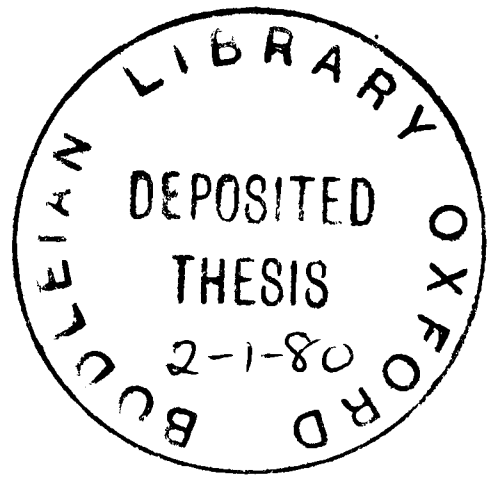
MACROSEGREGATION IN CASTINGS AND INGOTS.

K.M.FISHER, B.A.
St. Edmund Hall.

A thesis submitted in partial fulfilment for the degree of Doctor of Philosophy in the University of Oxford.



Department of Metallurgy and Science of Materials,
University of Oxford.
August 1979.

ABSTRACT

MACROSEGREGATION IN CASTINGS AND INGOTS

K M FISHER, ST. EDMUND HALL, OXFORD UNIVERSITY

SUBMITTED FOR THE DEGREE OF DOCTOR OF PHILOSOPHY, IN TRINITY TERM 1979

The various types of macrosegregation are described and their commercial importance discussed.

Previous work on macrosegregation reported in the literature is reviewed and those theories currently most popular for explaining the various segregates are summarised.

A number of commercial castings and ingots were examined. The majority were found to contain macrosegregation although its magnitude seldom exceeded ± 10% of the nominal composition. It was felt that contraction fluid flow had been the dominant segregation mechanism in operation, which was in line with the short freezing times of all the castings studied.

The critical solidification time required for the gravitational interdendritic fluid flow (GIFF) mechanism to produce significant amounts of segregation was determined. An alloy of Al-5½wt%Cu was cast into a series of sand moulds of different volumes, and the macrosegregation present in the solidified ingots was related to the various observed freezing times. A total freezing time of approximately 15 mins. had to be exceeded before gravity flow segregation became appreciable.

A detailed review is given of previous work concerning the nature and extent of 'GIFF', particularly with respect to position in the semi-solid zone. Inconsistencies between conclusions are highlighted and explained in terms of differences in presentation of results. It is shown that all previous work indicates that 'GIFF' is important in producing macrosegregation at high liquid volume fractions ($g_L > 0.80$) in the mushy zone, but that none of the work by design could indicate whether flow at lower g_L was important

An experiment was therefore set up to study the amount of segregation produced by 'GIFF' at various g_L in the mushy zone. A quenching technique was used. Thin section, 'slice castings' of Sn-5wt%Pb were grown undirectionally horizontally for various lengths of time under identical conditions and then quenched. The progress of segregation at given reproducible positions in these castings was determined and related to the progress of the semi-solid zone across the length of the castings. It was shown that although a large part of the final macrosegregation was produced in the region just behind the dendrite tips ($1 > g_L > 0.8$) a significant amount of segregation was produced by 'GIFF' up to approximately $g_L = 0.30$. A detailed description of the apparatus and experimental procedure employed is given together with a summary of the experiments conducted to ensure truly reproducible growth conditions between castings.

A radioactive tracer technique was used to provide direct visual evidence of fluid flow occurring deep within the semi-solid region of a casting. Radioactive material was inserted into the bulk liquid region of a solidifying 'slice casting' and the subsequent penetration of activity into the original mushy zone was studied. It was estimated from autoradiographs that 'GIFF' was still occurring up to at least $g_L = 0.40$, thus confirming the results of the 'slice casting' experiments.

A ternary Sn-Zn-Pb alloy with zero density change down its liquidus line was developed. This was a Sn-base alloy with a Zn:Pb ratio of 19.97:1 (atomic %) and a total solute content of < 15.2 at .%. The alloy was developed using a combination of a theoretical treatment and a highly accurate density measurement technique (pycnometer). It was confirmed using the 'slice casting' apparatus that such an alloy had no susceptibility to 'GIFF' segregation.

Finally, the analysis technique employed for composition measurements is described, and the operating conditions required for optimum analytical accuracy are discussed.

ACKNOWLEDGEMENTS

First I would like to thank my supervisor, Dr. J. D. Hunt, for all the advice, help, and encouragement he gave me during my time at Oxford: without his teaching and instruction this work would not have been possible. I would also like to thank Professor Sir P. B. Hirsch F.R.S. for the provision of laboratory facilities, and all those other members of the Department who gave me assistance. In particular I must thank Mr. J. Short who taught me how to use the workshop facilities, and helped me to realise my practical abilities. Finally my thanks go to Mrs. Celia Fisher for typing this thesis in such a speedy and excellent fashion, and to my wife, Kate, who fortunately has the patience of Job.

CONTENTS page no.

CHAPTER 1 INTRODUCTION

1.1 General 1
1.2 Types of macrosegregate, and their physical appearance. 2
1.3 Importance and commercial implications of macrosegregation defects. 5

CHAPTER 2 REVIEW OF PREVIOUS WORK ON MACROSEGREGATION AND EXAMINATION OF CURRENT THEORIES

2.1 Development of basic solidification theories and their effect on the understanding of macrosegregation. 9
2.2 Review of Previous Work relating to macrosegregates. 13
2.2.1. Inverse Segregation. 13
2.2.2. Exudations. 15
2.2.3. A Segregation. 17
2.2.4. Freckles. 21
2.2.5. Equi-axed, or Gravity, Segregation. 23
2.2.6. Positive Bottom Cone of Segregation. 25
2.2.7. Negative Bottom Cone of Segregation. 25
2.2.8. Under-riser Positive Segregation. 26
2.2.9. V Segregation. 26
2.3 Current Understanding of Macrosegregation. 27

CHAPTER 3 INVESTIGATION OF MACROSEGREGATION IN INDUSTRIAL CASTINGS AND INGOTS

3.1 Introduction. 30
3.2 Description of work performed. 31
3.2.1. General. 31
3.2.2. Racing car wheel - centrifugally casting. 32
3.2.3. Saloon car wheel - low pressure diecasting. 33
3.2.4. Brake cylinder - gravity diecasting. 34
3.2.5. Clutch housing - gravity diecasting. 36
3.2.6. Marine boat fitting - sand casting. 37
3.2.7. Transverse slices from semi-continuously cast ingots. . . 38
3.2.8. Gas turbine blade - investment casting. 40
3.2.9. Summary of work performed. 42
3.3 General data available from the literature. 44
3.4 Summary and Conclusions. 46

CHAPTER 4 INVESTIGATION OF THE TIME TAKEN FOR GRAVITY FLOW TO PRODUCE APPRECIABLE MACROSEGREGATION

4.1 Introduction. 47
4.2 Outline of the Experiment. 47
4.2.1. General Outline. 47
4.2.2. Reasons behind choice of casting process and alloy system. 48
4.2.3. Theoretical calculation of ingot freezing times. 49
4.3 Experimental Procedure. 52
4.3.1. Production of sand moulds. 52
4.3.2. Melting procedure. 53
4.3.3. Casting procedure. 54
4.3.4. Examination of ingots. 56
4.4 Results and Discussion. 58
4.4.1. Casting data, and physical measurements on solidified ingots. 58
4.4.2. Ingot Macrostructures. 59
4.4.3. Composition measurements. 60

page no.

4.4.4. Temperature measurements. 62
4.4.5. Macrosegregation mechanisms. 66
4.5 Summary of Results. 68

CHAPTER 5 REVIEW OF PREVIOUS WORK PERFORMED ON THE NATURE AND EXTENT OF GRAVITATIONAL INTERDENDRITIC FLUID FLOW

5.1 Introduction. 71
5.2 Review. 71
5.3 Discussion. 74
5.4 Summary and Conclusions. 77

CHAPTER 6 EXPERIMENTAL INVESTIGATIONS INTO THE RELATIONSHIP BETWEEN GRAVITATIONAL INTERDENDRITIC FLUID FLOW AND LIQUID VOLUME FRACTION IN A SEMI-SOLID REGION

6.1 Introduction 78
6.2 Outline of the Experiment. 79
6.3 Apparatus. 82
6.4 Experimental Procedure. 87
6.5 Results and Discussion. 94
6.5.1 Preliminary results on setting up apparatus. 94
6.5.2 Results on main series of samples. 98
6.5.2.1. Temperature measurements. 100
6.5.2.2. Macrostructure and interface shape. 102
6.5.2.3. Composition measurements. C vs. position. . . .105
6.5.2.4. Composition variation with time. C vs. t. . . .108
6.5.3 Observation of channeling. 112
6.6 Summary and Conclusions. 113

CHAPTER 7 OBSERVATIONS OF INTERDENDRITIC FLUID FLOW USING A RADIOACTIVE TRACER TECHNIQUE

7.1 Introduction 115
7.2 Outline of the Experiment. 115
7.2.1. General. 115
7.2.2. Choice of radioisotope, alloy system and composition, and detection method. 117
7.3 Experimental procedure. 119
7.3.1. Production of radioisotope. 119
7.3.2. Preparation of radioactive alloy slugs. 120
7.3.3. Insertion of radioactive alloy slugs into growing ingots. 122
7.3.4. Handling and machining of radioactive ingots. 122
7.3.5. Autoradiography of ingots. 124
7.4 Safety aspects. 125
7.5 Results and Discussion. 127
7.5.1. Thermal analysis of melts. 127
7.5.2. Thermal, and other, data obtained from ingot growth runs. .128
7.5.3. Dummy trials. 130
7.5.4. Radioactive trials. Insertion during growth. 132
7.5.5. Radioactive trials. Addition during pouring. 138
7.5.6. Activity measurements. 142
7.6 Summary and Conclusions. 145

CHAPTER 8 MEASUREMENT OF LIQUID METAL DENSITIES

8.1 Introduction 146
8.2 Theoretical calculation of required alloy composition. 148

page no.

8.3 Choice of density measurement technique. 151
8.4 Maximum Bubble Pressure Technique. 152
8.4.1. General Outline and Review. 152
8.4.2. Summary of Experimental Procedure and Results. 154
8.5 Pycnometer Technique. 157
8.5.1. General Outline and Review. 157
8.5.2. Apparatus. 159
8.5.3. Experimental Procedure. 161
8.5.4. Experimental difficulties and precautions. 164
8.5.5. Density Results and Calculations. 167
8.6 Slice Casting Experiments. 178
8.6.1. General Outline. 178
8.6.2. Results and discussion. 179
8.7 Summary and Conclusions. 182

CHAPTER 9 CHEMICAL ANALYSIS - ATOMIC ABSORPTION SPECTROPHOTOMETRY

9.1 Introduction. 184
9.2 Outline of analysis technique. 184
9.3 The Instrument. 185
9.4 Experimental Procedure. 186
9.4.1. Spectrophotometer Calibration. 186
9.4.2. Sampling Procedure. 191
9.4.3. Investigation of possible interference phenomena. 192
9.4.4. Sample Determination Procedure. 194
9.4.5. Practical aspects of spectrophotometer operation. 195
9.5 Error calculations. 197
9.6 Conclusions. 200

REFERENCES

APPENDICES

A.2.A. Production of macrosegregation by interdendritic fluid flow
A.4.A. Ccalculation of optimum hole size vs. position in ingot.
A.7.A. Calculation of the amount of Tl 204 required in the experiment.
A.7.B. Calculation of the irradiation time needed to produce the required activity of Tl 204.
A.7.C. Definitions of radioactivity terminology, and maximum permissible doses
A.7.D. Calculation of safe operating temperatures for molten thallium and its alloys.

SUGGESTIONS FOR FUTURE WORK

CHAPTER 1

INTRODUCTION

1.1 General

The vast majority of commercial metal products are alloys of two or more constituent elements. The non-uniform distribution of one or more of these constituents within the product is termed segregation. A distinction can be made between two broad categories of segregation, called microsegregation and macrosegregation. Microsegregation is the term used to describe localised fluctuations in alloy composition occuring over distances of the same order of magnitude as the cell or dendrite spacing. Macrosegregation refers to longer-range composition variations which may occur, for example, from the edge to centre, or from the top to bottom, of an article.

Segregation is an inherent feature of the solidification process. It is usually relatively easy to ensure that a liquid alloy is homogeneous throughout its volume, but it is practically impossible to carry over this homogeneity into the solid state even under laboratory conditions. Mostly, alloys solidify over some range of temperature, and at a given temperature within this range the composition of the solid phase is, in general, different to the composition of the adjacent liquid from which it is growing. Furthermore as solidification proceeds and the temperature falls within the freezing range so the composition of the growing solid and its adjacent liquid alter. Consequently a region of solid alloy freezing later in the solidification process has a different composition to one which froze earlier, and so a composition gradient is produced. Composition changes can only occur in the solid state by means of diffusion which is a relatively slow transport mechanism even at elevated temperatures. The limited times available for diffusion during the solidification of commercial castings and ingots therefore mean that it is impossible to cast homogeneous alloys.

1.2 Types of macrosegregate, and their physical appearance

Macrosegregation is such a common phenomenon in every kind of casting situation that it is likely that its existence and importance were recognised at the very beginnings of metallurgical science. One of the first references to it was made in 1540[1] when the problem of high tin content exudations on the outer surfaces of bronze gun barrels was noted. Since then many more kinds of macro-inhomogeneity have been recorded. Figures 1.1 to 1.7., which follow, show the physical appearance of the major types of macrosegregate commonly encountered. These figures, and the individual macrosegregates they illustrate, are described and discussed in turn below:-

(a) Fig. 1.1(a) is a schematic representation of the macrosegregation pattern commonly found in killed steel ingots. Four distinct types of macrosegregate are illustrated: A segregates, V segregates, under-riser positive segregation, and bottom negative cone of segregation. These terms refer specifically to defects found in steel ingots.

A segregates are discrete pencil-like stringers of highly solute-enriched material which usually extend from the columnar zone into the central equi-axed zone of the ingot macrostructure. They are arranged over the surfaces of cones whose apices are towards the top of the ingot. Consequently when seen in a longitudinal ingot section they appear inclined towards the axis of the ingot. The extent of this inclination varies from ingot to ingot but it is seldom greater than a few degrees from the vertical. Fig. 1.1(b) is a photograph of a sulphur print taken from a longitudinal section of a large, killed, steel ingot[2]. The A segregates are clearly shown up as dark lines on this print which indicates that they are very sulphur-rich (and hence solute-rich). They are also very well defined which indicates that the enrichment is extremely localised. Finally the discrete individual nature of A segregate stringers is illustrated very clearly by fig. 1.2(a), which shows a sulphur print of a tranverse section through the upper half of a steel ingot.[2]

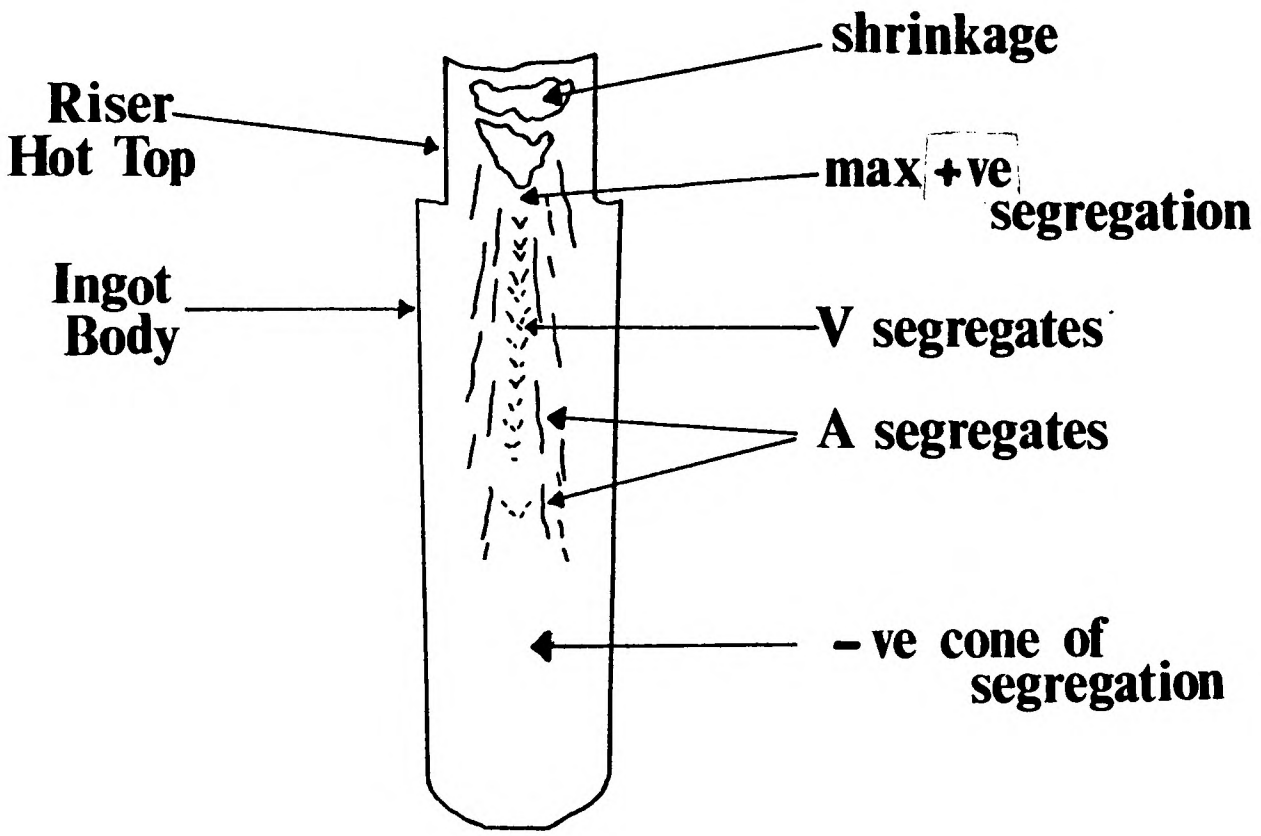


Fig. 1.1(a). Schematic representation of typical macrosegregation defects found in large, killed, steel ingots.

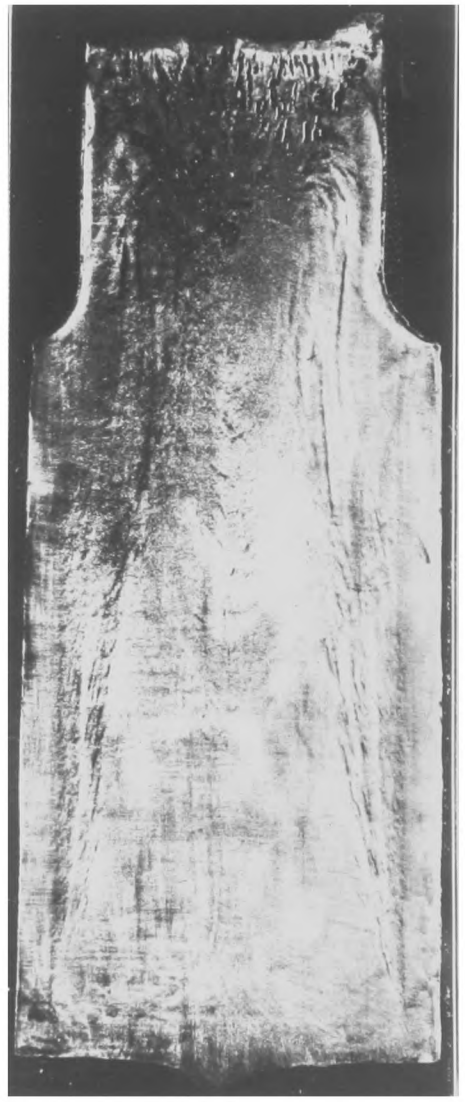


Fig. 1.1(b). Sulphur print taken from a longitudinal section of a 10½ ton steel ingot.[2] Top poured into an octagonal chill mould. (alloy comp^{n} given in fig. 1.3.) Magn × 0.04.

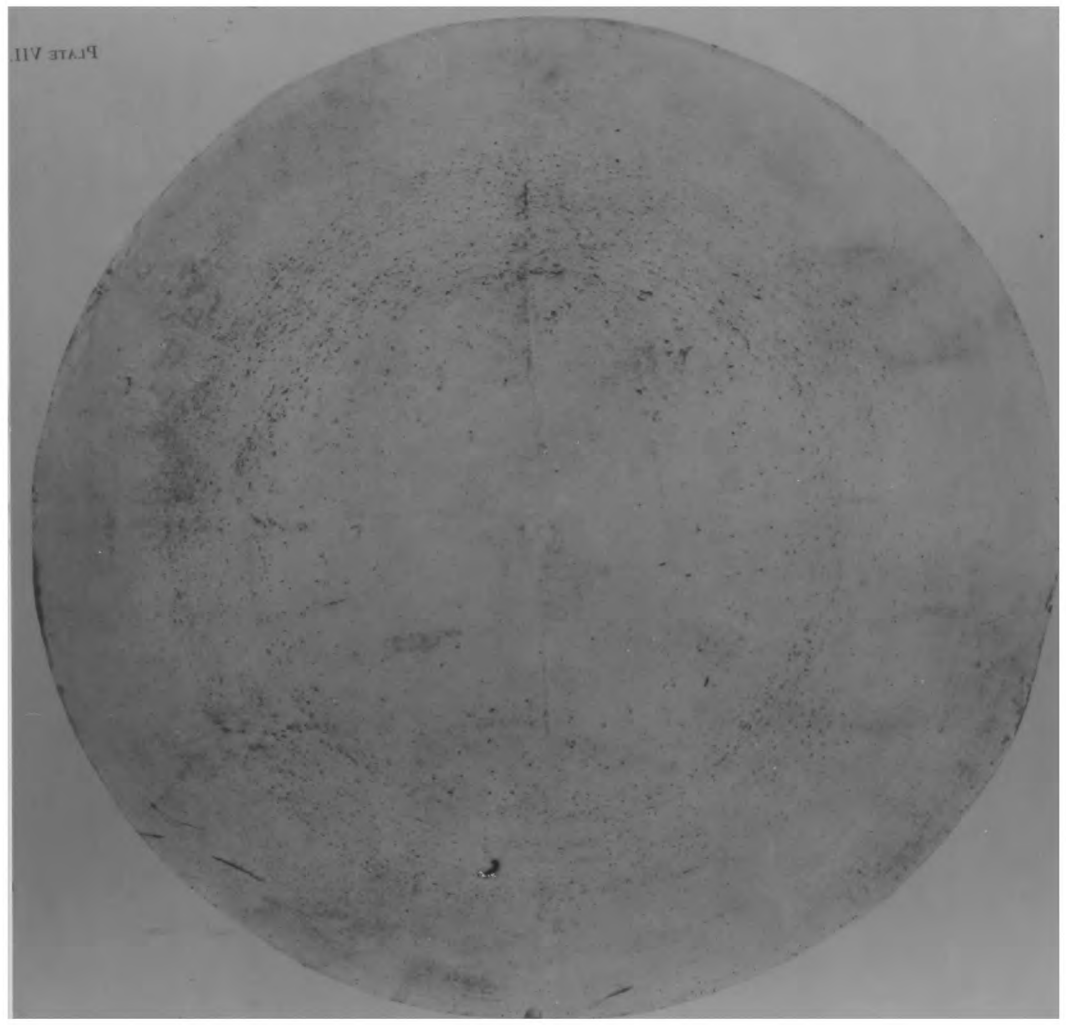


Fig 1.2(a). Sulphur print of the cross-section midway in the length of a bloom. This bloom had been taken from an ingot weighing 32 3/4 tons[2]. Magn x 0.1



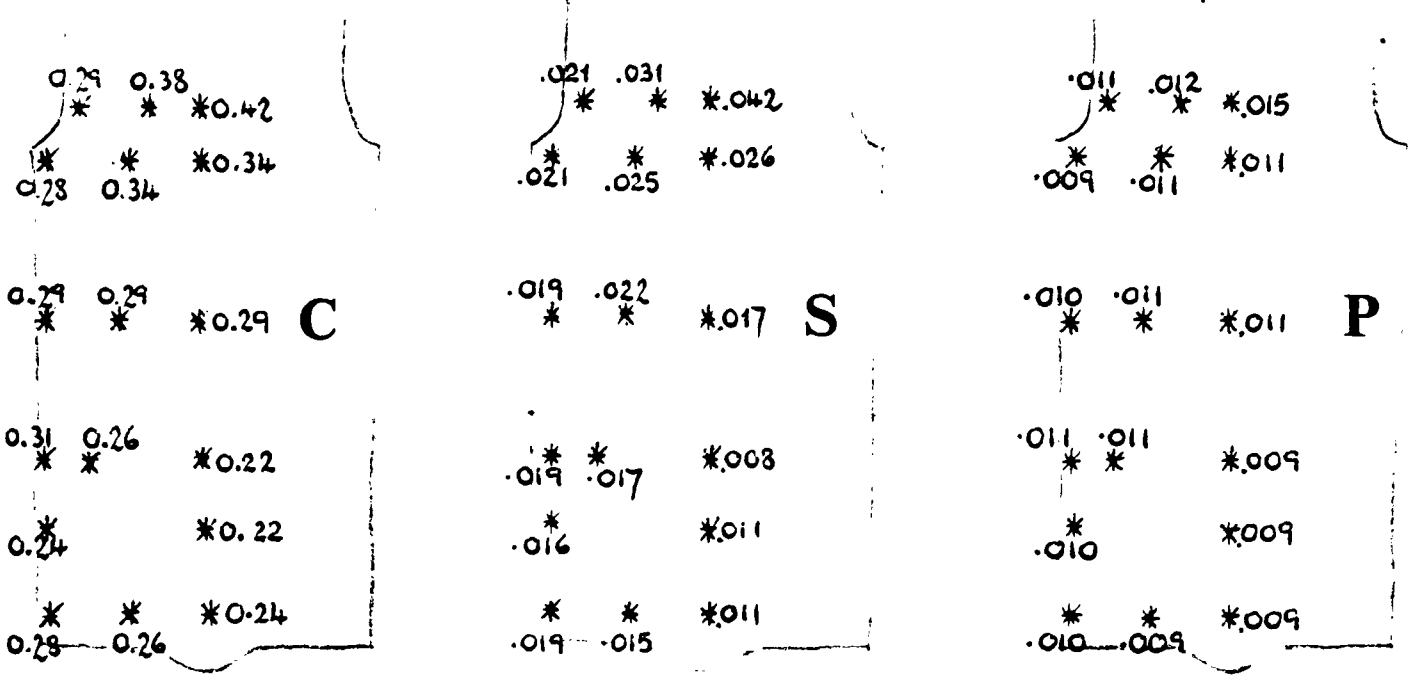
Fig. 1.2(b). Sulphur print from the longitudinal centre section of a 750 Kg., fully killed, steel ingot. The molten metal was inoculated with cerium during pouring. Gross macrosegregation of CeS inclusions is evident[4]. Magn x 0.1

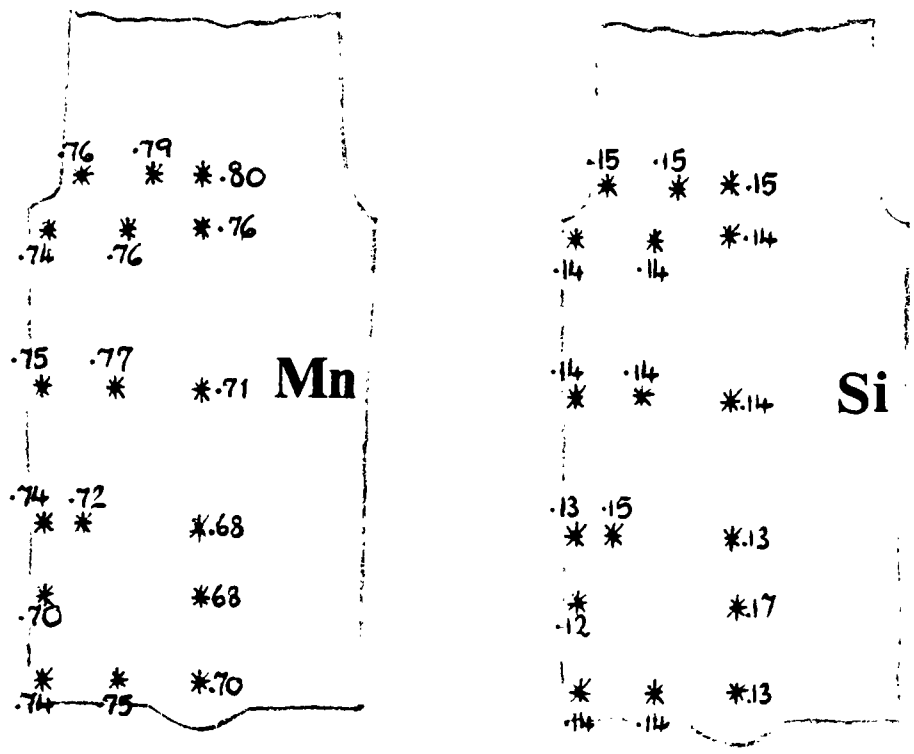
V segregates are also regions of high solute enrichment as shown by their dark appearance in fig. 1.1(b). They are more continuous and less pencil-like than A segregates, and are distributed over the surfaces of cones whose wide-ends are towards the top of the ingot. They always appear along the ingot centreline and are often found to be associated with pockets of porosity. They are particularly common in ingots which have a central equi-axed zone of crystals in their macrostructure.

The composition analyses reproduced in fig. 1.3. show how the terms under-riser positive segregation and bottom negative cone of segregation have arisen. The figure is a typical illustration of the way in which the solute elements become redistributed in a large steel ingot.[2] The majority of the solute elements have segregated towards the top of the ingot in and around the riser head, leaving the lower central regions of the ingot solute-depleted. It can be seen from fig. 1.3. that both of these forms of macrosegregate describe extended volumes of quite uniformly segregated material, in contrast to A and V segregation. With regard to ingot macrostructure the negative cone of segregation is invariably found to be associated with the bottom cone of equi-axed crystals, while the under-riser segregation extends through both the columnar and equi-axed zones at the top of the ingot.

(b) In fig. 1.3. it is clear that the distribution of silicates is in the opposite sense to that of the solute elements in the steel. This is quite a common feature in large steel ingots[3] where non-metallic, slaggy types of inclusions tend to form a 'positive bottom cone of segregation'. De-oxidation products such as Al_2O_3 and MnO are also found accumulated in this region which is invariably associated with the bottom cone of equi-axed crystals. A similar phenomenon has been observed in steel ingots[4] inoculated with cerium to remove the sulphur as CeS. Fig. 1.2. (b) is a sulphur print from such an ingot which shows the marked concentration of CeS particles towards the bottom centre of the ingot.

(c) Figs. 1.4. (a) and (b) illustrate a kind of macrosegregate known as Freckles which are often found in vertically-grown, iron-base and nickel-base





Cast Analysis Wt %
C = 0·30
S = 0.017
P = 0.010
Mn = 0.74
Si = 0·13

Fig. 1.3(a). Distribution of solute elements in the 10½ ton steel ingot shown in Fig. 1.1(b).[2]

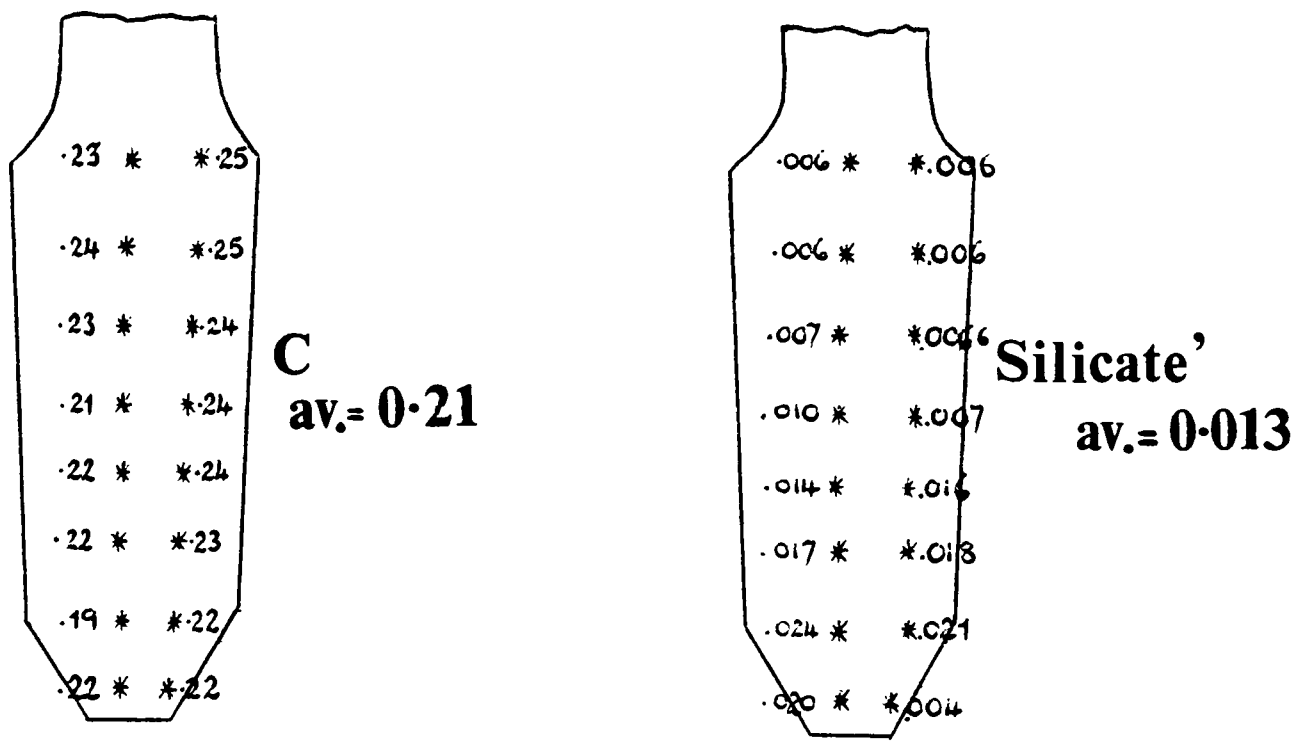


Fig. 1.3(b). Distribution of carbon and 'silicates' in a 12 ton killed steel ingot. (ref. 3)

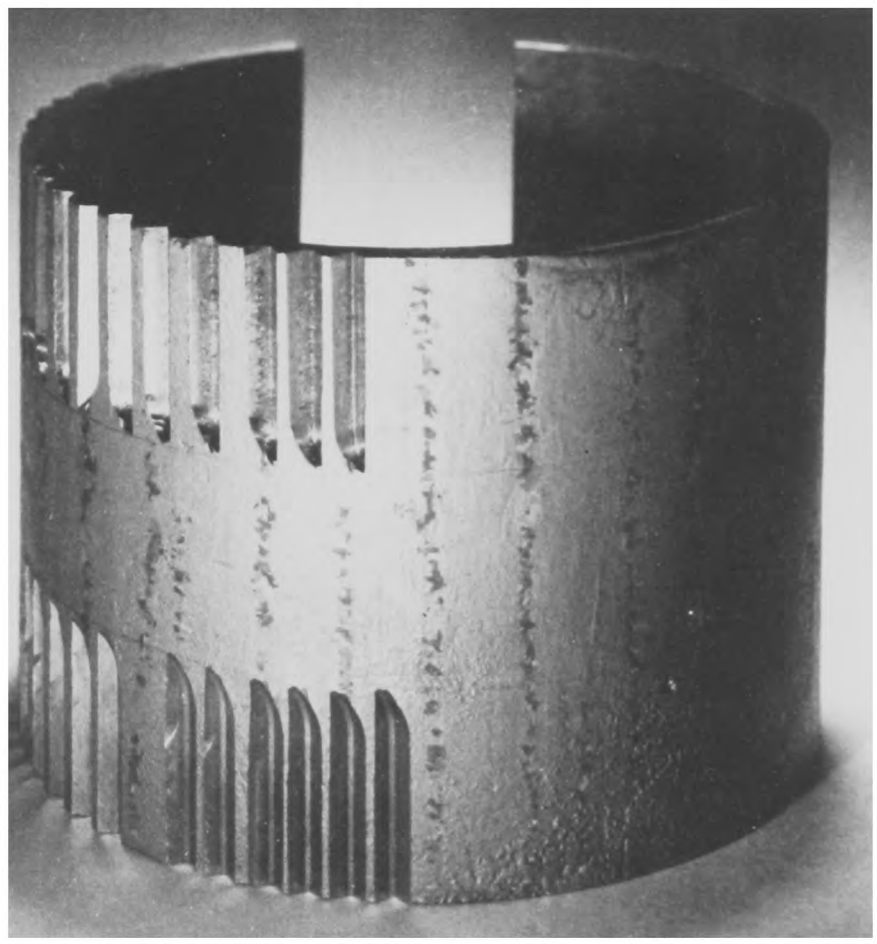


Fig. 1.4(a). Photograph of a vertically grown nickel-base superalloy ingot which has had its central portion trepanned away (ref. 5). The ingot was a single crystal apart from the freckle trails. Magn x 1.



Fig. 1.4(b) Close-up view of one of the freckle trails shown Magn. x 8 approx.

superalloy castings. Fig. 1.4. (a) shows a number of freckle trails around the outer surface of a nickel-base alloy casting which had been solidified unidirectionally upwards with the intention of obtaining a single crystal[5]. The freckles are vertical pipes of solute-rich material and they appear speckled because of their equi-axed structure, fig. 1.4. (b). The trails are roughly uniform in cross-section, and are often associated with feeding shrinkage indicating that they are the last regions to solidify. Freckles do not always appear on the outer surface of castings. In vertically grown, consumable arc-melted ingots of iron and nickel-base superalloys the trails are usually found in the interior of the ingot cross-section[6].

(d) The composition vs. position profile shown in fig. 1.5. (a) illustrates a kind of macrosegregation, known as inverse segregation, which is by far the commonest of all the macrosegregates. The term inverse segregation describes a region of moderate solute enrichment which exists towards the outer surfaces of virtually all chill castings and ingots. The profile shown in fig. 1.5. (a) was measured in a chill cast Al-4.6 wt.%Cu alloy ingot[7] and is a typical example of inverse segregation.

(e) Figs. 1.5. (b) and (c) show examples of a particularly exaggerated form of inverse segregation known variously as exudations, sweat, or bleed bands. These exudations are blobs of highly solute-rich material which are often found on the surfaces of chill castings. They are particularly common (as bleed bands) on the surface of direct chill, continuously cast, ingots. The magnitude of the solute-enrichment at the surface is much higher than that shown for the basic inverse segregation in fig. 1.5. (a). In bronze castings, for example, exudations appear quite white due to the large amount of tin they contain. This level of enrichment is, however, very localised at the surface and usually extends no more than a couple of millimetres into the body of the casting or ingot.

(f) Fig. 1.6. (a) and (b) show a type of macrosegregation called banding. This term describes layers of material lying parallel to the original solidification front which differ in composition and possibly structure from the bulk of the casting. It is a common defect in two widely different modes of solidification,

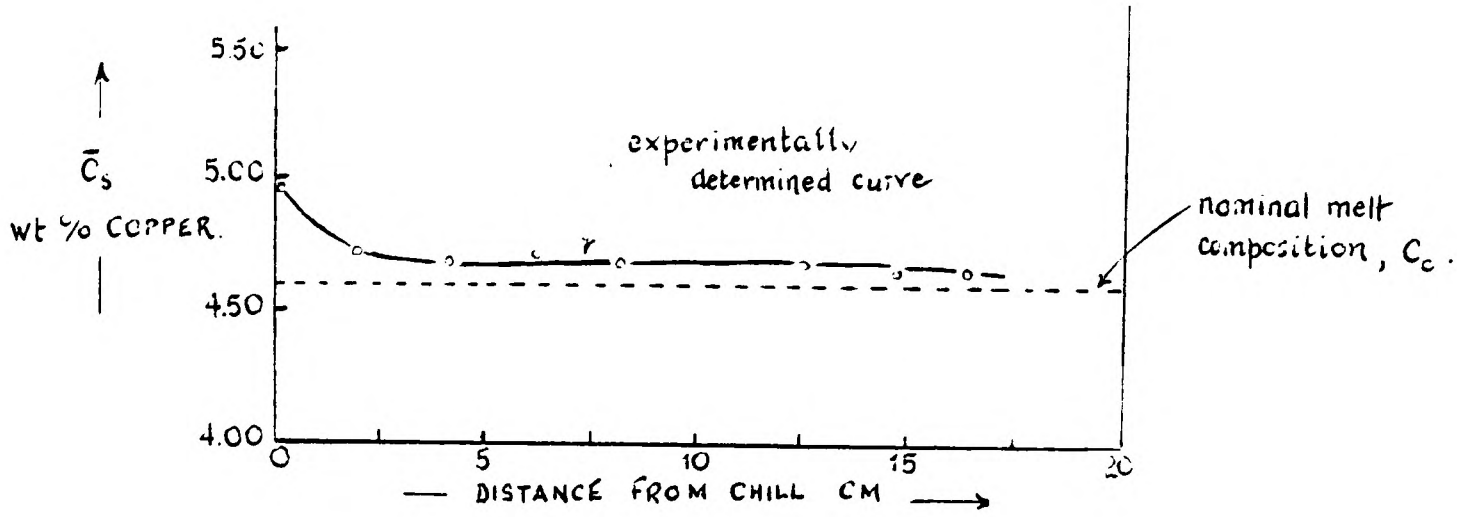


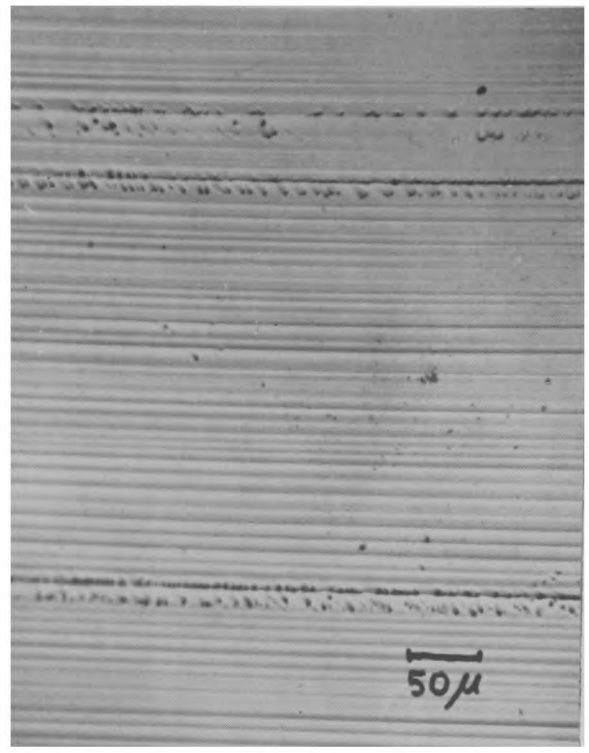
Fig. 1.5(a). Composition vs. position profile for an Al-4·6 wt % Cu ingot grown unidirectionally upwards from a water-cooled chill. (ref. 7)



Fig. 1.5(b). Phosphide eutectic 'sweat' on the surface of a grey iron casting. (ref 8).



Fig. 1.5 (c). Micrograph showing a massive sweat bead at the chill surface of an Al-10 wt % Cu ingot grown vertically upwards. (ref. 9). Magn. x 90.



Magn x 160

Fig. 1.6(a). Ge - 6 at% Si single crystal grown unidirectionally from melt with a planar solid / liquid interface. (ref. 10) Solute - enriched and -depleted bands lying parallel to the growth front are shown up by dislocation etch pits.

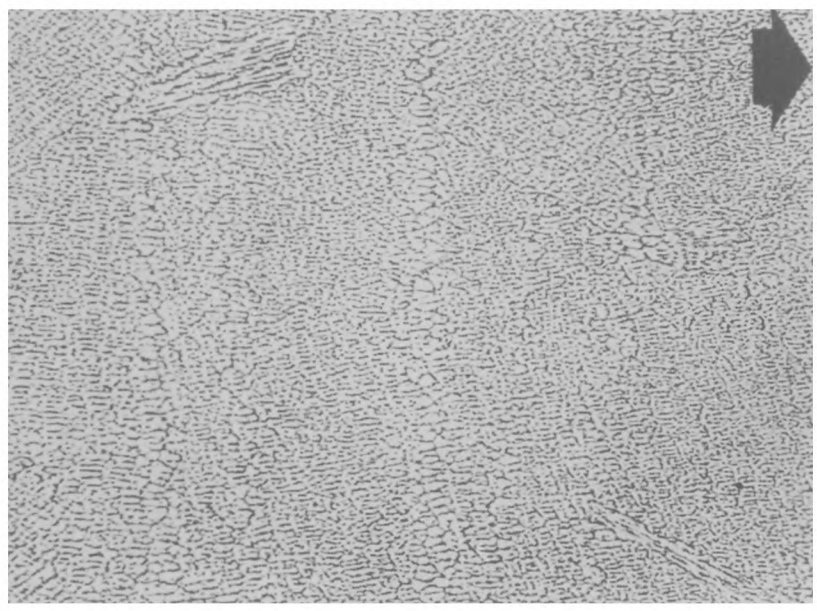


Fig. 1.6(b). Banding in a fusion weld of an Al - 1.5% Mg alloy. Solidification occurred in the direction of the arrow. (Ref. 11)

Magn x 320

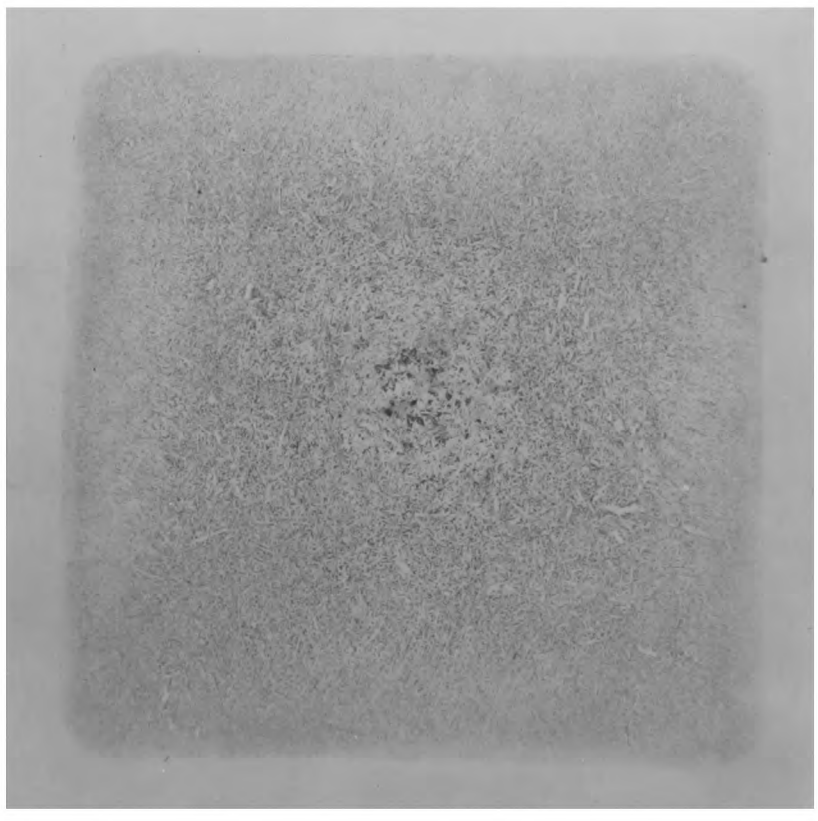


Fig. 1.6(c). Cross-section through a plain carbon steel billet. (Ref. 12). Rolled and cut from a continuously cast square-section strand.

Macroetched to reveal the carbon-enriched centreline.

Magn x 1

these being single crystal growth (where freezing occurs slowly with a planar solid/liquid interface morphology, see fig. 1.6. (a)) and in fusion welds (where freezing is very rapid and occurs with a columnar dendritic morphology, see fig. 1.6. (b)).

(g) Fig. 1.6. (c) is an example of a macrosegregate known as centreline segregation. This type of segregation is often observed in large ingots particularly where these have been continuously cast. It is a region of quite large solute enrichment which occurs locally at, and near, the centreline of an ingot. Fig. 1.6. (c) shows the carbon enrichment at the centre of a steel billet [12].

(h) Figs. 1.7. (a) and (b) show two examples of a type of macrosegregate called equi-axed, or gravity, segregation. These terms describe vertical segregates where one of the phases appears to have floated or sunk during solidification. In the 'kishing' of primary graphite flakes in hypereutectic grey irons, shown in fig. 1.7. (a), the flakes rise to the top surface of the casting. Similarly, in fig. 1.7. (b), the antimony dendrites have floated to the top surface of the antimony-lead alloy ingot leaving denser eutectic (lead-rich) material below.

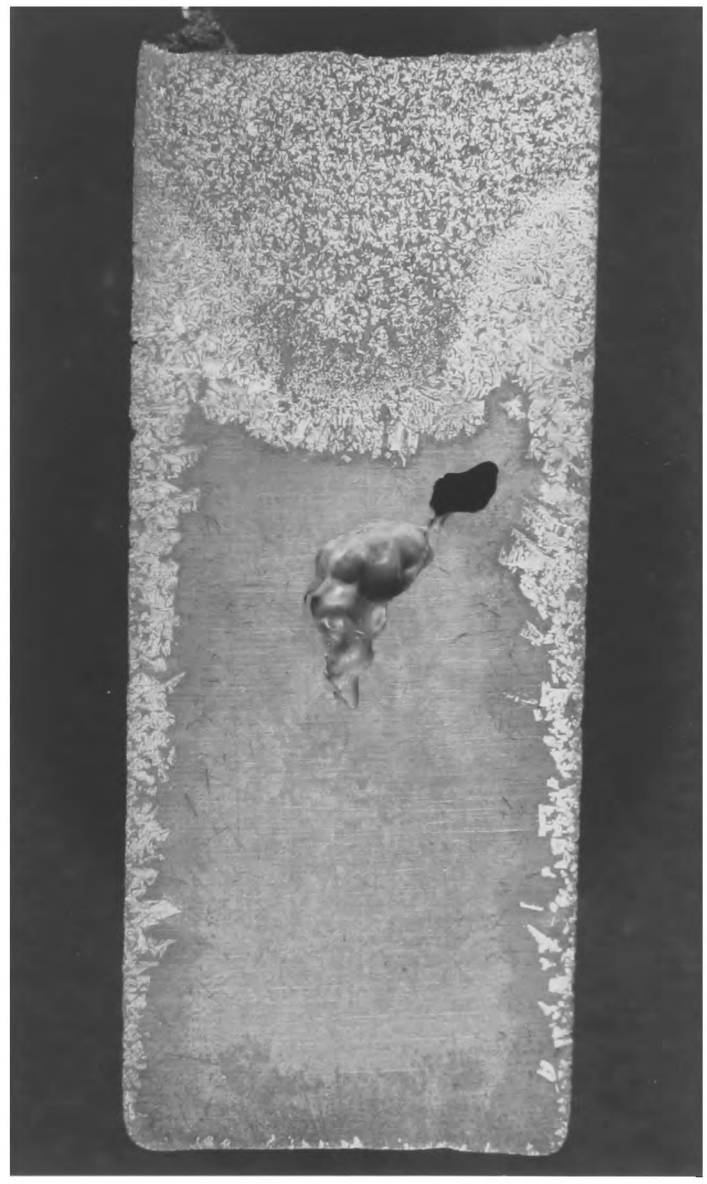
1.3 Importance and commercial implications of macrosegregation defects

Some of the macrosegregates shown in the previous section would appear to be fairly serious defects in their respective ingots and castings. Is this in fact correct? Do they cause problems when they appear? The answer to these questions is usually yes, and for several reasons. Macrosegregates can lead to a reduction in properties, loss of workability, loss of customer confidence, and an increase in manufacturing costs.

The mechanical, chemical, physical, and surface properties of an alloy vary with composition. Often this variation is quite pronounced even for relatively small composition changes. The alloy composition of any given component is chosen to optimise certain properties so that the component can give its best performance in the job for which it was designed. Segregation can



Fig. 1.7(a). 'Kishing' of primary graphite flakes in a hyper-eutectic grey iron casting (ref. 13). The graphite clusters have segregated to the side and upper surfaces of the casting, and some have been removed during the cleaning operation.



Magn. x 1

Fig. 1.7(b). Equi-axed gravity segregation in a Sb - 70 wt % Pb, furnace-cooled ingot (ref. 14). Primary facetted Sb crystals have segregated to the top third of the ingot, leaving Pb-rich eutectic material below (Sn-89 wt%Pb).

therefore lead to quite large local reductions in these properties, and the performance of the whole component may then be determined by the segregated regions. For example, solute enrichment can give rise to localised formation of harmful second phases. If these are brittle they may lower the ductility and impact strength of the component. If they are of low melting point they can seriously affect creep properties. The corrosion and fatigue properties of alloys are also particularly sensitive to chemical inhomogeneities, and it is because of this that banding can cause major problems in certain alloy steels.

A reduction in workability often occurs when macrosegregates are present. Examples of this can be found in the spalling of brittle surface exudations in bronzes; in the spreading of the cerium sulphide cloud in alloy steel ingots causing it to act like a giant elongated brittle phase; and in the internal cracking which can occur at accumulations of brittle second phases.

Customer confidence can obviously be adversely affected when defects appear, even when they do not detract from the properties of the casting. For this reason alone macrosegregation is commercially more of a problem when it manifests itself as a defect on the surface of an object. If it can be hidden in the bulk of the material then often it is simply overlooked - 'out of sight, out of mind' ! Problems can arise, however, even when the defects are hidden in the centre of ingots. If such ingots are given subsequent working and forming operations it is possible for the internal segregates to turn up on the surface of the worked product. Such defects are costly to the manufacturer. The rolling and annealing processes required to turn an ingot into sheet metal are expensive. If the sheet subsequently has to be rejected because it contains unacceptable surface flaws then a lot of money will have been wasted.

The thing which makes all of the above problems associated with macrosegregates so much more serious is the fact that once macrosegregation is present in a casting it is costly, difficult, and often, impossible to remove. Mechanical working of the ingot has little effect on macro-homogenisation and, in fact, can make the segregates even more of a problem. Heat treatment is also useless. The characteristic diffusion distance, x, for the movement of solute in

time, t, is given approximately by the formula $x = (D_s t)^{\frac{1}{2}}$, where D_s is the solid state diffusion coefficient. At temperatures just below the melting point D_s is at most only $10^{-8} cm^2/sec.$ for substitutional impurity atoms. An annealing time of 24 hours, or approximately 10^5 seconds, will therefore allow transport of solute over a distance of only 0.3mm, thereby making the operation impractical as a means of removing macrosegregation. Physical removal of the segregates by machining is, in fact, the only answer. Cropping and scalping of ingots after casting are accepted features in the processing of many materials. Inverse segregation and exudations can be removed by scalping the surface of the ingot or casting. This is a common operation on semi-continuously cast aluminium ingots, where as much as 20mm may sometimes have to be removed.[13] Cropping involves chopping off some part of the ingot. Steel ingots are usually cropped top and bottom before being worked. In a badly designed ingot as much as $\frac{1}{3}$ rd of the volume may have to be cropped off. Clearly much sound metal must also be lost in this case.

The total cost of segregation in terms of scrapping defective castings and machining material off ingots must be enormous, even allowing for the fact that the material can often be recycled. Consider for example the case of directionally solidified nickel-base superalloy castings reported by Streat.[15] In 1973 the cost involved in producing these castings in the United States was around 500 million dollars. The castings, which are designed for high temperature service, are susceptible to the freckle defect described earlier, and such defects seriously affect their strength and creep properties. There is a possible rejection rate of 20% and the cost of remelting the castings is about 40% of the cost of the product. Consequently the potential cost of this one type of casting defect alone was around 40 million dollars! It therefore becomes clear that considerable savings could be effected by controlling and eliminating macrosegregation. Because segregates are so difficult to remove, the problem of homogeneity control in the final product must be tackled at its source i.e. in the casting process itself. In order to do this, two separate areas of knowledge must be explored. It is necessary to

understand the fundamentals of the solidification process and of casting technology. It is also necessary to understand what mechanisms are causing the different types of segregate and under what conditions these mechanisms are likely to operate. Once these things have been understood, the casting process, alloy system, and casting conditions can be altered in order to yield a product free from defects and of the desired chemical, physical, and mechanical properties.

CHAPTER 2

REVIEW OF PREVIOUS WORK ON MACROSEGREGATION AND EXAMINATION OF CURRENT THEORIES

2.1 Development of basic solidification theories and their effect on the understanding of macrosegregation

The understanding of macrosegregation has inevitably tended to follow that of the solidification process as a whole. Hypotheses attempting to explain various of the macrosegregates observed in castings began to appear around the turn of this century. These were fairly naive, and in most cases incorrect, and this generally remained the case until the 1950s when major advances were made in basic solidification theory.

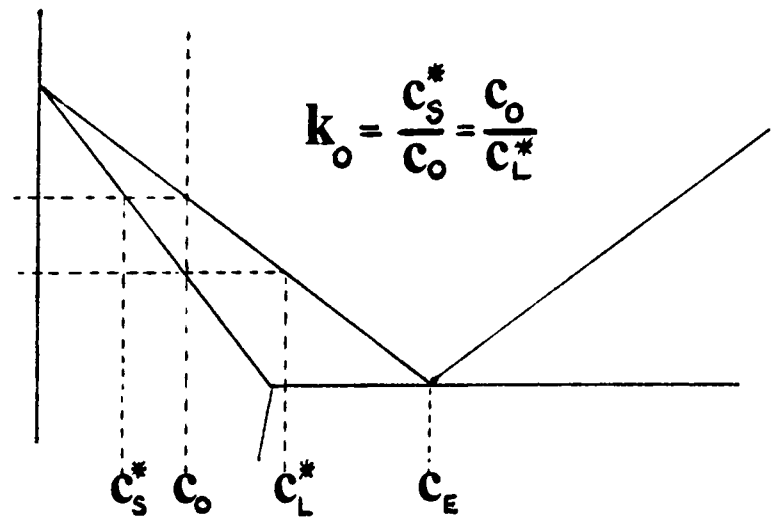
Studies of macrosegregation began with the observation of the defects produced by the various macrosegregation mechanisms.[1] Eventually the basis of alloy solidification theory was laid down with the realisation that the compositions of the solid and liquid phases were, in general, different during the freezing of an alloy, and that both of these compositions varied with temperature throughout solidification.[16] This idea was set out quantitatively at the latter end of the 19th century with the determination of the equilibrium phase diagrams of many binary alloy systems.[17]

The first theoretical treatments of solidification to appear concerned the rather simple situation of unidirectional growth with a planar solid/liquid interface.[18-20] Three models were proposed and in all of them it was assumed that the compositions of solid and liquid in contact across the interface at a given temperature could be specified from the relevant equilibrium phase diagram. This assumption was later shown by Jackson[21] to be valid for all conventional casting situations. The three models differed in the assumption which they made concerning the transport mechanism by which the rejected solute ($k_o<1$) was removed from the advancing solid interface; these being convection,[18] diffusion,[19] and a mixture of the two.[20] The well-known solute redistribution profiles for the planar growth of

alloy specimens using each of these assumptions are shown in fig. 2.1.

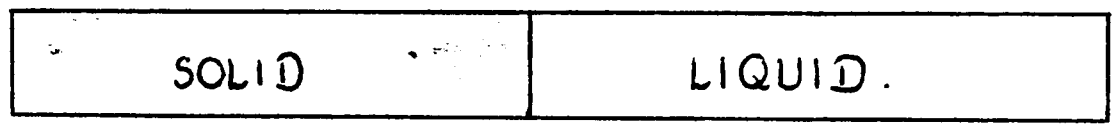
These treatments of planar growth proved to be very attractive to early workers in explaining certain of the types of macrosegregate observed in commercial ingots and casting. For example, the model of Tiller et al[19], where rejected solute is transported into the liquid by diffusion only, predicts a solute redistribution profile with a very localised positive segregation at the last region to freeze. Trapping of the diffusion layers ahead of the advancing growth fronts as they approach each other at the centre of an ingot was therefore suggested by several workers[22-24] as an explanation for the centreline segregation found in many ingots. Similar explanations have also been proposed to account for the formation of A segregates in steel ingots.[2, 26-30] The Tiller model further predicts that if the interface velocity fluctuates during growth then bands of solute-rich and solute-poor material are produced because of changes in the solute diffusion profile ahead of the advancing front. This mechanism seemed to provide a ready explanation for the banding observed in commercial ingots.[31] The Scheuer[18] and Burton[20] models predict solute redistribution profiles similar to those actually found in large commercial ingots where the solute concentration gradually increases towards the centre of the ingot. Bulk liquid convection currents sweeping away the solute diffusion layer ahead of the advancing growth fronts were therefore used as an explanation[32] for this type of segregation, which was termed 'Normal' because it was to be expected from the theoretical models. Segregation in the reverse sense, that is positive at the outside surfaces of the ingot in the first regions to freeze, was therefore the opposite, or inverse, of what was apparently logically expected and so became termed 'Inverse' segregation.

Over the last thirty years it has been shown that all of the theories listed in the above paragraph must be incorrect. This knowledge follows theoretical and practical studies of dendrite solidification, as well as experimental work on the larger-scale aspects of ingot solidification. It had long been appreciated that alloys froze dendritically under practical freezing rates, and that planar growth fronts were obtained only under conditions of high temperature gradients and low growth velocities. It was not, however, appreciated that there is a major

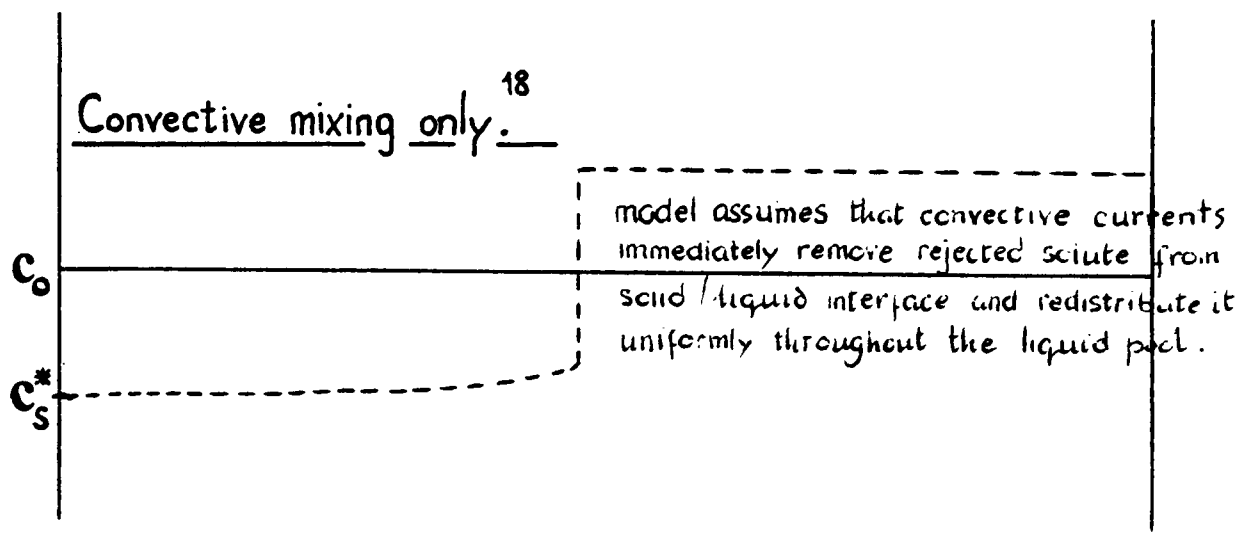


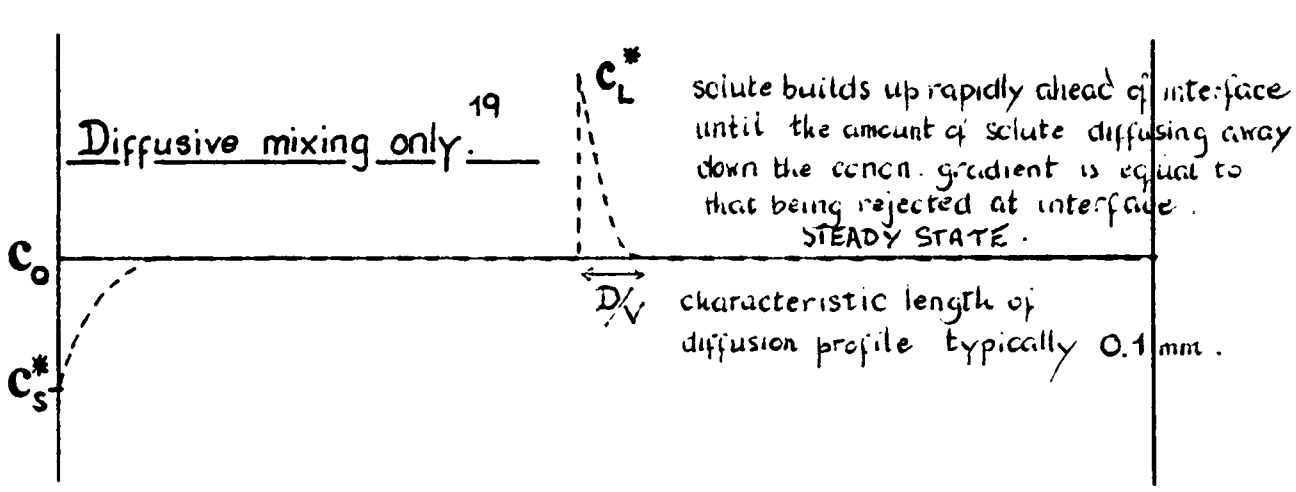
All three models assume :-

1. k_o is constant
2. k_o holds at solid/liquid interface
3. solid state diffusion of solute is negligible



nominal composition c_o





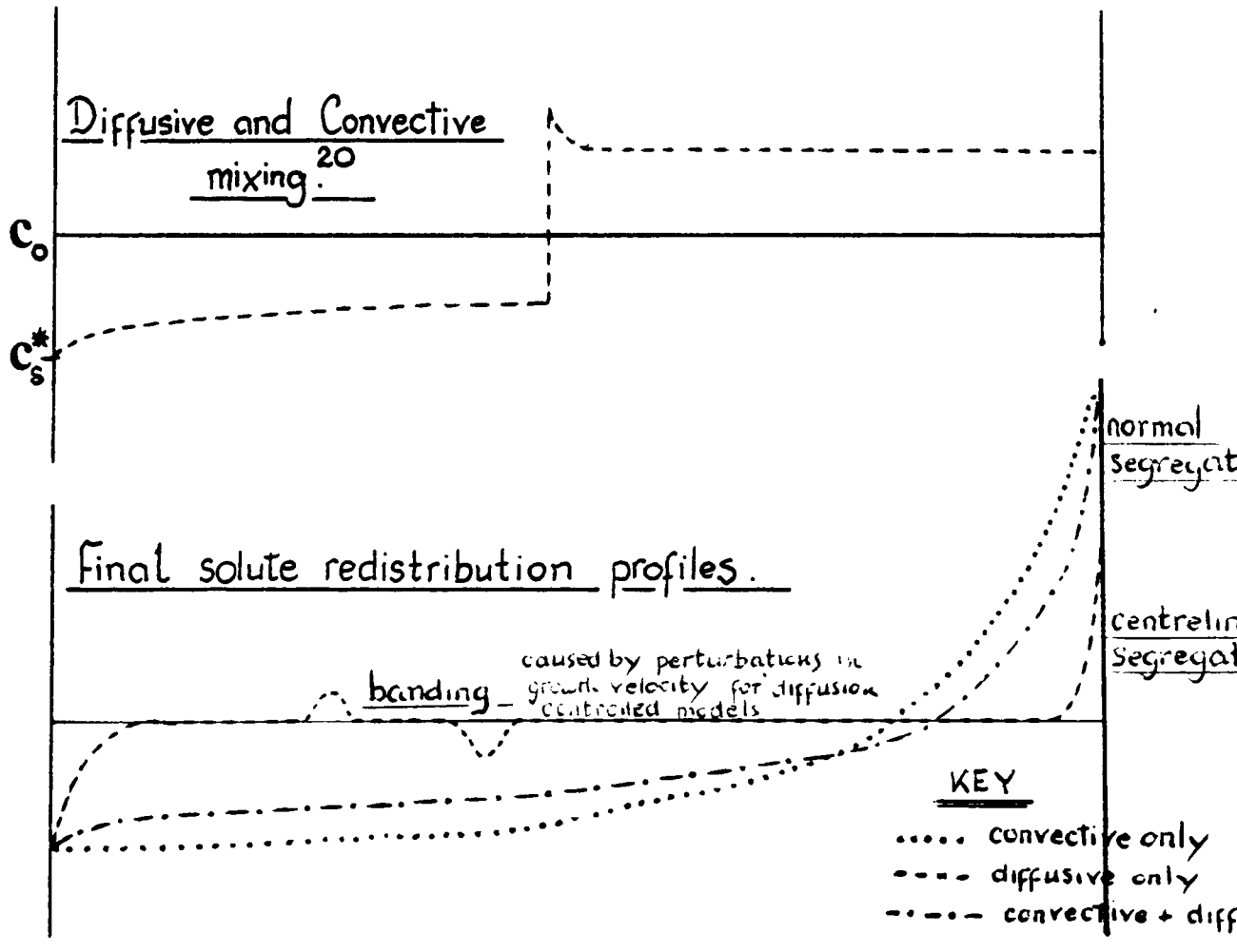


Fig. 2.1. Theoretical predictions of solute redistribution in planar growth.

difference in the nature of the solute redistribution which accompanies dendritic and plane-front growth. All of the early workers assumed that there was an appreciable amount of solute pushed ahead of an advancing dendritic front just as in planar growth. They were undoubtedly encouraged in doing this by the fact that theories based on such an assumption appeared to successfully explain many types of macrosegregate. However, recent work on dendritic growth has indicated that the solute diffusion layer ahead of a growing dendrite is extremely small.[35-40] It has been shown that solute rejection at a dendrite is not uniform at its surface but depends on the curvature of the surface. At highly curved surfaces such as the tip of the dendrite (typically 0.1 to 5 μ) very little solute is rejected.

The recent work on dendritic growth was triggered off by Rutter and Chalmers[33] in 1953. They developed a simplified theoretical treatment which successfully predicted the growth conditions at which a planar growth front would break down into a cellular morphology. Mullins and Sekerka[34] were later to treat the problem more elegantly and completely, but both approaches essentially demonstrated that the breakdown was caused by the ability of proturbences in the interface to reject solute laterally, parallel to the plane of the interface. This lateral rejection meant that less solute had to be rejected ahead of the interface, and this important feature of dendritic solidification has since been developed by many workers. Bolling and Tiller[36,37] measured the solute concentration at the centre of primary dendrite stalks and showed that this was $k_o c_o$, indicating the absence of a solute diffusion layer ahead of the dendrite tips. Brody and Flemings[38] developed a theoretical model to describe solute redistribution in dendritic solidification and made the assumption that there was 'negligible increase of solute in advance of the tips of growing dendrites'. In a later paper[39] they showed that their model accurately described the microsegregation observed in laboratory castings, thereby indicating that their assumption was valid. Burden and Hunt[40] accurately measured the growth temperature of cell and dendrite tips over a wide range of freezing conditions and demonstrated that the tip undercooling caused by solute rejection was very small for all growth velocities when the

temperature gradient in the liquid ahead of the dendrite was small.

The recent work on dendritic growth has been paralleled by an increased understanding of the macroscopic aspects of ingot solidification. A great deal of work has been performed in classifying the various zones of structure to be found in ingots [32,41-44] (e.g. chill, columnar, equi-axed), as well as in determining how the extents of these zones alter as casting parameters such as superheat, [45] alloy composition, [46] and ingot size [47] are altered. Various mechanisms have been proposed to account for the origins of the equi-axed zone. [48-52] Work has also been performed on the nature of fluid flow in the bulk liquid pool of a solidifying ingot. [53-60] Temperature measurements taken from solidifying ingots [53-57] have shown that the initial melt superheat is rapidly lost after pouring, and that the majority of solidification occurs with the bulk liquid pool at a nearly uniform temperature. Such measurements indicate that convection currents in the molten metal are initially very rapid due to pouring turbulence and the large temperature difference between mould and metal. They would appear to die down very quickly, however, leaving the bulk liquid pool fairly quiescent during the majority of solidification. Radiotracer work on laboratory-scale cells of liquid metal have shown that the fluid flow velocity is low for small horizontal temperature gradients. [58-60]

Stewart and Weinberg [61] suggested that bulk liquid convection currents could remove solute-enriched material from within the semi-solid zone behind the dendrite tip front. This would mean that certain of the 'planar growth' theories for macrosegregate formation could still be correct, in spite of the evidence against a diffusion layer ahead of a dendrite front. However, Verhoeven, [62] in laboratory scale experiements on Sn-Ag and Sn-Bi alloys, was unable to produce any mixing of interdendritic liquid into the bulk even with very vigorous, artificially induced, bulk liquid convection currents. It therefore seems unlikely that the sluggish bulk liquid convection currents observed in commercial ingots would be capable of penetrating the semi-solid region.

2.2 Review of previous work relating to macrosegregates

In this section the work which has been performed on the various individual forms of macrosegregation is reviewed. These forms have already been illustrated and described in section 1.2 of this thesis.

2.2.1 Inverse Segregation

This type of macrosegregate was one of the first to be correctly understood, although the arguments put forward to explain the proposed mechanism remained somewhat woolly for many years.

A paper by Vaughan[63] reviews work on inverse segregation to 1937. Vaughan described 8 theories which had been proposed to explain the segregation but pointed out that one of Bauer and Arndt[64] was generally accepted as being correct. These workers suggested that the segregation resulted from interdendritic flow of solute enriched liquid back down the temperature gradient. They did not, however, suggest why such flow should occur. Masing and Haase[65] proposed that the driving force for the movement lay in the volume contraction which accompanies the solidification process. Liquid flowed back between the dendrites to fill the contraction caused by the liquid which was solidifying deep within the semi-solid zone. The validity of this general mechanism for explaining inverse segregation was gradually established by a number of workers, notable amongst these being Scheil[66] and Adams.[67] Scheil[66] used the mechanism to derive an expression for the maximum segregation expected at the chill face for any given alloy composition, and reported good order of magnitude agreement with experimental data.[67] Adams performed extensive experiments on inverse segregation in Al-Cu ingots and gave a complete qualitative description of how the contraction flow mechanism could explain his results. Furthermore, he showed that a bismuth-6% tin alloy (which expands on freezing) gave a negative segregation at the chill face.

Kirkaldy and Youdelis[68] extended the theoretical treatment begun by Scheil to predict the concentration distribution along the whole length of a unidirectionally

solidified ingot in which the contraction flow mechanism had been operating. Their model showed good quantitative agreement with experimental data obtained on vertically-grown Al-Cu alloys. They pointed out in their treatment that steady state solidification produced no segregation, and so implied that solidification conditions had to be altering in order for contraction flow to cause segregation. Youdelis[9] later stated that an expanding semi-solid zone gives positive segregations, while a contracting zone causes negative segregations.

Most recently, Flemings and Nereo[69] have developed a general theoretical treatment for macrosegregation caused by fluid flow in the semi-solid region. They solved heat and mass balances in a differential volume element, considered to be representative of the whole of the semi-solid region, and obtained an expression relating the volume fraction of liquid in the element to the liquid composition. When integrated over the whole of the solidification range this expression was able to predict the macrosegregation caused by various combinations of heat flow and fluid flow. Flemings and Nereo used the model to predict an inverse type of macrosegregation profile in a specimen solidified under the relatively simple conditions of unidirectional heat and fluid flow. They considered contraction forces in the solidifying mushy zone to be the sole driving force for fluid flow. In a later paper[70] they showed that the predicted segregation profile agreed with that measured in an Al-Cu specimen solidified under the relevant conditions.

The 'local solute redistribution equation' developed by Flemings and Nereo has proved to be very useful in providing an explanation for many types of solidification phenomena. It shows that contraction flow of interdendritic liquid produces no macrosegregation unless the growth conditions are altering (i.e. the semi-solid zone is varying in length). It can also be used to show that contraction flow may be responsible for the types of macrosegregation known as banding, centreline segregation, and under-riser positive segregation. Flemings and Nereo[70,71] demonstrated that <u>banding</u> was the result of contraction flow of interdendritic liquid in the semi-solid region in association with sudden changes in growth conditions. For example, the abrupt formation of an air gap at a

mould-metal interface gives rise to 'reheating' of the solid skin thereby retarding the solidus isotherm and causing the length of the semi-solid region to expand. A solute-rich band of material is formed in the casting parallel to the mould wall at a position corresponding to this expansion of the semi-solid zone. Conversely a contraction in the length of semi-solid zone causes a solute-poor band to form. Banding is common in fusion welds where the periodicity of heat input may cause quite regular variations in semi-solid zone length. Banding in ingots may occur due to abrupt changes in heat transfer rate caused, for example, by air gap formation as mentioned above, or from thermal perturbations in the bulk liquid pool (e.g. at cessation of pouring, or upon gas evolution as in rimming steels).

Centreline segregation was shown by Flemings and Nereo[69] to be caused by the same mechanism as inverse segregation, namely interdendritic fluid flow to feed volume contractions. They demonstrated using their equation that such segregation was to be expected when, during the last stages of solidification, significant amounts of liquid flow occurred parallel to the isotherms in the semi-solid zone with a corresponding reduction in the flow velocity perpendicular to the isotherms.

2.2 Exudations

Four mechanisms have been proposed to account for the formation of exudations. All of these mechanisms are based on the back-flow of solute-rich interdendritic liquid from the semi-solid region to the outer surfaces of the casting. They differ, however, in the driving force proposed to account for this flow, these being solidification contraction; gas evolution within the body of the casting; pressure caused by withdrawal of the casting surface from the mould; and hydrostatic pressure of liquid metal acting down through the ingot height.

It was suggested by many early authors[32] that exudations were simply a severe form of inverse segregation, thereby implying that they, too, could be explained by interdendritic fluid flow in the semi-solid region under the influence of solidification contraction forces. It has been shown, however, that the magnitude

of solute-enrichment involved in exudations is far greater than the maximum chill face segregation calculated by Scheil[66], Kirkaldy[68], and Flemings[69] for flow under the influence of solidification contraction. Exudations cannot therefore be regarded as an extension of inverse segregation (see Section 1.2) but must be treated as a distinct macrosegregation phenomenon.

Gas evolution within the semi-solid region, giving rise to an internal pressure within the casting capable of forcing the interdendritic liquid out to the surface, has been proposed as a mechanism for exudation formation. It seems likely that this may be cause of exudations in bronzes where hydrogen is evolved in the later stages of solidification.

Youdelis[9] suggests that by far the most common mechanism responsible for exudation formation is the withdrawal of the solidified shell of a casting from the mould wall. This occurs under the influence of solid-state contraction and causes a marked reduction in the heat extraction rate. This results in a reheating of the solidified shell due to the continued heat transfer from the hot liquid core of the casting. If this reheating is sufficient to exceed the eutectic (or solidus) temperature at the casting surface then highly solute-rich interdendritic liquid will be forced out of the re-opened channels by the expansion pressure, thereby forming beads of exudation. In addition to the expansion pressure within the liquid, it has also been suggested that there may be a back-pressure due to a partial vacuum formed when the solidified casting skin withdraws from the mould. Such a pressure would be capable of'sucking' liquid out of the reheated channels. Youdelis[9] demonstrated the validity of the reheating mechanism by monitoring the thermal history of chill castings. He showed that exudations were only present when the outside surface of the casting reheated past the eutectic temperature. He also showed that exudations could be completely eliminated by applying a pressure to the solidifying casting because this prevented the surface of the casting from separating from the mould wall.

Finally, exudation as a result of hydrostatic liquid pressure has been used as an explanation for the bleed bands often observed on the surface of continuously cast ingots[73]. It has been suggested that these form when the solidified skin of the

casting ruptures under the stress caused by the weight of material below it. Solute-rich liquid then flows out of the semi-solid region to heal this crack under the influence of the hydrostatic head of liquid in the top molten pool.

2.2.3 A Segregation

'A' segregates in killed steel ingots have probably generated more interest and investigation than any other type of macrosegregate. There have accordingly been many conflicting theories as to their formation.

Early theories [2,26-30] tried to explain A segregates in terms of entrapment of the solute-rich layer which was believed to exist ahead of the advancing columnar dendritic fronts. Brearley et al [26] and Blank et al [29] suggested that the layer was trapped by equi-axed crystals growing in the bulk liquid; Standish [27] suggested that it was trapped between the advancing horizontal and vertical growth fronts; and in the 1st Report on the Heterogeneity of Steel Ingots [2] it was suggested that the layer was occasionally enveloped by the growing dendrite front itself. In other work by Blank et al [28] and also by Andrews et al [30] it was postulated that the impure liquid ahead of the dendrite front was swept down the interface by the convection currents and was then thrown out of cycle when it changed directions near the bottom of the ingot. This impure liquid was then trapped between the horizontal growth front and the equi-axed pile to produce the A segregates.

All theories based on a solute-rich layer ahead of a dendritic interface must now be considered highly unlikely in view of the recent work on dendritic growth discussed in section 2.1. In addition, none of the above theories explain the characteristic pipe-like morphology of A segregates nor the fact that they extend across the columnar/equi-axed interface. These same criticisms can be applied to a proposal made by Ohno [74] that A segregates are the result of the equi-axed zone tearing away from the columnar zone under gravitational forces.

Badenheuer [75] proposed that A segregates were formed by segregated liquid left in the wake of gas bubbles nucleating in, and rising through, the semi-solid zone. The mechanism has received much support since it obviously accounts for the

morphology of the segregates as well as for their near-vertical inclination. However, as Hultgren[76] points out, the gas content of killed steel ingots is by design very small, and furthermore a gas bubble mechanism cannot explain why A segregates are often observed to turn back towards the outside of the ingot when approaching the hot top liquid pool.

Several authors[76,77] have proposed that flow of liquid into the columnar region to feed solidification contraction is responsible for A segregates. Hultgren[76] suggested a mechanism based on shrinkage forces, bulk liquid flow down the advancing growth front, and equi-axed crystal attachment onto the front. Recent experimental[78] and theoretical work on columnar dendritic solidification has shown however that flow of liquid into a semi-solid zone causes solute depletion not enrichment. Contraction mechanisms cannot therefore be responsible A segregates.

The most recently proposed mechanism for A segregate formation is that of gravitational interdendritic fluid flow, and this is now generally regarded as being the correct explanation.[79] It was first suggested as a mechanism by Takahashi[80] who observed pipe-like defects in laboratory scale Al-4wt%Cu ingots. The idea only began to obtain wider acceptance however after the work of McDonald and Hunt.[81] They reproduced the classical form of A segregates using the transparent NH_4Cl-H_2O system in a model of a conventional ingot. They observed that in this system the A segregates were pipes of rapidly rising liquid within the semi-solid zone, and they postulated that this flow of liquid was caused by a solute driven convection cycle - the solute-rich interdendritic liquid of the NH_4Cl-H_2O system being less dense than the bulk liquid of nominal solute content. In a second paper[82] they demonstrated that the direction of the interdendritic fluid flow was reversed by adding $ZnCl_2$ to the NH_4Cl-H_2O system, since this was rejected by the growing NH_4Cl dendrites thereby making the interdendritic liquid denser than the bulk liquid. This reversal of the flow direction resulted in segregate channels which sloped inward towards the bottom of the model ingot, as observed by Takahashi in Al-Cu. McDonald and Hunt[81] developed a qualitative argument to explain the formation of the channels. This is given in Appendix 2.A.

They pointed out that during the part of the convection cycle where liquid was moving out of the semi-solid region it would be getting hotter. For an alloy system where $k_o < 1$ this liquid would therefore try and reduce its solute content in order to attain local equilibrium at each successively hotter temperature. This reduction in solute content could only be achieved by dissolution of solute-poor solid dendrites. This leads to channel formation causing a localised increase in fluid flow rate, which in turn leads to a widening of the channel. They therefore argued that fluid flow up the temperature gradient in a semi-solid region was unstable and tended to occur through a number of large channels.

The qualitative argument of McDonald and Hunt was later developed in a semi-quantitative fashion by Mehrabian, Keane, and Flemings[78]. These workers extended the theoretical model originally developed by Flemings and Nereo to take into account the influence of gravity on an interdendritic liquid of variable density. They stated that channel formation occurs when fluid flow occurs from colder to hotter regions of the semi-solid zone, in agreement with McDonald and Hunt. Unfortunately the assumptions they used in developing their model break down under such unstable flow conditions, and so their treatment cannot be used in predicting the form and magnitude of macrosegregation produced by the gravity flow mechanism. The model may only be used in the very restricted case where flow caused by solidification contraction outweighs that due to gravitational forces thereby preventing any flow of liquid back out of the semi-solid region. In a later paper, Mehrabian et al[83] produced experimental evidence of the macrosegregation caused by gravitational interdendritic fluid flow under such restricted growth conditions, and demonstrated that this agreed reasonably well with their theoretical predictions. They also demonstrated that channel-type segregates appeared in the macrostructure of their Al-Cu castings when growth conditions had been such that their model predicted unstable flow.

Hebditch and Hunt[84] used a radiotracer technique to demonstrate the existence of gravitational interdendritic fluid flow in model castings of Sn-6wt%Zn. These authors used the same model casting system to study the progress

of macrosegregation with time as the semi-solid region moved across their model ingot.[85] They employed growth conditions similar to those expected in large-scale ingots (i.e. slow growth rates - 10^{-2}cm/sec., low temperature gradients, and bulk liquid temperature just above the liquidus temperature), and observed that convective interdendritic fluid flow was the dominant macrosegregation mechanism in all their castings. This conclusion was inferred both from composition measurements and from the shapes of the quenched growth fronts in their ingots. This work was later extended by the present author using a similar model casting system,[86] and the same conclusions were reached concerning the importance of gravity flow as a macrosegregation mechanism. Fredriksson and Nilsson[87] also concluded that interdendritic convection was responsible for channel formation after they had studied Sn-Pb alloys in a quenchable casting technique.

Weinberg et al[88] have used the gravity flow mechanism to explain A segregate formation in their study of high carbon steel ingots. They observed differences in A segregate abundance and position according to the geometry of the ingot mould employed. The number of A segregates in ingots of comparable size was greatly reduced by employing big-end down (BED) moulds rather than the conventional big-end up (BEU) moulds. They attributed this to the fact that in BED ingots the isotherms sloped towards the centre of the ingot at the top. Upward flowing interdendritic liquid would not therefore have been moving from colder to hotter regions as it does in BEU ingots where the isotherms slope the other way. Channels would therefore not have formed so readily in the BED case.

Finally it has recently been reported that gravitational interdendritic fluid flow has been observed continuously and 'in-situ' in a metal alloy system.[89] This was achieved by using refined X-ray techniques on very thin section Al-Cu specimens. The suggestions[27,90,91] that analogue systems such as NH_4Cl-H_2O do not truly represent metal alloy solidification phenomena are therefore shown to be incorrect, as previously argued by Hunt.[93].

2.2.4 Freckles

The macrosegregation phenomenon known as freckling has been described and discussed in detail by Giamei and Kear[5]. Two main explanations appear in the literature concerning the origin of the freckle trails observed in directionally solidified castings and electro-slag refined (ESR) ingots of iron base, and nickel base, superalloys. These are gas evolution and gravitational interdendritic fluid flow.

Gould[6], noting that the freckle trails were always found parallel to the direction of gravity, suggested that they might be caused by gas bubbles forming in the semi-solid zone. These bubbles would tend to rise vertically out of the zone and might conceivably leave trails of solute-rich liquid in their wake. Gould reported, however, that the incidence and abundance of freckle trails in two susceptible alloys was unaffected by reductions in the oxygen, nitrogen and hydrogen contents of the melt.

Copley et al[94] proposed that freckle trails were simply pipes of rising, solute-rich liquid similar to A segregates in steel ingots. They suggested that freckles occurred in vertically solidified castings when the alloy composition was such that the interdendritic liquid became less dense as the solute content increased (for $k_o < 1$). Such a situation would lead to a density inversion in the semi-solid zone with the lightest liquid being at the bottom. This liquid would therefore have a tendency to rise, and in so doing would move from colder to hotter regions of the semi-solid. It would thus need to dissolve away solid dendritic material in order to lower its solute content and maintain local equilibrium, and so preferential channels for flow would be formed. Copley et al[94] confirmed this hypothesis with experiments on the transparent NH_4Cl-H_2O system. They reproduced the typical form of freckle trails by growing an alloy of NH_4Cl-70 wt $\%H_2O$ vertically upwards. Primary ammonium chloride dendrites formed at this composition and the interdendritic liquid became progressively lighter as more water was rejected into it, thereby giving the required density inversion. They observed that the freckle trails were caused by upward flowing jets of liquid

within the semi-solid zone. Dendritic debris was eroded from the sides of the channels and was carried along by the liquid jets, this being the cause of the classical 'speckled' or equi-axed appearance of the trails on their eventual solidification. Copley et al were able to demonstrate that the position of the freckles depended on the curvature of the isotherms within the semi-solid zone, and that this was consistent with the gravitational interdendritic fluid flow mechanism. In the same paper they also presented a semi-quantitative mathematical analysis of the mechanism. The treatment was limited in that it did not consider resistance to fluid flow in the semi-solid region, but they were able to use it to predict the effects on freckling behaviour of changes in growth conditions and alloy composition.

Streat and Weinberg[95] also developed a mathematical model for macrosegregation in vertically solidified ingots assuming that gravitational forces alone were responsible for fluid flow. They included the resistance to flow caused by the semi-solid zone by considering the zone to be a porous medium of variable porosity. They predicted that the magnitude of macrosegregation caused by gravity flow would increase as growth rate decreased, and as ingot height, temperature gradient, and primary dendrite spacing increased. They confirmed these trends experimentally using Pb-20%Sn alloy samples solidified unidirectionally upwards. Freckle trails were observed in some of these samples examined after solidification. Streat[96] pointed out that no gas evolution was observed in their Pb-Sn alloys even when they were solidified under vacuum,and so this could not be responsible for the freckles observed. Streat and Weinberg produced further evidence that gravity flow was the correct mechanism for freckle formation by growing Sn-4%Pb alloy samples in their apparatus. This alloy has a stable density gradient in the semi-solid zone when grown vertically upwards and no evidence of macrosegregation or freckling was observed in the samples.

The concept of unstable density gradients causing freckling is consistent with the observations of Smeltzer[97] who noted that the defect could be eliminated by changing the alloy composition. It is also consistent with the findings of Devries and Mumau[93] who reported that the incidence of freckling could be reduced

by altering the cooling conditions and decreasing the dendrite spacing. Burden and Hunt[99] have also used the gravitational interdendritic flow mechanism to explain the large variations which they observed in primary dendrite spacing with growth direction (see section 9.1).

2.2.5. Equi-axed, or Gravity, Segregation

Equi-axed segregation has tended to be a neglected area in work on macrosegregation - perhaps because the fundamental mechanism involved is so simple The effect which gravity has on objects has been recognised since Newton, and the motion of solid spheres in quiescent fluids has long been quantitatively described by the Stokes-Navier equation. It is not surprising, therefore, that it is taken for granted that the correct mechanism for explaining equi-axed types of segregation is one of gravitational forces acting on free-floating solid particles.[53,100-103]

The Stokes-Navier equation is:-

$$V = 2gr^2(D_s-D_l)/9n$$

where V is the terminal sink/float velocity of a spherical particle of radius r and density D_s in a stagnant liquid of density D_l and viscosity n. This equation may be applied, at least in a semi-quantitative fashion, to the motion of solid particles such as equi-axed dendrites and inclusions in liquid metals even though these are rarely spherical. This motion leads to vertical macrosegregation when the compositions of the solid and liquid phases (c_s and c_l) are different. The magnitude of the resulting segregation depends on three factors, these being (a) the magnitude of c_s-c_l; (b) the value of V , which is determined by the particle size and the density difference of solid and liquid; and (c) the time available for separation to occur. This time-dependency of the mechanism was stressed by Hebditch and Hunt[85] in their summary of macrosegregation mechanisms.

Some qualitative work has been performed on the macrosegregational effects of the mechanism, particularly in the fields of slag separation; floatation of kish graphite in cast irons;[104] separation of inclusion particles in copper

alloys;[105,106] and separation of intermetallic phases in Sn-Cu-Sb bearing alloys.[107,108]

Davies[109] has suggested that the sink/float tendency of solid particles under the influence of gravity may be overcome and even reversed by vigorous thermal convection currents in the liquid melt. He reported the anomalous floatation of the primary Cu_6Sn_5 solid intermetallic phase in a Sn-5wt%Cu sample which had been unidirectionally solidified in a horizontal furnace. Density measurements indicated that the phase should have sunk. Davies also proposed that this anomalous effect might have been caused by a surface energy gradient within the melt. He cited the work of Kawai and Keller[110] who pointed out that in a liquid containing composition and temperature gradients there exists a gradient of interfacial free energy with respect to a solid object placed in it. This would tend to modify the gravitational effect particularly wher the surface area to volume ratio of the solid phase is large, as in the case of the Cu_6Sn_5 needles reported by Davies.

Sinking of primary equi-axed dendrites has been used to explain both the negative and positive bottom cones of segregation found at the bottom of large steel ingots. These cones are invariably associated with the bottom pile of equi-axed crystals.[51] Southin, in particular, has demonstrated how dendritic debris from the top semi-solid skin of castings sinks through the bulk liquid pool.

Gravity segregation has also been shown to be a problem when remelting alloys.[111] Strangman and Kattamis have shown that primary dendritic fragments can survive and even coarsen at temperatures above the liquidus of the nominal alloy composition. This is because such fragments are solute-depleted and hence of higher melting point. They tend to sink to the bottom of the melt and dissolve only slowly, particularly when a stable composition gradient is developed in the liquid above them. Partial melting is often a problem in commercial practice particularly when hardener alloys of high solute content are added to a melt to make up the required alloy composition.[112] Streat and Weinberg[113] also experienced incomplete melting problems in their work on Pb-Sn alloys. Gravity segregation of phases has even been reported in eutectic alloys after repeated solidification and

melting cycles on the same sample.[114,115]

Gravity segregation has also been reported to occur in the liquid phase when there is a liquid miscibility gap in the phase diagram, as for example in the Cu-Pb system.[116]

2.2.6 Positive bottom cone of segregation

A thorough review of the mechanisms proposed for the formation of this type of segregation is given by Standish.[117] Two theories have attracted most attention. The first is that the inclusions are carried down in front of the solidifying columnar fronts to the bottom of the ingot by bulk liquid convection currents[28,30,118]. At the bottom they are then thrown out of the convection stream as it changes direction. Such an explanation now seems unlikely, however, in view of the sluggish nature of the convection currents in conventional ingots. The second theory is that the inclusions are carried down by primary equi-axed dendrites as they sink to the bottom under gravitational forces[3,4,119,120]. This proposal certainly accounts for the fact that the positive segregation of inclusions is associated with the bottom pile of equi-axed crystals and the region of negative segregation of solute elements. Some workers have suggested that the equi-axed crystals actually nucleate on the inclusions,[119,120] while others have proposed that the falling crystals act like flypaper and sweep inclusions down to the bottom of the ingot by trapping them between their growing arms.[3,4]

2.2.7 Negative bottom cone of segregation

It has generally been recognised that gravitational forces are responsible for causing this macrosegregate. As mentioned in the previous section many workers have proposed that the negative cone is caused by the settling of solute-poor, primary, equi-axed crystals to the bottom of the ingot[3,4,51,119,120]. It has also been pointed out that gravitational interdendritic fluid flow could be responsible for the negative cone in steel ingots.[103] The solute-rich interdendritic liquid in the advancing horizontal columnar zones of a steel ingot

is lighter than the bulk liquid and so will tend to flow upwards. In order to complete the convection cycle, liquid must therefore flow into the semi-solid zone towards the bottom of the ingot, thereby causing a negative segregation in this region (see Appendix 2.A). It has also been suggested that the negative bottom cone could be formed by the upward movement of the lighter solute-rich liquid away from the equi-axed pile, rather than from the settling of the pile itself.[23] Such flow is indeed possible, as observed by Copley et al[94] and by Burden,[99] but it does seem unlikely in large steel ingots in view of the overall fluid flow pattern.[81]

2.2.8 Under-riser positive segregation

Two mechanisms have been suggested to account for this macrosegregate. Flemings and Nereo[70,71] proposed that the segregation was caused by interdendritic fluid flow to feed contraction. They used their local solute redistribution equation to demonstrate that positive segregations could be produced by flow of liquid from a riser to feed contraction forces in the top of the ingot under the shoulders of the riser.[81] McDonald and Hunt observed a density-stable, solute-rich layer of liquid at the top surface of their model NH_4Cl-H_2O ingots. They proposed that this was formed by non-equilibrium flow of solute-rich liquid from the A segregate channels in the semi-solid regions, and observed such flow in their ingots. They therefore concluded that under-riser positive segregation in steel ingots was simply another feature of interdendritic fluid flow under the influence of gravity, as were A segregates and the negative segregation at the bottom of the ingots.

2.2.9 V Segregates

The first mechanism proposed for this segregate was one of layering in the bulk liquid.[23] It was suggested that impurities in the bulk liquid pool arranged themselves in horizontal layers, and that these layers were eventually sucked down at the centre of the ingot in the last stages of freezing due to contraction forces. The explanation which is most commonly accepted, however, is that the V segregates

are formed by the influence of contraction forces acting on the solid dendritic network.[81] It is believed that the initial solid framework which is formed in the ingot once the growth fronts have reached the centreline is fairly weak. The framework is therefore likely to collapse under the combined forces of its own weight and the contraction it experiences as it cools down. This collapse will be more marked in that part of the framework at the centreline of the ingot because it is both weaker and less well supported. The collapse therefore causes V shaped voids to be formed which are then partially or completely filled by solute-rich interdendritic liquid depending on the amount available for feeding.

2.3 Current Understanding of Macrosegregation

Alloy solidification involves solute redistribution on a microscopic scale. There exists a diffusion field of solute around a solid particle growing in a liquid alloy. Macrosegregation can only occur if this solid particle is somehow macroscopically separated from its solute diffusion field. There must be some relative movement of the solid and liquid phases on a macroscopic scale. Macrosegregation mechanisms differ only in the manner in which this separation is achieved.

It can be seen from the review of work given in the previous section that some of the apparently different forms of macrosegregation occur by essentially the same mechanism. In fact, in all the theories discussed only 4 driving forces have been used to explain the necessary separation of solid and liquid. These are gravitational forces, contraction forces, diffusion, and gas evolution, and of these the first two are by far the most important. The various types of macrosegregate observed in castings and ingots are produced by one of these driving forces acting on either the solid or the liquid phase.

Figure 2.2., overleaf, shows how gravitational and contraction forces may account for all of the forms of macrosegregation found in commercial castings and ingots. The chart is divided according to whether the solid phase exists in a free-floating condition or as a semi-rigid framework, and it is further sub-divided according to whether the force acts primarily on the solid or the liquid

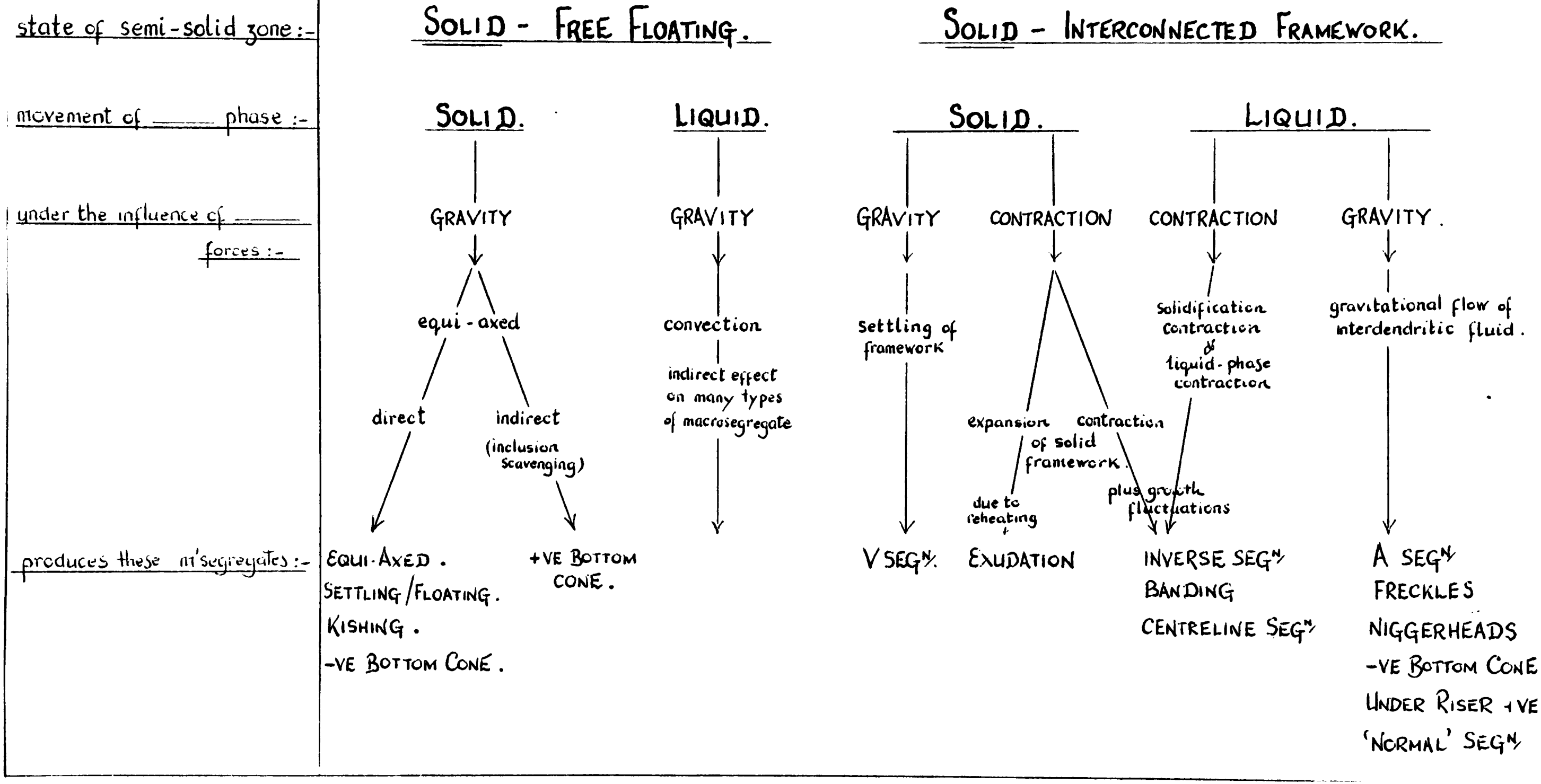


Fig.2.2. Chart showing how gravity and contraction forces may account for various types of commercially importa macrosegregatic.

phase. Where more than one combination of these factors is capable of producing a given type of segregate this has been noted.

Diffusion is basic to the production of microsegregation without which macrosegregation could not occur. However, on its own it can only produce macrosegregation under specialised conditions. These are diffusion controlled planar front solidification where initial and terminal transients of composition are formed, and the even more unusual case of a stagnant liquid held in a temperature gradient (Ludwig-Soret effect).

Gas evolution may be responsible for several types of segregation in connection with one of the other driving forces, although conclusive evidence of this has not been produced. It may, for example, cause banding (in connection with contraction forces) by giving rise to growth fluctuations of the semi-solid region. It may also be responsible for forcing liquid back between dendrites to cause exudations.

Our understanding of macrosegregation mechanisms is now such that qualitative predictions can be made on how to minimise the defects. Segregates produced by gravitational forces may, in general, be removed by reducing the total solidification time of the casting. Shortening the vertical height of the casting should also be beneficial in reducing such segregates by decreasing the driving force. Gravity induced segregates may be eliminated completely by using electromagnetic fields to balance gravitational forces in the casting. Contraction driven segregates may be reduced by causing the casting to solidify slowly without sudden changes in growth conditions. Exudations may be minimised by adequate melt degassing and by casting into non-rigid moulds. All types of segregation, apart from those associated with equi-axed segregation, are less severe in a casting of equi-axed macrostructure compared with one of columnar macrostructure. Equi-axed segregation may be reduced by vigorous stirring of the liquid metal, either thermally, mechanically, or electromagnetically.

Burden et al[121] have pointed out that the best way of producing a homogeneous sample under laboratory conditions in an alloy where the interdendritic liquid gets denser as freezing progresses is to grow the material vertically upwards under

steady state conditions with horizontal planar isotherms. In commercial practice the size and shape of the casting design obviously limit the scope for reducing macrosegregation, as does the type of casting process which must be used. This will be further discussed in the following chapter. However, in general terms, castings should be produced with their shortest overall dimension in the vertical plane, with an equi-axed structure, and they should be made to solidify in as short a time as possible without producing too great an initial chilling effect. For ingot solidification 'dumpy' ingots are to be preferred, in which equi-axed growth is encouraged in connection with artificially induced stirring. These conditions, of course, do not take into account other casting problems such as shrinkage porosity, incomplete feeding etc., but they should minimise macrosegregation.

CHAPTER 3

INVESTIGATION OF MACROSEGREGATION IN INDUSTRIAL CASTINGS AND INGOTS

3.1 Introduction

Previous work carried out in this Department, including some by the author, has tended to be concentrated on the gravitational interdendritic fluid flow mechanism for macrosegregation. It was decided at the beginning of the present work that a broader look should initially be taken at the field of macrosegregation as a whole. It was hoped that this would lead to the identification of the most important mechanisms and types of segregate, and that further research could then be concentrated on specific aspects of these mechanisms.

The majority of the literature survey presented in Chapters 1 and 2 was performed at the start of the present work in order that a broad picture of segregation could be obtained. It seemed from this survey that the major mechanisms contributing to the formation of the various macrosegregates were reasonably well understood. However, it also seemed that the relative abundance and importance of the different types of segregation in commercial castings and ingots had not been correspondingly well investigated. The only wide-ranging examination which had been performed on commercial macrosegregation had been for steel ingots.[2,23,122] It was therefore decided that some sort of survey should be carried out into the relative importance of the segregates in commercial solidification. To this end a number of industrial companies and research organisations were contacted with a view to the supply of castings and ingots for investigation. Unfortunately their response was very limited and only a very restricted survey could be carried out. The results of those castings which were examined are presented and discussed in the following section, together with a summary of the quantitative data from commercial

castings which was already available in the literature.

3.2 Description of work performed

3.2.1 General Outline

Two of the organisations which were contacted for help actually supplied castings. Alcan International Ltd. at Banbury supplied the several aluminium alloy castings and ingots described in sections 3.2.2. to 3.2.7., inclusive. Rolls-Royce Ltd. at Bristol supplied the nickel-base superalloy gas turbine blade casting described in section 3.2.8.. Of the aluminium castings supplied by Alcan only the semi-continuously cast ingot slices described in section 3.2.7. were actually manufactured at Banbury. All the other castings had been submitted to Alcan by their customers for evaluation.

Composition analyses were performed by atomic absorption spectrophotometry using the sampling and analysis techniques described in detail in Chapter 9. The accuracy of each set of composition measurements has been noted on the relevant figure or table.

The nominal compositions of those alloys examined in this work are given in Table 3.1., below:-

Table 3.1

Alloy Designation	Balance	Composition wt %				
		Si	Mg	Mn	Cu	Zn
L99	Al	6.5/7.5	0.2/0.45	-	-	-
LM9	Al	10.0/13.0	0.2/0.6	0.3/0.7	-	-
LM12	Al	-	0.2/0.4	-	9.0/11.0	-
LM6	Al	10.0/13.0	-	-	-	-
LM10	Al	-	9.5/11.0	-	-	-
AA 7075	Al	-	2.1/2.9	-	1.2/2.0	5.1/6.1
AA 2014	Al	0.5/1.2	0.2/0.8	0.4/1.2	3.9/5.0	-
AA 2017	Al	0.2/0.8	0.4/0.8	0.4/1.0	3.5/4.5	-

		Co	Cr	Mo	Ti	Al	V
IN-100	Ni	15.0	9.5/10.5	2.75/3.5	5.0	5.5	1.0

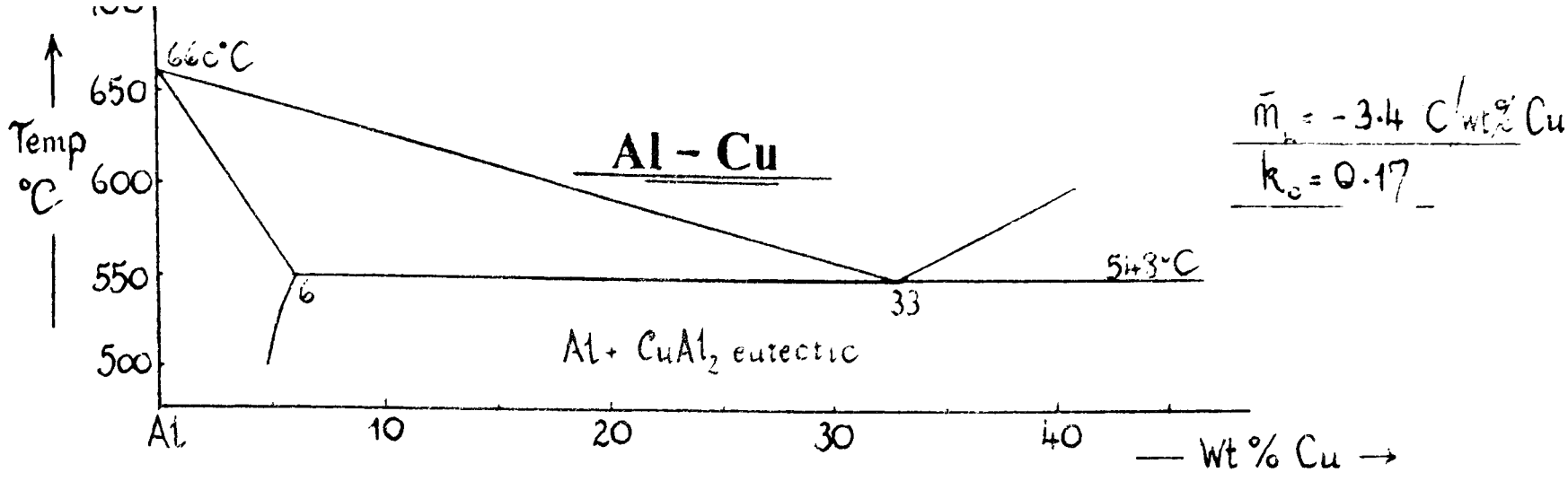
The binary equilibrium phase diagrams for the Al-Si, Al-Cu, Al-Mg, and Al-Zn systems are reproduced in fig. 3.1., while those for the Ni-Cr and Ni-Co systems are given in fig. 3.2..

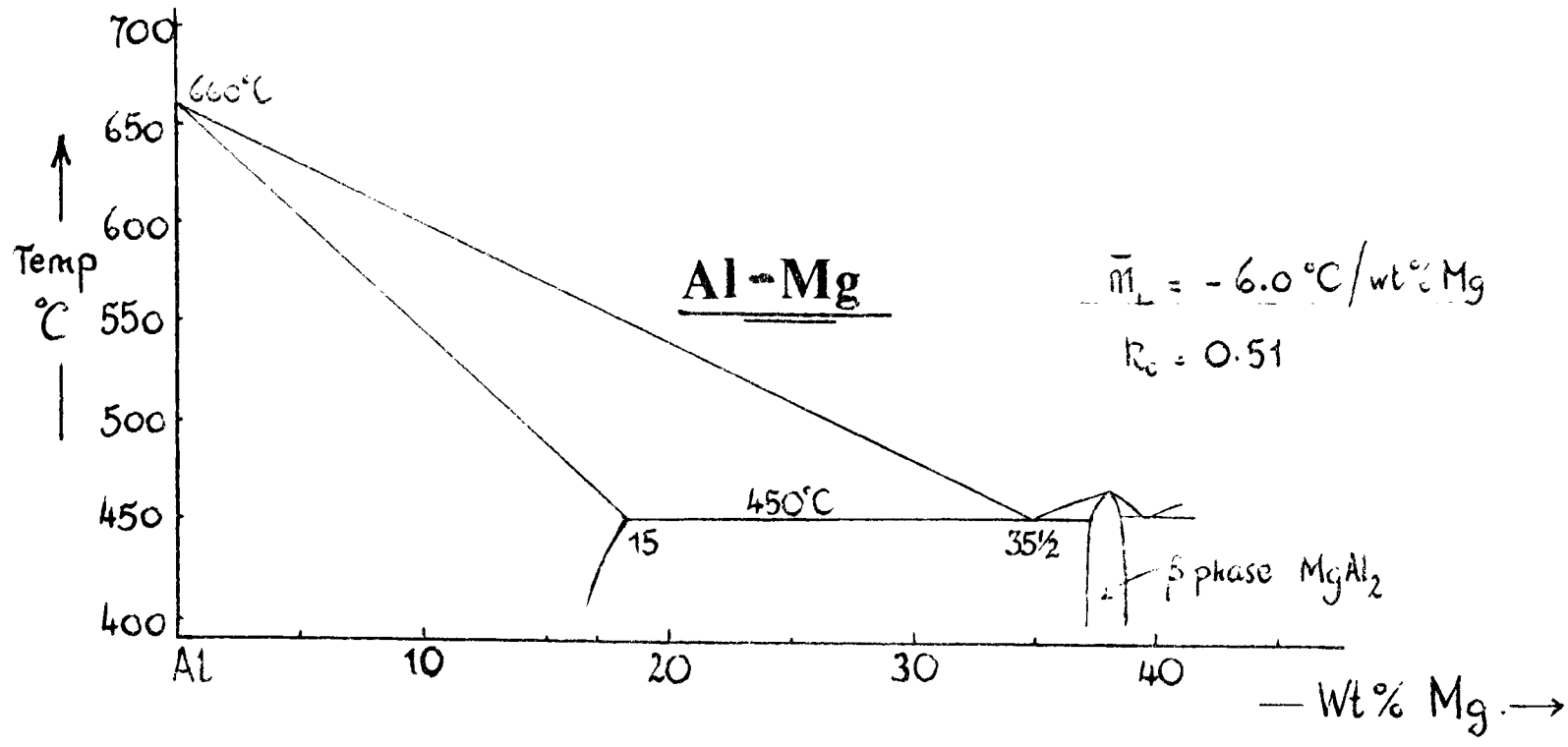
3.2.2 Racing Car Wheel - centrifugally cast

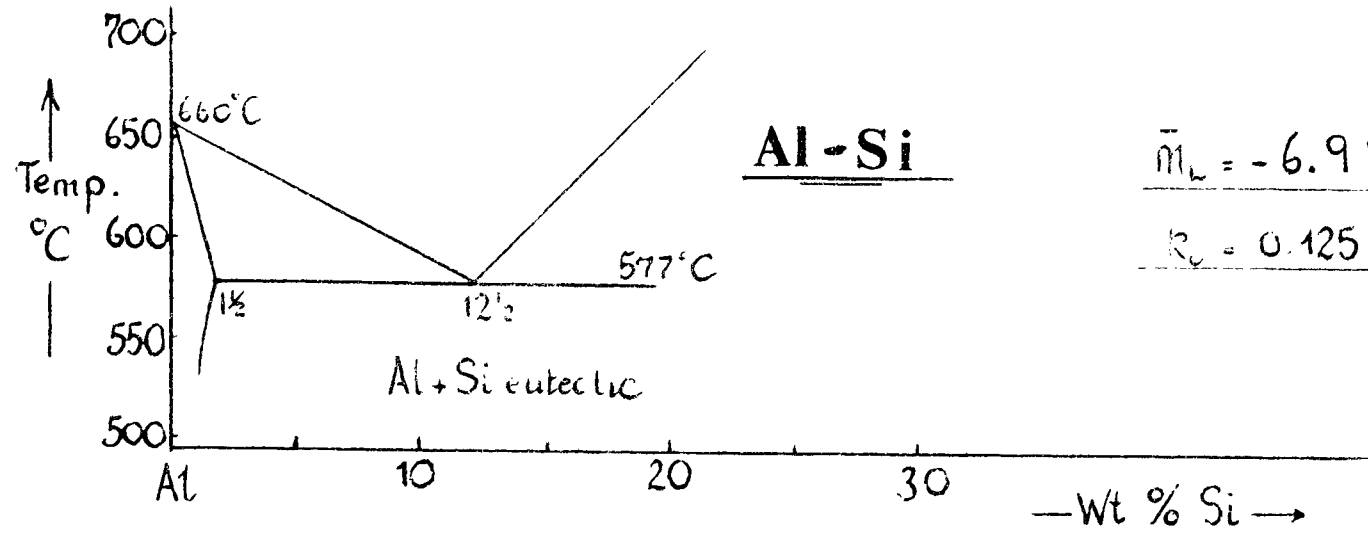
This was a spoked wheel made by Dialloys Ltd., Cardiff, for use in the U.S.A. A radial section of the wheel was supplied, the elevation view of which appeared as shown in the diagram in fig. 3.3. The wheel was centrifugally cast in a ceramic-coated metal mould, the radial section being horizontal. Molten alloy was poured into the die through the hub section, and the casting was fed from this position. Data for rotation speed was unknown but the solidification time was thought to be less than 2 minutes. Alloy composition was L99 (Al-7wt %Si).

Several samples were drilled from the radial section in the positions shown in fig. 3.3. In addition, samples were milled from a circumferential section towards the bottom of the rim at various depths through the rim thickness. Analysis was performed on the silicon content of these samples. The results obtained from the various positions are shown in fig. 3.3. The average composition obtained was 6.5wt %Si, the error on the composition values being $\pm$ 0.2 wt %Si. The only value found to lie outside this error range from the average composition was on the wheel rim at its intersection with the hub. Microstructures taken from various positions of the wheel section showed that the structure was reasonably uniform throughout, although the as-cast structure had been disguised by heat treatment. The structure essentially consisted of aluminium dendrites surrounded by a spheroidised Al-Si eutectic.

It is felt that the radial macrosegregation observed in this wheel was caused by the centrifuging of the primary equi-axed aluminium dendrites to the outer end of the hub section. In Al-Si alloys the primary aluminium-rich dendrites are denser than the bulk liquid [123] and so would tend to move towards the outside of the wheel under the influence of centrifugal forces. The







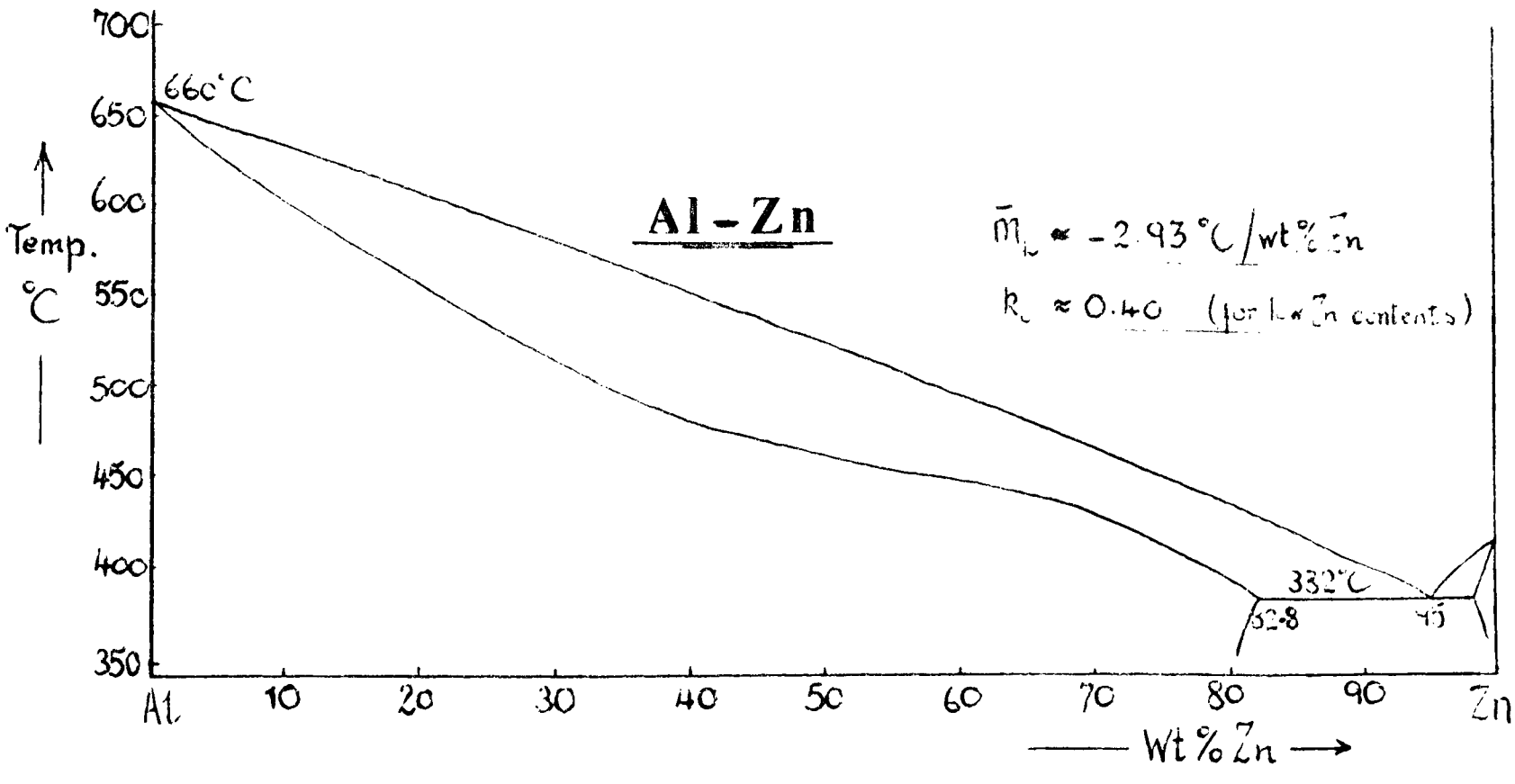
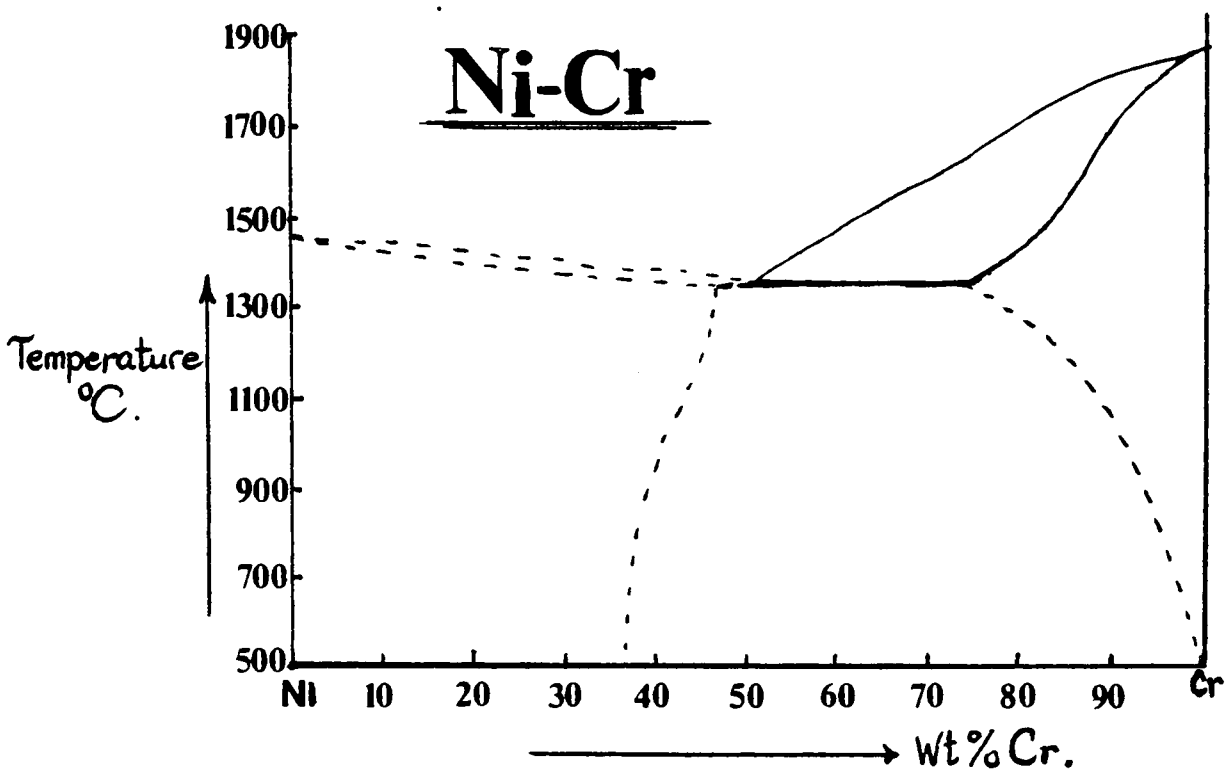


Fig 3.1. Part binary equilibrium phase diagrams

3.1



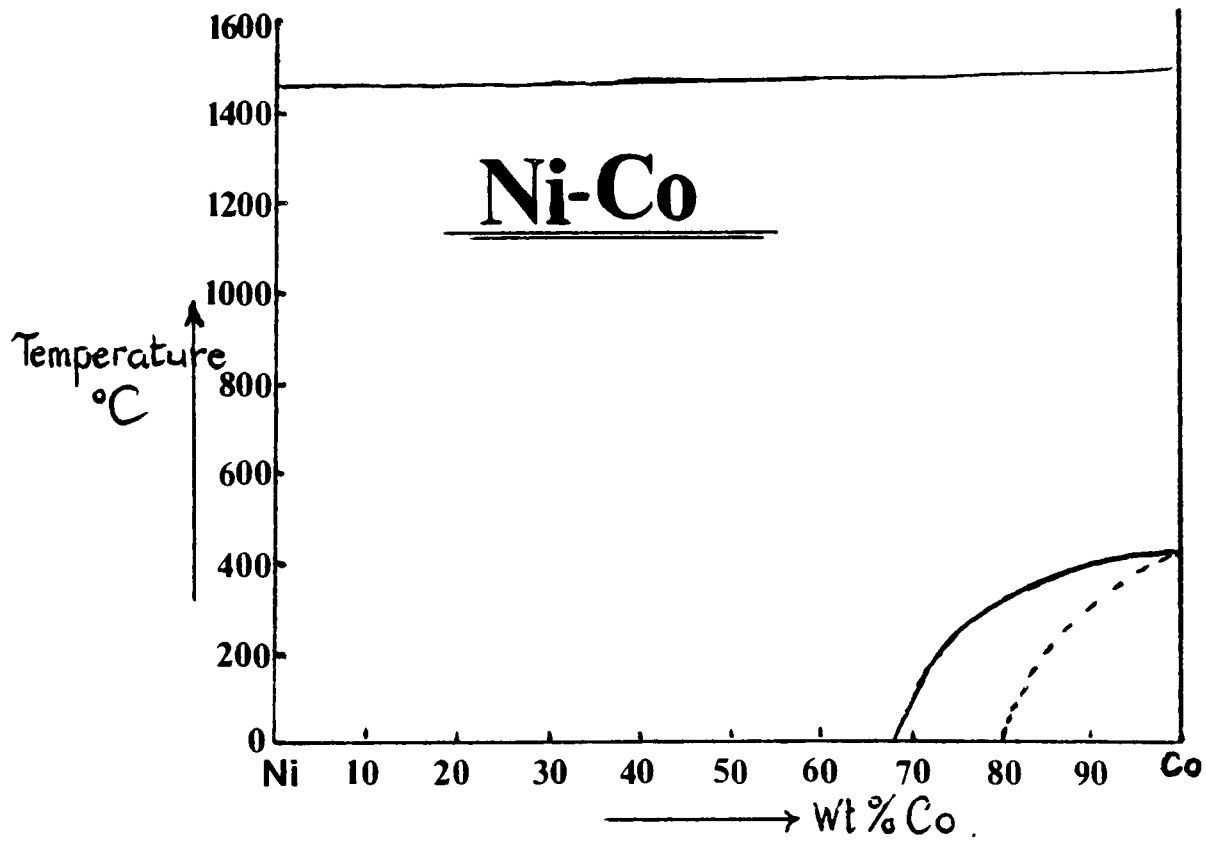
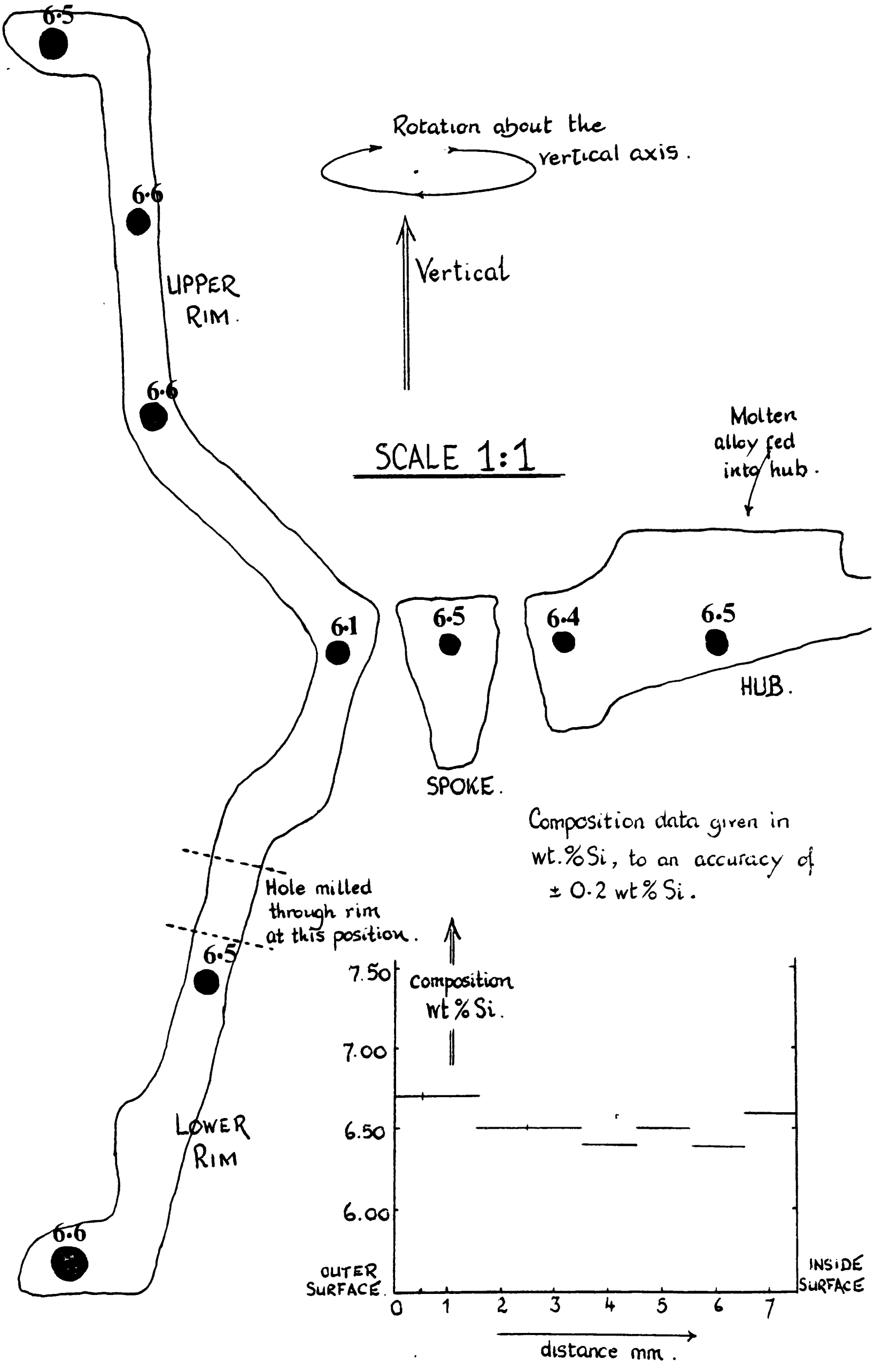


Fig 3.2. Binary equilibrium phase diagrams of the Ni-Cr and Ni-Co systems.



Segregation profile through the lower rim of the wheel, at the position shown

Fig. 3.3. Work performed on centrifugally cast wheel.

increased gravitational forces experienced in centrifugal casting must allow equi-axed mechanisms to produce macrosegregation in shorter times than in conventional gravity castings. However the fact that the majority of the wheel rim was of nominal composition suggests that it was only in the thicker hub section that sufficient time was available during solidification for appreciable movement of the solid phase to occur .

There was some evidence of inverse segregation through the thickness of the rim although the magnitude of this was within the error range on the nominal composition figure.

3.2.3 Saloon car wheel - low pressure diecast

Once again a radial section of the wheel was supplied, the etched macrostructure of which is shown in fig. 3.4. The wheel was cast as shown in the figure, with the radial section horizontal and below the level of the majority of the rim. A metal mould was used to which a ceramic coating had been applied in order to reduce the solidification rate. Die temperature would have been around 250°C. The feed from the molten metal reservoir was attached to the centre of the hub section, and so die cooling would have been arranged to ensure that solidification proceeded from the top of the rim down to the centre of the hub in order to obtain the maximum benefit from the applied pressure. The total solidification time of the wheel was reported to have been approximately 5 minutes, although the wheel rim had probably solidified within 2 minutes of filling the die. The alloy used was LM9 (Al-11Si).

The macrostructure of the wheel showed quite a large amount of shrinkage porosity, particularly in the hub section. The grain structure was equi-axed, with very large equi-axed dendrites at the bottom of the hub section. The dendrites were clearly delineated by the aluminium-silicon eutectic, the silicon being in the modified condition. The structure was as-cast.

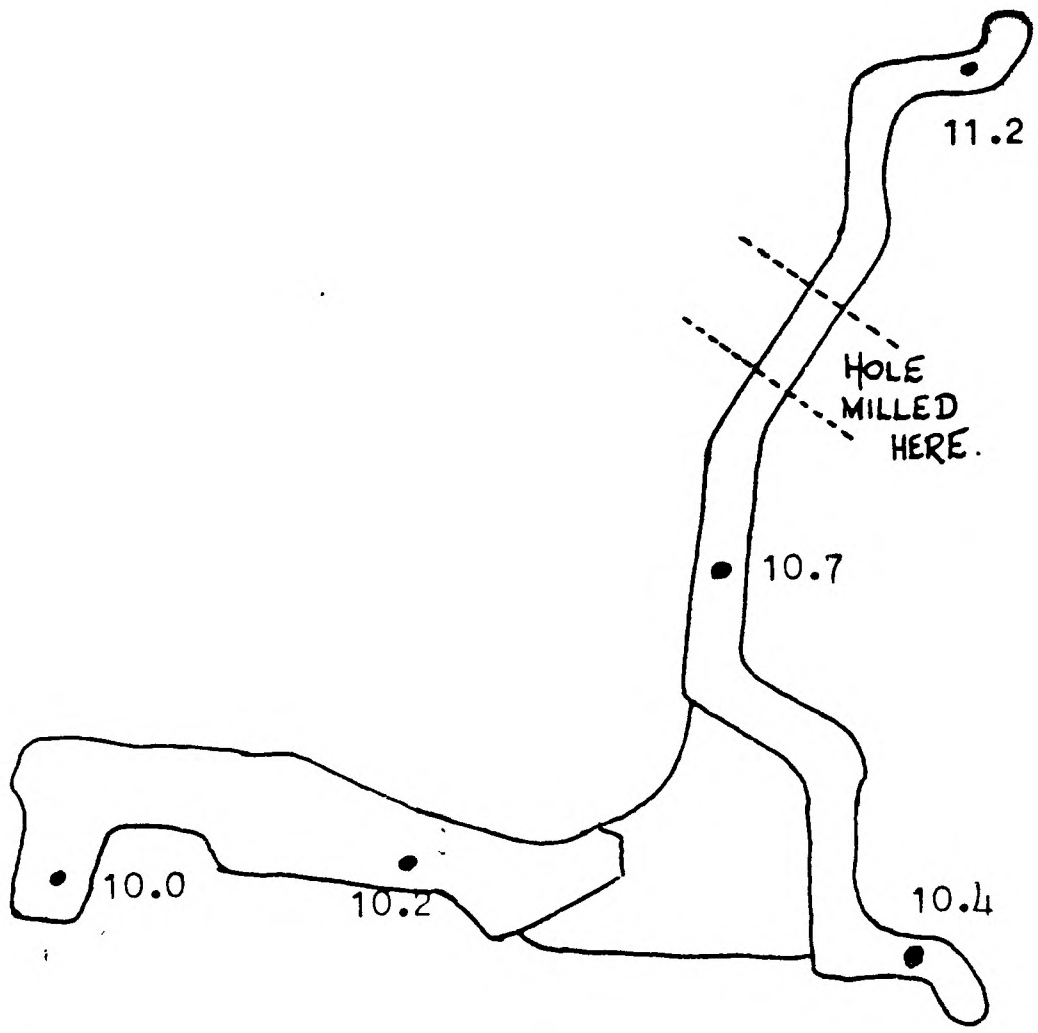
The macrosegregation observed in this wheel was of a vertical nature, as shown in fig. 3.4., which suggests that gravitational driving forces were



Macrostructure of radial section

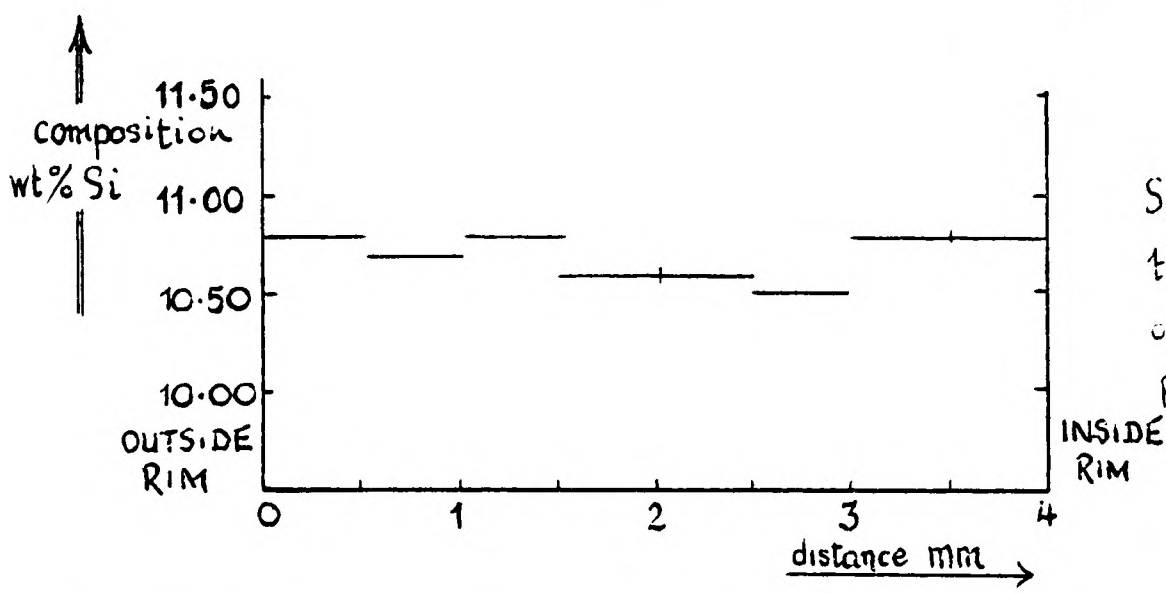
Magn x 0.4

Vertical



Composition analyses performed. Data given in wt % Si, correct to ± 0.35 wt % Si.

Average composition of analyses performed was 10.50 wt % Si.



Segregation profile through the upper rim of the wheel, at the position shown above.

Fig. 3.4. Summary of work performed on low-pressure diecast wheel.

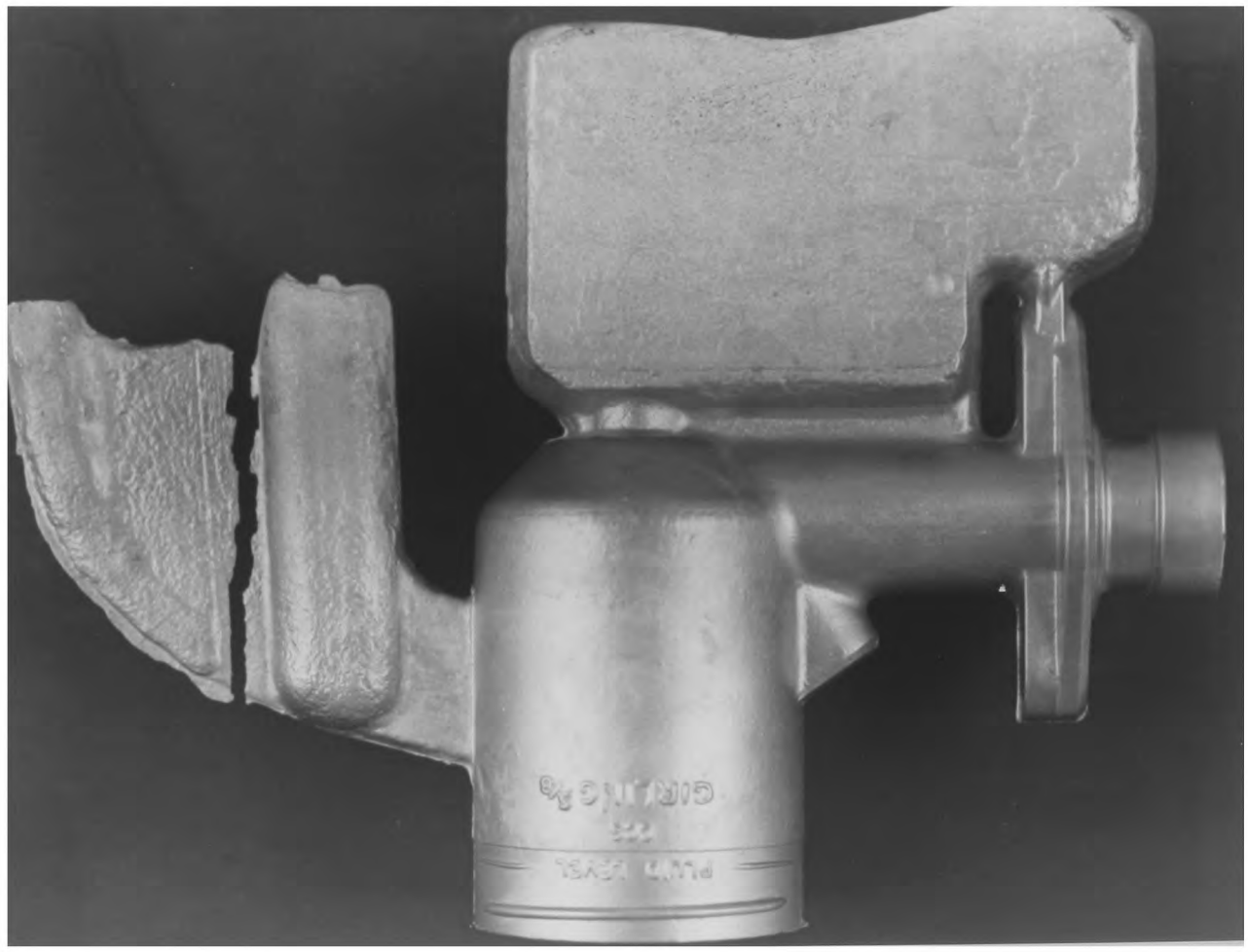
responsible for causing it. It seems likely that settling of equi-axed crystals was the mechanism responsible for the segregation in view of the large, coarse, equi-axed dendrites observed at the bottom of the casting. The segregation could not be explained by the gravitational interdendritic fluid flow mechanism. The operation of this mechanism in the casting would have led to segregation in the opposite sense to that observed, because in Al-Si alloys the density of the interdendritic liquid increases with increasing silicon content.[124] Liquid in the mushy zone would therefore have had a tendency to move downwards. The contraction flow of interdendritic fluid may possibly have been responsible for the segregation because of the directionality of the solidification from top to bottom in the casting. Presumably the application of pressure to the casting (typically 10 lbs/ins^2) would enhance the contraction flow mechanism by forcing liquid back into the mushy zone to feed solidification shrinkage.

There was no evidence of any inverse segregation in the samples taken through the rim of the casting.

3.2.4 Brake cylinder - gravity diecast (chill cast)

This casting was supplied complete with its risers as shown in fig. 3.5. The alloy specification was LM12 (Al-10Cu), the nominal copper content of the melt being 10.0 wt%Cu. The casting was produced by first pouring metal into riser 1 (fig.3.5) until the cavity was filled and the level of metal reached the top of the riser. A few seconds were then allowed for the thin section at the bottom of the riser to freeze off, at which point riser 2 was topped up with extra molten alloy. Exact freezing times were unknown but it was estimated[125] that the casting would have solidified within 20 seconds and the risers within 40 seconds. A graphite-coated steel die was used, with retractable steel cores forming the internal casting cavities.

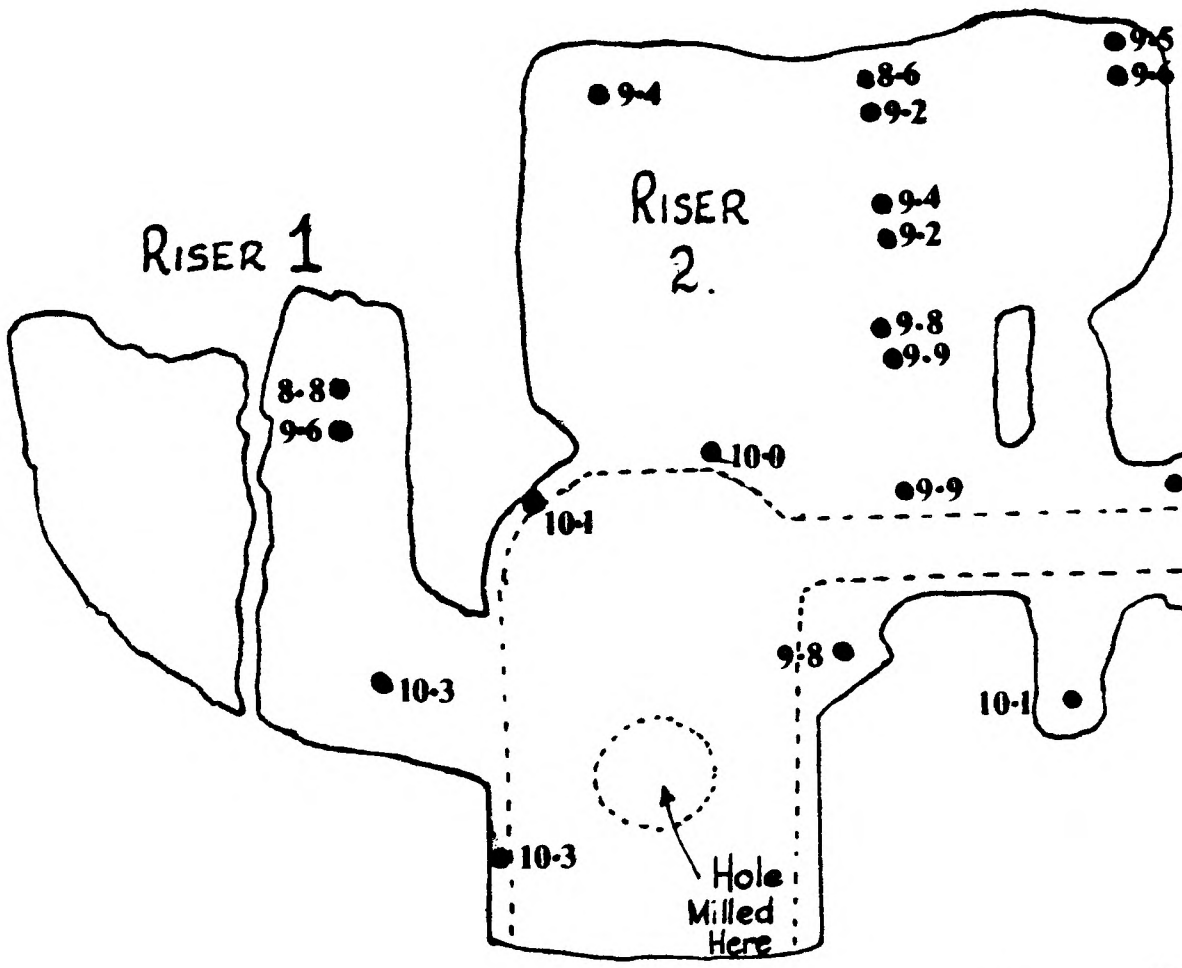
The macrostructure of the casting and risers consisted of fine equi-axed dendrites delineated by Al-Cu eutectic. The structure was relatively uniform



Macro - appearance of casting.

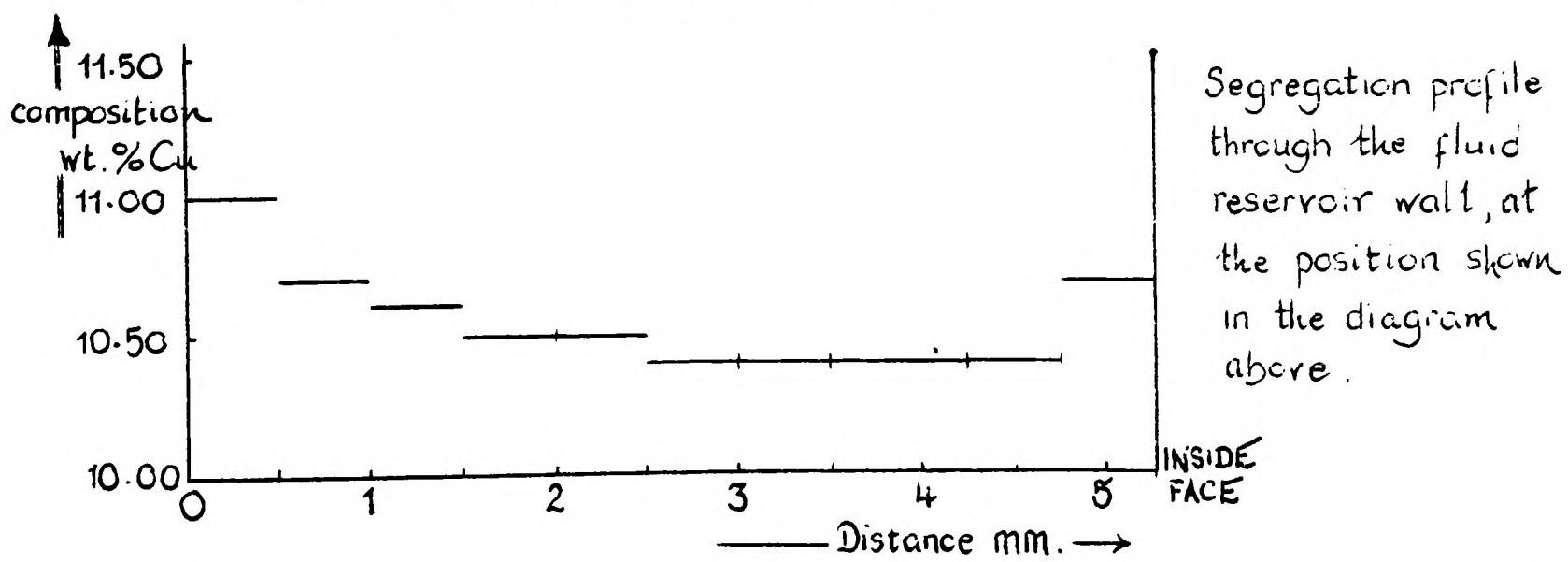
↑ Vertical

Magn x 0.5



Nominal Composition 10.0 wt% Cu

Composition data obtained from casting. Values given are in wt.% Cu.
Data are correct to ± 0.20 wt.% Cu.



Segregation profile through the fluid reservoir wall, at the position shown in the diagram above.

Fig. 3.5. Work performed on gravity diecast brake cylinder.

throughout the volume, although a certain amount of porosity was present at the top of both risers.

The composition analyses performed on the casting showed up two types of macrosegregation, as illustrated in fig. 3.5. There was a positive segregation at the outer surface of the fluid reservoir section of the casting, and there was a general vertical segregation in the risers and casting with solute-poor material at the tops of the risers and some evidence of solute enrichment in the casting beneath. The vertical segregation had every indication of being caused by gravitational driving forces. In Al-Cu alloys the interdendritic liquid becomes denser as the copper content increases and so would tend to sink and cause positive segregations towards the bottom of castings. In addition, the solute-poor aluminium dendrites tend to float in Al-Cu alloys with copper contents of greater than 10wt%Cu, [78,133] and so the equi-axed mechanism could have lead to the observed solute depletion at the tops of the risers. However, the short solidification time of the casting coupled with its observed uniformity of structure suggests that time-dependent, gravity-driven mechanisms could not have been responsible for the segregation. Instead it seems likely that it was caused by interdendritic fluid flow to feed solidification contraction in the casting. The way in which the two risers were successively poured would have meant that the casting would have frozen directionally upwards. Liquid would therefore have flowed down from the risers to feed contraction and this would have caused positive segregations in the casting due to the rapidly changing growth conditions. Towards the top of the risers at the last positions to freeze the mushy zone would have been contracting and there would have been insufficient liquid for complete feeding, thereby causing negative segregations in these regions.

The segregation observed through the thickness of the reservoir wall had the classical form of inverse segregation and was undoubtably another feature of the interdendritic fluid flow occurring in the casting. Solidification conditions would have been changing rapidly at this part of the casting. The

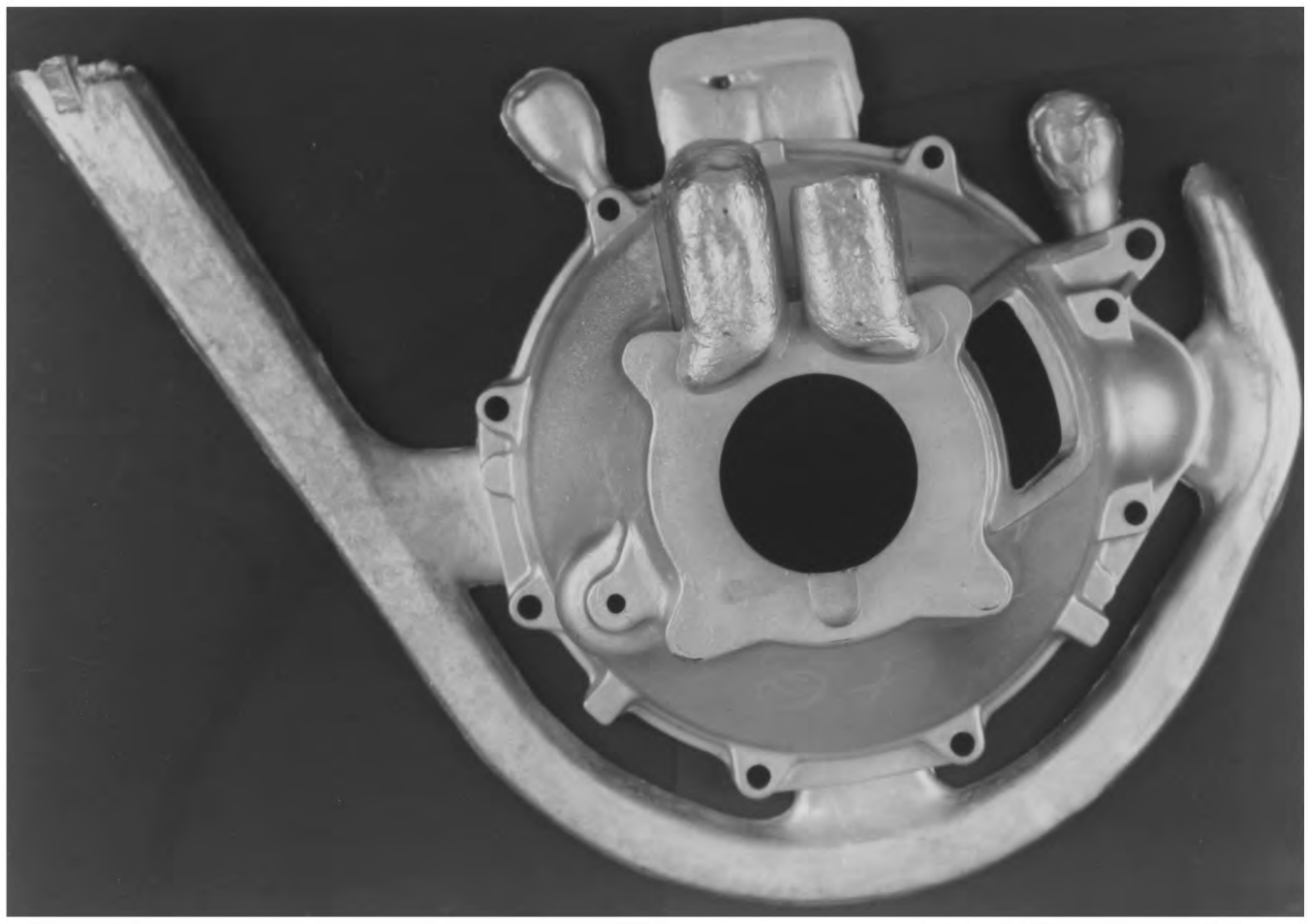
highest positive segregation was observed on the outside surface of the reservoir wall and so presumably growth advanced from the outer to the inner wall. The composition measured at the inner wall was also higher than the nominal melt composition, however, which is consistent with fluid flow occurring vertically downwards from the riser to completely feed contraction (positive segregation similar to centreline segregation).

3.2.5 Clutch housing - gravity diecasting

This casting was also supplied complete with its runner and riser systems, as shown in fig. 3.6. It was the largest casting examined, weighing approximately 8 kg., and was made from alloy LM6 (Al-11%Si). The nominal melt composition was unknown. The casting was almost hemispherical, and was cast in the vertical plane shown in fig. 3.6. Graphite-coated steel dies were used as the mould, the part-line being vertical and forming the back surface of the component and runner system. Retractable steel pins formed the holes around the perimeter of the casting, and the front half of the die split to allow ejection of the two risers on the central boss section. The section thickness of the casting was typically about 5mm, the maximum thickness being 15mm in the region around the central boss. Freezing time was estimated to be approximately 40 secs. for the casting and 60 secs. for the runner and risers.

The microstructure of the casting consisted mainly of un-modified Al-Si eutectic with a few small, primary, equi-axed, aluminium dendrites. No appreciable variation in the distribution of these dendrites was observed in the casting volume.

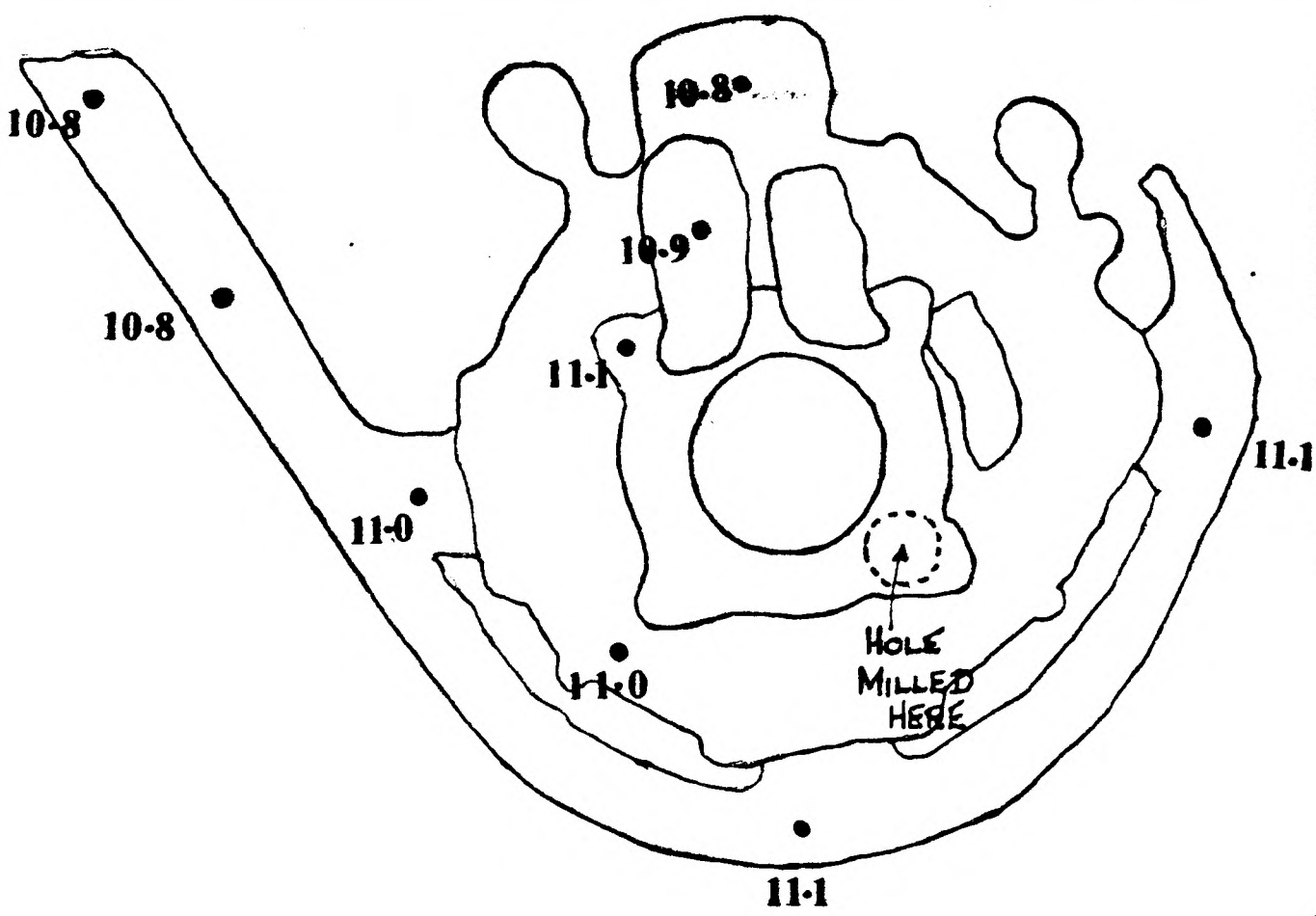
The silicon contents of the various samples taken from this casting are given in fig. 3.6. The average silicon content of these was 11.0 wt%Si. Only two of the sample compositions lay outside the error range of $\pm$ 0.35 wt% Si on this average composition. The casting as a whole was essentially uniform in composition, with some small negative segregations towards the tops of the runners and risers. There was some inverse segregation evident through the thickness of the casting adjacent to both mould walls. These segregations were



_Macro-
_appearance
of casting.

↑ Vertical

Magⁿ x 0.15



Average
Composition
determined as
11.00 wt % Cu.

Composition data obtained from casting. Values are given in wt. % Si.
Data are correct to ± 0·35 wt % Si

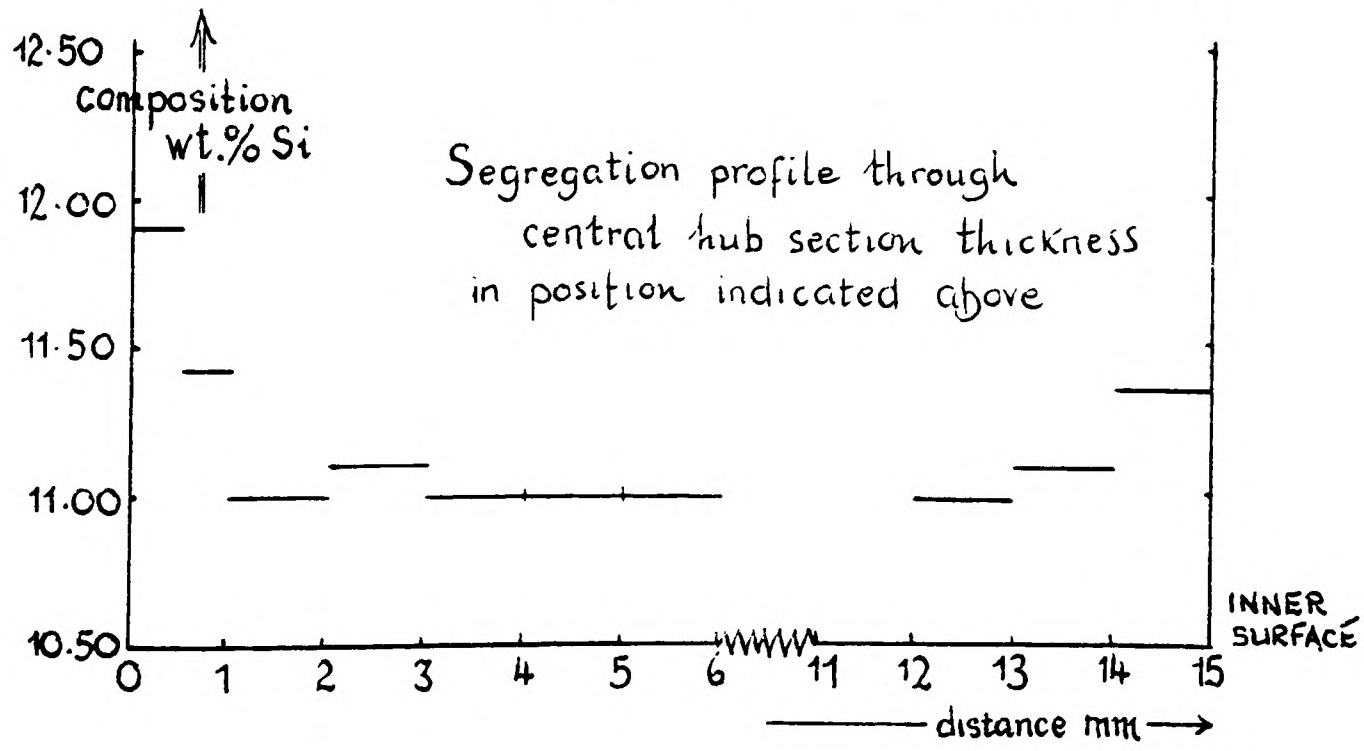


Fig. 3.6. Work performed on gravity-diecast clutch housing.

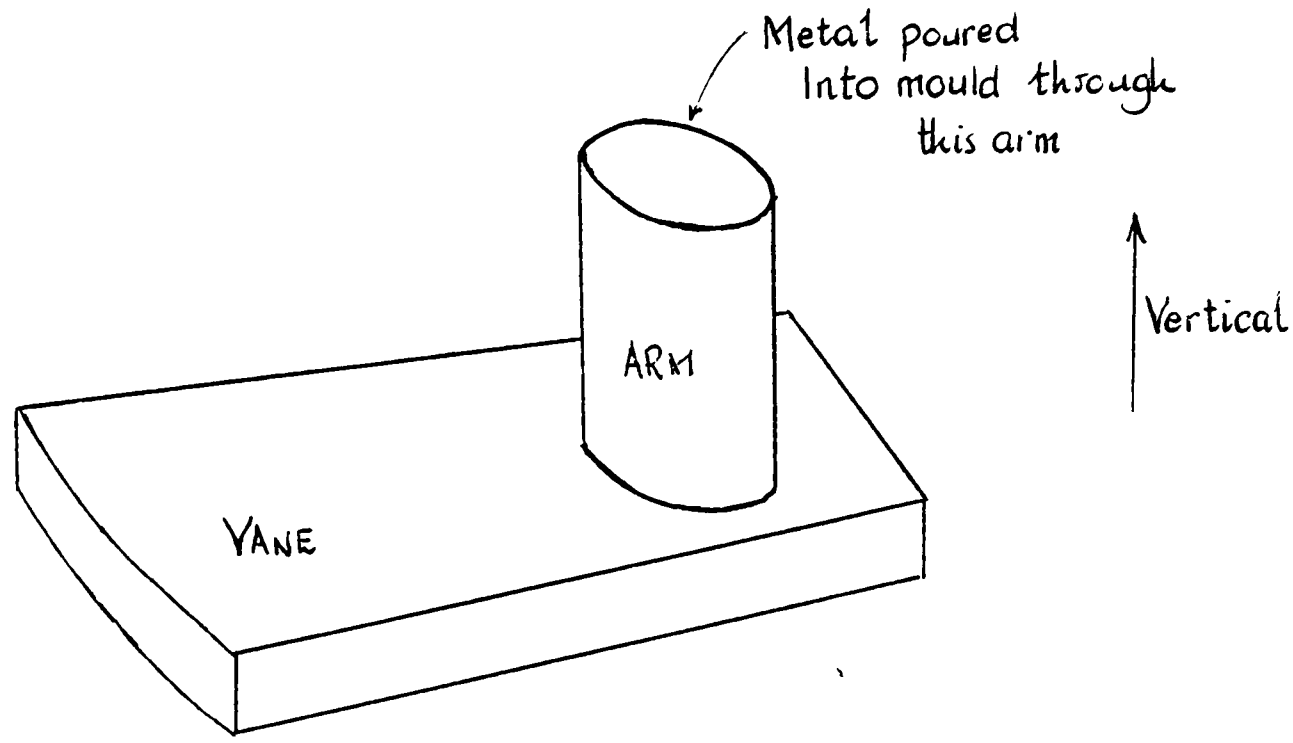
caused by the contraction flow mechanism as explained for the brake cylinder casting in the previous section. The magnitude of the vertical segregation observed in this casting was much smaller than in the brake cylinder for two reasons. Firstly, the runner and risers were so arranged that feeding occurred at several positions in the casting. Secondly, the alloy was very close to the eutectic composition thereby restricting the freezing range and giving little opportunity for interdendritic microsegregation and fluid flow.

3.2.6 Marine boat fitting - sand casting

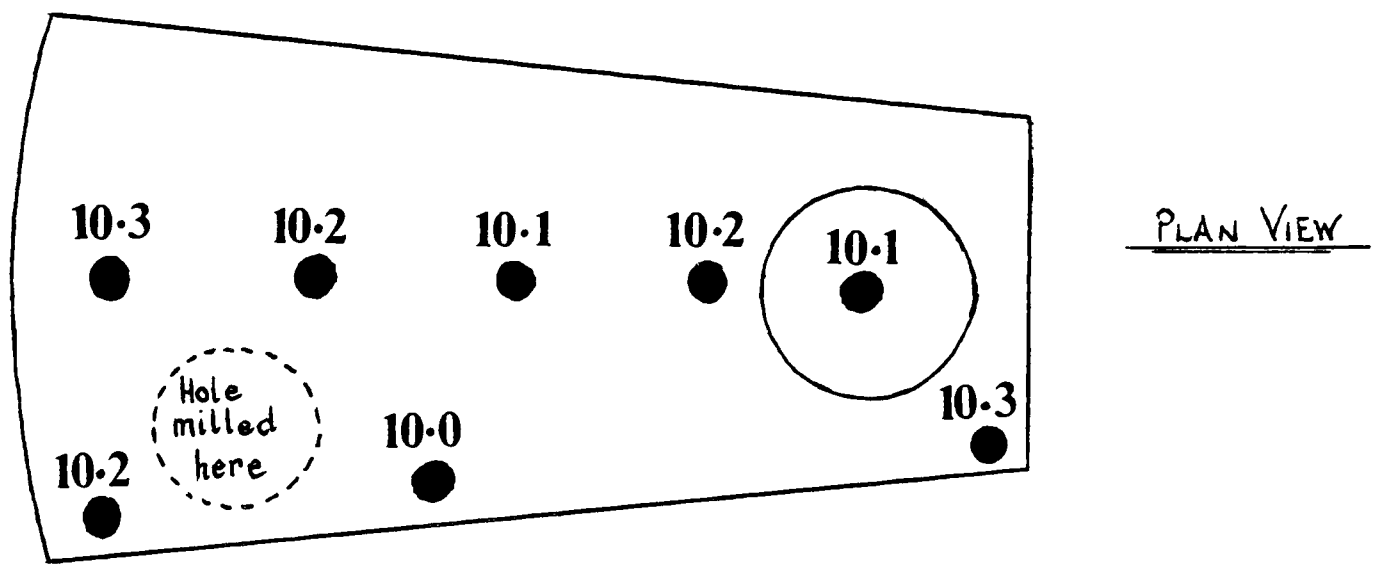
A schematic drawing of this casting is shown in fig. 3.7. The casting was some kind of boat fitting, and was made from LM 10 (Al-10 %Mg) which has good marine corrosion resistance. The nominal alloy composition was again unknown. The casting was quite small, weighing less than 200 grams, and had been made in a sand mould with its vane section horizontal. Pouring and feeding had been performed through the vertical arm of the component which had been machined off to size. It was estimated that the freezing time of the component would have been approximately 30 seconds.

The microstructure of the component consisted uniformly of fine, primary, equi-axed, aluminium dendrites with Al-Mg eutectic in the grain boundaries. The casting had been supplied in the as-cast condition.

It may be seen from fig. 3.7 that virtually no segregation was detected from the composition analyses performed on the casting. The average composition was 10.2 wt %Mg , and all the samples lay within the error range of this value. This is not surprising in view of the small size of the casting which would have minimised gravitational mechanisms. The contraction flow mechanism would also have been less important in this casting than in the two previous ones described because the sand mould would not have caused such large fluctuations in solidification conditions as the metal dies. There was, in fact, some small amount of inverse segregation present adjacent to the mould walls, as shown in fig. 3.7.

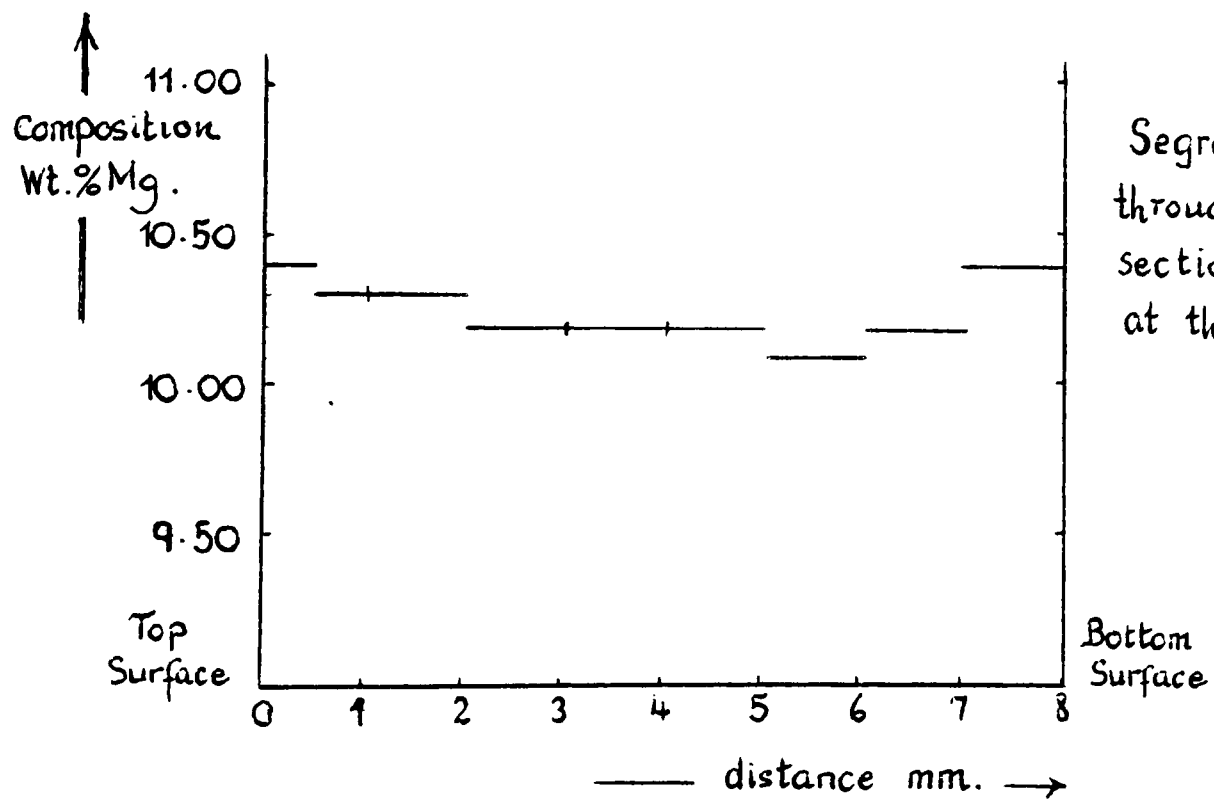


SCALE 1:1



PLAN VIEW

Composition data obtained from casting. Values given are in wt.%Mg.
Data are correct to ± 0·2 wt.% Mg



Segregation profile through the vane section of the casting at the position shown.

Fig.3.7. Work performed on sand cast marine fitting.

3.2.7 Transverse slices from semi-continuously cast ingots

Three slices were examined from three separate ingots. Two of these were Al-Cu alloys and the other was an Al-Zn-Mg alloy. The semi-continuous casting process employed at Alcan is shown schematically in fig. 3.8(a). Ingots approximately 5 metres in length were produced, and these slices were taken from roughly mid-length. The growth of material within them should therefore have been at 'steady state' and not subject to end-transient growth conditions. The depth of the liquid pool and mushy zone during growth of the ingots depends on liquid metal superheat, cooling rate at (and below) mould surface, withdrawal rate of floor (and hence of ingot), and alloy system and composition. Exact figures were not available for the first three of these variables in the ingots examined, but according to Alcan[125] they would have been arranged such that the mushy zone took around 2 minutes to grow past a given transverse plane in the ingots during steady state growth.

The Al-Zn-Mg slice examined was circular in cross-section, of radius 147 mm and thickness 25 mm.. The macrostructure of the ingot slice consisted mainly of fine equi-axed aluminium dendrites with a skin of columnar dendrites extending in from the circumference to a depth of approximately 5 mm.. The results of the composition analyses performed on it are shown in fig. 3.9. Clearly the majority of the ingot section was homogenous with all the radial analyses lying within the experimental error range of the nominal zinc content of the alloy, 3.95 ± 0.10 wt %Zn. The samples milled in from the edge of the slice showed a marked positive segregation at the outer surface of the ingot. This segregation had a maximum value of 7.00 wt %Zn but extended for only $1\frac{1}{2}$ mm. into the ingot before the nominal composition was re-attained. The microstructure at the surface of the ingot is shown in fig. 3.9(c). It may be seen from this photograph that the solute-enrichment corresponded to the layer of eutectic material at the ingot surface. This was presumably exuded as the shell of the ingot reheated once it had dropped below the water-cooled mould ring. The driving force behind the exudation could either have been the

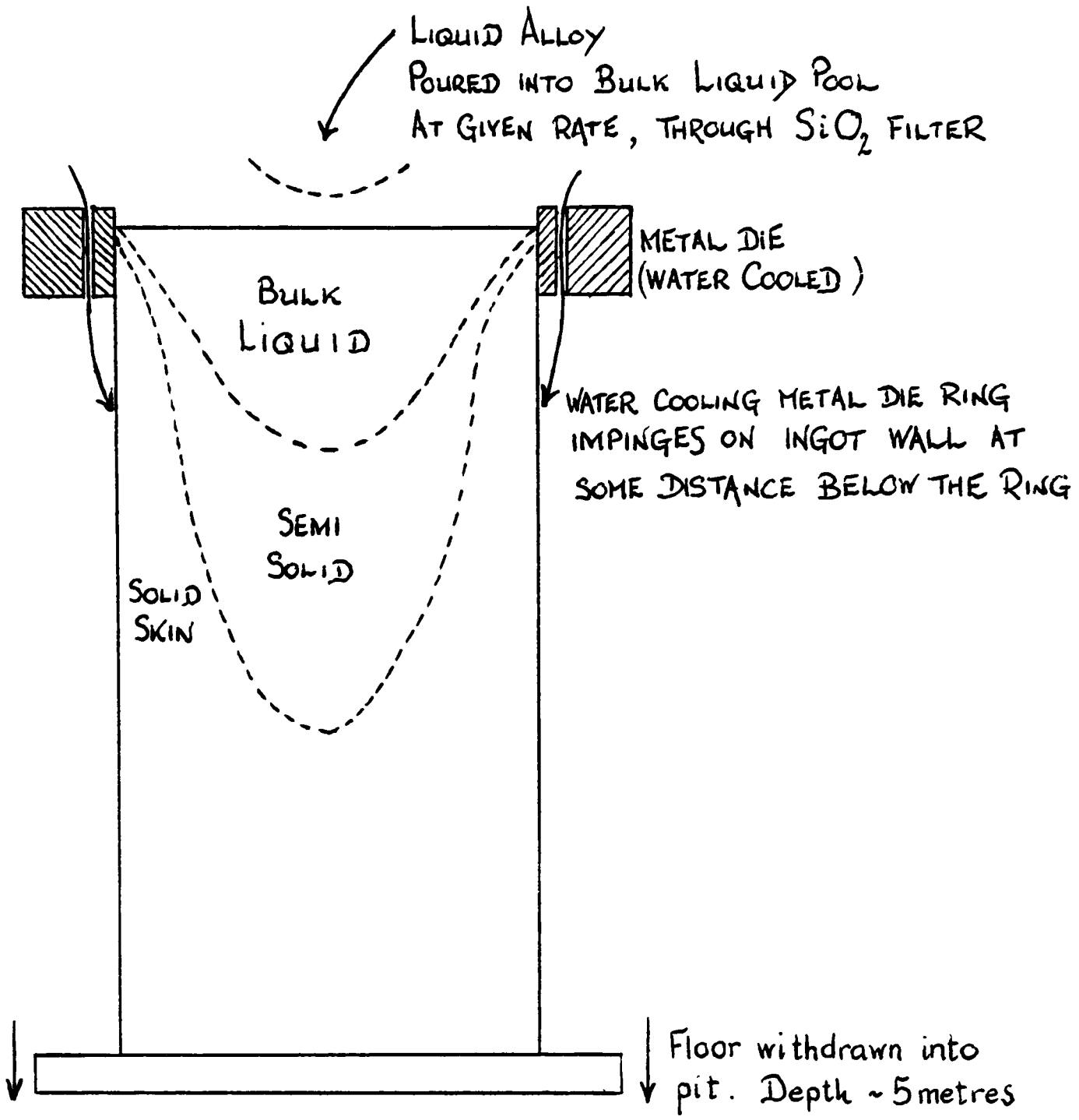


Fig 3.8(a). General schematic representation of semi-continuous casting process employed at Alcan, Banbury.

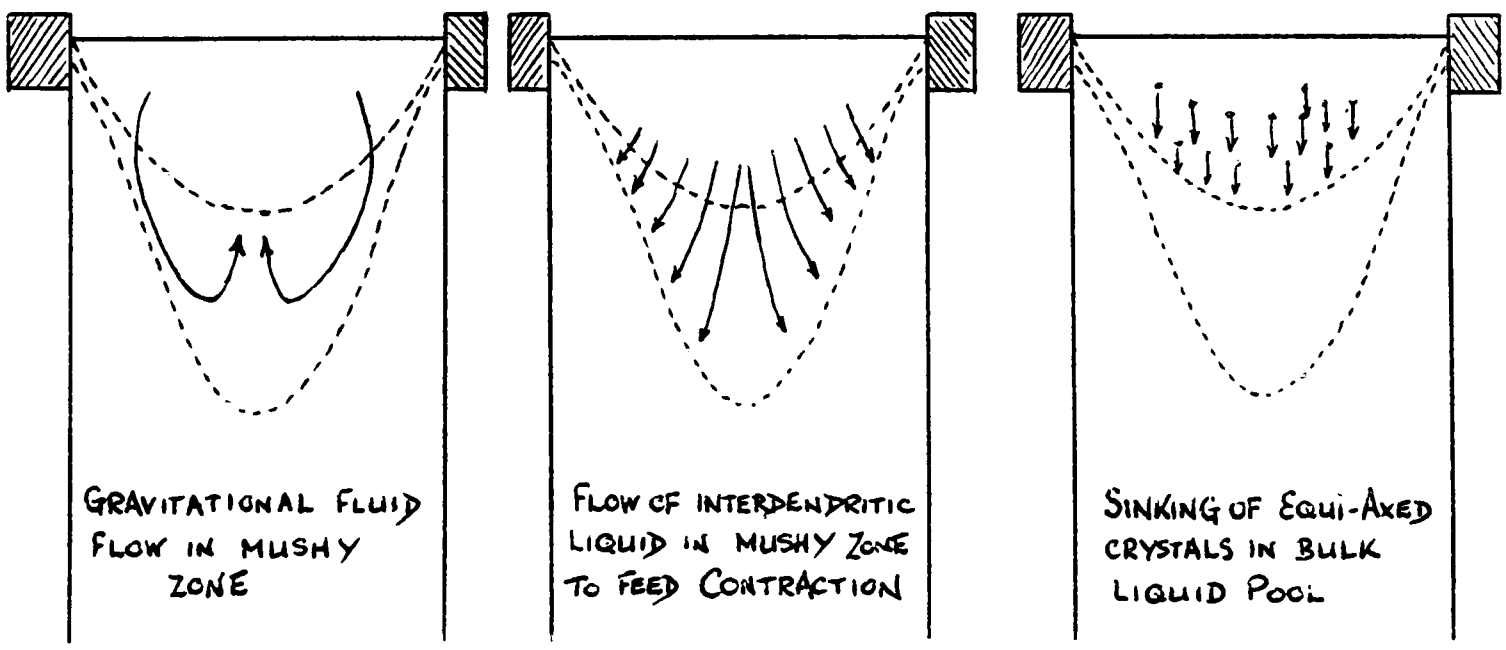


Fig 3.8(b). Possible mechanisms for macrosegregation in semi-continuously cast ingots.

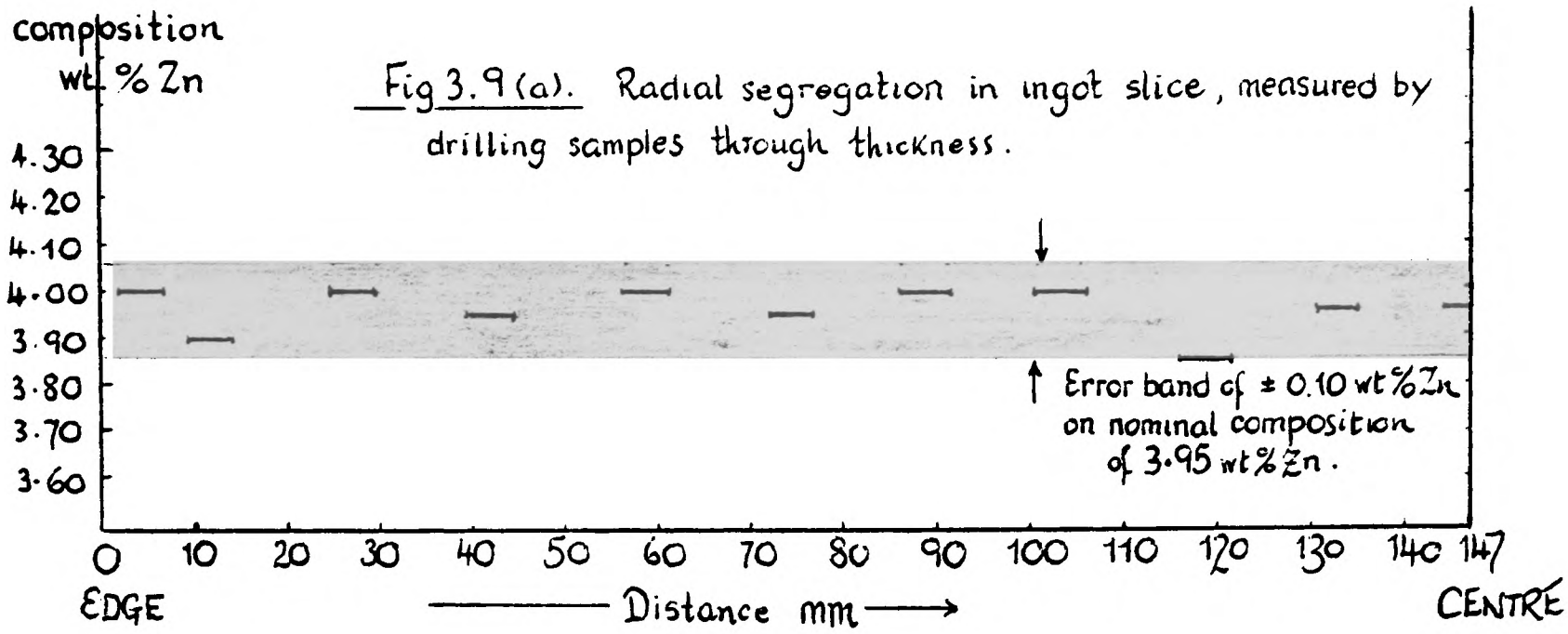


Fig 3.9 (a). Radial segregation in ingot slice, measured by drilling samples through thickness.

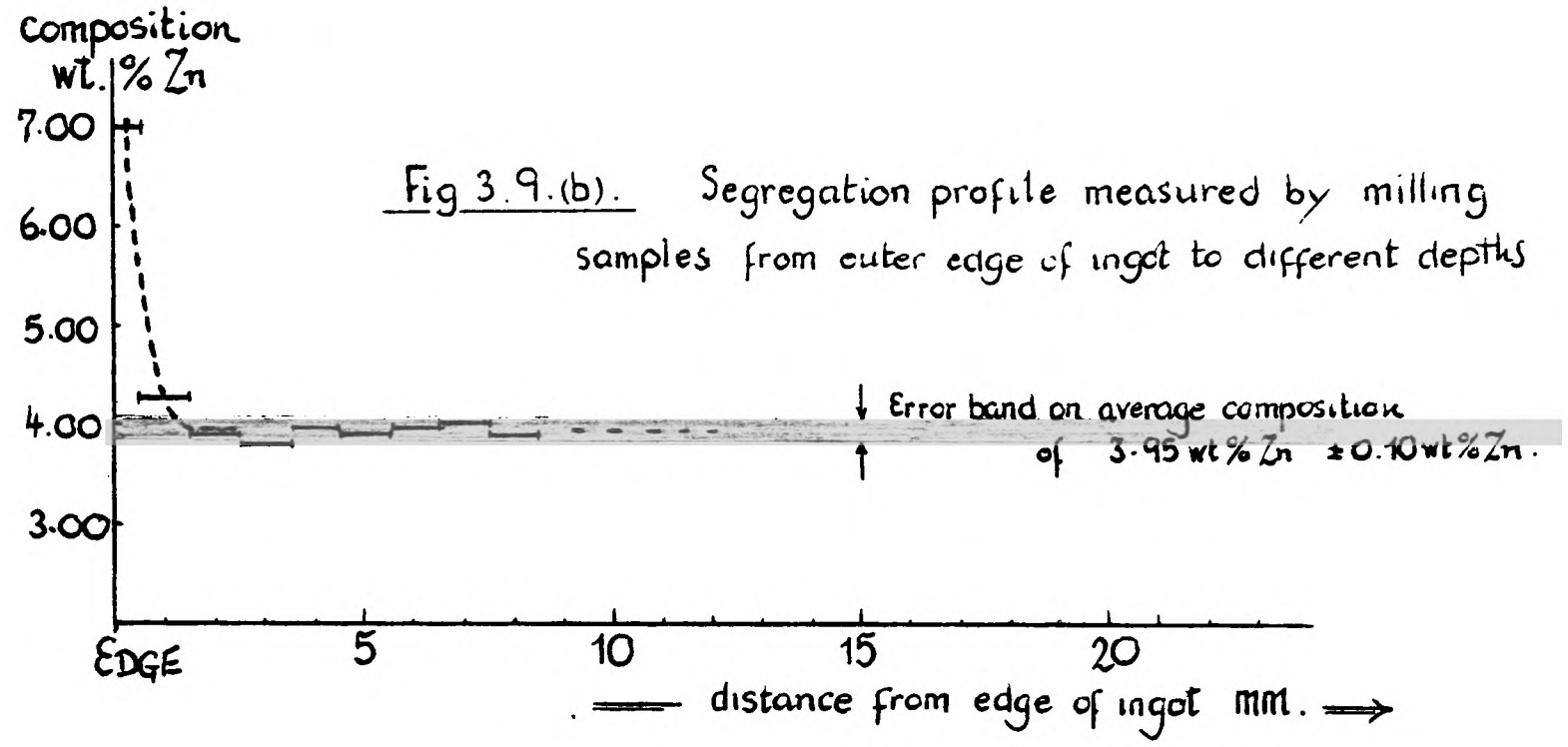


Fig 3.9. (b). Segregation profile measured by milling samples from outer edge of ingot to different depths

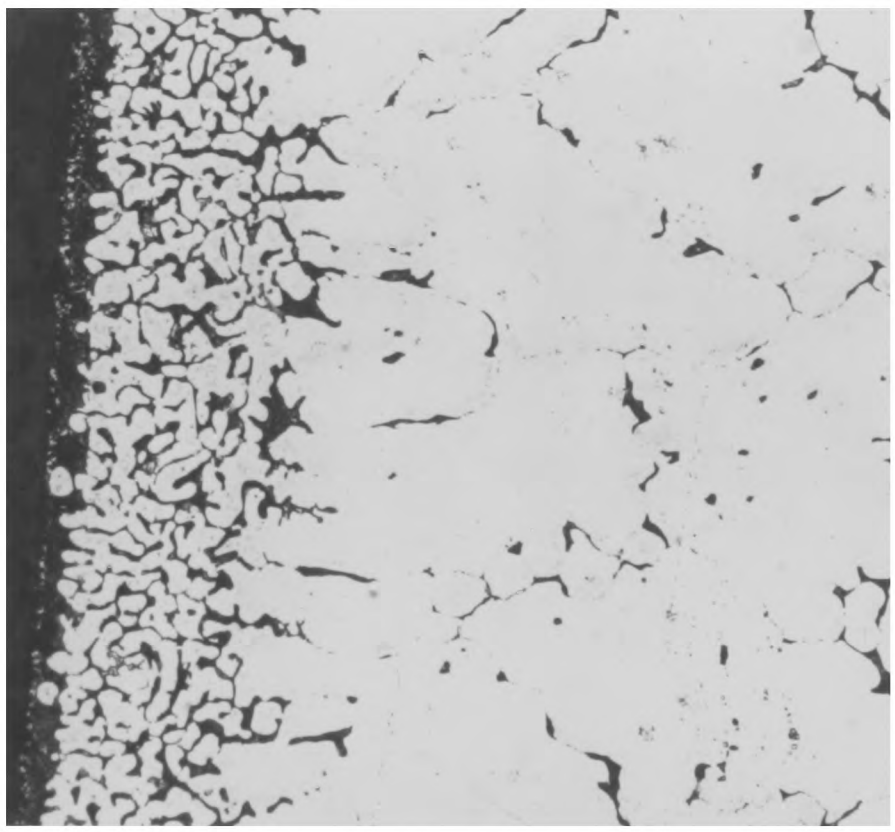


Fig. 3.9 (c). Etched microstructure at surface of ingot showing the layer of exuded, solute-rich eutectic material.

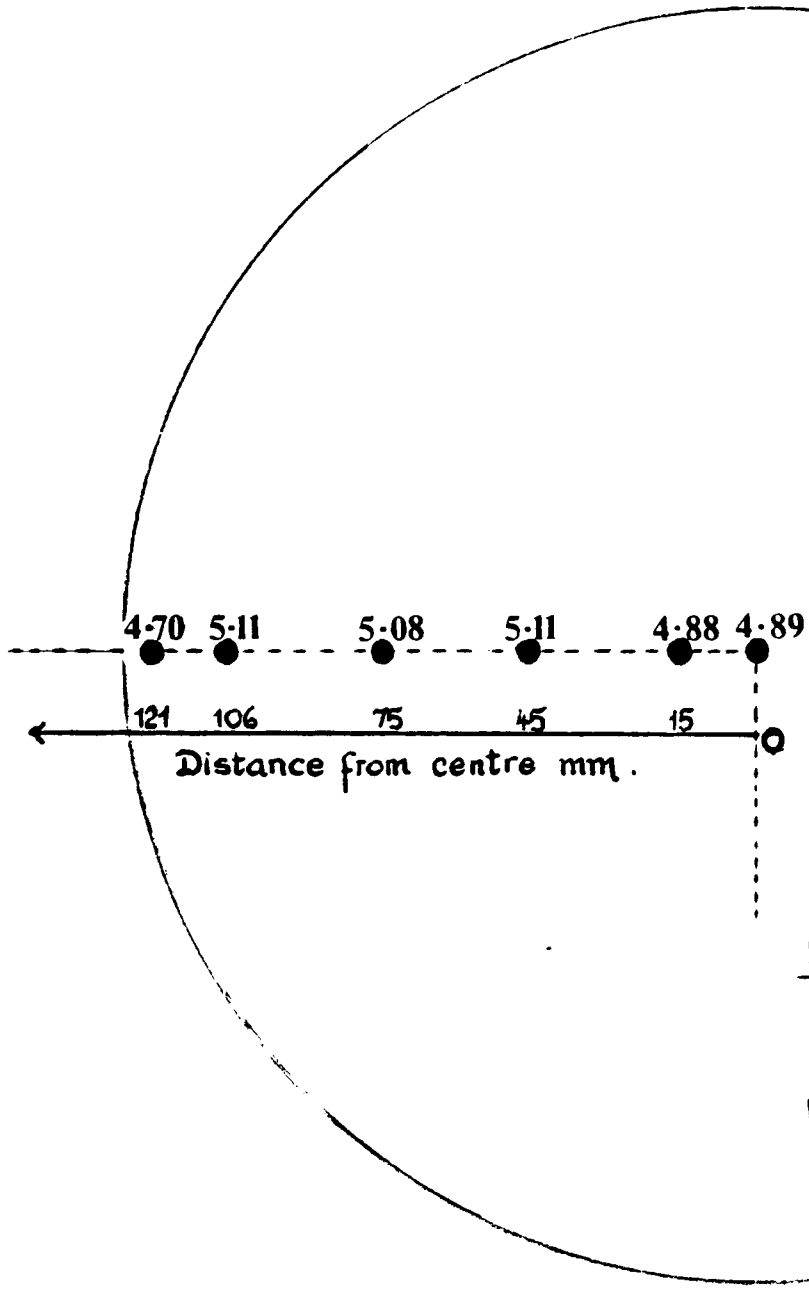
Magn x 50

Fig. 3.9. Work performed on Al-Zn-Mg slice from semi-continuously cast ingot. (circular section)

expansion pressure of the remelting interdendritic liquid, or the hydrostatic pressure of the liquid in the bulk liquid pool above. The segregation was far too sharply defined to have been caused by the contraction fluid flow mechanism.

An Al-Cu ingot slice of circular cross-section and similar dimensions to the Al-Zn-Mg slice was also studied. The macrostructure of this slice was similar to that of the Al-Zn-Mg slice, the equi-axed dendrites being somewhat coarser and the columnar zone extending up to 10 mm. into the ingot section. The nominal copper content of the alloy was 5.04 wt% Cu.[125] The results of the composition analyses performed on this ingot slice are given in figure 3.10. There was a layer of solute-rich, exuded eutectic at the surface of this ingot slice, similar to that observed in the Al-Zn-Mg slice. The maximum solute enrichment was measured as 8.00 wt % Cu in a layer up to $\frac{1}{2}$ mm. below the surface, and the solute-enriched region extended for approximately 3 mm. into the ingot. There was also some more general segregation across the radius of this ingot slice. The pronounced negative segregation detected at a distance of 7 mm. from the ingot surface could have been caused by a number of mechanisms. It is consistent with gravitational interdendritic fluid flow of copper-rich liquid down through this outer columnar skin. It could also be explained by contraction fluid flow in the mushy zone, in connection either with a general feeding pattern from centre to edge (see fig. 3.8(b)), or with a rapid change in heat transfer conditions as when the water jets impinged on the outer surface of the ingot (banding). The slight negative segregation observed towards the centre of the ingot section could also have been caused by the contraction flow of interdendritic fluid from centre to edge. Another possible explanation for this segregation is the sinking of solute-poor, equi-axed dendrites through the bulk liquid pool to the bottom central region of the ingot, see fig. 3.8(b).

The third ingot slice to be examined had a rectangular cross-section as shown in fig. 3.11. The alloy had a composition similar to A.A. 2017 (Al-4% Cu), with a nominal copper content of 4.01 wt %Cu. The slice had a columnar outer



Composition data given in wt. % Cu. to an accuracy of ± 0.13 wt % Cu

INGOT SLICE was circular section with 128 mm. radius and 20 mm thick.

Nominal composition quoted as 5·04 wt % Cu

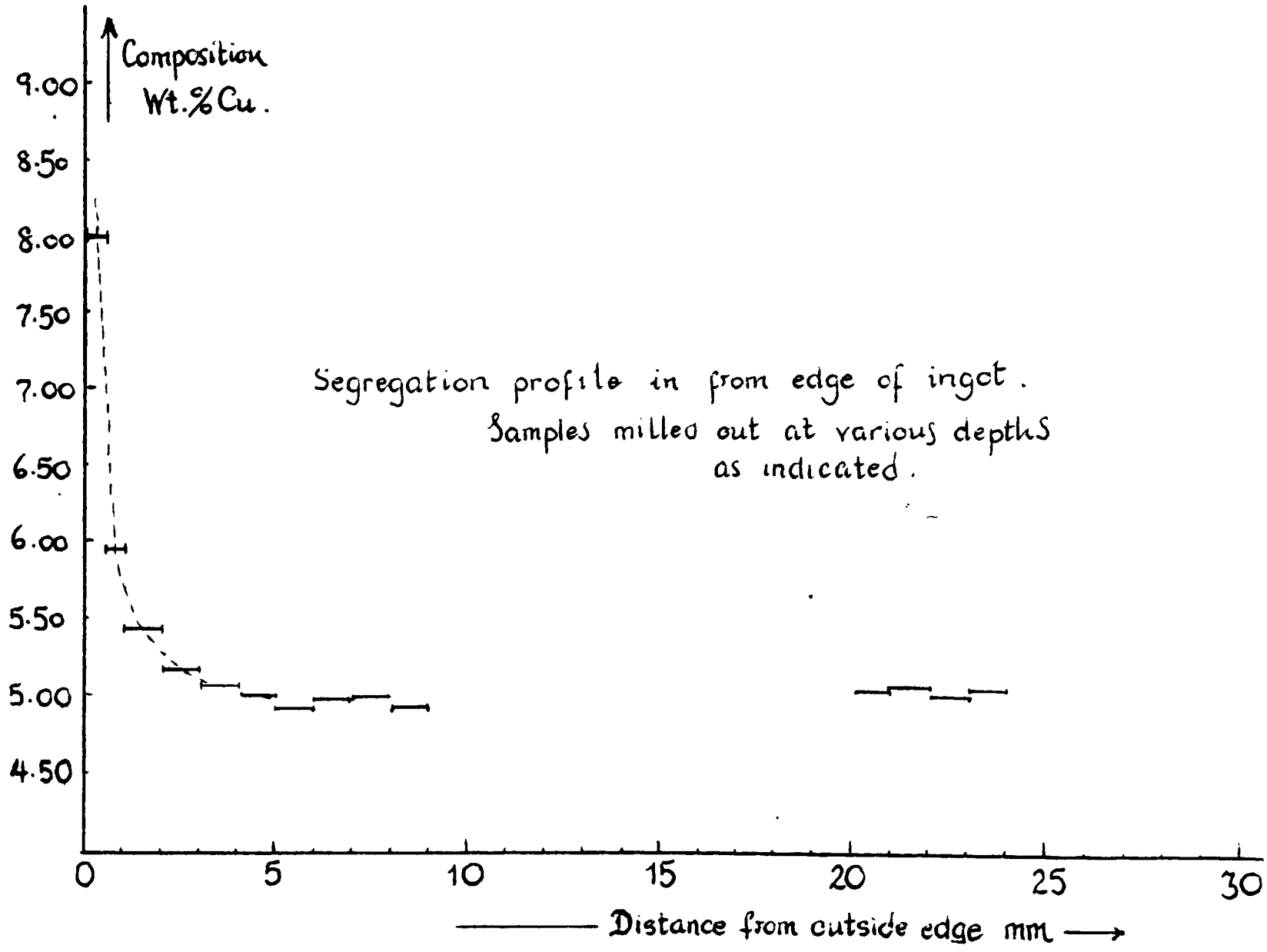


Fig 3.10. Work performed on semi-continuously cast Al-Cu (circular section) ingot slice.

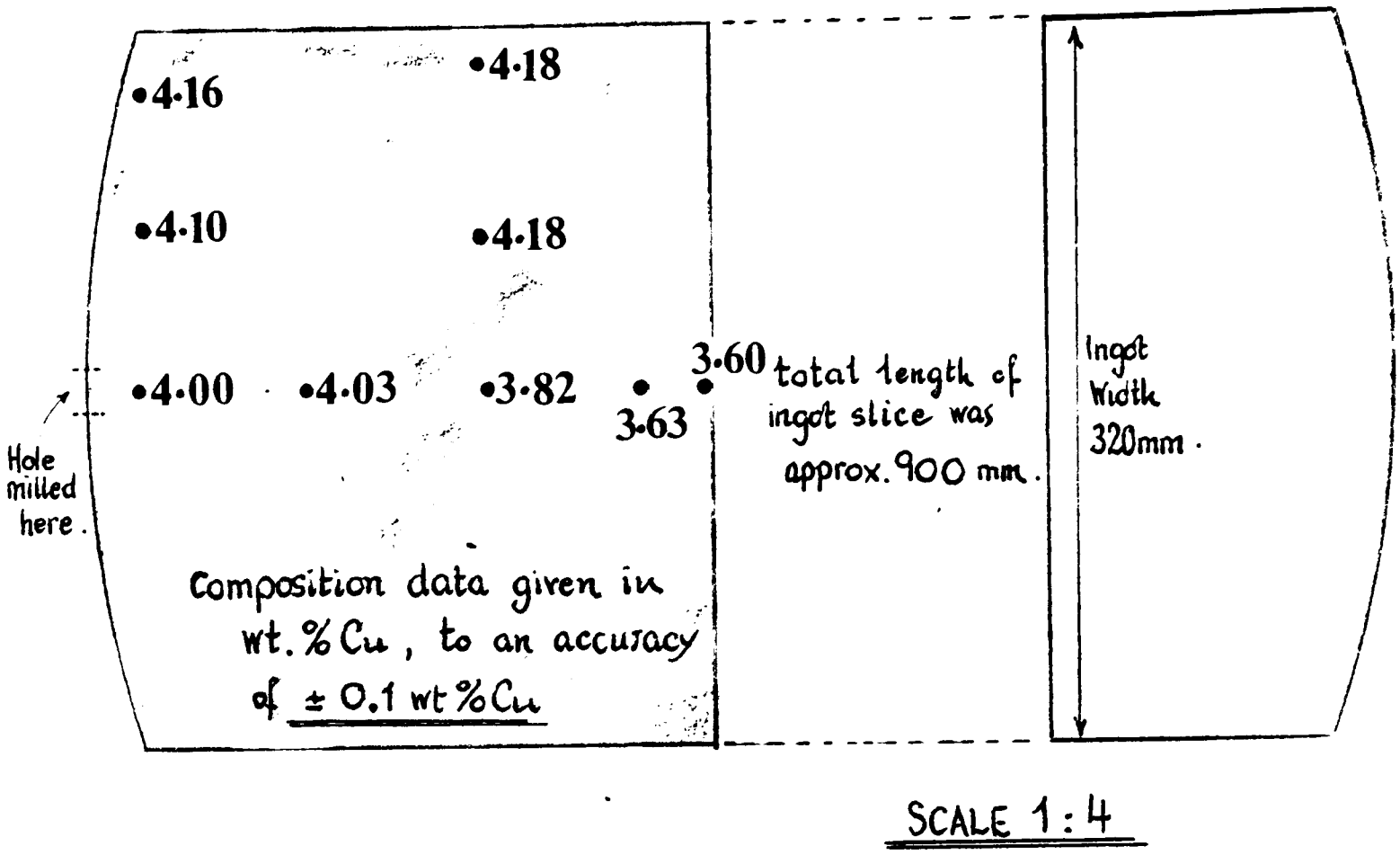


Fig. 3.11(a). Composition data obtained from samples drilled down through thickness of slice in the positions shown above. Shaded portion was piece supplied by Alcan. Nominal alloy content was 4.01 wt % Cu.

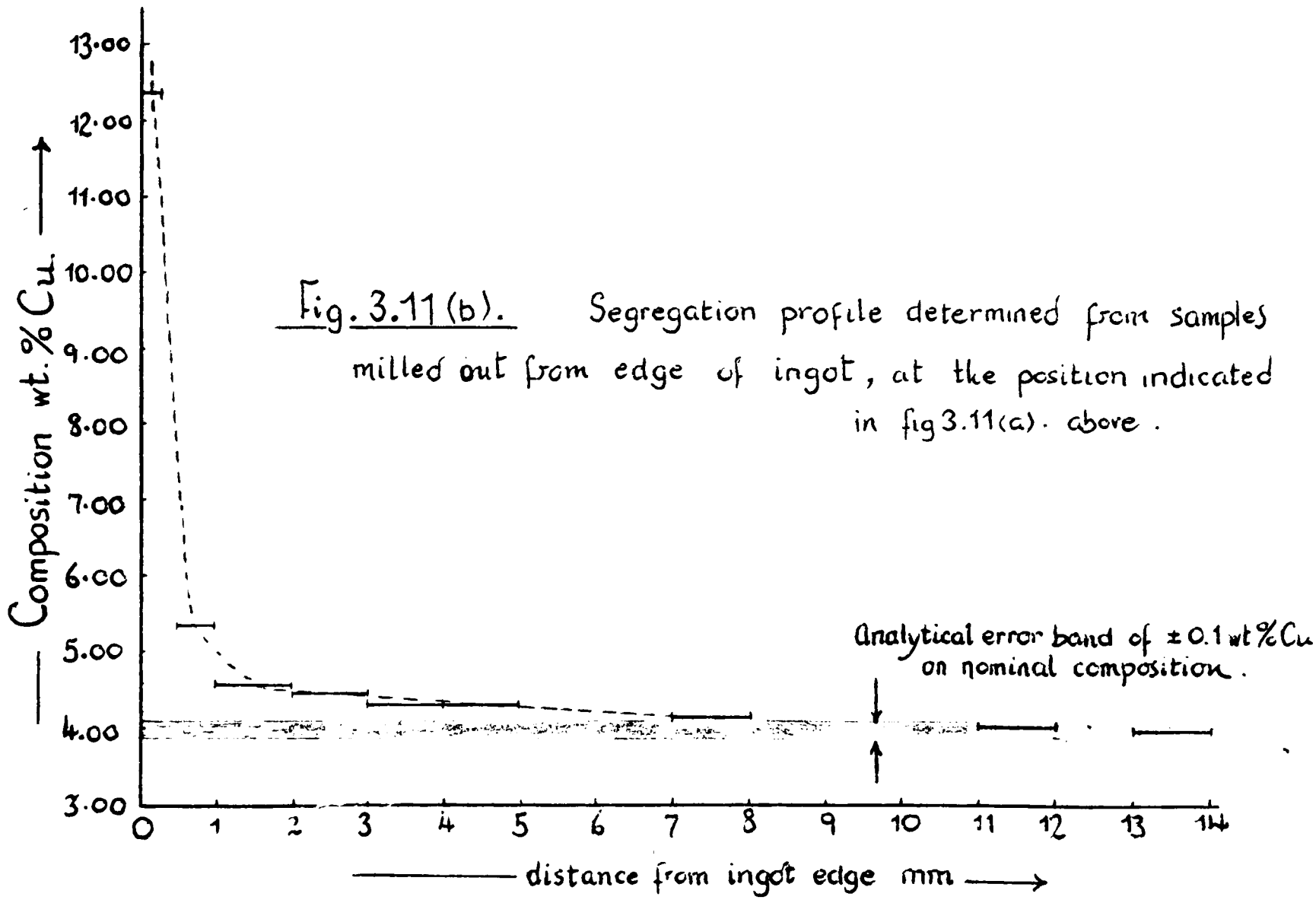


Fig. 3.11(b). Segregation profile determined from samples milled out from edge of ingot, at the position indicated in fig 3.11(a). above.

skin extending up to approximately 25 mm. into the section with a core of moderately fine equi-axed dendrites. The composition measurements made on the ingot are shown in fig. 3.11(a) and (b). Once again there was a layer of solute-rich exuded eutectic material at the surface of the ingot. A fine skim taken from the surface to a depth of 0.25 mm. showed a copper concentration of 12.4 wt % Cu. This is far too high for inverse segregation due to solidification contraction fluid flow and so must have been caused by exudation mechanisms. The solute enriched zone extended up to approximately 8 mm. below the ingot surface. The solute depletion observed towards the centre of the ingot section could have been caused either by contraction flow of liquid in the mushy zone,or sinking of solute-poor, equi-axed dendrites in the bulk liquid pool, as mentioned for the other Al-Cu ingot section examined. The relatively large magnitude of the negative segregation at the centre of this ingot coupled with the larger size of the ingot suggested that the time-dependent, equi-axed mechanism may well have been responsible for its formation. Gravity flow of interdendritic liquid would have produced segregation in the opposite sense at the ingot centreline and so could not have been operating as a major macrosegregation mechanism in this ingot.

3.2.8 Gas turbine blade - investment casting

The blade examined is shown in fig. 3.12(a). It was intended for use in the Rolls-Royce 'Olympus' jet engine, but had been scrapped because of a 'mould inclusion' in the blade root. The blade was made by Rolls-Royce Ltd. at their investment foundry in Bristol. It was cast as part of a 'tree' of four ceramic moulds which were arranged vertically around a central sprue. Feeding was uphill through the thick blade root section which was at the bottom of the moulds. The alloy employed was a nickel base superalloy, IN-100, with the nominal composition given in fig. 3.12(b). This was cast at a temperature of around 1450°C under vacuum into the ceramic mould arrangement which had been preheated to a temperature of around 1000°C. The mould arrangement was then immediately removed from the furnace and allowed to cool in air.

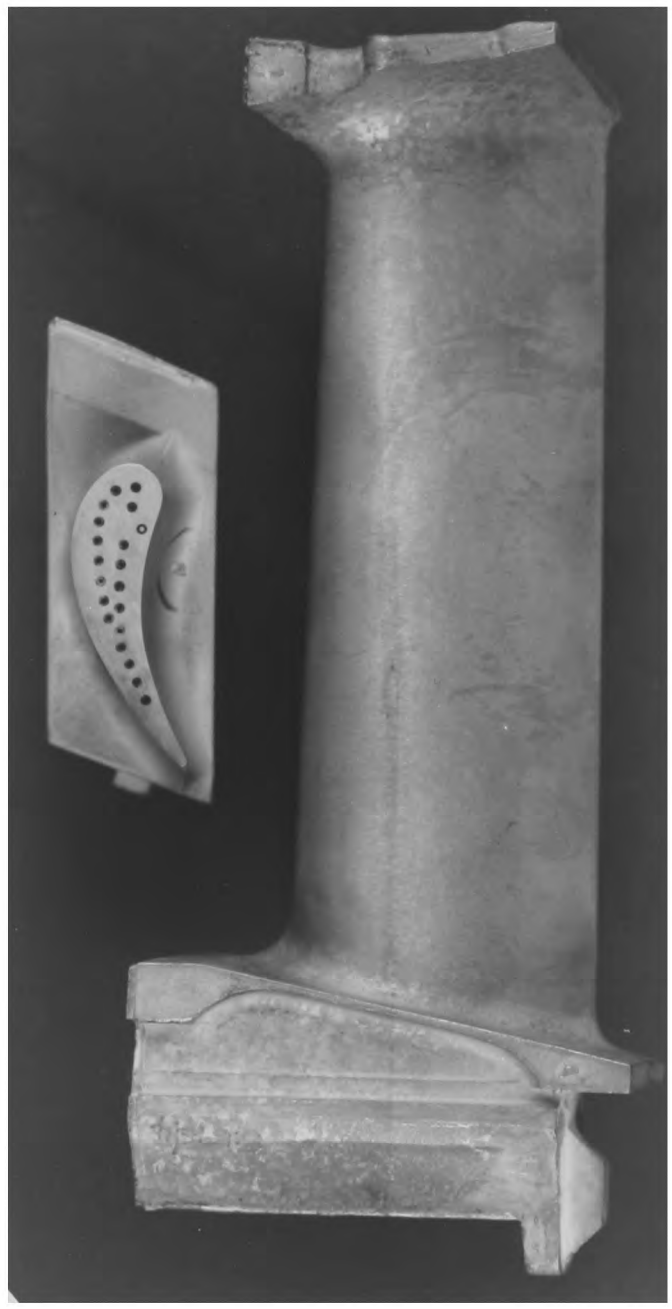


Fig 3.12 (a).

Macro - appearance of turbine blade casting.

A section taken through the aerofoil part of the blade is shown alongside.

Magn x 0·5

Vertical

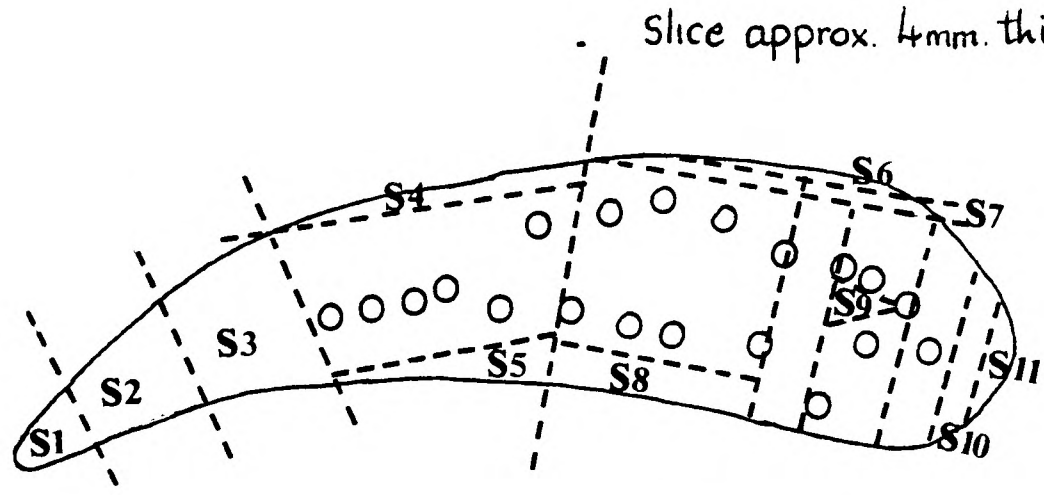


Fig. 3.12(b). Positions of sample cuts made in transverse slice through aerofoil.

TABLE 3.2

Nominal solute contents of alloy :- Co - 15·5 wt%
Cr - 9.1 wt %

Element	Composition Wt %											Errors
	S1	S2	S3	S4	S5	S6	S7	S8	S9	S10	S11	
Cobalt	15.8	16.1	16.3	16·1	15.9	16·7	17·0	15.5	13·3	14.0	14.5	± 0.2 wt%
Chromium.	5.8	5.9	6.0	5.9	6.1	6·0	6·2	5·8	4.6	5.4	5.6	± 0.1 wt%

Thermocouples were positioned at mid-section along the height of one of the blades in the tree. These showed that freezing was directional from top to bottom of the blade (as shown in fig. 3.12(a)). The top part of the blade vane was completely solid within 40 seconds, while the lowest (and thickest) part of the vane took approximately 2 minutes to solidify. The thick blade root section took around 5 minutes to freeze. Alloy liquidus temperature was determined as 1330°C with a freezing range of approximately 90°C.

The superalloy was found to be very hard and almost impossible to machine, which made it very difficult to obtain samples for metallographic study and chemical analysis. A carbide cut-off wheel had eventually to be used to obtain thin transverse slices through the blade section at various positions along its length. Some of these slices were then macro-etched in aqua-regia to reveal the grain structure, and others were slit into several pieces on a fine diamond rotary wheel for chemical analysis. The positions of the cuts made in one of the transverse slices taken from the middle of the blade length are shown in fig. 3.12(b). These samples were analysed for cobalt and chromium since these were not only the two major alloying elements of the superalloy but also the most easily analysed using the spectrophotometer technique. The results of the analyses performed on the samples are given in Table 3.2., below fig. 3.12(b). These show a definite negative segregation at the centre of the blade section and towards the outer surface at the leading edge of the blade, with a more general and less severe positive segregation towards the trailing edge of the blade and around its outer surface. This 'inverse' type of segregation is consistent with the operation of the contraction flow mechanism, particularly since the macrostructure of the blade consisted of coarse columnar crystals which extended from the edge to the centre of the blade section. Equi-axed mechanisms could not therefore have been responsible for the segregation observed. In view of the complexity of the alloy it is difficult to predict whether gravitational interdendritic fluid flow could have been responsible for the segregation in the sense observed, but the

relatively short freezing time of the blade section would suggest that this mechanism could not have produced it.

It should be noted that the chromium figures quoted in Table 3.2. are considerably lower than the nominal chromium content of the alloy. This was presumably caused by one of the other alloying elements interfering with the chromium ions in the analysis technique (see Chapter 9). Trials showed that neither nickel nor cobalt were responsible for the interference, and it was felt that a further, more complete, study was not worthwhile in view of the alloy complexity. Furthermore the chromium analyses reproduced the behaviour of the cobalt analyses and so presumably the extent of the interference was similar in each sample.

Finally it should be noted that the binary phase diagrams for the Ni-Co and Ni-Cr systems, shown in fig. 3.2., both exhibit very limited freezing ranges for the alloy contents of this material. This would ordinarily suggest that macrosegregation should be rather small in such systems. However the appreciable amount of cobalt and chromium segregation observed in this blade presumably mean that the freezing ranges have been extended by the complex nature of this alloy, and that appreciable amounts of interdendritic liquid were present in the columnar zones during freezing.

3.2.9 Summary of work performed

The scope of the present work on macrosegregation in industrial castings and ingots was unfortunately far more limited than had originally been envisaged. The response of the various industrial organisations contacted was very disappointing, with the notable exceptions of Alcan and Rolls-Royce. This lack of interest probably reflects the apathy (or ignorance) which the metallurgical profession and industry show towards the phenomenon of macrosegregation. Indeed it seems that most people in industry never regard an alloy as being anything other than homogenous!

In spite of the poor response a wide range of casting processes were covered, although admittedly only in aluminium-base and nickel-base alloys.

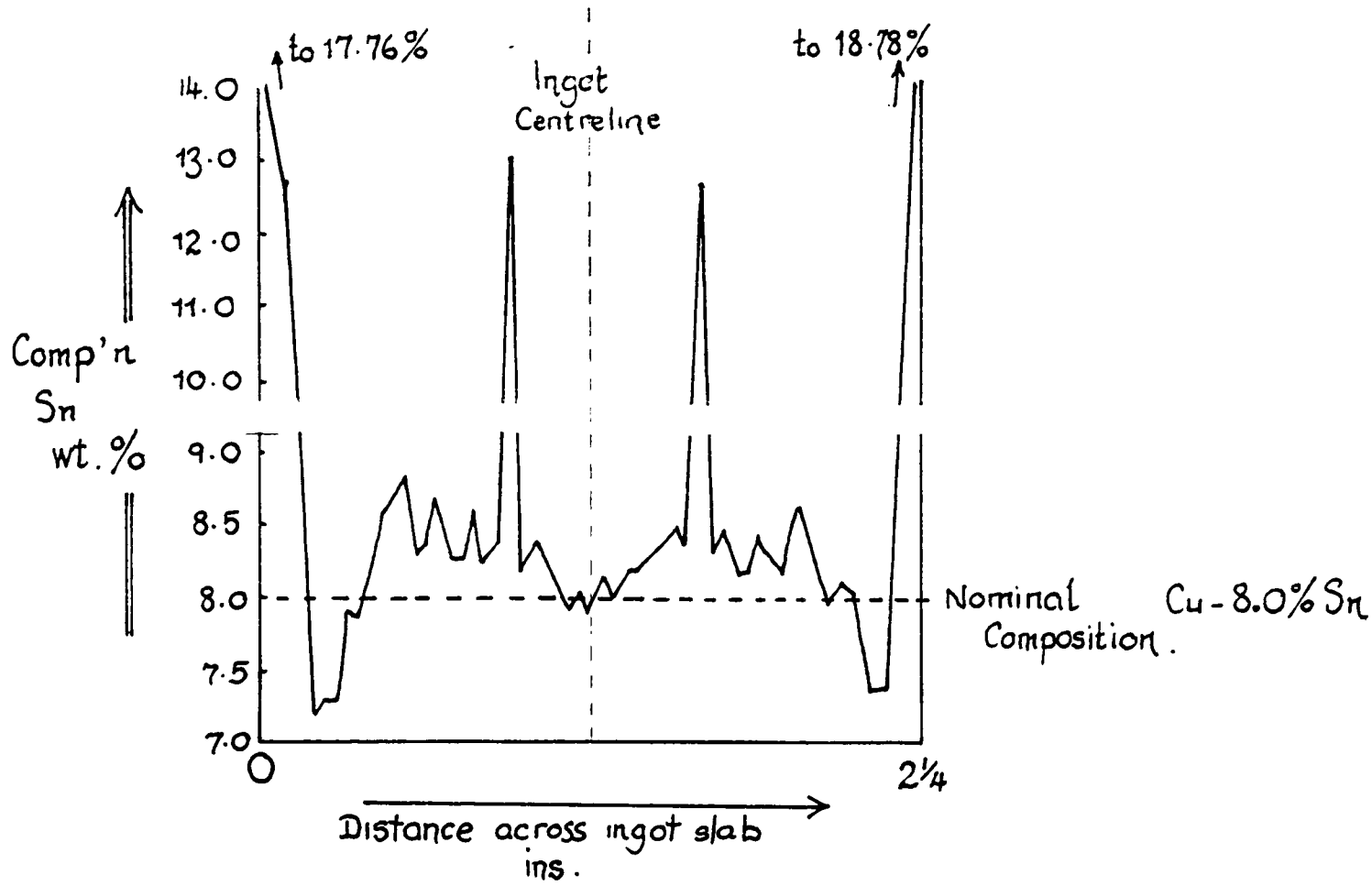
Inverse segregation and other manifestations of the contraction fluid flow mechanism were present in most of the castings examined except for the low pressure diecast wheel and the sand cast marine fitting. Exudations were present on the surface of all three semi-continuously cast ingots due either to the expansion pressure of remelting interdendritic liquid or to the hydrostatic pressure exerted by the bulk liquid pool. There was little evidence of gravitational interdendritic fluid flow having occurred in the castings, although it may possibly have operated in the chill-cast brake cylinder and the circular section, Al-Cu, semi-continuously cast ingot. There was some evidence of equi-axed mechanisms for segregation in the two car wheels examined and also in the two semi-continuously cast Al-Cu ingots. The general pattern of macrosegregation in these castings was therefore one of contraction fluid flow being the dominant mechanism with gravity-driven mechanisms appearing only occasionally. This is not surprising in view of the fact that the majority of the casting were of fairly thin section ($<\sim 25$ mm) and froze fairly quickly ($<\sim 2$ mins.). Even the large section, semi-continuously cast ingots froze in such a way that material was only in the semi-solid zone for two to three minutes. It should also be noted that the magnitude of the macrosegregations observed in these castings was generally fairly small, being mainly less than $\pm$ 10% of the nominal alloy composition with the exception of the very localised exudations on the surface of the semi-continuously cast ingots. However, only the sand cast marine fitting exhibited no appreciable macrosegregation, which illustrates that segregation must be considered as an important, and probable, defect in any alloy casting. Finally, it may be seen that a particular macrosegregate can often be explained by the operation of several different mechanisms. This is the reason that model experiments must usually be set up in order to study the nature and operation of any one particular mechanism.

3.3 General data available from the literature

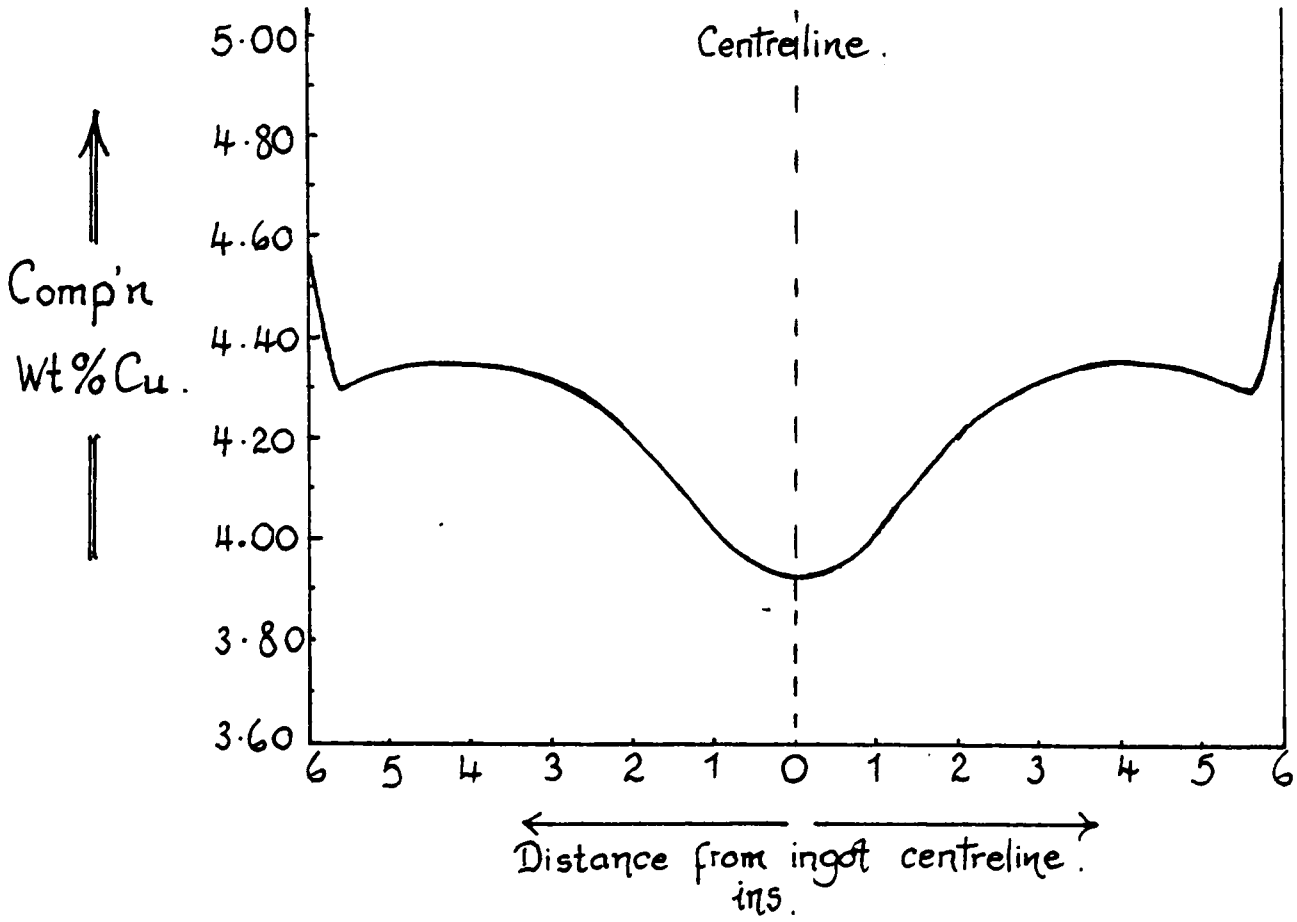
The most comprehensive investigation which has been conducted into quantitative macrosegregation was that of the Iron and Steel Institute on steel ingots. Ten reports were produced on 'The heterogeneity of steel ingots' in the period from 1926 to 1943, a full review of the work performed being given in the last of these.[122] The data provided in these reports has since proved to be invaluable in the development and understanding of many macrosegregation mechanisms, particularly those driven by gravitational forces. In total 78 ingots were examined during the course of the work, the majority of these being made from fully killed plain carbon steel. A typical set of analyses obtained from one of the ingots was given in fig. 1.3. The reports established the general pattern of macrosegregation found in killed steel ingots (fig. 1.1), which is now quoted as a matter of course in most works on macrosegregation.[101] It has since been shown that these segregation features are the result of a number of mechanisms all of which are associated with gravitational forces. A segregates and under-riser positive segregation are formed by gravitational interdendritic fluid flow;[81] negative and positive bottom cones of segregation are formed by sinking of equi-axed dendrites through the bulk liquid pool;[4,120] and V segregates are formed by the collapse of the initial dendritic framework.[81] Gravitational mechanisms are so predominant in such steel ingots because of the large freezing times involved (typically 20 minutes for an ingot of 40 cm. diameter weighing 750 kg.[126]).

Other quantitative work on macrosegregation in commercial practice has tended to be very sparse and fragmented.

Some pieces of work have been performed on continuously cast ingots. Data from two of these is reproduced in fig. 3.13. overleaf.[13,101] It can be seen that exudations are a particular problem in such ingots because of the reheating of the solidified shell once this moves below the water cooled chill.[13] Inter-dendritic gravitational flow can cause segregation and channeling in alloys such as bronzes and steels where the semi-solid mushy zone extends for long



Variation of Sn content across a 2¼ inch thick slab of tin bronze (Cu - 8 wt % Sn.) (ref 13).



Segregation profile across the diameter of a cylindrical, continuously cast, Al-Cu ingot produced under relatively poor casting conditions (ref 101).

Fig 3.13. Quantitative data from two sources[13,101] concerning macrosegregation in continuously cast ingots.

distances below the chill ring.[127] Flemings[70] has also shown that contraction flow of liquid in the mushy zone can cause the centreline type of segregation commonly observed in such ingots.

Macrosegregation was mentioned in a review of centrifugal casting by Howson.[25] Gravitational mechanisms should be exaggerated in such castings since forces may be as high as 50 G,[128] and indeed equi-axed segregation is often observed. Beardsley[128] reports the segregation of a number of lighter phases to the internal bore of centrifugally cast pipes. These include carbon nodules and magnesium sulphide inclusions in hyper-eutectic, spheroidal cast irons, and manganese sulphide inclusions in grey cast irons.[129] Northcott and Dicken reported the 'centrifuging' of denser primary equi-axed dendrites to the outer surface of pipes in Al-6 wt % Cu, Cu-6 wt%Sn, and Cu-30 wt%Zn alloys. They also noted inverse segregation at the outer surface of the pipes, particularly in the bronze alloy, which they observed decreased in magnitude as the rotation speed increased. They attributed this to the increasing amount of negative segregation produced by the centrifuging of equi-axed dendrites to the outer surface as gravitational forces increased. They also observed banding in the pipes which was associated with vibration in the machine.

Macrosegregation reported in cast irons has tended to be associated with gravitational mechanisms. Kishing of primary graphite flakes in hypereutectic grey cast irons is a commonly encountered type of macrosegregate,[8] and is caused by the equi-axed mechanism. Floatation of magnesium sulphide inclusions in large, horizontally cast, iron rolls has also been reported.[130] Gravitational interdendritic fluid flow often leads to defects known as 'niggerheads' in large, vertically cast, steel-base rolls (approximately 2 wt % C).[131] These defects are pipes of solute-enriched material which extend vertically upwards through the roll, and may be as large as 20 mm. in diameter. The niggerheads may be reduced by lowering the pouring superheat, and raising the carbon content to nearer the eutectic composition. Both of these variables reduce the time available for the gravity flow mechanism to operate.

3.4 Summary and Conclusions

A survey of the literature revealed a lack of quantitative information on macrosegregation present in commercial castings and ingots. The data that was available mainly related to large-scale ingots and castings and indicated the importance of gravitational mechanisms in producing macrosegregation in such situations. The scope of the practical work performed on industrial castings in this study, and described in this chapter, was limited by time and, unfortunately, by the poor response of those organisations which were contacted for help. The castings examined were all of relatively short freezing time, and the major macrosegregation mechanism found to be operating within them was contraction fluid flow. All except one of the nine castings examined was found to exhibit some form of macrosegregation, but the magnitude of this segregation seldom exceeded $\pm$ 10% of the nominal composition.

CHAPTER 4

INVESTIGATION OF THE TIME TAKEN FOR GRAVITY FLOW TO PRODUCE APPRECIABLE MACROSEGREGATION

4.1 Introduction

The industrial castings and ingots described in section 3.2 and investigated in the present study contained little evidence of macrosegregations which could be attributed to the gravitational fluid flow mechanism. It was concluded that this was due mainly to the short overall freezing times of these castings which prevented any appreciable operation of the time-dependent gravity flow mechanism.

In view of this conclusion it was decided that an experiment should be set up to investigate how long a material could grow and exist in a semi-solid state before detectable gravity flow macrosegregation occurred. The time dependency of gravitational fluid flow had previously been discussed only in a qualitative manner. The aim of the experiment was to provide some quantitative idea of the figures involved. It was not intended that the experiment should provide absolute time values for every combination of alloy and casting process. Clearly the critical time required for segregation depends upon the particular alloy system and composition involved, upon the casting process employed, and upon the cooling conditions which prevail. It was felt, however, that a quantitative measure of the critical time for one particular alloy system and casting situation would provide a useful starting point, which could be used to predict approximate times for other systems and situations.

4.2 Outline of the Experiment

4.2.1 General Outline

In order to measure the time required for gravity flow to produce significant macrosegregation, it is necessary to find some means of performing

composition analyses on an alloy sample which has been allowed to grow for different periods of time. A simple way of doing this is to use a series of static castings of similar shape but increasing capacity, cast under identical conditions from the same melt. The freezing times of these castings will vary according to their volumes, and should increase as the volume increases. The critical time required for gravity flow macrosegregation to occur can then be obtained by determining the freezing time of the smallest ingot found to contain such segregation.

The ingots described in this chapter were produced using the facilities at Alcans research laboratories, Banbury, and with the help and guidance of Dr. R. Jordan and Mr. K. Latimer. The alloy employed was a simple binary of aluminium and copper, with a nominal composition of Al-5 wt% Cu. 140 kg. of alloy was melted up in a single melting pot, without a grain refining addition. The molten alloy was cast with a superheat of approximately 90°C into a series of five green sand moulds. These moulds were cylindrical in shape with a fixed aspect ratio (h/r = 4), each one having a different radius. The time taken for each ingot to freeze was monitored using thermocouples positioned in the mould cavity. The solid ingots were sectioned longitudinally, and structural examinations and composition analyses performed on them.

4.2.2 Reasons behind choice of casting process and alloy system

The proposed experiment required the manufacture of a number of moulds, all of which were to be used once only. The cheapest, and indeed the easiest, way of producing an article which is required only in small numbers is to use sand moulds, especially when casting simple shapes. Sand as a mould material had other advantages in the context of this experiment. The time taken for a given volume of metal to freeze in a sand mould is much larger than in an equivalent metal mould. It was hoped that the largest ingot would take at least 30 minutes to solidify, and it was thought that the amount of metal needed to give such a freezing time in a metal mould would be prohibitively large. The use of chill moulds would also have enhanced the contraction flow mechanism for

macrosegregation. This might have tended to obscure any gravity flow macrosegregation present, especially in ingots with low solidification times.

Unfortunately there were no facilities in the laboratory either for sand casting or for melting large quantities of metal. A number of industrial organisations were therefore contacted in the hope that they would provide assistance with the casting operation. As mentioned in the previous section help was offered by Alcan International.

It was felt that the results of the experiment would be of more general interest if an alloy system of commercial significance was used. Further advantage was therefore taken of Alcans offer by using an aluminium-base alloy. The aluminium-copper system was chosen because gravitational fluid flow ought to be quite pronounced in alloys from this system. There is a large density difference between the two components, a large freezing range, high liquidus slope, and low distribution coefficient (see fig. 4.1). The composition Al-5 wt% Cu was chosen because this alloy is widely used in commercial casting. Indeed slices from two Al-Cu semi-continuously cast ingots had previously been examined (section 3.2.7), and so it was hoped that a useful comparison could be made between them and these static sand castings.

The casting conditions were chosen to minimise all macrosegregation mechanisms other than gravity flow. Columnar growth was encouraged in order to suppress equi-axed mechanisms. This was done by pouring the metal with a high superheat, using an alloy of low solute content, and making no grain refinement additions to the melt. The superheat used was at the upper end of the superheat range employed commercially. As mentioned earlier, any operation of the contraction flow mechanism was hopefully minimised by employing sand as the mould material.

4.2.3 Theoretical calculation of ingot freezing times

In order to set up the experiment it was necessary to have some idea of how the freezing times of Al-Cu sand cast ingots varied with ingot diameter. Unfortunately very little experimental data could be found in the literature for

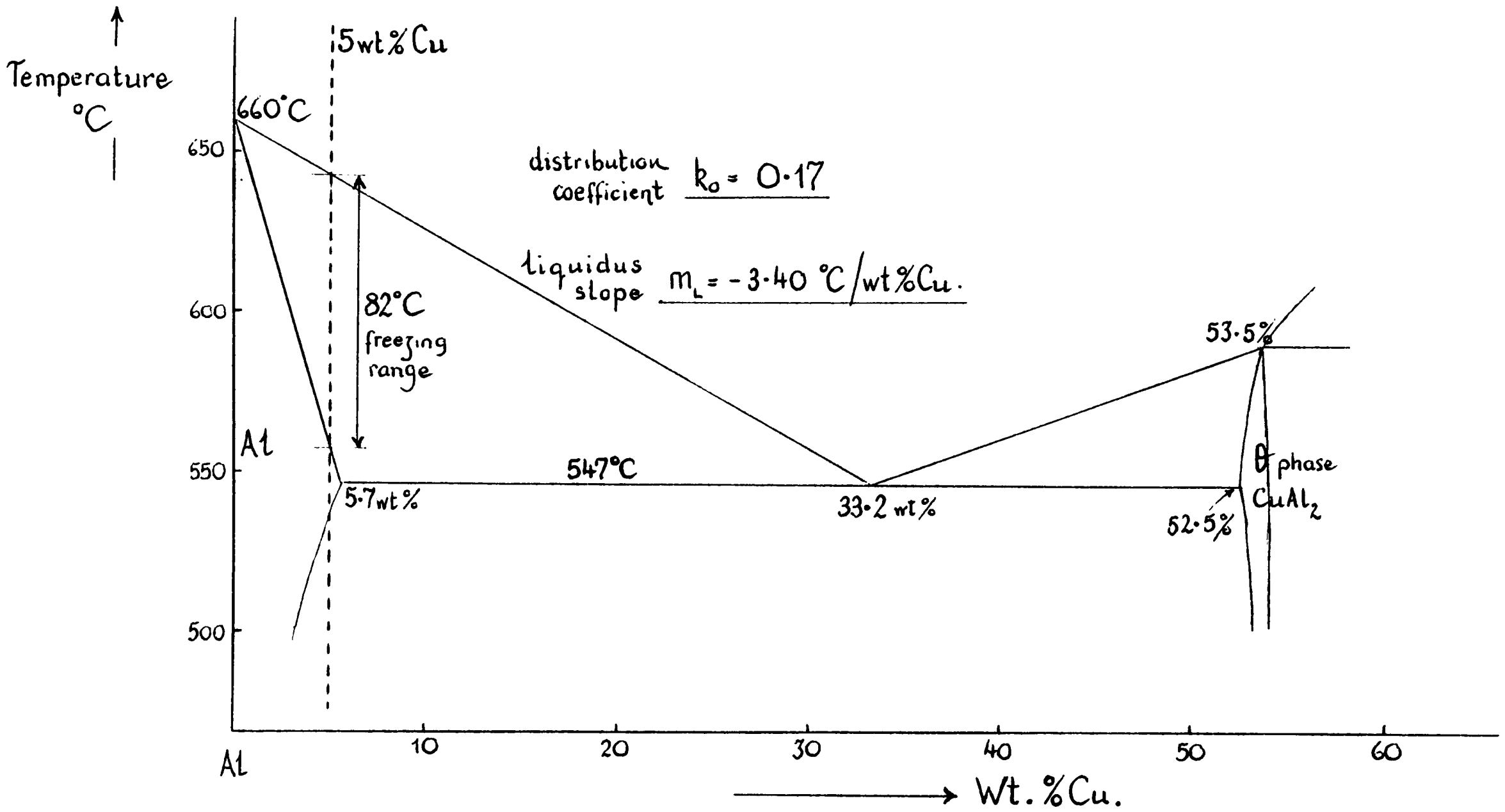


Fig. 4.1. Part equilibrium phase diagram of the Al-Cu binary system.

these freezing times, and the Alcan foundry had no experience of casting such alloys into sand. It was therefore necessary to attempt a theoretical treatment of the problem. It was found, in this context, that many authors [41,100,101] pointed to the success of 'Chvorinov's' rule [132] in predicting solidification times for sand castings. This rule states that:-

$$t_f = C(V/A)^2$$

where t_f is the total solidification time of the ingot; V is the total volume of metal solidified; A is the surface area of the mould in contact with the metal; and C is a constant which depends on various mould and metal parameters. This type of relationship may be derived theoretically and a value for C thereby obtained. The treatment essentially involves equating the amount of heat evolved by the solidifying metal with the amount of heat entering the mould.

Consider a pure metal with zero superheat, poured against a flat sand mould wall of semi-infinite thickness, and solidifying with a planar growth front (see fig. 4.2(a)). The expression for the solid metal thickness S at time t is given by [101] :-

$$S = \frac{2}{\sqrt{\pi}} \left(\frac{T_L - T_o}{\rho_s H_f} \right) \sqrt{k_m C_m \rho_m} \sqrt{t} \qquad - 4.1$$

i.e $$S = K\sqrt{t} \qquad - 4.2$$

where T_L = melting point of pure metal; T_o = initial mould temperature; ρ_s = solid metal density; H_f = latent heat of fusion; k_m = thermal conductivity of sand; C_m = specific heat of sand; and ρ_m = density of sand.

If the assumption is now made that a given area of mould surface has a fixed ability to absorb heat regardless of its contour or location then the term S in equation 4.2 can be replaced by V_s/A, where V_s is the volume of metal solidified at time t and A is the total area of mould-metal interface (see fig.4.2(b)),

i.e. $$V_s/A = K\sqrt{t} \qquad - 4.3$$

And if t_f is the total solidification time of a casting of volume V then:-

$$V/A = K\sqrt{t_f} \qquad - 4.4$$

or $t_f = C(V/A)^2$, which is Chvorinov's rule.

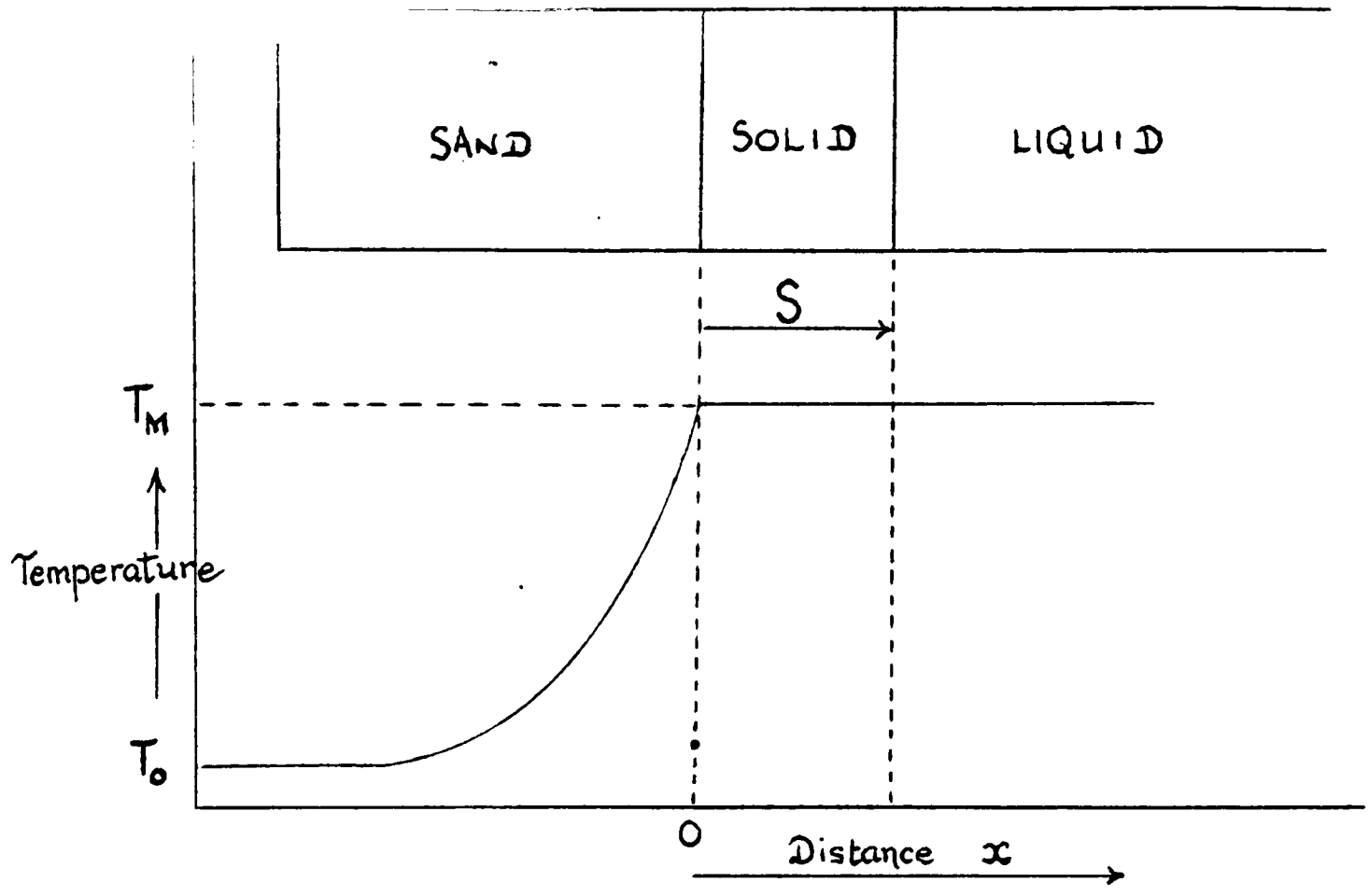
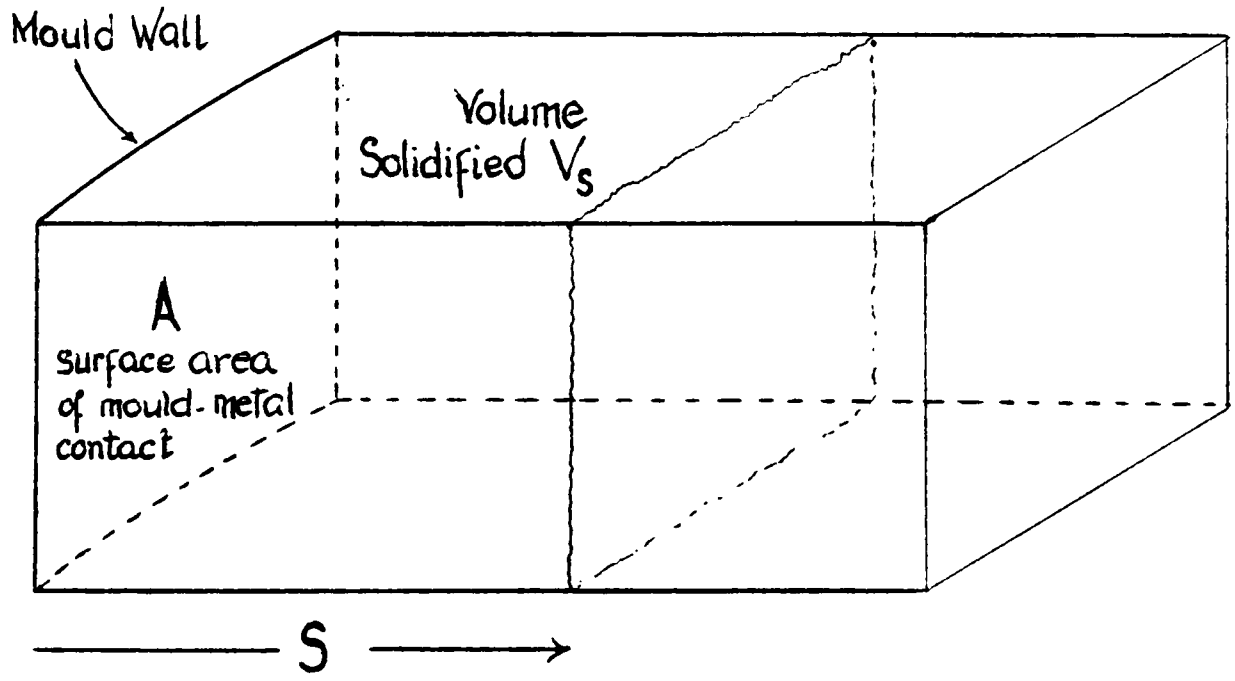


Fig. 4.2(a). Approximate temperature profile for the solidification of a pure metal poured at its melting point, T_m, against a flat sand mould wall of semi-infinite thickness and at an initial uniform temperature T_o.



$$V_s = AS$$

$$\therefore \quad S = V_s/A$$

Fig. 4.2(b). Assumption that mould has a fixed ability to absorb heat regardless of its contour

Now, for an open-topped cylindrical mould

$$V/A = \pi R^2 h / (2\pi Rh + \pi R^2) \qquad - 4.5$$

and the moulds used in this work had aspect ratio h/R = 4.

$$\text{Therefore } V/A = 4R/9 \qquad - 4.6$$

which in equation 4.4 gives:-

$$R = 9/4\ K \sqrt{t_f} \qquad - 4.7$$

Substituting the following values into K for the particular materials used in this experiment:-

$T_L = 647^\circ C$; $T_o = 20^\circ C$; $\rho_s = 3$ gms/cc; $H_f = 93$cal/gm; $k_m = 14.5 \times 10^{-4}$ cal/cm $^\circ C$ sec; $C_m = 0.27$ cals/gm $^\circ C$; $\rho_m = 1.5$ gms/cc.

then $K = 6.145 \times 10^{-2}$ cm $\sec^{-\frac{1}{2}}$ - 4.8

$C = K^{-2} = 266.5$ secs cm^{-2} - 4.9

and so $\underline{R = 0.1383 \sqrt{t_f}\ cm}$ - 4.10

and $\underline{t_f = 52.3\ R^2\ secs}$, - 4.11

for the casting conditions employed.

These expressions were used to estimate the sizes of ingot needed for the experiment. It was felt that the critical time required for gravity flow segregation to occur would be around 20 minutes. The sequence of five ingots was therefore arranged to straddle this time. From equation 4.7, for

$t_f = 20$ mins = 1200 secs

$$\underline{R = 4.8 \text{ cm}}$$

and it was arbitrarily decided that the ratio of freezing times should be approximately 3:1 for consecutive ingots, meaning $R_x : R_{x+1} = 1:3$. Ingot moulds of radii 1.6 cm, 2.8 cm, 4.8 cm, 8.3 cm, and 14.4 cm were therefore specified, these having calculated freezing times of 2 mins., 7 mins., 20 mins., 60 mins., and 180 mins. respectively.

It should be emphasised that the treatment outlined in this section contains several approximations and important omissions and that it was therefore only intended to give a rough idea of ingot freezing times.

4.3 Experimental Procedure

4.3.1 Production of sand moulds

The type of sand used to make the moulds for this experiment was Mansfield Red, which is a naturally occurring, clay-bonded sand. Prior to the moulding process water was added to the sand in order to plasticise the clay and thereby make the sand grains bind together. The moisture content was measured to be 4%, which was slightly over that required to give optimum strength properties to the sand mix. This excess of water was added because the moulds had to be made up two days prior to the casting runs, thus giving them some time to dry out. The moisture content of a control sample of sand was remeasured at the time of casting and the value had fallen to 3.4%, which was almost the optimum value for the type of sand used.

The moulds were made by hand-ramming. The technique used is shown schematically in fig. 4.3. First an outer metal container was taken and the moist sand rammed down into the bottom leaving a flat, smooth surface. The depth of sand in the container was adjusted until the distance h_1 (fig. 4.3(c)) was equal to the height required for that particular casting. A pre-formed stainless steel cylinder, of the correct diameter for the casting concerned, was then placed centrally on top of the sand in the container, and further sand was packed around it. When the sand level had reached the top of the container the steel liner was carefully removed, thereby leaving a cylindrical cavity of the desired diameter and depth. Finally a thin sheet of asbestos paper was laid across the bottom of the mould in order to protect the sand from the molten metal stream during pouring.

The containers used for the five moulds were simply those which could be found at the time. Cylindrical cast iron pots were used for the smaller three moulds, a cubical steel bin for the second largest, and a large galvanised iron dustbin for the largest mould. The values for the depth of sand below the mould cavity, and the thickness of sand at the sides of the cavity, Y and X respectively fig. 4.3 (f), are given for each of the five

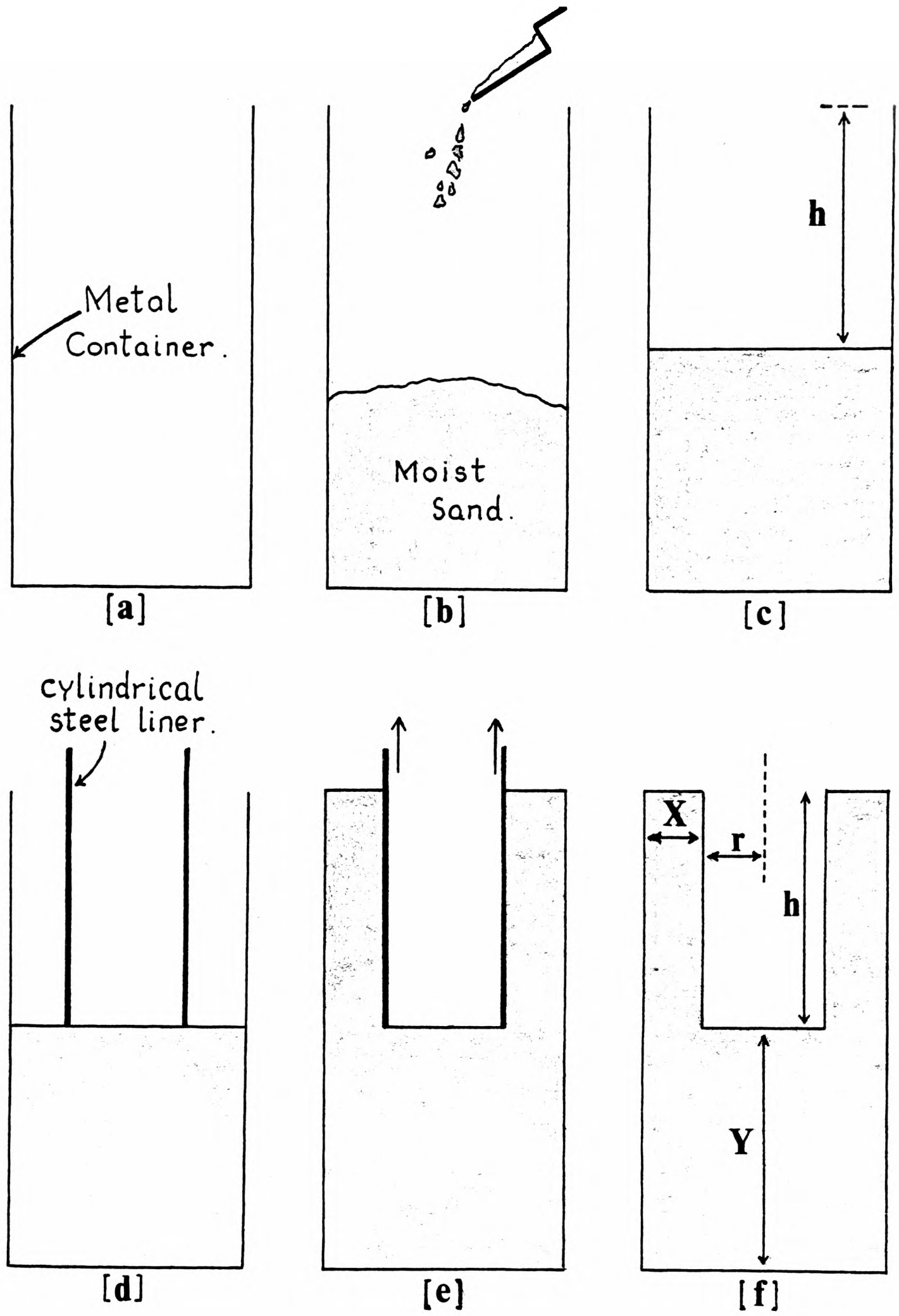


Fig.4.3. Technique used for the preparation of inget moulds.

Ingot No.	X cm.	Y cm.	r cm.	h cm.
1	3·4	11·3	1·6	6·7
2	4·8	6·0	2·7	12·0
3	5·3	10·9	4·7	19.1
4	7·8	15·2	7·7	30·8
5	9·3	28·0	13·2	52·0

Table 4.1

moulds in Table 4.1.

The cylindrical liners used to form the inner surface of the moulds were produced by bending a thin sheet of stainless steel around an expandable mandrel then spot welding along the seam. All the liners were of uniform cross-section along their length except for the largest one, which was too long to fit completely onto the mandrel. Consequently this liner could not be removed from its mould after ramming without destroying the inner sand surface. The problem could not be overcome even by giving the liner a slight taper. It therefore had to be left in the mould cavity during casting.

4.3.2 Melting Procedure

The molten alloy of Al-5 wt % Cu was prepared by heating up pre-weighed amounts of commercial purity aluminium and copper together in a firebrick-lined electrical resistance furnace. Approximately 140 kg. of metal was charged, the capacity of the furnace being around 160 kg.. The furnace plus charge was left to heat up overnight ready for casting the following day. Next morning, however, it was discovered that there was still some solid copper lying on the bottom of the furnace, despite the fact that the melt temperature was measured to be well over 700°C. The casting procedure was therefore postponed until the afternoon, and the melt was stirred vigorously by hand at intervals throughout the morning in order to ensure that all of the copper was dissolved.

The current passing through the resistance windings of the furnace was controlled so that a melt temperature of 750 $\pm$ 5°C could be maintained. The melt temperature was monitored using a chromel/alumel thermocouple in a long alumina sheath, attached to a robust foundry voltmeter.

The charge was degassed twenty minutes before the first casting was due to be poured by plunging four 3 ounce tablets of hexachloroethane to the bottom of the melt using a long iron rod. (Chlorine is liberated from the tablets and rises to the surface of the melt releasing any entrapped gases, of which hydrogen can be a particular problem). The noxious fumes produced were removed by a strong overhead extractor. It should be noted that commercial

hexachloroethane tablets often contain additions of a grain refiner. The tablets used in this experiment did not contain any such addition. After degassing the large amount of oxide and surface scum which had accumulated was removed, leaving the surface clean and the melt ready for pouring.

4.3.3 Casting Procedure

The three smaller ingots were cast using a hand-held ladle which had a maximum capacity of around 5 kg. of molten metal. The ladle was lowered into the melt and stirred around for about 1 minute before any metal was taken up. This helped to keep the melt well mixed and uniform in temperature, and it ensured that the ladle did not chill the metal in it appreciably. The temperature of the molten alloy in the ladle was monitored using the furnace monitoring thermocouple. When it had fallen to around 715°C the alloy was carefully poured from the ladle into one of the ingot moulds. Any excess alloy remaining in the ladle after filling the mould was returned to the melt in the furnace.

The two larger ingots were cast by tilting the furnace about its axis and pouring the molten alloy down an asbestos-lined launder into the moulds. The launder was positioned so that there was a slight downward slope from furnace to mould. The metal was simply allowed to run down the slope and over the end of the launder into the mould. Care was taken to ensure that the launder was well supported so that its weight would not damage the mould, and that the molten metal stream did not splash or erode the walls of the mould. The temperature of the pouring stream was monitored at the bottom end of the launder. The metal was found to have cooled by approximately 20°C in the launder, giving a pouring temperature of approximately 730°C.

The progress of solidification in the ingots was monitored using thermocouples. Two thermocouples were used in each ingot, except for the smallest which only had one. Each pair was set-up prior to pouring, so that one lay approximately on the axis of the cylindrical cavity, the other lay approximately at mid-radius, and so that the beads were at approximately

mid-height. In the smallest ingot only a single central thermocouple was used. The thermocouples were held in position, somewhat precariously, by an arrangement of stands and clamps which extended over the mould cavity. Care was taken during pouring to ensure that the thermocouples were not moved by the metal stream.

Chromel-alumel type thermocouples were used, sheathed in long alumina tubes. The ends of these alumina tubes were left open so that the thermocouple beads could be in direct contact with the metal, thereby ensuring rapid response to changes in temperature. The chromel and alumel wires were individually sheathed above the bead so that they would not short out if metal rose up the open outer tube.

The voltage signals from the thermocouples were monitored on a two channel Oxford Instruments pen recorder, using a cold junction ice bath and a constant back-off potential of 20mV. This recorder set-up meant that only two temperature signals could be monitored at any one time. In order to obtain full information about the freezing process in each ingot it was therefore necessary to cast the ingots in sequence rather than all together. Thus the second ingot was not cast until the first one had completely solidified and the recorder leads had been transferred to the pair of thermocouples in the next ingot.

The time which elapsed between pouring the first casting and pouring the fifth one was around three hours. In order that a reasonable comparison could be made between the ingots it was therefore necessary to ensure that the temperature and composition of the melt remained constant throughout the period. The temperature of the melt was continuously observed and adjusted. As the charge in the furnace was used up so the current passing through the furnace windings was decreased to ensure that the temperature did not rise above 750^{o}C. In addition, samples were taken from the melt at the beginning and end of the casting sequence. These were poured into small iron chill moulds to provide standard test pieces for subsequent composition analysis. In this way any long-term variation of melt composition with time could be detected.

Normal foundry precautions were observed throughout the casting

programme, special care being taken during the pouring, sampling, and stirring of the melt. A safety helmet, fitted with a visor was worn at all times, and asbestos gloves, leggings, and an apron were put on when dealing directly with the molten metal.

4.3.4 Examination of Ingots

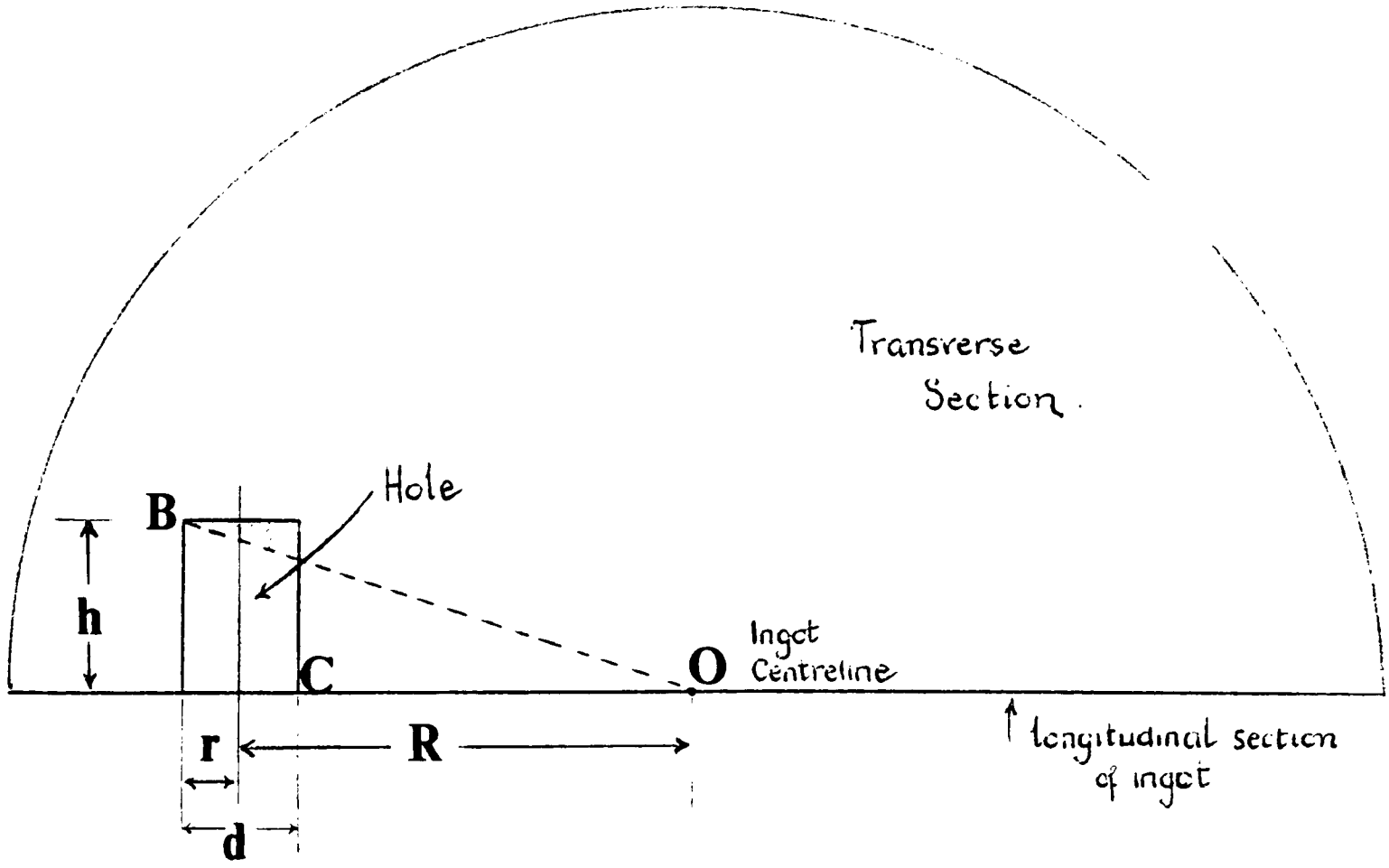
The five ingots were all sectioned longitudinally into two equal halves in the plane containing the two thermocouples. In the three smaller ingots one half was used for macrostructure studies and the other half for composition analysis. For the two larger ingots only a central longitudinal slice was supplied by Alcan so the same section had to be used for both macrostructure and composition work.

The sections intended for macrostructure work were first degreased and then given a rough machining operation using a flycutter on a milling machine. Ingot 5 was unfortunately too large to fit onto the machine and so it had to be cut into two pieces which were then machined separately. After flycutting, the surfaces were progressively hand-ground on 60, 100, and 220 grade silicon carbide papers. They were then etched in a variety of etchants, the best of which was found to be 10% HNO_3; 10% HF; 80% H_2O. This was used cold and was applied to the surface of the ingots by swabbing. The optimum etching time was around 2 to 3 minutes. Any staining of the surface could be removed by quickly wiping it over with concentrated nitric acid.

Samples for composition analysis were taken from the longitudinal ingot sections by drilling out material from specific positions. The sample collector, described in section 9.4.2., was used to ensure the complete collection of all material swarf and fragments from each position. The samples were dissolved into acid solution, as described in section 9.4.4., and these solutions were then analysed for copper content using atomic absorption spectrophotometry (see chapter 9).

The diameter of the drill used to take each sample, and the depth to which the hole was drilled, were varied according to the position of the hole

with respect to the ingot centreline. This was done in order to obtain samples which were the most representative of particular regions, and was a consequence of the curvature of the ingots below the central sampling section. Consider figure below, which shows a hole of diameter d and depth h drilled into the longitudinal face of a half-ingot at a radius R from the centreline of the ingot. In this situation material is effectively sampled from distances between OC and OB from the centreline O. The 'effective diameter' of the hole OB-OC can be minimised at each value of R by a certain value of d and h, while at the same time keeping the total volume of the hole constant. This calculation is set out in Appendix 4.A. The optimum values of drill diameter (d) and depth (h) against distance from the centreline (R) are given by the curves shown in figure 4.4.



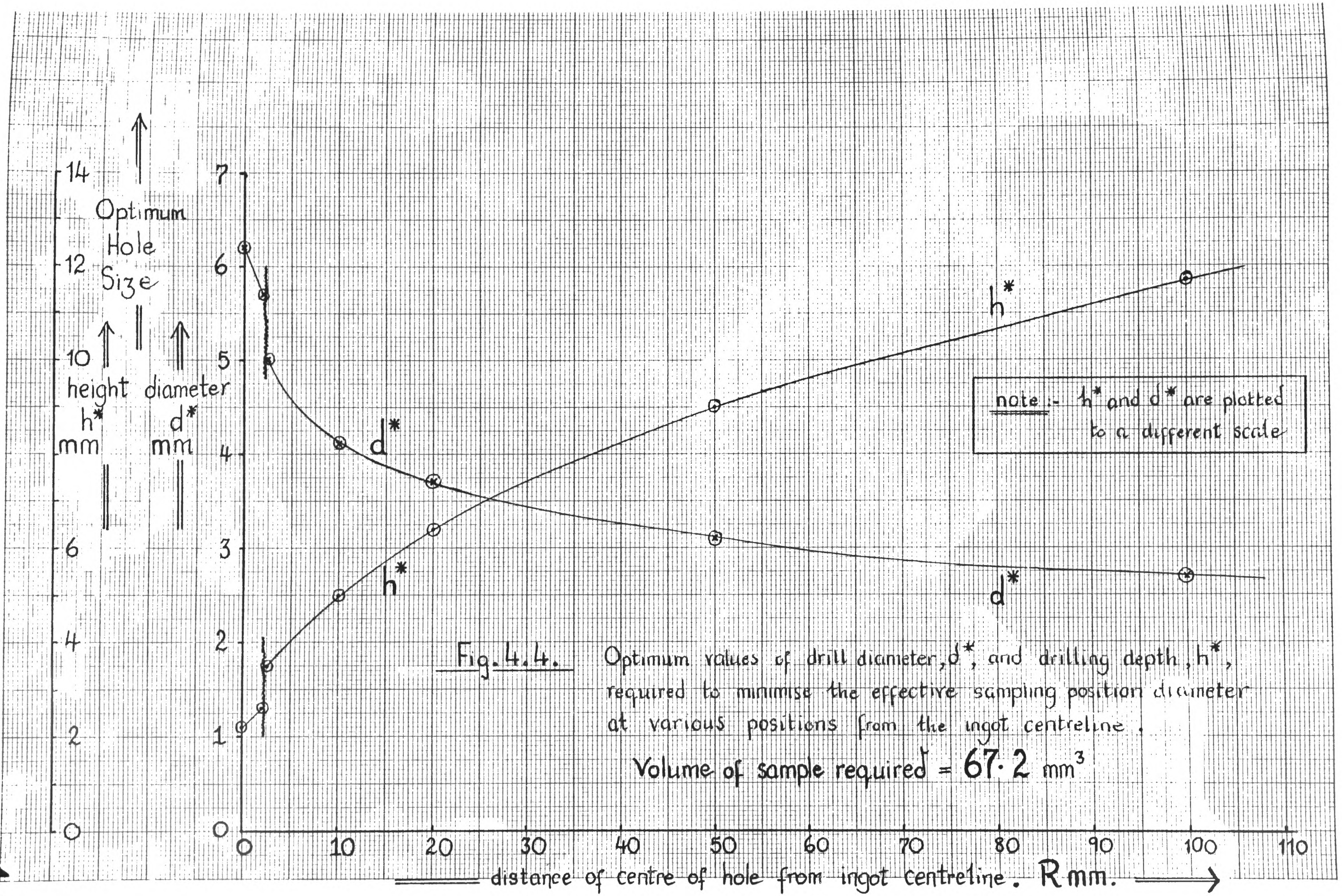


Fig. 4.4. Optimum values of drill diameter, d^*, and drilling depth, h^*, required to minimise the effective sampling position diameter at various positions from the ingot centreline.

Volume of sample required = 67·2 mm^3

4.4 Results and Discussion

4.4.1 Casting data and physical measurements on solidified ingots

The relevant information concerning pouring temperatures, ingot weights, dimensions etc. has been gathered together in table 4.2., shown below:-

Table 4.2

Ingot Number	Ingot Weight Kg.	Ingot Diameter mm.	Ingot Height(av) mm.	Pouring Temperature °C	Casting Sequence (A first)
1	0.152	32.4	69.6	715	C
2	0.739	54	124	715	B
3	3.50	94	193	715	A
4	15.10*	154	312	730	D
5	74.4*	264†	523	730	E

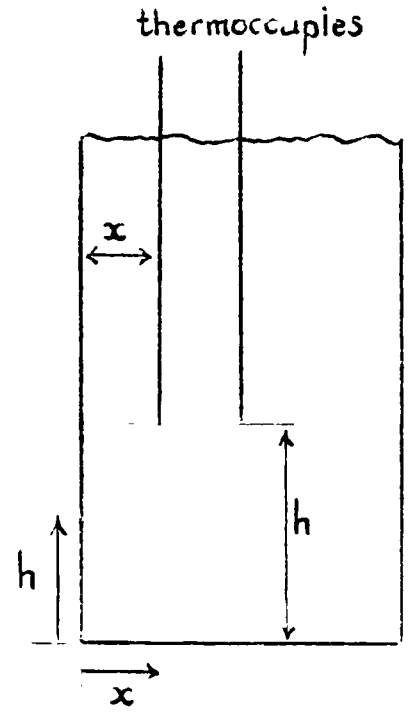
† ingot was tapered - this was value at half-height.

* estimated value - central region only supplied.

The positions of the thermocouple beads within each ingot were determined by sectioning the ingots once all metallographic and composition work had been completed. These are given in table 4.3., shown below:-

Table 4.3

Ingot Number	Thermocouple Positions mm.			
	Outer		Centre	
	x	h	x	h
1	-	-	14	24
2	16	60	25	62
3	24	105	47	105
4	28	147	71	150
5	70	272	124	275



As indicated on the diagram h represents the height of the bead from the bottom mould surface, and x represents the radial distance of the bead from the edge of the casting.

4.4.2 Macrostructures of Ingots

The macrostructures of the five ingots are shown in plates 4.5 to 4.9. Different magnifications have been used for each photograph in order to show the structure of each one as clearly as possible. Unfortunately this has tended to disguise the size difference between the ingots. The transparent overlays to the photographs show the extent of the columnar and equi-axed regions in the ingots, and also the positions of the thermocouple beads in each one.

It can be seen from the macrostructures that solidification has occurred in a largely columnar fashion. Ingots 1 and 2 have fully columnar structures. Ingots 3,4, and 5 do have an equi-axed zone in their bottom central region, but the extent of this zone is fairly limited.

In the two smaller ingots growth has occurred solely from the vertical sides of the mould. In the three larger ingots, however, growth has also proceeded from the top surface of the molten liquid pool, and to a lesser extent from the bottom mould surface. There are therefore three distinct columnar regions in each of these larger ingots.

The two halves of ingot 5 shown in plate 4.9 have clearly responded differently to the etchant. This was due partly to the fact that the etchant had to be applied by swabbing, which lead to variations in attack, and partly to the fact that there was a large amount of porosity present in the lower half of the ingot which meant that the etch could not easily be washed away. The columnar nature of the structure at the edges of the lower half has unfortunately been masked in the photograph by this etching effect. It could, however, be clearly seen by viewing the structure through a low-magnification binocular microscope.

Regions of gross porosity are clearly visible in the interior of ingots 3,4, and 5. This porosity was essentially caused by poor casting design. Hot tops were not employed and so a rigid solid crust formed across the top surface of the ingots shortly after pouring. The high solidification contraction of



Fig.4.5. Etched macrostructure of INGOT 1.

MAG^{N} x 1½

thermocouple bead position marked with red dot •



Fig.4.6. Etched macrostructure of INGOT 2.

MAG^{N} x 1



32·4 mm.

Fig.4.5. Etched macrostructure of **INGOT 1.**

MAGN x 1½



54 mm.

Fig.4.6. Etched macrostructure of **INGOT 2.**

MAGN x 1

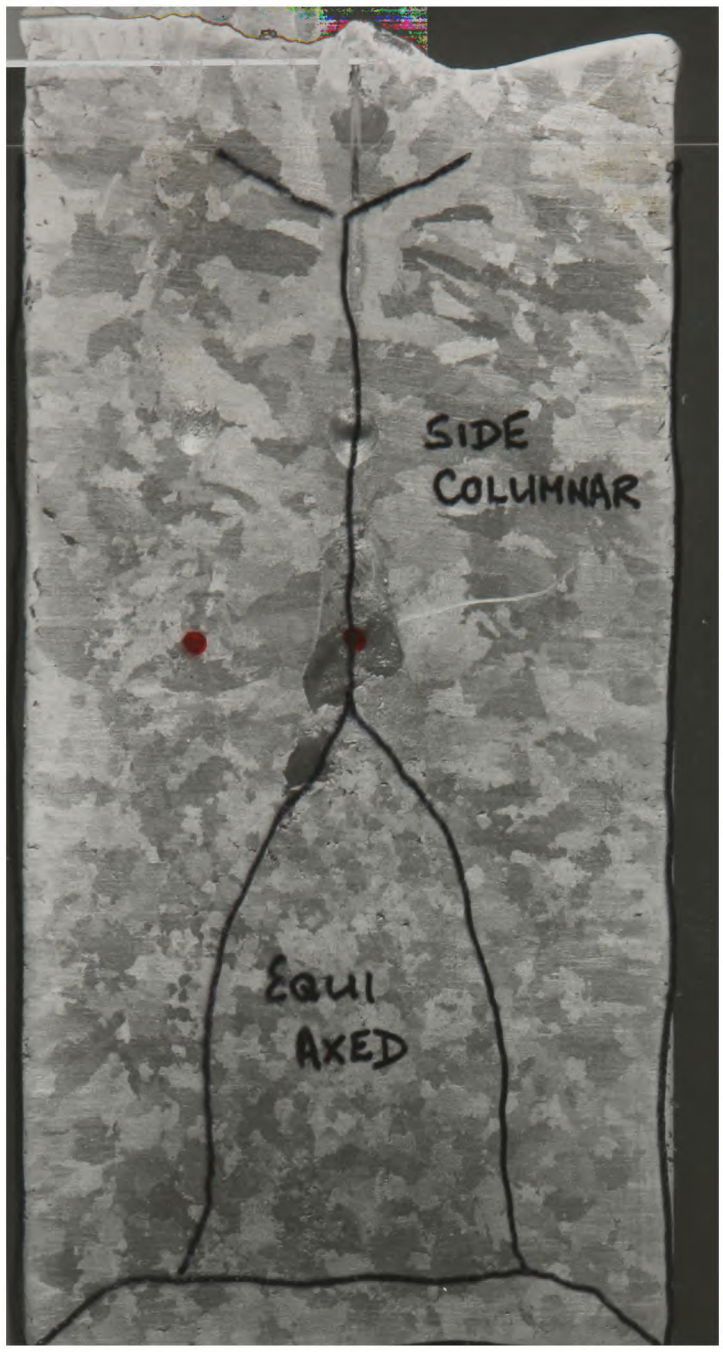


Fig. 4.7. Etched macrostructure of INGOT 3.

MAG^{N} x 2/3

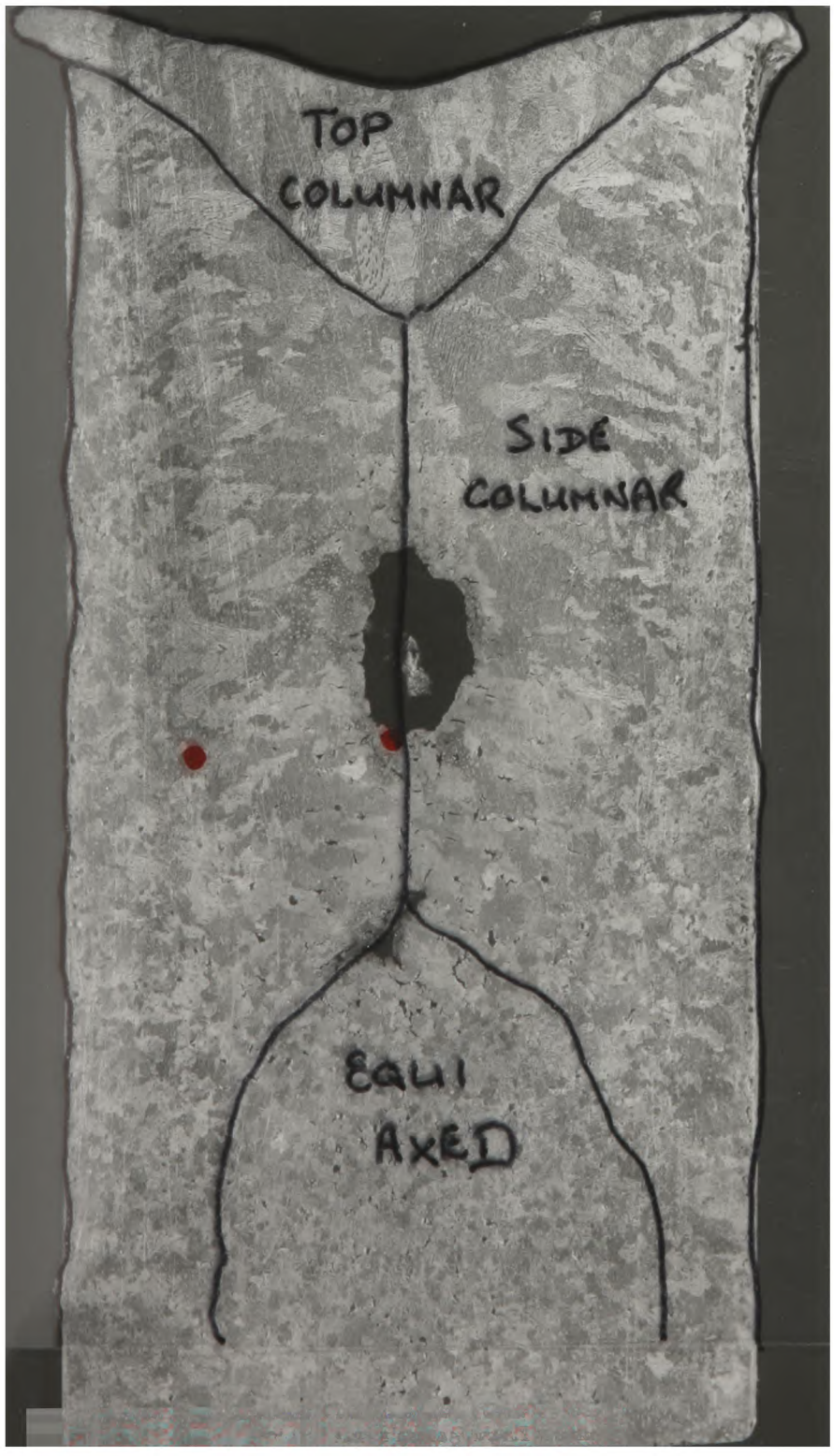


Fig. 4.8. Etched macrostructure of INGOT 4.

MAG^{N} x 1/2



Fig. 4.7. Etched macrostructure of INGOT 3.

MAGN x 2/3

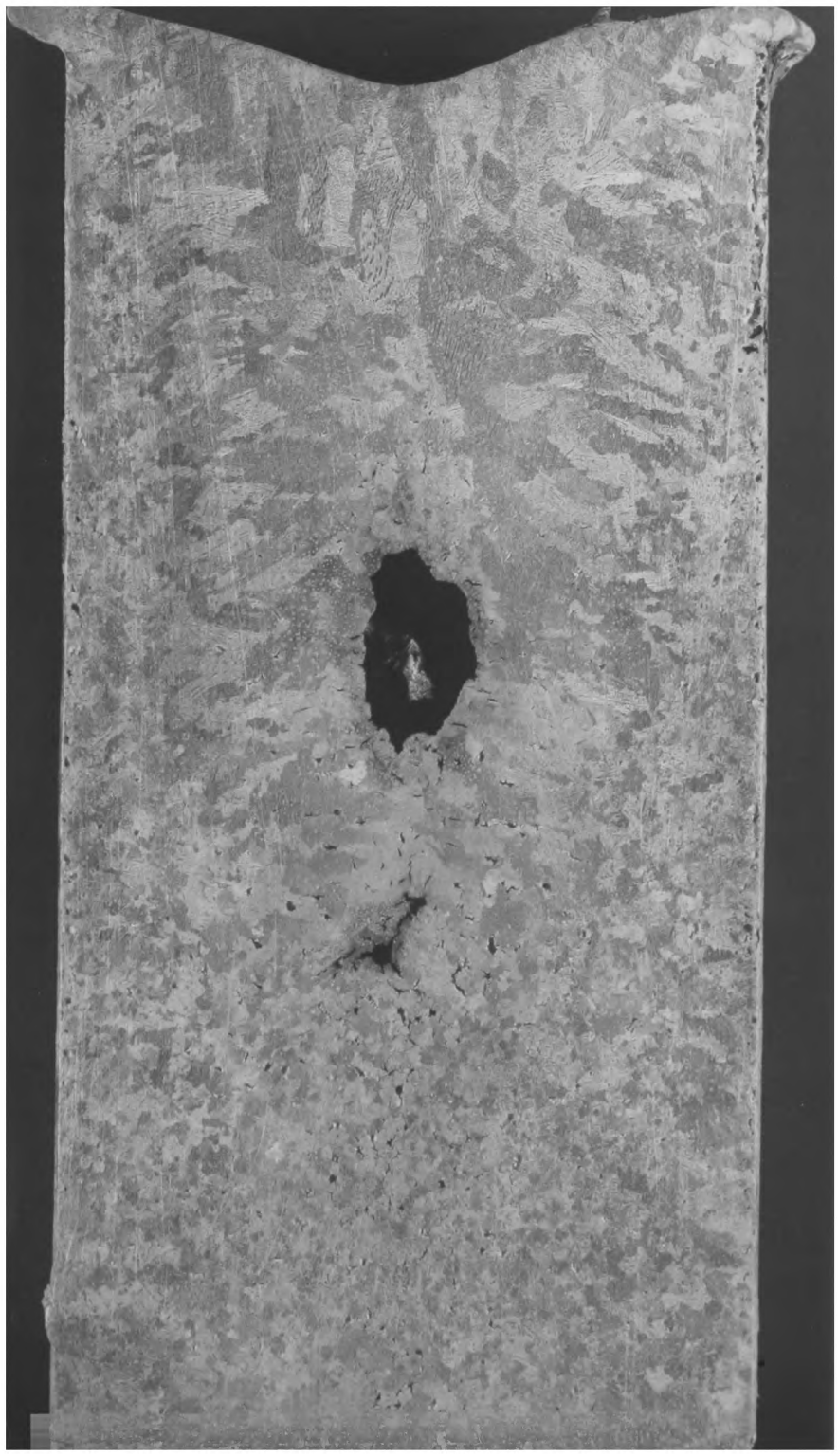


Fig. 4.8. Etched macrostructure of INGOT 4.

MAGN x 1/2

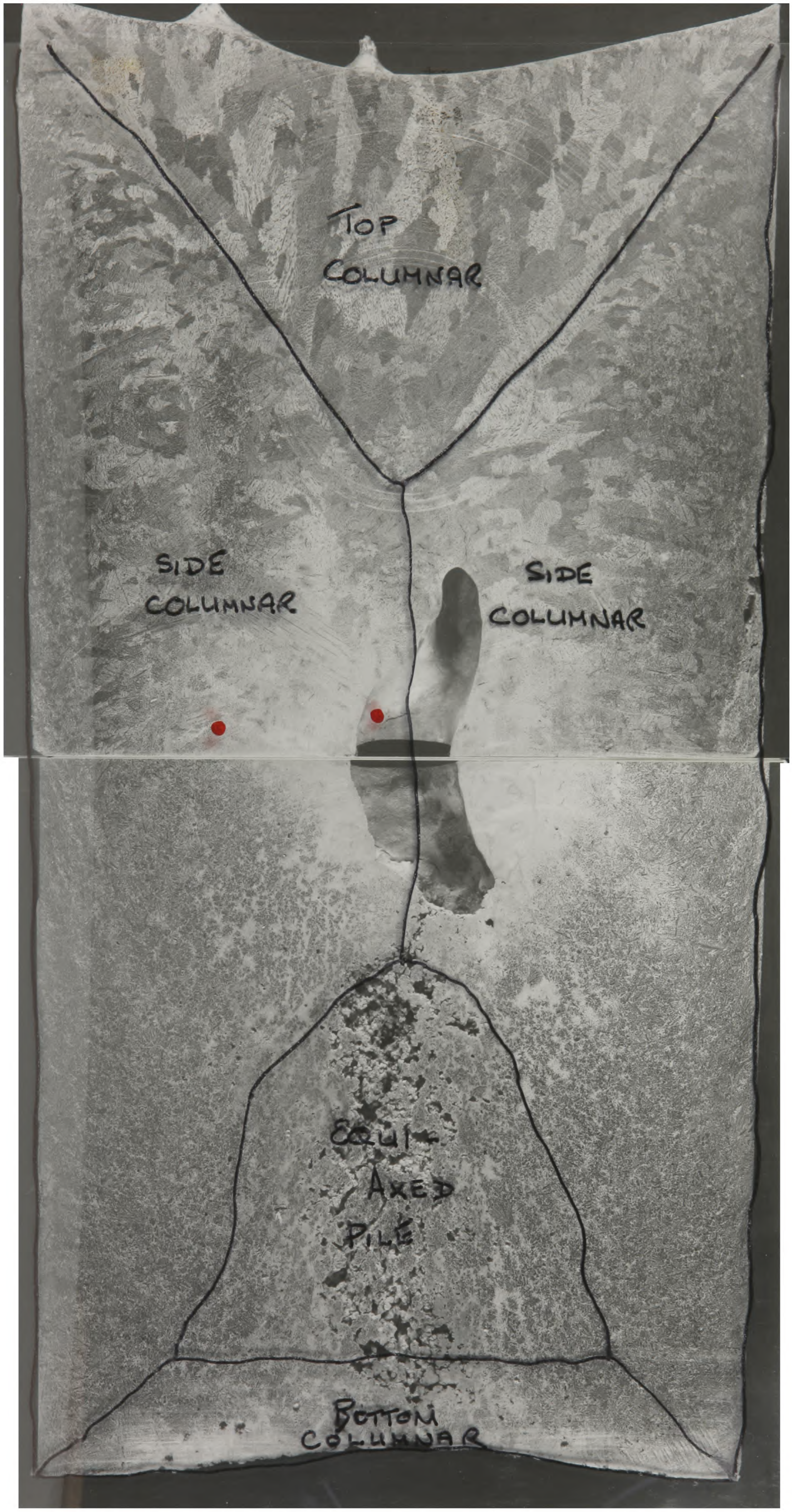


Fig. 4.9. Etched macrostructure of **INGOT 5.** MAG^{N} x ½



264 mm

Fig. 4.9. Etched macrostructure of **INGOT 5.** MAG^{N} x ½

the molten aluminium had therefore to be taken up internally within the body of each ingot. A further factor which probably contributed to the very large size of the central pores was that the alumina thermocouple sheaths were open-ended. Air might well have been sucked down the central thermocouple sheath to take up the contraction of the last liquid to freeze. It can be seen from plates 4.7 to 4.9 that the central thermocouple positions are associated with this region of gross porosity.

4.4.3 Composition Measurements

The samples which were taken from the melt at the beginning and end of the casting sequence and cast into chill moulds were found to have compositions of Al-5.7wt%Cu and Al-5.6wt% Cu respectively. The accuracy of $\pm$2% in the analysis technique for copper (see section 9.5) means that these values are correct to within $\pm$0.1wt% Cu. The variation between them therefore lies within the limits of experimental error, meaning that there was no significant change in melt composition during the casting sequence.

Figures 4.10 and 4.11 show the composition versus position plots obtained from the five ingots.

It can be seen from figure 4.10 that there has been no appreciable macrosegregation in either of the two smaller ingots. The average of the composition values in each of these ingots is 5.6wt% Cu, which is identical to that of the second melt sample. The value of 5.6wt% Cu has therefore been taken as the nominal melt composition for all of the ingots.

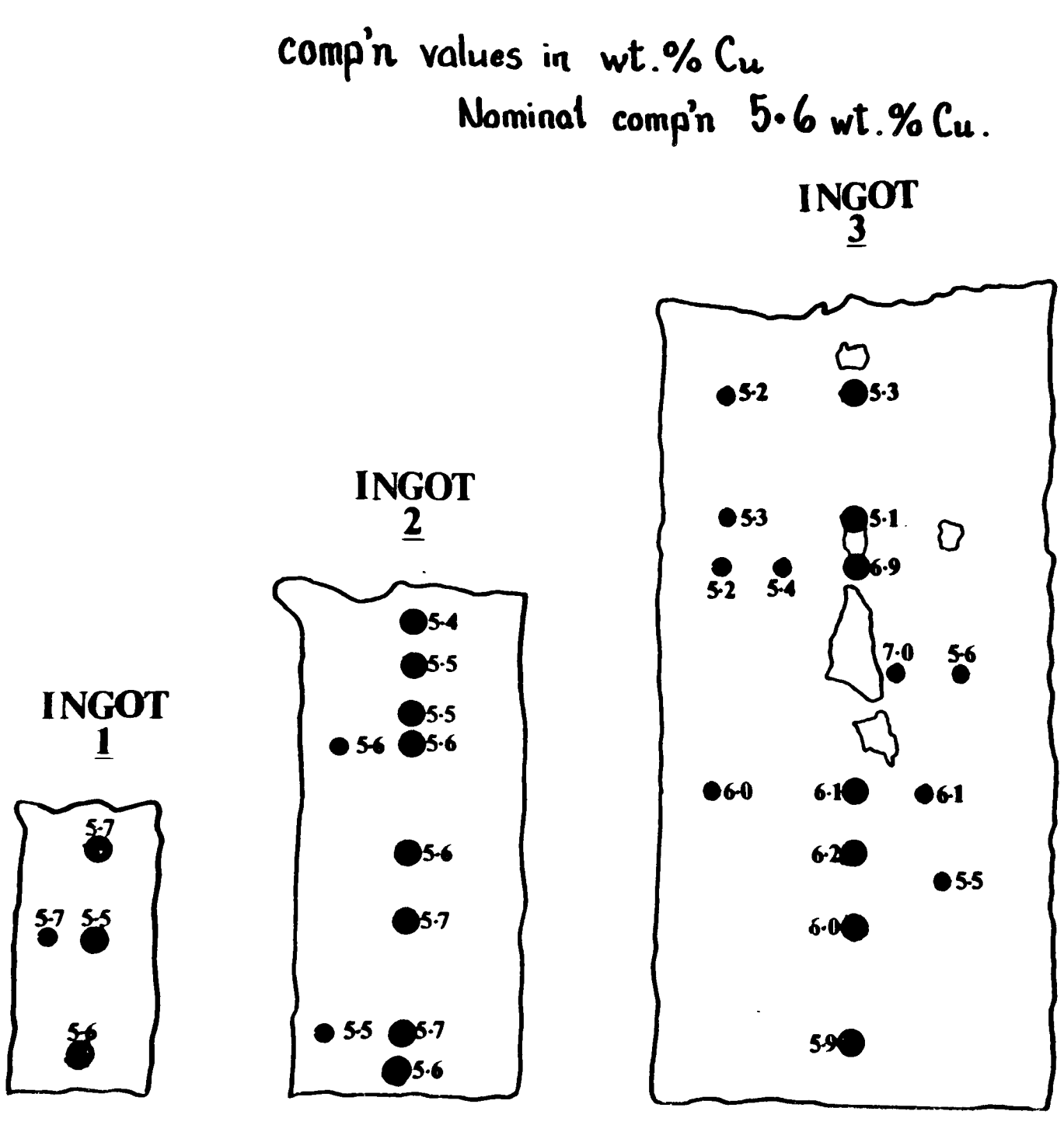
The only composition value in ingots 1 and 2 which lies outside the nominal range of 5.6$\pm$0.1wt% Cu is that at the top centre of ingot 2. This low value was probably caused by slight pick-up of fragments of the alumina thermocouple sheath in the swarf sample. These would have added to the observed sample weight, thereby 'diluting' the specimen and making the composition appear lower than its true value .

Ingot 3 is the smallest of the castings to exhibit any evidence of macrosegregation, as shown in figure 4.10(c). Clearly, therefore, one (or more)

Fig 4.10. Comp'n vs. position plots determined in Ingots 1; 2; 3 and 4.

Comp'n values in wt.% Cu

Nominal comp'n 5·6 wt.% Cu.



INGOT 5.

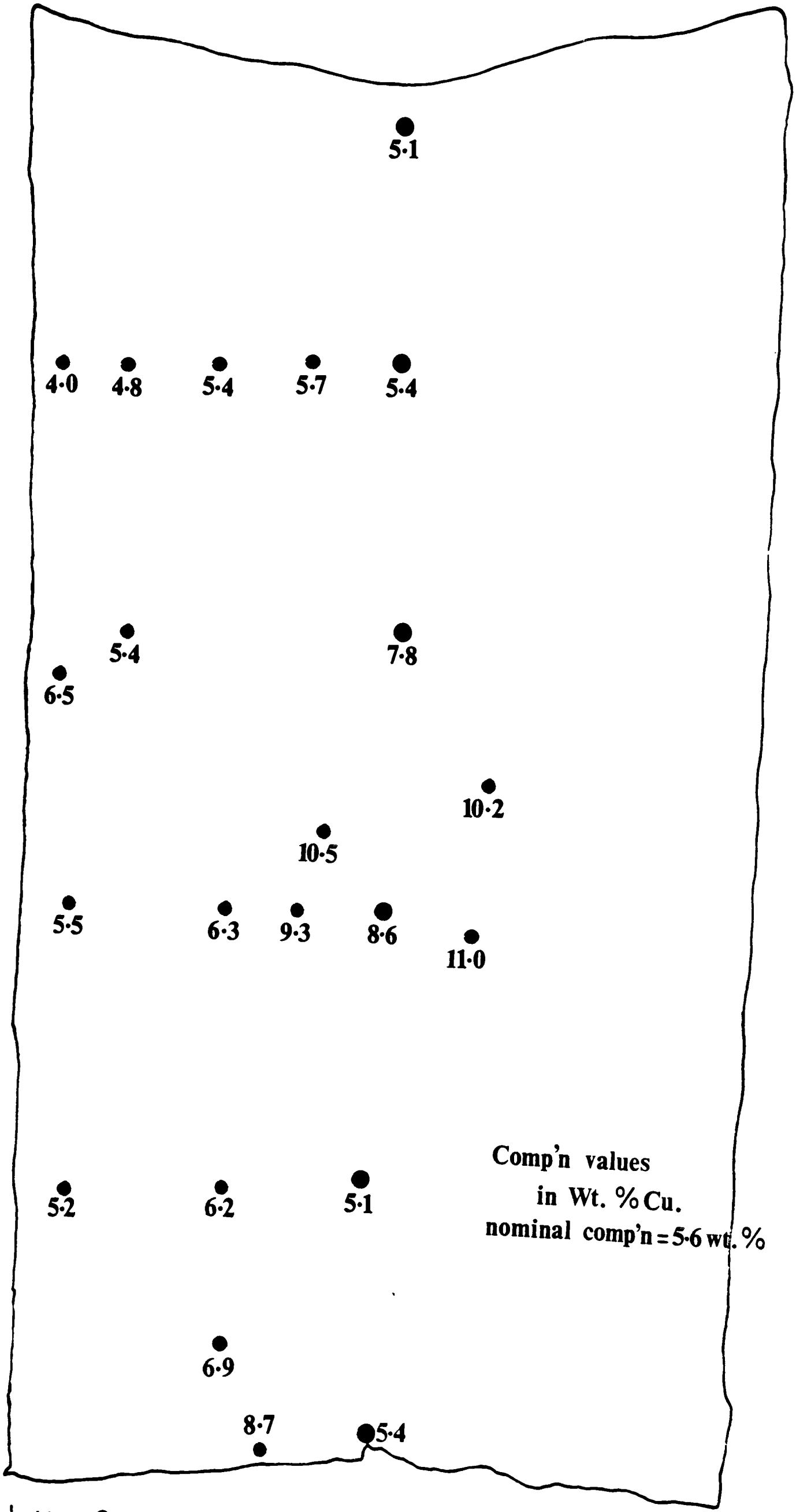


Fig 4.11. Composition vs position plot determined in Ingot 5.

of the time-dependent macrosegregation mechanisms has begun to produce appreciable segregation at some point in between the freezing times of ingots 2 and 3. Indeed the mechanism(s) must have been operating for quite a considerable time in ingot 3 because the alloy has become very inhomogenous. Segregation has occurred chiefly in a vertical direction with solute depletion at the top of the ingot and solute enrichment at the centre and bottom. The highest observed values of composition appear at approximately mid-height in the ingot near to the centreline, where the solute enrichment is up to 25% above the nominal solute content of the alloy. It should be noted that these high composition values lie close to the central shrinkage cavities, indicating that the region of maximum solute enrichment was also that of the last liquid to freeze.

The pattern of macrosegregation observed in ingots 4 and 5 and shown in figures 4.10(d) and 4.11 respectively, is very similar to that of ingot 3. There is pronounced vertical segregation in the ingots. In addition, in these two larger ingots there is also an appreciable amount of radial segregation throughout the ingot height. This type of segregation can be seen to a lesser extent in ingot 3, its magnitude in this ingot probably being camouflaged by the sampling positions which were chosen. A solute depleted region occupies the top quarter of each of these three ingots and this spreads down the outer sides of ingots almost to their base. The solute enriched region on the other hand is somewhat conical in shape with its apex extending up to approximately two-thirds of the height of each ingot in a narrow region around its centreline.

The regions of maximum solute concentration in ingots 4 and 5 were measured to be around the centreline of the ingots at a height of approximately 0.4h above the base. This is somewhat lower than in ingot 3. However these regions are again associated with the gross centreline porosity indicating that they correspond to the last liquid to freeze. The magnitude of the observed macrosegregations increases with increasing ingot size, which confirms that a time-dependent mechanism is responsible for their formations. The maximum solute enrichment determined in ingot 5 was 11.0 wt% Cu which is 79% above the

nominal solute content.

4.4.4 Temperature Measurements

Figure 4.12. shows the complete temperature versus time (T vs. t) traces recorded by the two thermocouples in ingot 2. After an initial rapid loss of the melt superheat both traces exhibited a plateau at the same temperature, just below the calculated liquidus of the alloy. The trace from the outer thermocouple left this plateau earlier than that from the centre thermocouple. Both traces fell gradually from the plateau and eventually recombined at a temperature of around 610°C. They then continued to fall together until the eutectic temperature was reached at which a sharp arrest was observed.

The T vs. t plots obtained from the thermocouple pairs in the other ingots were of this same general form, except for one particular feature which appeared in the three larger ingots. This feature is illustrated in figures 4.13(a) to (c) which show the first part of the T vs. t traces from the thermocouples in ingots 3, 4, and 5 respectively. It involves the way in which the trace of the central thermocouple fell from the 'liquidus' plateau temperature. In ingots 1 and 2 this occurred smoothly with a gradual increase in the rate of temperature loss. In the larger three ingots, however, the fall from the plateau was initially steeper than for ingots 1 and 2, and this rate of temperature loss was observed to be constant for a certain period of time. Furthermore, in ingots 4 and 5 the central thermocouple trace exhibited several subsequent plateaux at lower temperatures, before settling down to the gradually increasing decline in temperature observed in ingots 1 and 2.

The traces from the outer thermocouples of ingots 4 and 5 were incomplete as shown in figures 4.13(b) and (c) because of lack of foundry time which meant that the casting of these two larger ingots had to be overlapped, and facilities were available only for monitoring two thermocouple signals at any one time.

The times and temperatures which are considered to be of importance have been denoted by the symbols on the traces in figure 4.12., and their values in each of the ingots are given in table 4.4 which accompanies the figure. The

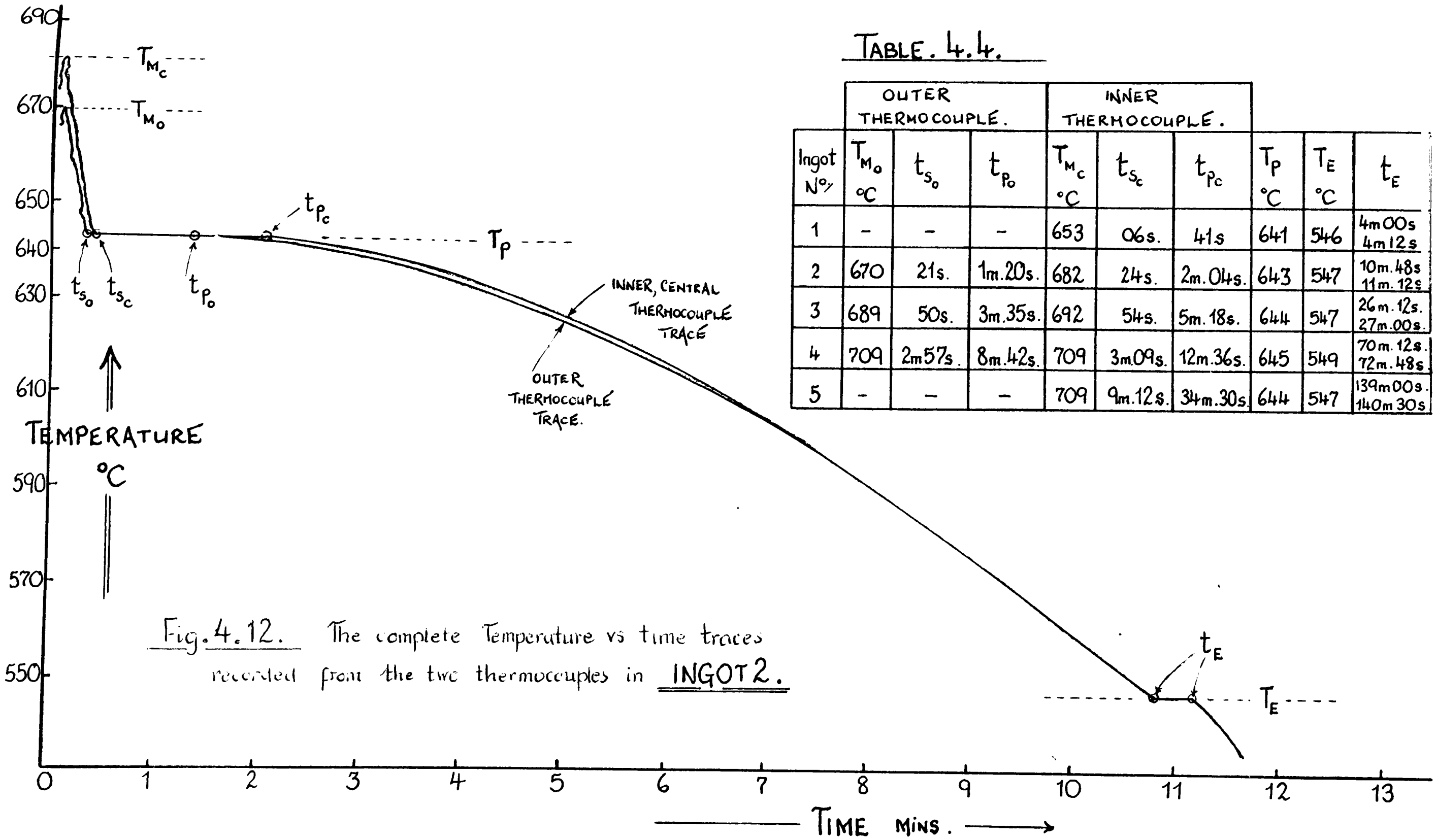


Fig. 4.12. The complete Temperature vs time traces recorded from the two thermocouples in INGOT 2.

TABLE. 4.4.

	OUTER THERMOCOUPLE.			INNER THERMOCOUPLE.					
Ingot N°	T_{M_o} °C	t_{S_o}	t_{P_o}	T_{M_c} °C	t_{S_c}	t_{P_c}	T_P °C	T_E °C	t_E
1	-	-	-	653	06s.	41s	641	546	4m00s 4m12s
2	670	21s.	1m.20s.	682	24s.	2m.04s.	643	547	10m.48s 11m.12s
3	689	50s.	3m.35s.	692	54s.	5m.18s.	644	547	26m.12s. 27m.00s.
4	709	2m57s.	8m.42s.	709	3m.09s.	12m.36s.	645	549	70m.12s. 72m.48s.
5	-	-	-	709	9m.12s.	34m.30s.	644	547	139m00s. 140m30s

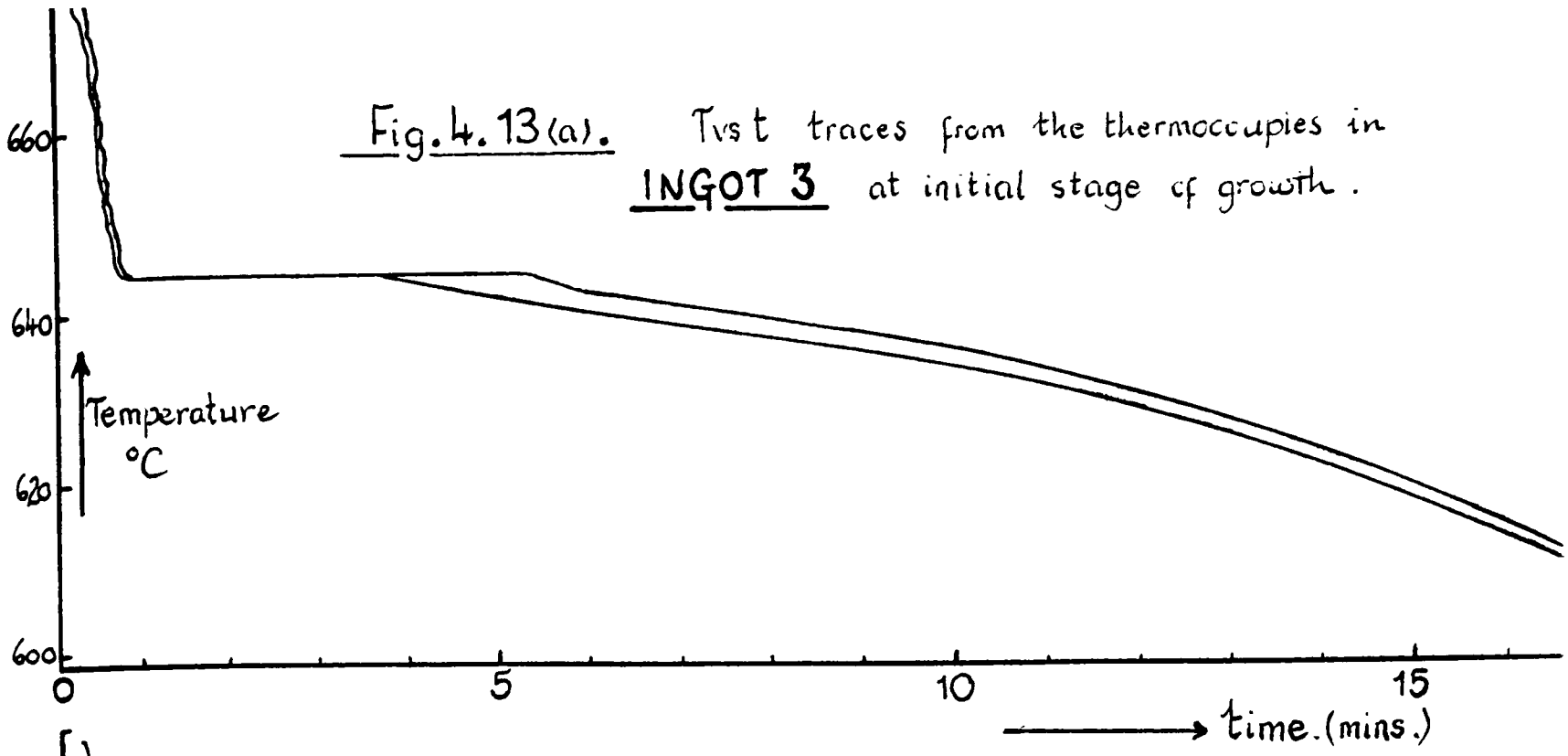


Fig.4.13(a). T vs t traces from the thermocouples in **INGOT 3** at initial stage of growth.

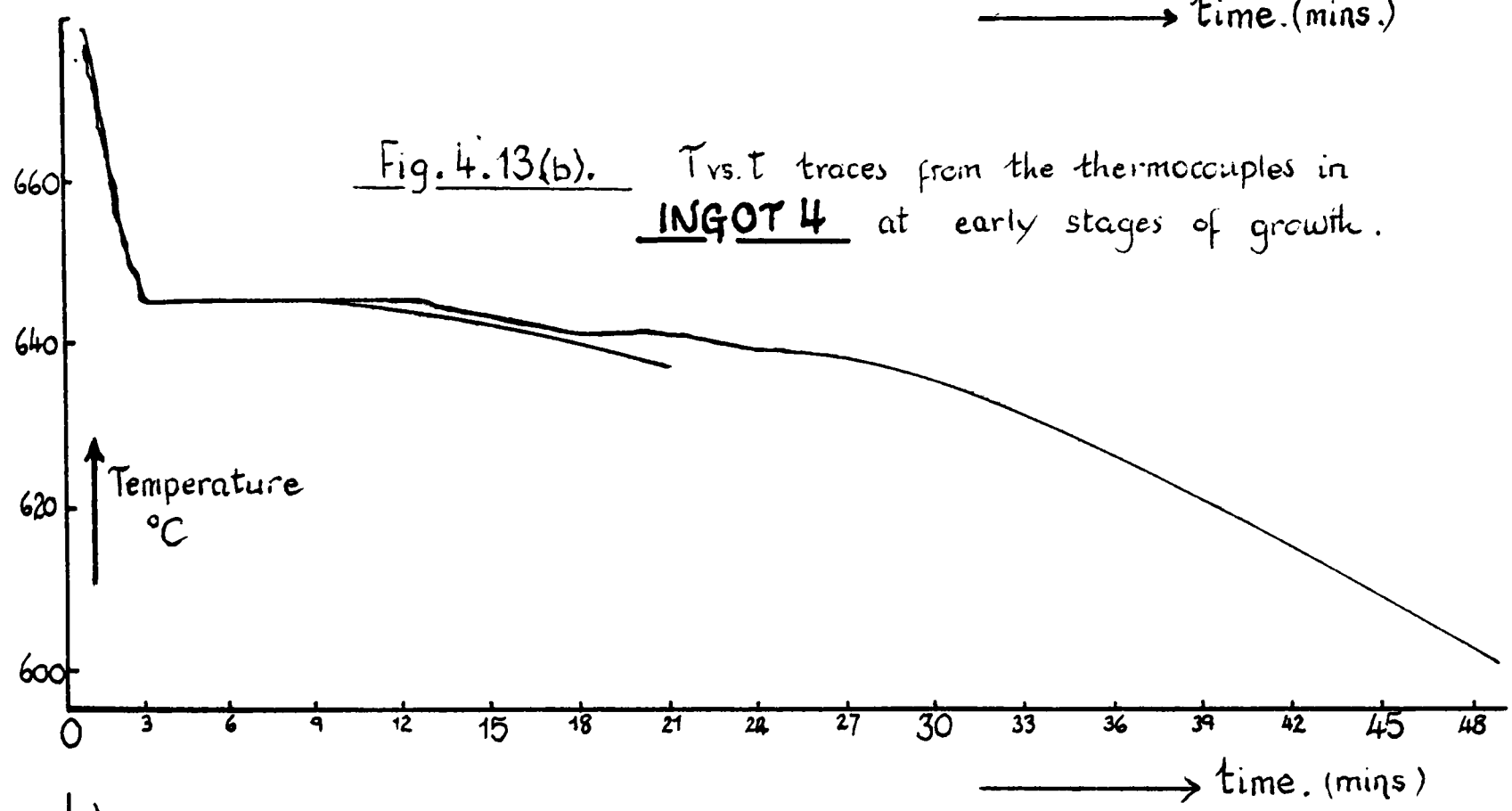


Fig.4.13(b). T vs. t traces from the thermocouples in **INGOT 4** at early stages of growth.

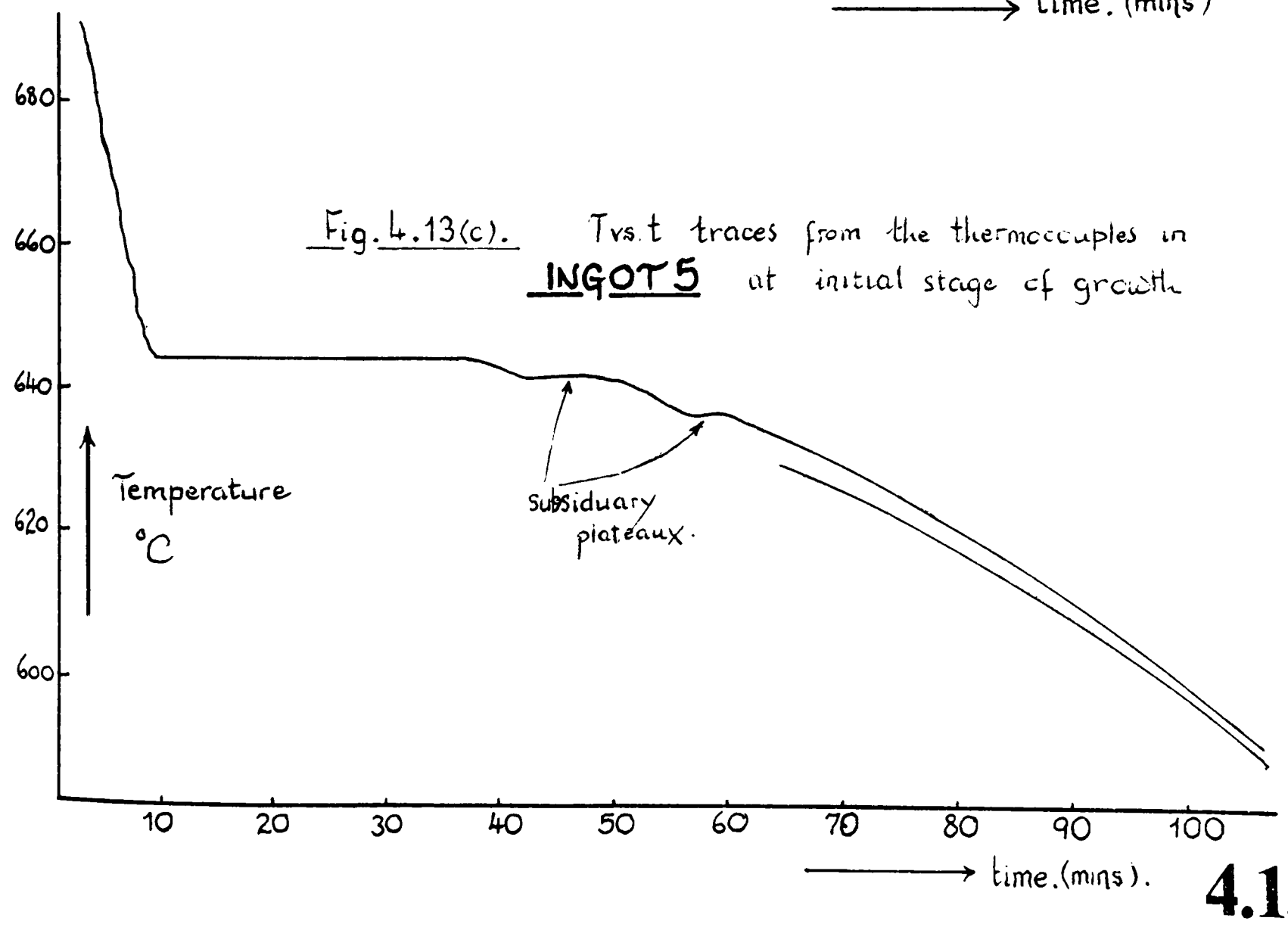


Fig.4.13(c). T vs.t traces from the thermocouples in **INGOT 5** at initial stage of growth

values given for tp_c for ingots 3,4, and 5 relate to the time at which the trace fell from the initial plateau. The values given for T_p, T_E and t_E relate to both centre and outer thermocouples in each ingot, since at these points the traces coincided. Times were measured from the moment that metal was first poured into the mould. The accuracy of both time and temperature measurements for each ingot are given in Table 4.4.

The interpretation of T vs. t curves from thermocouples positioned in solidifying ingots has been well established for cases of columnar growth by both Backerud[55] and Burden.[56] The rapid loss of the melt superheat is caused by vigorous convection currents within the melt resulting both from pouring turbulence and from the large temperature gradients which initially exist across the molten pool. Very little growth occurs away from the sides of the mould during this initial period until the pouring superheat is lost. The plateau region of the traces corresponds to the growth of columnar dendrites in from the mould walls towards the thermocouple positions. The bulk liquid pool is practically uniform in temperature during this period (i.e. the plateau temperatures of the two thermocouples coincide) and so must be relatively stagnant. The plateau temperature represents the growth temperature of the advancing columnar dendrite tips and so is undercooled slightly from the equilibrium liquidus temperature of the alloy. Each trace begins to fall from the plateau temperature once the relevant thermocouple has been passed by the advancing columnar interface. For cases of columnar growth the value of $(tp_c - ts_c)$ measured by the central thermocouple therefore represents the time taken for the semi-solid zone to advance from the edge to the centre of the ingot. The values of $(tp_c - ts_c)$ measured from the ingots in this experiment are given in Table 4.5 below:-

Table 4.5

Ingot Number	1	2	3	4	5
$t_{p_c} - t_{s_c}$	35s	1m40s	4m22s*	9m27s*	25m18s*

The values for ingots 3,4 and 5 are marked with an asterisk because there is

some doubt whether these values actually do represent the times taken for the advance of the semi-solid zones from edge to centre. For columnar growth the fall of the trace from the plateau temperature occurs gradually and the rate of temperature loss steadily increases with time. This can be seen in the traces from ingots 1 and 2 where growth was completely columnar. The secondary plateaux and linear temperature falls observed in the T vs. t traces of ingots 3,4 and 5 do not follow this classical pattern. It seems likely that these features were caused by a combination of two factors; equi-axed crystal growth and macrosegregation in the bulk liquid pool. Ingots 3, 4, and 5 all have equi-axed zones in their macrostructure. Growth of equi-axed crystals within the bulk liquid pool would have caused more heat to be extracted from this region than for columnar growth alone. Ingots 3, 4, and 5 also contain large amounts of macrosegregation. During growth the average composition of the bulk liquid pool in these ingots would therefore have been continually increasing. The equilibrium liquidus temperature of the material in the bulk liquid pool would correspondingly have been falling, which in turn would have induced the growth temperature of the advancing columnar dendrites (which determines the bulk liquid temperature) to have fallen. Both equi-axed growth and macrosegregation could therefore have caused the temperature trace of the central thermocouple to leave its initial plateau before the columnar fronts reached the ingot centreline.

The temperature gradients in the semi-solid zones were small in all five ingots. In ingot 2, for example, the maximum temperature difference observed between the two thermocouple traces was only $2^{o}C$ which corresponds to a temperature gradient of $2\frac{1}{4}^{o}C/cm$.. Furthermore it can be seen from figure 4.12 that the two traces actually coincided near the end of the freezing process. This is typical of alloys of wide freezing range and high conductivity, such as Al-5wt% Cu, cast into sand moulds.[101] The castings essentially solidify as a near-uniform mush once the columnar fronts have advanced to the centre.

Al-5.6wt% Cu is fairly dilute alloy composition (C_E = 33.0wt% Cu) and so the majority of solidification occurs near the liquidus temperature.

Table 4.6., below gives the equilibrium volume fraction liquid (g_L) at various temperatures within the solidification range of this alloy, calculated using the Scheil equation.[66]

Table 4.6

T °C	644	640	635	620	610	600	548
g_L	1.00	0.78	0.60	0.35	0.28	0.22	0.11

Clearly g_L has fallen to 0.60 at only 9°C below the liquidus temperature.

The time taken for the central thermocouple trace to fall to a temperature of 613°C is given for each of the ingots in Table 4.7 below.

Table 4.7

Ingot No.	1	2	3	4	5
$t_{613°C}$	2m14s	6m18s	16m35s	43m24s	89m00s

These times are considered to be of significance because they correspond roughly to the point when g_L fell below 0.30 in the centre of each ingot. In Chapter 6 of this thesis it is shown that gravitational fluid flow ceases to produce macrosegregation at $g_L < 0.30$.

The final time of interest is that of the eutectic arrest. A sharp eutectic arrest was observed in the thermocouple traces from all five ingots. The times at which the traces came off this arrest have been taken as the total solidification times of the ingots. These are listed in Table 4.8., below, together with the theoretical freezing times predicted for these ingots by the treatment described in section 4.2.3.

Table 4.8

Ingot No.	1	2	3	4	5
Predicted freezing time t_f	2m17s	6m21s	19m16s	51m42s	151m55s
Actual total freezing time t_E	4m12s	11m12s	27m00s	72m48s	140m30s

It can be seen from the Table that the actual freezing time was greater than the predicted freezing time in every ingot except the largest, although the difference between the values was not too marked. The theoretical treatment had therefore clearly fulfilled its purpose in providing ingots of approximately the required freezing times.

4.4.5 Macrosegregation Mechanisms

The segregation observed in ingots 3,4, and 5 was essentially of a vertical nature with solute depletion at the top of the ingots and solute enrichment towards the bottom. This form of segregation is consistent with the operation of the gravity flow mechanism in these ingots, and, indeed, gravity flow is the only macrosegregation mechanism which can account for it.

Figure 4.14(a) is a simple schematic representation of the way in which solidification must have progressed in the three larger ingots. There are columnar regions advancing from the sides and bottom of the ingot moulds as well as from the top free surface, and equi-axed crystals are growing in the bulk of the melt. Now in hypo-eutectic Al-Cu alloys, such as the Al-5.6wt% Cu composition used in this experiment, copper atoms are rejected by growing dendrites. This means that in columnar regions the interdendritic liquid becomes progressively more enriched with solute as growth proceeds, and consequently becomes progressively denser (Atomic Wt. Al = 27; Cu = $63\frac{1}{2}$). Convection currents in those semi-solid regions growing horizontally from the mould walls in these ingots would therefore have been as shown in figure 4.14(a). The dense interdendritic liquid would have had a tendency to sink with respect to the purer bulk liquid and so would have flowed out of the semi-solid zone towards the bottom of the ingot. Bulk liquid would then have flowed into the semi-solid zone towards the top of the ingot to complete the convection cycle. Such flow would indeed have led to the observed solute depletion at the top of the ingot and solute enrichment at the bottom. Furthermore, any solute enrichment at the bottom of the bulk liquid pool represents a gravity-stable situation. This, coupled with the sluggish nature of the bulk liquid convection

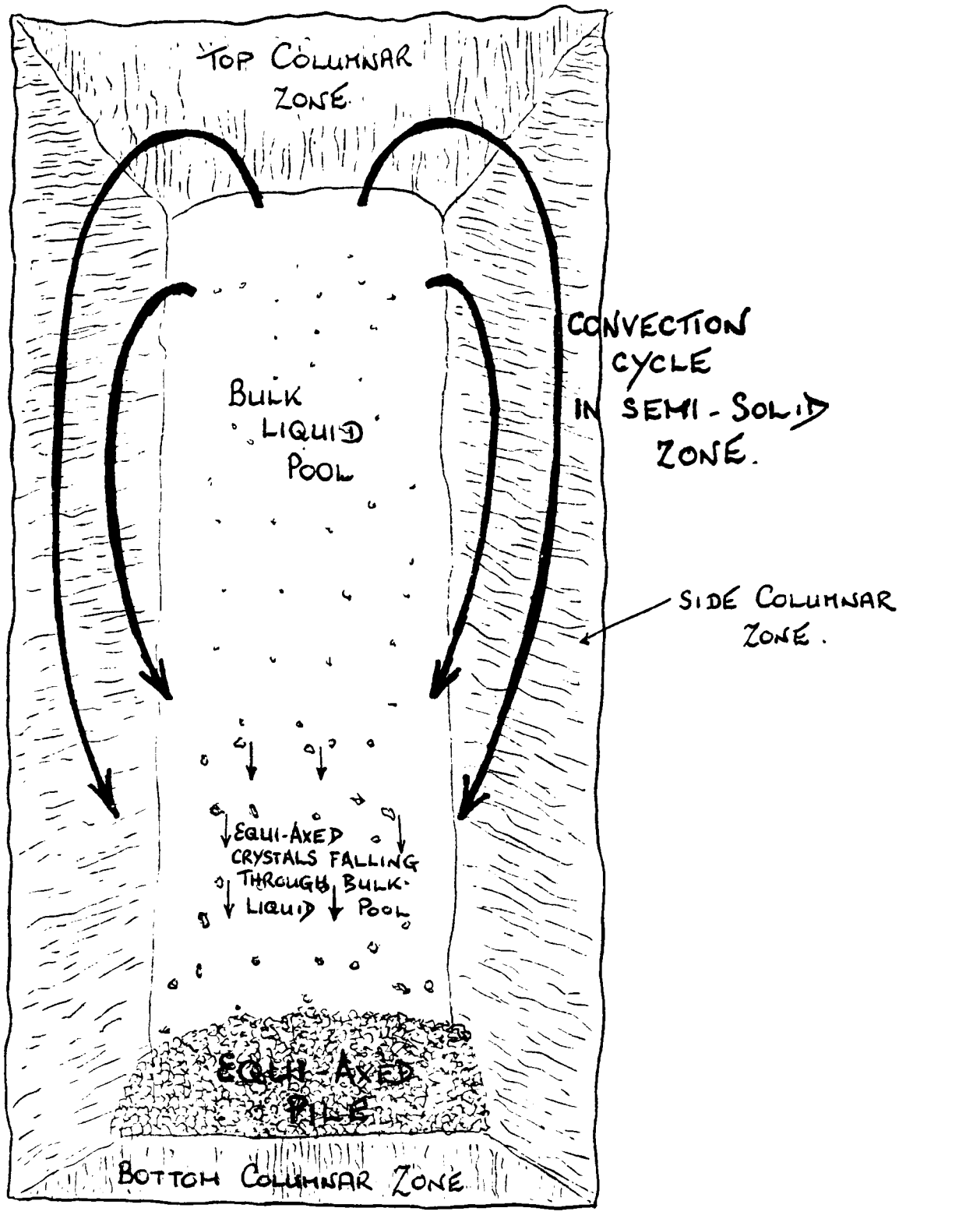


Fig. 4.14(a) Schematic illustration of expected freezing process in ingots 3, 4, and 5 at an intermediate stage of growth.

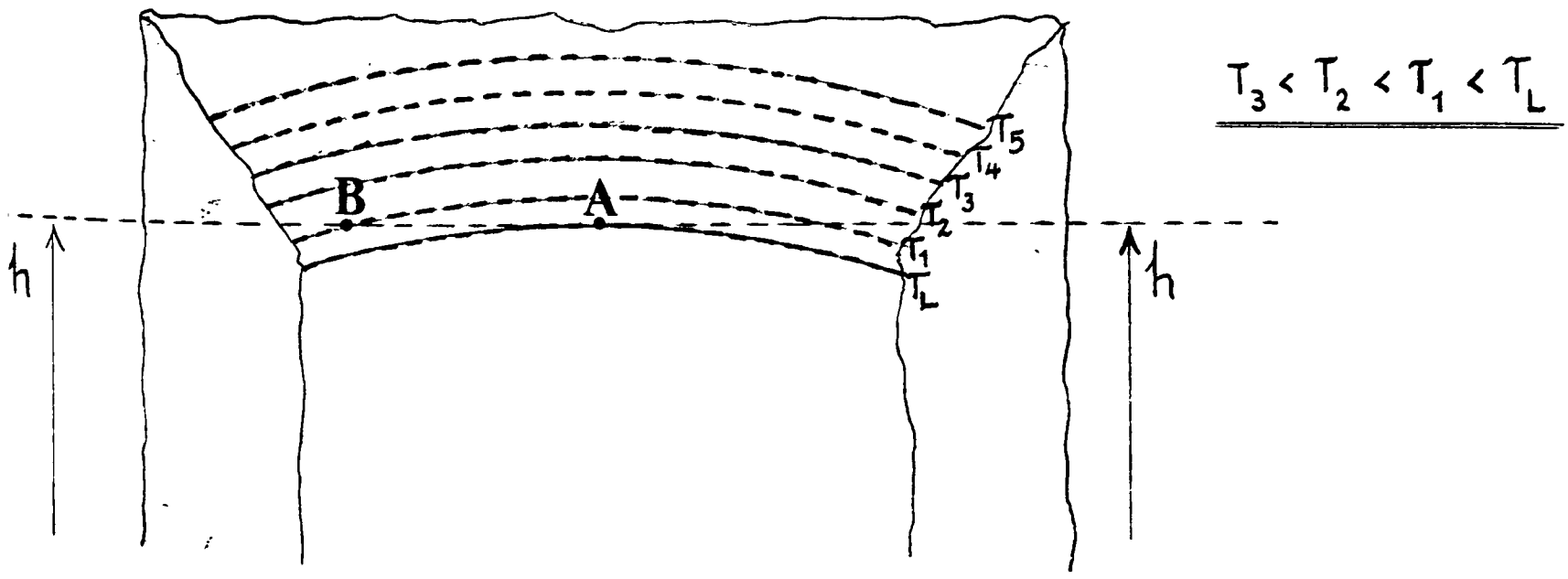


Fig. 4.14(b). Schematic representation of expected isotherm curvature near top of ingot in semi-solid crust.

currents during growth, meant that solute simply accumulated at the bottom of the pool and was not mixed into the bulk of the liquid; this accounts for the very large magnitudes of positive segregation observed in these ingots.

The columnar region growing down from the top free surface of the ingots would probably have taken the contour shown in figure 4.14(a) with the isotherms convex to the surface. This seems likely since heat would have been extracted from this region through the mould walls as well as through the free surface. Also any convection currents remaining in the bulk liquid pool would have been throwing hotter liquid up towards this top interface in the centre of the ingot. Such an isotherm curvature would have meant that, at a given height in the ingot, h,figure 4.14(b), interdendritic liquid at B near the edge of the ingot was colder than that at A near the centre of the ingot. Liquid at B would therefore have contained more copper than that at A and so would have been denser, thus leading to the type of convection cycle shown in figure 4.14(a) for this top semi-solid region. Such a cycle would have lead to solute depletion in the top central region of the ingots and very localised solute enrichment around the top circumference. This was the type of segregation pattern observed in these regions. Indeed, large vertical indentations could be seen around the outside surface towards the top of ingots 4 and 5, and these had probably been solute-enriched channels which were insufficiently fed in the last stages of freezing.

Channels comparable with A segregates in steels could not be readily observed in the macrostructures of these ingots. This is because the alloy composition was such a long way from that of the eutectic. The solute enriched liquid in these channels which undoubtably did exist during solidification would have eventually been plated out onto existing dendrites, thereby camouflaging the channels in the final structure. The high readings of 6.0wt% Cu and 6.5wt% Cu observed towards the sides of ingots 3 and 5 respectively, (figures 4.10(c) and 4.11),were presumably a result of the sampling position intersecting some part of a solute enriched channel.

Equi-axed crystals do appear in the macrostructures of the three larger

ingots in spite of the steps taken to minimise their formation. Equi-axed segregation mechanisms cannot, however, be used to explain the observed solute patterns. In the Al-Cu system primary dendrites are denser than the liquid from which they form for alloys with copper contents of less than 9.9wt% Cu.[78,133] The solute-depleted dendrites in these ingots would therefore have sunk in the bulk-liquid pool, and, indeed, the equi-axed zones do appear towards the bottom of the ingots. Such movement would have led to negative segregation in these regions, which is opposite to the general pattern observed. Consequently although an equi-axed mechanism has undoubtably operated in these ingots its effects have been largely swamped by those of the gravity flow mechanism. It may well explain however why the maximum positive segregations appear so high up in the ingot sections, and also why there are some negatively segregated areas near to the bottom of ingot 5. Finally, it should be noted that equi-axed crystals only appear in the three larger ingots where the gravity flow mechanism has operated. It may well be, therefore, that the gravity flow mechanism was responsible for their formation by partially remelting and detaching dendrite arms from within the columnar regions.[50,51]

4.5 Summary

In this experiment five ingots of an aluminium - 5.6wt% copper alloy were cast into sand moulds. These ingots were cylindrical in shape and of fixed aspect ratio (h/r = 4/1) but different volumes. Composition measurements performed on the ingots after solidification showed that macrosegregation became significant only in the three largest ingots. It was demonstrated that the form of the observed macrosegregation was consistent with the operation of the gravitational interdendritic fluid flow mechanism, and that it could not have been produced by any other mechanism. Temperature measurements were taken during solidification from thermocouples positioned in the melts. The T vs. t traces produced were of the classical form[55,56] for this type of casting situation, and so it was possible to interpret them in terms of the way in which the growth process was progressing in the ingots. Values were therefore obtained

for the times taken by the columnar fronts to advance from the edge to the centre of the ingots, as well as for the overall freezing times of the ingots. Furthermore, by using the Scheil equation in conjunction with the T vs. t traces it was possible to estimate the times at which the volume fraction of liquid at the centre of the ingots fell below 0.30. This is the value of g_L (predicted in Chapter 6 of this thesis) below which fluid flow ceases to cause significant macrosegregation.

The critical region for the onset of appreciable gravity flow segregation lay between ingots 2 and 3 in this experiment. Table 4.9., below, summarises the values of those size and freezing time parameters considered to be of significance in these ingots.

Table 4.9

Ingot No.	Volume ccs.	Ingot Weight Kg.	Ingot Diameter mm.	$t_{pc} - t_{sc}$	t_{613}	Total Freezing Time t_E
2	284	0.739	54	1m40s	6m18s	11m12s
3	1,339	3.500	94	4m22s	16m35s	27m00s

In view of the large magnitude of macrosegregation observed in ingot 3 it seems likely that the critical values of the above parameters for the onset of gravity flow segregation lie closer to those given for ingot 2 than those for ingot 3. Consequently it can be stated with some confidence that to avoid gravity flow macrosegregation with aluminium-copper alloys then castings must be small enough to be completely mushy within 2 minutes and fully solidified within 15 minutes. Furthermore, it should be noted that although these critical time values apply strictly only to un-nucleated Al-5½% Cu sand castings, it is likely that the corresponding times for other alloys and casting situations will be similar. The critical size values suggested by Table 4.9 for Al-Cu sand castings are a volume of approximately 400 ccs. and a weight of approximately 1200 gms.. This critical volume is likely to be roughly applicable to sand (or other insulating mould) castings of other alloys but it will not apply to

chill moulds where the critical volume for macrosegregation will be much higher, owing to the increase in freezing rate in such moulds.

CHAPTER 5

REVIEW OF PREVIOUS WORK PERFORMED ON THE NATURE AND EXTENT OF GRAVITATIONAL INTERDENDRITIC FLUID FLOW

5.1 Introduction

Fluid flow in the semi-solid zone of a casting under the influence of of gravitational forces is now generally accepted as being an important mechanism for macrosegregation.[79] The operation of the mechanism has been demonstrated visually in transparent analogue systems[81,82,94] and in experiments involving radioactive additions to solidifying ingots.[61,84] It has also been inferred from composition measurements made on laboratory castings,[85,86] and it provides a ready explanation for the channel and freckle defects often observed in large ingots.[2,5] Little quantitative work has been performed, however, to discover whereabouts in the semi-solid region the majority of gravitational fluid flow occurs, or to discover what proportions of the segregation is caused by flow at different depths in the semi-solid. Those pieces of work which have looked into these questions have apparently reached quite diverse conclusions about the nature and extent of interdendritic fluid flow.

In this chapter the various papers relating to the nature and extent of gravitational interdendritic fluid flow are reviewed, and an explanation is given for the apparent contradictions in their conclusions. Furthermore, from this review an insight is gained into how the extent of fluid flow with position in the semi-solid zone may be studied without ambiguity.

5.2 Review

The first piece of work to examine the nature of gravitational fluid flow, albeit rather qualitatively, was that of McDonald and Hunt.[81,82] They used the transparent ammonium chloride-water analogue system to study interdendritic flow and channel formation. Pipes of rapidly rising liquid were seen in the semi-solid regions of their model ingots similar in appearance to the A segregates found in large steel ingots. They observed that these pipes were

formed behind the dendritic front and concluded that they were produced by convective interdendritic flow occurring 'deep within the semi-solid zone.'

Copley et al[94] also used the NH_4Cl-H_2O system for their study of freckle formation in vertically solidified ingots. They too observed jets of solute-rich liquid moving up and out of the semi-solid region. These were seen to originate near to the bottom of the mushy zone. They therefore concluded that freckles were localised columns of convection having their origins deep in the semi-solid zone.

Stewart and Weinberg[61] employed a radiotrace technique to look at fluid flow in a metallic system. They grew a number of Sn - x Pb alloy specimens in a thin section mould (x=2;5;12.5;20 wt%). A temperature gradient was maintained across the horizontal length of the ingot, as shown in figure 5.1(a). Growth was made to proceed horizontally and unidirectionally from one end of the mould to the other by lowering the average temperature. At a certain stage in the growth process a small amount of liquid alloy containing a radioactive addition was added to the top of the bulk liquid pool. Growth was quenched 30 secs. afterwards, and any radioactive penetration of the semi-solid region was observed. They found that the tracer penetrated the semi-solid only up to quite small volume fraction solids, g_s=0.12→0.22. Their plot of penetration versus alloy composition is reproduced in figure 5.1(b), together with their table of results. In addition to this series of specimens they allowed a Sn-2wt%Pb sample to grow the whole length of the mould after insertion of the radiotrace. The available time for flow was of the order of one hour. They compared an autoradiograph from this specimen with one taken from a Sn-2wt%Pb ingot quenched 30 secs. after radiotrace addition, and suggested that the amount of penetration was similar in each one. They therefore concluded that the observed flow was caused by penetration of the solid-liquid region by bulk liquid convection currents, and that no appreciable fluid flow occurred in the semi-solid for $g_L < 0.80$.

Hebditch and Hunt[84] also used a radiotrace technique to study fluid flow in the semi-solid. They employed a model casting system similar to that of

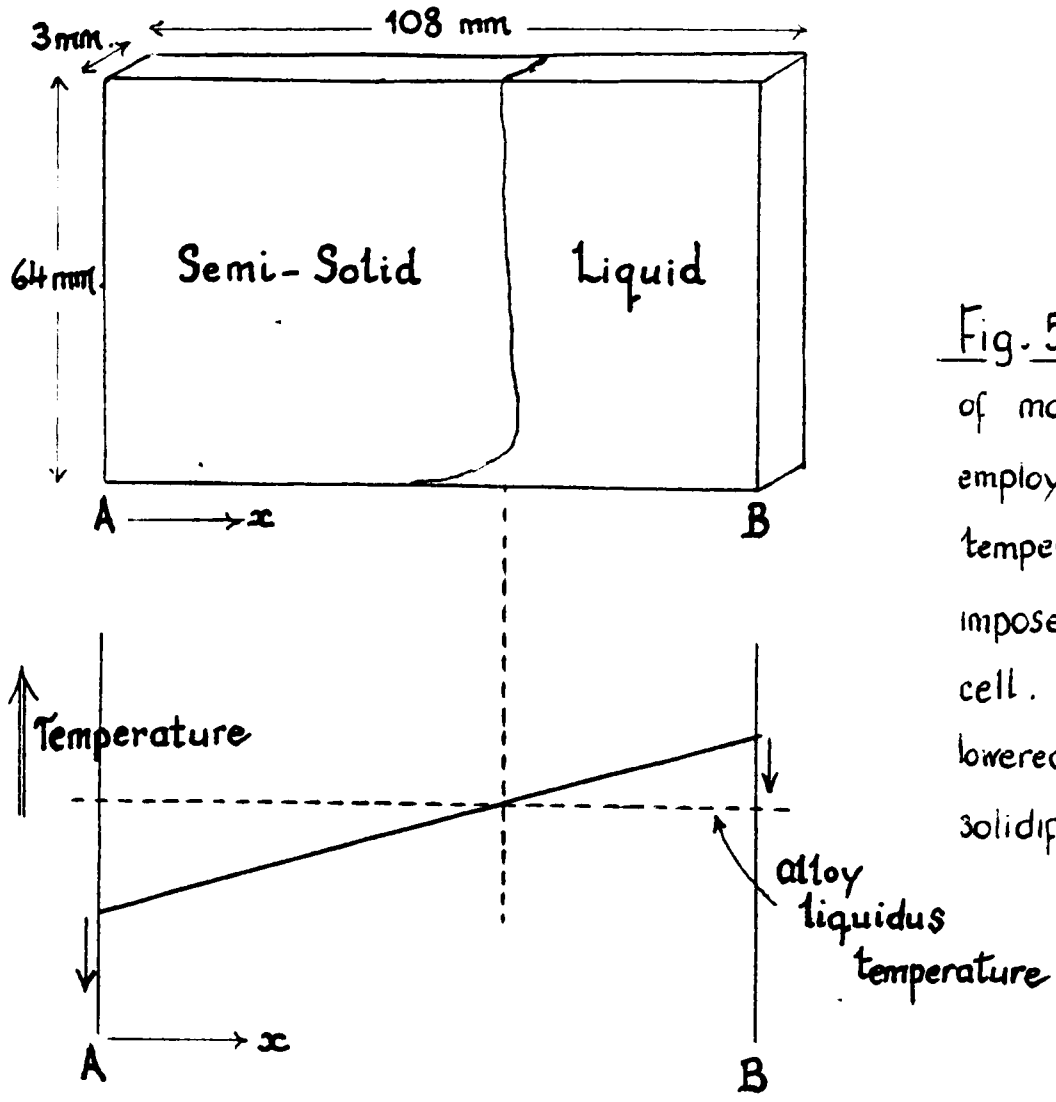


Fig. 5.1(a). Schematic view of model casting system employed by Stewart.[61] A temperature gradient was imposed along the length of the cell. Temperature of faces A & B lowered at same rate to produce solidification from A to B.

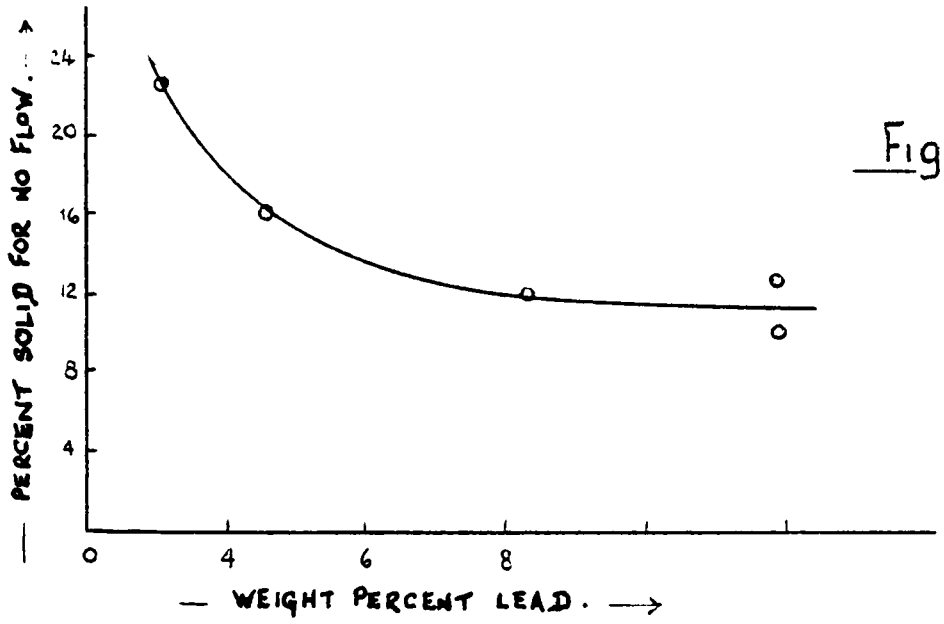


Fig. 5.1(b). Plot of the volume fraction solid (g_s) present at the point of deepest flow penetration against alloy composition.[61]

TABLE 5.1. Experimental measurements on flow penetration obtained from radiographs by Stewart and Weinberg. (ref. 61)

Alloy Composition C_o Wt.% Pb.	Temperature Gradient in semi-solid zone. G_s °C/cm.	Average distance of flow penetration cm.
2	3·69	0·20
5	3·08	0·37
12·5	5·20	0·40
20	3·50	0·89
20	4·07	0·61

Stewart and Weinberg. The technique differed, however, in that their thin section mould containing the alloy charge was held initially in an isothermal enclosure rather than in a temperature gradient. Growth proceeded horizontally unidirectionally away from a vertical copper chill block, as shown in figure 5.2(a). A number of ingots of Sn-6wt%Zn were grown at different rates. A glass syringe arrangement, containing small amounts of the alloy with a radioactive tin addition, was fixed at the same position in each ingot. The tracer was injected into the heart of the semi-solid zone when the temperature at the tip of the syringe was mid-way between the liquidus and eutectic temperatures. Growth was allowed to proceed to completion before removing the mould from the furnace. The distribution of the radioactive material was studied by contact autoradiography. The fact that the ingots had been grown at different rates meant that different amounts of time were available for flow in each one. Hebditch and Hunt observed by comparison of the ingots that the radioactivity spread out into a 'cloud' which moved upwards and back towards the chill with time. They reported that this movement was consistent with gravitational interdendritic flow since the alloy density was found to increase down the liquidus line. They also pointed out that the observed flow could not have been caused by penetration of bulk liquid convection currents into the semi-solid because these would have been moving in the opposite sense in their ingots (i.e. downwards at the interface).

Hebditch and Hunt[85] later used their model casting system to grow a number of thin section Sn-Pb, Pb-Sn, and Sn-Zn ingots, and subsequently examined these for evidence of macrosegregation. The casting system was designed so that the growth process in the ingots could be quenched at any stage. Details concerning fluid flow were inferred from composition measurements made on the quenched ingots. They inscribed a fine-scale grid of 2.5mm squares across the dendrite tip interface in several of their quenched ingots (see figure 5.2(b)). Samples were taken for analysis from each grid point using a 1.5mm diameter drill. Their results for two grids in a Sn-5wt % Pb ingot are reproduced in figure 5.2(c). These showed a gradual decrease in

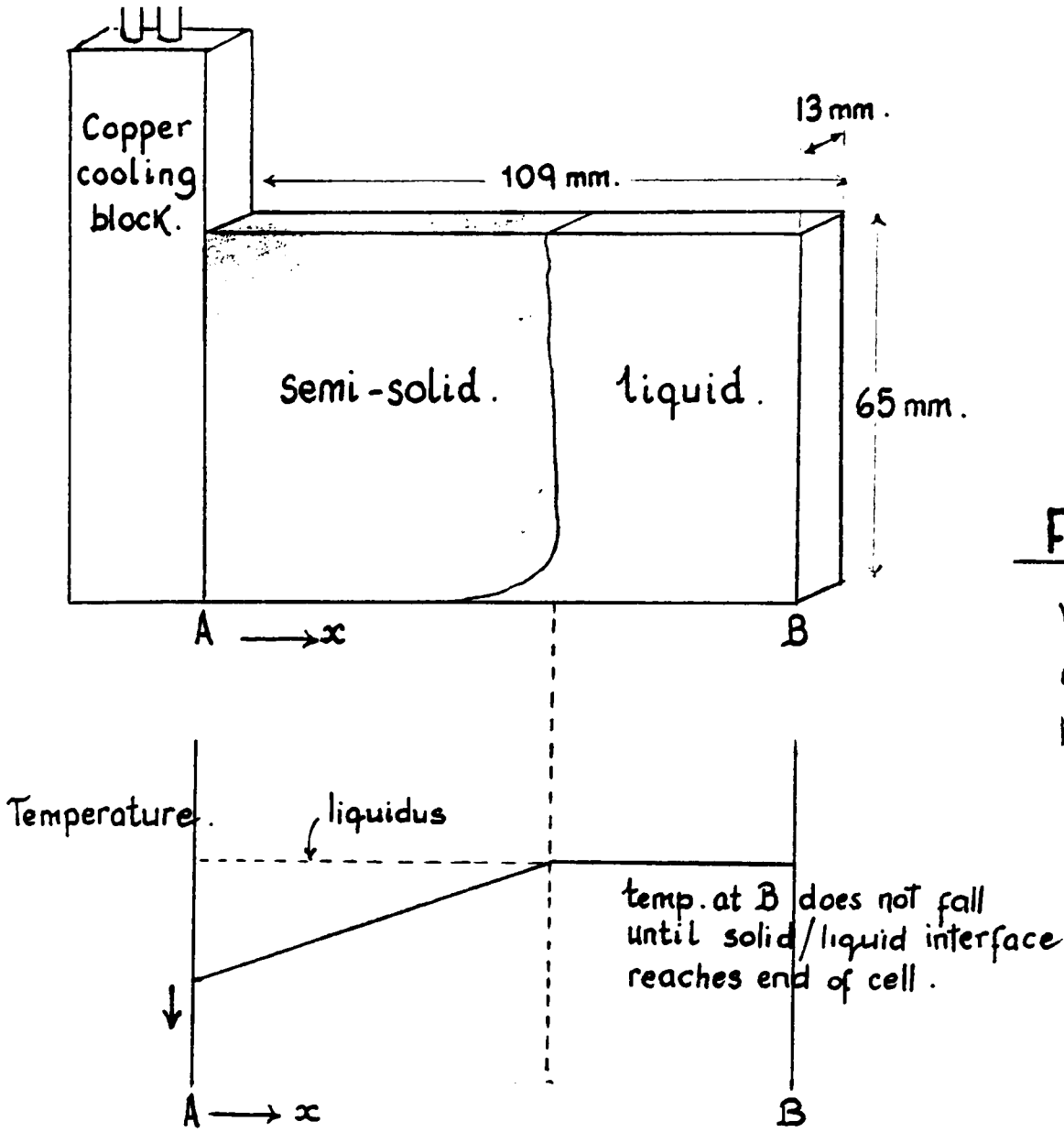


Fig. 5.2(a). Schematic view of model casting apparatus employed by Hebditch.[34,35]

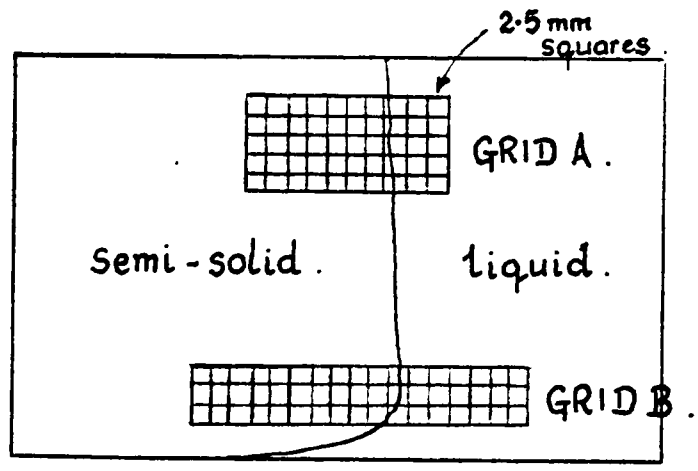


Fig. 5.2(b). Elevated section of quenched ingot, showing typical position and appearance of fine-scale grids inscribed prior to composition analysis.[85]

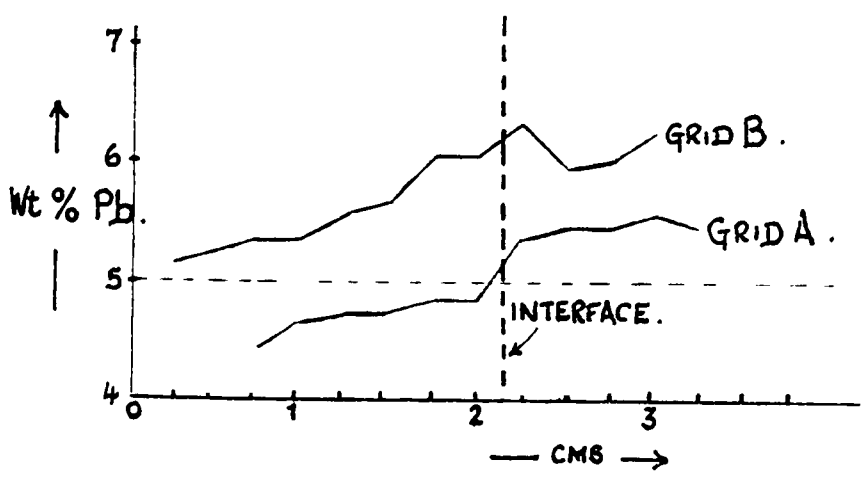


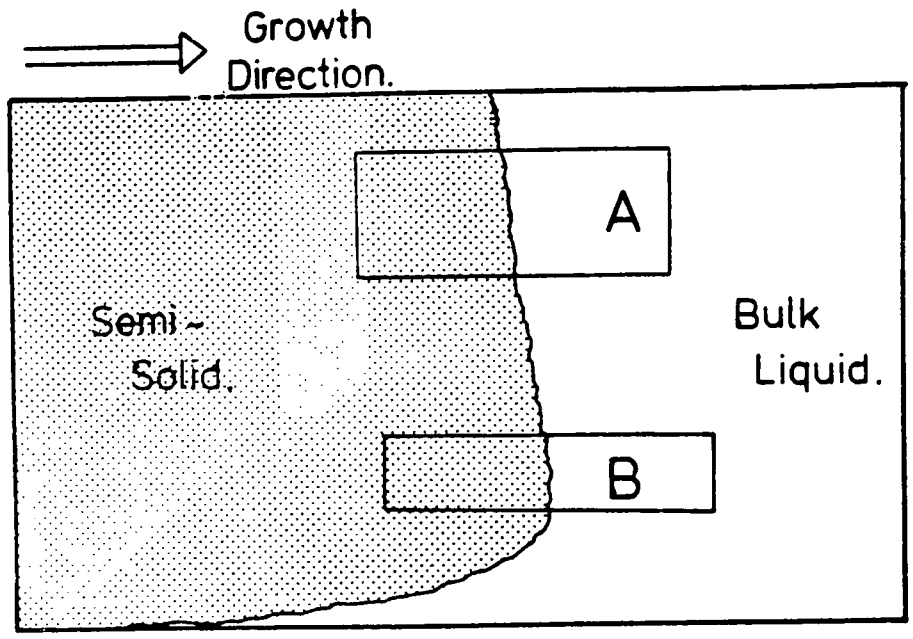
Fig. 5.2(c). 'Average comp'n' versus 'position relative to solid/liquid interface' plots for two grids in a Sn-5wt% Pb ingot.[85]

composition which tended to flatten out at a distance of around 2 cm. behind the interface in the ingots. They concluded that macrosegregation was occuring gradually behind the interface as a result of gravitational interdendritic fluid flow, and not as a sharp discontinuity at the interface itself.

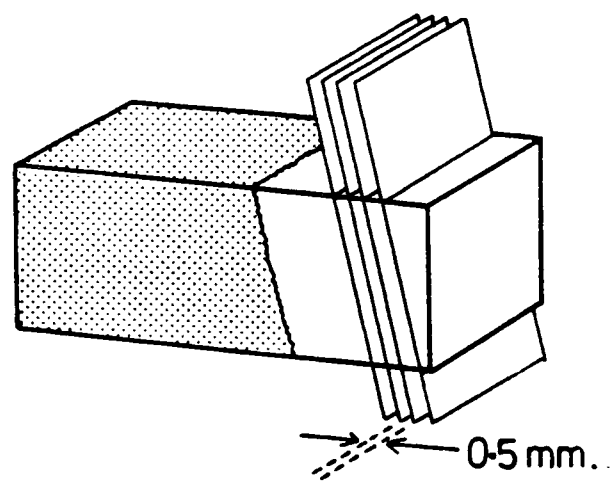
This fine-scale work was subsequently repeated by the present author[86] using an improved sampling technique. The same basic casting system was employed, and Sn-Pb ingots of various alloy compositions (0.5; 2; and 5 wt% Pb) were quenched during growth. Pieces were cut from these ingots, as shown in figure 5.3(a), across the dendrite tip interface. Skims were then taken off the end of each piece parallel to the plane of the interface at 0.5 mm intervals, figure 5.3(b). The swarf from each skim was collected and analysed. Figure 5.3(c) shows the composition versus position plots for two pieces cut from a Sn-5wt% Pb ingot. Similar results were obtained for pieces cut from ingots of the other compositions. The graphs show that fluid flow in the region immediately behind the interface had quite a considerable effect on the macrosegregation of solute. The distances involved, X in figure 5.3(c), were approximately 5mm, 3mm, and 1.5mm, for the Sn-5wt% Pb; -2wt% Pb; and 0.5wt% Pb ingots respectively. The technique allowed observations on the structure of the semi-solid to be made between skims. These showed that the composition began to fall only after the dendrite tips could be seen on the skimmed section, and that the region of rapid composition change corresponded to that in which large interdendritic liquid channels existed. The odd increase in composition following the large drop was thought to be a quenching artefact. It was concluded from the results that gravity flow was only important in causing segregation in the region just behind the dendrite tips.

5.3 Discussion

The pieces of work described in the review reached seemingly diverse conclusions concerning the nature and extent of interdendritic flow. The transparent analogue studies and the radiotracer work of Hebditch suggested that



(a.)



(b.)

(c.)

Fig. 5.3. Composition work on Sn-Pb model ingots previously performed by the author.[86]

(a) Positions from which pieces were cut

(b) Sampling technique - material skimmed parallel to interface plane.

(c) C vs x plots for two specimens from a Sn-5%Pb. ingot.

appreciable flow was occuring well inside the mushy zone. The composition work of Hebditch, and later Fisher, suggested that the important region for flow lay just behind the interface, and implied that little flow was occurring in other regions of the semi-solid. Finally the radiotrace work of Stewart suggested that gravity flow did not occur at all in the semi-solid, but instead that there was a limited amount of flow just behind the dendrite tips caused by penetration of bulk liquid convection currents.

The major cause of these apparent discrepancies lies in the fact that only one of the pieces of work made any attempt to relate position in the semi-solid region with liquid volume fraction. For example, the two analogue investigations both demonstrated in a very qualitative sense that fluid flow occurs deep in the semi-solid zone in NH_4Cl-water castings. However, it should be noted from the phase diagram shown in figure 5.4(a), that at the compositions employed in the two experiments the structure would have been very open even at the eutectic temperature. Assuming, as a first approximation, that the Scheil equation can be used to specify volume fraction liquid g_L:-

$$g_L = (C_o/C_L)^{1/1-k_o}$$

and that $k_o=0$; and C_o= initial composition = 30wt% NH_4Cl, then even at the eutectic temperature:-

$$g_L = (70/80.4) = 0.87$$

Clearly, therefore, the statements that 'flow was observed to occur deep in the semi-solid zone' are not synonymous with flow at small g_L.

A similar observation can be made concerning the radiotrace work of Hebditch and Hunt. They inserted their tracer alloy when C_L=7.5wt% Zn. Again using the Scheil equation, with C_o=6wt% Zn, and assuming $k_o=0$ (see fig.5.4(b)), then:-

$g_L = (6/7.5) = 0.80$ at the position of insertion

and $g_L = (6/9) = 0.66$ at the eutectic temperature

The Sn-Pb ingots studied by Hebditch, Fisher, and Stewart, on the other hand, had structures which were much less open. For example, in the Sn-5wt% Pb specimen grown by Stewart the penetration distance of only 3.7 mm

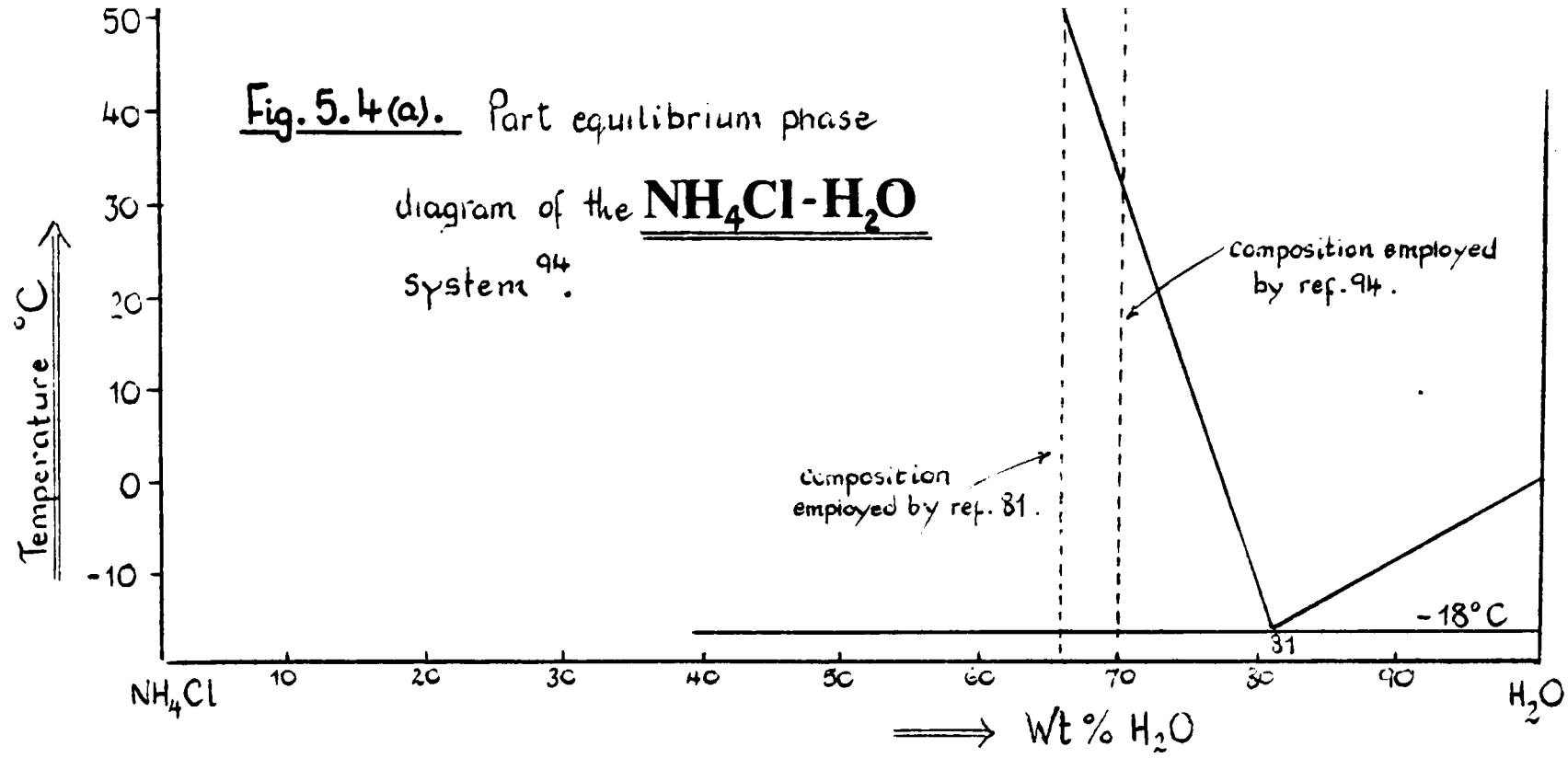


Fig. 5.4(a). Part equilibrium phase diagram of the **NH_4Cl-H_2O** system.[94]

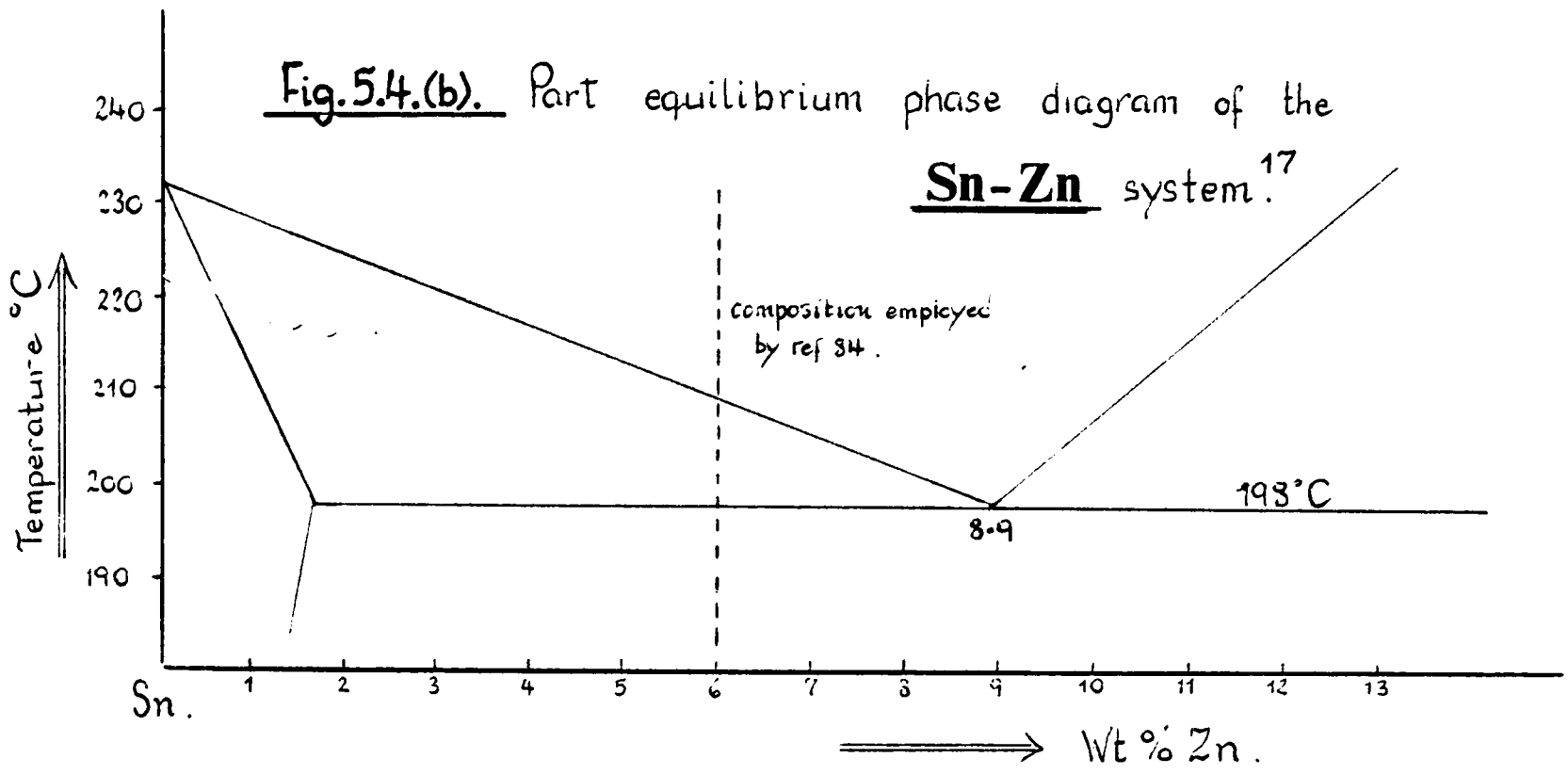


Fig. 5.4.(b). Part equilibrium phase diagram of the **Sn-Zn** system.[17]

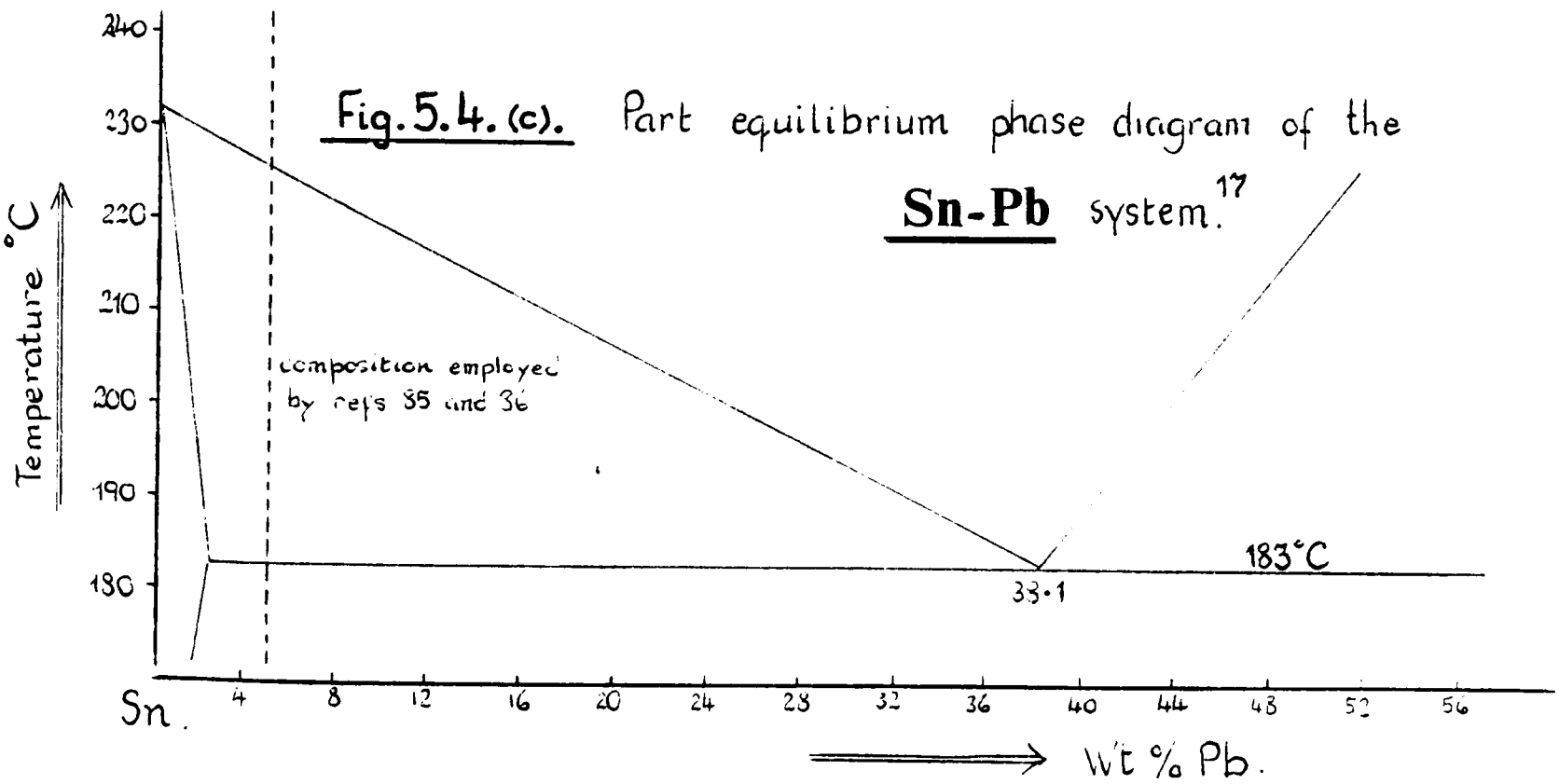


Fig. 5.4.(c). Part equilibrium phase diagram of the **Sn-Pb** system.[17]

Fig. 5.4. Part equilibrium phase diagrams showing the relationship of the sample compositions used in the various experiments to the eutectic comp".

equated with a liquid volume fraction $g_L = 0.84$. Values of g_L were not quoted in the works of either Hebditch or Fisher. However, the temperature gradients in the semi-solid regions of their ingots (G_S) were similar to those given by Stewart, and so g_L should also have fallen quite rapidly behind the interface in their specimens.

Values of g_L corresponding to the distance X measured by Fisher, fig. 5.3(c), are given in the table below, using the Scheil equation and values of G_S quoted by Fisher. Values of $k_o = 0.07$, and $m = -1.29^{\circ}C/wt\%$ Pb are assumed.

Table 5.2

C_o wt%Pb	X cm	G_S °C/cm	$C_L=-G_SX/m$ wt%Pb	g_L
5	0.50	3.6	6.40	0.77
2	0.30	3.2	2.74	0.71
0.5	0.15	3.4	0.90	0.54

It would therefore appear, from these conversions of distance into volume fraction liquid, that the results of these pieces of work are not in contradiction with each other. They all agree, in fact, that an important region for fluid flow in the mushy zone is that in which g_L is large. However, it should be noted that none of the experiments, by design, can give any indication of the extent and importance of fluid flow at lower values of g_L:-

(a) The experiements on NH_4Cl - water and Sn-Zn were such that g_L was still large even at the eutectic temperature.

(b) The fine scale works of Hebditch and Fisher were both wrong in inferring from their results that flow at low g_L was negligible. Both of the experiments studied the composition vs. position patterns in individual ingots quenched after particular times of growth. The growth process in the ingots examined was not, however, at steady state. Consequently no information could correctly be inferred from their results concerning any subsequent variations in composition at a given position.

(c) The radiotrace work of Stewart and Weinberg relied on comparison of the interface shape at the time of insertion with the region of activity

observed after quenching. This could only be done accurately in the ingots quenched soon after radiotrace addition. The method was therefore little suited to measuring any deep inflow into the semi-solid region, since this should have been relatively slow for the time-dependent gravity flow mechanism. In the Sn-2wt% Pb ingot grown to completion the original interface shape was inferred from that observed in the quenched Sn- 2wt% Pb ingot. However, Stewart and Weinberg made no attempt to show that growth was, in fact, reproducible from one ingot to another. Their conclusion that the depth of penetration did not alter with time must therefore be regarded with suspicion. Indeed in the two autoradiographs they show for the Sn-2wt% Pb ingots it would appear that flow had occurred further back towards the chill in the one grown to completion.

Finally, it should be noted that the penetration distances quoted by Stewart in Table 5.1, are very similar to those observed by Fisher, Table 5.2. The bulk liquid convection currents would however have been much more sluggish in the latter's experiment. It therefore seems likely that the flow observed by Stewart was caused by solute-driven convection currents in the liquid just behind the dendrite tips rather than by penetration of bulk liquid convection currents.

5.4 Summary and Conclusions

Previous work into the nature and extent of gravitational interdendritic fluid flow has been reviewed. Inconsistencies between the conclusions of these pieces of work have been highlighted. It is proposed that these inconsistencies arose because the results of the various works had been presented in different ways. It is shown that the results of all works are consistent when fluid flow is related to the volume fraction liquid values (g_L). Furthermore it is shown that although past experiments have all indicated the importance of gravity flow in producing macrosegregation at high g_L (> 0.80), none of them were designed to be able to study the effect of fluid flow at low g_L(< 0.60). This therefore suggests the need for further experimentation into the nature of interdendritic fluid flow particularly at low g_L.

CHAPTER 6

EXPERIMENTAL INVESTIGATIONS INTO THE RELATIONSHIP BETWEEN GRAVITATIONAL INTERDENDRITIC FLUID FLOW AND LIQUID VOLUME FRACTION IN A SEMI-SOLID REGION

6.1 Introduction

The work described in this chapter has been summarised and presented as a paper[72] at the 'Sheffield International Conference on Solidification' organised jointly by Sheffield University and The Metals Society in 1977.

The work was performed in order to investigate the extent and importance of gravitational interdendritic fluid flow (G.I.F.F.) at all volume fractions of liquid within a semi-solid zone. It was concluded in the review of previous work on this topic, given in chapter 5, that this objective had not hitherto been achieved. Such knowledge would be an important step towards the complete understanding, and hence control, of the gravity flow mechanism for macrosegregation. It might also indicate certain approximations regarding 'GIFF' which could be used in any future model of the mechanism (e.g. at what value of g_L flow becomes negligible in producing further segregation).

It was felt that the best way of determining the relationship of fluid flow (and hence segregation) with position in the semi-solid zone would be to study the variation in the composition ($\bar{c}$) of a given small volume element within an ingot as solidification progressed. The plot of $\bar{c}$ vs time thus obtained could then be related to the development of growth within the ingot, and in particular to the passage of the semi-solid region through the volume element. This would then allow a plot of $\bar{c}$ vs g_L (volume fraction liquid) to be drawn. The variation of $\bar{c}$ could then be related directly to the extent of 'GIFF' providing that no other macrosegregation mechanism was operating, and the required plot of 'GIFF vs g_L' could therefore be obtained.

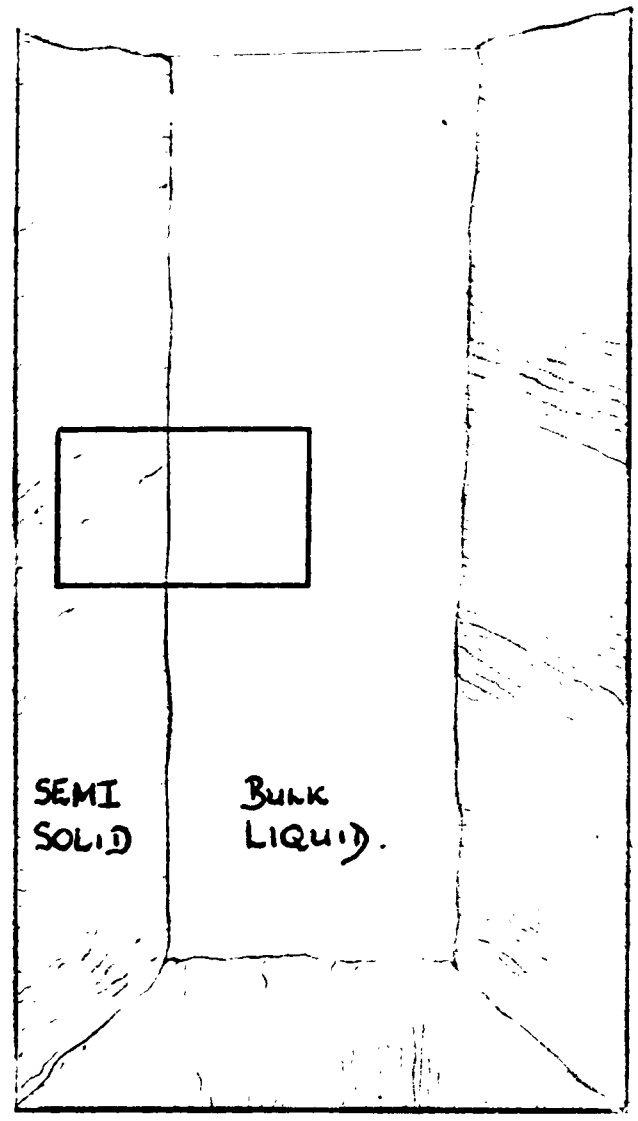
Unfortunately there exists no easy method of measuring the average composition of a fixed volume element in an ingot. In order to obtain a

$\bar{c}$ vs t plot some property of the alloy is required which varies continuously with $\bar{c}$ and which can be readily monitored 'in situ' within the molten alloy. X-ray absorption and radioactive emission were both considered as possible properties but the penetration distances of these radiations in metallic specimens is usually quite small. It would therefore be necessary to use for monitoring either an 'in situ' probe capable of operating at high temperature, or very thin specimens with an external measuring device. It was felt, however, that a probe would be difficult to manufacture and might well disturb flow locally, while very thin specimens would be expected to inhibit any interdendritic flow.

In view of the large experimental difficulties envisaged in measuring $\bar{c}$ 'in situ' it was decided that a quenching technique should be used to obtain $\bar{c}$ vs. t data. This involved solidifying a number of ingots under identical experimental conditions so that growth and, hopefully, macrosegregation were reproducible in each one. The growth process was then quenched after a different period of time in each ingot, and the compositions at identical positions in each one were determined. In this way a picture of $\bar{c}$ vs. t at a number of positions could be built up. Such a quenching technique is intuitively less satisfactory than one which studies $\bar{c}$ continuously in a single ingot. Provided, however, that growth and macrosegregation can be made macroscopically reproducible in each ingot then the technique ought to be just as accurate.

6.2 Outline of the Experiment

The quenching aspect of the experiment meant that a thin-section mould had to be employed in order for the growth process to be quenched rapidly and reproducibly. Gravity flow segregation is, however, commercially most important in large-scale ingots taking long times to freeze. The apparatus was therefore so designed, and the freezing conditions were so arranged, that the mould could be assumed to be equivalent to a thin radial slice taken at mid-height and mid-radius from a large static ingot, as shown in fig. 6.1. The conditions listed in the figure as being typical of those found in a large



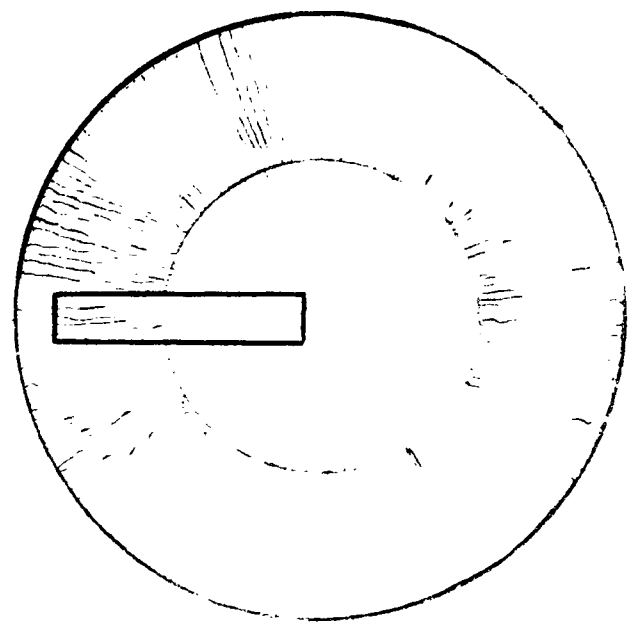


Fig. 6.1 Schematic view of a large static ingot at an intermediate stage of freezing. Slice mould apparatus was so designed to reproduce the growth conditions in the thin radial slice shown.

CONDITIONS expected to prevail in a large static ingot at an intermediate stage in the freezing process:-

(a) Heat extraction unidirectional and horizontal through one end of radial slice.

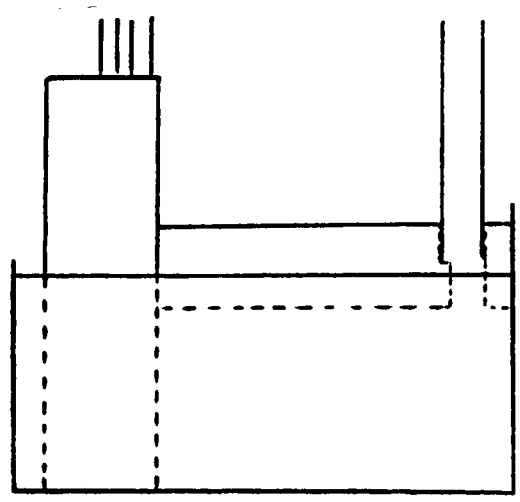
(b) Bulk liquid maintained at a temperature just above the alloy liquidus temperature as semi-solid zone advances.

(c) Growth in a columnar mode, with the dendrite tip front advancing at a reasonably steady rate of between 10^{-2} and 10^{-3} cm/sec.

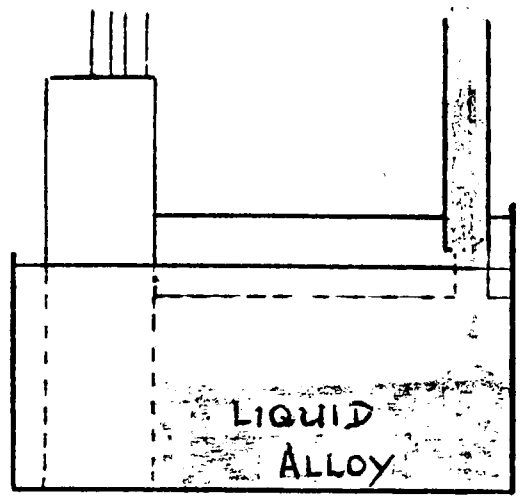
(d) Temperature gradient in semi-solid zone less than 5°C/cm.

ingot at an intermediate stage in the growth process were taken as those which had to be reproduced by the apparatus. Such steady-state growth conditions together with the columnar mode of growth also had the advantage of minimising the operation of the contraction fluid flow and equi-axed mechanisms for macrosegregation in the slice casting. Any variation in the average composition $\bar{c}$ of a volume element in the casting could therefore be confidently connected with the operation of the gravity flow mechanism.

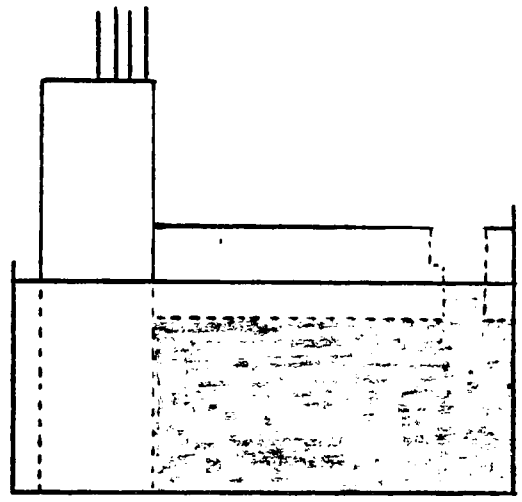
The same basic slice casting apparatus was employed for this experiment as that used previously by Hebditch[84,85,103] and myself.[86] It was however necessary to make major modifications to both the apparatus and the experimental procedure in order to obtain the accurately reproducible growth conditions essential to the success of the experiment. The apparatus consisted basically of a thin-section mould which fitted down into a slot-shaped furnace enclosure. An outline of the experimental procedure employed is shown diagramatically in fig. 6.2. The alloy charge was first melted in a separate furnace, while the mould was pre-heated in the furnace enclosure to a temperature above the alloy liquidus temperature. The alloy charge was then poured into the mould, and the heaters around the furnace enclosure were individually adjusted until the temperature of the charge was stable and just above its liquidus. The charge was then made to grow unidirectionally along the length of the mould (condition (a), fig. 6.1) by passing air through the cooling block fixed at one end of the mould. Progress of growth was monitored by thermocouples positioned in the alloy along the centreline of the mould cavity at various distances from the chill block. Growth could be quenched after any length of time by simply removing the bottom plate from the furnace enclosure and forcing the mould down through the slot into the quench bucket below. The quenched ingot was then removed from the mould, and swarf samples were taken for composition analysis from fixed positions within the ingot using a rotary saw wheel on a milling machine. A picture of $\bar{c}$ vs. t could then be built up at the various sampling positions



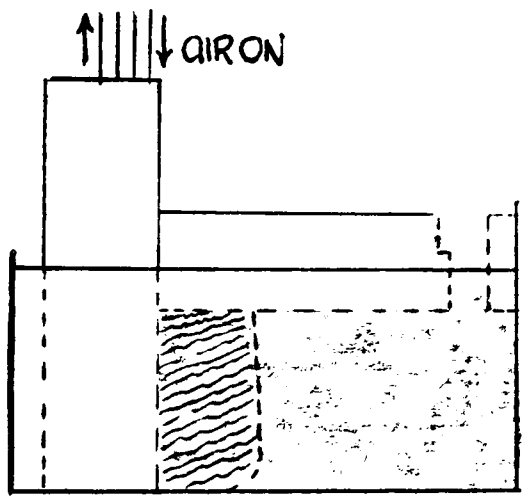
Step 1 Slice mould pre-heated in slot furnace, and alloy charge melted in separate vacuum furnace



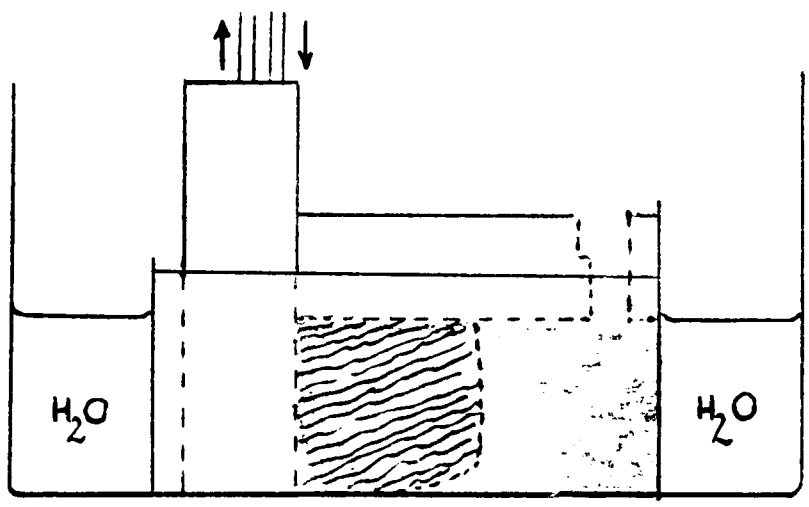
Step 2. Alloy charge poured into slice mould, and filling funnel removed.



Step 3. Heaters around furnace adjusted until mould and furnace slot isothermal, at temperature of approx 2°C above alloy liquidus



Step 4 Air cooling turned on through the copper cooling block at the end of the mould. Alloy charge grows unidirectionally along length of mould.



Step 5 Progress of growth monitored by sample thermocouples in alloy charge. Growth quenched by forcing the mould down through the slot into the quench bucket below.

Fig. 6.2 Schematic outline of experimental procedure

within a series of ingots.

The slice mould was insulated from its surroundings within the furnace enclosure by asbestos blanket so that there was very little heat loss or gain through the sides of the mould during growth. The temperature of the 'hot' end of the mould therefore remained just above the liquidus of the alloy while the dendrite tip front advanced along the length of the mould, as required in condition (b), fig. 6.1. The interface velocity, (v), and temperature gradient in the semi-solid zone, (G), could be altered by varying the air flow rate through the cooling block, and so this was adjusted to give the values of v and G required in conditions (c) and (d), fig. 6.1. Columnar growth was ensured by correct choice of alloy system and nominal composition (c_o), and by nucleating the melt prior to cooling (condition (c), fig. 6.1).

The Sn-Pb alloy system was used for this work. A low temperature system had to be employed because the sindanyo boarding from which the furnace was constructed had a maximum continuous operating temperature of 350°C. The Sn-Pb system was chosen because it had been widely studied in previous work.[61,84-86] The system has a simple eutectic phase diagram with wide freezing ranges and there is a large density difference between the two elements - factors which favour the operation of the gravity flow mechanism. Sn-5 wt%Pb was the composition mainly employed. Previous experiments had shown that growth could be maintained as completely columnar at this composition while still obtaining appreciable amounts of gravity flow segregation.[85,86] At higher Pb concentrations there is a tendency for equi-axed crystal formation, while at lower Pb concentrations the freezing range is constricted and the amount of material required for accurate chemical analysis becomes too large.

The initial experiments performed with the apparatus, and described in detail in section 6.5.1., were involved with commissioning the apparatus and with ensuring that reproducible growth conditions could be obtained. Now the extent of interdendritic gravitational fluid flow is, in general, a function of the alloy system; nominal solute composition (c_o); dendrite growth velocity (v); temperature gradient in mushy zone (G); primary dendrite spacing; growth

morphology (columnar/equi-axed); and the shape and size of the ingot which determines both the time available for flow and the hydrostatic driving force behind the flow. Within this list both the primary dendrite spacing and the growth morphology are themselves dependent on c_o, v, and G. In view of these factors the following variables within the experiment were identified as being crucial to its reproducibility:- c_o, initial heat capacity of the melt and furnace prior to growth, heat extraction rate of the cooling system during growth, quenching technique, and sampling procedure after quenching. Table 6.1., overleaf, lists these variables and the precautions which were taken to ensure that they were made reproducible between each and every growth run. Detailed descriptions of the apparatus and experimental procedure are given in the following two sections, 6.3. and 6.4.

6.3 Apparatus

The layout of the apparatus when fully assembled is shown schematically in fig. 6.3. All relevant dimensions may be obtained from this figure.

Figure 6.4(a)., is a photograph of the furnace used in the experiment. It was essentially a box built around a central, vertical, rectangular slot, open at both top and bottom. The sides of the slot and the box itself were constructed of $\frac{1}{2}$ inch thickness asbestos board. The main heating source for the furnace was provided by a kanthal resistance element wound evenly around the length of the slot. The space inside the furnace was tightly packed with an insulating material (Triton kaowool). The furnace was rigidly mounted on an angle-iron frame. This raised it off the bench surface and so allowed a quench bucket to be inserted under the bottom of the slot when required, fig. 6.4(b).

The bottom of the slot was closed off during growth runs by a removable bottom heater, fig. 6.5(a). This was made from two pieces of $\frac{1}{2}$ inch thickness asbestos board firmly bolted together. The top piece had been cut so that it just fitted up into the slot. A kanthal resistance wire heating element was wound inside this insert evenly along its length. The bottom piece had larger dimensions. It could be held tightly up against the bottom of the furnace

TABLE 6.1

VARIABLE.	PRECAUTIONS TAKEN.
C_o.	Accurate weighing of pure elements, from which oxide layer had previously been removed. Reproducible vacuum melting procedure. Thorough stirring of molten charge.
Initial Heat Capacity.	Volume of metal charge made reproducible by weighing; C_o (and hence density) of charge reproducible. Volume of mould cavity rigidly fixed. Transfer of metal into cavity always complete thanks to filling funnel arrangement. Welded box mould prevented leakage of metal charge during holding period. Initial charge holding superheat made reproducible (uniformity and control of isothermal temperature enclosure important - efficient temperature controllers employed; all thermocouple circuits calibrated; and copper jacket fastened to inside of slot enclosure surface to eliminate any temperature inhomogeneities caused by uneveness in the heater windings).
Heat Extraction Rate.	Air flow rate through cooling block calibrated and hence made reproducible in each growth run. The cooling circuit was regularly tested for leaks and blockages which might have altered the calibration. The alloy charge was nucleated to provide consistent initial growth conditions.
Quench technique.	Standardised to fixed procedure, taking same length of time in each growth run.
Sampling Procedure.	Accurate machining techniques employed to ensure reproducibility in sampling position.

SCALE 1:4

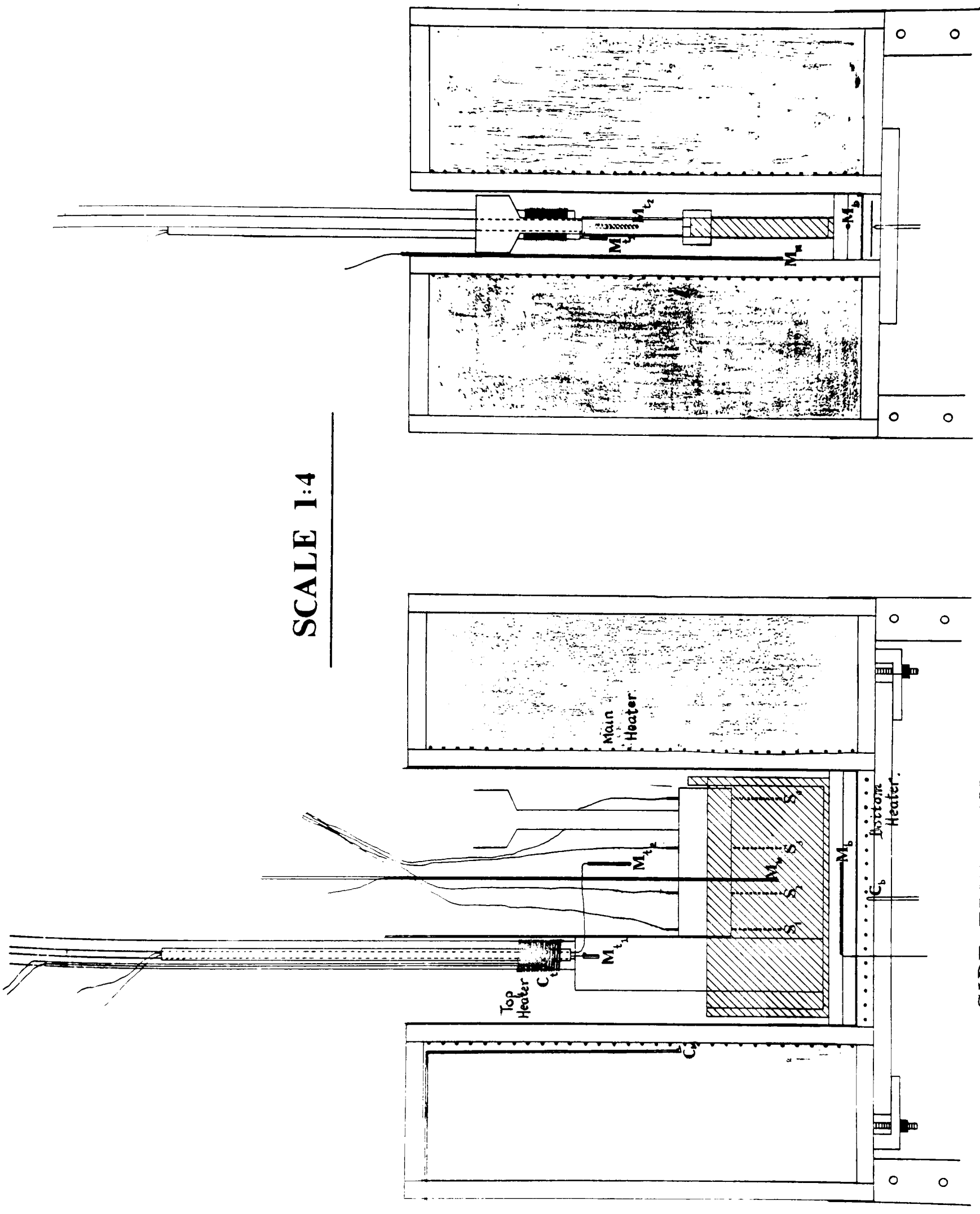


Fig 6.3. Slice casting apparatus.

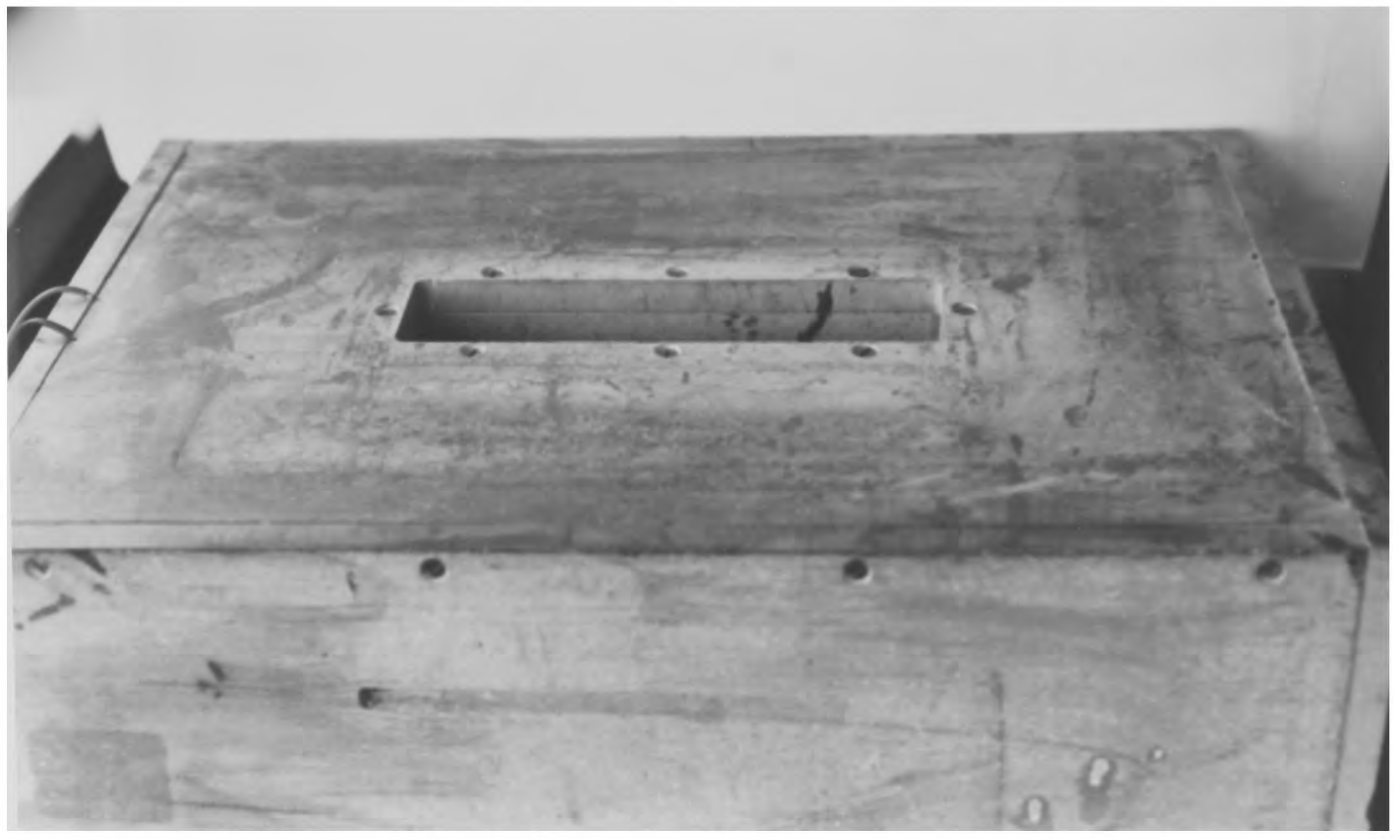


Fig.6.4(a). Furnace - showing central rectangular slot.

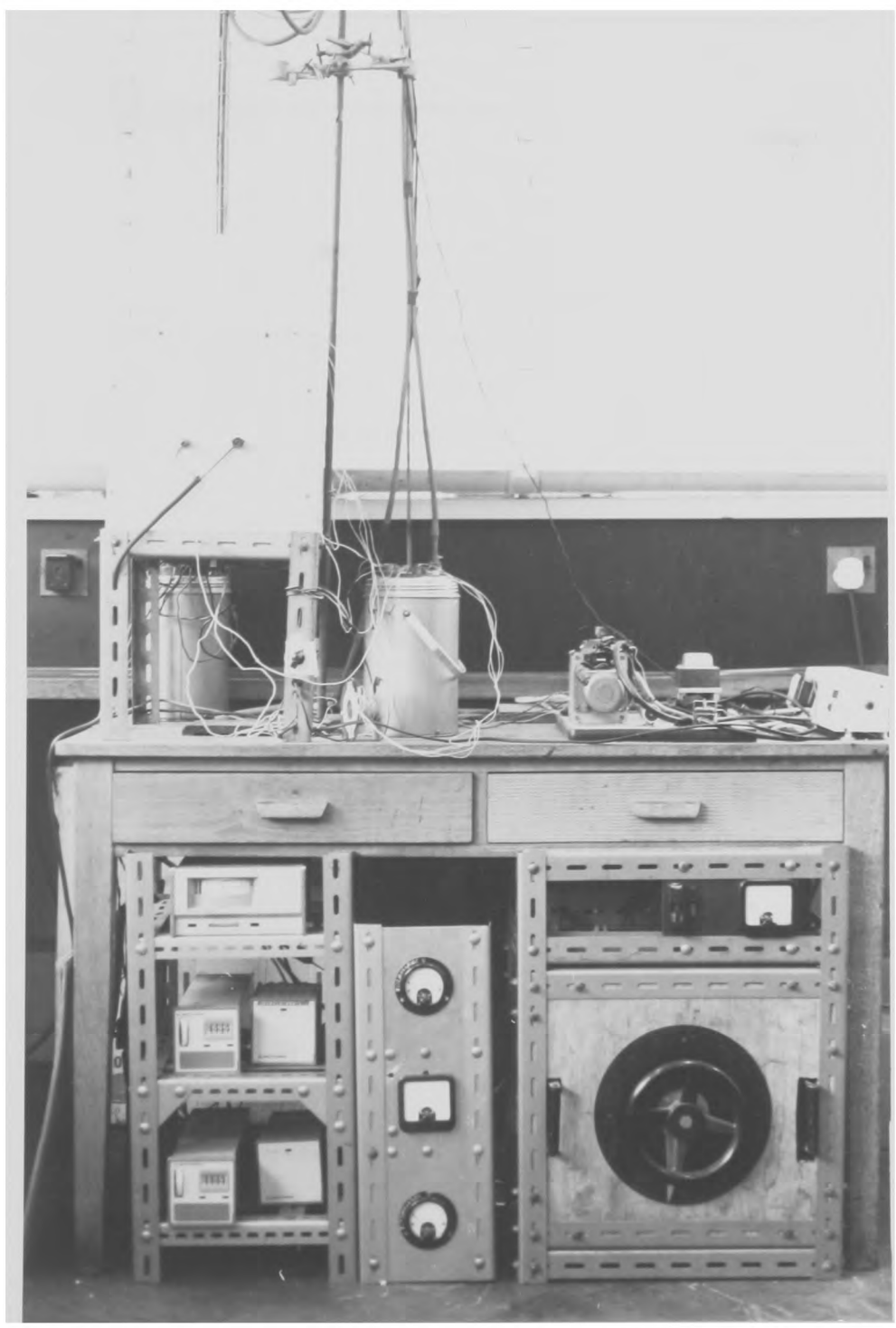


Fig.6.4(b). General apparatus layout - angle iron framework raised furnace off bench and allowed insertion of quench bucket below slot.



Fig. 6.5(a). Removable bottom heater plate, and kaowool insulation.

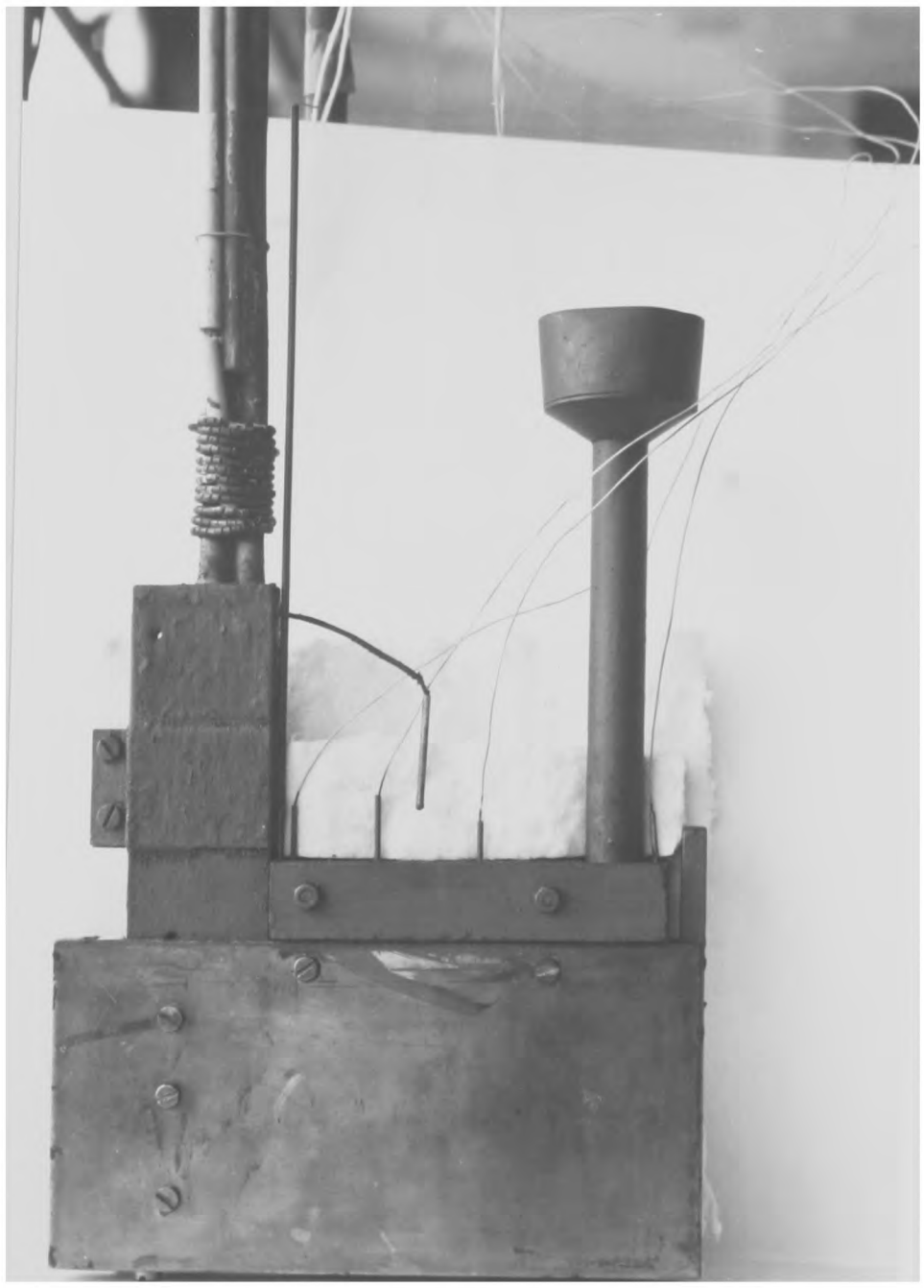
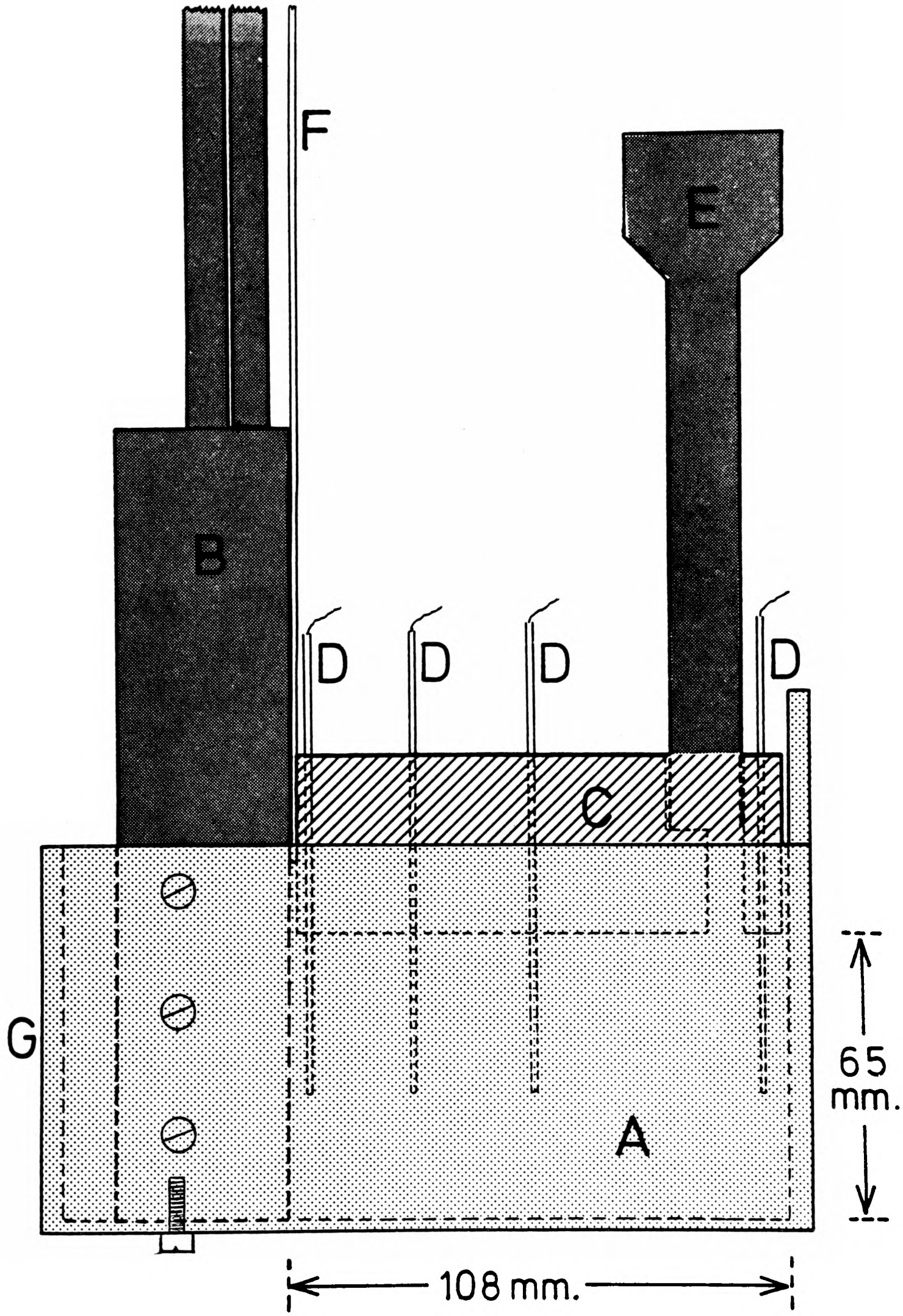


Fig. 6.5(b). Thin section mould.

using two adjustable clips, once the top piece had been inserted into the slot.

Thin sheets of copper were fixed onto the inside surfaces of the slot and onto the top surface of the bottom heater insert, as shown in fig. 6.3. This was done as a precaution against any uneven-ness in the heater windings. Since asbestos is such a poor conductor any uneven-ness might otherwise have caused hot-spots in the furnace enclosure.

A photograph of the mould employed in this experiment is shown in fig. 6.5(b), and a schematic diagram of it is given in fig. 6.6. It was comprised essentially of three parts: a welded stainless steel box (G, fig. 6.6.) open along its top surface, a copper cooling block (B) which fitted tightly down inside the box, and an asbestos insert (C) which closed off the top of the mould cavity (A). The long sides of the stainless steel box were cut from 1.7 mm. thickness sheet, while 6.3 mm. thickness plate was used for the bottom and end pieces. These relatively thick sections had to be used in order to give the pieces sufficient rigidity to prevent them buckling during welding. The copper cooling block formed one of the vertical ends of the mould cavity. It was held in place in the box by three screws which passed through clearance holes in the sides of the box and the block itself, and also by another screw which passed up through the bottom of the box into a tapped hole in the block, see fig. 6.6. This figure also shows that a space was left between the copper block (B) and the end of the box mould (G). This was filled with insulating material once the mould had been assembled prior to a growth run. The space was left in order to ensure that the block could be removed easily once the alloy sample had solidified in the mould cavity (A). The top asbestos insert ensured a reproducible cavity volume and protected the surface of the molten alloy pool from oxidation. It was also used to hold the sample thermocouples in position in the cavity, and it provided a convenient mounting for the copper filling funnel (E, fig. 6.6). The stainless steel tube, marked F in fig. 6.6, was held up against the copper chill block by the top asbestos insert. This



A — mould cavity.

B — copper cooling block.

C — asbestos insert.

D — sample thermocouples.

E — copper filling funnel.

F — stainless steel tube, 2mm I.D.

G — stainless steel box mould.

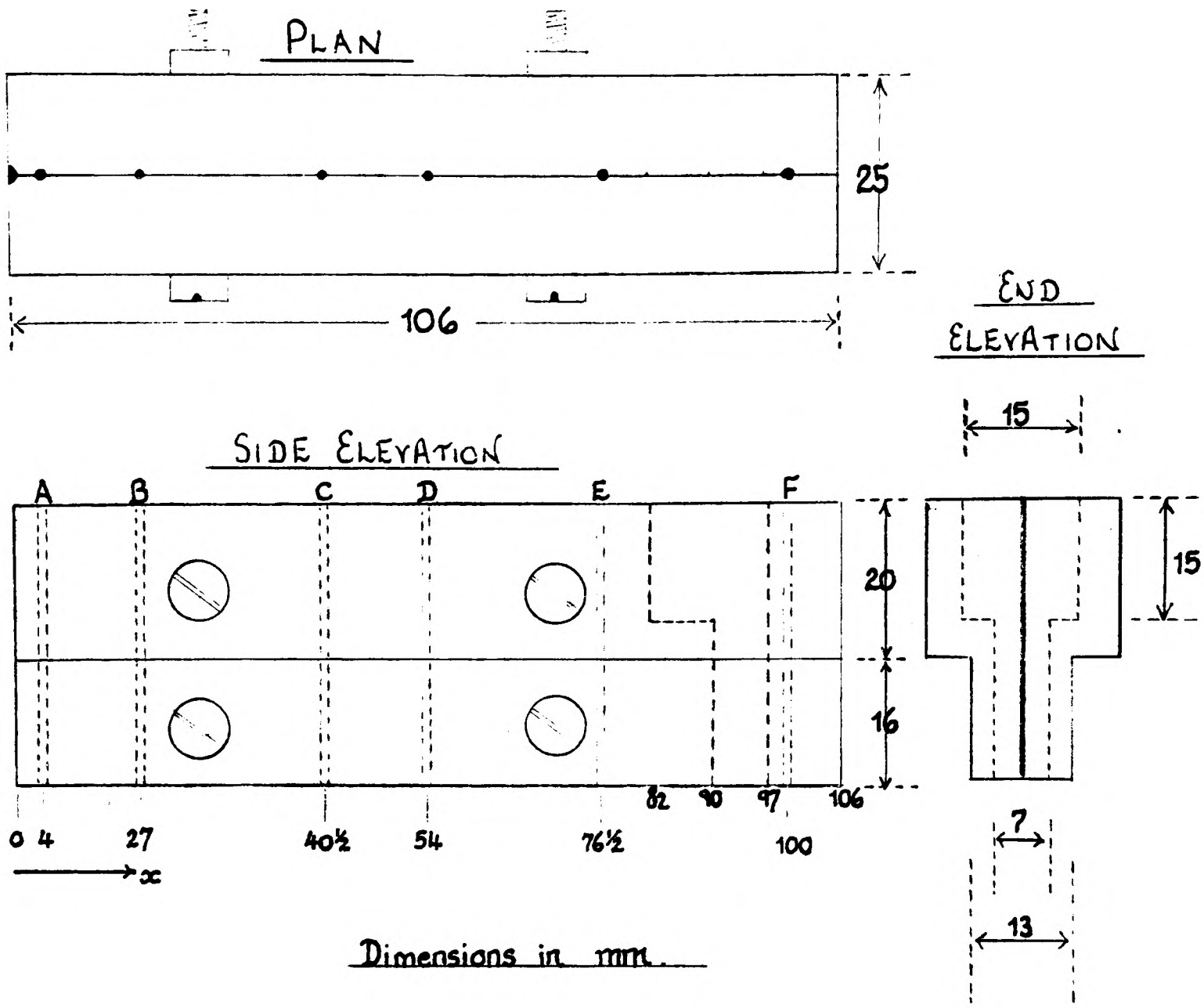
Fig. 6.6. Schematic diagram of the thin-section mould employed in this work.

tube was sufficiently long to project up to just below the top of the furnace slot, and it was used as a convenient channel down which to insert the nucleant wire into the molten metal pool once cooling had begun.

The mould cavity was made 108 mm. long; 65 mm. tall; and 13 mm. wide. These dimensions were essentially a compromise between a number of factors. The mould had to be sufficiently long for the growth front to take a significant time to advance from the chill end to the 'Hot' end with a typical velocity of 5×10^{-2} cm./sec., thereby allowing growth to be quenched at a reasonable number of intermediate stages. It also had to be sufficiently tall and wide to permit convection cycles to operate in the semi-solid and bulk liquid regions of the casting. However the length and height of the mould both had to be restricted in order that the construction of an isothermal furnace enclosure for the mould did not become too difficult. Furthermore the width of the mould had to be reasonably small in order to allow a rapid quench of the growth process. The mould cavity was made to be squat (height:length < 1) because previous work had shown that this made the columnar dendritic structure more stable and less likely to break down into equi-axed crystals.

The construction of the top asbestos insert of the mould is shown schematically in fig. 6.7(a). It was made from two pieces of $\frac{1}{2}$ inch thickness asbestos board held together by two nuts and bolts. These pieces were machined into the shape shown in fig. 6.7(a), so that 16 mm. of the insert fitted down tightly into the top of the box mould. Several 1.2 mm. diameter holes, in which alumina thermocouple sheaths could be gripped, were drilled down through the insert along the line where the two pieces met. A 7 mm. diameter hole was also drilled down through the insert near one end, through which the molten alloy charge could be poured into the mould cavity. A larger diameter hole of 15 mm. was drilled over this in the thicker part of the insert to provide a socket for the copper filling funnel. The insert was fastened into the box mould by two nuts and bolts which passed through matching clearance holes in the sides of the box and the thin part of the insert.

Air, taken direct from the laboratorys compressed air supply, was used as



Dimensions in mm.

Fig. 6.7(a). Drawing of top asbestos insert. SCALE 1:1

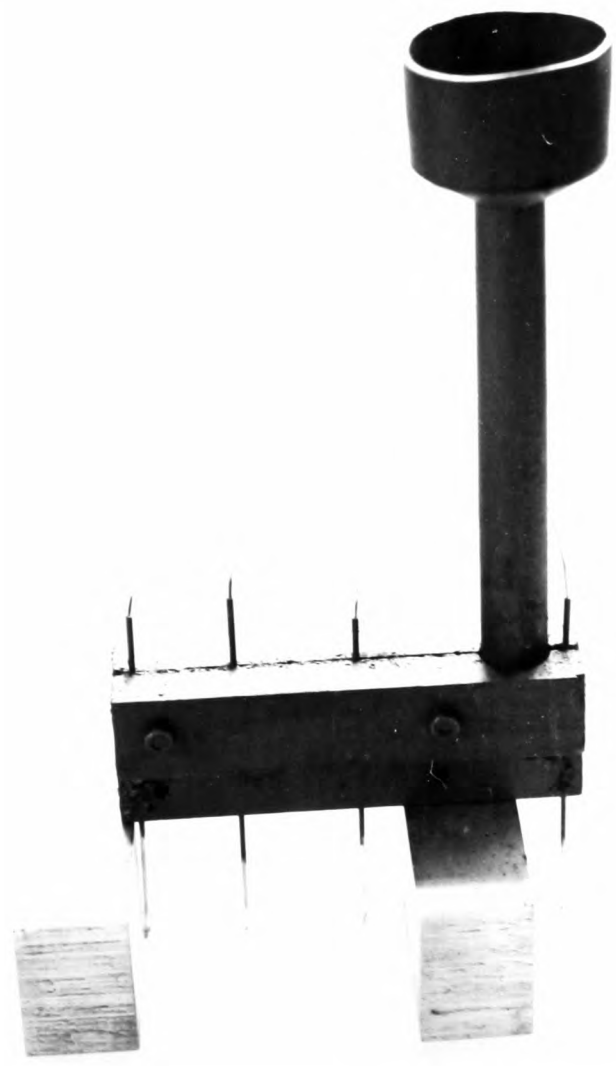


Fig 6.7(b). Photograph of top insert when fully assembled with sample thermocouples and copper filling funnel. Blocks ensure thermocouple beads are fixed depth below insert.

the cooling medium for the experiment. This was passed through a 4 mm. diameter channel drilled out of the copper cooling block, as shown in fig. 6.8(a). The air was led into, and out of, the furnace through two long copper tubes brazed into the holes on top of the copper block. The air flow rate was measured using a rotameter connected in the exit arm of the cooling circuit. Thick walled rubber tubing was used for all connections in the cooling circuit outside the furnace.

In addition to the two long copper tubes mentioned above, the 'cooling column' was made up of a steel rod and an alumina tube of 3.5 mm. I.D. The steel rod was brazed onto the tubes to provide the column with rigidity. The alumina tube was fastened to the column by a number of wire clips and was used to bring the leads for the two top monitoring thermocouples into the furnace. A kanthal heating element was wound around the cooling column just above the copper block (fig. 6.3), since it was recognised that the column would constitute a large heat sink. The element was insulated from the metal parts of the column by threading ceramic beads onto the kanthal wire before winding.

In summary, therefore, the heating for the furnace was supplied by three kanthal resistance-wire elements; one wound around the outside of the main furnace slot, one wound inside the bottom insert to the slot, and one wound around the cooling column on the mould. The heat supplied by each of the elements was independently adjustable, so that an isothermal enclosure could be obtained. Three Eurotherm thyristor temperature controllers were used to control the temperatures of the heaters. The three thermocouples by which these controllers operated (C_m, C_b, C_t, in fig. 6.3) were positioned close to the respective heating elements. Chromel/alumel (Titan) thermocouples were employed, made from uninsulated, 0.24 mm. diameter, chromel and alumel wires. The beads were formed by mechanically joining the wires together and then melting this join in an oxy-gas flame. The thermocouple leads were taken from the furnace to separate junctions in an ice/water reference bath before being connected to the controllers.

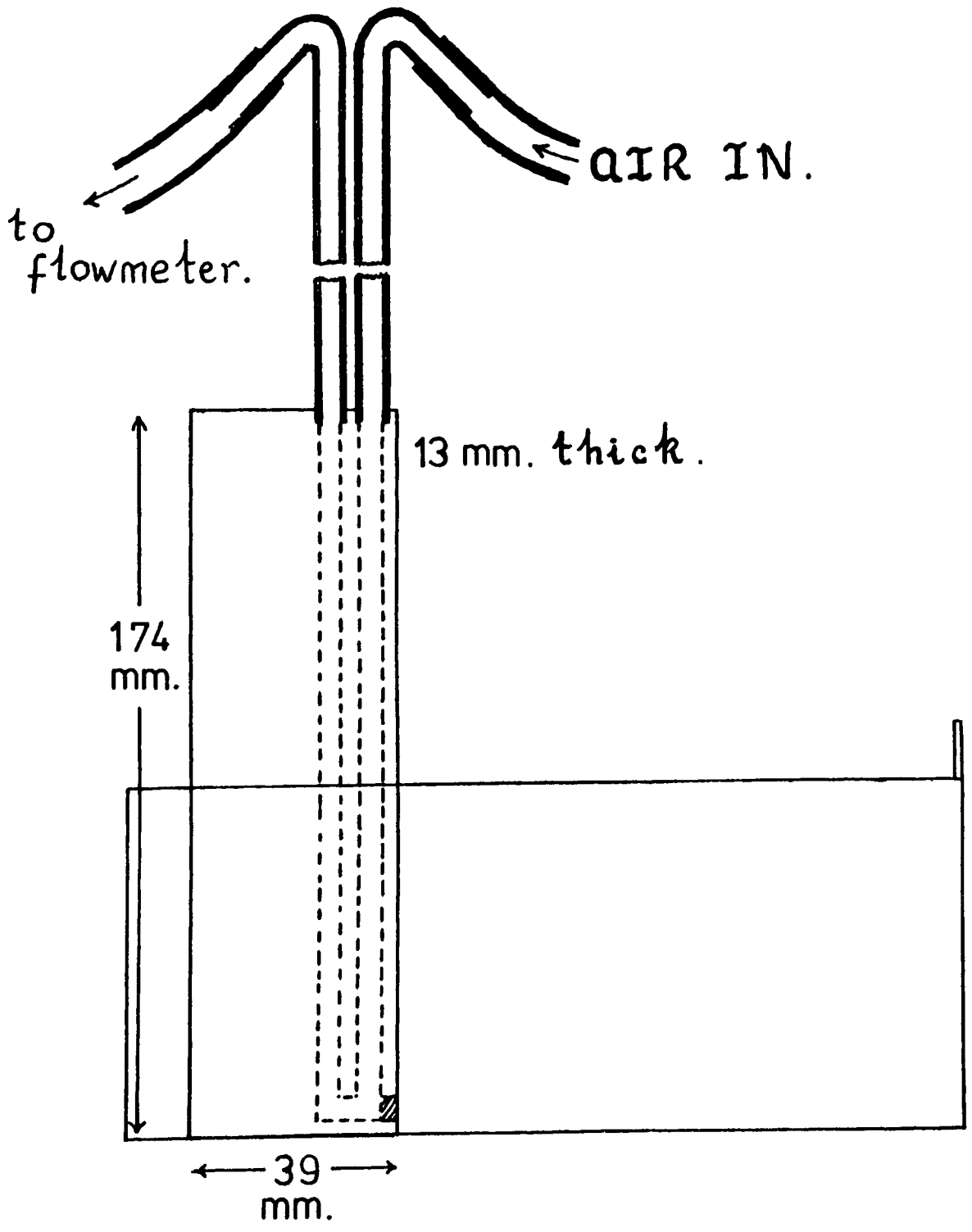


Fig. 6.8(a). Dimensions of copper cooling block and position of air cooling channels

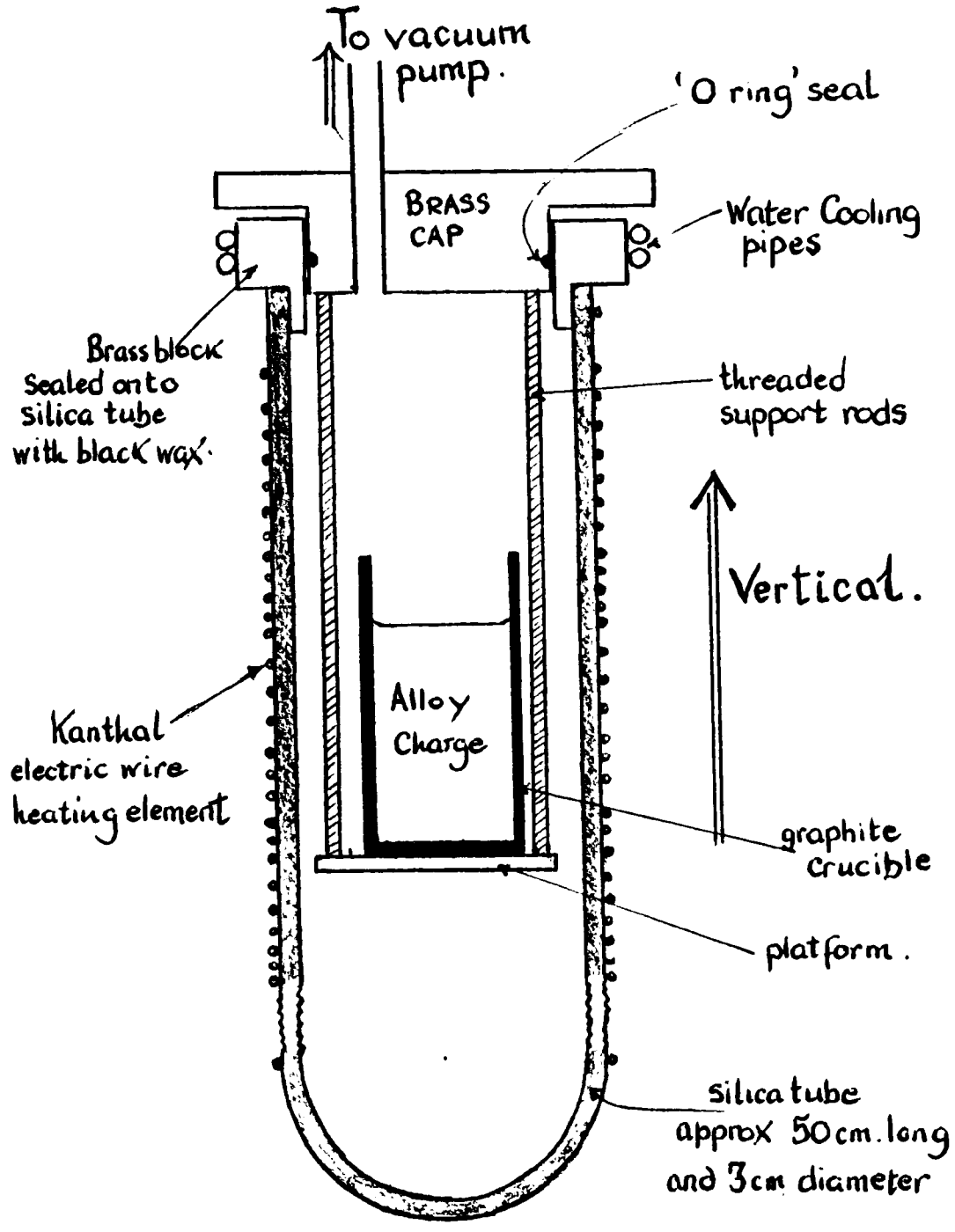


Fig. 6.8(b). Schematic view of melting furnace arrangement.

Four chromel/alumel thermocouples were used to monitor that the furnace slot constituted an isothermal enclosure. These were positioned as shown in fig. 6.3., M_b, M_m, M_{t1}, M_{t2}. A further four chromel/alumel couples were used to read the temperature of the molten alloy at fixed positions in the mould cavity (S_1-S_4, fig. 6.3). These could be arranged in any of the six positions drilled out of the top insert. The wires for these thermocouples were supplied by 'The Saxonia Electrical Wire Co.' to B.S. 1827 specification, in the form of lapped conductors - lapped overall with insulation. Two separate batches of wire were used. That for the monitoring thermocouples had an overall (insulated) diameter of 1.3 mm., while that for the sample thermocouples had an overall diameter of 0.55 mm.. The individual conductors in both batches were 0.12 mm. in diameter. The beads for these thermocouples were made by removing the insulation at the ends of the wires and then spark welding the bare conductors together under water. Recrystallised alumina sheaths were employed to protect the beads. The sheaths were closed off at one end in an oxy/gas flame. Those used for the sample thermocouples were 0.8 mm. I.D., 1.2 mm. O.D., and approximately 80 mm. long. Those used for the monitoring thermocouples were 1.5 mm. I.D., 2.0 mm. O.D., and of different lengths.

The leads from the four monitoring thermocouples were led out of the furnace by various routes (fig. 6.3) and were taken directly to an ice/water reference bath. The positive (chromel) wires had separate cold junctions while the negative wires were fixed to a common junction. The copper wires leading from the positive junctions were soldered onto the terminals of a four-way, manually-operated switch. The output wire from the switch together with the copper wire from the negative cold junction were connected to the input terminals of a Tinsley digital potentiometer. This was used to back-off accurately a large part of the thermally-generated E.M.F., so that the remainder could be fed into a sensitive recorder. One channel of a double-channel Kipp and Zonen BD6 chart recorder was used for this purpose.

The circuit for the sample thermocouples was very similar. Instead of a manual switch an automatic switch was employed. This switched between the four

couples at six second intervals, so that the voltage from each one was observed at eighteen second intervals. A separate potentiometer was used from that in the monitoring thermocouple circuit so that a different back-off potential could be used in the two circuits. The remaining voltage signal from the potentiometer was fed into the second channel of the Kipp recorder.

The furnace used for melting the alloy charge is shown in fig. 6.8(b). It was made up of a long ceramic tube, closed at one end, which was heated by a kanthal element wrapped evenly around it along its length. The tube and windings were surrounded by insulation blanket and were mounted vertically in an asbestos box. A length of copper tubing was wrapped around the top of the ceramic tube where it projected from the box. Water was continuously passed through this copper tubing when the furnace was in operation in order to keep the top of the ceramic tube cool. This enabled a brass cap to be fitted over the top of the tube onto an O-ring seal, and so allowed the tube atmosphere to be evacuated when required. Three threaded rods were screwed into tapped holes on the underside of the brass cap and these supported a platform which rested at approximately mid-height in the furnace tube when the cap was placed on the O-ring. The alloy charge was melted in a graphite crucible which fitted onto this platform.

6.4 Experimental Procedure

The first part of a growth run involved the assembling of the slice mould. Since the four sample thermocouples had to be sacrificed in the solid ingot after each run, it was first necessary to remake the beads on the sample thermocouple leads and fit them into their protective alumina sheaths. The two parts of the top alumina insert were then loosely bolted together with the alumina sheaths inserted down the required holes. The beads were kept at the same depth below the bottom of the insert in each run by using the technique shown in fig. 6.7(b). The insert was supported on two blocks of aluminium 35 mm. tall and the alumina sheaths were allowed to rest on the bench below. The bolts through the insert were then tightened up, thereby holding the

thermocouple sheaths firmly in position. Once the top insert had been assembled all parts of the mould likely to come into contact with the molten metal were painted with colloidal graphite. This was done in order to prevent corrosion of the mould by the melt, and to make removal of the solidified ingot from the mould easier. After leaving the pieces to dry off for approximately thirty minutes, the copper cooling block and the top insert were slotted into the welded steel box and fixed rigidly in position. Care was taken not to break the alumina sheaths during this operation. Assembly of the mould was completed by fitting the copper filling funnel into its hole in the top insert, and by filling the space behind the cooling block with insulation.

After assembling the mould the next step was to surround it with insulation before placing it in the furnace slot. A small, pre-cut, piece of insulation 'blanket' (10 mm. thick x 100 mm. long x 40 mm. high) was placed above each half of the top insert to hold the top monitoring thermocouple M_{t2} in position, see fig. 6.3. The sides and ends of the mould were then completely covered with pre-cut pieces of insulation blanket (15 mm. thick), held in position by two elastic bands. The empty mould, together with its insulation wrapping, was then lowered gently down into the furnace slot until it rested on the layers of insulation above the bottom heater insert. The thickness of insulation used was intended to make the mould plus insulating jacket quite a tight fit in the slot. Care was therefore taken during lowering not to ruck the insulation around the mould. Care was also taken not to pull the sample thermocouples up out of their sheaths during this process. Once the mould was inside the furnace loose insulation 'wool' was carefully packed down on top of it, until the furnace slot was filled with insulation. A small piece of insulation blanket was laid inside the top of the filling funnel to prevent any loose insulation from falling into the mould cavity. The main furnace monitoring thermocouple M_m was then pushed down between the side of the furnace and the insulation. Finally two pieces of insulation blanket were wrapped loosely around the mould column where it projected out of the furnace. This was done to prevent the column being cooled by draughts in the laboratory. The

appearance of the furnace and mould at this stage (i.e. set up for a run) is shown in fig . 6.4(b)

Prior to commencing a run the thermocouple circuits were checked. The two ice-baths used for the thermocouple reference junctions were filled with an ice-water slurry, and the two potentiometers which provided the back-off voltages in the sample and monitoring thermocouple circuits were standardised. The Eurotherm controllers to the three heating elements were then pre-set to the required holding temperature and the heaters switched on. Warm-up to 230°C took around two hours, and during this period the traces of the sample and monitoring thermocouples were observed to check that everything was proceeding satisfactorily.

The melting furnace was switched on at the same time as the slice-casting furnace. The current was adjusted so that the furnace would heat up rapidly to a temperature around 100°C above the liquidus temperature of the alloy being used. When this was attained the current was turned down until it became just sufficient to maintain that temperature. An exact amount of alloy charge was then carefully weighed out from the pure component metals, and was put into the graphite crucible. This was, in turn, fitted onto its platform and lowered down into the furnace. The furnace tube was then evacuated down to around 1 mm. Hg. pressure, for a period of around 25 minutes. Air was let back into the tube at this point and the now molten charge was carefully and thoroughly stirred for several minutes. The melt was then lowered back into the furnace, and the vacuum replaced, until the sample thermocouples in the slot furnace indicated that the temperature of the slice mould was above the alloy liquidus temperature. The crucible was then once again taken out of the melting furnace and the melt was re-stirred. A small amount of alloy was then removed from the crucible, using a graphite-coated spoon, for subsequent composition analysis. The temperature of the molten alloy was crudely monitored using a chromel/alumel thermocouple connected directly to a simple galvanometer. When it had fallen to around 70°C above the alloy liquidus temperature the crucible was picked up in a long pair of tongs and taken over to the slot furnace. The loose insulation was

then removed from above the filling funnel, and the whole of the alloy charge was very carefully poured down the mouth of the funnel. The funnel was then removed from the furnace, using the tongs, and the loose insulation was replaced.

It took around two hours for the alloy to lose the majority of its superheat. The sample thermocouple traces were carefully checked towards the end of this period to ensure that they were not going to fall below the alloy liquidus temperature. Slight adjustments were made to the heater controller settings until the sample thermocouples registered a temperature slightly above the previously determined liquidus value ($1\frac{1}{2} \rightarrow 2^{\circ}C$), and until the monitoring thermocouples all registered the same temperature as each other (to within $\frac{1}{4}^{\circ}C$). This was quite a slow process often taking several hours. Firstly, owing to the insulation, there was a long delay between altering a heater setting and this alteration being passed on to the relevant monitoring thermocouple, and hence to the mould. Secondly, altering one heater setting often caused the temperatures registered by all four monitoring thermocouples to change (by different amounts).

Once an isothermal enclosure a couple of degrees above the liquidus had been obtained the alloy was ready for solidification. The cooling procedure was as follows. The top heater was switched off and immediately after this air was passed through the cooling block. The flow rate measured on the rotameter was quickly adjusted to the required value by altering the tap setting on the compressed air supply. The pieces of insulating blanket were then removed from around the cooling column, thereby exposing the top of the thin steel nucleant tube. At $20 \rightarrow 25$ seconds after cooling had begun a pre-measured length of pure tin wire was inserted down the steel tube into the melt. Nucleation and subsequent growth were then followed by observing the traces of the sample thermocouples on the chart recorder. When the dendrite tip front passed a thermocouple the temperature it registered began to fall sharply. The traces of the monitoring thermocouples were also recorded during growth of the alloy.

That of M_{t1} was recorded at the start of cooling in each run in order to give a check on the reproducibility of the cooling rate.

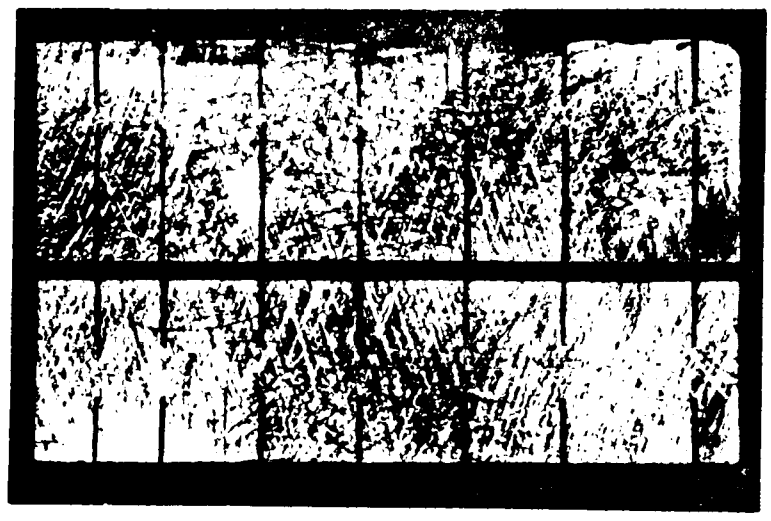
The growth process in the alloy specimen could be quenched when required by using the following procedure. First, a clamp was attached to the cooling column just above the top of the furnace to hold the mould firmly in position. The bottom heater was then switched off, and the bottom heater insert removed from the furnace slot after loosening the clips which held it in place. A plastic bucket containing cold tap water to a depth of 70 mm. was then placed underneath the furnace slot, the clamp on the column was undone, and the mould was forced down through the slot into the quench bucket. This procedure took around forty seconds, and so it was begun this length of time before quenching was actually required. The depth of water in the quench bucket was just sufficient to reach up to the top rim of the steel box mould. Water was not allowed to overflow into the mould and hence come into direct contact with the molten metal. Once the ingot was judged to have completely solidified (approximately fifteen seconds), water was vigorously splashed over the top insert to cool it down and prevent it from reheating the metal.

After quenching, the dry insulation left in the furnace slot was removed and kept for further runs. The main furnace heater was switched off and the mould was brought back up through the furnace slot and rested on top of the furnace. The mould was then dismantled by first removing the copper chill and then the top insert. Usually the removal of the top insert in one piece forced the solidified ingot up off the bottom of the mould. It could then easily be removed from the steel box by levering it up using a long-shafted screwdriver. Occasionally the ingot did not leave the bottom of the mould, in which case several sharp taps with a hammer on the bottom of the mould were found to loosen it.

When the ingot had been removed from the mould it was washed clean of graphite, any small pieces of flash were cut from its edges, and the alumina sheaths which had contained the sample thermocouples were broken off at the top surface. The ingot was then weighed and its dimensions were checked using a

pair of vernier callipers. A skim of exactly 2.5 mm. was then removed from one of the large faces of the ingot using a fly-cutter on a milling machine. The material was removed in 0.5 mm. steps and so five passes of the cutter were required. For best results the cutting edge of the tool employed had to be kept very sharp, the spindle speed high (300 r.p.m.,with paraffin lubrication),and the traverse speed low (1 cm./min.). The skimmed face was then lightly ground on 600 grade silicon carbide paper taking care not to embed the carbide particles in the soft alloy surface. The ingot was then immersed skimmed-side up in a dish of etching solution for several minutes in order to bring out the macrostructure. This was photographed, and any interesting details of the ingot microstructure (e.g. channels) were examined after re-grinding and polishing in the usual way. The ingot was then ready for sampling, if this was required.

The sampling process involved the accurate machining of material from identical positions in each ingot, and its collection for subsequent composition analysis. The machining was performed with a 1 mm. thick circular saw on a milling machine. Figure 6.9 shows the appearance of an ingot after sampling and the positions of the cuts. These were made through the full thickness of the ingot at fixed distances from its chill end, and at fixed heights from its bottom surface. It can be seen from figure 6.9 that the ingots were cut into two parts for sampling, along a line drawn parallel to their bottom edge and 28 mm. from it. This was done in order to obtain specimens from interior positions of the ingots. A 2 mm. diameter circular saw had to be used for the purpose since thinner diameter saws were insufficiently rigid and were found to be easily deflected from the cutting line. The sampling procedure was as follows. Lines were scribed around the ingot at 25 mm., 30 mm., and 35 mm. from its bottom surface to act as reference marks. The ingot was then stood upright on a flat in the vice of the milling machine, see fig. 6.10(a). The 2 mm. thick saw with its blade horizontal was then touched on the top surface of the flat, the bed of the miller lowered exactly 28 mm., and the ingot was cut in two. A



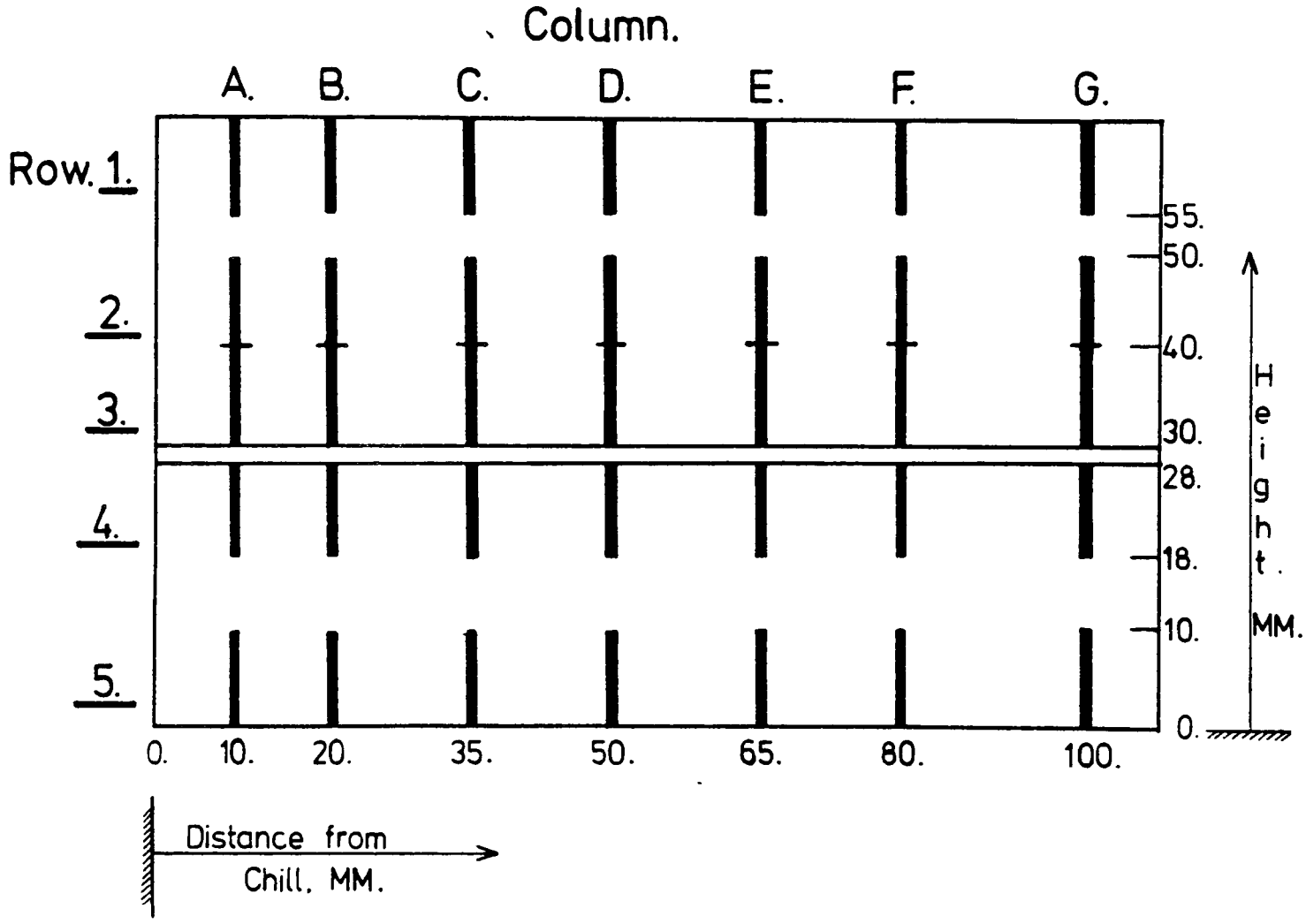


Fig. 6.9. Appearance of ingot after sampling, and the position (and reference code) of each cut.

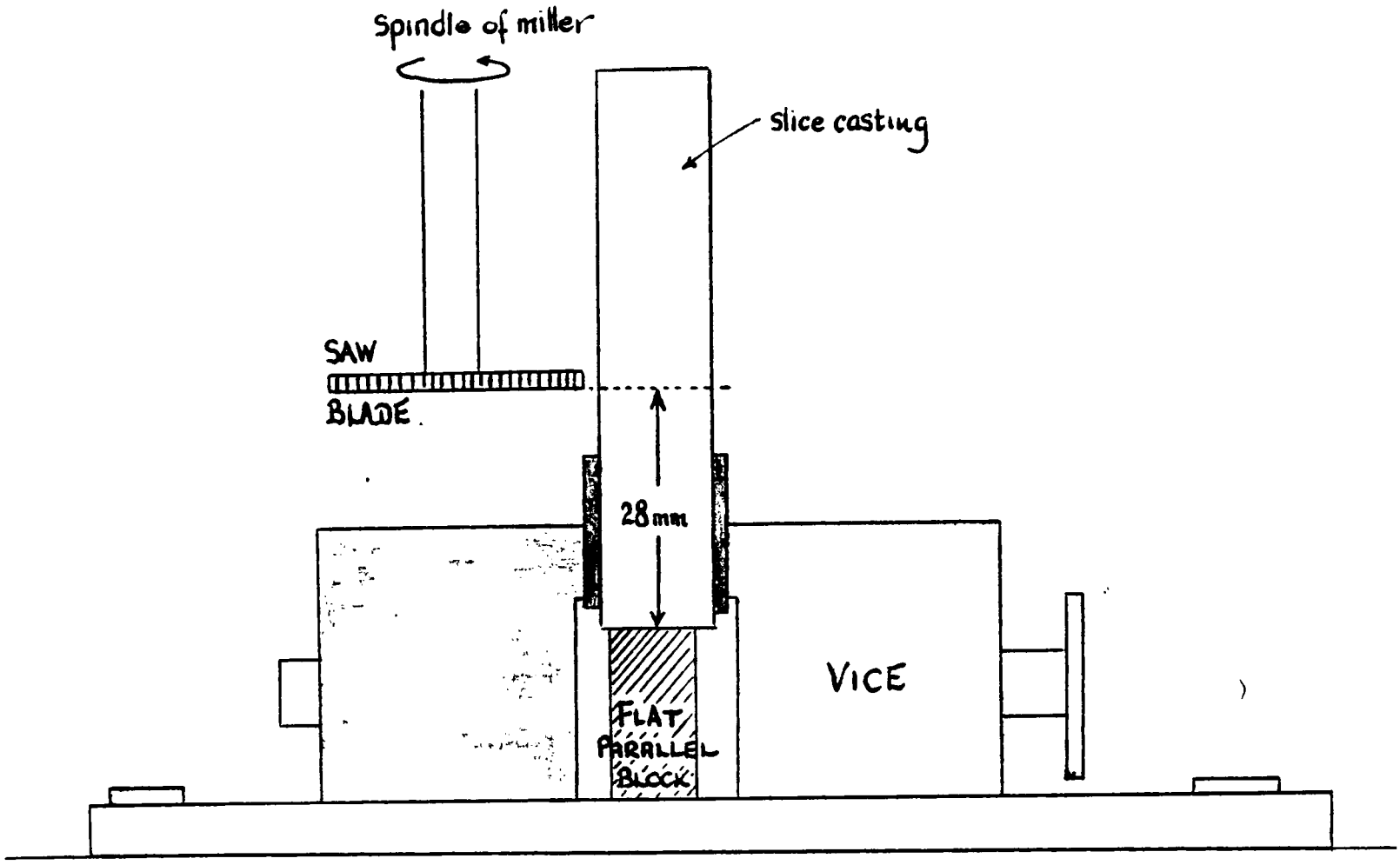


Fig 6.10 (a). Schematic illustration of initial machining operation prior to sampling - cutting slice casting into two pieces along a horizontal line.

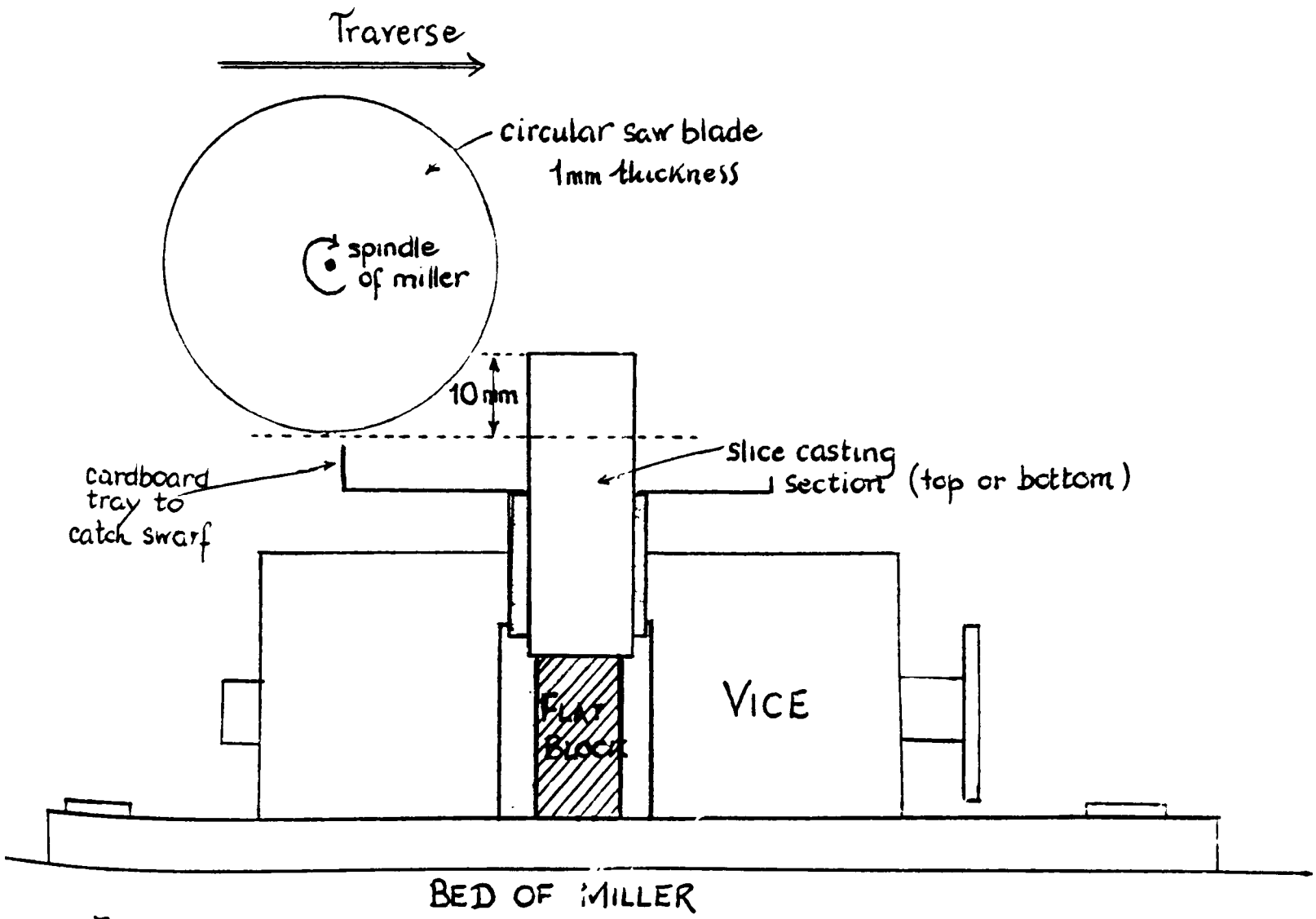


Fig 6.10(b). Schematic illustration of sampling procedure.

slow manual traverse was employed together with a slow cutting speed and copious amounts of paraffin lubrication. A light skim was then given to the two cut surfaces using a flycutter to ensure that they were flat and parallel to their respective reference lines. After this operation the miller and surrounding workshop area were meticulously cleaned in order to prevent contamination of the samples which were to be taken. All traces of oil, paraffin, and grease were removed from the machine together with any metal swarf. The arrangement employed for actually taking the samples from the ingot pieces is shown in fig. 6.10(b). A tray made from stiff card, and cut so that the ingot piece fitted exactly into the slot in the tray, was used to ensure that no material taken from a given position could be lost. The 1 mm. thick saw with its blade vertical was touched against the top of the flat and then the end of the ingot. These two surfaces acted as reference positions and the readings on the traverse and height gauges of the miller were noted when the surfaces were touched by the blade. The position of the blade with respect to the ingot section was then adjusted using the gauges on the miller until a standard sampling position (as shown in fig. 6.9) had been reached. The saw was then set into motion at a speed of approximately 60 r.p.m. and was manually traversed through the ingot section in a single pass. Care was taken to ensure that all pieces of swarf from the sampling position fell into the cardboard tray surrounding the ingot. Some pieces were found to lodge into the teeth of the saw and these were carefully removed with a pair of tweezers after each pass and put into the tray. All the swarf was then sucked up into a glass sampling jar using the sample collection device described in section 9.4.2. It was estimated that by using this technique the reproducibility of any sampling position was approximately $\pm$0.1 mm. between ingots.

The composition value of the swarf sample taken from each position was determined by atomic absorption spectrophotometry. The analysis technique is described in detail in chapter 9, and was developed and refined until accuracies of around $\pm$1% of the composition values could be achieved.

6.5 Results and Discussion

This section is split into two parts. The first describes the initial trials used to set up the apparatus and obtain the required growth conditions for the slice castings. The second describes the results obtained from the series of slice castings grown under reproducible conditions in order to obtain data concerning the change of composition with time at various fixed positions in the castings.

6.5.1 Preliminary results on setting up the apparatus

The first castings to be grown in the apparatus were of the Sn-Pb eutectic composition. It was felt that such castings would be particularly useful for observing basic faults in the apparatus and experimental technique since the eutectic alloy solidifies at a single temperature. The complicating effects of macrosegregation should therefore have been eliminated in such castings. The etched macrostructures of four of these castings are shown in fig. 6.11(a) to (d). The melt composition used for casting number 1, shown in fig. 6.11(a)., was made up to the eutectic composition of Sn-38.1wt%Pb given by Hansen.[17] Primary dendrites were observed in its quenched macrostructure, however, and since these had tended to sink to the bottom of the casting they were assumed to be lead-rich. The remaining eutectic castings were therefore made up to a composition of Sn-37.4 wt%Pb and no further problems were encountered with primary dendrite formation. This agrees with the work of Burden and Hunt[173] on the extent of the eutectic range in the Sn-Pb alloy system which suggested that the true eutectic composition was as low as Sn-35.5 wt % Pb .

The other three castings whose quenched macrostructures are shown in fig. 6.11(b) to (d) all indicated faults in the initial apparatus design. In casting 2, fig. 6.11(b)., growth of eutectic occurred off the bottom of the mould during cooling because the bottom monitoring thermocouple had been giving an erroneous high reading during the holding period, and the bottom heater had consequently been turned down too low. After this casting all three monitoring

Fig 6.11. Sn-Pb eutectic alloy growth run in apparatus used to correct faults.

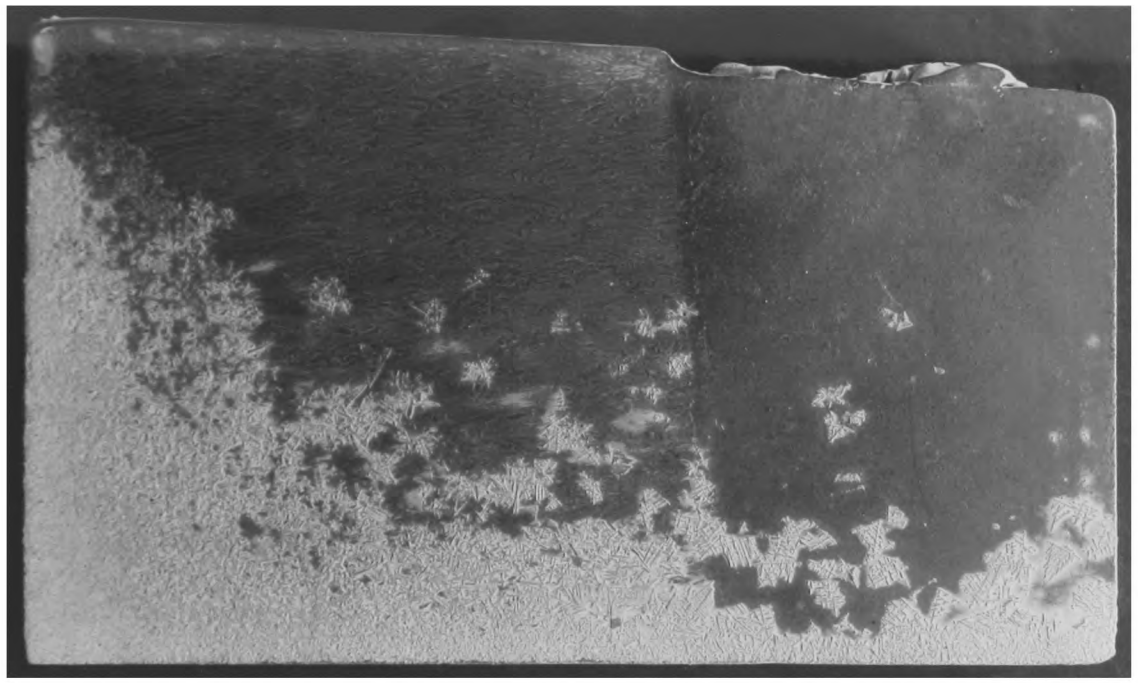


Fig 6.11.(a). CASTING 1 - off eutectic composition

MAG^N
x 1

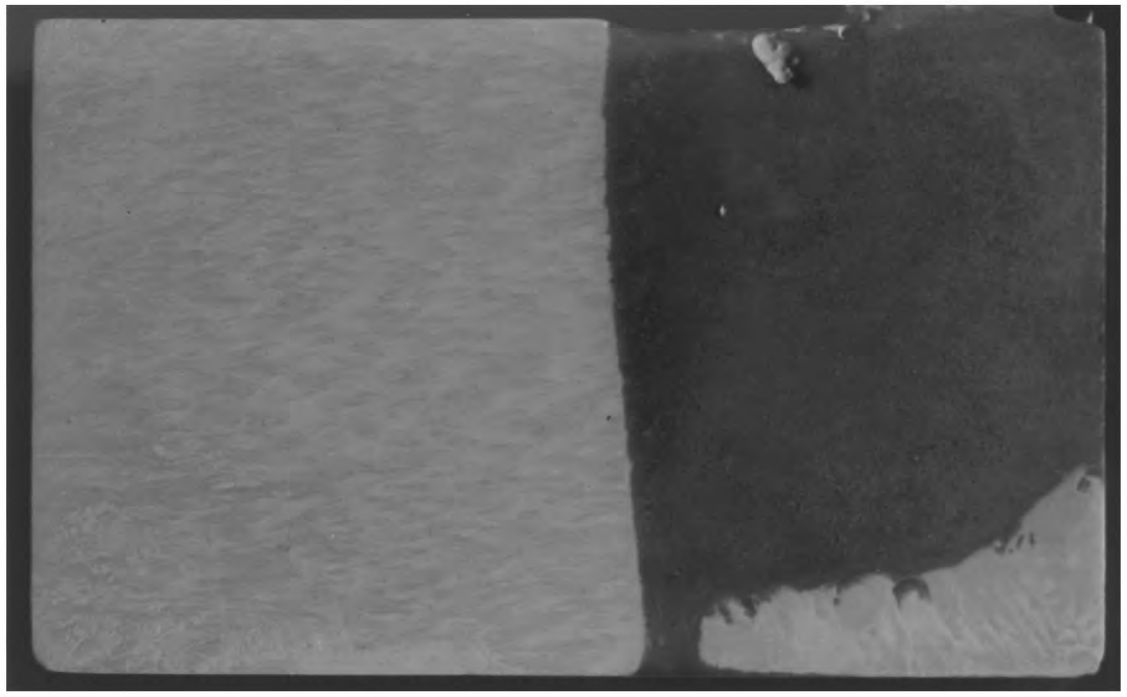


Fig 6.11(b). CASTING 2 - bottom heater too low, fault in monitoring thermocouple

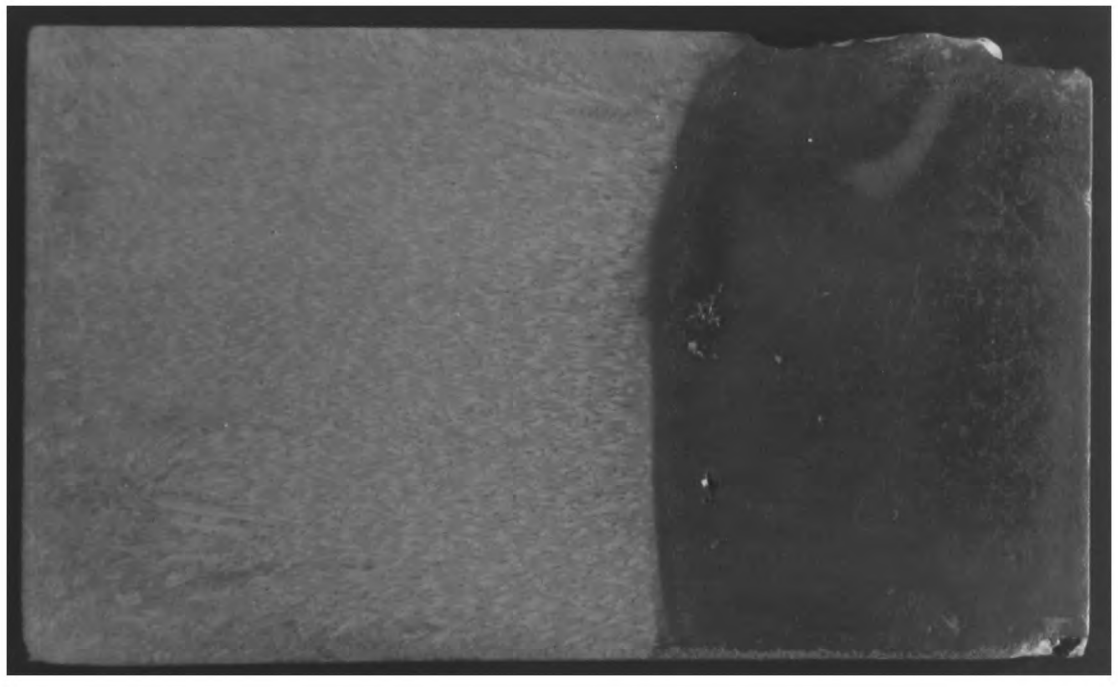


Fig 6.11(c). CASTING 3 - stainless steel top insert, constituted too large a heat sink.

Growth from left to right →

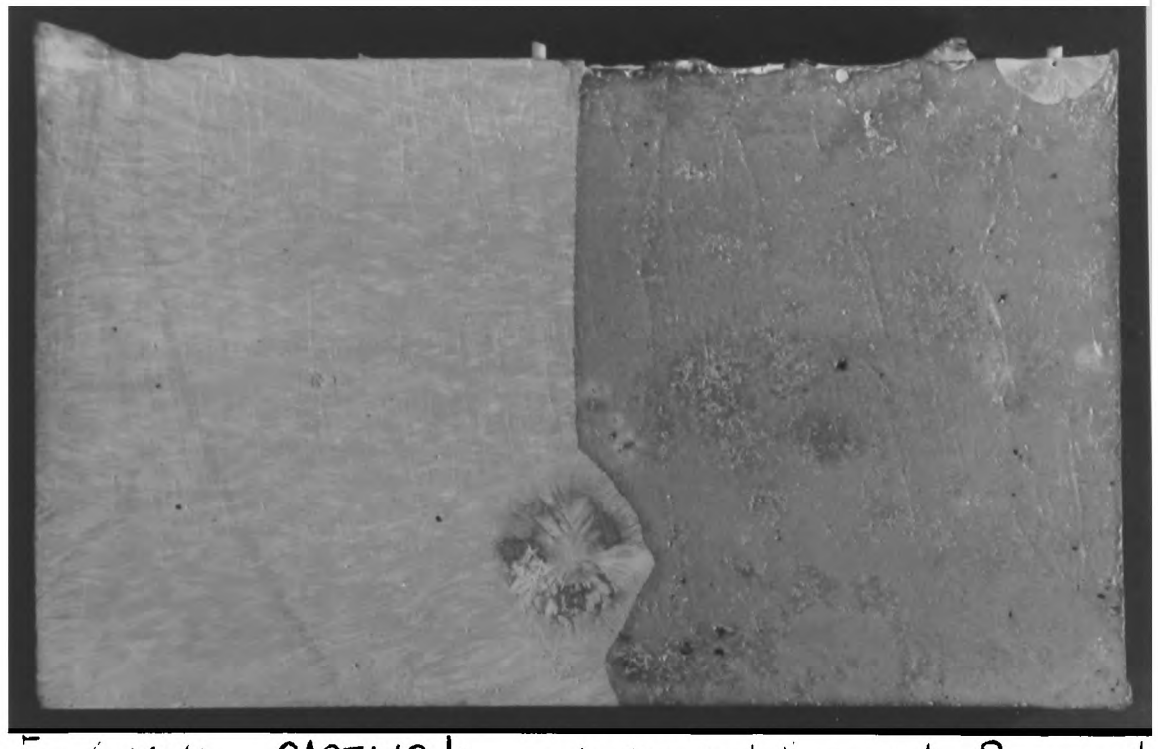


Fig 6.11(d). CASTING 4 eutectic nodule present. Pre-growth holding temperature too low. Calibration of thermocouples.

thermocouples were replaced and the new ones were all made from the same batch of wire. In casting 3, fig. 6.11(c)., it was observed that the original top insert of the mould, made from stainless steel, had acted as a heat sink during cooling. It was therefore replaced with the sindanyo insert described in section 6.3. Finally, in casting 4, fig. 6.11(d), eutectic noduli were observed floating in the quenched bulk liquid pool. These had presumably formed during the holding period prior to growth, therefore suggesting that the holding temperature had been slightly below the eutectic temperature. This was confirmed by calibrating the three monitoring thermocouple beads against the freezing point of pure lead. It was found that the millivolt reading registered by all three thermocouple was 0.12 mV ($3^{o}C$) higher than the freezing point of lead on standard tables. In fact it was later discovered that this error was within the error range of the thermocouple wire calibration quoted by the manufacturer.[174] In subsequent growth runs this difference of $3^{o}C$ between the readings of the thermocouples and standard table values was taken into account when adjusting the temperature of the furnace during the holding period.

The effects of variations in air flow rate through the cooling block on cooling rate were examined to determine how critical this variable was in terms of reproducibility. A rotameter was connected up in the air line on the exit side of the cooling block to measure air flow rates. The scale of this meter was only calibrated up to flow rates of 15 litres/minute and so a by-pass was used in parallel with the meter when higher flow rates were being monitored. The true rate of air was then determined by taking the air line outlet into a 5 litre flask inverted under water and measuring the time taken to displace the water from the flask. Initial experiments were performed with a thermocouple attached directly to the side of the cooling block in the mould cavity and with no metal charge. The mould was heated up in the furnace enclosure to a steady temperature of around $225^{o}C$, the top heater on the mould column was switched off air was passed through the cooling block at a rate given by the rotameter, and the variation of cooling block temperature with time was monitored via the thermocouple readout. The plots of T vs t obtained for the different air flow

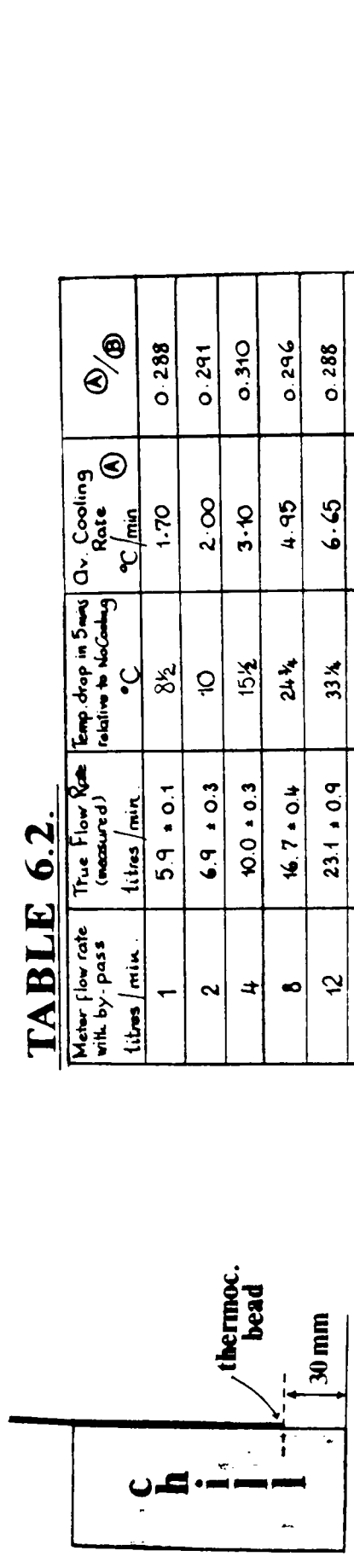
rates are shown in fig. 6.12. In Table 6.2., given with the figure, the average cooling rate over the first five minute period from the start of cooling is listed against the true air flow rate through the cooling block. It is clear both from the figure and the Table that the cooling rate of the block showed a marked, and almost linear, dependence on air flow rate.

Further trials were performed on air flow rate through the cooling block to determine the optimum rate for the particular growth velocity and temperature gradient required in this experiment (see section 6.2). Three Sn-Pb eutectic castings were grown using different flow rates through the cooling block. The rates used were 10, 16.7, and 23.1 litres/min. (true flow rates). The superheat of the alloy charge was $1^{\circ}C$ before cooling in each of the growth runs. The trace recorded by the thermocouple positioned nearest to the chill at the start of cooling is reproduced for each of these three growth runs in fig. 6.13. It may be seen that the cooling rate of the alloy charge was initially proportional to the true air flow rate through the cooling block, the ratio being $0.294^{\circ}C/min/litre/min$.. The time taken for the eutectic interface to pass between thermocouples C and D (fig. 6.13) was also noted. (The T vs t trace registered by the thermocouples began to fall once the eutectic interface had passed the thermocouple position). The velocity of the eutectic interface as measured between positions C and D in each run is given in Table 6.3 on fig. 6.13. It may be seen from this that the growth velocity varied significantly with true air flow rate through the cooling block although the relationship was not linear. It was decided that a true flow rate of 10 Litres/minute should be used for the subsequent castings in the experiment.

It may be seen from the thermocouple traces shown in fig. 6.13 that there was an appreciable degree of supercooling of the metal charge just after the start of cooling and prior to the start of growth. This is a common feature in tin-base melts because tin dendrites are difficult to nucleate. In order to check whether this supercooling would lead to non-reproducibility in growth two castings of Sn-5 wt % Pb were grown under identical conditions for the same length of time before quenching. The T vs t traces obtained from two of the

TABLE 6.2.

Meter flow rate with by-pass litres/min.	True Flow Rate (measured) litres/min.	Temp drop in 5 secs relative to No Cooling °C	Av. Cooling Rate Ⓐ °C/min	Ⓐ/Ⓑ
1	5.9 ± 0.1	8½	1.70	0.288
2	6.9 ± 0.3	10	2.00	0.291
4	10.0 ± 0.3	15½	3.10	0.310
8	16.7 ± 0.4	24¼	4.95	0.296
12	23.1 ± 0.9	33⅛	6.65	0.288
15	39.1 ± 3.0	54½	10.90	0.279



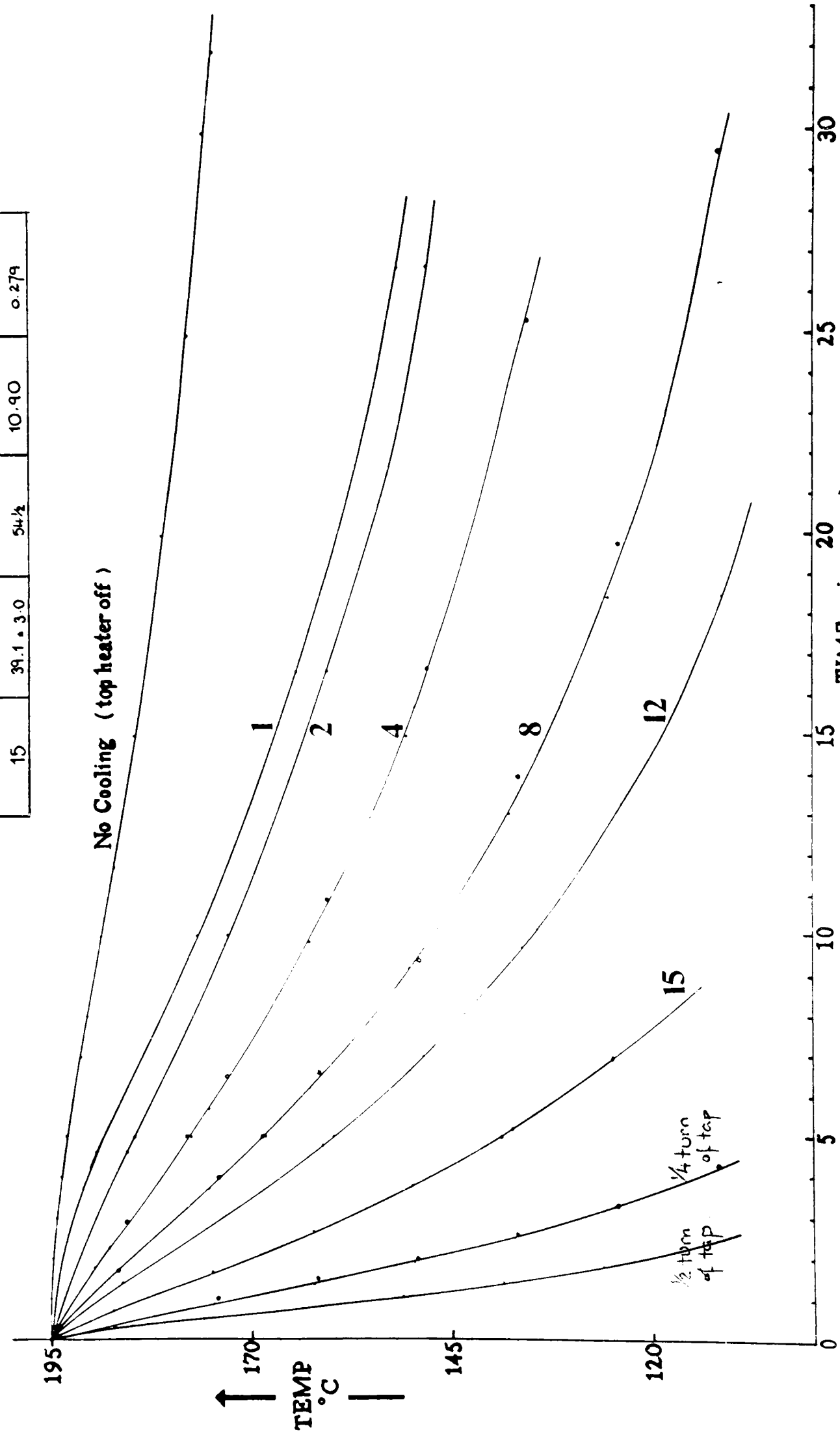
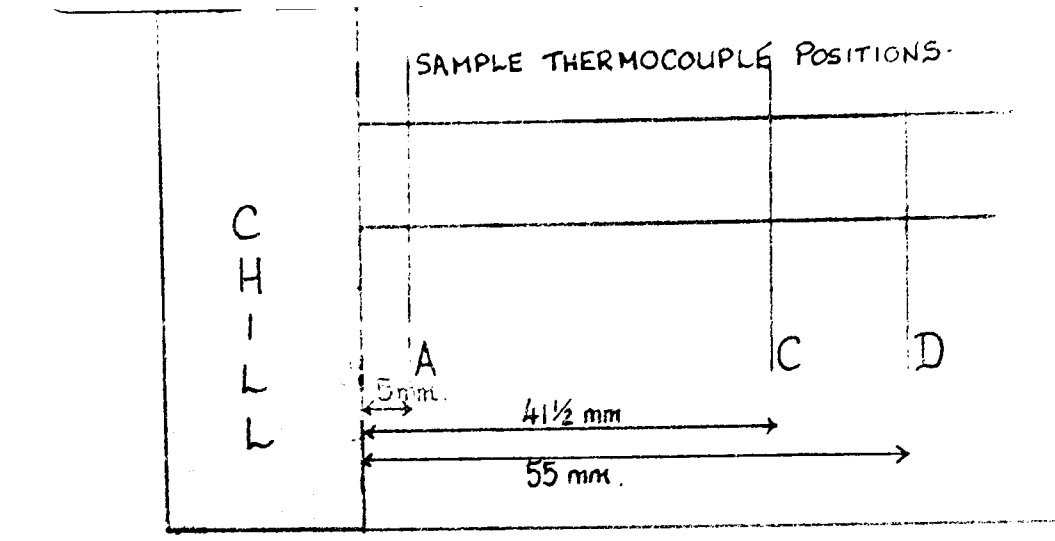


Fig 6.12. Cooling curves for various air flow rates through the cooling block.



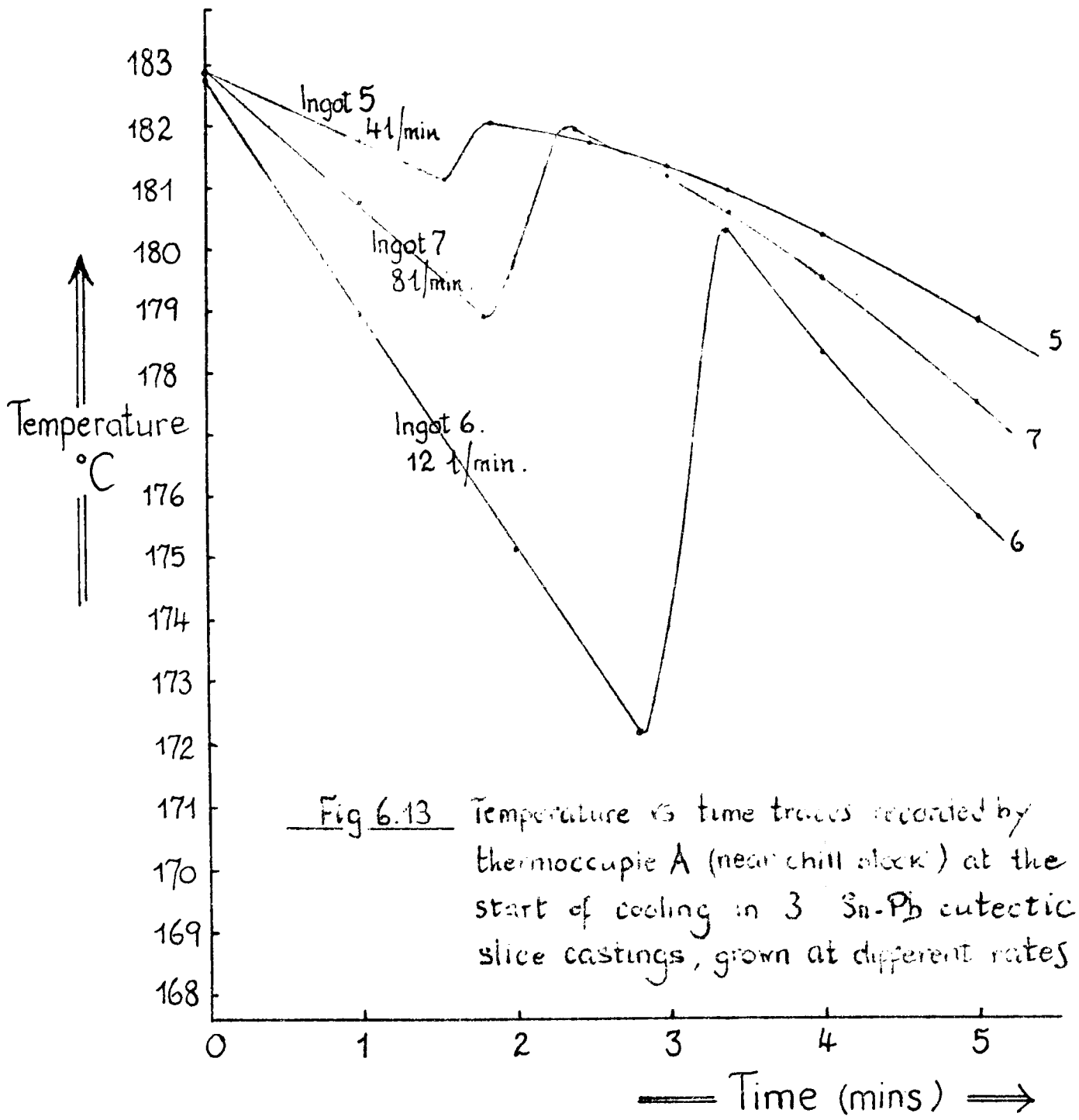


Fig 6.13 Temperature vs time traces recorded by thermocouple A (near chill block) at the start of cooling in 3 Sn-Pb eutectic slice castings, grown at different rates

TABLE 6.3

Ingot No.	Meter flowrate l/min.	True air flowrate l/min.	t_C from start	t_D of cooling	$x_{C \to D}$ cm.	Interface velocity $V_{C \to D}$ cm/sec.
5	4	10·0	14m08s	18m42s	1·35	4.92×10^{-3}
7	8	16·7	12m27s	16m23s	1·35	5.72×10^{-3}
6	12	23·1	11m27s	14m54s	1·35	6.51×10^{-3}

thermocouples in these ingots are shown in fig. 6.14(a) and (b). It may be seen from these that ingot 8 took 6 minutes 10 seconds to nucleate after the start of cooling while ingot 9 took 5 minutes 19 seconds, both melts having an initial melt superheat of $4\frac{1}{2}^{o}C$. The thermocouples nearest the chill registered a supercooling of $9\frac{1}{2}^{o}C$ and $7\frac{3}{4}^{o}C$ in ingots 8 and 9 respectively, and all four thermocouples fell below the liquidus temperature prior to nucleation in both growth runs. The growth rates of the dendrite tip interfaces measured from the thermocouple traces were initially very rapid (14×10^{-3}cm/sec.), but they slowed down considerably with time. They were not reproducible between the two ingots. Both of the growth runs were quenched at 14 minutes 46 seconds after the start of cooling and their quenched macrostructures are shown in fig. 6.15(a and (b). Although the major part of the dendrite tip front had advanced the same distance from the chill block in each ingot it was clear that the proturbences at the bottom of the interfaces were not reproducible. It was felt that these proturbences were a product of the whole melt supercooling at the start of freezing since this probably allowed a stable layer of 'cold' liquid to survive the recalescence. They were felt to be very undesirable features not only in terms of non-reproducibility but also because they showed a tendency towards fragmentation and equi-axed crystal formation. Trials were therefore conducted to nucleate the melt at the start of cooling. The first attempt was made using strands of copper wire poked down the tube fixed to the chill block. This failed to produce any improvement in nucleation, all four sample thermocouples supercooled below the alloy liquidus temperature as in figs. 6.14(a) and (b). Copper wire coated with tin was then tried and this proved to be partially successful, with only the sample thermocouple closest to the chill monitoring any supercooling, fig. 6.14(c). The quenched macrostructure of this ingot, number 10, is shown in fig. 6.15(c), and it is clear that the bottom interface proturbence had been eliminated by preventing the bulk of the melt from supercooling. Finally, in ingot 11, cold pure tin wire was inserted into the molten metal near to the chill at the start of cooling and this proved to be completely successful in eliminating supercooling. The thermocouple traces

Fig 6.14(a). Run n° 5 - un-nucleated

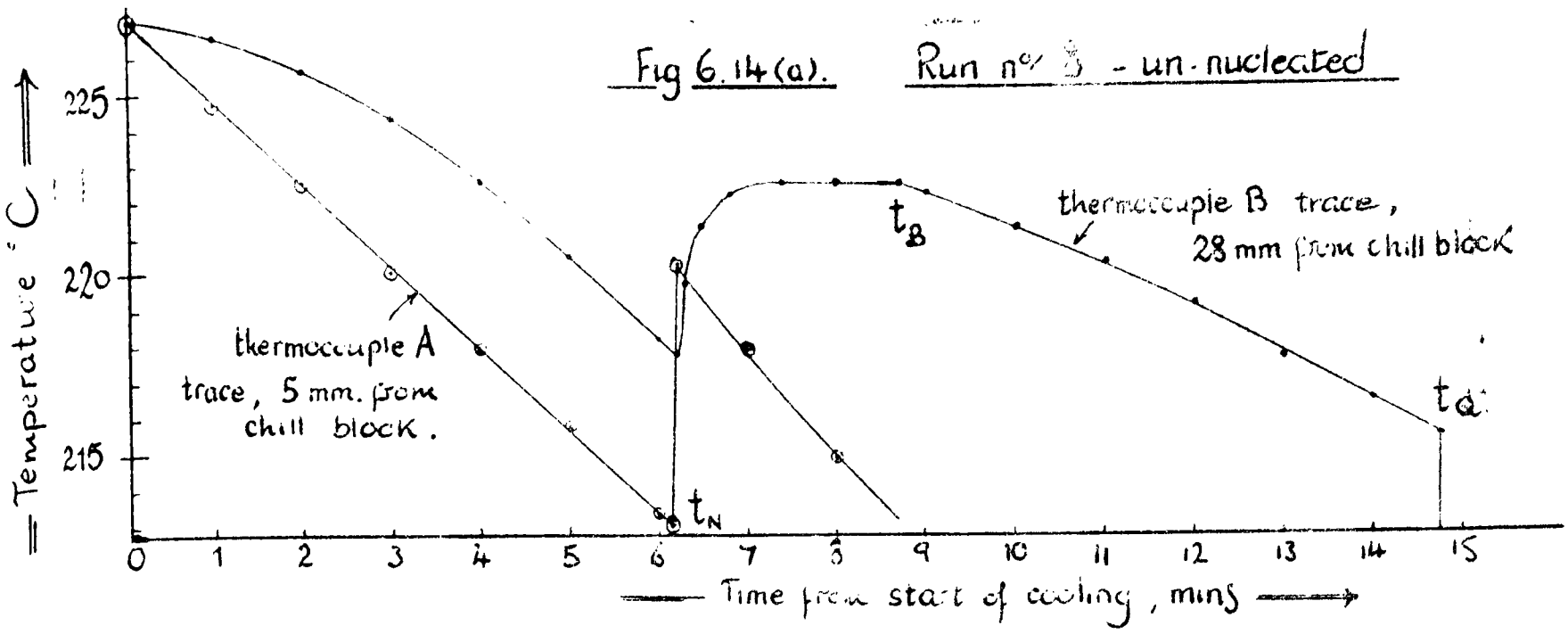


Fig 6.14(b). Run n° 9 - un-nucleated

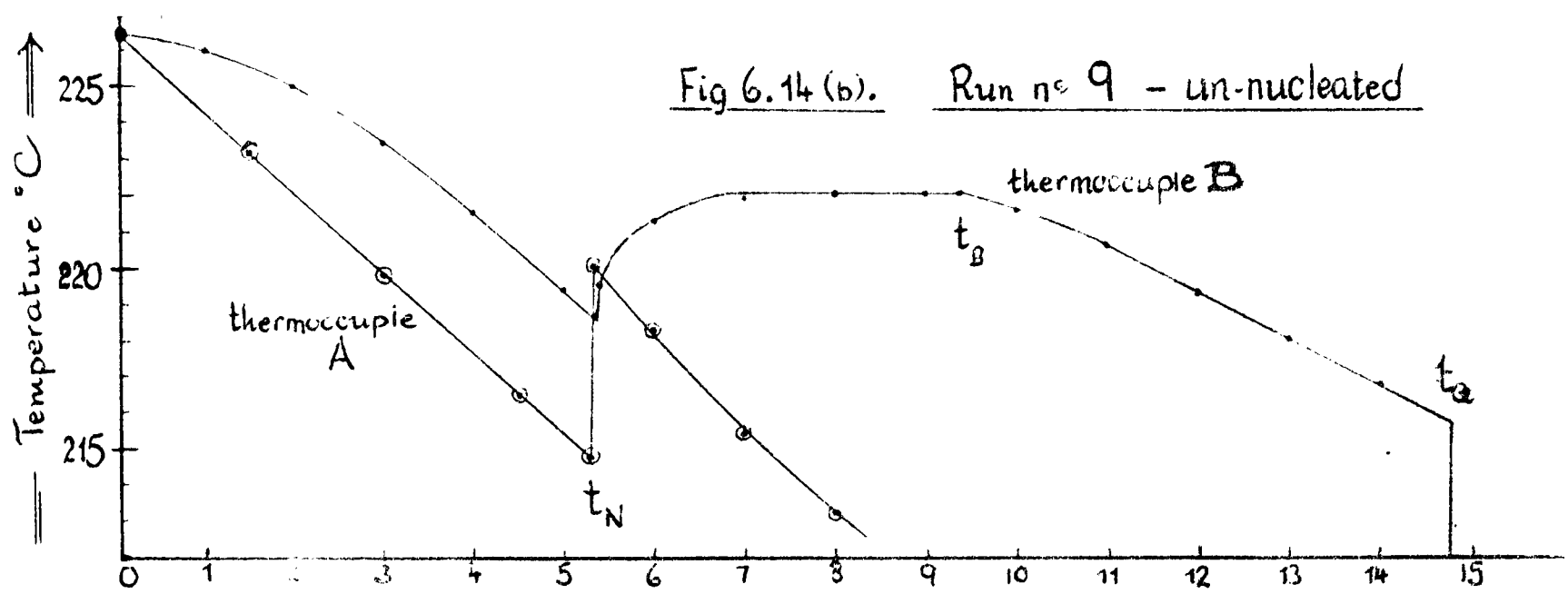


Fig 6.14(c). Run n° 10 - nucleated with tin coated, copper wire

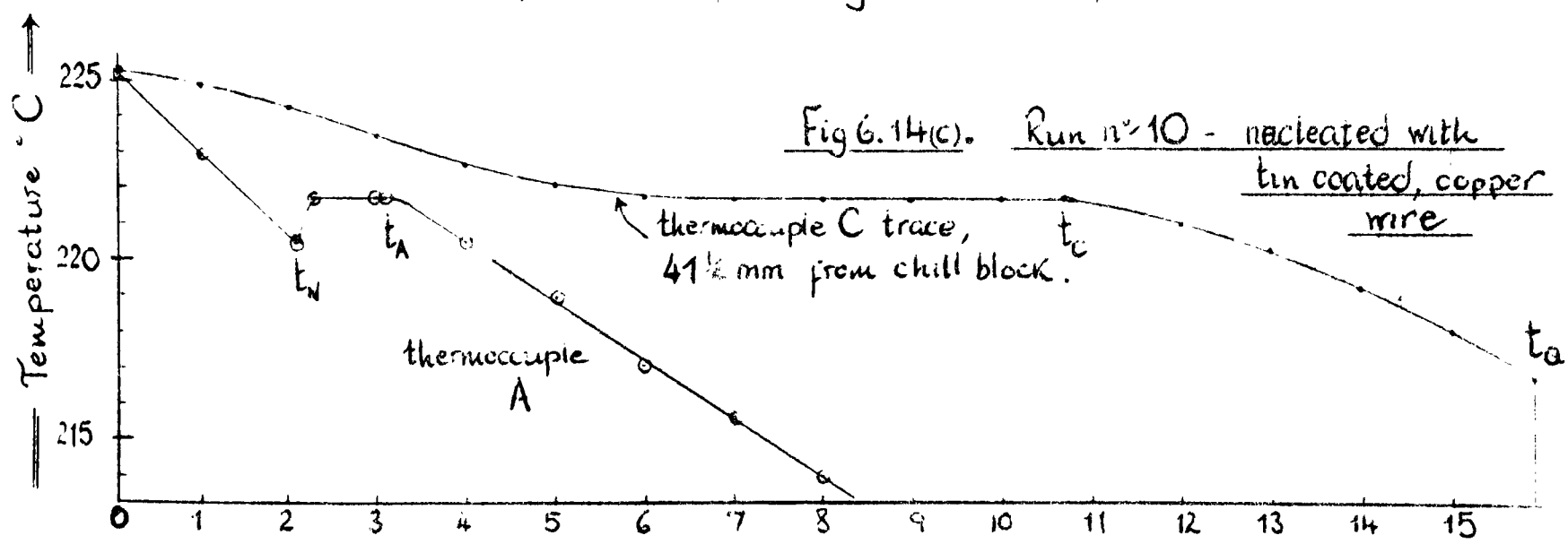
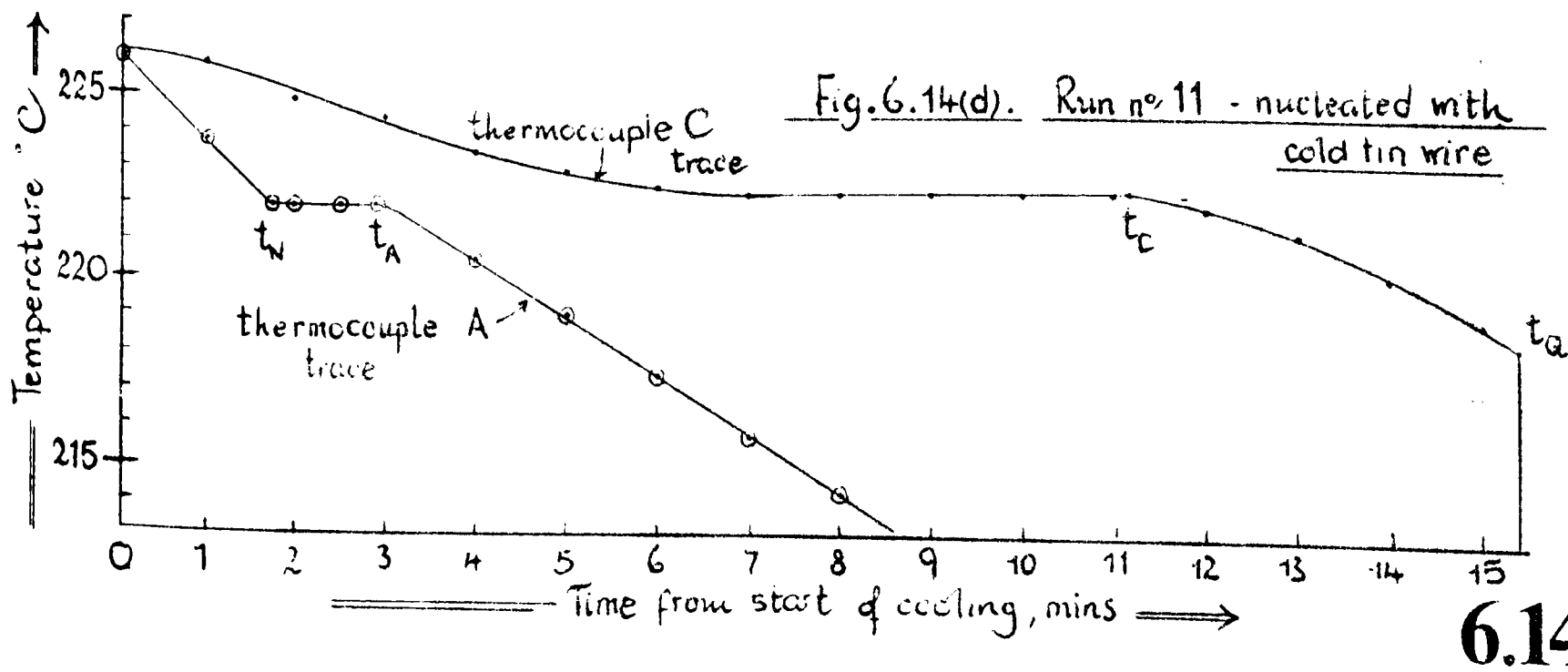


Fig. 6.14(d). Run n° 11 - nucleated with cold tin wire



6.14

Fig 6.15. Macrostructures of four 3-5 wt.% Pb castings quenched after similar growth times. Each casting nucleated in a different way.



Fig 6.15(a). CASTING 8 - No nucleation

MAG^N
×1

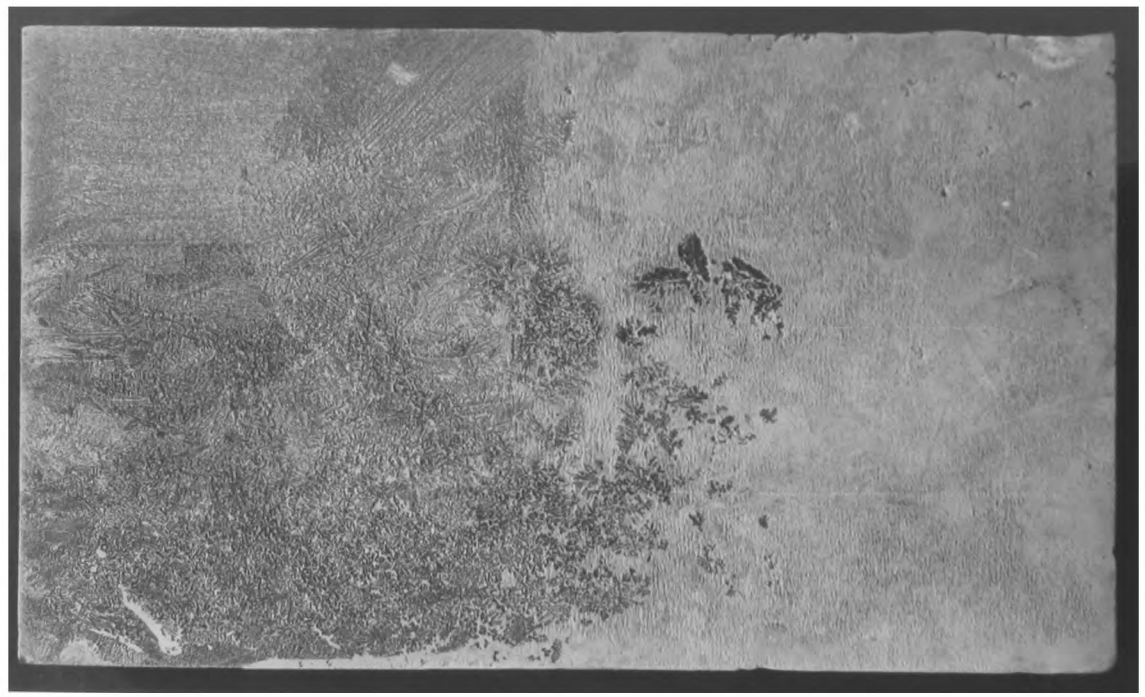


Fig 6.15(b) CASTING 9 - No nucleation.



Fig 6.15(c) CASTING 10 - nucleated with tin-coated, copper wire

Growth from left to right →

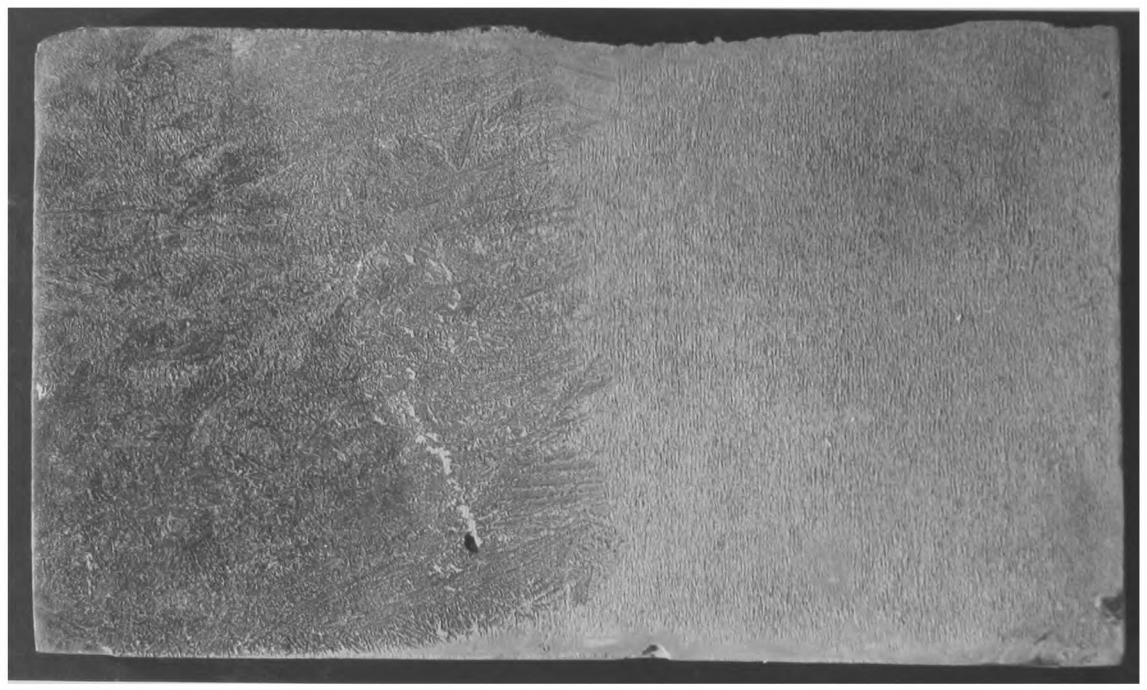


Fig 6.15(d) CASTING 11 - Nucleated with cold, pure tin, wire

6.15

and ingot macrostructure are shown in figs. 6.14(d) and 6.15(d) respectively.

Finally a Sn-Pb eutectic casting was grown under the optimum conditions developed for the main series of slice casting described in the next section (i.e. 2°C holding superheat, 10 l/m air flow rate through cooling block, nucleated with cold tin wire). The casting was quenched after growth had progressed almost half-way along the ingot in order to check the macroscopic eutectic interface shape (and hence the isotherm shape in the slice castings). This may be seen in fig. 6.16. The isotherms were parallel to the chill block for the majority of its height in the casting although there was a certain amount of curvature away from the chill at both the top and the bottom. It may be seen from the macrostructure of the solidified eutectic region that this was caused by growth from the top insert and the bottom mould surface. The extent and magnitude of the isotherm curvature was not considered to be sufficiently large to affect the validity of the experiment in terms of monitoring macrosegregation in a series of castings. Table 6.4., overleaf, gives the relevant growth data for this eutectic casting.

6.5.2 Results of major series of castings

Twelve ingots were cast altogether in the series of samples which made up the major part of the experiment; that is those which were cast under identical conditions in order to determine the variation of composition with time at various positions within the ingots. The casting data for this series of ingots are given in Table 6.5., on page 99.

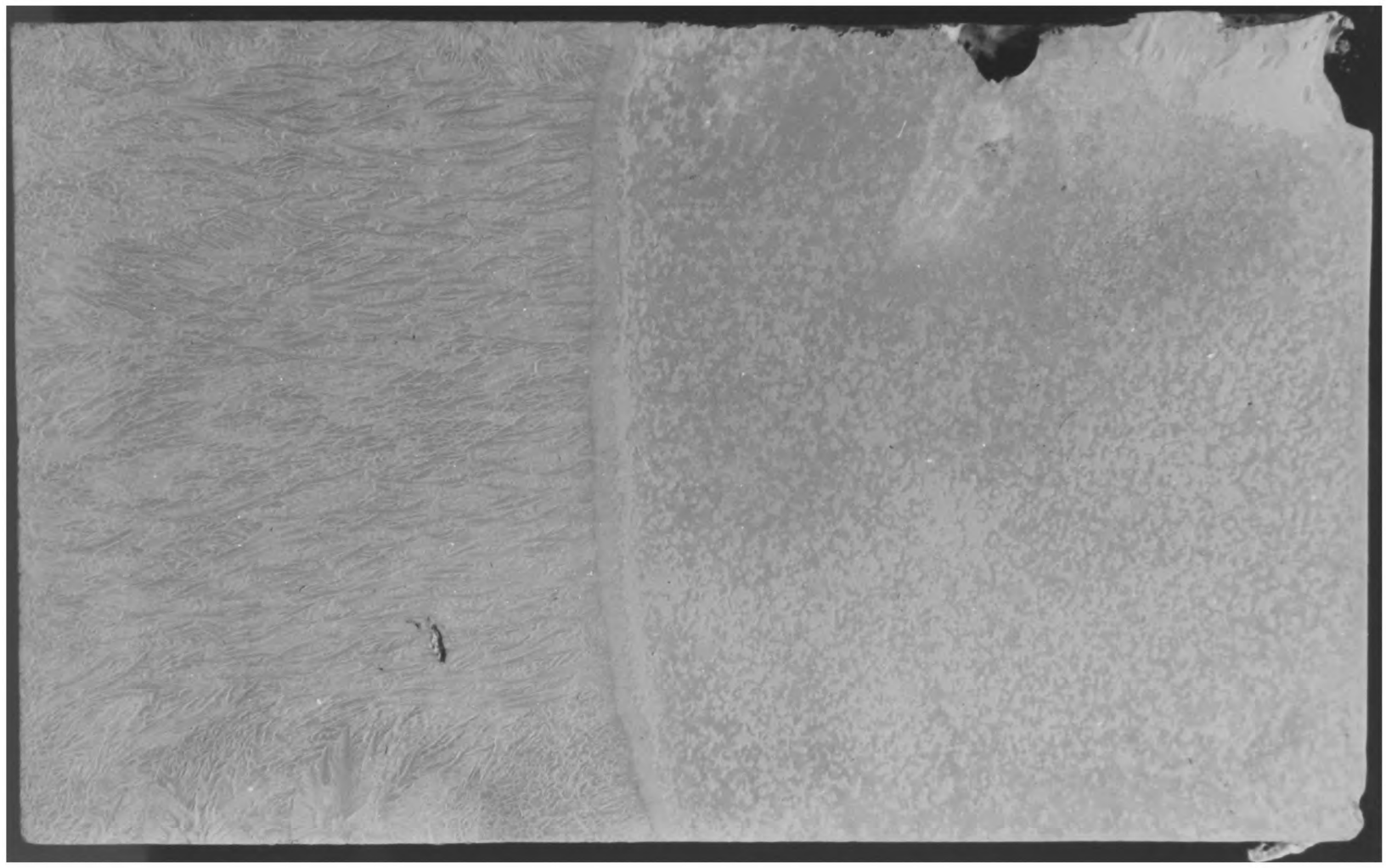


Fig 6.16. Etched macrostructure of Sn-Pb eutectic slice casting (run number 191), quenched after 18m 14s of cooling.

Magn x 1·5

Table 6.4

Holding Superheat $\Delta T_s = 2\frac{1}{2} \pm \frac{1}{4}\ ^\circ C$

Times measured from start of cooling.	Nucleation Time t_N	Time at which interface passed the relevant sample thermocouple.			Quench Time t_Q.
		t_A	t_B	t_C	
	1m 25s	3m 05	11m 06s	15m 52s	18m 14s

Distance of the sample thermocouple beads from the chill block, as measured with travelling microscope on quenched and sectioned casting.

A	B	C	
5.0 mm	27.8 mm	41.3 mm	± 0.1 mm

Distance of quenched interface from chill block = 47.0 ± 0.5 mm
(measured from casting macrostructure, see fig 6.16. above)

Interface velocity between various positions (from above data) cm/sec.	$\bar{V}_{CHILL \to A}$	$\bar{V}_{A \to B}$	$\bar{V}_{A \to C}$	$\bar{V}_{CHILL \to QUENCH}$
	5.00×10^{-3}	4.74×10^{-3}	4.73×10^{-3}	4.66×10^{-3}

Table 6.5

Ingot Number	Cooling time t_Q (Cooling on → quench)	Ingot Weight gms	Compn. of melt sample Wt % Pb
14	0m 00s	642	5.00
17	8m 32s	643	4.95
21	10m 40s	639	4.99
24	15m 19s	639	5.02
11	15m 24s	642	-
12	15m 28s	645	-
23	18m 39s	643	4.99
15	22m 54s	645	5.07
16	22m 55s	638	4.96
20	30m 35s	643	4.98
13	47m 35s	641	4.99
22	75m 06s	643	4.97
Errors	±01s	$\pm\frac{1}{4}$	±0.05

The cooling time, t_Q, was measured with a stopwatch and represents the time interval from the start of cooling to the moment at which the mould was plunged into the quench bucket. The series of ingots ranged from one which was quenched before cooling (no. 14), to one which was quenched after complete solidification (no. 22). The table shows that the as-cast, ingot weight was reproducible to better than $\pm$ 1%. It also shows that the nominal compositions of the ingots, determined from samples taken from the melt before pouring, all lay within the error range of the analysis technique, $\pm$ 1.3%.

The sample thermocouple temperature traces, macrostructure, and composition data obtained from each of the castings in this series are summarised and discussed in the following three sections.

6.5.2.1 Temperature Measurements

The T vs. t traces recorded by the four sample thermocouples in ingot 23 are shown in fig. 6.17. These thermocouples were in positions A, B, D, and F in the top insert of the mould (see fig. 6.18.). The general form of these traces is typical of that obtained from the thermocouples in the other ingots of the series. It can be seen from figure 6.17. that the liquid metal in the mould was isothermal prior to cooling; all four thermocouples indicating the same temperature, T_H. Once cooling had begun the trace of thermocouple A nearest the chill fell steeply and steadily until a sharp plateau was observed at t_N. This was taken to be the time at which nucleation of solid material occurred at the chill block. The traces of the other three thermocouples fell less steeply on cooling and exhibited no change in slope at t_N. The effects of nucleation were therefore confined to the vicinity of the chill block. No undercooling was observed in any of the ingots prior to nucleation.

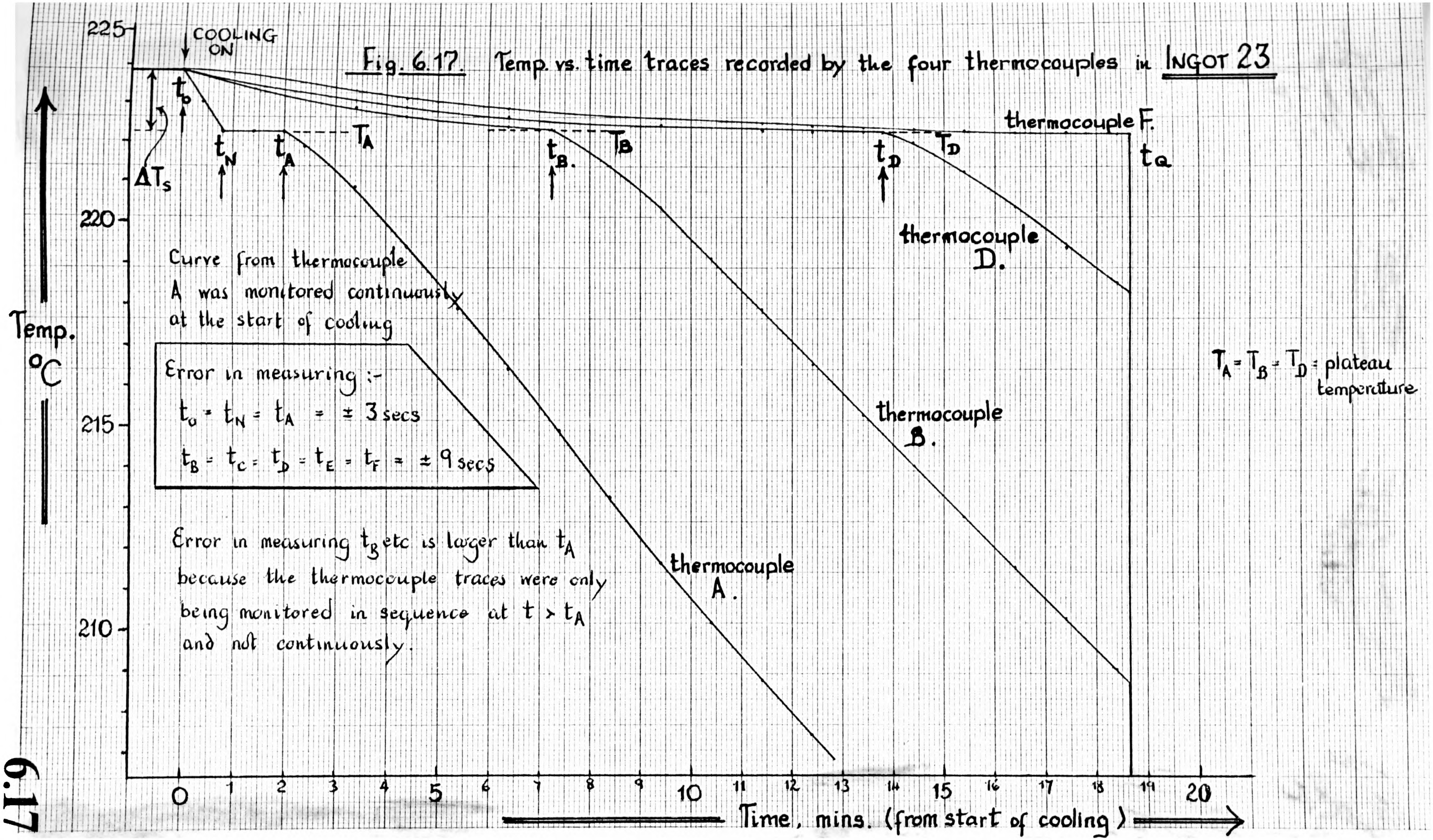
Figure 6. 17. also shows that each of the thermocouple traces eventually fell to a plateau in temperature, and that these plateaux were all of the same value ($T_A=T_B=T_D$). This temperature was taken to be the growth temperature of the advancing dendritic front, T_p, which would have been slightly below the equilibrium liquidus temperature of the alloy.[40] The holding superheat in each run was calculated simply by subtracting T_p from T_H. Table 6.6., below, lists the values of superheat measured in the ingots and compares them with the corresponding values for t_N measured from the thermocouples at position A.

Table 6.6

Ingot Number	23	20	21	16	24	15	22	17	12	11	13	Error
Plateau Temperature °C	222¼	222¼	222	223	222	222	222½	222½	222	222	222½	
Superheat °C	1½	2	2	2	2	2	2¼	2½	3½	4	4¼	± ¼
t_N Secs	48	60	60	61	66	72	72	74	90	106	117	± 6s

It can be seen from this Table that for each $\frac{1}{2}$°C of superheat the nucleation time was delayed by approximately 15 seconds.

Fig. 6.17. Temp. vs. time traces recorded by the four thermocouples in INGOT 23



6.17

The absolute value of the plateau temperature in each ingot (T_A etc.) was obtained by calibrating the sample thermocouples against the freezing point of pure lead (99.99%) before the start of each growth run. A thermal analysis technique was used. This involved simply melting up a charge of pure lead, inserting the thermocouple into the centre of the molten pool, switching off the furnace, and allowing the charge to cool very slowly. The thermocouple trace fell slowly until solidification of the charge began at which point a plateau was observed. The length of this plateau corresponded to the growth of columnar crystals from the edge of the crucible to the centre of the molten pool. Tin was not used as the calibration metal because of the large initial undercoolings experienced during freezing. A calibration was required before each growth run because the sample thermocouple beads had to be re-made after the previous run. It should be noted that the plateau temperatures obtained in the slice casting experiment were approximately $1^{o}C$ lower than those obtained from identical Sn-5wt%Pb alloy melts in the thermal analysis technique. This was presumably due to the slower growth rate in the furnace-cooled, thermal analysis melts, and it would help to explain why the plateau temperatures measured from the slice castings were apparently as much as $3\frac{1}{2}^{o}C$ lower than the calculated liquidus temperature of the alloy ($225\frac{1}{2}^{o}C$).

The time at which each thermocouple trace fell from its plateau temperature (t_A, t_B, etc. in fig. 6.17.) was taken to be that at which the growing dendrite tip interface passed that thermocouple position in the ingot. It was found that these times were not consistent from one ingot to another. For example, t_A varied from 1m 58secs in ingot 23 to 3m 09secs in ingot 11, and t_D varied from 13m 41secs in ingot 20 to 14m 48secs in ingot 13. This would seem to suggest that growth had not occurred reproducibly between the ingots. If, however, the nucleation times (t_N) are subtracted from these cooling times (t_A etc.) to give actual growth times (t_A-t_N, etc.) then the figures become much more consistent. This is illustrated in Table 6.7., overleaf, where the growth times to the various thermocouple positions

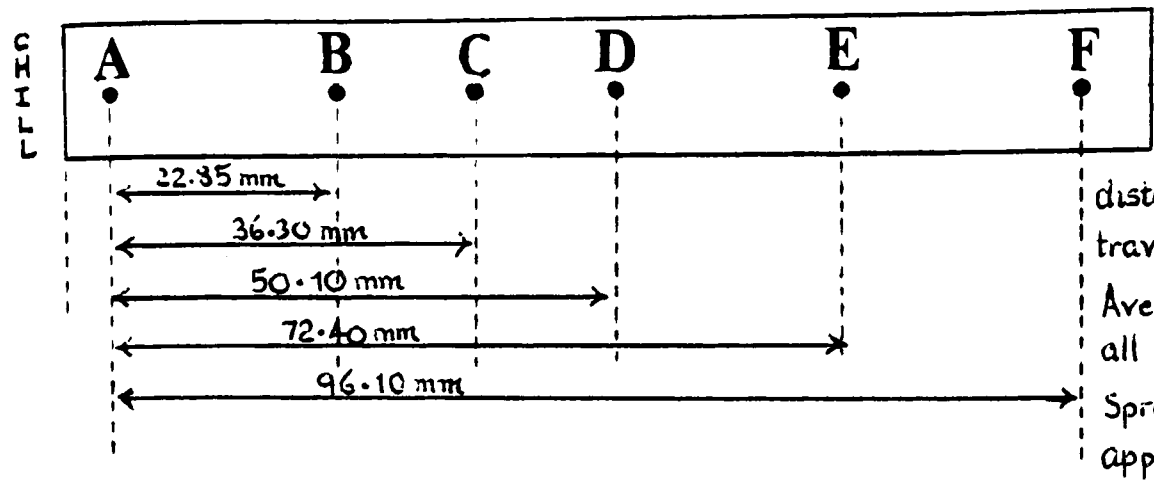


Table 6.7

Run No.	Nucl^n Time t_N.	Growth times for dendrite tip interface to advance from chill to the various thermoc. positions. $t_A - t_N$	$t_B - t_N$	$t_C - t_N$	$t_D - t_N$	$t_E - t_N$	$t_F - t_N$	Total Growth Time. $t_G = (t_Q - t_N)$
17	1m14s	1m13s	6m27s	-	Q	-	Q	7m18s
21	1m00s	1m00s	6m28s	-	Q	-	Q	9m40s
11	1m46s	1m09s	-	9m26s	12m36s	Q	-	13m38s
12	1m30s	1m13s	6m23s	9m30s	12m32s	-	-	13m58s
24	1m06s	1m09s	6m39s	-	?	-	Q	14m13s
23	0m48s	1m10s	6m27s	-	12m58s	-	Q	17m51s
15	1m12s	1m03s	-	9m24s	-	17m29s	Q	21m42s
16	1m01s	0m59s	-	9m19s	-	?	Q	21m54s
20	1m00s	1m03s	6m16s	-	12m41s	-	25m24s	29m35s
13	1m57s	1m09s	6m22s	-	12m49s	-	25m01s	45m38s
22	1m12s	1m08s	6m32s	-	12m39s	-	25m04s	73m54s
Error	±06s	±06s	±12s	±12s	±12s	±12s	±12s	±07s
Average Value		1m07s	6m27s	9m25s	12m43s	19m18s	25m10s	

Table 6.8

Positions	Distance A→X cm	Time for interface to move from positions A→X secs.	Average growth velocity $\bar{V}_{A\to X}$ cm/sec.
A→B	2.285	320	7.14×10^{-3} (±0.35)
A→C	3.630	498	7.19×10^{-3} (±0.24)
A→D	5.010	696	7.20×10^{-3} (±0.17)
A→E	7.240	1091	6.90×10^{-3} (±0.14)
A→F	9.610	1503	6.39×10^{-3} (±0.06)

are listed for each ingot. Also listed in the Table are the average growth times to the positions, taken over the whole series of ingots. The variation of the individual values from these average times lies in all cases within the error range of the experimental measurements. The variations which occurred in metal superheat throughout the series therefore had an effect on cooling times but not on growth times. It may be concluded from this that growth occurred in a reproducible manner within all of the ingots.

Table 6.8 lists the average growth rates of the advancing dendrite front between the various interface positions. It can be seen from the Table that the velocity of the interface was constant at 7.20 ($\pm$ 0.20) x 10^{-3} cm/sec. in the initial stages of growth. However, once the interface had moved beyond approximately 6 cm. from the chill block it began to slow down slightly, so that its average velocity across the whole length of the mould was around 6.30×10^{-3}cm sec.. The dendrite tip front must therefore have reached the end face of the mould at around 29 minutes after nucleation. The distances between the various thermocouple positions used in the calculation of these velocities were average values of measurements taken from quenched ingots on the surface sectioned at 30 mm. from the ingot base. Measurements were made using a calibrated travelling microscope.

Figure 6.19 shows the temperature profiles which existed in the ingots immediately prior to quenching. The temperature gradient in the majority of the semi-solid region was linear and constant at around 3.60°C/cm. during the period when the tip front was advancing across the length of the mould. The eutectic isotherm passed thermocouple A in ingots 13 and 22 after approximately 42 minutes from nucleation, and reached thermocouple F in ingot 22 at 69 minutes from nucleation. Ingot 22 was therefore fully solid on quenching.

6.5.2.2 Macrostructure and interface shape

The etched macrostructures of the series of ingots are shown in figs. 6.20 to 6.23. The ingots were etched for approximately 15 minutes in a mixture of 1 pt.HNO_3: 3 pts.HCl : 2 pts. H_2O. This etchant clearly distinguished the

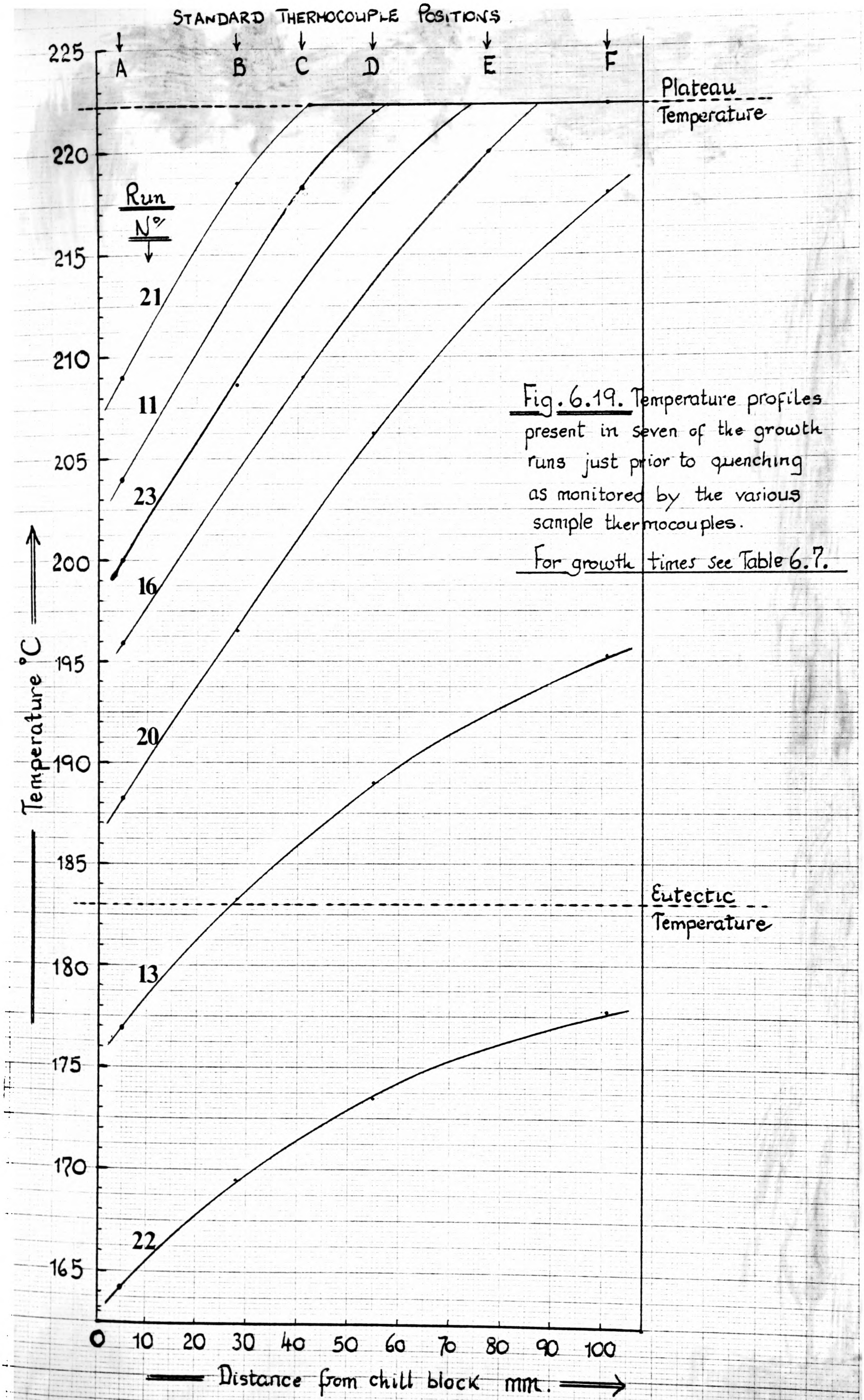


Fig. 6.19. Temperature profiles present in seven of the growth runs just prior to quenching as monitored by the various sample thermocouples.

For growth times see Table 6.7.

original semi-solid and bulk liquid regions of the ingots, as well as bringing out the dendritic structure within the semi-solid zones. There was no evidence in any of the ingot macrostructures to suggest that equi-axed crystal growth had occurred. Growth had apparently been completely columnar and unidirectional away from the chill block (left to right in the macrostructures presented in figs. 6.20 to 6.23). The quenched bulk liquid regions appeared relatively featureless with no general indication of primary dendritic fragments. The nucleation technique employed had therefore clearly been successful in preventing gross undercooling of the liquid pool and consequent equi-axed growth.

The progress of the macroscopic dendrite tip interface across the length of the ingot mould, which can be seen clearly from this series of photographs, is plotted diagrammatically in fig. 6.24. The interfaces exhibited a characteristic cut-back towards the chill at the bottom of the mould, and this became more pronounced as growth proceeded. This cut-back was a result of macrosegregation caused by the convective flow of interdendritic liquid within the growing semi-solid region. The interdendritic liquid in the mushy zone would have been denser than the bulk liquid since it was both colder and richer in lead. It would therefore have had a tendency to move downwards through the semi-solid zone, causing the flow cycle shown in fig. 6.20 (a). Flow of liquid towards the chill at the top of the mushy zone in the ingots would have caused a relatively uniform region of negative segregation owing to an increase in the amount of solid being deposited on the dendrites. Flow of liquid away from the chill near the bottom of the mushy zone would have tended to redissolve the dendrites. Such flow would not, however, have produced a corresponding uniform region of positive segregation because it is unstable and would have broken down into localised regions of preferential flow through large liquid channels. Such channels may indeed be seen towards the bottom of the semi-solid region of the majority of the quenched ingot macrostructures. Non-equilibrium liquid enriched in Pb would have been transported from within the mushy zone through these channels. This liquid would then have tended to remain as a gravity-stable

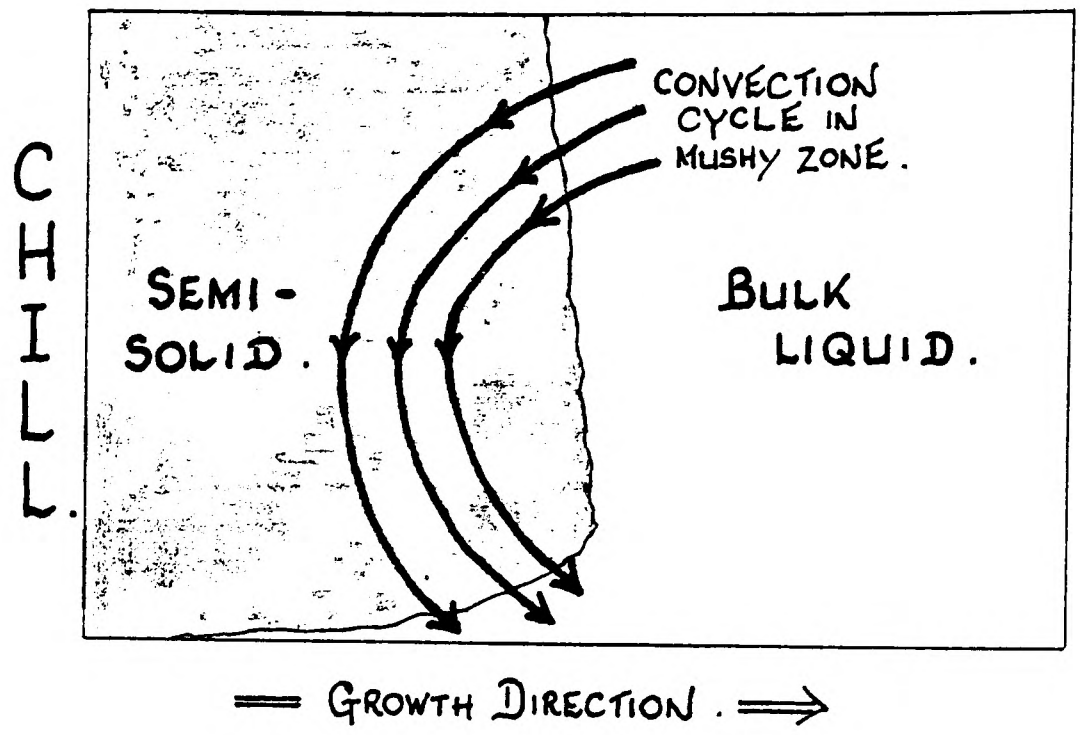


Fig. 6.20(a). Schematic representation of mushy zone flow cycle for horizontal unidirectional growth of Sn-5 wt.% Pb ingots.

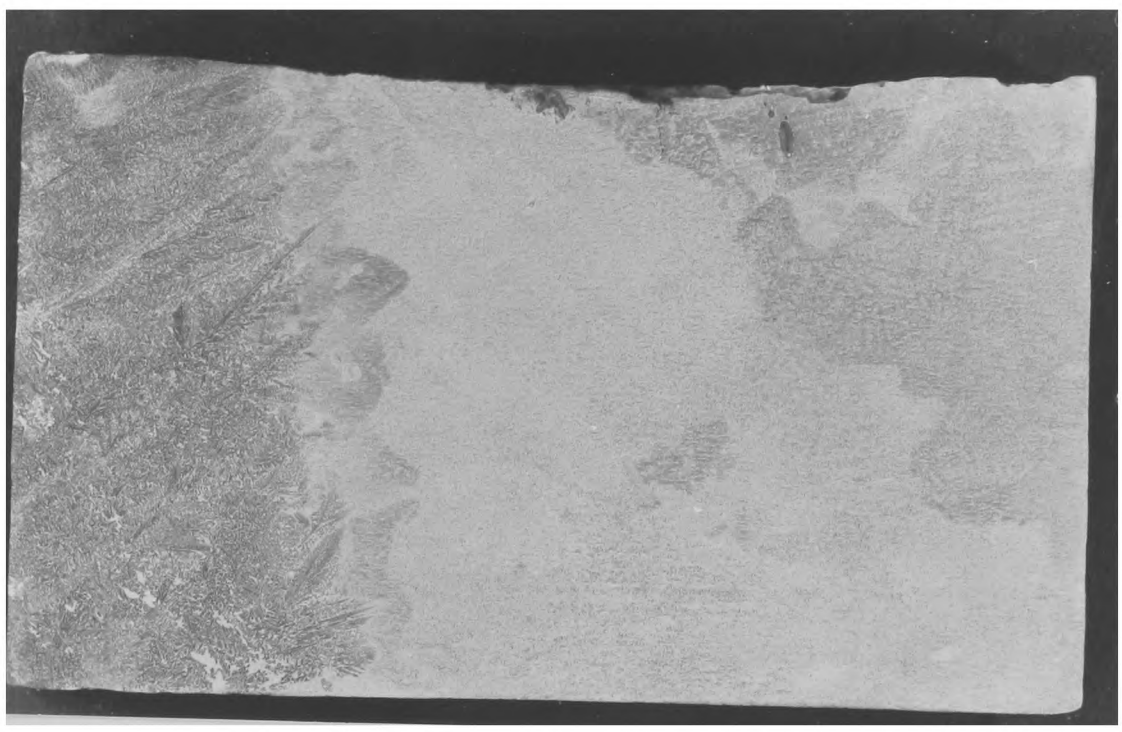


Fig. 6.20(b).

Ingot 17

Growth time 7m 18s

(growth from left to right away from vertical chill. Macrostructure brought out by etching in 1pt HNO_3 : 3pts HCl : 2pts H_2O for 15 mins.)

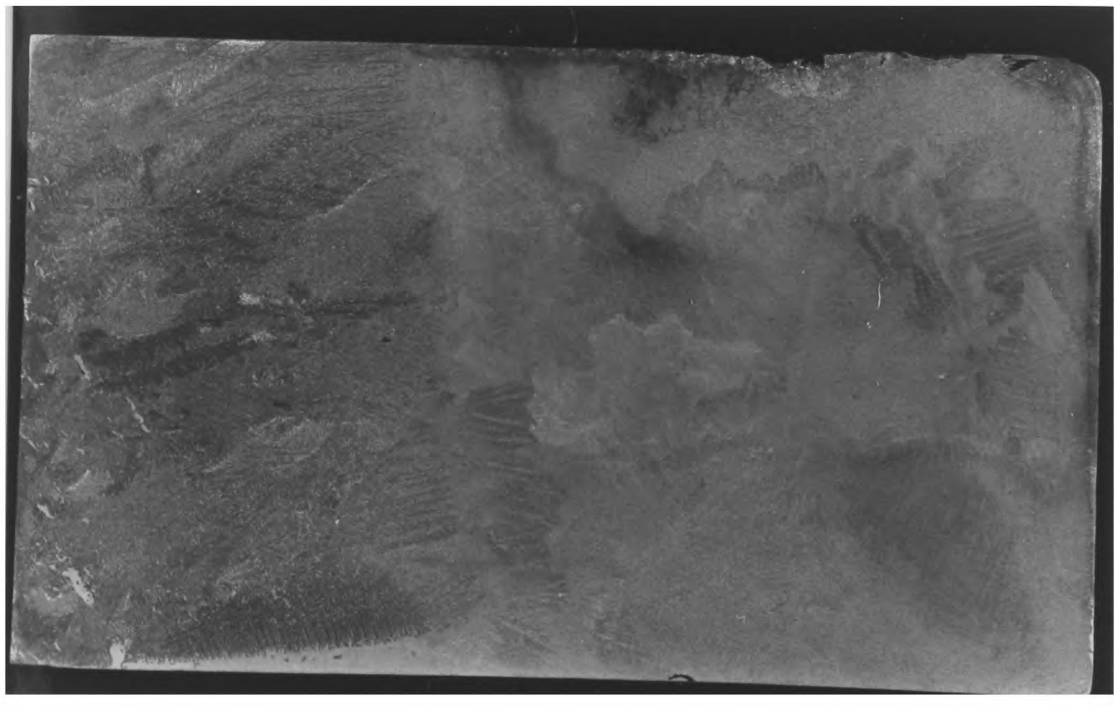


Fig. 6.20(c).

Ingot 21

Growth time 9m 40s.

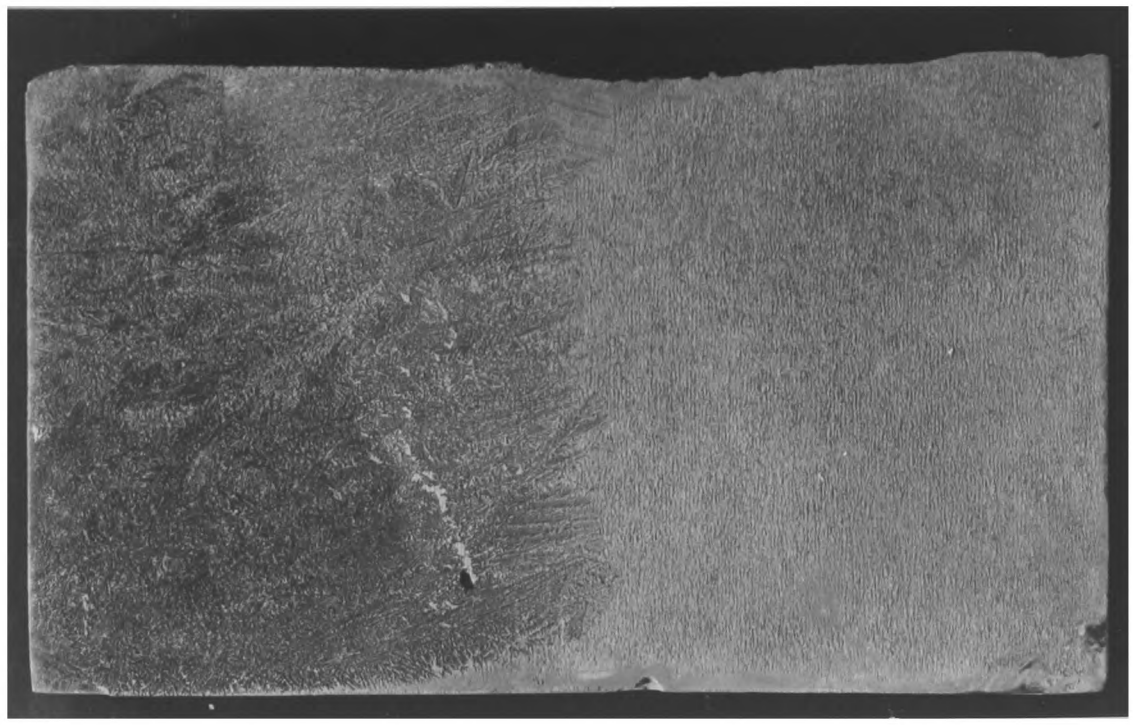


Fig. 6.21(a)

Ingot 11

Growth time 13m 38s.

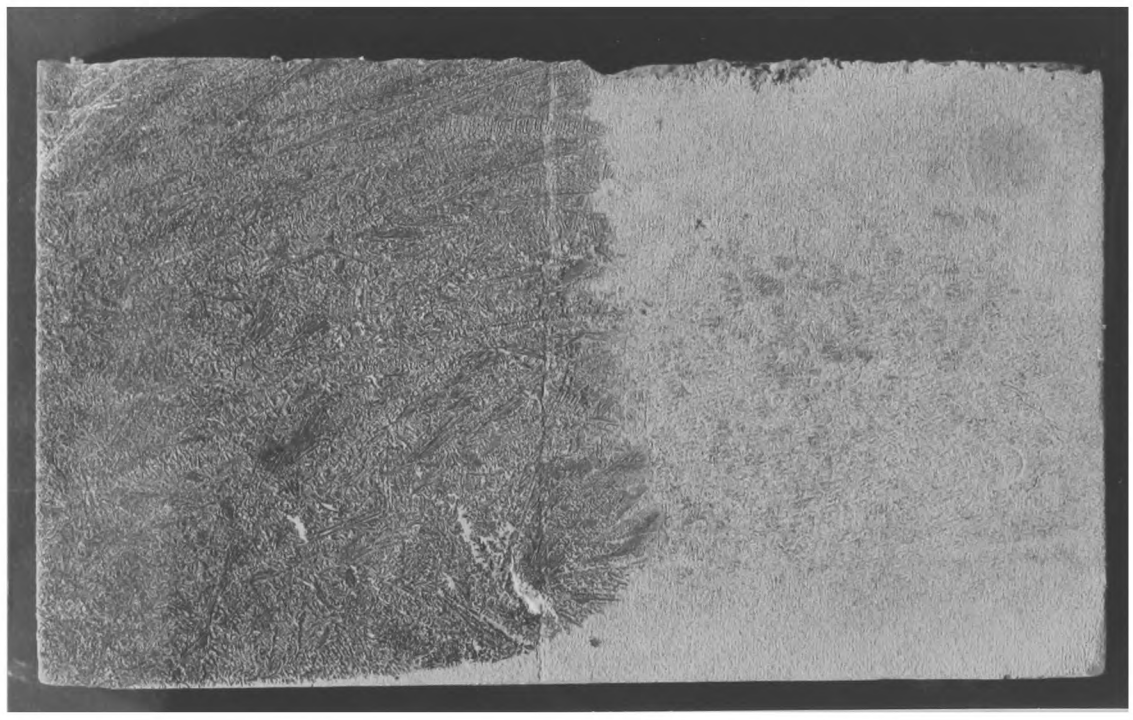


Fig. 6.21 (b).

Ingot 12

Growth time 13m 58s



Fig. 6.21(c).

Ingot 24

Growth time 14m 13s.

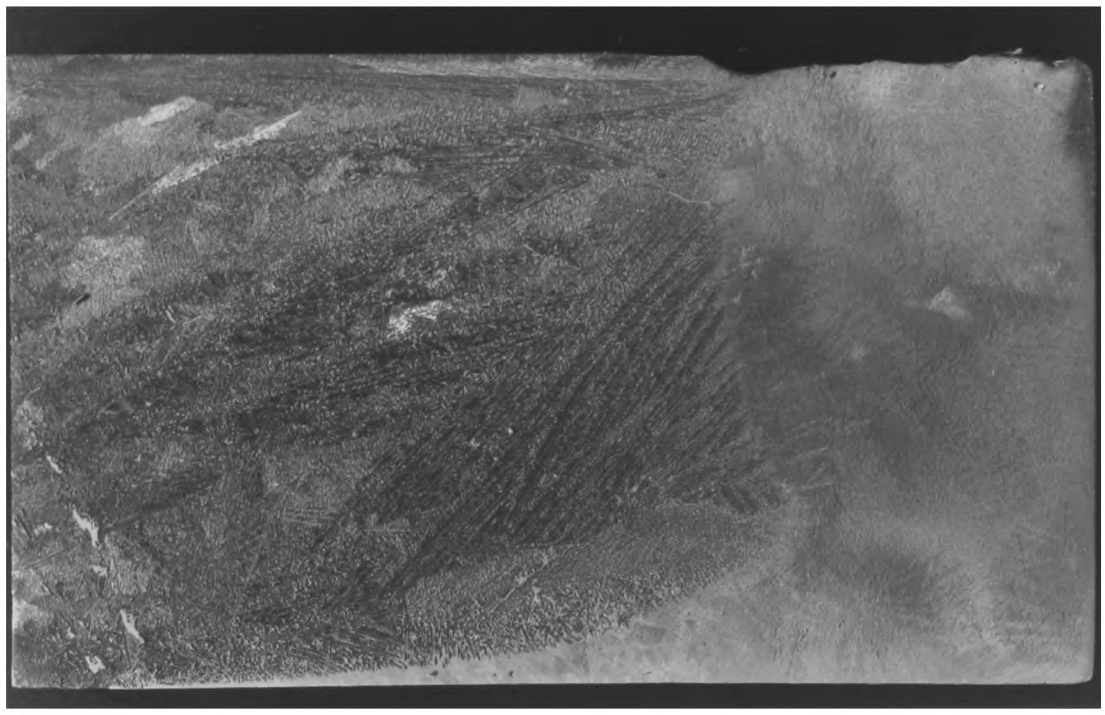


Fig. 6.22 (a).
Ingot 23
Growth time 17m 51s

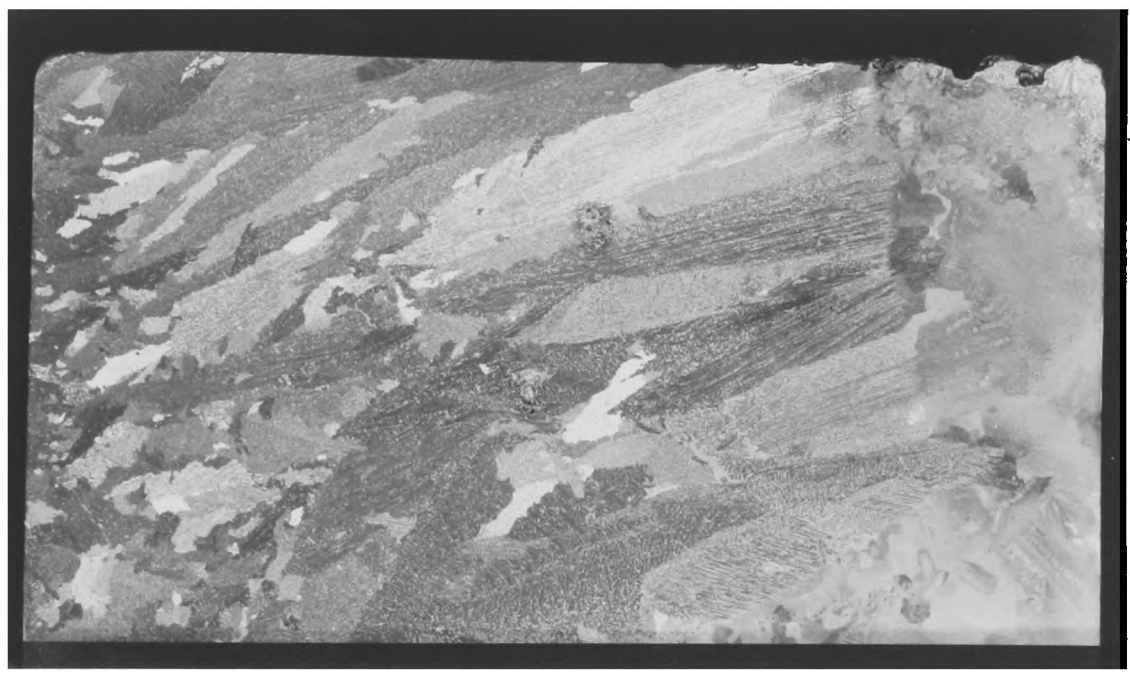


Fig. 6.22 (b).
Ingot 15.
Growth time 21m 42s.



Fig 6.22 (c).
Ingot 16
Growth time 21m 54s



Fig. 6.23 (a).
Ingot 20
Growth time 29m 35s.



Fig. 6.23 (b).
Ingot 13
Growth time 45m 38s

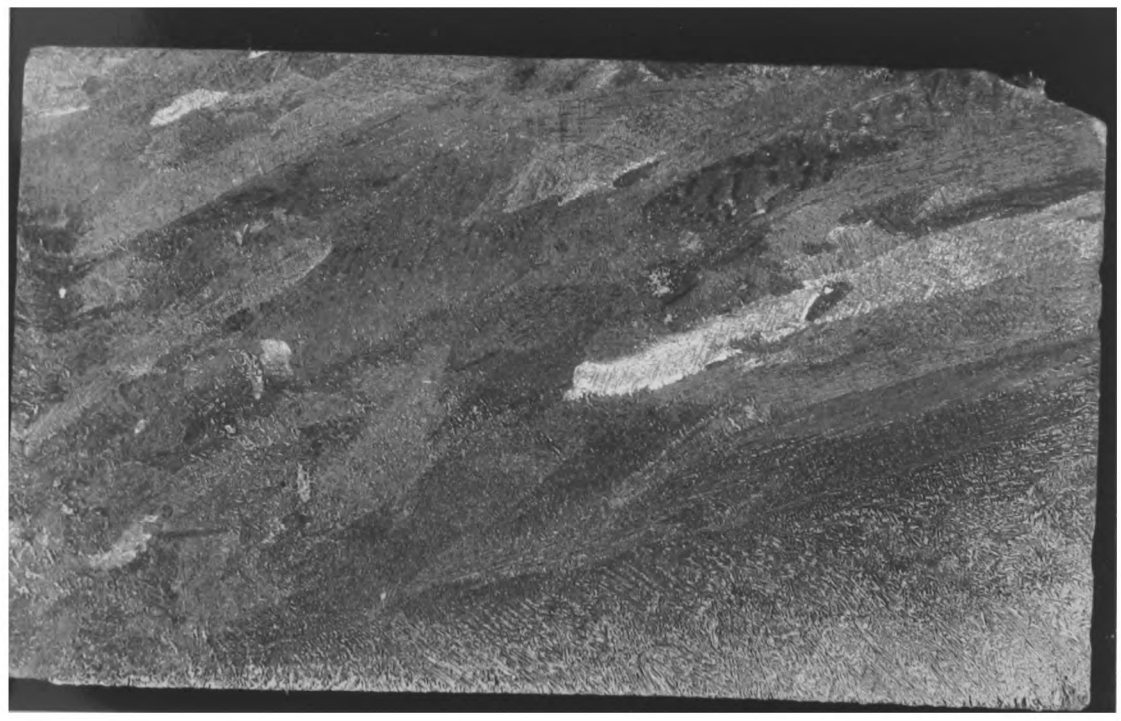


Fig 6.23 (c).
Ingot 22
Growth time 73m 54s

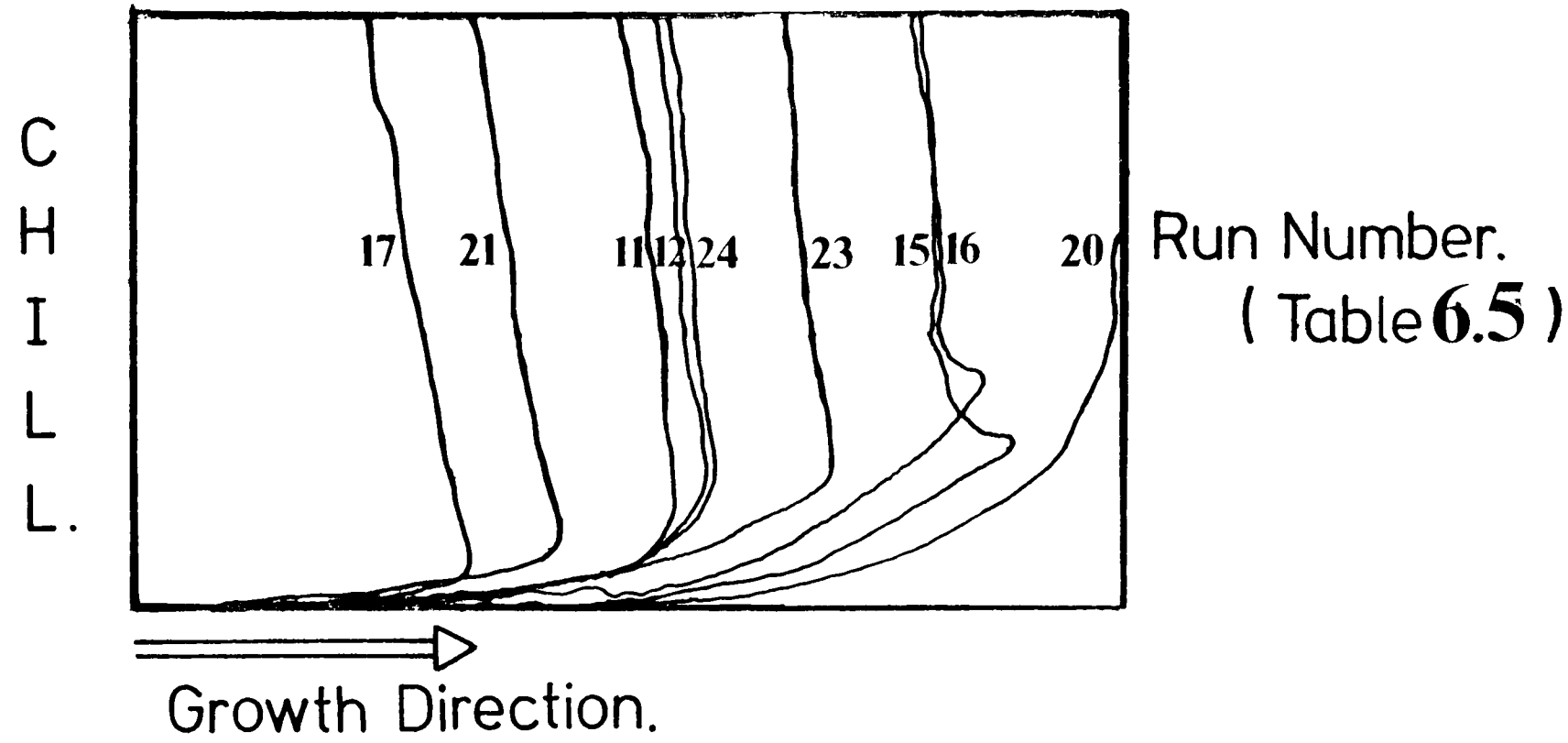


Fig. 6.24. Progress of macroscopic dendrite tip interface across the length of the inget mould as determined from the quenched ingots

layer along the bottom of the mould because it was rich in Pb and so denser than the bulk liquid. It would then have tended to retard solidification at the bottom of ingots because of its lower liquidus temperature and so would have caused the observed cut-back in the macroscopic dendrite tip interface. This cut-back became more pronounced with time of growth because of the continued operation of the gravity flow mechanism in the mushy zone, which would have lead to progressively larger build-up of Pb at the bottom of the ingots with time. Quantitative evidence of this solute build-up is presented in the next section.

The macroscopic reproducibility of the apparatus may be demonstrated by comparing the quenched interface positions of ingots 11, 12, and 24, fig. 6.21(a) (b), and (c) respectively. These ingots were quenched after similar times of growth (see Table 6.7) and the interface position and shape show good reproducibility between them, once allowance has been made for the slight difference in growth times. Good reproducibility may also be observed between the macroscopic interface shape and position in ingots 15 and 16, fig. 6.22(b) and (c), which were allowed to grow for similar periods of time (Table 6.7). It should be noted, however, that the positions of the solute-enriched channel segregates observed in the quenched mushy zone of these ingots were not reproducible. This is both understandable and, unfortunately, inevitable because the position of these channels will be determined by the microstructure within the mushy zone of each of the ingots, and this is a factor which cannot be made reproducible. The effect of this on the composition measurements is discussed in the next section.

The distance to which the dendrite tip front had advanced from the chill in each of the quenched ingots is given in Table 6.9 overleaf. In view of the slope of the interface towards the top of the ingots the distance was measured at a standard height of 30 mm. from the ingot base. Also listed in the Table are the growth time and the calculated interface velocity.

Table 6.9

INGOT NO.	17	21	11	12	24	23	15	16	Errors
$t_G = t_Q - t_N$. secs.	438 s.	580 s.	818 s.	838 s.	853 s.	1071 s.	1302 s.	1314 s.	±8 s.
Av. distance of quenched interface from chill at a height of 30 mm.	3·15 cm.	4.20 cm.	5.80 cm.	6.00 cm	6.10 cm	7·40 cm.	8·65 cm	8·75 cm	±0.15 cm.
Av. growth velocity. cm/sec.	7.19×10^{-3} (6.73 → 7·67)	7.24×10^{-3}	7.09×10^{-3}	7.16×10^{-3}	7.15×10^{-3}	6.90×10^{-3}	6.64×10^{-3}	6.66×10^{-3} (6·51 → 6·31)	

The velocity data calculated from the quenched interface positions and given in Table 6.9 are in very good agreement with the velocities measured from the sample thermocouple traces — given in Table 6.8. They confirm that the interface velocity begins to fall after approximately 60 mm. of growth.

6.5.2.3 Composition Measurements C vs. position

The composition values obtained from specimens taken from the standard sampling positions in this series of ingots are given in figs. 6.25 to 6.28. The progress of macrosegregation within the ingots may be assessed by following these composition vs. position plots through from fig. 6.25(a) (ingot 14, no growth) to fig. 6.28(c) (ingot 22, full growth). The shape and position of the quenched dendrite tip interface is shown superimposed on the composition data for each ingot.

Analysis of samples from the no growth ingot, fig. 6.25(a), shows that there was no appreciable macrosegregation present in the ingot prior to growth. Only one value lay outside the analytical error range of the nominal ingot composition (5.00 ± 0.07 wt %Pb). This low value at position 3F (fig. 6.9) was probably a result of the quenching process. It could have arisen either through insufficient liquid feeding of this region during the rapid solidification which followed from quenching, or by an inverse segregation type of mechanism with liquid from the reservoir in the top mould insert flowing through this region to

Figs. 6.25 to 6.28. Composition values of swarf specimens taken from ingots in the standard sampling positions. Figures are given in wt % Pb, to an accuracy of ± 1·3 % of the figure (i.e 4.00 ± 0.05 wt % Pb.).

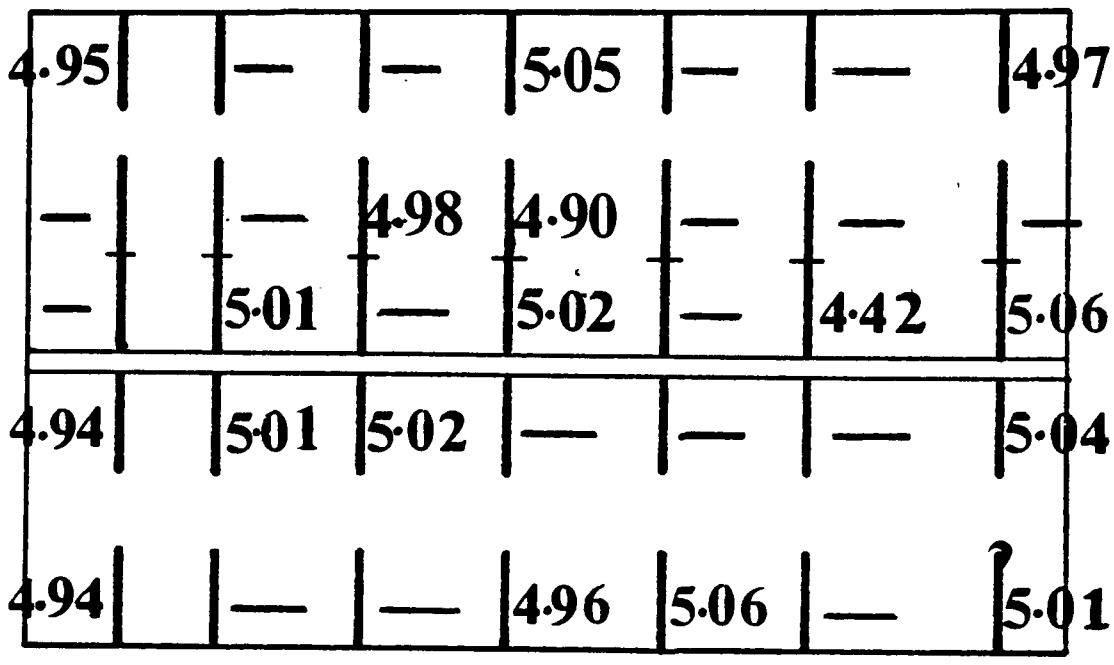


Fig. 6.25 (a). INGOT 14 No growth.

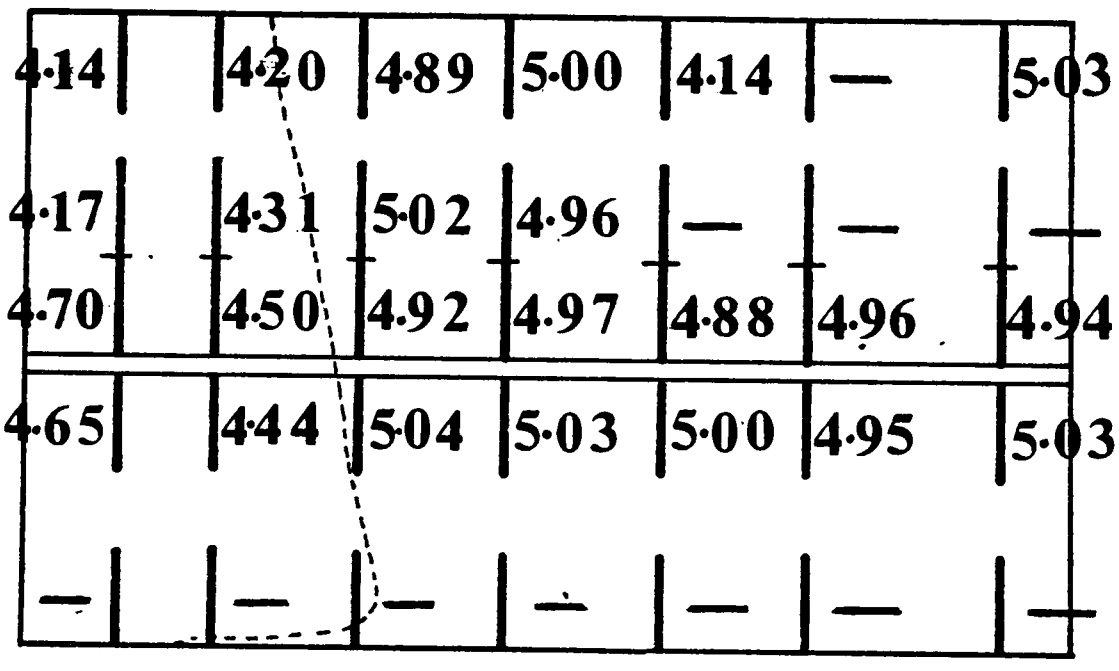


Fig. 6.25 (b). INGOT 17 Growth time, $t_Q - t_N$ = 7m 18s

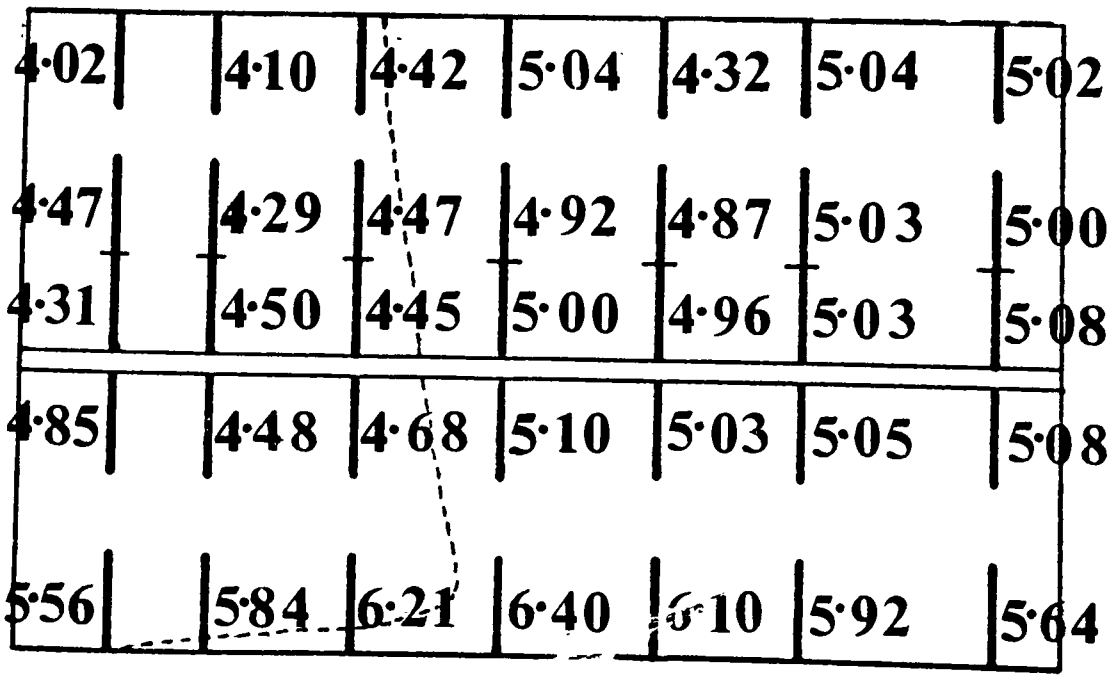


Fig. 6.25 (c). INGOT 21 Growth time, $t_Q - t_N$ = 9m 40s.

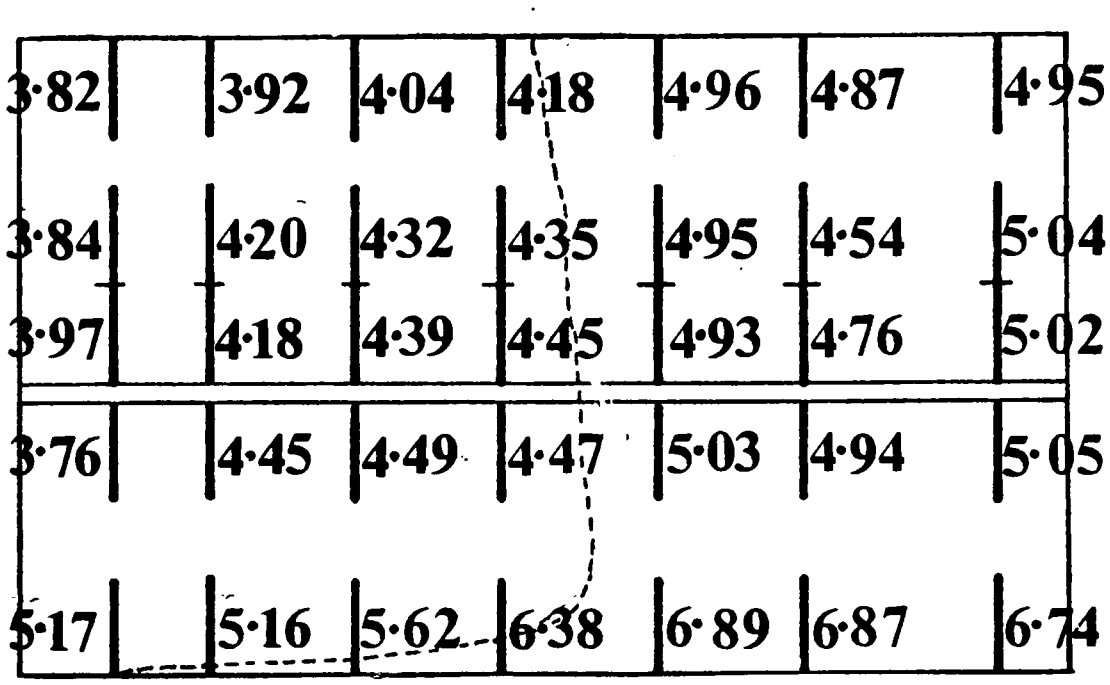


Fig 6.26(a). INGOT 11 Growth time, $t_Q - t_N$ = 13m 38s.

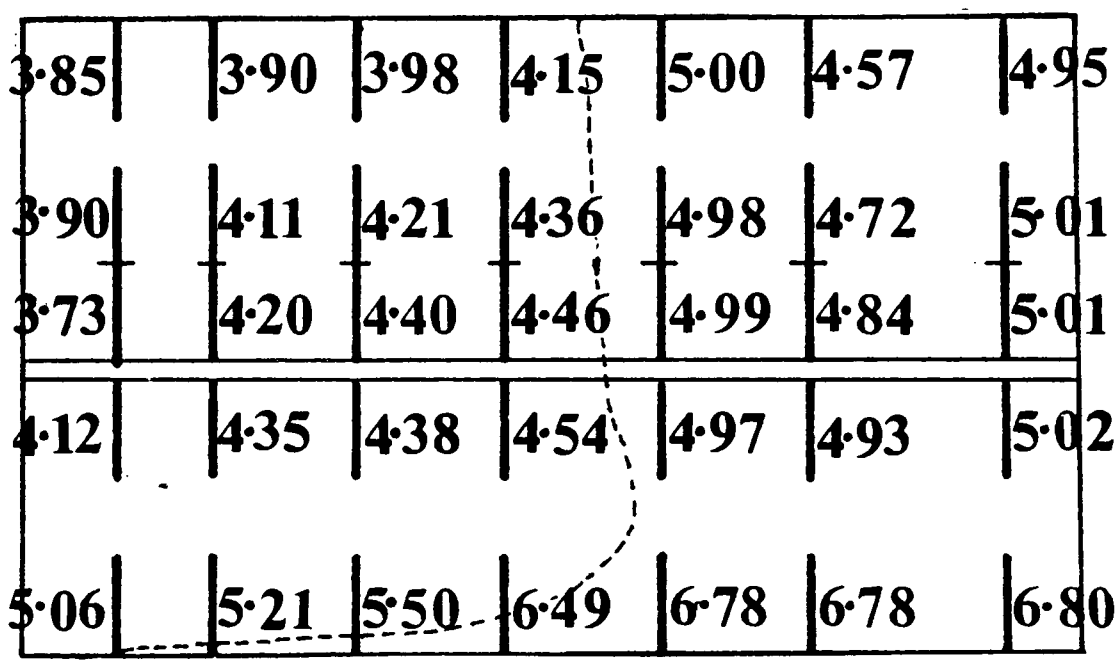


Fig. 6.26(b). INGOT 12 Growth time, $t_Q - t_N$ = 13m 58s

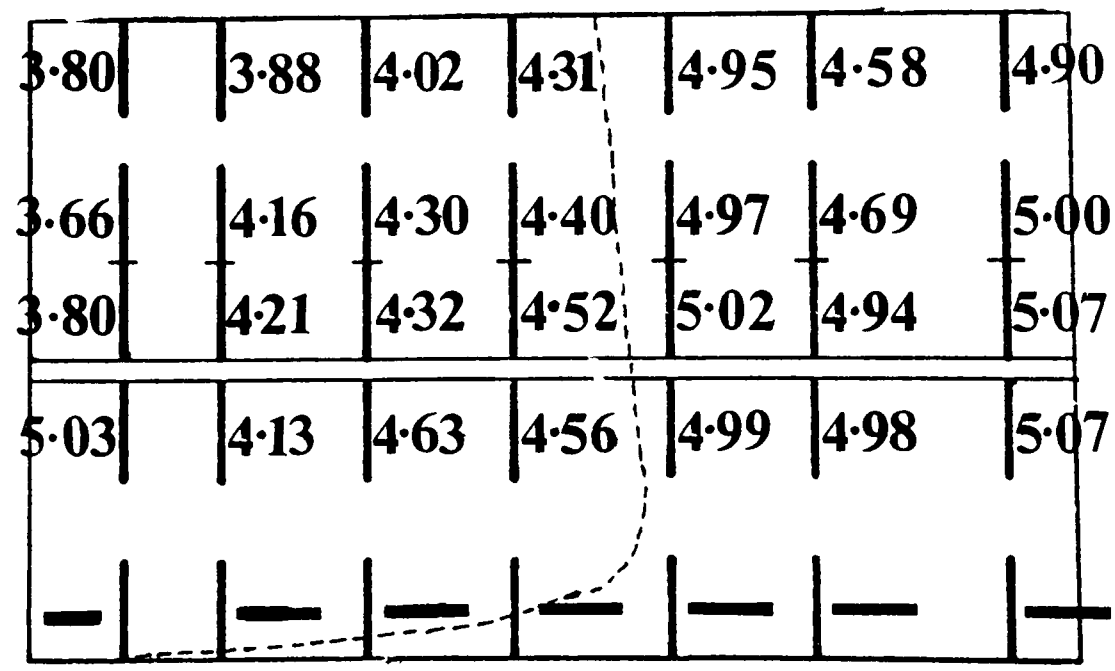


Fig. 6.26(c). INGOT 24 Growth time, $t_Q - t_N$ = 14m 13s.

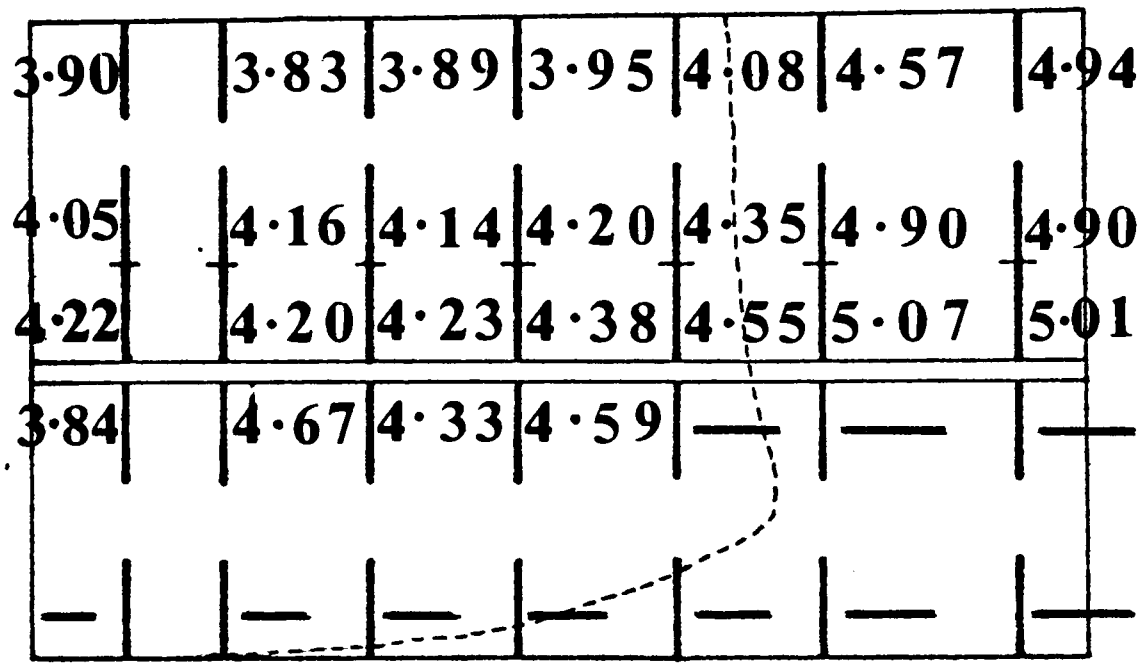


Fig. 6.27(a). INGOT 23 Growth time, $t_Q - t_N$ = 17m51s

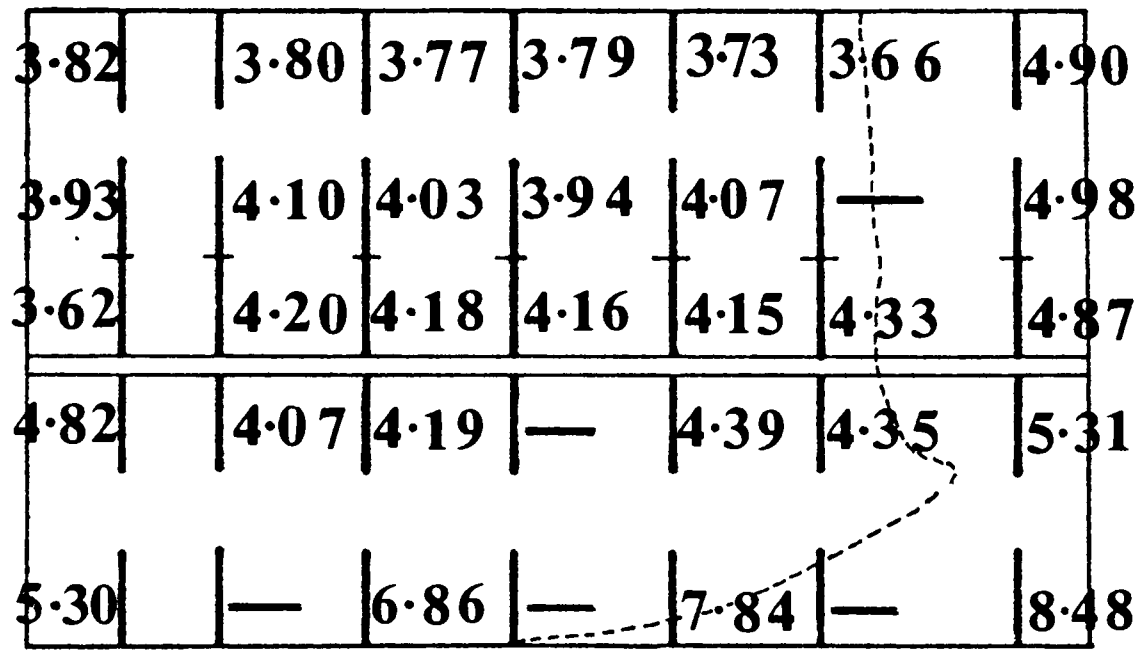


Fig. 6.27(b). INGOT 15 Growth time, $t_Q - t_N$ = 21m42s

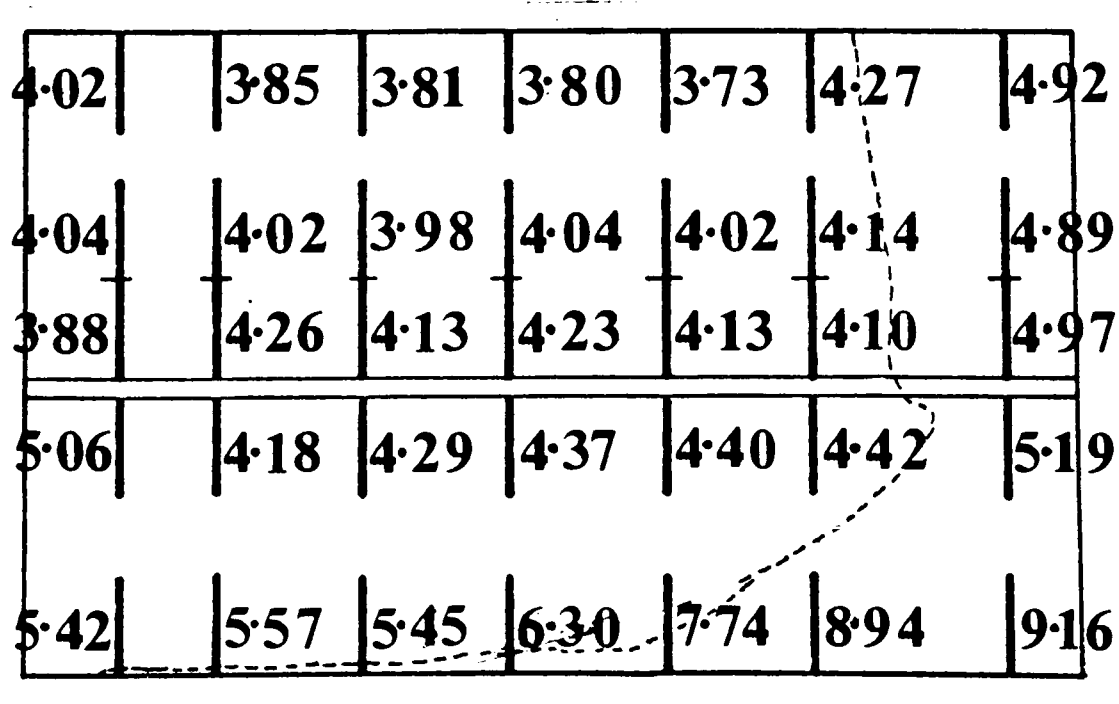


Fig. 6.27(c). INGOT 16 Growth time, $t_Q - t_N$ = 21m54s.

4·11	3·91	3·84	3·81	3·75	3·90	4·33
4·26	4·14	4·11	3·97	4·00	4·16	4·44
4·09	4·45	4·20	4·18	4·18	4·33	4·56
3·90	4·44	4·70	4·43	4·54	4·68	6·22
5·39	5·40	5·44	6·25	7·93	9·70	11·21

Fig. 6.28(a). INGOT 20 Growth time, $t_Q - t_N$ = 29m 35s

—	—	—	—	—	—	—
4·10	4·10	4·05	4·02	3·98	—	—
4·70	4·34	4·20	—	4·21	4·29	4·74
4·59	4·39	4·42	4·25	—	—	—
—	—	—	—	—	—	—

Fig. 6.28(b). INGOT 13 Growth time, $t_Q - t_N$ = 45m. 38s.

4·07	3·91	3·81	3·72	3·77	3·90	4·77
4·19	4·09	4·04	4·05	4·10	4·20	—
3·75	4·80	4·19	4·17	4·22	4·20	—
3·90	4·45	—	—	4·40	4·60	6·52
6·06	6·04	7·85	7·37	8·49	9·81	12·05

Fig. 6.28(c). INGOT 22 Growth time, $t_Q - t_N$ = 73m. 54s.

feed other parts of the casting.[71] There was no evidence of any solute-depleted layer at the top surface of the ingot as observed by Hebditch[103] in his no-growth model castings.

In the remaining ingots grown unidirectionally for different periods of time the vertical nature of the macrosegregation produced during this growth can clearly be seen. In ingot 11, fig. 6.26(a), for example, the majority of the mushy zone was negatively segregated with the largest negative segregations (>20% of nominal composition) being towards the top surface of the ingot. Some positions of positive segregation were determined at the bottom of the mushy zone but these were undoubtably associated with the layer of highly solute-enriched liquid which was gradually built up at the bottom of ingots during the growth process. This layer would have itself been responsible for the observed interface cut-back at the bottom of the ingots. The layer of solute-enrichment is very localised at the bottom of the bulk liquid pool, the majority of the pool remaining at the nominal solute composition of the melt. This is understandable since the apparatus was designed so that temperature gradients in the bulk liquid pool would be small and hence convection currents sluggish. Furthermore, the positively segregated bottom layer, being enriched in lead, would have been denser than the remainder of the liquid in the pool, and it formed a gravity stable layer.

The final solute distribution observed in the fully grown ingot, fig. 6.28(c), shows the majority of the ingot to be negatively segregated. The corresponding zone of solute enrichment lies along the bottom surface of the ingot up to a height of probably less than 10 mm. from the bottom, except at the end of the ingot furthest from the chill where the positive segregation reaches up to approximately 30 mm. from the bottom surface. The magnitude of the positive segregation reaches an enormous value of 12.05 wt % Pb (approximately 140% greater than the nominal composition) at the bottom corner of the ingot furthest from the chill.

The reproducibility of the model casting system in terms of the segregation patterns produced may be assessed by comparing the composition data

obtained from ingots 11, 12, and 24, fig. 6.26(a), (b), and (c) respectively. It may be seen that at the majority of the sampling positions in the top portions of the three ingots (rows 1, 2, and3) the composition values are remarkably consistent. In fact out of the 21 sampling positions in the top three rows it is only in 6 positions that the composition values of the three ingots lie outside the analytical error range of each other ($\pm$1.3% of average composition of position). Furthermore, 3 of these positions lay in the bulk liquid region in column F where quenching effects were probably predominant in causing non-reproducibility. Of the remaining 3 positions,two were in column A (position 3A ingot 11 too high, position 2A ingot 24 too low), and one was in column D (position 1D ingot 24 too high). The agreement between composition values in the bottom two rows of the three ingots is less convincing, particularly within the quenched mushy zone. This must be due to the instability of the fluid flow in these regions which leads to non-reproducible channel formation. These solute-enriched channels may intersect a sampling position in one ingot and not another, depending on the developing mushy zone microstructure in the ingots. This explanation probably also accounts for the discrepancies in composition values observed at positions 2A and 3A in these ingots, since channel-type segregates could be seen in the ingot macrostructures around these positions close to the chill face.

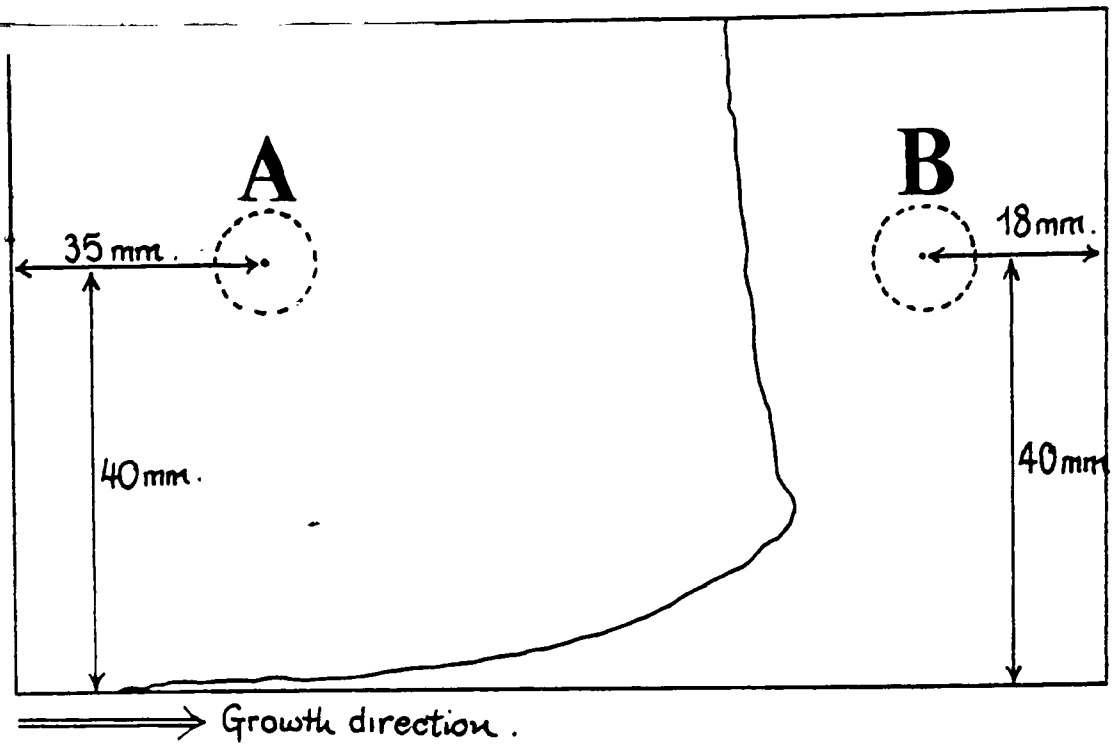
Ingots 15 and 16 were also quenched after similar times of growth and the composition data obtained from them shows the same generally good reproducibility as did those from ingots 11, 12, and 24. It may be seen, from figs. 6.27 (b) and (c), that,of the 21 sampling positions in the top three rows,again only 6 of them showed appreciable differences in composition between the two ingots. These six positions were made up the three in column A (caused by non- reproducibility of channels) and the three in column F. These positions in column F were in the mushy zone just behind the dendrite tip interface where composition was changing rapidly with position. Small variations in interface position might therefore have been responsible for these discrepancies. They might also have been caused by spurious quenching effects

at this position connected with liquid feeding from the metal reservoir in the top mould insert. It should be noted that there are spuriously low values of composition at these positions in the bulk liquid pools of ingots 17 to 23, figs. 6.25(b) to 6.27(a) inclusive. It seems very unlikely that such localised regions of solute depletion could actually have existed in the bulk liquid pools during growth, and it would seem likely that they were caused by the same quenching mechanisms as those proposed to explain the low composition value observed at position 3F in ingot 14 (no growth).

The variation of composition through the thickness of the ingot slice was investigated to determine whether the depth of the skim of metal removed from the side of the ingot prior to macroetching had any effect on the composition values subsequently determined. This was done using a 10 mm. diameter end-miller. Samples were taken at 1 mm. intervals through the thickness of ingot 23 in two positions, as shown in fig. 6.29. No significant variation of composition with thickness was observed in the samples milled from the quenched mushy zone position, and only a slight amount of inverse segregation at the edge of the ingot was detected from samples taken from the quenched bulk liquid position. The depth of the skim was therefore not critical, although it was maintained at around 2 mm. for all the ingots in the series.

6.5.2.4 Composition measurements c vs. time

The main aim of this experiment was to grow a series of ingots under reproducible growth conditions so that the variation of composition at fixed positions within a 'standard' ingot could be examined. It has been shown by the various results presented in the previous three sections that this aim of growth reproducibility was essentially attained. Observations concerning the variation of composition at a given position in an ingot grown under the conditions employed in this experiment may therefore correctly be made by simply comparing the composition vs. position plots obtained from the various ingots and given in figs. 6.25 to 6.28.



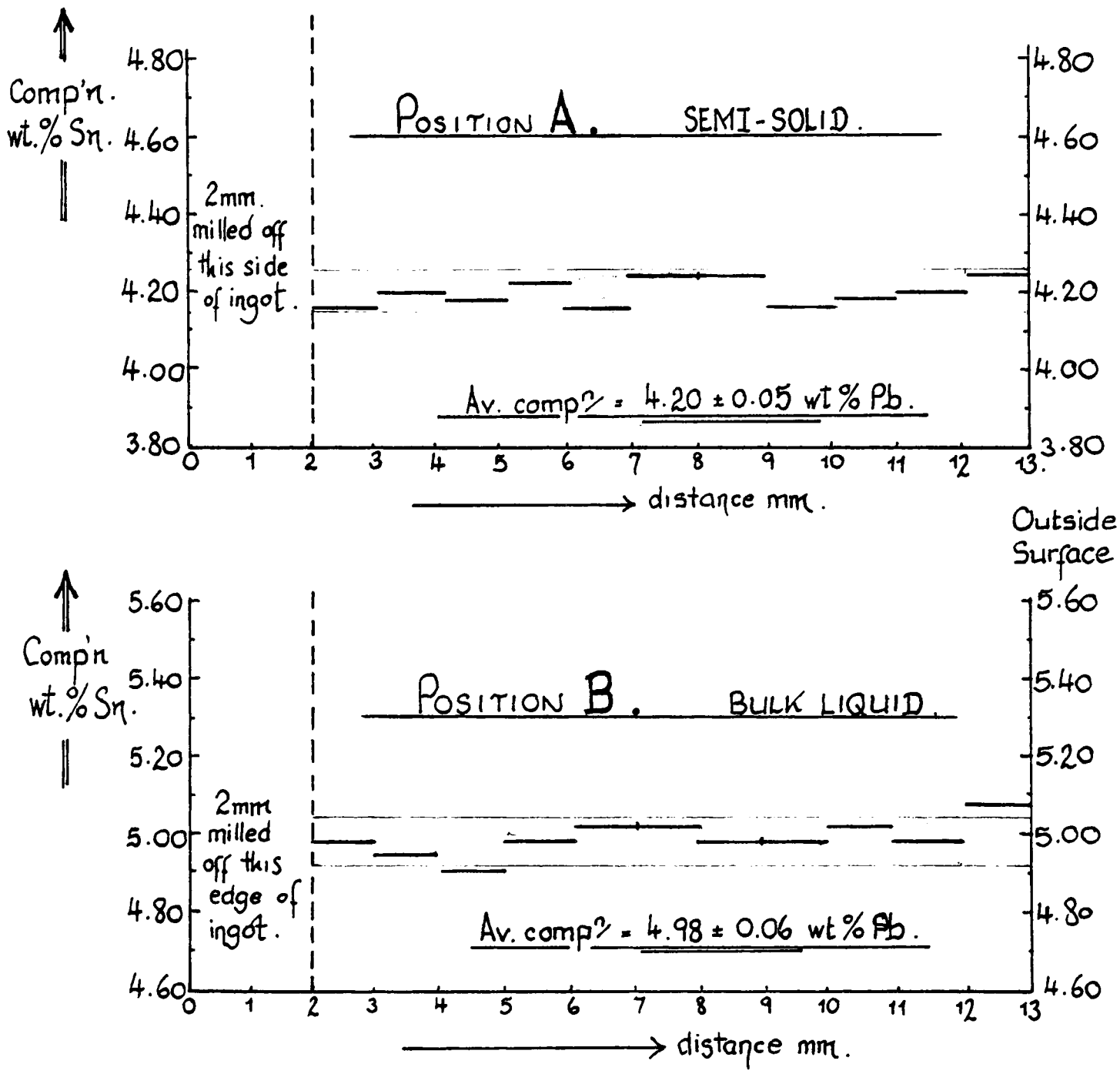


Fig. 6.29. Variation in composition at various distances through the thickness of the slice cast ingot number 23 at positions A and B ; semi-solid region and bulk liquid region respectively.

A comparison of the figures shows that there is a large fall in the composition of a given volume element in the period just after the dendrite tip interface moves through it (see, for example, positions in column C in ingots 17 and 21, fig. 6.25(b) and (c)). This rapid fall in composition across the interface occurs even for positions near to the bottom of the ingot where the trend is generally one of solute enrichment. After this rapid fall there follows a more gradual decrease in composition with time at the majority of the positions within the mushy zone of the ingot.

A more quantitative picture of composition variation with time may be obtained from figs. 6.30 to 6.32. These figures show the composition versus time plots obtained at the standard sampling positions in the top three rows. The dotted lines on the curves indicate the times at which the dendrite tip interface passed each of the positions. These times were calculated from the growth velocity data obtained from the sample thermocouple traces (Table 6.8) and from the quenched interface positions (Table 6.9). The calculations are outlined in Table 6.10., below:-

Table 6.10

Distance from chill of standard sampling positions x cm.	Av. growth velocity to position x. $\bar{V} \times 10^3$ cm/sec	Time taken for interface to advance from chill to standard position t secs.
0.9 → 1.0	7.14 (± 0.35)	133 (± 6)
1.9 → 2.0	7.14 (± 0.35)	273 (± 13)
3.4 → 3.5	7.20 (± 0.20)	479 (± 13)
4.9 → 5.0	7.20 (± 0.20)	688 (± 19)
6.5 → 6.6	7.03 (± 0.15)	932 (± 20)
8.0 → 8.1	6.78 (± 0.10)	1187 (± 23)
10.0 → 10.1	6.26 (± 0.10)	1605 (± 25)

These times apply strictly only to positions in row 3, since these are at the same height in the ingots as the sample thermocouple beads. The times used for interface intersection with positions in rows 1 and 2 have therefore been

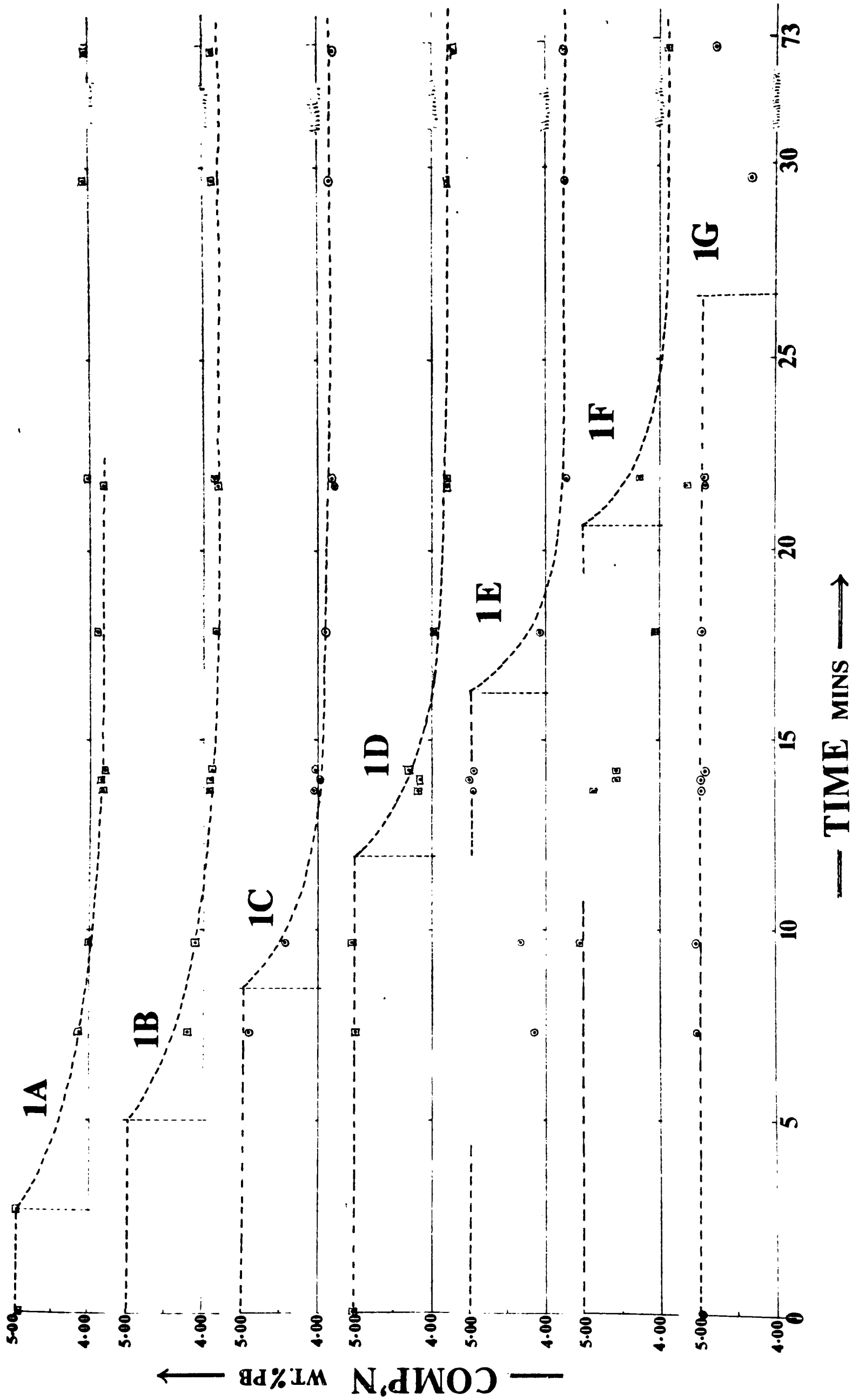


Fig.6.30. Compn vs time of growth plots for each of the standard positions in Row 1.

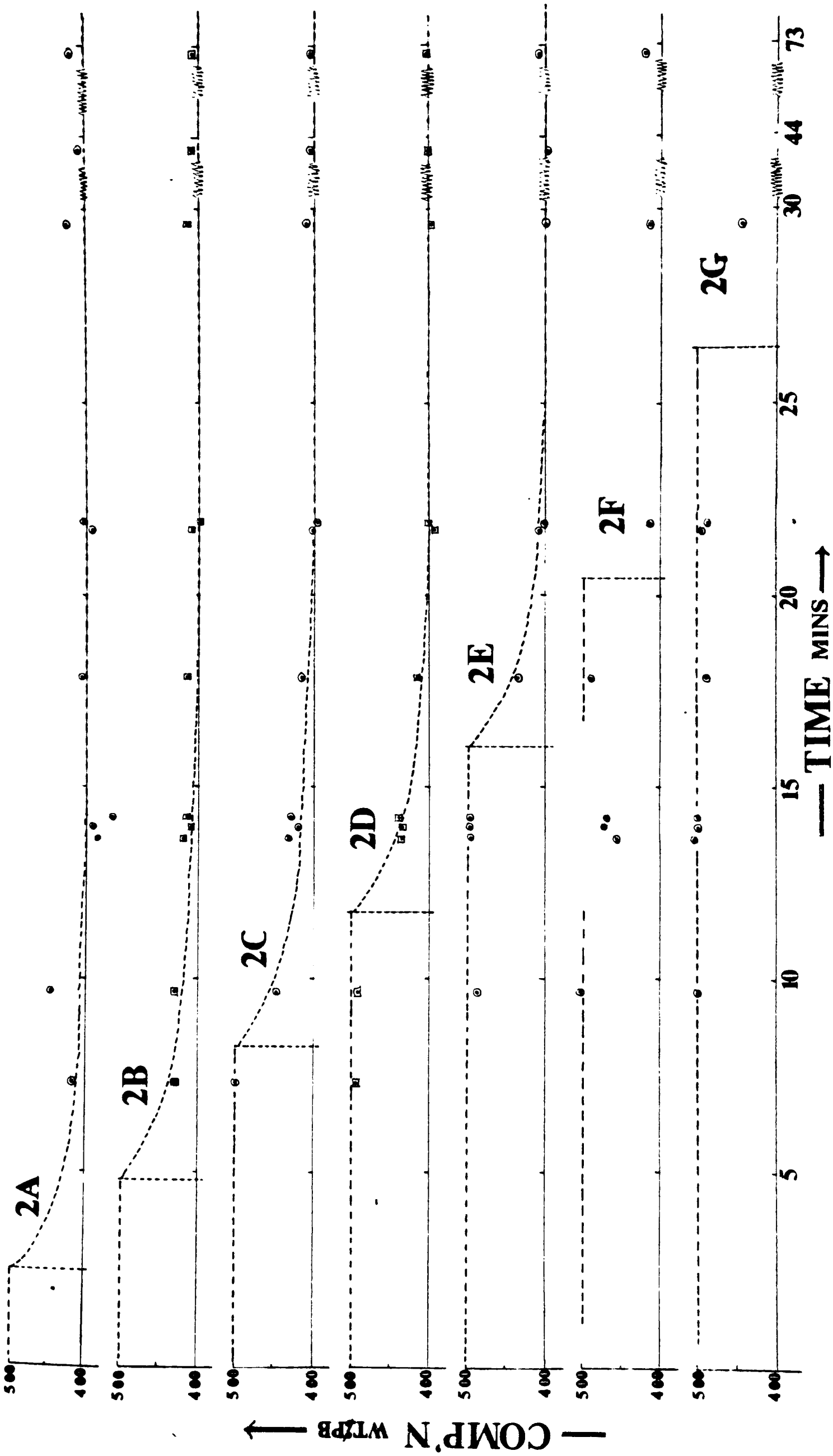
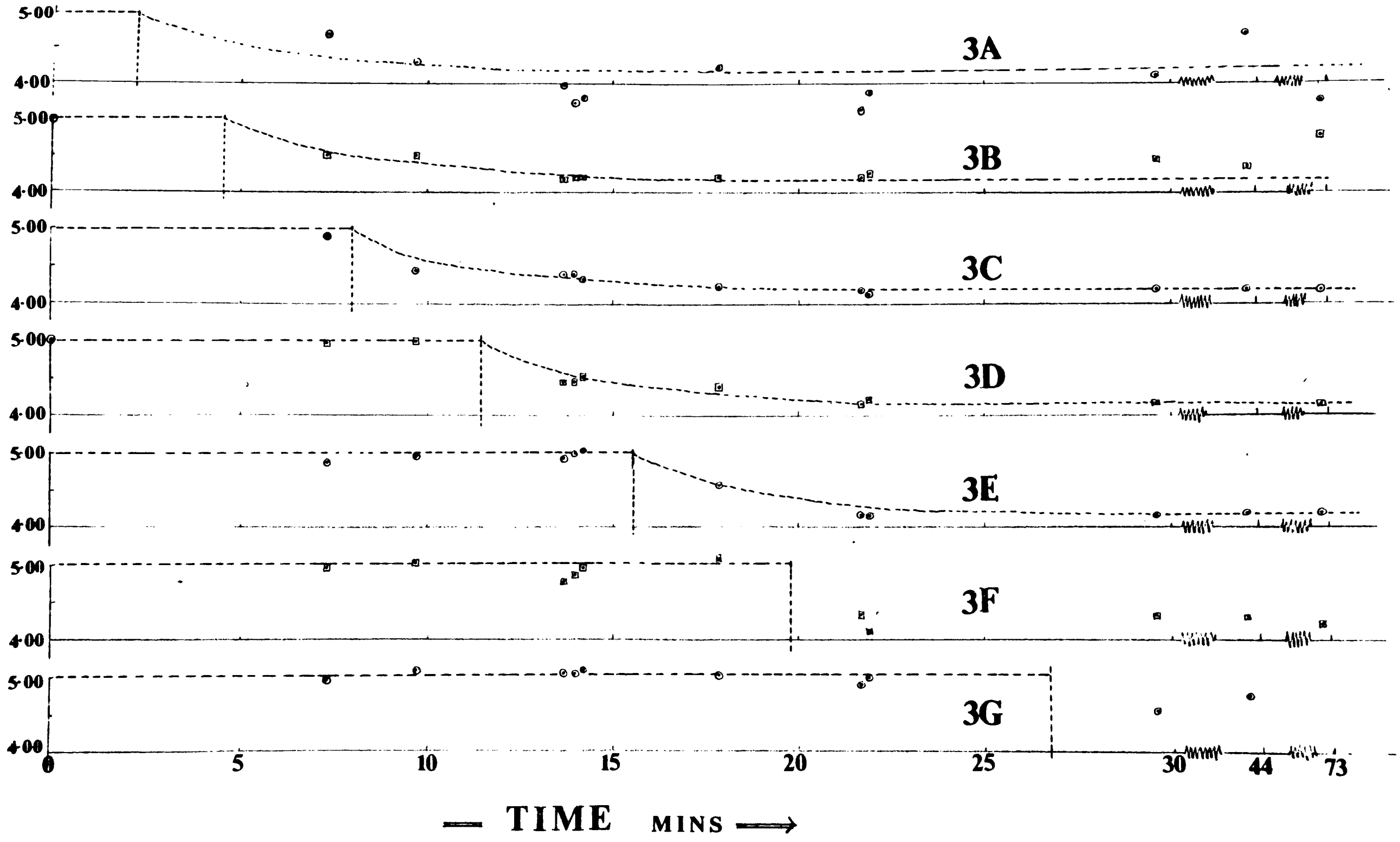


Fig.6.31. Comp'n vs time of growth plots for each of the standard positions in Row 2

Fig. 6.32. Compn vs time of growth plots for each of the standard positions in Row 3



6.32

corrected slightly to allow for the small slope-back in interface position towards the top of the ingots.

The important features of the composition versus time curves shown in figs. 6.30 to 6.32 are as follows:-

1. At every position the composition fell rapidly in the first 2 minutes after the dendrite tip front had passed. The magnitude of this fall was, at most positions, approximately 10% of the nominal composition value.

2. Following this initial sharp fall there was a more gradual decrease in composition over a further time period of 7 to 8 minutes (i.e. approximately 9 to 10 minutes after the front had passed). The magnitude of this further decrease varied from 15% of the nominal composition for certain position in row 1 to 8% of the nominal composition for most positions in row 3.

3. After approximately 10 minutes from the dendrite tip interface passing a position there was no further appreciable change in the composition value.

4. The composition data determined at position 3A, and to a lesser extent 2A, exhibit inconsistencies. The composition seems to have risen and fallen with time. This type of behaviour was also found to occur at the majority of positions in rows 4 and 5. As explained previously it is thought that this is due to the non-reproducibility of channel formation within the ingots. Channels were definitely visible in the macrostructure of certain ingots in the region of positions 2A and 3A.

It may be concluded from the curves that gravitational interdendritic fluid flow in these ingots not only produced macrosegregation very rapidly in the region just behind the dendrite tips but it also continued to cause appreciable amounts of macrosegregation at quite large distances into the semi-solid zone. If the average interface velocity is taken to be 7.15×10^{-2} mm/sec. then the time periods of 2 minutes and 10 minutes mentioned in points 1 and 3 above correspond to distances of 8.6 mm. and 43.0 mm. behind the dendrite tip interface

In order that this experiment should not fall into the same traps as those described in chapter 5 it is necessary to relate these times and distances to liquid volume fraction within the semi-solid zone. Consider the standard

position 2C. Figure 6.33 shows the variation of several parameters with time at this position in these ingots. Figure 6.33(a) shows again the experimentally determined variation in the average composition ($\bar{c}$) at the position with time. Figure 6.33(b) gives the temperature variation at the position with time of growth, calculated from the known temperature gradients in the ingots (see figure 6.19). Figure 6.33(c) shows the interdendritic liquid composition (C_L) variation with time calculated using the T vs. t data, shown in figure 6.33(b), together with the liquidus slope of the Sn-Pb equilibrium phase diagram (m_L = -1.29 ^{o}C/wt % Pb). Finally figure 6.33(d) gives the variation of the volume fraction liquid (g_L) at the position with time. Two curves are shown for this. Curve 1 was drawn by substituting the C_L values from figure 6.33(c) into the Scheil equation:-

$$g_L = \left(\frac{C_o}{C_L}\right)^{1/1-k_o}$$

where C_o = nominal composition = 5 wt % Pb

k_o = equilibrium distribution coefficient = 0.07

therefore:-

$$g_L = (5/C_L)^{1.07}$$

Curve 1 gives an over-estimate of g_L at all times because the Scheil equation does not allow for any fluid flow (and hence macrosegregation). In these ingots at this position fluid flow has caused negative segregation by a decrease in g_L.

Curve 2 was drawn by substituting the values of $\bar{c}$ and C_L from figures 6.33(a) and 6.33(c) into the equation:-

$$\bar{D}\,\bar{C} = \bar{D}_s\bar{C}_s(1-g_L) + D_LC_Lg_L$$

which conserves solute mass within the volume element. The average solid composition, $\bar{C}_s$, was taken as 0.5 wt % Pb and the average densities of the various phases were assumed to be equal $\bar{D} = \bar{D}_s = D_L$.

It may be seen from the curves in figure 6.33(d) that to a rough approximation the time values of 2 minutes and 10 minutes after the dendrite tip interface passed the position correspond to volume fractions liquid of 0.65 and

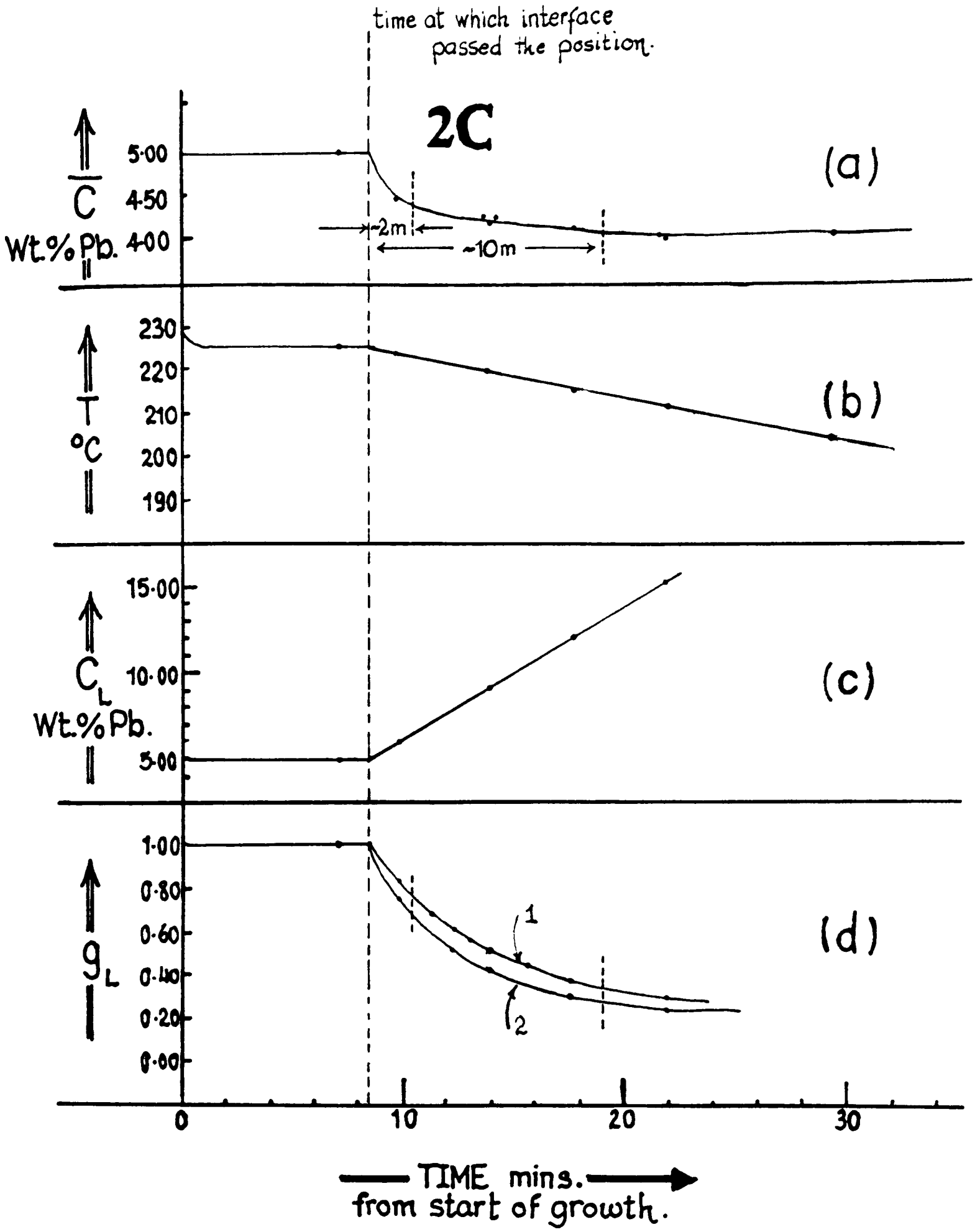


Fig.6.33. Curves showing the variation of several parameters with time of growth, at the standard position 2C.

(a) average composition, $\bar{C}$, (measured).

(b) temperature, T, (measured).

(c) average liquid composition, $\bar{C}_L$, (calculated).

(d) liquid volume fraction, g_L, (calculated).

0.30 respectively. It may therefore be concluded that interdendritic gravitational fluid flow was producing appreciable amounts of macrosegregation up to volume fractions liquid of around 0.30 in these ingots, i.e. deep within the semi-solid zone.

6.5.2.5 Obervation of Channeling

Channel-type macrosegregates were clearly outlined in the macrostructure of most of the ingots. These lay close to the chill face of the ingot and also towards the bottom of the semi-solid zone. Characteristically they sloped downwards and away from the chill face which is in keeping with them having been formed by gravitationally induced convection cycles sweeping down through the mushy zone. Their solute-enrichment was evidenced both by their etching behaviour (relatively unattacked, whereas the solute-poor Sn dendrites were heavily eaten away) and by the occasional high composition measurement obtained from positions in the lower halves of the quenched ingot mushy zones.

The very large channel at the bottom of the semi-solid region of ingot 16 (figure 6.22(c)) was examined in more detail, as shown in figure 6.34. Figure 6.34(a) is simply a higher magnification of the etched macrostructure, while figure 6.34(b) shows the channel after re-polishing and etching in dilute hydrochloric acid to bring out the microstructure. It appears from these photographs that the channel mouth was blocked off by columnar dendrites, althoug this is presumably an illusion caused by the channel moving out of the plane of the section at this position. There are several very important features on these photographs. First, it can clearly be seen that the liquid in the channel has dissolved away portions of the primary dendrite stalks which run across the section. This is very significant in proving that gravitational interdendritic fluid flow has been operating in these ingots. Second, and presumably connected with the first point, there is a large amount of dendritic debris visible both within the channel and at its mouth. Third, the side of the channel nearer to the chill appears to be much smoother and less open than the side further from the chill. This may be accounted for by considering that the liquid in the



Fig. 6.34(a). Magⁿ x 2·7

MACRO-ETCHED

Channels at bottom of semi-solid region in CASTING 16 (see fig 6.22(c). for complete macrostructure)

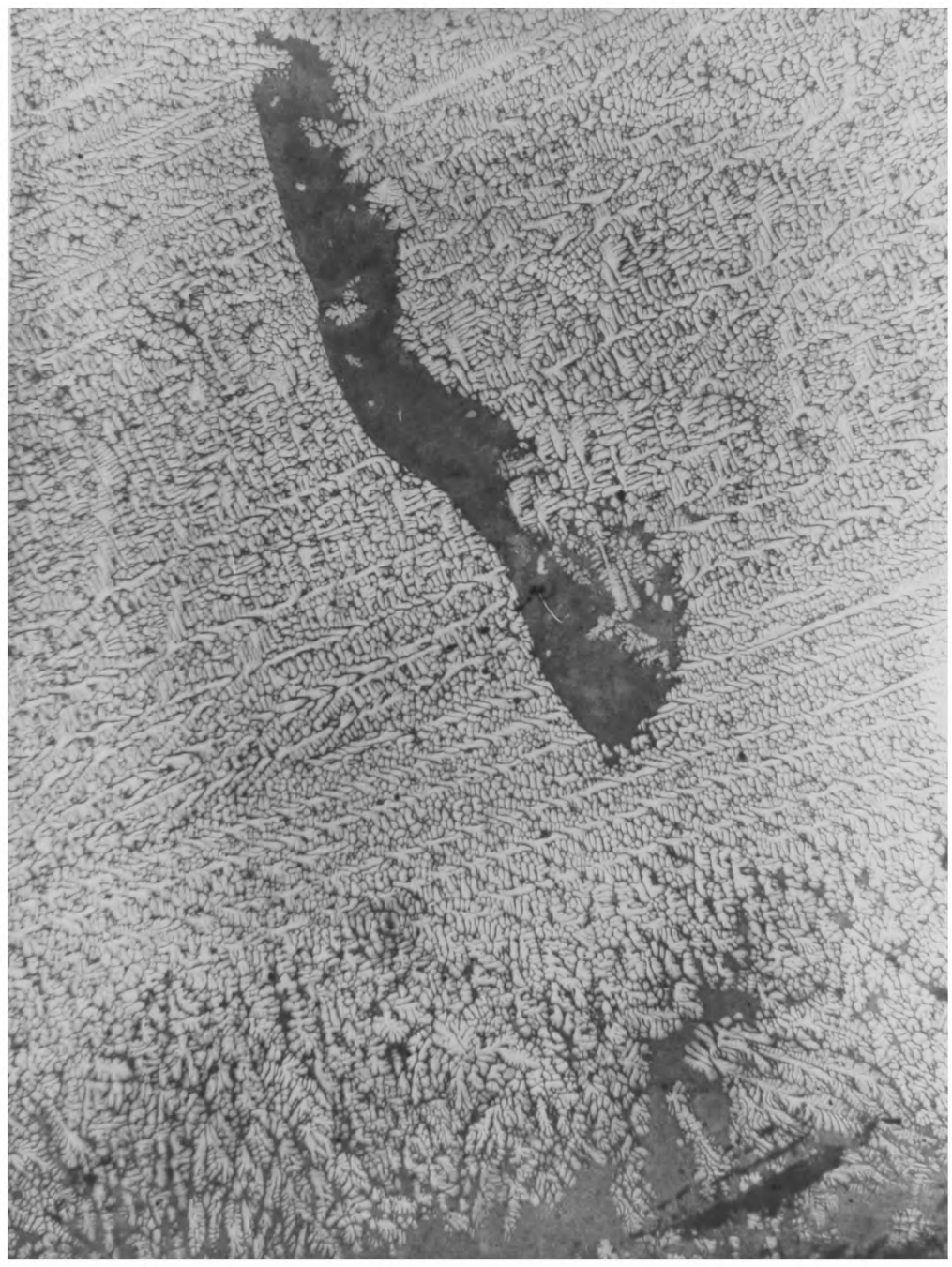
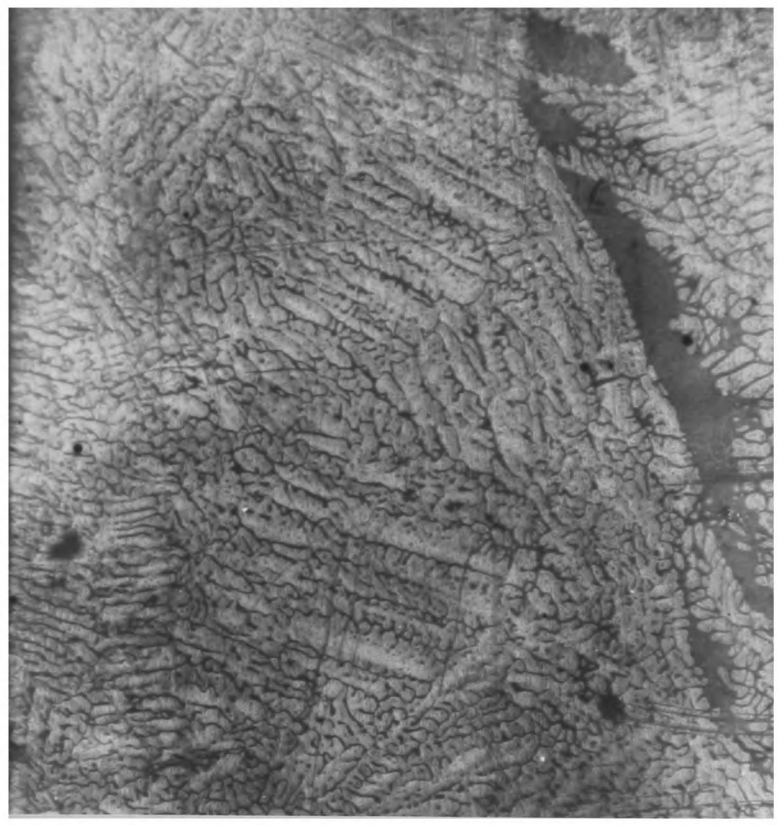


Fig. 6.34(b). Magⁿ x 8

MICRO-ETCHED SECTION

Channel has clearly dissolved away primary columnar dendrite stalks of original semi solid region.

CHILL FACE



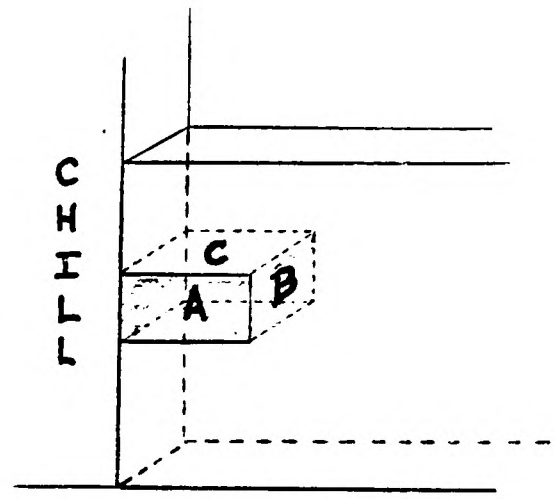


Fig 6.35 (a). Surface A
Ingot 20.

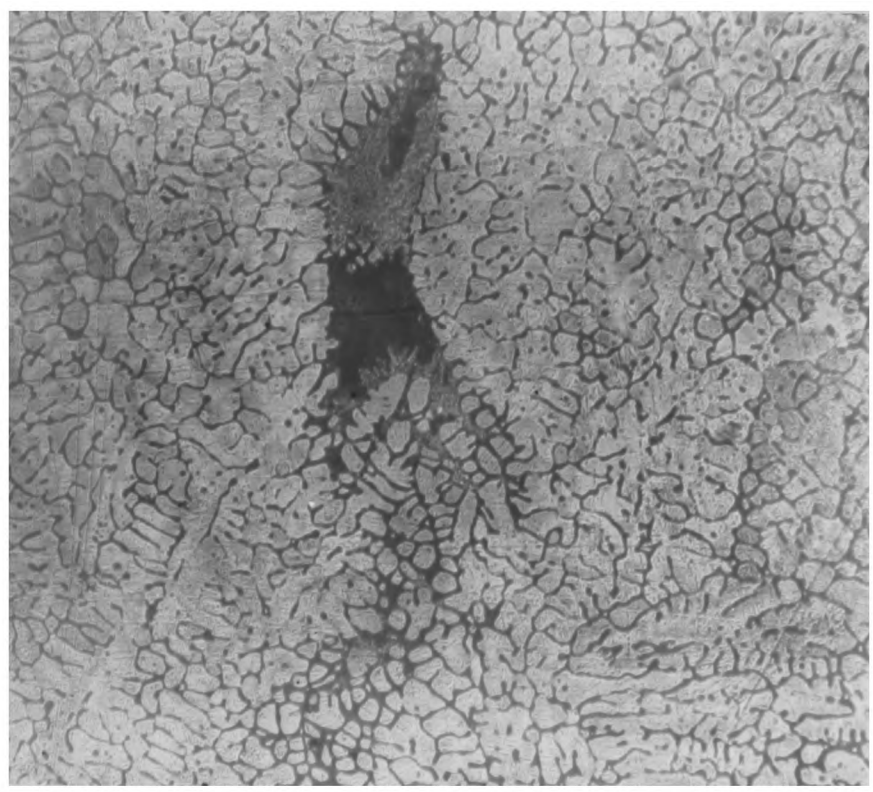


Fig. 6.35 (b). Surface B
Ingot 13

CHILL FACE



Fig. 6.35 (c). Surface C
Ingot 13

Fig. 6.35. Orthogonal sections cut through the channel-type segregates observed near to the chill block in the quenched semi-solid region of ingots 13 and 20. Sections as indicated on diagram.

channel must feed solidification shrinkage in the surrounding areas of the mushy zone. When this flow is towards the chill, as on the chill side of the channel, then the highly solute-enriched liquid in the channel will cause negative segregation by an increase in the volume fraction of solid. The chill side of the channel therefore appears smoother and less open. On the other side of the channel any liquid flow to feed shrinkage occurs up the temperature gradient and so results in positive segregation by dendrite dissolution, thereby causing this side of the channel to appear more open.

Figure 6.35(a), (b), and (c) show orthogonal sections cut through channels near to the chill face in ingots 20 and 13. These micrographs also illustrate that the side of the channel nearest to the chill has a smoother morphology than the side further from the chill. The pipe-like cross-section of the channels is clearly illustrated by figure 6.35(c).

6.6 Summary and Conclusions

The progress of macrosegregation in model castings has been followed using a quenching technique. Ingots of Sn-5wt%Pb were grown under identical conditions and quenched after different lengths of time. Samples were taken from identical positions in each casting for composition analysis. The reproducibility of the method was confirmed (a) by following the sample thermocouple traces in each ingot, and (b) by comparing the macrostructures and solute distributions of three ingots quenched after similar times of growth. The observed macrosegregation was consistent with the operation of the gravitational interdendritic fluid flow mechanism. Channel-type segregates were observed in the majority of the quenched ingots towards the bottom of the mushy zone and near to the chill face.

A picture was built up from the composition analyses performed on individual ingots of the way in the composition at various positions in the ingots varied with time. This showed that the composition at a given position fell rapidly in the first 2 or 3 minutes after the dendrite tip front had passed the position. It also showed that there was a more gradual, yet

significant, fall in composition up to 9 or 10 minutes after the front passed a position. These time values corresponded to distances of 8.5 mm. and 43 mm. into the semi-solid region. The liquid volume fraction values at these positions were calculated to have been approximately 0.65 and 0.30 respectively It must therefore be concluded that macrosegregation caused by the interdendrit gravitational fluid flow mechanism is developed throughout the majority of the semi-solid zone and not solely in the region of high volume fraction liquid behind the dendrite tip front.

CHAPTER 7

OBSERVATION OF INTERDENDRITIC FLUID FLOW USING A RADIOACTIVE TRACER TECHNIQUE

7.1 Introduction

The work presented in this chapter was undertaken in an attempt to corroborate certain of the findings and conclusions made in the previous chapter concerning interdendritic fluid flow. In that experiment flow was studied indirectly by correlating it with the change in macrosegregation with time determined through composition measurements. In this piece of work a radioactive tracer technique was used to provide direct visual evidence of fluid flow occurring deep within the semi-solid region of a casting. This was achieved by inserting radioactive material into the bulk liquid region of solidifying castings and studying the subsequent penetration of activity into the original semi-solid zone.

The work also looked at the way in which the activity of an initially homogeneous radioactive liquid alloy charge becomes redistributed after solidification. Channels of solute enriched materials were observed and the general composition pattern was found to be the same as that in the ingots of Chapter 6.

It was felt necessary to provide corroborationfor the results obtained in Chapter 6 because of the work of Stewart and Weinberg,[61] (described in detail in Chapter 5), which reached very different conclusions about the nature and extent of fluid flow. This experiment is essentially a repeat of their work, with the doubts about the reproducibility of their technique being removed by using the apparatus developed and described in the previous chapter.

7.2 Outline of the Experiment

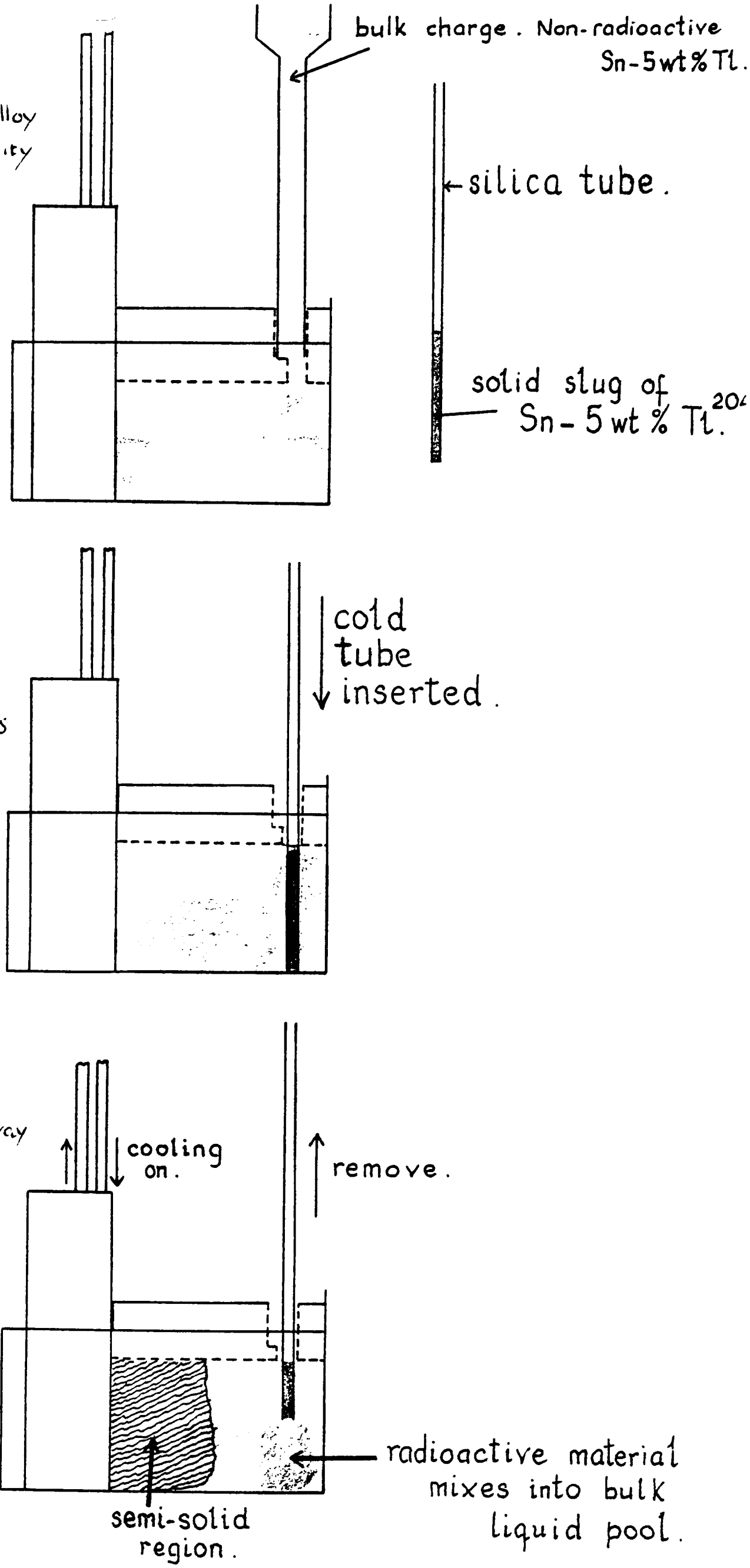
7.2.1 General

The basic technique of the experiment was to grow an alloy charge in

the model casting system in the same manner as described in Chapter 6. During growth, when the dendrite tip front had advanced a known given distance across the length of the mould, radioactive material was introduced into the bulk liquid pool. Growth was then allowed to proceed in the normal manner for a given period of time after which the ingot was quenched. Autoradiographs were then taken from the large surface of the ingot in order to observe how the activity was distributed within the ingot. Any penetration of radioactivity into the original semi-solid region (i.e. that which had grown prior to insertion of the radiotrace) was taken as evidence of interdendritic fluid flow. Tin - 5wt% thallium was the alloy system and composition employed, with thallium 204 as the radioistope.

Figure 7.1 shows the procedure used for introducing the radioisotope into a growing ingot. Superheated molten alloy was first charged into the mould cavity in the usual way. Shortly afterwards a cold silica tube, open at both ends and containing a pre-cast solid slug of radioactive Sn-5wt% Tl alloy, was plunged quickly into the melt so that it rested vertically on the bottom of the mould cavity. The slug of radioactive alloy rapidly became molten but could not flow out of the bottom of the silica tube since this was resting on the floor of the mould. The length of the slug was also cut so that on melting the hydrostatic pressure would be the same both inside and outside the tube. Molten radioactive alloy of nominal solute content was therefore present within the mould cavity, but separated from the bulk alloy charge by the walls of the silica tube. This radioactive alloy could be added to the bulk liquid pool at any stage before or during growth by simply raising the silica tube vertically out of the mould.

This insertion technique meant that the temperature of the radioactive material was the same as that of the surrounding bulk liquid throughout the growth process. It also had the advantage that little turbulence was created by inserting the radiotrace providing the silica tube was removed slowly and carefully. Any possible disturbance of the growth process (and hence of its reproducibility, upon which the success of the experiment depended) was



Step 1
Non radioactive alloy charged into mould cavity in usual fashion

Step 2
Silica tube inserted into cavity.

Step 3
Radioactive alloy slug melts, but remains inside the tube since this is resting on the bottom of the mould.

Step 4
Cooling turned on - growth proceeds away from chill.

Step 5
After a known time the silica tube is withdrawn from the mould allowing the radioactive alloy to mix into the liquid pool.

Fig. 7.1. Showing the technique employed to insert the isotope into a growing ingot.

therefore minimised. It was also felt that the technique allowed the radiotrace to mix more quickly and evenly throughout the height of the bulk liquid pool than if it were poured onto the top of the pool, which was the insertion method used by Stewart.[61]

7.2.2 Choice of radioisotope, alloy system and composition, and detection method

Thallium 204 was chosen as the most suitable radioisotope for this experiment because it combined the following advantages:-

(1) it is a practically pure β^- emitter giving out very little electromagnetic radiation on decay.

(2) it can be produced easily, and without contamination from other radioisotopes, by neutron irradiation of pure thallium, and

(3) it has a moderately long half-life of 3.8 years.

These factors were considered advantageous in the context of this experiment for the following reasons:-

(a) β^- particles are the only type of radiation which combine a moderate ionising power with limited penetration properties. Limited penetration properties were prefereable so that the effects of the radioactive source could be confined to a given limited area. This was particularly important since the experiment involved the use of unsealed radioactive sources in an undesignated laboratory where other people were working. Electromagnetic radiations such as γ rays were considered undesirable because they have approximately 100 times the penetrating power of β^- rays of equivalent energy. The ionising power was required because the detection method, autoradiography, relies upon the radiation ionising the chemicals in the photographic emulsion to produce a picture.

(b) Neutron irradiation of a pure metal sample was found to be the cheapest and simplest way of obtaining a radioisotope in the form required for this experiement. The process involves bombarding the stable nuclides of the sample with neutrons inside an atomic reactor, thereby transforming some of them by

neutron capture into nuclides with a mass number increased by one, viz :-

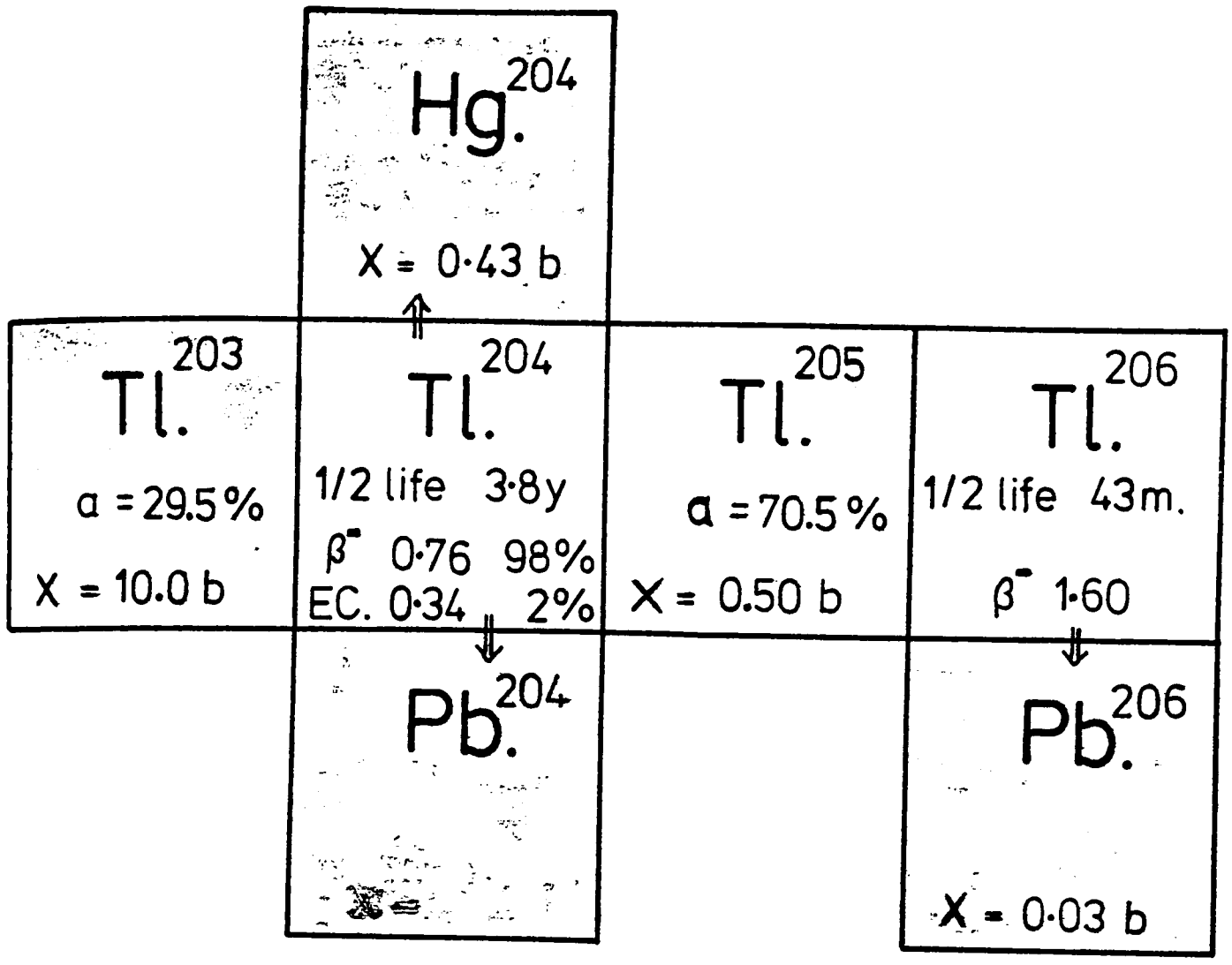
$$X_a^b + n_o^1 \rightleftharpoons X_a^{b+1}$$

Thallium 204 can be produced by this process from the stable isotope Tl 203. Furthermore, thallium has only two stable isotopes, Tl 203 and Tl 205, which yield just two radioisotopes, Tl 204 and Tl 206, after neutron bombardment (see figure 7.2). Thallium 206 has a short half-life of only 43 minutes and so decays away quickly, leaving Tl 204 as the sole radioisotope in the sample.

(c) The long half-life of Tl 204 allowed the experiment to be performed without undue haste, and meant that the activity of the source did not effectively alter over the duration of the experiment. Hebditch used tin 121 (half-life 27 hours) in his radioactivity work and found that such a short half-life created severe problems in the planning of his experiments.[103]

The most obvious choice of alloy system and composition for this work was Sn-5wt% Pb in view of the large amount of data concerning interface positions which had already been obtained for such ingots. Unfortunately, however, no suitable isotope of lead or tin could be produced by neutron irradiation of the pure metals. Tin has ten stable isotopes which yield significant quantities of five different radioisotopes on irradiation. Four of these emit γ radiations, while the pure β^- emitter Sn121 has only a short half-life. Lead has four stable isotopes which produce just two radioisotopes, Pb 205 and Pb 209, on irradiation. These isotopes, however, have half-lives of 10^7 years and 3.3 hours respectively, which makes them totally unsuitable for this experiment.

It was originally intended that a trace amount of radioactive thallium (say 0.1wt%) should be used in a master alloy of Sn-5wt% Pb in order to combine the advantages of using Tl 204 as the radiotrace with those for using Sn-5wt% Pb as the alloy system. However the amount of radioactive material which could be inserted into the casting without disturbing the growth process was felt to be quite small, and it was calculated that the activity of the thallium source required to produce acceptable autoradiographs was at least 15 mci/gm. of



KEY

Shaded Squares – Stable nuclides.

a = natural abundance. %.

X = thermal neutron capture cross-section. barns.

β^- = β rays.

E.C. = orbital electron capture.

Figures by radiations - E_{max} MeV.

$$_{81}Tl^{203} + _{0}n^{1} \longrightarrow {}_{81}Tl^{204} \xrightarrow{\beta^-} {}_{82}Pb^{204} + {}_{-1}e^{0} + \bar{\upsilon}$$

$$_{81}Tl^{204} \xrightarrow{O.E.C.} {}_{80}Hg^{204} + \upsilon$$

$$_{81}Tl^{205} + {}_{0}n^{1} \longrightarrow {}_{81}Tl^{206} \xrightarrow{\beta^-} {}_{82}Pb^{206} + {}_{-1}e^{0} + \bar{\upsilon}$$

Fig. 7.2. Irradiation and decay schemes for neutron irradiation of thallium metal.

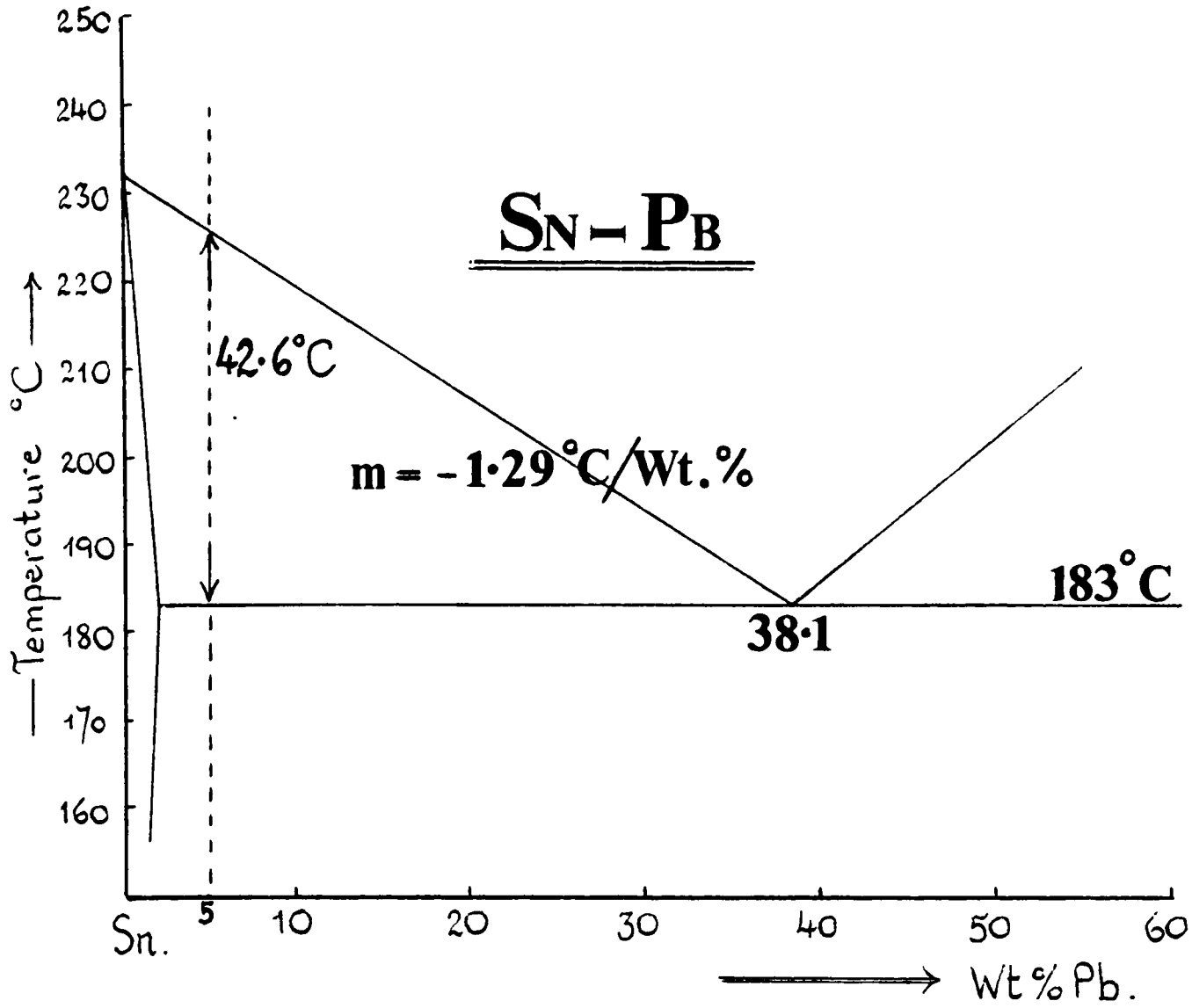
thallium for an alloy containing only 0.1wt% Tl (see Appendix 7.A). This was far in excess of the maximum safety value for the experiment of 1 mci/gm., which had been stipulated by the Radiation Protection Office. A thallium content of at least 1.5wt% was therefore needed in the radioactive alloy 'slug' and so it was decided that a binary Sn-Tl alloy should be used for the experiment. Luckily thallium metal is both chemically and physically very similar to lead, and there is also a close similarity between the Sn-Tl and Sn-Pb phase diagrams as shown in figure 7.3. Consequently it was expected that the Sn-Tl ingots would grow in a similar fashion to the Sn-Pb ingots in the model casting system. An alloy composition of Sn-5wt% Tl was therefore chosen for the experiment because Sn-Pb ingots of this solute content had exhibited large amounts of gravity flow segregation.

7.3 Experimental Procedure

7.3.1 Production of radioisotope

A length of 99.999% purity thallium metal rod was taken and the oxide layer scraped from its surface. Five pieces were cut from the rod, each weighing approximately 1 gm., and the total weight of the pieces was accurately measured. These five pieces were carefully wrapped up into individual pockets in a strip of aluminium foil, as shown in figure 7.4(a), which was then coiled inside an aluminium 'A can' supplied by Harwell. The 'A can' plus contents were then sent to Harwell for irradiation, together with specifications for the activity of Tl 204 required and the date at which the radioactive material should be delivered to the laboratory.

Thallium is a very dense metal and so there can be quite severe problems with self-shielding of the sample from the neutron flux in the reactor. It was for this reason that the sample had to be in 1 gm. pellet form. The pellets were packaged in aluminium foil in order to facilitate handling of the sample after irradiation, and because the aluminium strip could be coiled in the 'A can' thereby ensuring that the individual lumps of thallium would not be shielding



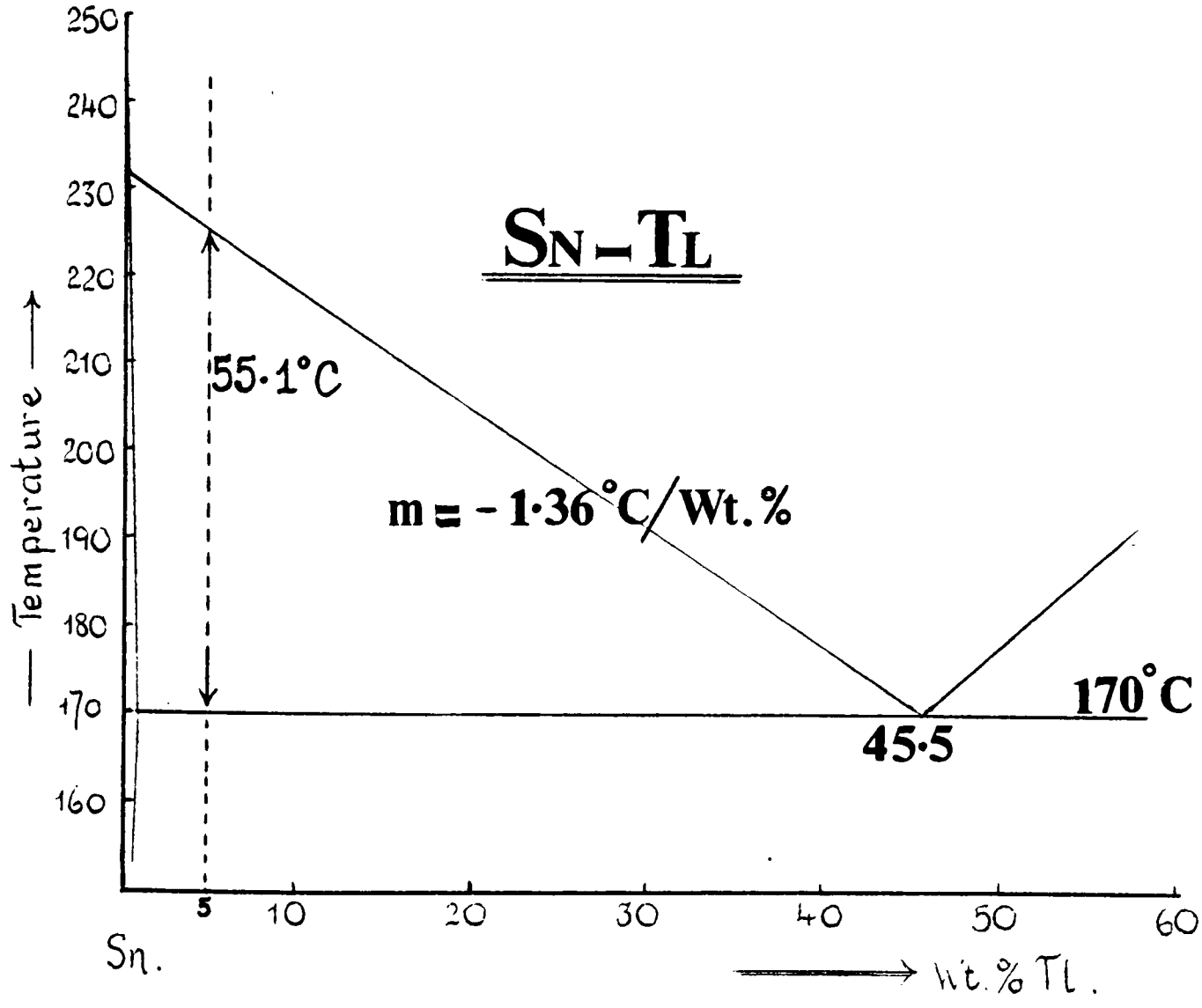


Fig. 7.3. Comparison of the binary equilibrium phase diagrams of the Sn-Pb and Sn-Tl systems.[17]

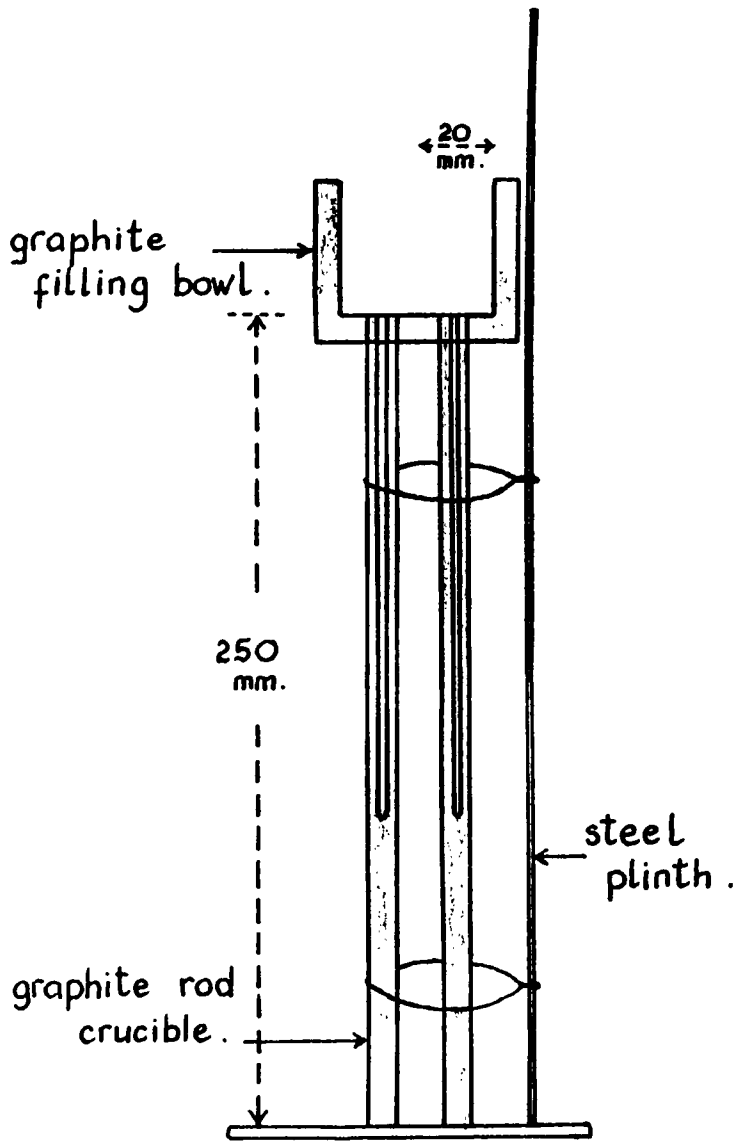
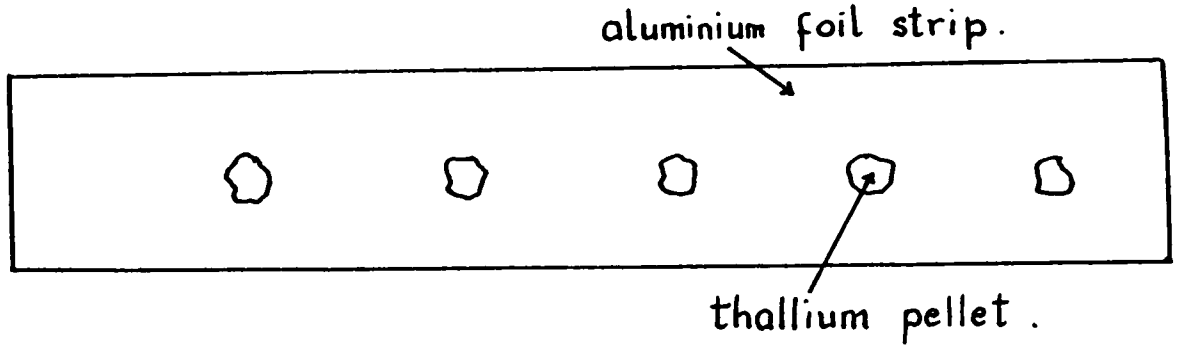
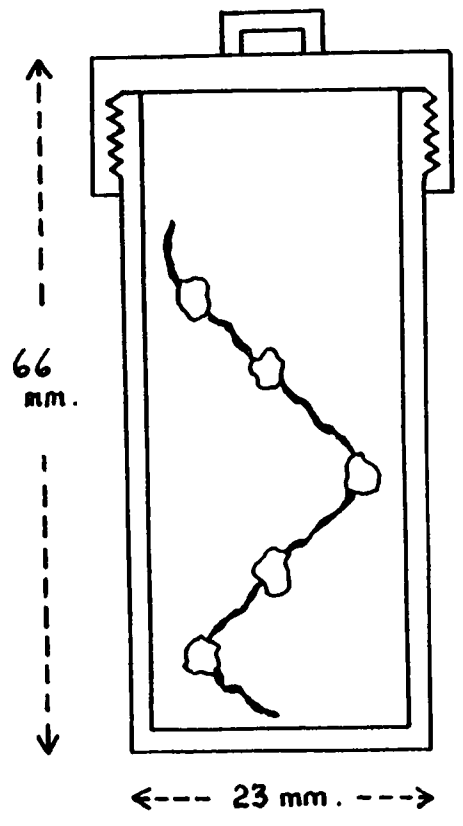


Fig. 7.4(b) Assembly employed to manufacture the radioactive alloy rods.







standard aluminium 'A' can.

Fig. 7.4(a). Packaging of thallium metal prior to irradiation.

each other in the reactor.

Irradiation of the sample was performed by inserting the 'A can' into the PLUTO reactor at Harwell. The sample was exposed to a thermal neutron flux of 7×10^{12} neutrons/cm^2/sec for a period of 40 hours. This irradiation time was calculated to be that required to produce an activity of approximately 1 millicurie of Tl 204 per gram. of thallium for that flux of neutrons. The calculation is given in Appendix 7.B. After being removed from the reactor the can was allowed to 'cool' for 12 days. This permitted the short half-life, very active, isotopes like Tl 206 and Al 28 to decay away. The foil strip containing the sample was then removed from the can and put into a 'dead' A can before being sent back to Oxford. This operation was particularly important from a safety aspect. Hebditch[103] had found that his irradiated 'A can' gave off very hard and long-lived gamma rays, presumably due to impurities in the aluminium.

7.3.2 Preparation of radioactive alloy slugs

When the radioactive thallium was received back from Harwell the pellets were carefully removed from the aluminium foil wrapping and put into a preweighed alumina crucible. The crucible plus thallium was then weighed thereby checking the weight of thallium. An amount of 99.99% tin sufficient to make an alloy of nominal composition Sn-5.00($\pm$0.01)wt% Tl was then measured out and added to the crucible.

The charge was melted up in a small vertical resistance furnace. The alumina crucible was placed in an iron pot before being inserted into the furnace in order to contain any leakage if the crucible were to break. Care was taken during melting not to raise the temperature of the molten charge above 400°C (see Appendix 7.D) because of the poisonous nature and radioactivity of the thallium vapour. As an additional precaution melting was carried out in a fume cupboard. Once the charge had melted it was thoroughly stirred to ensure homogeneity, care being taken to ensure that no splashing occurred. Thermal analyses (see section 6.5.2.1.) were performed on the radioactive melt as a check on

the alloy composition. The charge was thoroughly re-stirred after melting between each determination.

The apparatus employed to produce the pre-cast slugs of radioactive alloy used in the experiment is shown in figure 7.4(b). The graphite filling bowl was turned from a larger piece of graphite rod. The graphite crucibles were made by carefully drilling and reaming 4mm. diameter holes down the axes of 8mm. diameter graphite rods using a precision lathe. The crucibles push-fitted tightly into 8mm. holes drilled through the bottom of the filling bowl.

When completed the whole assembly was fastened onto a plinth so that it could be placed into the vertical tube furnace described in section 6.3. It was then heated to a temperature of around 350°C, removed from the furnace, and quickly transferred to the fume cupboard in which the radioactive charge was being melted. There it was rigidly clamped in position over a deep enamelled metal tray as a precaution against leaks or spills.

When the radioactive charge had melted and been sufficiently stirred it was taken from the furnace with a pair of long-handled tongs and carefully poured into the graphite bowl. A long thin alumina tube was then inserted down the full length of each crucible cavity in turn. This acted as a vent for any trapped air pockets within the cavities and so helped ensure complete filling of the crucibles. It was in order to give time for this operation to be performed that the graphite assembly was pre-heated, the radioactive alloy solidifying over a period of approximately 4 minutes.

When the assembly had cooled to room temperature the graphite crucibles were broken open using a pair of pliers and the radioactive alloy rods were cut off from the base of the graphite bowl. Two 62mm. lengths were then cut from each alloy rod using a pre-cut template as a gauge. These 'slugs' were then put in a lead-lined container until they were required for use. Care was taken not to bend or otherwise deform the rods during the process. Precautions were also taken to ensure that the pieces of graphite from the broken crucibles did not escape from the enamelled tray.

7.3.3 Insertion of radioactive alloy slugs into growing ingots

The procedure adopted for growing the slice cast ingots in this experiment was similar to that described in section 6.4., the only differences being in those aspects which involved the insertion of the radioisotope into the mould cavity using the silica tube technique already outlined in section 7.2.1 and illustrated in figure 7.1.

Silica had several advantages as a sheath material. It was inert to the molten alloy, of low heat capacity, and a poor conductor. It also had a low thermal expansion coefficient which allowed it to be plunged cold into molten metal without shattering.

The silica tubes were cut to a length of 300mm., long enough to handle conveniently without them projecting from the top of the furnace. The internal diameterof the silica tube matched the diameter of the slugs; this meant the slugs were held in place (with one end flush with the end of the tube) by friction once they had been pushed inside the tubes.

The tube complete with slug was inserted into the mould cavity approximately two minutes after pouring the main alloy charge into the cavity. It was lowered into the cavity until it was resting on the bottom of the mould. The tube remained vertical because the hole in the top mould insert was only slightly larger than the outside diameter of the tube. In order to ensure that the tube did not have a tendency to float up in the melt a removable brass collar (approximately 17 gms.) was fastened onto the tube near the top.

Once the slug had melted the radioactivity could be released into the bulk of the alloy charge simply by raising the silica tube slowly and gently out of the cavity.

7.3.4 Handling and machining of radioactive ingots

On removal from the mould each ingot was dried on a large sheet of absorbent paper. Any flash from around the edges of the ingot was then carefully cut off with a sharp bladed scalpel, and any pieces of graphite or

loose metal were cleaned from the surfaces of the ingot using moist tissue swabs.

In order to obtain autoradiographs of an acceptable quality from the ingots it was found necessary to machine away the rough outer-cast faces. This was done using a flycutter on a milling machine, a thickness of approximately 3 mm. being removed from one of the large faces of each ingot. The operation required a great deal of advanced preparation and planning in order to cope with the radioactive swarf produced, and involved the workshop being closed to other users for several days. Consequently the ingots were stored until all of the radioactive growth runs had been completed, and were then all machined in one batch.

The arrangement used to ensure containment of the radioactive swarf during the milling operation is shown in plate 7.5(a), and schematically in figure 7.5(b). Four separate levels of safeguard were employed. The ingot was first placed in a deep oblong tray made from stiff cardboard. These trays were disposable, a different one being used for each ingot. The floor of each tray had a shallow groove running along its length into which the ingot fitted. The ingot and tray were then clamped in the vice on the miller. The vice itself sat inside a large, deep-sided, plastic bucket and was fastened down to the bed of the machine through holes drilled in the bottom of this. Underneath the bucket the bed of the miller was completely covered with two large cardboard trays which were fastened together by tape. Finally, and in case anything escaped from these three containers, the floor area surrounding the miller was cleared, cleaned, and then covered with thick plastic sheeting. In addition to these precautions the milling machine itself was thoroughly degreased and cleaned of any detectable dirt and metal swarf prior to setting up the equipment.

The milling operation was performed using a very sharp tool, no lubrication, and the slowest spindle and traverse speeds available (60 r.p.m. and 0.5 cm. per minute respectively). The material was removed in six passes each of 0.5 mm.. The swarf came off the ingot surface in large chips which, at the low cutting and spindle speed employed, were simply pushed away by the

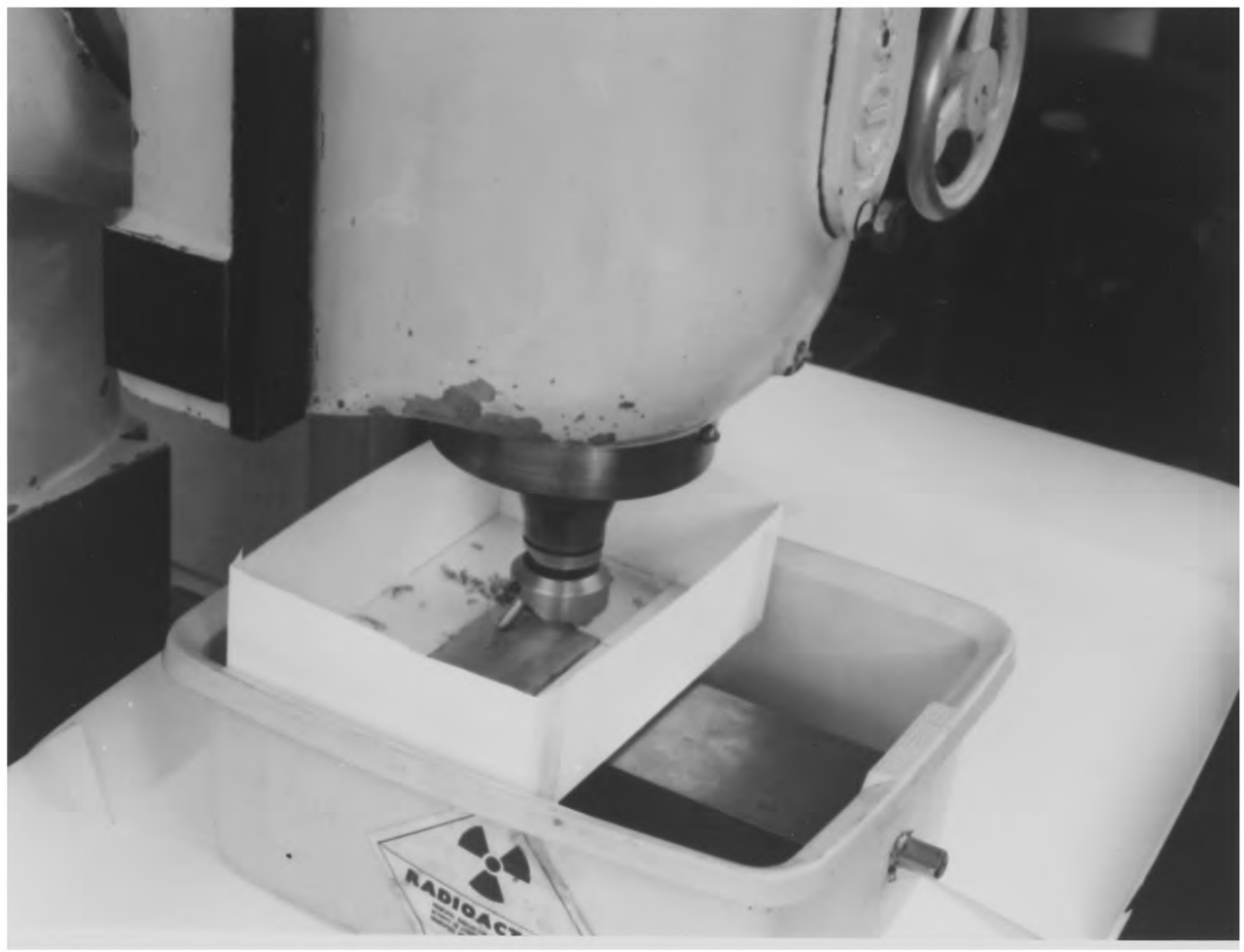


Fig. 7.5(a). Photograph showing the milling operation in progress.

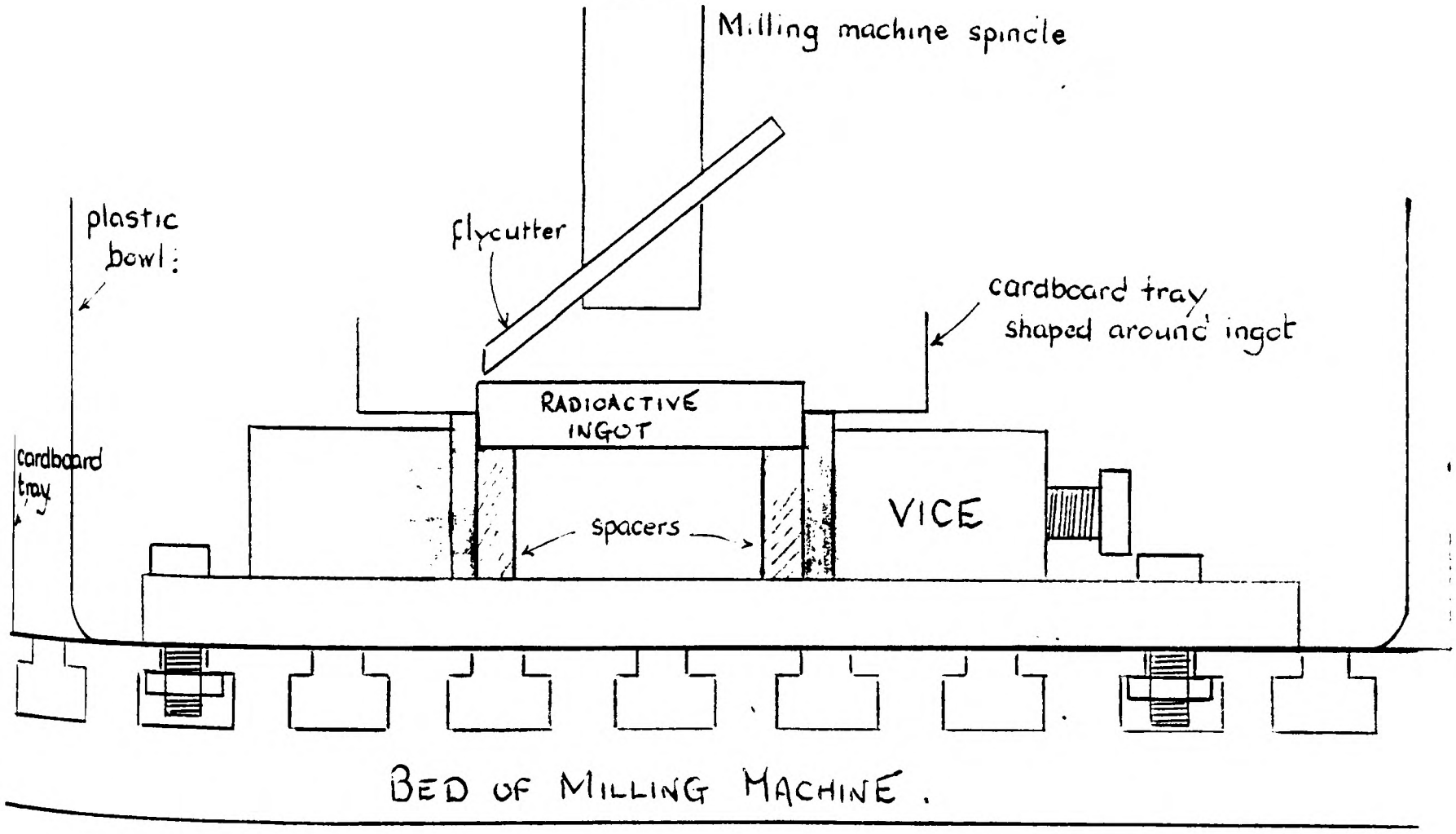


Fig. 7.5(b) Schematic illustration of the arrangement used to contain radioactive swarf during the milling operation.

revolving tool. All of the swarf was therefore easily contained within the first cardboard tray.

After the machining operation was completed the ingot was carefully released from the vice and all loose pieces of swarf adhering to it were brushed back into the tray. The tray plus swarf were then put into the radioactive waste bin. Once all the ingots had been machined a thorough check was made on the machine and surrounding workshop area to ensure that there had been no contamination.

7.3.5 Autoradiography of ingots

This part of the work was carried out in an ordinary photographic darkroom, which had therefore to be temporarily designated as a radioactive area. All exposures were performed in a large metal tray covered with a disposable paper lining in order to avoid any possible contamination of the darkroom. Ilford 'industrial G' X-ray film sheets were used to produce the autoradiographs. Yellow safelights could be used with this film. This was considered to be an important factor, since it was not felt safe to try and handle the radioactive ingots in total darkness. The paper envelope supplied with each sheet of film was removed prior to exposure in order to give optimum resolution on the radiograph and decrease the required exposure times.

The exposure procedure involved taking a sheet of film and laying it on top of a larger piece of black card in the metal tray. This was done so that the edges of the film sheet could be easily distinguished under the safelights. The ingot to be radiographed was then taken and laid on the film with its machined surface in contact with the film. The weight of the ingot itself ensured that a firm, even contact was made between the two. Pre-cut pieces of stainless steel were then slid up against the four edges of the ingot on the film in order to minimise fogging and thereby produce a clear outline of the ingot face. Finally a large sheet of lead was laid over the entire arrangement in order to prevent any accidental exposure of other workers. Exposure times were varied according to the detail required.

7.4 Safety Aspects

Radiations are harmful because they interfere with vital processes within the living cell. The biological effect of radiation is related to the energy absorbed per unit weight of tissue. The absorbed dose depends on the amount of radioactivity within the source, the type of radiation emitted, the energy of the radiations, the distance of the source from the tissue and the nature of the material between them. The accepted maximum permissible doses for radiation workers are set out in Appendix 7.C., together with the definitions of the important units of radioactive dose.

The use of radioactive materials in the University is governed by the rules set out in the national 'Code of Practice for Ionising Radiations'[134] and in the 'Oxford Local Regulations'.[135] It was necessary to obtain approval for the proposed experiment both from the University radiation protection officer and from the departmental safety officer. This piece of work was carried out under 'approved scheme B'[135] of the Local Regulations, which meant that:-

(a) the total quantity of radioactivity involved in the whole experiment had to be less than 10 millicuries (of β^- or γ radiation)

(b) the author had to register as a 'radiation worker' with the protection office and

(c) a film badge and laboratory coat had to be worn at all times.

By keeping within the boundaries of the approved scheme it was possible to perform the experiment in an ordinary undesignated laboratory. This was essential since no special facilities were available within the department for radioactive work.

Strict precautions were observed during the experiment in order to guard against the hazards involved in using a radioactive substance. The minimum strength of source capable of performing the experiment was employed. A safe operating distance was always maintained away from sources, and screening was used whenever possible. Sources were never touched, but always handled with tongs and rubber gloves. Inhalation of radioactive material was avoided by

keeping dust in the laboratory to a minimum, and by exercising special care when melting the radioisotope.No smoking, eating, or drinking was permitted in the laboratory in order to avoid ingestion dangers. Sources were kept within a specific area of the laboratory, most of the work being carried out in a large, deep, enamelled tray. Contamination of equipment and apparatus was kept to a minimum and carefully monitored. Contamination was a particularly serious problem with the Tl 204 isotope used in the experiment because of its long half-life. All radioactive waste and pieces of contaminated equipment were sealed into plastic bags and placed in a large metal bin until the experiment was completed. This bin was then taken to A.E.R.E. at Harwell for disposal.

A contamination monitor, described in detail in section 7.5.6., was used to check on the amount of activity present in any given source. The readout from this monitor gave the activity in counts per second but this was recalibrated in terms of millirads per hour using a standard source. The maximum whole body dose rate considered to be tolerable in this experiment was one millirad per hour.

Precautions were also taken against the chemical toxicity of thallium. The soluble compounds of the element are used in rodenticides, and the metal itself is extremely toxic. Its effects are similar to those of lead. It is however more dangerous than lead because it is readily absorbed through the skin, and the copious amounts of oxide which it forms on contact with air do not adhere to the metal surface and so can easily be inhaled as dust. Care was therefore taken not to handle the metal directly, and to ensure that the oxide dust was not allowed to enter the laboratory atmosphere. The safety threshold for thallium vapour in air is given [136] as 0.1 mg/m^3. The vapour pressure calculation given in appendix 7.D. shows that this threshold would be exceeded by raising the temperature of liquid thallium above 700°K. Care was therefore taken not to exceed this temperature during any of the melting operations in the experiment.

The safety threshold for Airborne Tl 204 (either as dust or as vapour)

is given ^{137} as 3×10^{-4} mci/m^3. The activity of the source used in this experiment was 1 mci/gm., and so the airborne concentration should not have exceeded 0.3 mg/m^3. This concentration limit was clearly in excess of that for the poisonous nature of thallium itself.

7.5 Results and Discussion

Six ingots were grown as part of this experiment, all of nominal composition Sn-5.00 ($\pm$0.01)wt% Tl. Runs number 28 and 29 were dummy trials in which a 'dead' liquid alloy addition was made to the bulk liquid pools during growth of the ingots. Information obtained from these ingots was used to set up runs number 33 and 34 in which actual radioactive alloy was inserted into the pools during growth. Finally, in runs number 35 and 36 the radioactive addition was made shortly after pouring the bulk alloy charge into the mould cavity. These runs were used to study how tracer was distributed throughout the bulk liquid during the holding period, and how it was redistributed in the solid ingot by the growth process.

7.5.1 Thermal analysis of melts

Composition determinations were not attempted in this experiment owing to the high cost of providing a thallium lamp for the spectrophotometer for such a limited number of analyses. Instead a rough comparison of the composition of the various charges was made using the thermal analysis technique described in section 6.5.2.1. Care was taken to ensure reproducibility of cooling rate in every determination so that a valid comparison could be made. The average plateau voltages obtained from the various charges are given in table 7.1 below:-

TABLE 7.1.

Run No.	28	29	33	34	35	36	Radioactive Melt
No. of determinations	5	2	3	2	2	2	2
$\bar{V}_p$ mV	9.005	9.00	9.005	9.00	9.01	8.995	8.99

The accuracy with which the determinations could be made was estimated to be

$\pm$ 0.01 mV. The sequence of five determinations performed on the charge of run 28 was carried out over a period of 25 hours. The individual plateau voltages are given in Table 7.2. below. The holding temperature during this period was 350°C.

time hrs.	$\frac{1}{2}$	1	$1\frac{1}{2}$	24	25
V_p mV	9.00	9.02	8.995	9.015	8.995

TABLE 7.2.

The spread of these values lies within experimental accuracy and no systematic variation with time can be observed. This indicates that there was no large change in composition (due to preferential oxidation of one of the components) when holding the molten alloy at this temperature.

The values of $\bar{V}p$ given in table 7.1. also lie within the experimental accuracy of the technique, indicating that all charges were of roughly the same composition. Unfortunately the technique is not particularly suited to measuring small variations in alloy composition. The average liquidus slope for Sn-Tl alloys is -1.36 °C/wt% Tl (figure 7.3). Consequently the experimental accuracy of $\pm$ 0.01 mV(or $\pm \simeq \frac{1}{4}$°C) means that composition changes smaller than $\pm$ 0.18wt% Tl cannot be detected. The technique was useful, however, in checking that there were no major variations in composition between the alloy charges themselves, or between the charges and the radioactive melt.

7.5.2 Thermal and other data obtained from the ingot growth runs

The data obtained from the sample thermocouples in the six runs is given in table 7.3 overleaf. The T vs. t traces obtained from these thermocouples during growth in the Sn-Tl ingots were of the same general form as those shown in figure 6.17.for Sn-Pb ingots. The time values, t_x, quoted in table 7.3 are taken from the start of cooling, and are considered correct to within $\pm$12 seconds.

The holding superheats employed in these runs were slightly larger than those used in the majority of the Sn-Pb ingots of Chapter 6. This was done intentionally in order to ensure that the radioactive alloy did not begin to

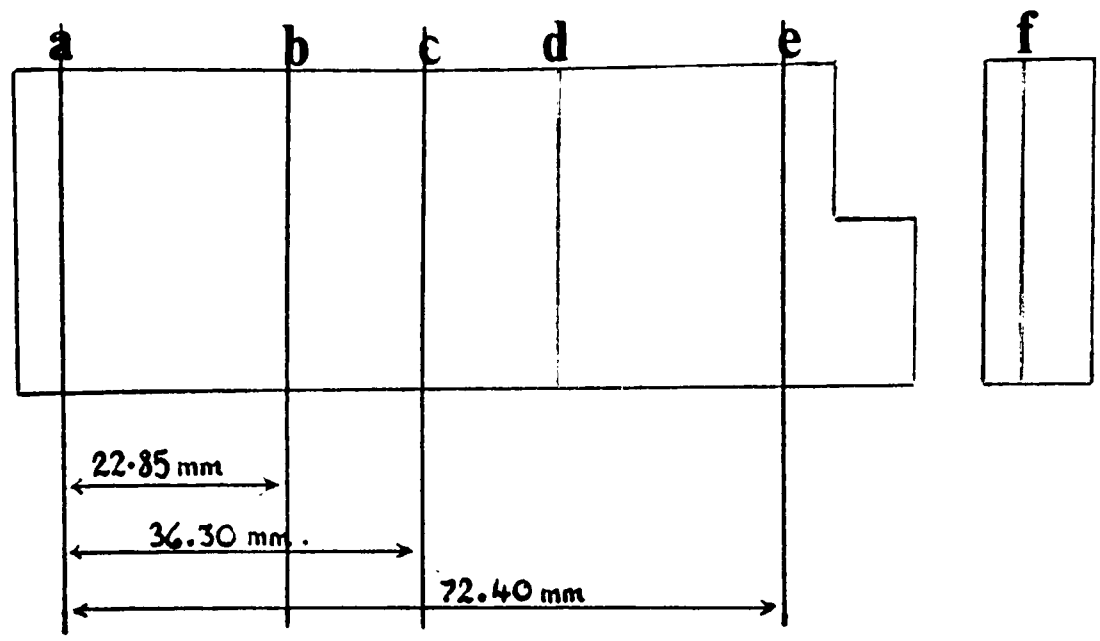


TABLE 7.3

Thermal data obtained from the sample thermocouple traces in the Sn-Tl radiotracer growth runs.

Run N^0		28	29	33	34	35	36
Av. holding superheat	ΔT_s °C	3½	2½	2½	3	3	4
Nucleation time	t_n	1m 47s	1m 24s	1m 18s	1m 33s	-	2m 00s.
Time at which the solid-liquid interface passed the thermocouple position.	t_a	3m 00s	2m 36s	2m 30s	2m 54s	-	3m 12s
	t_b	8m 06s	7m 51s	7m 45s	8m 27s	-	8m 36s
	t_c	11m 33s	10m 42s	10m 30s	11m 18s	-	11m 06s
	t_e	-	-	20m 06s	-	-	20m 18s
Quench time	t_q	13m 00s	12m 30s	32m 42s	14m 25s	0m 00s	74m 00s
Time at which radiotracer inserted	t_i	at quench.	9m 45s	12m 30s	12m 55s	on pouring	on pouring
Total Growth time	$t_q - t_n$	11m 13s	11m 06s	31m 24s	12m 52s	0m 00s	72m 00s
Available flow time for radiotracer	$t_q - t_i$	NONE	2m 45s	20m 12s	1m 30s	-	-
	$t_i - t_n$	11m 13s	8m 21s	11m 12s	11m 22s	-	-
Average interface temperature	T_p mV	8·965	8·960	8·955	8·960	-	8·960
	$t_b - t_a$	5m 06s	5m 15s	5m 15s	5m 30s	-	5m 24s
	$t_c - t_a$	8m 33s	8m 06s	8m 00s	8m 24s	-	7m 54s
	$t_e - t_a$	-	-	17m 36s	-	-	17m 06s

Times measured from start of cooling. Errors t_q, t_i ±01s ; t_N ±06s ; t_A, t_B, t_C, t_E ±12s

TABLE 7.4

Other casting data from radiotrace runs.

Run Number	28	29	33	34	35	36
Charge Weight gms.	632	634	633	633	635	630
Ingot Weight gms.	635½	636½	634	636	639	634
Pouring Temperature °C	350	350	345	345	350	355
Temperature at which radiotracer tube inserted °C	310	305	302	305	-	-
Air flow rate l/min.	10	10	10	10	-	10
M_{t_1} temp. drop in 1 min °C	6¾	6¼	7	6¾	-	-
" " " " 5 mins °C	23¼	23¼	24	23¼	-	-
" " " " 10 mins °C	33¼	33½	34½	33½	-	-

TABLE 7.5

Temperature (in mVolts) registered by the sample thermocouples 11m00s after nucleation.

Run Number	28	29	33	34	35	36	Av.
overall cooling time (t_N+11m)	12m47s	12m24s	12m18s	12m33s	-	13m00s	-
T_a mV	8.365	8.375	-	8.38	-	8.36	8.37
T_b mV	8.74	8.74	8.725	8.75	-	8.755	8.74
T_c mV	8.92	8.905	8.89	8.91	-	8.905	8.905
T_e mV	8.97	8.97	8.96	8.96	-	8.965	8.965

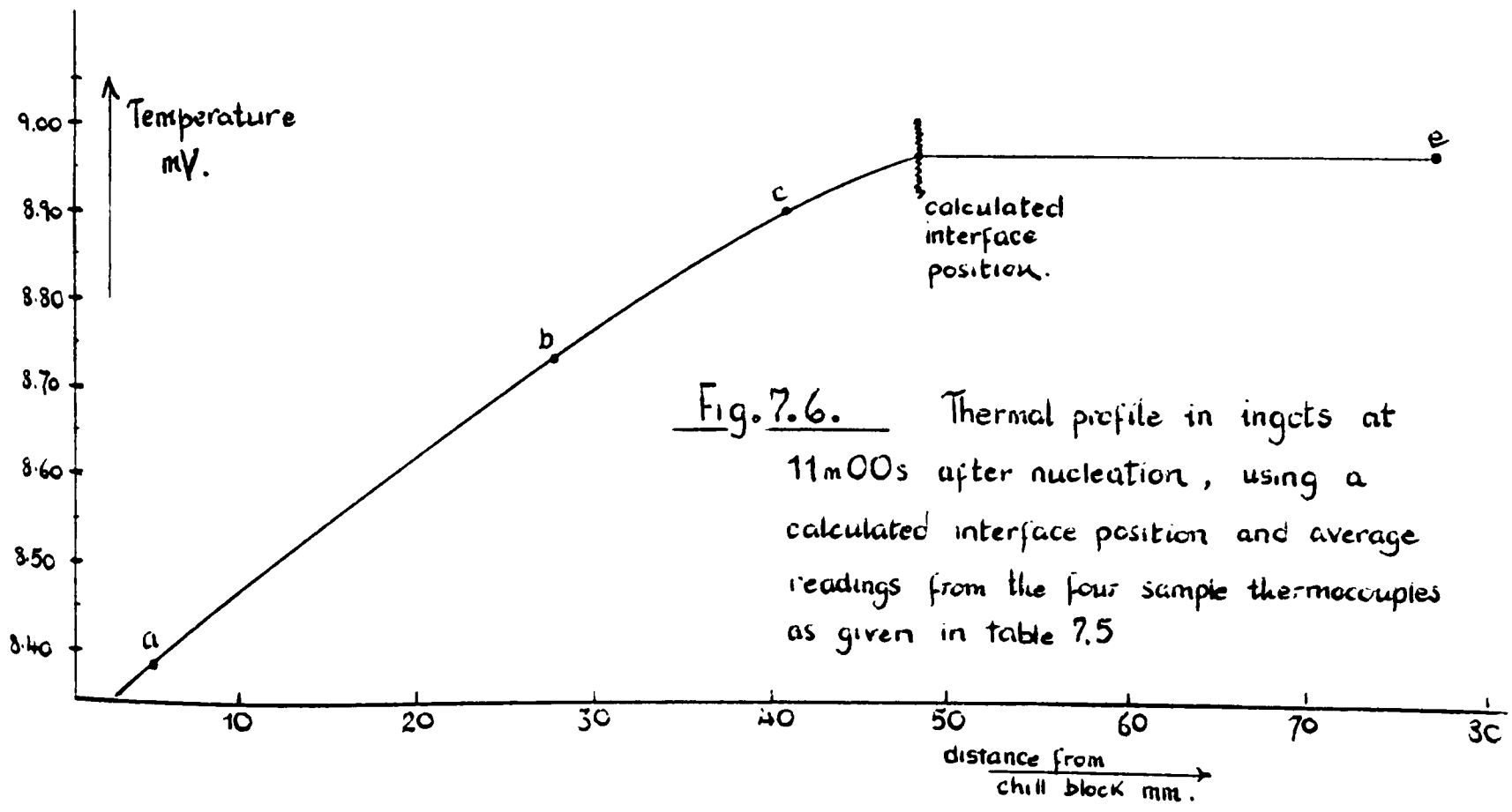


Fig. 7.6. Thermal profile in ingots at 11m00s after nucleation, using a calculated interface position and average readings from the four sample thermocouples as given in table 7.5

solidify inside the silica tube during the holding and cooling periods. A value of superheat of 3°C ($\pm \frac{1}{2}$°C) was considered sufficient for this purpose since other precautions had been taken to prevent the tube from acting as a heat sink.

It can be seen from table 7.3 that there was a definite relationship between the nucleation time (tN) and holding superheat (ΔT_s) just as in the Sn-Pb ingots of the previous chapter. The nucleation time altered by approximately 15 seconds for every $\frac{1}{2}$°C change in superheat.

It can also be seen that the times taken by the interface to advance between the thermocouple positions in the various runs, $t_x - t_y$, all lie within the experimental error range of $\pm$ 12 seconds. This would suggest that growth was consistent in each one. The average interface velocities between the various positions are worked out below, using time values averaged over the six runs.

$$(t_B-t_A)\text{av.} = 318 \pm 12 \text{ secs.} \quad \bar{V}AB = \frac{2.285 \pm 0.01}{318 \pm 12} = 7.19(\pm 0.40) \times 10^{-3} \text{ cm/sec}$$

$$(t_C-t_A)\text{av.} = 492 \pm 12 \text{ secs.} \quad \bar{V}AC = \frac{3.63 \pm 0.01}{492 \pm 12} = 7.37(\pm 0.27) \times 10^{-3} \text{ cm/sec}$$

$$(t_C-t_E)\text{av.} = 1041 \pm 12 \text{ secs.} \quad \bar{V}AE = \frac{7.24 \pm 0.01}{1041 \pm 12} = 6.95(\pm 0.12) \times 10^{-3} \text{ cm/sec}$$

It should also be noted from table 7.3 that the dendrite tip temperatures registered by the sample thermocouples were again approximately 0.04 mV (1°C) lower than the average plateau temperature observed by thermal analysis (see section 6.5.2.1).

Table 7.4 gives other data noted during the growth runs. The alloy charge weight was 633 g $\pm$ 3g, somewhat lower than in the Sn-Pb runs in order to allow for the metal displaced by the silica tube. Pouring temperatures were high in order to ensure that the bulk alloy charge was not chilled too far on insertion of the cold silica tube into the mould cavity. The reproducibility of the cooling rate during growth is confirmed by the values given for the temperature drops registered by the monitoring thermocouple on the chill block (M_{t1}) 1 minute, 5 minutes, and 10 minutes after the start of cooling.

Finally table 7.5 gives the voltage readings of the four sample thermocouples in the ingots at 11 minutes after nucleation. The reproducibility of these values within the ingots is clearly demonstrated, again indicating good growth reproducibility. Using the value of $\bar{V}AC$ calculated in this section the interface should have advanced to a position of 4.85 cm ($\pm$0.15cm) from the chill in this time. The thermal profile in the semi-solid zones at this time was therefore as shown in figure 7.6. The temperature gradient is not linear but slightly curved, being shallower just behind the interface.

7.5.3 Dummy trials. Runs 28 and 29

In these two runs a 'dead' alloy addition was made to the bulk liquid pool during growth of the ingots using the silica rod technique described in section 7.2.1. It was necessary to perform these dummy runs for a number of reasons, these being:-

(a) to check that the insertion technique worked satisfactorily, i.e. that the alloy sample inside the silica tube was molten and flowed out of the tube on its removal from the mould.

(b) to check whether the removal of the tube disturbed the semi-solid structure.

(c) to check that the Sn-Tl system did not present any unusual problems in itself, i.e. that a good columnar structure and plenty of gravity flow macrosegregation could be obtained.

(d) to obtain thermal data for Sn-5.00wt% Tl ingots, so that growth reproducibility could be demonstrated and interface position with time accurately predicted, and

(e) to check that there were no unexpected snags in the experimental procedure which might have caused dangerous problems when using 'real' radioactive material.

The relevant thermal data for these runs are given in tables 7.3 to 7.5. It can be seen from table 7.4 that the temperature of the bulk alloy charge on insertion of the cold silica tube was around 300°C in both runs.

The temperature of the charge, as monitored by the sample thermocouples, did not fall below 232°C (m.p. of pure tin) until 45 minutes after insertion. It was felt that this time period should have been sufficient to alloy any of the bulk alloy chilled by the insertion of the silica tube to remelt, and also to ensure that the whole of the inserted alloy slug was melted.

Table 7.3 shows that the overall growth times in these two runs were very similar. The difference between the runs lies in the fact that the 'dead' tracer alloy was inserted into the bulk liquid pool during growth in ingot 29, but not in ingot 28. In run 29 the ingot was grown for 8m 21s ($\pm$8s) at which time the silica tube was carefully removed from the mould cavity, thereby inserting the 'dead' tracer. Growth was then allowed to proceed for a further 2m 45s after which the ingot was quenched. In run 28 the ingot was grown for a period of 11m 18s ($\pm$8s) before quenching. The silica tube was not removed during growth although it did pull out of the mould in the quenching process.

The etched macrostructures of the two ingots are shown in plates 7.7(a) and 7.7(b). The structures are clearly columnar and the large cut-backs at the bottoms of the ingots indicate that large amounts of interdendritic fluid flow have taken place during growth. A large channel (containing dendrite fragments) is also clearly visible near the chill in the structure of ingot 28, giving further evidence of flow.

The macroscopic interface positions are virtually identical in the two ingots. The distance of the interface from the chill at a height of 30mm. from the ingot base is 4.95cm($\pm$0.15cm) in both ingots. The relatively large error range in this measurement is a result of having to draw 'average' interface positions through the various protrusions and hollows on the actual interfaces. This measured distance is consistent with the predicted interface positions in these ingots, calculated using the average interface velocities quoted in the previous section, i.e. :-

Ingot 28 $\quad d_{chill} = 673(\pm 8s) \times 7.37(\pm 0.27) \times 10^{-3}$cm. $= 4.96 \pm 0.24$ cm.

Ingot 29 $\quad d_{chill} = 666(\pm 8s) \times 7.37(\pm 0.27) \times 10^{-3}$cm. $= 4.91 \pm 0.24$ cm.

The interfaces in both ingots slope back towards the chill at the top



Fig. 7.7(a). Etched macrostructure of ingot 28 quenched after 11m 06s of growth. 'Dead' radiotracer inserted 2m 45s. prior to quenching.

Magn x 1·5

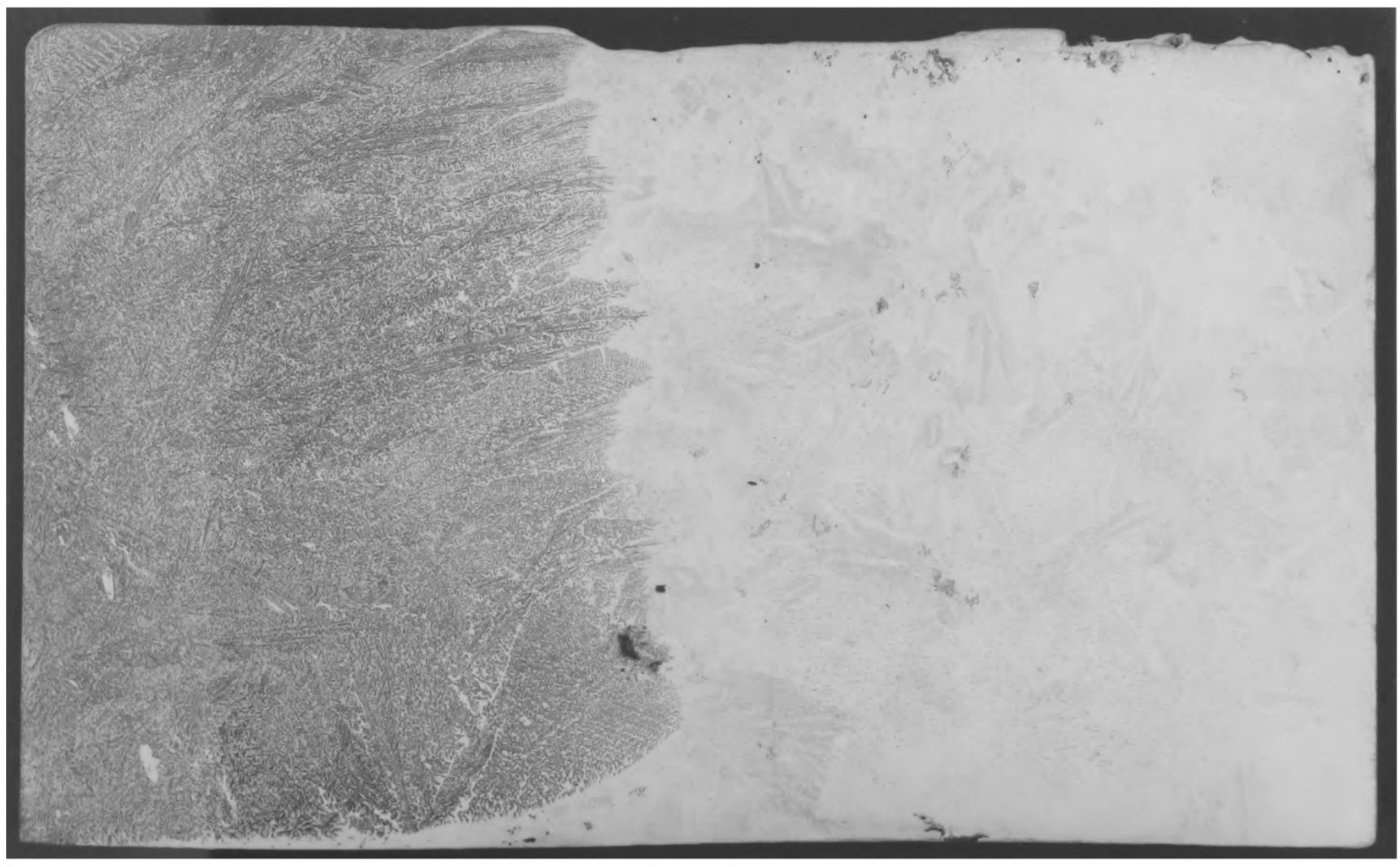


Fig. 7.7(b). Etched macrostructure of ingot 29 quenched after 11m 18s of growth. 'Dead' radiotracer added on quenching.

Magn x 1·5

of the ingots. The measured distance of the interface from the chill at the top surface of the ingots is 4.50cm ($\pm$0.15 cm).

It is therefore clear both from the macrostructures and from the thermal data presented in the previous section that the casting apparatus was providing reproducible growth conditions for Sn-Tl ingots. It is also clear from a comparison of the etched macrostructures that the removal of the silica tube during the growth of ingot 29, and the consequent insertion of 'dead' tracer alloy into the bulk liquid pool, had no appreciable disturbing effect on the original semi-solid structure or on the subsequent growth process. This is confirmed by the T vs. t traces of the sample thermocouples during growth of ingots 28 and 29, which showed no significant difference between the two runs.

In both runs the molten alloy slug flowed easily from the silica tube when it was removed from the mould. Only trace amounts of metal were left on the surfaces of the tubes. It would appear from the macrostructures of the quenched ingots that the 'slugs' were completely molten on insertion. A few small dendritic fragments were visible dispersed throughout the bulk liquid regions of both ingots, but their presence is not considered significant. As discussed earlier it is unlikely that they originate from the chilling effect of the cold silica tube on its insertion into the mould. They could not be from the inserted 'dead' tracer material since they are observed throughout the bulk in ingot 28 where insertion was not made until quenching. It is more likely that they come from the growing semi-solid region itself as a result of dendrite detachment in the channels. Finally, it should be pointed out that the odd 'structure' present in the bulk liquid region of ingot 29, plate 7.7(b), is caused by pieces of graphite which have presumably become detached from the sides of the mould.

7.5.4 Radioactive trials. Runs 33 and 34. Insertion during growth

Having established that the silica tube insertion technique worked satisfactorily run 33 was performed in which a radioactive liquid alloy 'slug'

was added to the bulk liquid pool during growth. The radioactive addition was made to the ingot 11m 12s($\pm$8s) after the bulk charge had nucleated and begun to grow. Growth was then allowed to proceed for a further 20m 12s after insertion, at which time the ingot was quenched.

A contact autoradiograph taken from the skimmed surface of the ingot is shown slightly magnified in plate 7.8(a). The outline of the ingot can be faintly discerned; the dark regions on the photograph indicate the presence of the radioisotope. The success of the experiment hinges on how accurately the interface position at the time of insertion can be established, so that this may then be compared with the darkened areas on the autoradiograph. It can be seen from table 7.3 that the sample thermocouple traces in this ingot were almost identical to those obtained from ingot 29 and very similar to those from ingot 28. Furthermore, the time between nucleation and insertion in run 33 was the same as the total growth times of ingots 28 and 29 within experimental error. It therefore follows that the interface position of insertion of the radiotrace in run 33 should have been the same as the quenched interface position in ingots 28 and 29. This position is given by the dashed line on the transparent overlay for plate 7.8(a). Confirmation that this is the correct position can be obtained by examining the position of the step which appears on the top surface of the ingot (faintly visible in plate 7.8(a)). This was formed on withdrawal of the silica tube from the mould cavity; the level of the bulk liquid pool dropping by approximately 1mm.. This step occurs at a distance of 46mm. from the chill in ingot 33, which agrees well with the distance of 45$\pm$1.5mm. measured as the interface position in ingots 28 and 29.

When the estimated interface position is overlayed on the autoradiograph of the ingot it is quite clear that the radioactived liquid inserted into the bulk liquid pool has penetrated the original semi-solid region to quite an appreciable extent. The sweeping curve which marks the maximum boundary of observed penetration provides very good evidence for the convective nature of the flow. The majority of the radioactive liquid would appear to have entered

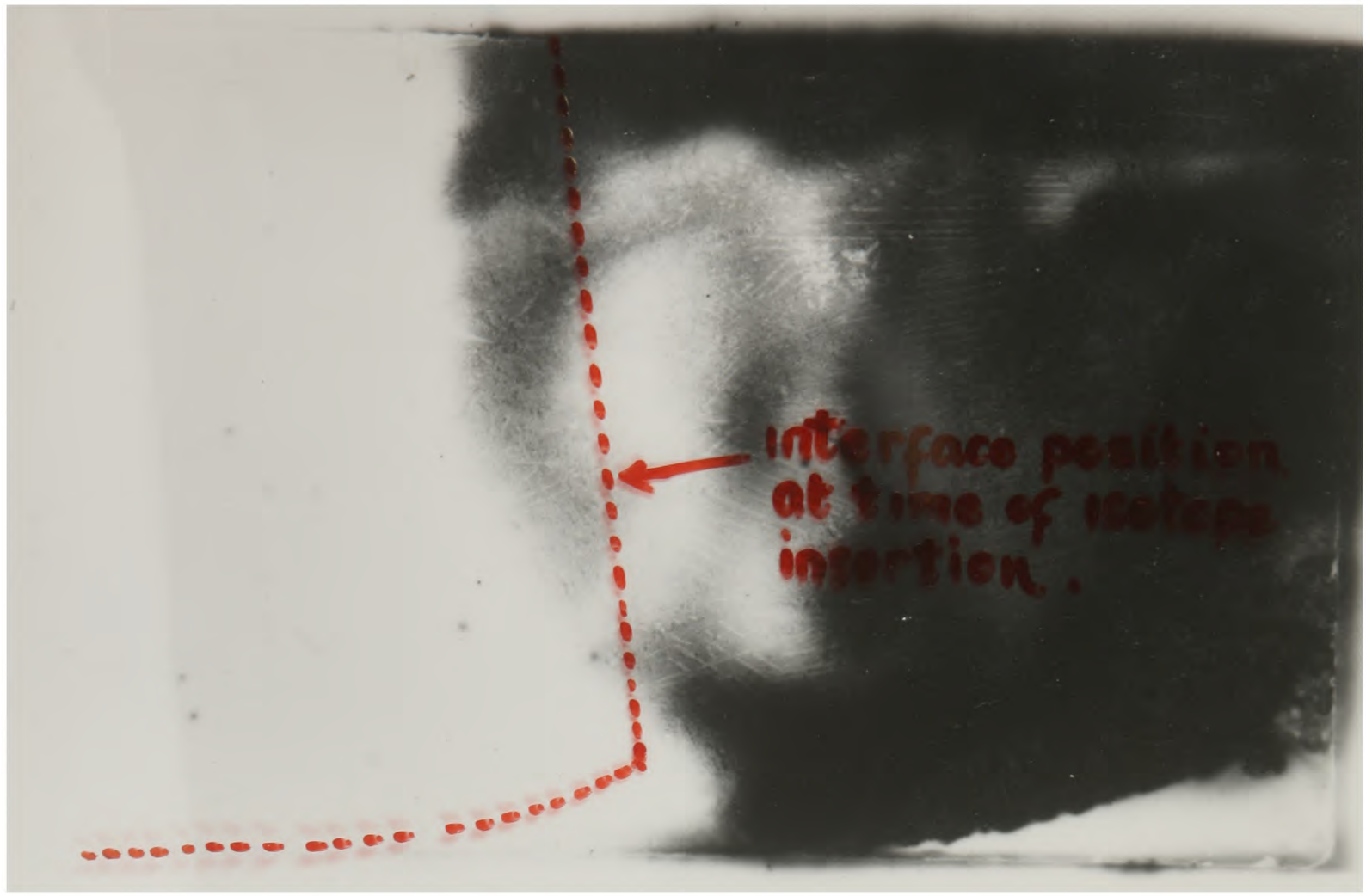


Fig. 7.8(a). Ingot 33. Contact autoradiograph with ingot resting on X-ray film. 4 days exposure. Dark regions indicate radioactivity. Magn x 1·5

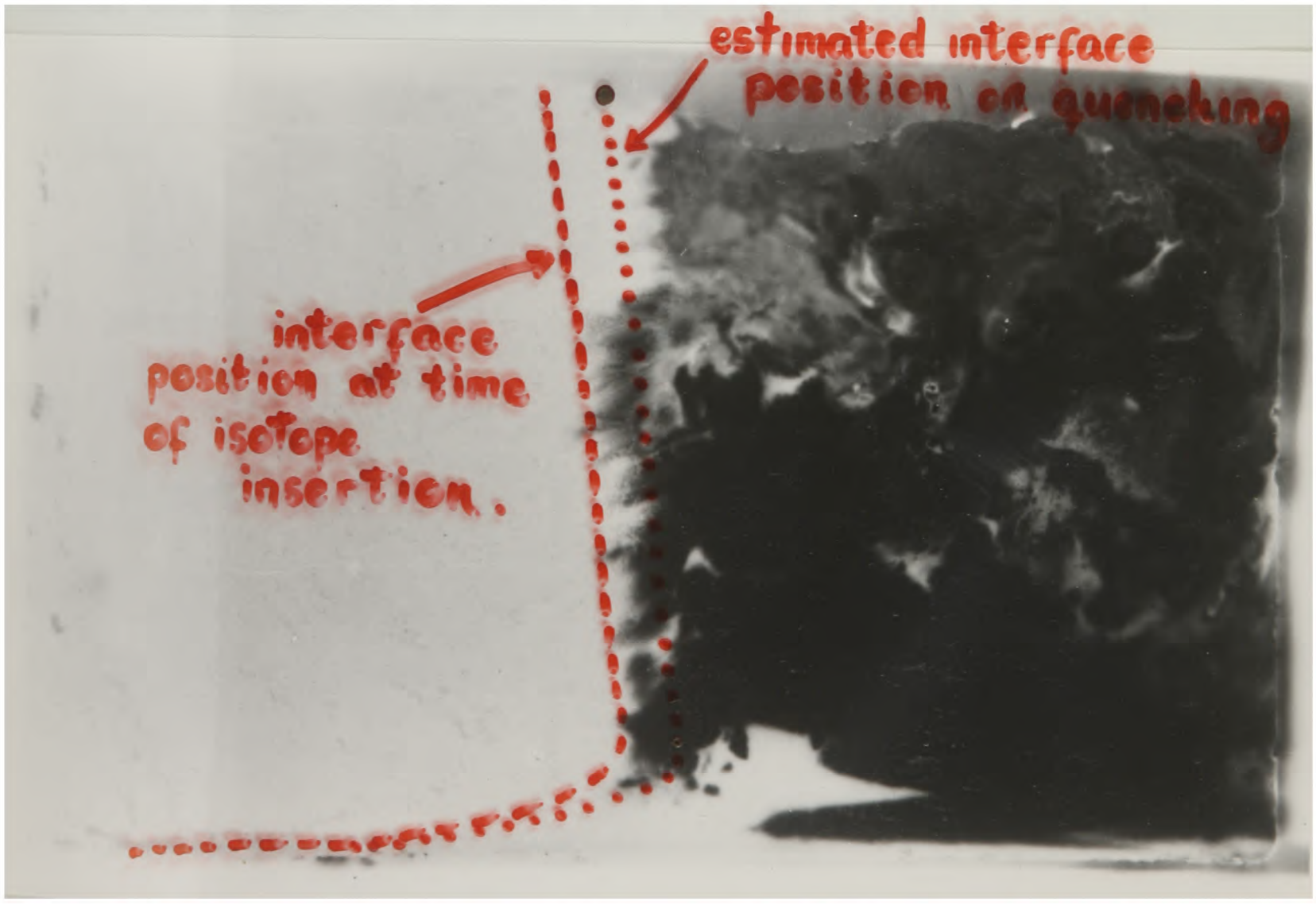


Fig. 7.8(b). Ingot 34. Contact autoradiograph. 4 days exposure. Magn x 1.5.



Fig. 7.8(a). Ingot 33. Contact autoradiograph with ingot resting on X-ray film. 4 days exposure. Dark regions indicate radioactivity. Magn x 1.5



Fig. 7.8(b). Ingot 34. Contact autoradiograph. 4 days exposure. Magn x 1.5.

the semi-solid near to the top of the ingot, before flowing down and then finally out again at the bottom of the ingot. The apparent penetration distance varies from around 8mm. behind the interface at the top of the ingot to a maximum of 11mm. behind the interface at half-height. In fact because the interface was continually moving away from the chill the actual penetration distances may well have been much greater than these, especially when it is considered that interdendritic fluid flow rates should be fairly slow.

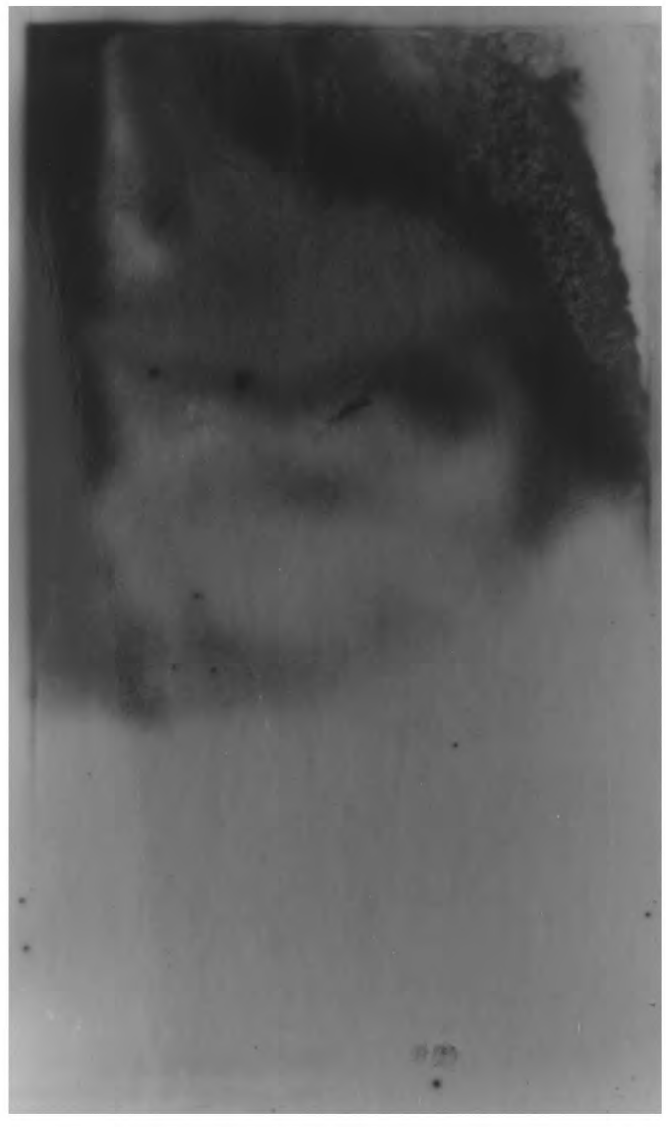
In order to check that the observed penetration had not occurred very quickly soon after insertion of the radiotrace (i.e. in the semi-solid region of high g_L just behind the interface) a further ingot was grown. Radioactive alloy was inserted into the bulk liquid pool of this ingot at roughly the same stage of growth as in ingot 33. However, this ingot was then allowed to grow for only a further 90 seconds before being quenched. A contact autoradiograph taken from the skimmed surface of ingot 34 is shown in plate 7.8(b). The thermal data taken from the growth run and given in table 7.3 show that growth proceeded in the same manner in this ingot as it had in the others. The insertion of the radioactive alloy was however slightly delayed in comparison with run 33 and so it is likely that the dendrite tip interface would have advanced a further 1mm. in this ingot. This is confirmed by the position of the step on the top surface of the ingot which occurs at a distance of 47mm. from the chill. The estimated interface position on insertion of the radiotrace is shown by the dashed line on the overlay to plate 7.8(b). The dotted line on this overlay gives the estimated interface position on quenching the ingot. This was calculated using the average growth velocity calculated in section 7.5.2 In the 90 seconds between insertion and quenching the interface should have advanced:-

$$d = 7.37(\pm 0.27) \times 10^{-3} \times 90 = 0.65 \text{ cm}$$

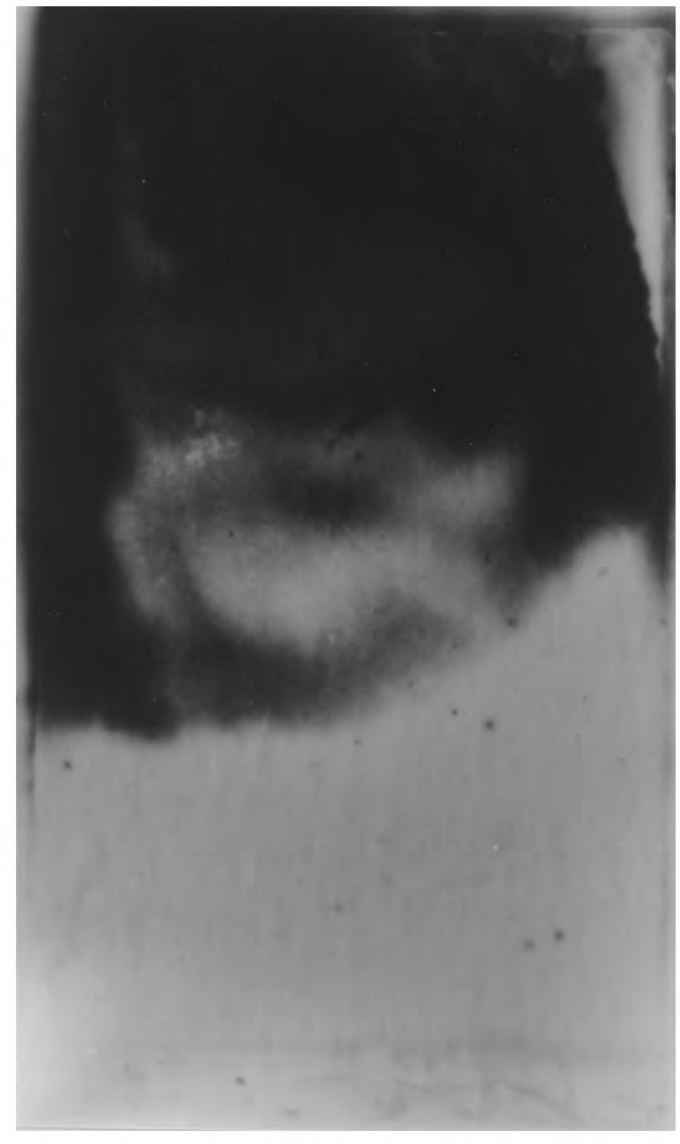
It is clear from a comparison of interface position with the region of activity in the autoradiograph of ingot 34 that there has been no penetration

of radioactive alloy into the original semi-solid region of the ingot. Furthermore there has been only partial penetration of radioisotope into the semi-solid region which grew between insertion and quenching. It can therefore be concluded that the penetration observed in the radiograph of ingot 33 (plate 7.8(a)) must have occurred by flow of radioactive liquid into the semi-solid zone over a long period of time (i.e. deep in the semi-solid zone at low g_L). This corroborates in a qualitative sense the conclusions drawn from the composition measurements in the previous chapter. Assuming that had ingot 34 been allowed to continue growing the position of maximum radiotrace penetration would have been the same as that found in ingot 33, then at the top of the ingot penetration would have had to occur up to 16mm. behind the quenched interface position. Even assuming that interdendritic flow rate equalled growth rate this would mean that flow was occurring over3cm. behind the interface. Using the thermal data given in table 7.5., and assuming the Scheil equation holds, a distance of 3cm. into the semi-solid zone corresponds to g_L = 0.40 for a Sn-5wt% Tl alloy. In fact it is unlikely that interdendritic flow rates would be as high as the growth rate of these ingots and so this value of g_L is likely to be an over-estimate. The ingots therefore also provide a semi-quantitative confirmation of the results of chapter 6, where the limiting value of g_L for flow to be appreciable was estimated as 0.30.

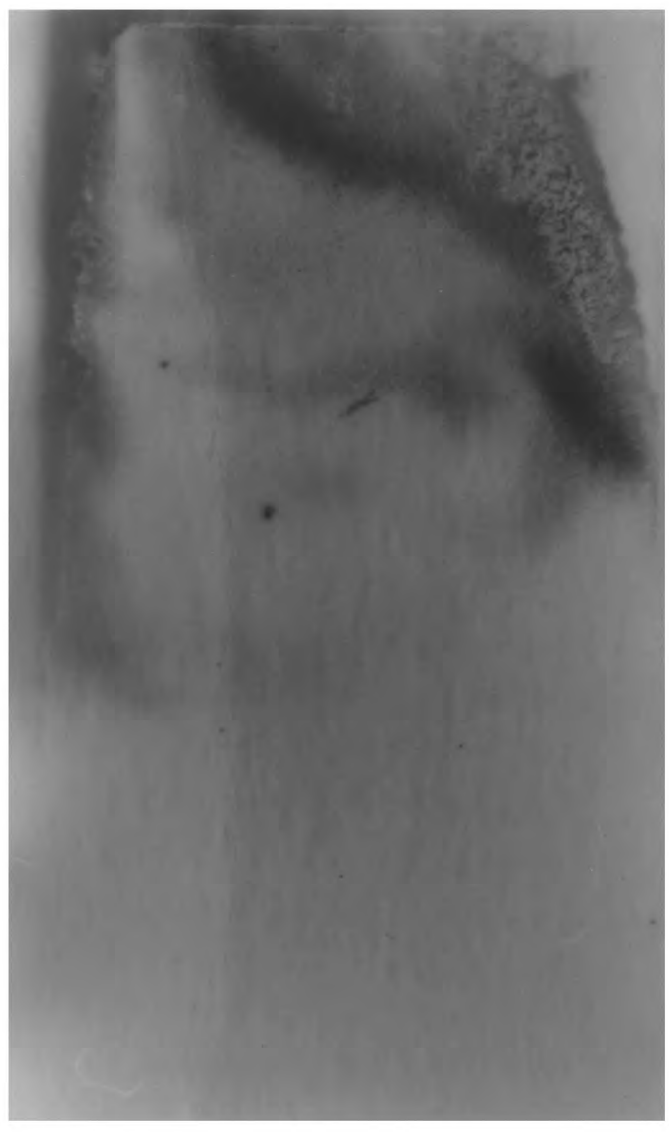
In addition to the major conclusion to be drawn from the experiment and described above, there are several other interesting features in the autoradiographs of these two ingots. These can be seen more clearly by studying the sequences of radiographs shown in plates 7.9 and 7.10., taken from ingots 33 and 34 respectively. Each of these radiographs was developed in identical conditions for the same length of time. The graduation in darkness within each sequence is due to the variation in exposure time of the film to the ingot. It is clear from the sequences how such variations in exposure can enhance, or disguise, different features on the radiographs. The following



(b) 13 hrs.



(d) 7 days

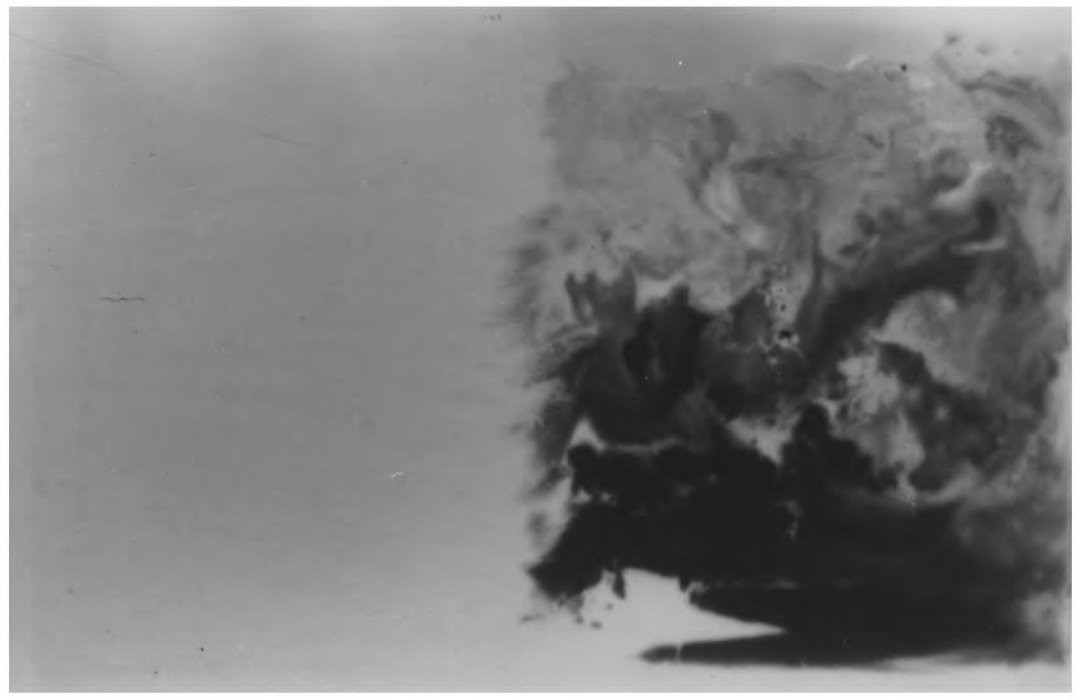


(a) 4 hrs.



(c) 24 hrs.

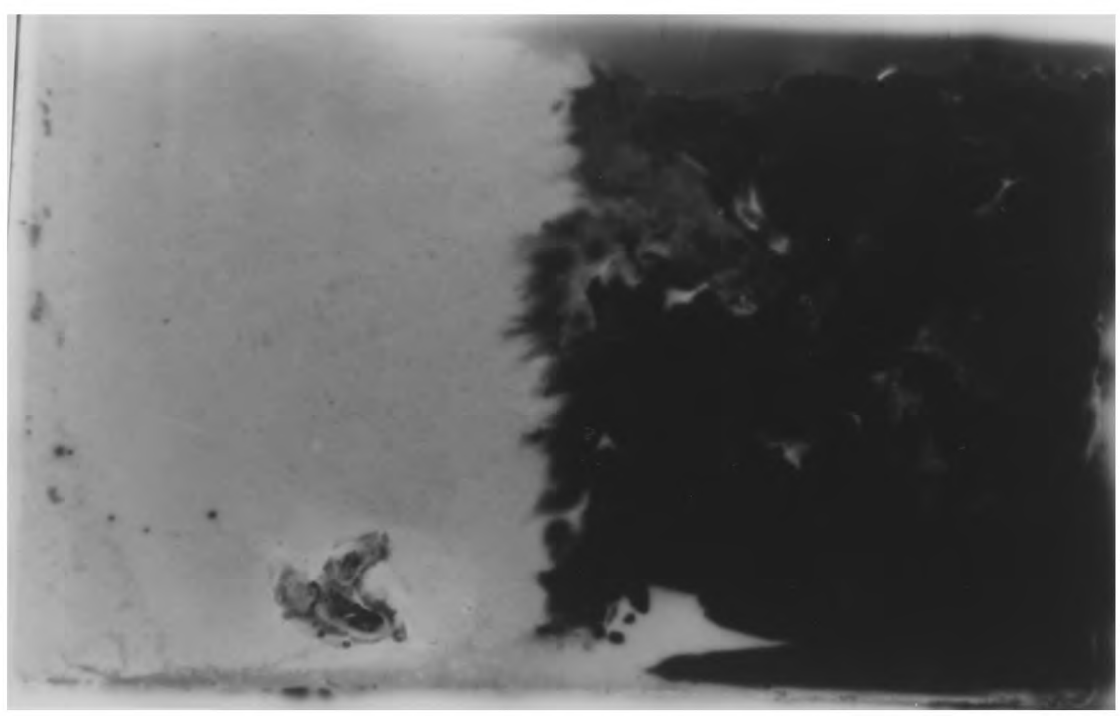
Fig. 7.9. Sequence of autradiographs from ingot 33 exposed for different periods of time, as indicated in captions (a) to (d) Mag² x 1



(a) 13 hrs.



(b) 24 hrs.



(c) 7 days.

Fig. 7.10. Sequence of autoradiographs from ingot 34 exposed for different periods of time. Magn x 1

points are worthy of mention:-

From plates 7.9 (ingot 33)

(a) The radiotrace clearly delineates the structure in the regions which have grown after its addition, although this is obscured when exposure times become long. A definite channel can be seen at half-height in the original bulk liquid region.

(b) The small black dots which appear at different points in the radiographs are not significant. They are caused by small pieces of radioactive swarf adhering to the ingot surface.

(c) There was clearly no penetration of radioactive alloy into the bottom corner at the 'hot' end of the ingot. This was most probably the result of a gravity-stable layer of dense, inactive, thallium-rich liquid lying on the bottom of the mould, and set up there by gravity flow segregation which had occurred in the growing semi-solid prior to insertion. It is also possible that the feature might have been caused by the angular geometry of the mould cavity preventing convection currents from reaching completely into the corner.[58,59] A similar region to this was present in the Sn-2wt% Pb ingot grown to completion by Stewart and Weinberg.[61] It seems probable from the low exposure radiographs that the material in this corner was still liquid on quenching the ingot, although the growth front can clearly be seen to have reached the end of the ingot over the majority of its height.

(d) Some very faint detail is beginning to emerge in the original semi-solid area in the radiograph exposed for seven days. This is thought to be caused by a very slight amount of seepage occurring from the radioactive 'slug' into the bulk alloy charge during the holding period prior to growth.

From plates 7.10 (ingot 34)

(e) A similar seepage must have occurred in this run although to a somewhat greater extent. The structure of the original semi-solid is clearly delineated after exposure for seven days. There is a very obvious build-up of solute at

the bottom of the ingot, and this is clearly causing a 'nose' of solute-enriched liquid to accumulate ahead of the interface at the bottom of the ingot which is not being mixed into the bulk (as delineated by the major radioactive addition).

(f) The radioactive liquid alloy has clearly not had sufficient time to mix uniformly into the bulk liquid pool in this ingot. This is not surprising since the convection currents must have been fairly sluggish and only ninety seconds elapsed between insertion and quenching. It is discussed further below.

(g) There is a layer of liquid laying at the bottom of the liquid pool in this ingot which has not been penetrated by the radiotrace. This is again probably a gravity-stable, thallium-rich layer formed prior to insertion.

There is some doubt arising from these sequences of radiographs concerning the mixing of the radioactive alloy into the bulk liquid pool. In plates 7.9(b) and (c) it can be seen that there appears to be an accumulation of activity at the top surface of ingot 33. In plates 7.10 on the other hand the majority of the activity seems to have stayed at the bottom of the pool in ingot 34. A possible explanation for these features might be that the radioactive 'slug' inserted into these ingots were not of the same composition as the bulk alloy charge. For example, if in ingot 33 the slug contained less than 5wt% thallium then the liquid would be expected to rise to the top of the pool on insertion. Once at the top some of it might very well not be mixed into the bulk liquid by convection. The activity in it would then remain undiluted and would therefore give the impression on an autoradiograph of being a region rich in thallium. A similar explanation could be proposed for the feature observed in ingot 34 if the slug contained more than 5wt% thallium. If this explanation is correct it seems likely that the inhomogeneity between slugs must have arisen for the technique of casting them into graphite moulds. The fact that two 'slugs' were cut from each cast rod may well have been a cause of inhomogeneity. Such an explanation would not invalidate the main conclusions

drawn from these ingots regarding flow in the semi-solid region. If a gravity-stable layer depleted in thallium did exist at the top of ingot 33 after insertion then it would have acted as a hindrance to convective flow, if anything. It would also have caused more solid to be deposited in this region, so that the observed penetration could not have been the result of dissolution by the liquid.

Finally plates 7.11(a) and (b) show how much poorer the resolution is when the X-ray film is laid on the ingot surface rather than vice versa. Fogging of the film from activity on the edges of the ingot is also a problem, making the ingot outline less well defined. Plate 7.11(b) was taken from the unskimmed side of ingot 33 and in spite of the lack of detail it can be seen that the general position of the radiotrace is much the same as in the skimmed surface. This therefore demonstrates that there are no edge effects associated with the sides of the mould - a point which is important with respect to the composition measurements of Chapter 6.

7.5.5 Radioactive trials. Addition during pouring. Runs 35 and 36

The purpose of these two runs was to observe how the radioactivity of an initially homogenous radioactive liquid alloy charge could be distributed after freezing the charge. By making the solute element the radioactive component of the alloy it was hoped that these runs would corroborate the picture of solute redistribution obtained in Chapter 6 from composition measurements on slice-cast ingots.

These runs fall outside the main experiment described in this chapter because the silica tube technique for inserting the radioactive alloy was not employed. Instead, one of the solid radioactive alloy 'slugs' was dropped into the mould cavity just before the bulk alloy charge was poured in. It was felt that the large pouring superheat of the bulk charge would quickly melt the 'slug', and that the pouring turbulence and subsequent convection currents would be sufficiently vigorous to mix the radioactive solute uniformly throughout the alloy volume.

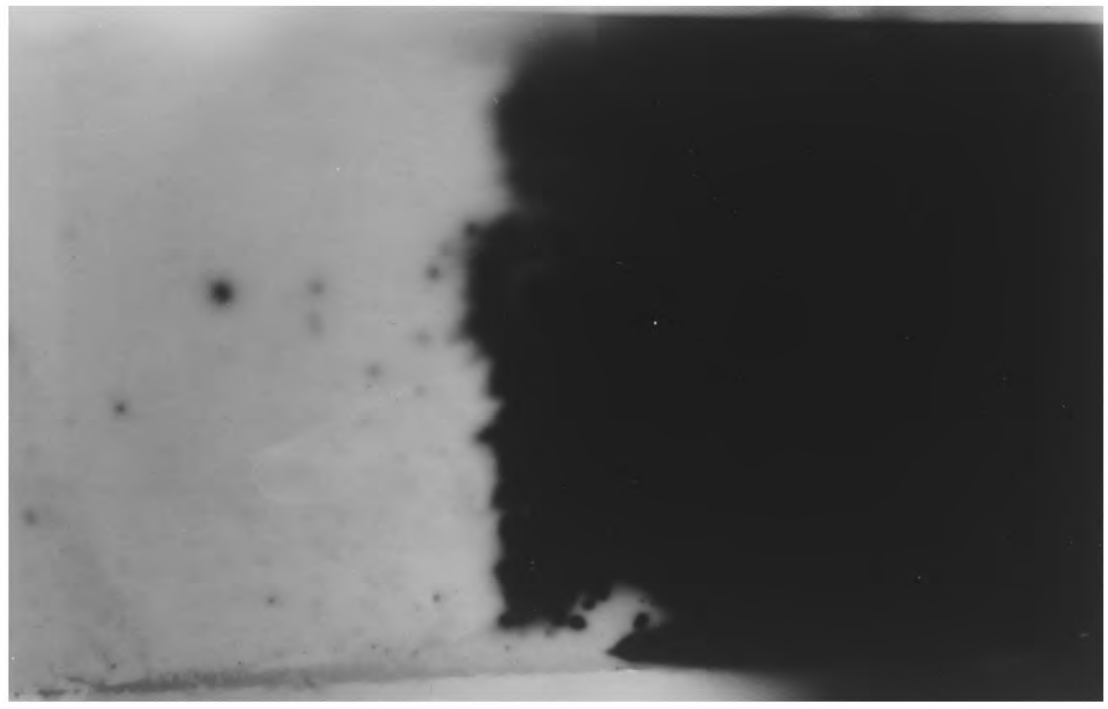


Fig. 7.11(a) Ingot 34. Radiograph after 3 days exposure with the film resting on the ingot. Shows lack of resolution and poor detail obtained using this technique. Magn x 1

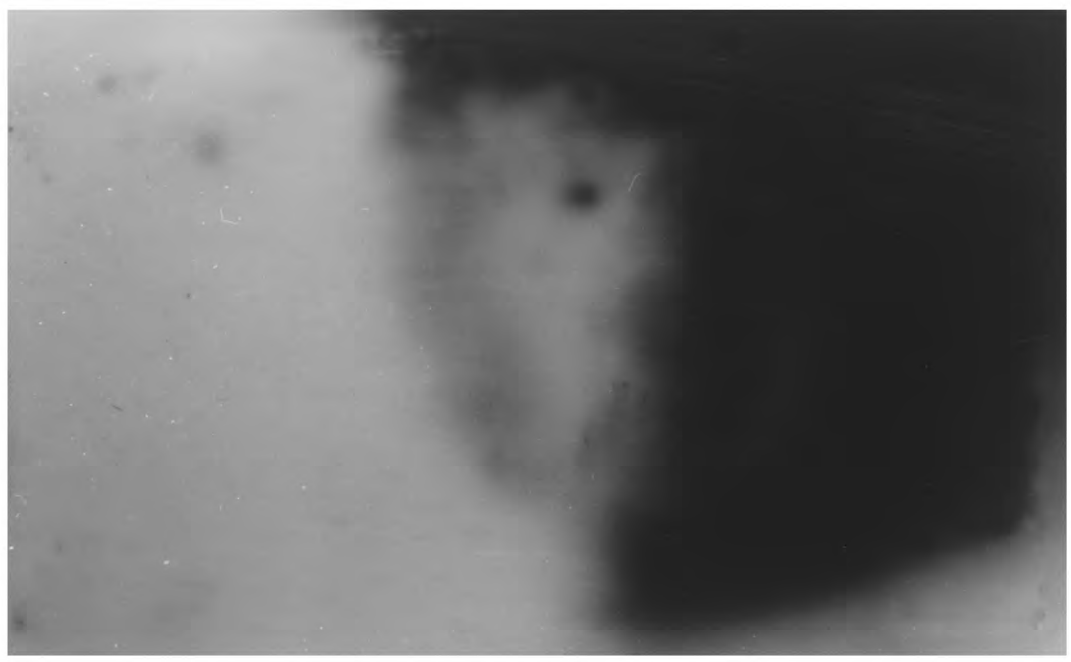


Fig. 7.11(b) Ingot 33. Radiograph after 1 day exposure with the film resting on the unskimmed surface of the ingot. Shows that penetration into the semi-solid zone was uniform throughout the ingot section (cf fig 7.9(c).)
Magn x 1

In order to check that the technique did produce an initial uniform distribution of radioactivity a 'no growth' run (run 35) was performed. In this run the radioactive addition was made on pouring and the alloy charge was then allowed to lose the bulk of its superheat as normal. However, once the charge had attained a stable temperature just above the liquidus temperature of the alloy it was quenched. No air cooling was passed through the copper chill block. Plate 7.12(a) is a photograph of a contact autoradiograph taken from the skimmed surface of the quenched ingot. The radiograph appears uniformly dark over most of the ingot surface indicating good homogeneity. There are a few large light patches towards the bottom of the radiograph which were found to correspond exactly to shrinkage pores on the ingot surface. The smaller and fainter light patches near the top of the radiograph were also thought to correspond to shrinkage pores although some of these must have been lying below the ingot surface.

In the light of this good initial uniformity the insertion technique was used for a second run, run 36, in which the alloy charge was grown almost to completion before quenching. The total growth period was 72m00s($\pm$8s), see table 7.3. The temperatures registered by the four sample thermocouples on quenching were:-

TABLE 7.6.

thermocouple	A	B	C	E
distance from chill cm ($\pm$0.02cm)	0.49	2.78	4.12	7.73
Temperature ^{o}C ($\pm\frac{1}{4}^{o}$C)	163$\frac{1}{2}^{o}$C	170^{o}C	172$\frac{1}{2}^{o}$C	177$\frac{1}{2}^{o}$C

It can be seen from these that solidification was practically complete, with the eutectic isotherm (170^{o}C) approximately 28mm from the chill block on quenching.

Plate 7.12(b) is a photograph of a contact autoradiograph taken from the skimmed surface of ingot 36. The autoradiograph shows very clearly how the radioactive thallium solute had been redistributed during the solidification process (compare with plate 7.12(a) which was how the ingot would have appeared before growth). The dendritic structure has been outlined clearly by the

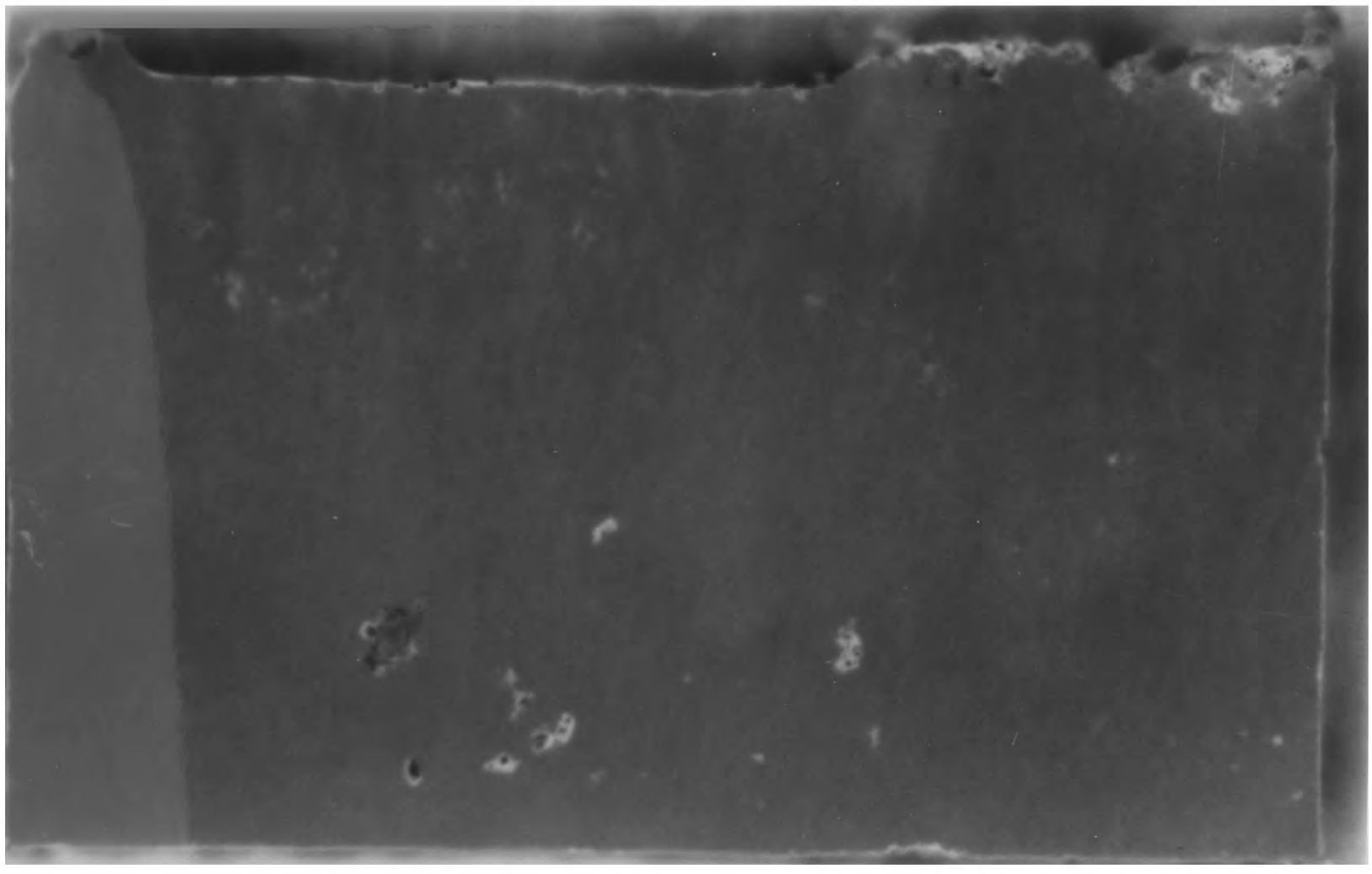


Fig. 7.12(a). Ingot 35 (No growth). Contact autoradiograph with skimmed surface. 24 hours exposure. Magn x 1·5



Fig. 7.12 (b) Ingot 36 (Full growth). Contact autoradiograph with skimmed surface. 24hrs. exposure. Magn x 1·5

microsegregation of radioactive thallium which occurred during growth. This structure is clearly columnar and is very similar in appearance to the etched macrostructure of the 'full growth' Sn-Pb ingot shown in plate 6.23(c).

There is a very obvious build-up of solute along the bottom of the ingot. This is very localised at the bottom surface near the chill end of the ingot, but gradually spreads upwards towards the mid-height of the ingot at the hot end. The 'blackest' region (i.e. that most heavily enriched in solute) appears from the radiograph to be around 2 cm from the chill face.

The remainder of the ingot section generally appears much lighter on the radiograph than the bottom region thereby indicating a fairly uniform solute distribution. That the solute content is much lower than the nominal value of 5.00wt% Tl in this the majority of the section can be demonstrated by comparing plates 7.12(a) and (b). Identical conditions were used in the production of these photographs. The pieces of X-ray film were exposed to their respective ingots for identical periods and then developed in the same tank for identical lengths of time. Similar precautions were taken in producing the photographs of the radiographs. Furthermore the pieces of radioactive alloy stick added to the charges were of roughly the same weight (6g $\pm$0.05g). Consequently the 'degree of darkness' of areas in plate 7.12(b) relative to that of ingot 35 in plate 7.12(a) should give at least a qualitative measure of the solute content. A comparison of the two plates does indicate that the composition of the majority of ingot 36 lay below 5.00wt% Tl. This visual comparison of 'darkness' is admittedly rather unsatisfactory and so a counting technique described in the next section was used to confirm these measurements.

In addition to the positively segregated region at the bottom of the ingot, heavily segregated 'channels' of material are clearly present in the bottom quarter of the ingot section near the chill face. Their general position and direction provide further remarkably good evidence of the gravity-driven fluid flow cycles which must exist in these ingots during growth. The angle at which the channels slope from the chill is identical with the direction of the lower half of the flow cycle delineated by the radiotrace in ingot 33. The

channels are present mainly in the bottom half of the radiograph although they can be seen to originate near to the chill in the top half. These were the positions at which the composition analyses of Chapter 6 were inconsistent, which helps to confirm the explanation proposed for this.

On studying plate 7.12(b) closely it can be seen that there is a very solute-depleted region running down between the two main channel streaks. This is not simply a phenomenon associated with incomplete film development since several radiographs were taken from the ingot and it appeared on all of them. It seems most likely that the extra solute depletion in this region is caused by the channels leaching solute locally. This would be done by an increase in the interdendritic fluid flow rate (down the temperature gradient) in this region in order to feed the large flow of liquid in the channels. A further, and possibly connecting, explanation is that the non-equilibrium liquid in the channel furthest from the chill has to feed this region during growth. Because this liquid is richer in solute than it should be then more solid (of low solute concentration) needs to be put down to re-attain equilibrium. This could lead to the large solute depletion observed. It should be noted that anomalously low solute compositions were occasionally observed in the Sn-Pb ingots of Chapter 6 in the regions associated with channels.

It is clear from the above paragraphs that the radiograph of ingot 36, shown in plate 7.12(b), does corroborate the picture of solute redistribution built up in Chapter 6. The bulk of the ingot is negatively segregated. There is a thin ($\simeq$3mm) layer of positively segregated material along the bottom of the ingot which spreads up to approximately mid height at the 'hot' end (c.f. the six values of positive segregation in ingot 22, figure 6.28(c)). A number of very localised solute enriched channels are present near the chill face and in the bottom half of the ingots. These, together with seemingly related areas of large solute depletion, confirm the explanation proposed for anomalous composition measurements at certain positions in the Sn-Pb ingots of Chapter 6.

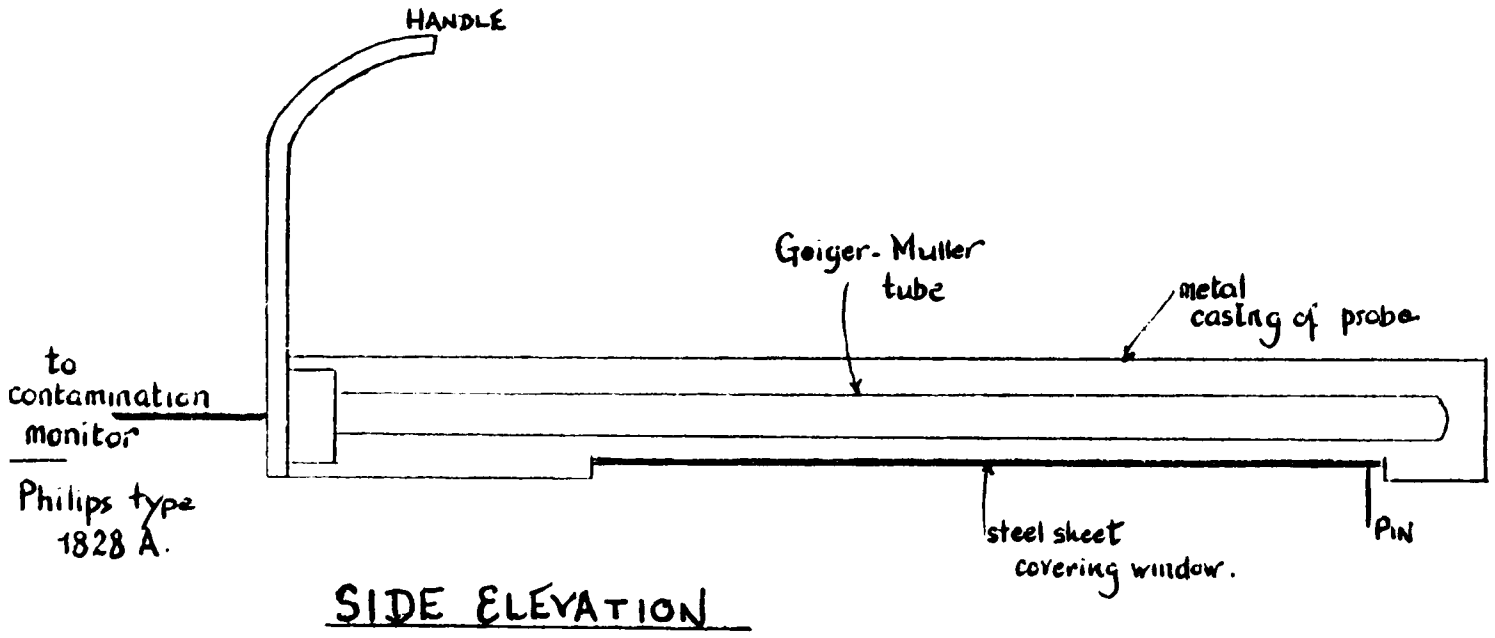
A further point worthy of note is that the solute enrichment in the channels is very localised in position. The surrounding semi-solid material is

clearly depleted in solute. This is a consequence of channel formation. Flow from cold to hot regions is non-uniform. Once a channel forms all the flow up the temperature gradient in that region tends to occur through it. Surrounding material is then fed from the channel and becomes negatively segregated.

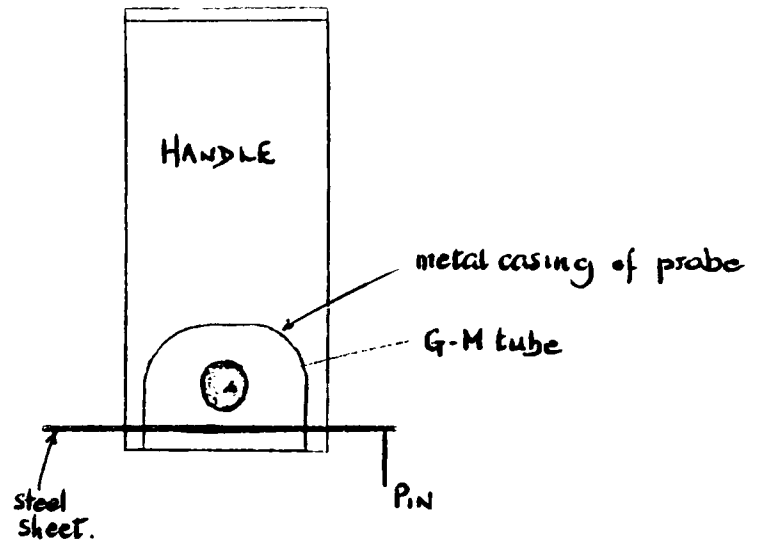
7.5.6 Activity Measurements

These measurements were intended for use in conjunction with the autoradiographs which have been presented. They give a more quantitative idea of the distribution of radioactivity within the ingots. The readings were taken using the contamination monitor mentioned previously. The probe for the monitor consisted of a long Geiger-Muller tube inside a cylindrical metal case. This case had an open window running down its length, as shown in figure 7.13. For this part of the experiment a flat,1mm. thick,steel sheet was fastened onto the probe over the window in order to reduce the effective monitoring area. The sheet was sufficiently thick to stop the β^- particles given off by thallium 204 from reaching the G-M tube. An 8mm. diameter hole drilled in the centre of the plate provided the reduced window for the tube. A pin of length 1cm. was fastened tightly onto a hole drilled in one of the corners of the steel sheet. This acted as a reference pointer so that the exact position of the hole in the plate could be calculated during counting. The counting procedure was as follows. The ingot to be studied was placed on a sheet of graph paper and the positions of the ingot edges noted. Activity readings were then taken from the ingot with the steel sheet of the probe resting flat on the ingot surface. The position of the hole for any reading was estimated from the position of the pin point just above the graph paper. The gauge of the counter was calibrated logarithmically in counts per second (c.p.s.), the most accurate part of the scale being in the range 10→200c.p.s. A hole size of 8mm. diameter in the steel plate was found by trial and error to give readings in this range from the activities present in these ingots.

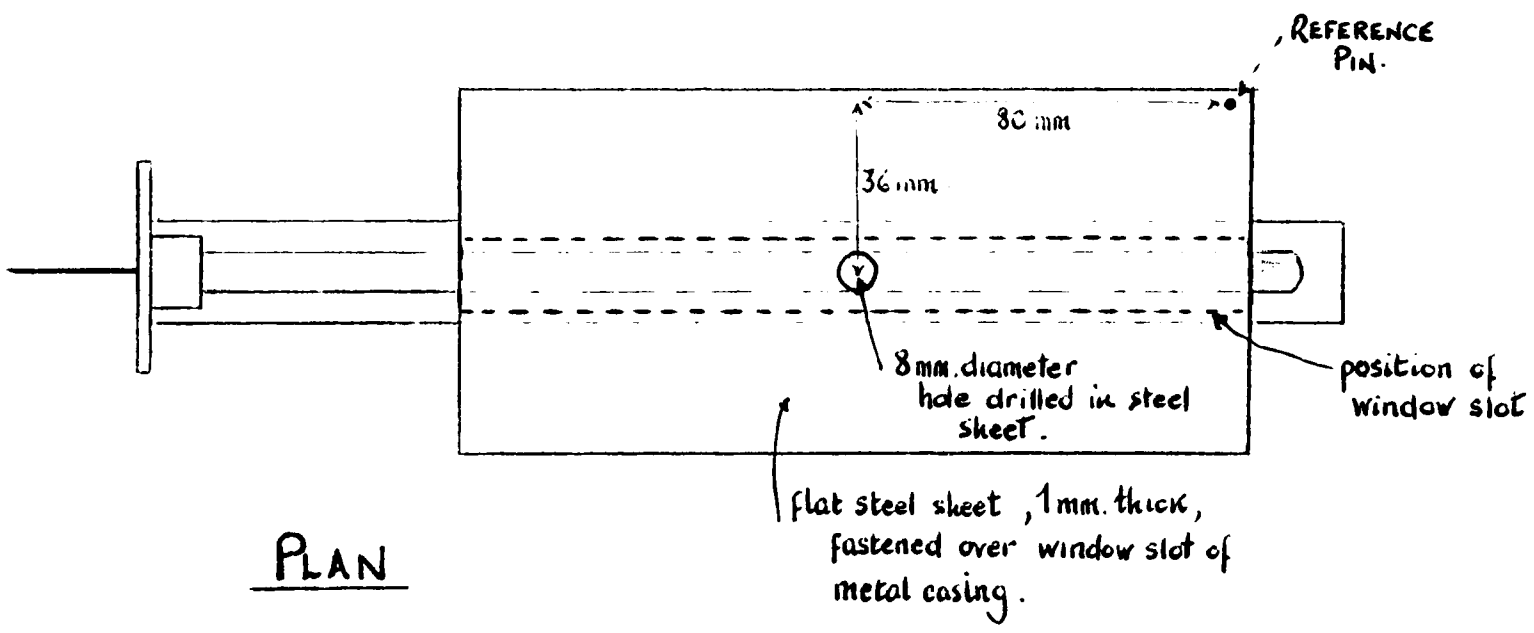
Measurements taken from ingot 35 (no growth) using this technique are given in figure 7.14(a). The count rate from the skimmed surface of the ingot



SIDE ELEVATION



END ELEVATION.



PLAN

Fig. 7.13. Arrangement employed for making activity measurements on radioactive ingots.

SCALE × 0.5

was 30 c.p.s.$\pm$5 c.p.s. and was uniform all over the surface within these limits (except for the shrinkage areas noted in the radiograph). The count rate on the unskimmed surface was also uniform but was slightly higher. This would indicate that there was a certain amount of inverse segregation from edge to centre, occurring on quenching the bulk liquid (see section 6.5.2.3). Count rates were also taken from the four narrow faces of the ingot. The 8mm. hole was less than the ingot thickness and so it was completely covered. The readings show quite large increases in activity over that obtained from the large skimmed surface. At the end in contact with the copper chill block the reading of 90$\pm$10 c.p.s. suggests a thallium concentration of around 15wt% Tl. These high count rates are presumably a result of surface exudation of thallium rich interdendritic liquid. The large thermal capacity of the copper chill, and to a lesser extent that of the sindanyo insert and the thick steel end and bottom pieces, would probably have slowed down the quenching process in the material adjacent to them. These segregations must have been very localised at the surfaces of the ingot since no significant increase could be detected in count rate near the edges of the large sides of the ingot, even when using a smaller diameter orifice on the G-M tube.

It is clear both from these activity measurements and from the autoradiographs taken from ingot 35 that the alloy charge remained homogenous during the time it was held in the furnace. There was no evidence of any gravity-stable, tin-rich, layer at the top of the liquid pool as was found by Hebditch[103] in his experiments.

The measurements taken from ingot 36 (full growth) are given in figure 7.14(b) and are obviously very different to those taken from ingot 35. The redistribution of solute as a result of solidification and ingot growth is immediately apparent. The majority of the ingot volume is depleted in solute. The count rate over much of the skimmed surface is below 20 c.p.s. as compared with a count rate of around 30 c.p.s. taken from ingot 35 for the nominal solute content of 5.00wt% Tl. Count rates of 30 c.p.s. and above are found only towards the bottom surface of the ingot. It is clear from the measurements taken from

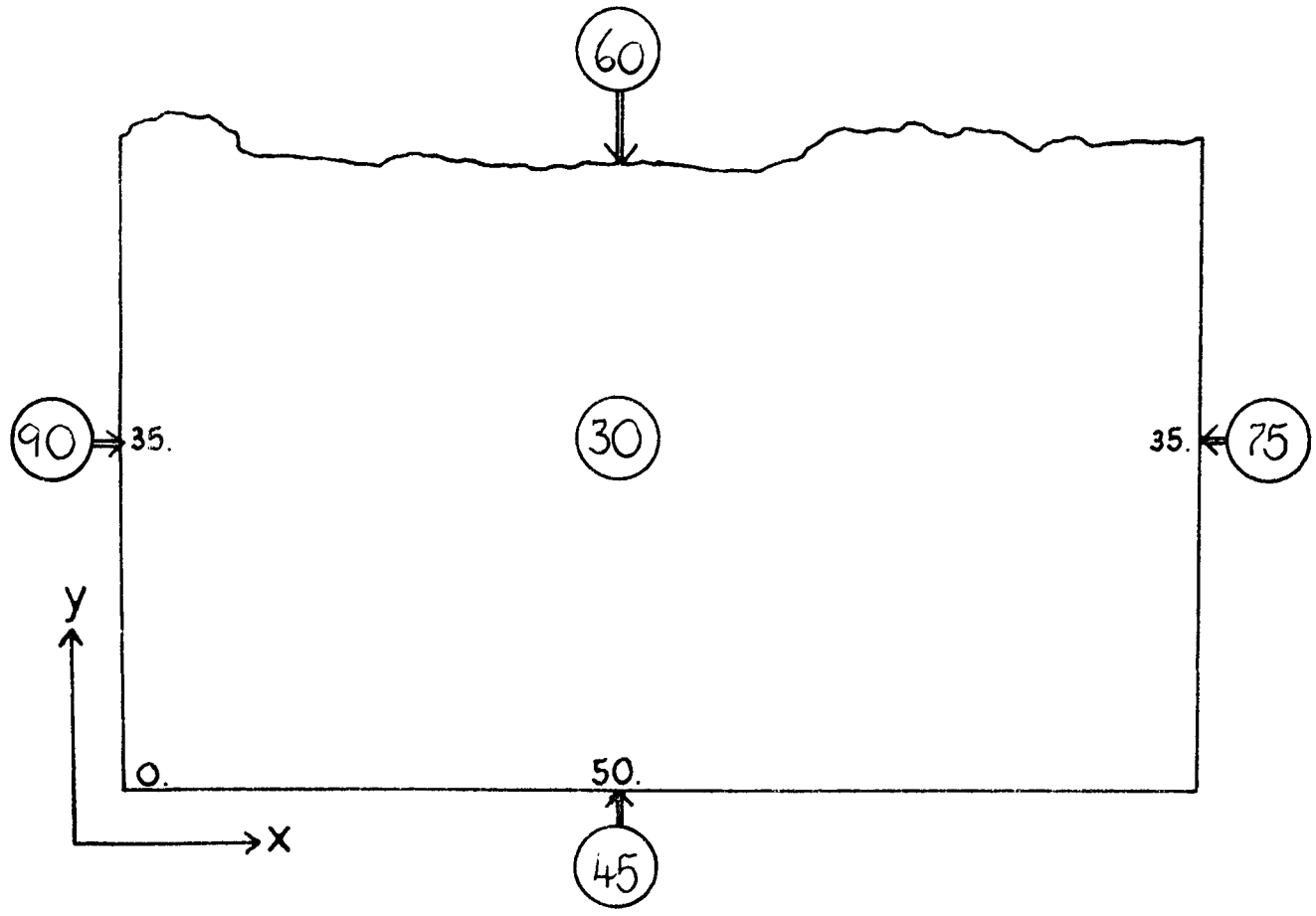


Fig. 7.14(a). Activity measurements taken from the surface of ingot 35 (No growth)

Key.

(A)	Reading through an 8 mm. diameter orifice in c.p.s.
x;y	Position of centre of orifice in mm. from reference position at bottom chill corner of ingot.

Typical errors in Measurements.

0 → 20	c.p.s.	error ± 3 c.p.s.
20 → 80	c.p.s.	error ± 5 c.p.s.
80 → 150	c.p.s:	error ± 10 c.p.s.
150 → 200	c.p.s.	error ± 15 c.p.s.

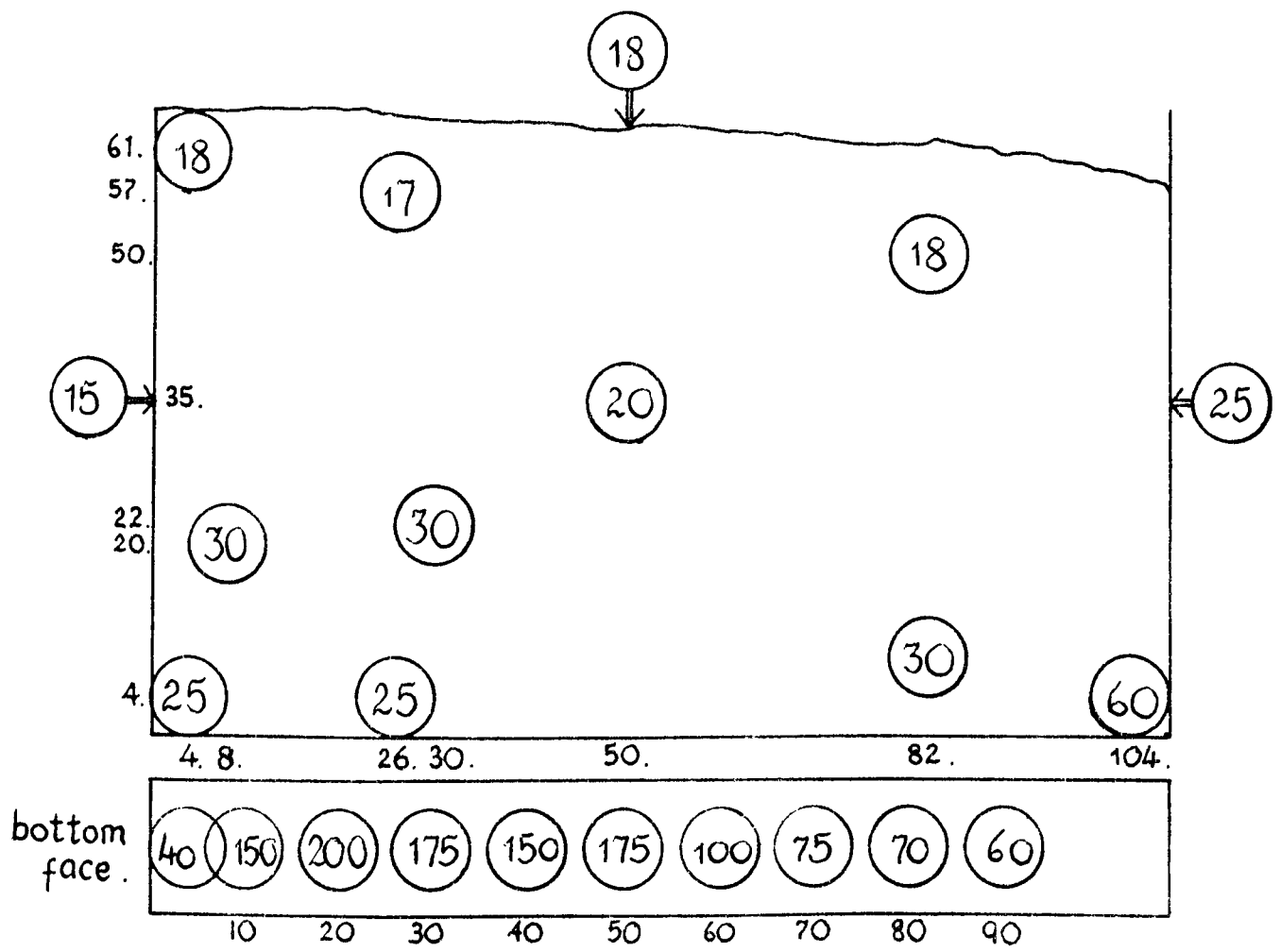


Fig 7.14(b) Activity measurements taken from the surface of ingot 36 (Full growth)

the bottom surface itself that there is a very large solute build-up there. Indeed the count rates of 175 c.p.s. measured towards the chill end of the bottom surface suggest an average composition of around 30wt% Tl. This build-up must however be very localised (in say the bottom 1 or 2mm.) since the readings taken on the skimmed surface in this region are only 25 c.p.s. The count rate on the bottom surface decreases to around 60 c.p.s. at the 'hot' end of the ingot, suggesting a composition of around 10wt% Thallium. This solute enrichment is far less localised, a similar count rate being observed in this region on the skimmed surface.

Measurements were also taken from the skimmed surface of ingot 36 in the regions where the channel streaks were observed in the autoradiograph, plate 7.12(b). The count rates from these regions were found to be 30 c.p.s. ($\pm$5 c.p.s as compared with an average background count of 20 c.p.s. ($\pm$3 c.p.s.) from surrounding areas of the ingot surface. Assuming that the solute-enriched channels took up around $^1/_{10}$th of the area of the counter window then the actual activity of the channel regions, 'a' c.p.s., say, would be given by:-

$$0.1\ a + 0.9 \times 20 = 30$$

$$\text{Therefore } a = 120 \text{ c.p.s.}$$

which would be equivalent to a solute content of around 20wt% thallium, although the calculation is only intended to give a rough idea of the large amounts of solute present in the channels.

Finally, there is no evidence of any inverse segregation having occurred at the edges or sides of ingot 36 during growth. This is understandable given the uniform growth conditions which prevailed, and confirms that the large positive segregations found on the edges of ingot 35 were caused by the quenching process.

Activity measurements were also taken from ingots 33 and 34. These are shown in figures 7.15(a) and 7.15(b) respectively. A direct comparison of count rate with that of ingot 35 is not possible since in these ingots the radiotrace was injected during growth. However, injection was performed at approximately half growth and so if the tracer had mixed uniformly into the bulk liquid pool

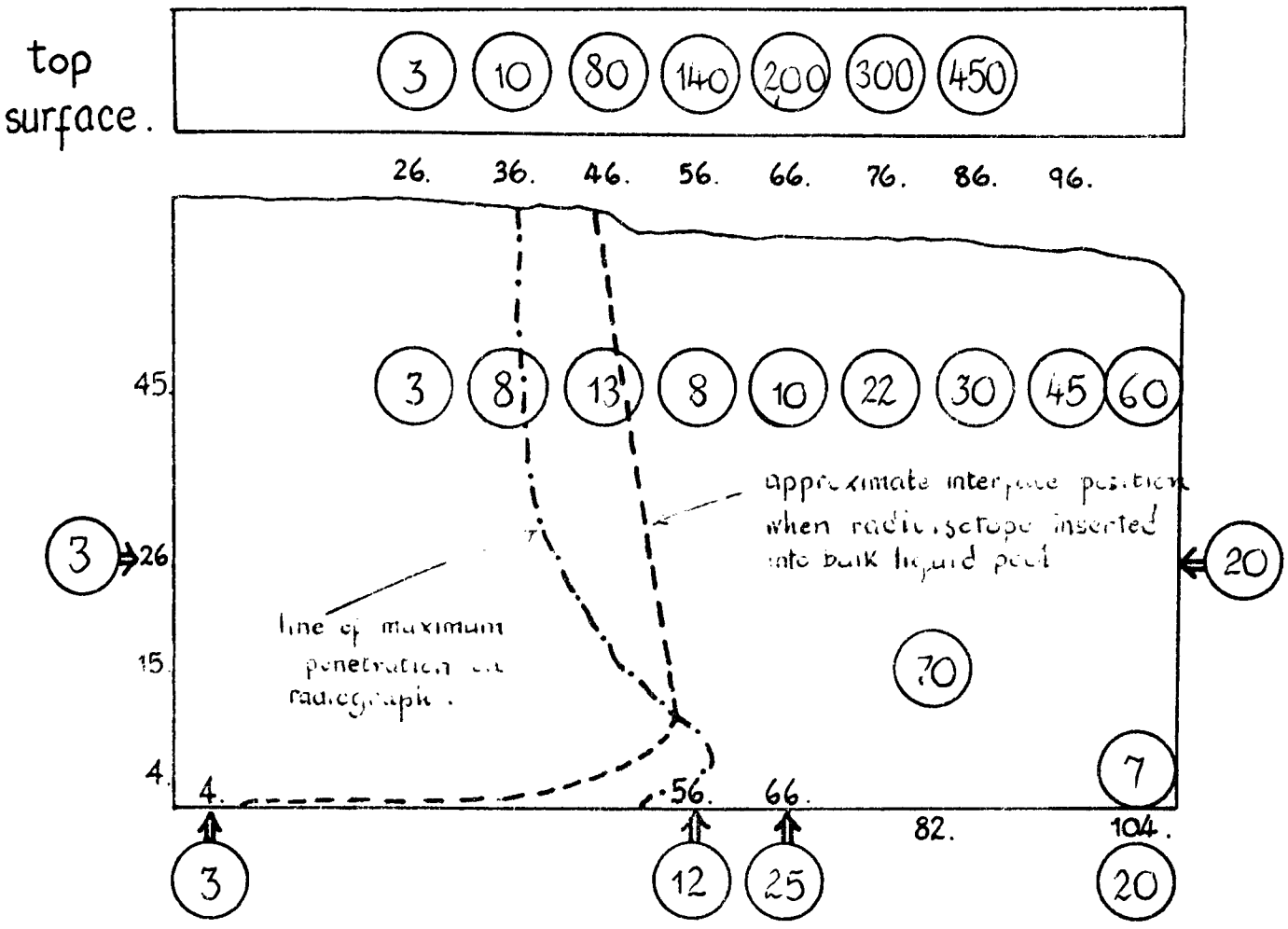


Fig. 7.15(a). Activity measurements taken from the surface of ingot 33.

Key - as for Fig. 7.14.

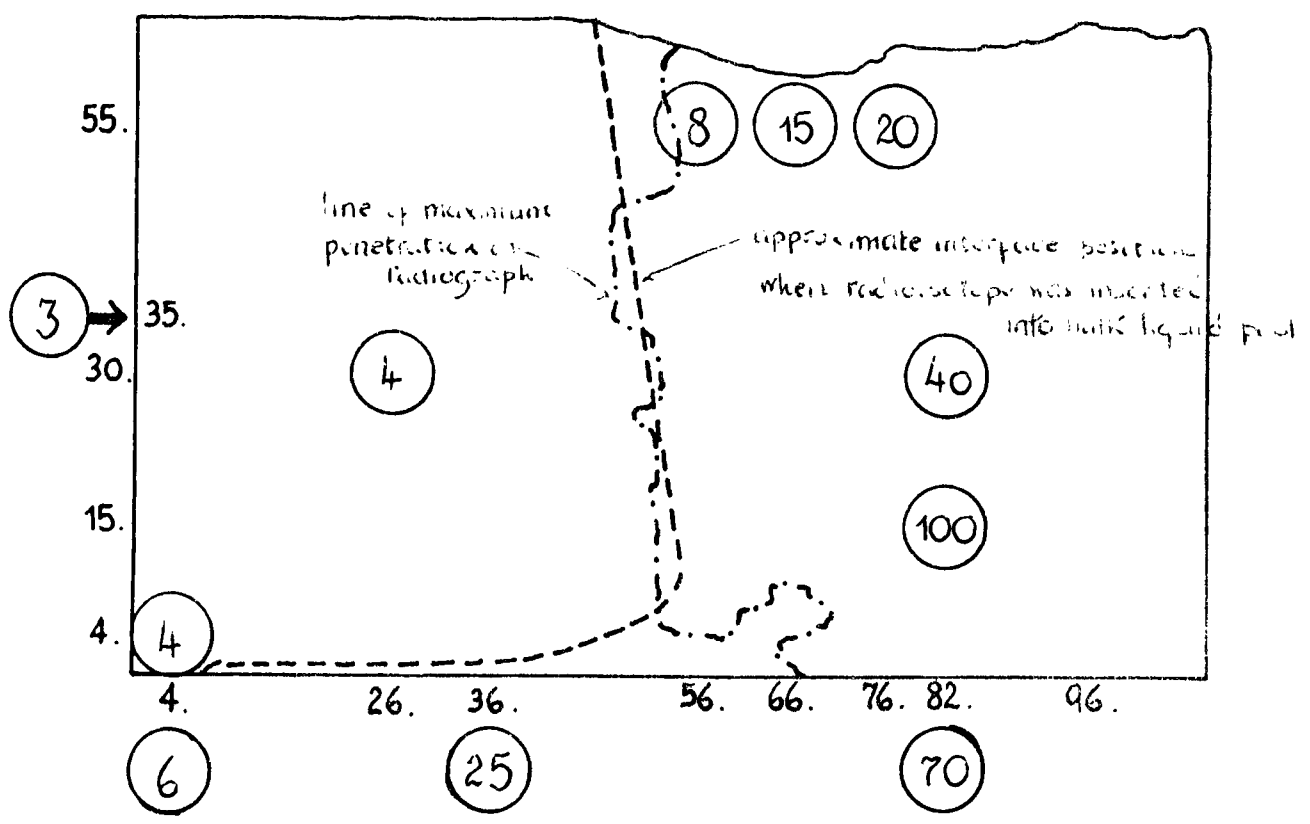


Fig. 7.15(b). Activity measurements taken from the surface of ingot 34.

the expected activity would have been around 60 c.p.s. (twice that of ingot 35). It can be seen from the measurements that the tracer has not mixed uniformly on either ingot. In the case of ingot 34 this may well have been, as suggested earlier, due to the lack of time between insertion and quenching. However the very high count rates observed on the top surface of ingot 33 could only have been caused by floatation of the inserted radioactive alloy liquid, as suggested in section 7.5.4.

7.6 Summary and Conclusions

(a) The model casting system provided reproducible growth conditions for the ingots produced in this experiment.

(b) The silica tube insertion technique was simple, efficient, and did not disturb the semi-solid structure of the growing ingots.

(c) Radioactive liquid was observed to have penetrated deep into the semi-solid zone from the bulk liquid pool. It was estimated that interdendritic fluid flow was still occurring up to at least $g_L = 0.40$. The conclusions of Chapter 6 concerning the extent of fluid flow were therefore corroborated.

(d) The extent of fluid flow in the semi-solid zone was the same throughout the ingot cross-section, indicating that edge effects were minimal.

(e) Highly solute enriched channels were observed in the radiograph of the fully grown ingot, and there was evidence of a gravity-stable, thallium-rich layer adjacent to the bottom surface in all ingots where growth had occurred.

CHAPTER 8

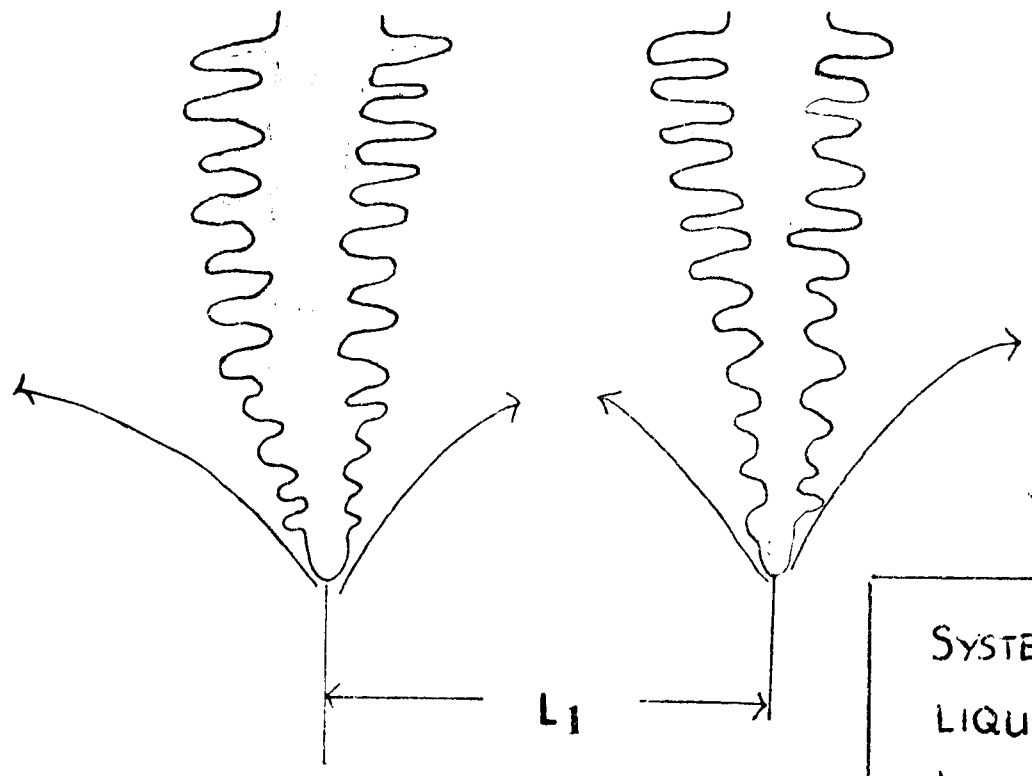
MEASUREMENT OF LIQUID METAL DENSITIES

8.1 Introduction

The work described in this chapter involved the measurement of liquid metal densities with a view to developing an alloy where the density of the interdendritic liquid remained constant throughout the freezing range. Gravitational interdendritic fluid flow would be eliminated in such an alloy through lack of driving force. This would allow other types of macrosegregation, such as inverse and equi-axed, to be studied more satisfactorily, and it would also permit accurate measurements of dendrite spacing to be made without the complicating influence of gravitational flow.

Experimental studies on primary dendrite spacings in metals and alloys have in the past often exhibited marked differences in their results. Hunt[145] has attributed this to a hitherto unexpected variable in the experiments, namely the direction of growth with respect to gravity. Burden and Hunt[99] have recently demonstrated that in the transparent NH_4Cl/H_2O system the average primary dendrite spacing was ten times greater for growth vertically downwards than for growth vertically upwards under otherwise identical growth conditions. Burden[146] has observed similar variations of dendrite spacing with growth direction in continuously cast steel ingots produced on a curved mould machine. Burden and Hunt[99] explain this variation in terms of the gravitational interdendritic fluid flow mechanism, see fig. 8.1(a), and they conclude that for dendrite spacing measurements to be meaningful they should be carried out under conditions of controlled fluid flow.

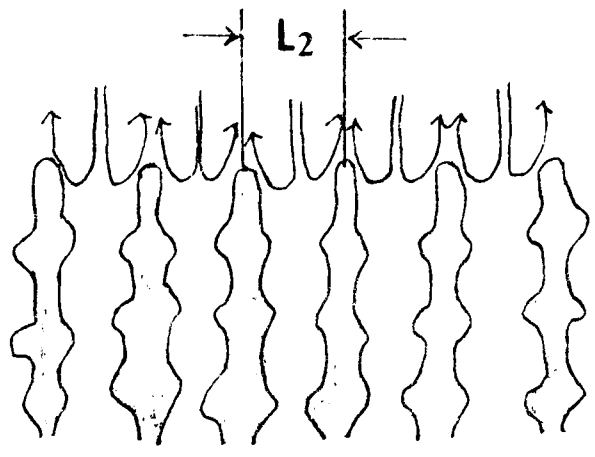
In order to overcome gravitational effects some workers have in the past arranged that the alloy growth direction in their experiments be such that a stable density gradient was produced in the interdendritic liquid. For example, Flemings and co-workers[70] in their studies of inverse segregation grew their



Growth vertically downwards.
Lighter, solute-enriched liquid in mushy zone gives a gravity-stable situation.

SYSTEM WHERE INTERDENDRITIC LIQUID BECOMES LESS DENSE AS SOLUTE CONTENT INCREASES (e.g $NH_4Cl - H_2O$)

$L_1 \gg L_2$



Growth vertically upwards.
Lighter, solute-enriched interdendritic liquid has a tendency to float out of the mushy zone - aids solute rejection - dendrites grow closer together.

Fig 8.1 (a) Schematic illustration of Burden & Hunt[99] arguement to explain the large difference in primary dendrite spacing (L) between columnar dendrites growing vertically upwards and downwards

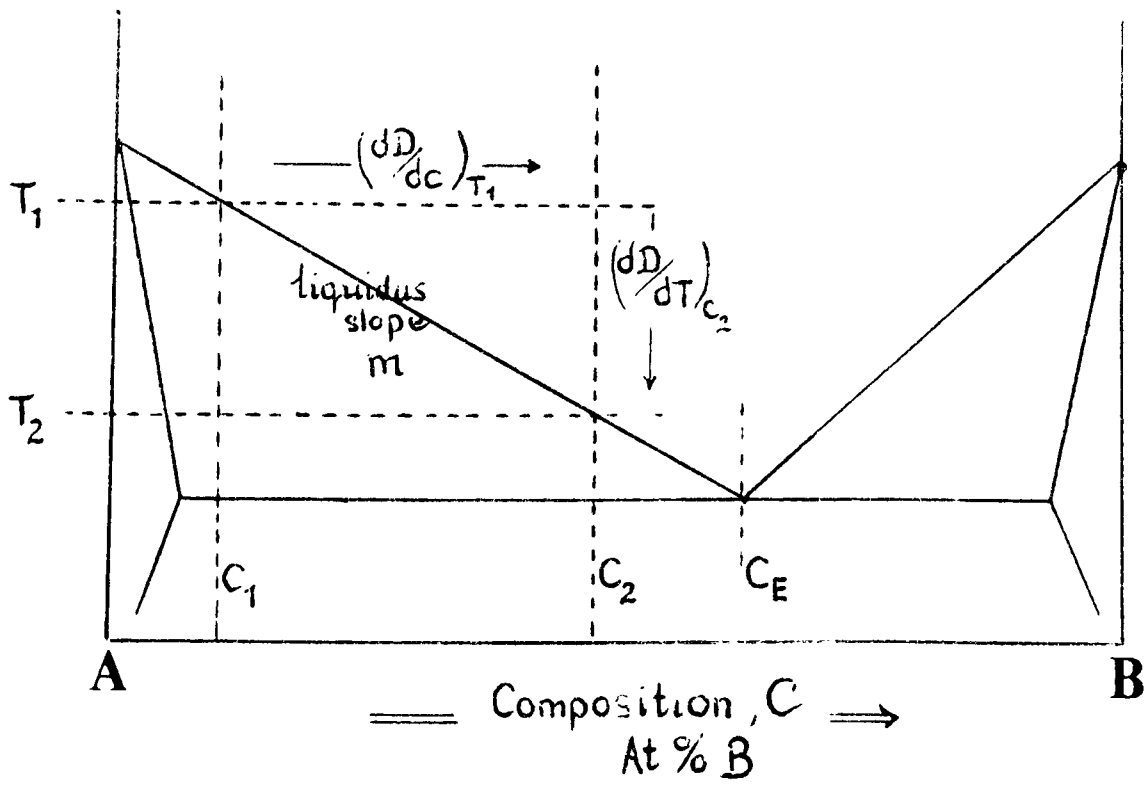


Fig 8.1 (b). Idealised equilibrium phase diagram for binary alloy system AB.

Al-Cu alloys vertically upwards because the interdendritic liquid became denser as freezing progressed. However, it has been demonstrated by both Burden et al [147] and the present author [86] that gravity flow may occur even in such cases of supposedly stable density gradient if the isotherms are not perfectly horizontal.

In view of the pieces of work described in the preceding paragraphs it was felt that the best alloy system to use for dendrite spacing measurements would be one in which the interdendritic liquid density did not alter during freezing. Such an alloy would also be very useful in studying macrosegregation mechanisms other than gravity flow. It was therefore concluded that attempts should be made to develop such an alloy. It was eventually decided that the best way of doing this would be to set up a precision technique for measuring liquid metal densities. This was felt to be a more acceptable approach than simply using the absence of gravity flow phenomena as a guide to zero interdendritic liquid density change. Furthermore it was felt that a precision density measurement technique, if successful, could provide a great deal of quantitative information about the magnitude of the driving force behind gravity flow in many alloy systems. Such information is at present sparse and often inaccurate, but it would be of great use to any future theoretical model of the gravity flow mechanism.

The precision density measurement technique was used in connection with a quantitative theoretical treatment of liquid metal alloy density variations. This treatment is described in detail in the following section. It was used to give an approximate prediction of an alloy system and composition where density change down the liquidus surface would be zero. This alloy was then studied using the density measurement technique to identify what, if any, variations in density occurred. If variations were observed, then adjustments were made to the alloy composition until the correct composition for zero density change was obtained, this being verified by the density measurement technique. An alloy of the correct composition was then grown in the slice

cast apparatus described in chapter 6 to corroborate that it exhibited no gravitational flow effects.

8.2 Theoretical Calculation of required alloy composition

Consider fig. 8.1(b) which shows an idealised equilibrium phase diagram for a binary alloy system AB. The liquidus slopes are assumed to be linear and there is a eutectic at C_E At.%B. Consider further the two alloy compositions C_1 and C_2 At.%B and their intersection with the A-rich liquidus line. Now if the density of liquid of composition C_1 at temperature T_1 is D_1, and that of C_2 at temperature T_2 is D_2 then the two densities may be related by the equation

$$D_2 = D_1 + \left(\frac{dD}{dC}\right)_{T_1} (C_2 - C_1) + \left(\frac{dD}{dT}\right)_{C_1} (T_2 - T_1) \qquad (8.1)$$

assuming that $(dD/dc)_{T_1}$ and $(dD/dT)_{c_1}$ are constant in these temperature and composition ranges respectively. Furthermore,

$$m = (T_2 - T_1 / C_2 - C_1) \qquad (8.2)$$

and this combined with eqn. (8.1) gives:-

$$D_2 - D_1 = (C_2 - C_1)\left[\left(\frac{dD}{dc}\right)_{T_1} + m\left(\frac{dD}{dT}\right)_{c_1}\right] \qquad (8.3)$$

This equation may be extended to cover the density variation of the liquid down the whole length of the liquidus line. Assuming that m is constant, and that $(dD/dc)_{T_1}$ and $(dD/dT)_{c_1}$ may each be represented by a single constant value over the whole temperature and composition range of the liquidus line ($T_M < T < T_E$ and $C_M < C < C_E$) then:-

$$\left(\frac{dD}{dc}\right)_{\text{liquidus}} = \left(\frac{dD}{dc}\right)_T + m\left(\frac{dD}{dT}\right)_c \qquad (8.4)$$

Equation (8.4) represents the change in density of an A-rich liquid as its composition falls down the liquidus line. It has been demonstrated by several workers[66,148] that the composition of interdendritic liquid closely follows the liquidus line of the equilibrium phase diagram as freezing progresses. Consequently for an alloy with no density change in interdendritic liquid then:-

$$(dD/dc)_{\text{liquidus}} = 0 \qquad (8.5)$$

therefore

$$\left(\frac{dD}{dc}\right)_T + m\left(\frac{dD}{dT}\right)_c = 0 \qquad (8.6)$$

In eqn. (8.6) the term $(dD/dT)_c$ is always negative. For an alloy with $k_o < 1$ then m is also negative, and so the product $m(dD/dT)_c$ is always positive. Therefore in order to satisfy eqn. (8.6) the term $(dD/dT)_c$ must be negative, i.e. the solute must be less dense than the solvent. It should be noted however that the magnitude of $m(dD/dT)_c$ is usually quite small (typically $<10^{-3}$ g/cc/°C) and so the densities of solute and solvent cannot be too dissimilar.

Owing to the limited experimental facilities available it was necessary to confine investigations to the lower melting point alloy systems ($T_M < 450$°C). The common elements which fall into this category are listed in Table 8.1, below, together with their accepted liquid phase density at 450°C.[149]

Table 8.1

Element	Tl	Pb	Bi	Cd	Sn	In	Zn
D_{450} g/cc	11.1	10.5	9.83	7.87	6.87	6.80	6.54

It is clear from this table that the most promising binary systems are Sn-In and Sn-Zn. However, it was shown by Hebditch[103] that alloys from both of these systems are subject to gravitational interdendritic fluid flow. For primary tin alloys the interdendritic liquid increases in density with increasing indium content and decreases in density for increasing zinc content. In view of these findings it was felt that eqn. (8.6) would only be satisfied in a three element system where the proportion of the two solute elements could be suitably adjusted to give $(dD/dc)_T$ of the required sign and magnitude.

Consider fig. 8.2 which shows the liquidus surface in the A-rich corner of the ternary AXY equilibrium phase diagram. Assume firstly that the liquidus composition an alloy of initial composition C_x^o At %X, C_y^o At %Y falls down the surface such that $C_x : C_y$ remains constant (as shown in fig. 8.2(b)). This then allows the ternary alloy to be treated as a pseudo-binary AB, where C_B

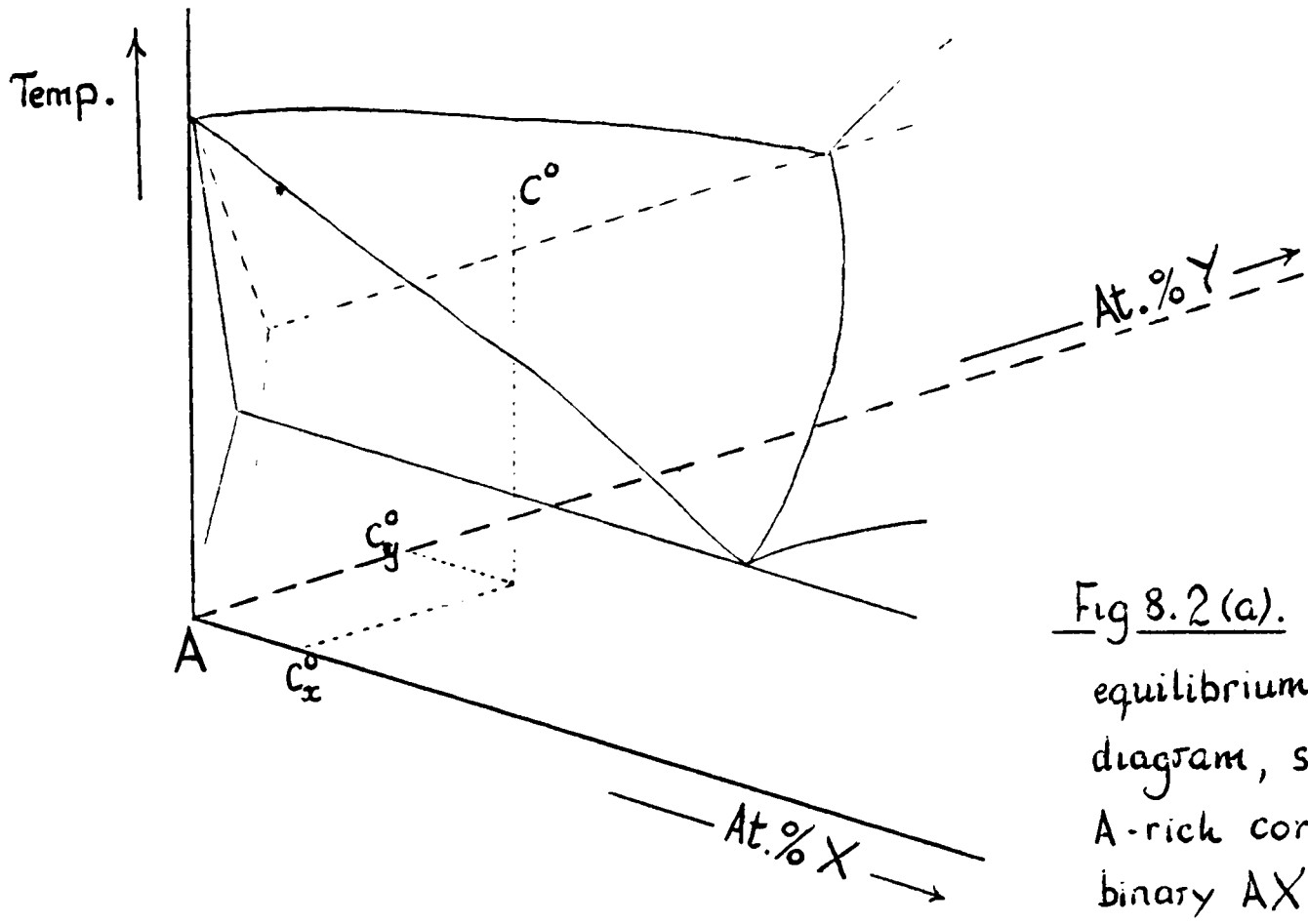


Fig 8.2(a). Ternary equilibrium phase diagram, showing A-rich corner. The binary AX and AY systems both have simple eutectics.

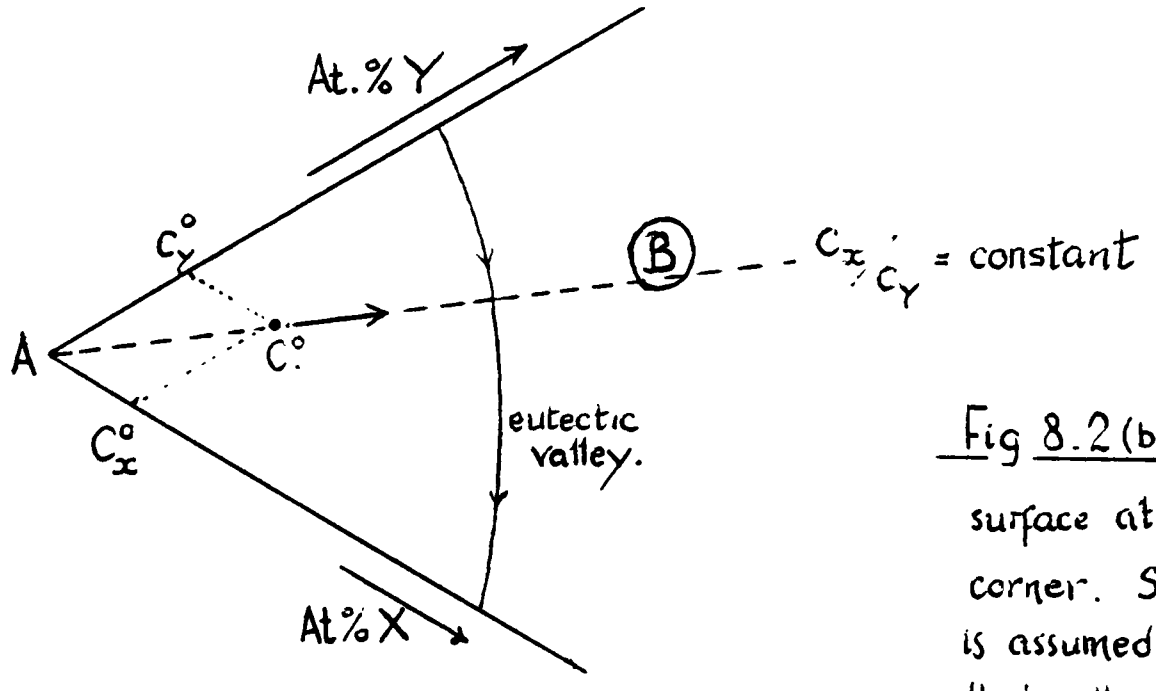


Fig 8.2(b). Liquidus surface at the A-rich corner. Slope of surface is assumed to be such that alloy of initial comp^n C° falls down surface such that C_x/C_y remains constant as shown.

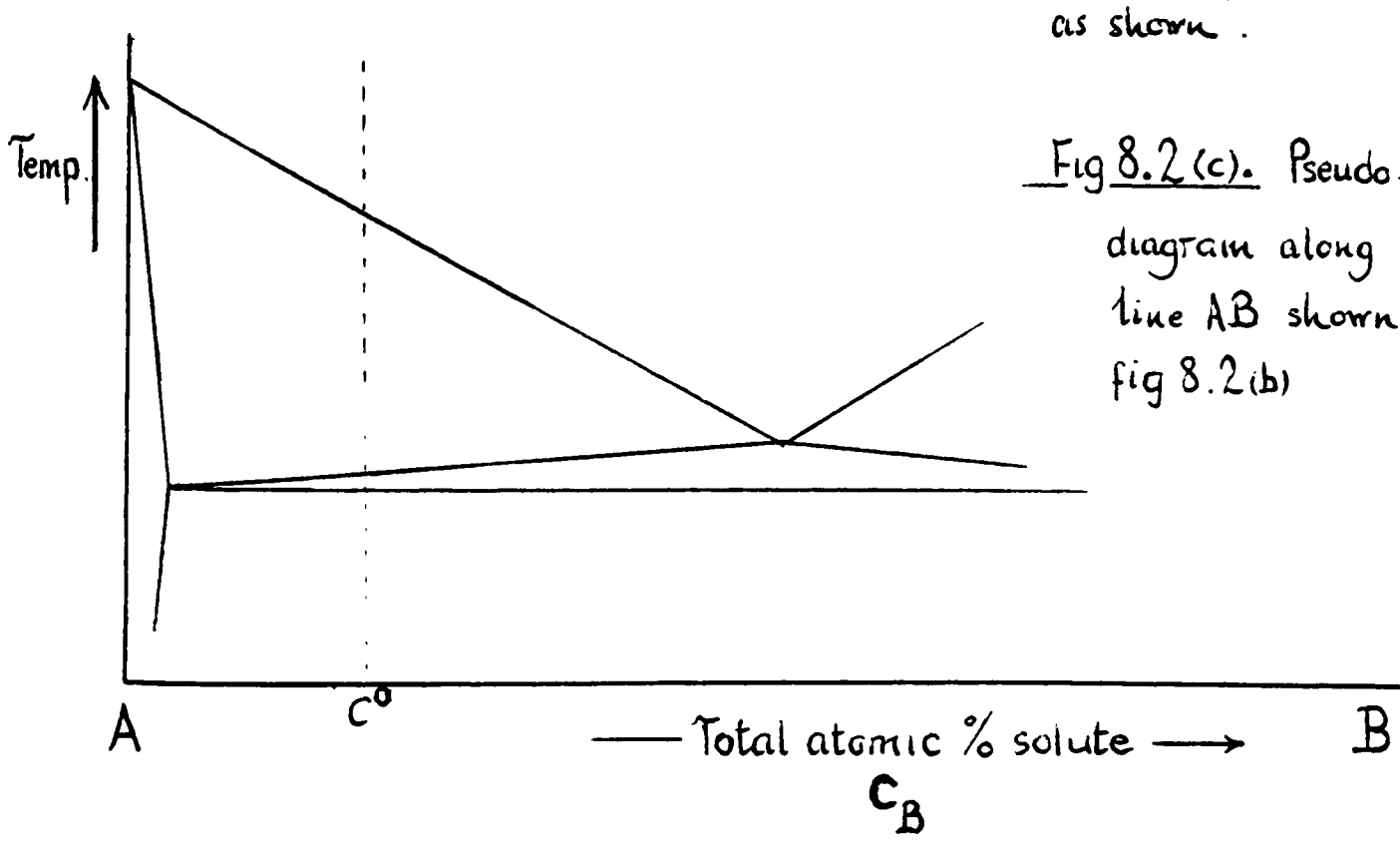


Fig 8.2(c). Pseudo-binary diagram along the line AB shown in fig 8.2(b)

is the total atomic % of solute in the alloy, see fig. 8.2(c). Assuming also that the terms $(dD/dc_B)_T$ and $(dD/dT)_{C_B}$ of the pseudo binary may be calculated from an atom fraction combination of the relevant binary A-X and A-Y terms (i.e. that the alloy is an ideal solution), then

$$\text{for } C_x/C_y = R \quad \text{where R is a constant} \tag{8.7}$$

we have

$$\left(\frac{dD}{dT}\right)_{c_B} = \left(\frac{dD}{dT}\right)_{c_x}\left(\frac{R}{R+1}\right) + \left(\frac{dD}{dT}\right)_{c_y}\left(\frac{1}{R+1}\right) \tag{8.8}$$

and

$$\left(\frac{dD}{dC_B}\right)_T = \left(\frac{dD}{dC_x}\right)_T\left(\frac{R}{R+1}\right) + \left(\frac{dD}{dC_y}\right)_T\left(\frac{1}{R+1}\right) \tag{8.9}$$

Substituting eqns. (8.8) and (8.9) into eqn. (8.4) gives an expression for the density variation down the liquidus line of the pseudo-binary A-B as:-

$$\left(\frac{dD}{dC_B}\right)_{\text{liquidus}} = \frac{1}{R+1}\left[R\left(\frac{dD}{dC_x}\right)_T + \left(\frac{dD}{dC_y}\right)_T + m_{AB}R\left(\frac{dD}{dT}\right)_{C_x} + m_{AB}\left(\frac{dD}{dT}\right)_{C_y}\right] \tag{8.10}$$

Therefore for a ternary alloy with no density change down its liquidus line, we may equate eqn. (8.10) to zero, and re-arrange to give an expression for R of the form:-

$$R = -\frac{(dD/dc_y)_T + m_{AB}(dD/dT)_{c_y}}{(dD/dc_x)_T + m_{AB}(dD/dT)_{c_x}} \tag{8.11}$$

It was felt that the assumptions used in deriving eqn. (8.11) were most likely to be valid in an alloy where one of the solute elements (Y, say) was present in only small quantities, so that the supposed pseudo-binary section would be very similar to the A-X binary.

It was decided that the best system to use as the major A-X binary would be Sn-Zn. It was known from Hebditchs work[103,150] that, for tin-rich alloys in this system, the value of $(dD/dc)_{\text{liquidus}}$ was negative but not very far removed from zero. Small amounts of a third, denser element should therefore be able to increase the value of $(dD/dc)_T$ sufficiently to make eqn. (8.4) equal to zero. The Sn-Zn system also had the advantage of having a eutectic

reaction at a composition of only 15.2 At.% Zn. This means that the assumption of constant m, $(dD/dT)_c$ and $(dD/dc)_T$ used in deriving eqn. (8.4) are more likely to be valid.

Lead was chosen as the denser minority solute element of the ternary alloy. Its density is sufficiently far removed from that of tin to make $(dD/dc_{Pb})_T$ large and positive, and the binary Sn-Pb phase diagram shows a single eutectic at 26.1 At.% Pb. Furthermore, a considerable amount of apparently reliable work had already been performed on the liquid density values of binary Sn-Pb alloys by Thresh et al,[151] and others[152,153] from which values of $(dD/dc_{Pb})_T$ and $(dD/dT)_{c_{Pb}}$ could be readily calculated.

Equation (8.11) for the Sn-Zn-Pb ternary becomes:-

$$R = - \frac{(dD/dc_{Pb})_T + m_{AB}\,(dD/dT)_{c_{Pb}}}{(dD/dc_{Zn})_T + m_{AB}\,(dD/dT)_{c_{Zn}}} \qquad (8.12)$$

Data for $(dD/dc_{Zn})_T$ and $(dD/dT)_{c_{Zn}}$ were not available in the literature and so it was first necessary to obtain values for these coefficients of the Sn-Zn binary system using the precision density measurement technique. These experimentally determined coefficients were then used with the corresponding coefficients for the Sn-Pb binary system calculated from Thresh's work[151] to predict a value for R.

8.3 Choice of Density Measurement technique

Two major reviews[153,154] of liquid metal density measurement techniques were found in a search of the literature. These indicated that those techniques which had been used in the past could be split up into four main areas, namely:-

(a) Methods employing Archimedes' Principle - i.e. measuring the upthrust which the liquid metal exerts on an inert sinker, or measuring the upthrust experienced by a container filled with the liquid metal in an inert fluid.

(b) Pycnometer methods, which involve measuring the weight of liquid metal required to fill a container of known volume.

(c) Dilatometric methods, which involve measuring the volume, and change in

volume, of a known mass of liquid metal.

(d) Hydrostatic pressure methods, which involve measuring the pressure required either to maintain a column of liquid to a known height, or to just force a bubble of gas from a tube immersed to a certain depth in the liquid metal (known as the maximum bubble pressure technique).

Careful study of the literature indicated that the two techniques capable of providing the optimum accuracy in density measurements were the pycnometer and maximum bubble pressure methods. Of these two the latter seemed initially to be the best suited to this experiment because it would allow a continuous assessment of density over a range of temperature, thereby permitting an easy determination of $(dD/dT)_c$. The bubble pressure technique was therefore chosen to perform the density measurement in this work.

It should be noted that the degree of accuracy required from the chosen technique could be judged from Hebditch's work on the Sn-Zn binary system.[84] He estimated that the variation in density down the Sn-rich liquidus line was less than 0.04 g/cc between pure Sn at 232°C and Sn-Zn eutectic at 198°C. The average density was around 7 g/cc and so this density variation represented a change of only 0.57%. However, Hebditch still observed gravitational flow in the interdendritic liquid of Sn-Zn alloys. Consequently the density measurement technique had to be capable of a reproducibility of at least 0.1% in the density determinations if it was to be of use in establishing an alloy with zero gravity flow.

8.4 Maximum Bubble Pressure Technique

8.4.1 General Outline and Review

This technique was first developed by Jaeger[26] to measure surface tension forces, but it has since been employed by many workers as a method for measuring liquid metal densities. It essentially involves the measurement of the pressure required to just detach a bubble of an inert gas from the tip of a capillary tube immersed to a certain depth in the molten metal. The

calculation of this pressure is given beneath fig. 8.3, overleaf. In order to eliminate the surface tension terms in this expression the pressure required to detach a bubble from the tube at a different known depth is measured. The measured difference in maximum pressure then gives an expression for the density of the liquid metal in terms of the difference in the immersion depths of the tube, as in eqn.(8-13.).

Veazey and Roe[153] in a review article on liquid metal density measurement conclude that 'the maximum bubble pressure method is probably the most convenient and reliable method available at present, and is capable of yielding a reasonable degree of accuracy.'

A comprehensive search of the copious amount of literature available on the technique uncovered the following important points:-

(a) The accuracy of the technique was claimed by various workers to lie between $\pm$ 2 x 10^{-4} %[156] and $\pm$ 2%.[157] Lucas and co-workers, in recent work on low melting-point alloy systems,[158,159] claimed accuracies of between $\pm$ 0.08% and $\pm$ 0.30%, and these values were typical of the majority of work using the technique. The technique therefore appeared to be capable of achieving the accuracies required in the present experiment providing it was refined to its optimum performance.

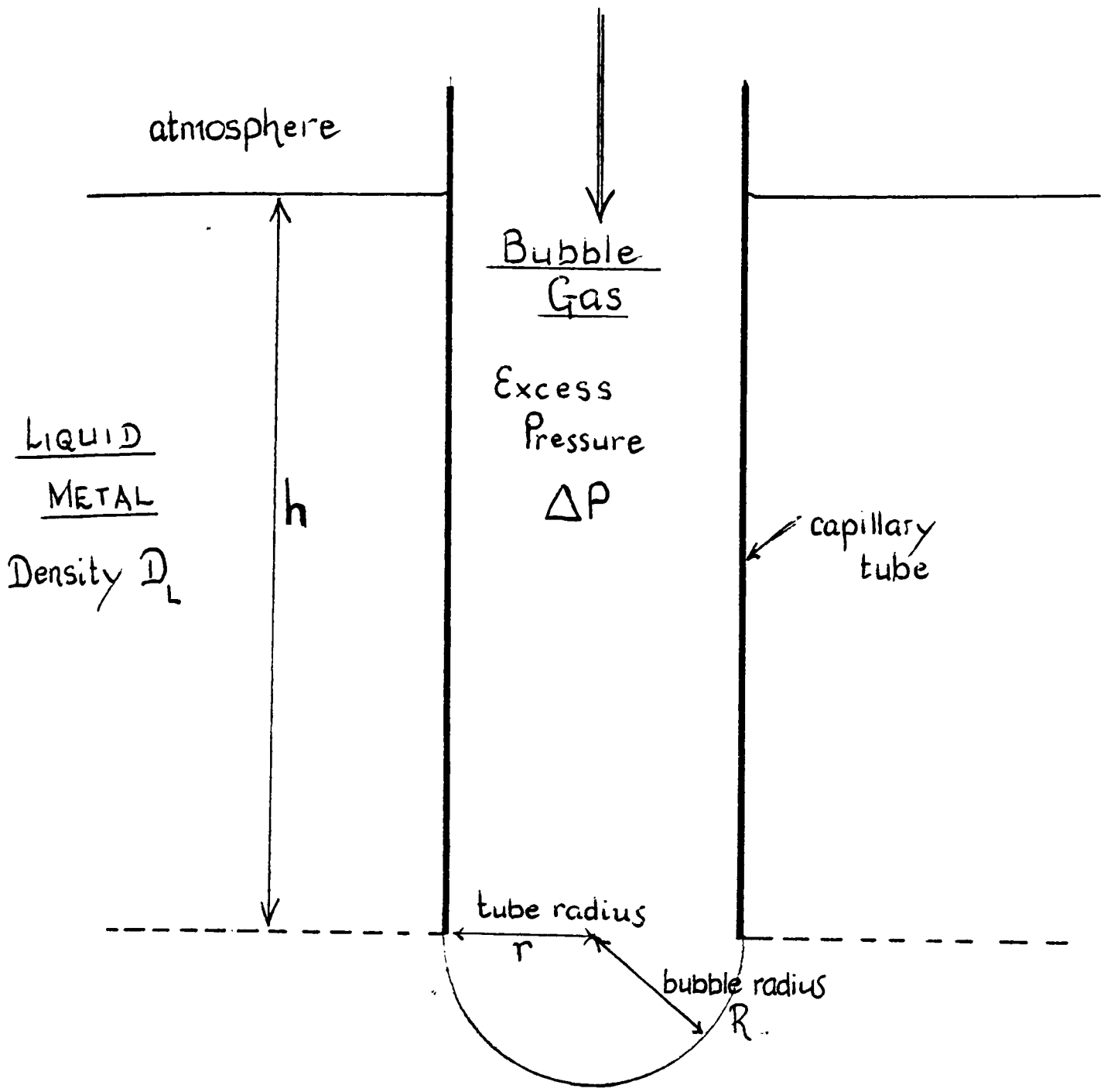
(b) Two designs of bubbling system were used; either a single tube connected to a device capable of precise measurement of vertical displacement,[161,162] or two tubes with identical end geometry set parallel to each other with ends a fixed distance apart.[152,156-160]

(c) It is essential that all traces of oxygen and water vapour are removed from the bubble gas to prevent oxidation.[153]

(d) The magnitudes of the internal and external diameters of the bubble tube are important in determining whether the maximum pressure corresponds to the bubble breaking from the internal or the external circumference of the tube.[172]

(e) The rate of rise of gas pressure in the tube (and hence bubble rate) must be very slow, typically two bubbles per minute, for reproducible results.

The salient features of the more reliable pieces of work performed



Consider the capillary tube, shown above, of radius r, whose end projects below the liquid metal surface to a depth h. If the liquid metal density is D_L^T, at the test temperature T, then the excess pressure required to blow a bubble of radius R at the end of the tube is ΔP where :-

$$\Delta P = D_L^T g h + {}^{2S}/_{R}$$

[g = gravitational force
S = gas/liquid surface tension.]

Now ΔP is maximised when the bubble is a hemisphere of radius r,

$$\Delta P_m = D_L^T g h + {}^{2S}/_{r}$$

Thus, if ΔP_m is measured while blowing a bubble from identical tubes at different immersion depths h_1 & h_2 then :-

$$\Delta P_{m_1} - \Delta P_{m_2} = D_L^T g (h_1 - h_2) \quad \text{—(8-13)}$$

using the technique are given in Table 8.2 overleaf.

8.4.2 Summary of Experimental Procedure and Results

A great deal of time and effort were spent in setting up the apparatus for this technique, and subsequently in modifying it to try and obtain reproducible bubble results. Unfortunately, results of a sufficient accuracy were never obtained on the molten metals examined and so the technique was eventually abandoned in favour of the simpler pycnometer method. A detailed description of the apparatus and experimental procedure used for the bubble pressure technique in this work is given by Johnson [163] together with the results obtained and the numerous experimental difficulties encountered. This work will only be summarised here, in view of the failure of the technique to yield accurate density measurements.

A double-tube technique was employed. Two sets of apparatus were used at various times in the experiment, and these were continually developed and modified. The first experimental arrangement, shown schematically in fig. 8.4, was relatively simple, the furnace being open to the atmosphere. The second arrangement, shown in fig. 8.5, was more refined and utilised a furnace with a vacuum facility. The manometer consisted of two 1 metre lengths of silica tubing joined by glass blowing. The pressure was observed using a travelling microscope arrangement converted to function in a vertical plane. This was used in conjunction with a 1 metre rule fastened rigidly to the manometer tubes so that displacements of the manometer fluid in excess of the ordinary microscope traverse could be measured.

The major, insoluble, problem of the technique was non-reproducibility of maximum bubble pressure, particularly over the long periods of time required to obtain density measurements from the apparatus. The consistency of the maximum bubble pressures obtained for molten tin and lead was at best only $\pm$ 0.2% over short periods, and was typically $\pm$ 1 to 2% over long periods. Indeed a phenomenon was quite often encountered where the pressure indicated by the manometer remained stationary at some value below the previously

Table 8.2

Author.	Paper Ref. No.	Metal systems studied.	Bubbler Tubes.				Bubble Gas.		Quoted Accuracy	Comments.
			Type	Size	Number of.	End Geometry.	Type	Treatment		
Greenaway	161	Pb-Sb. Cd-Sb.	silica & stainless steel	2.5 → 3.0 mm O.D.	2	polished, flat.	H_2 & N_2	Passed over dried $CaCl_2$ and heated Cu turnings.	–	1 bubble/min. Inconsistent results near liquidus
Kirshenbaum	162	Sb.	Vycor		2	polished, flat			±0.09%	
Taylor	157	Na	stainless steel	1.5mm O.D.	1	fine polished, flat	Ar	Passed over hot calcium and a liquid Na-K alloy	± 2.0%	Measured surface tenjion. Problems with 'pulsing' in manometer.
Lucas	158	Ag Cu Fe	alumina	6mm O.D. 4mm I.D.	1	Bevelled 45°	Ar	dried with P_2O_5, de-oxidised with Fe at 200°C and Mg at 500°C	< ±0.5%	
Coy	160	Al Al alloys.	alundum.	6mm O.D.	1	Bevelled 45°	Ar	dried over P_2O_5		
Philips	152	Pb-Sn Sb-Cd	Quartz.	3.5mm O.D. 2.0 mm I.D.	1	polished, flat	H_2	Passed over :- Pd catalyst, $CaCl_2$, Magnesium perchlorate, activated alumina.	–	Used KBr/CdBr flux to prevent dressing in Cd-Sb alloys.
Lucas	159	Sn-Zn.			1					
Lang	156	Sn, Bi, Pb, Hg.	SiO_2, ThO_2, Al_2O_3, Pt-10%Rh	1.2 mm → 2.0 mm O.D. Fine wall thickness	1	polished, flat.	Ar	Pd catalyst Silica gel Magnesium turnings 400°C	$\pm 2 \times 10^{-4}$ %	Measured surface tension Noted 'channeling' effect

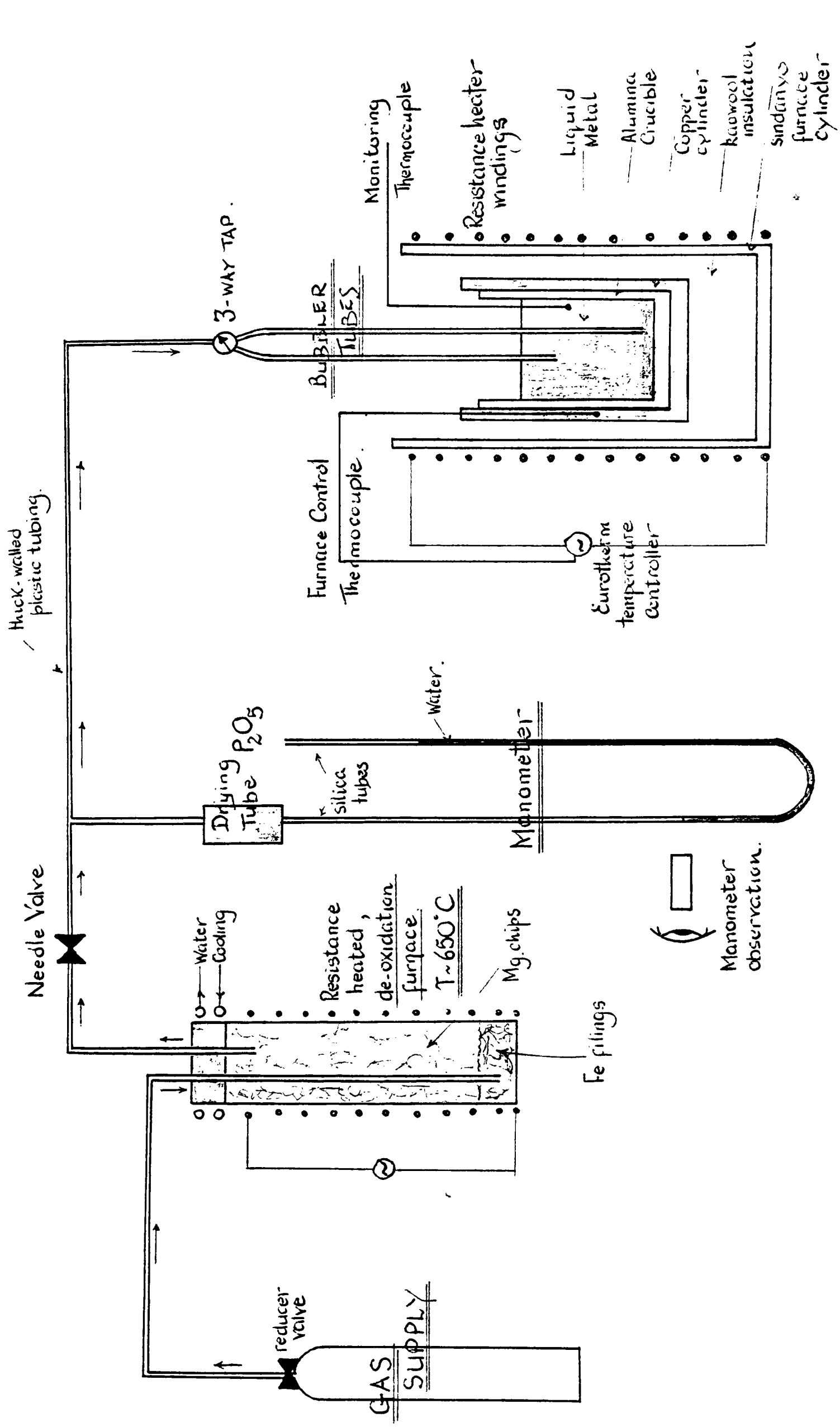


Fig 8.4. Schematic illustration of first experimental arrangement for maximum bubble pressure measurements.

observed maximum value even though gas was still escaping from the bubble tube. It was eventually concluded that the cause of the inconsistency was metal oxide build-up and formation at the tips of the bubbler tubes and on the surface of the melt. The experimental observations which led to this conclusion were as follows:-

(a) Bubble pressure reproducibility was improved on reducing the oxygen content of the gas supply, and became very much poorer if oxygen was artificially introduced into the gas line.

(b) The results obtained for molten lead and tin became more consistent as the melt temperature was raised. This was presumably due to a shift in the metal- metal oxide equilibrium making the oxide less stable at higher temperatures.

(c) Copious amounts of oxide were formed on the surface of an unprotected melt during the course of a bubble pressure determination. Even when the melt surface was protected by an inert atmosphere,oxide was found to be present on it after a determination had been performed. This must have arisen from oxygen in the gas supply.

(d) If the ends of the bubble tubes were protected by graphite caps as they were lowered through the surface of the melt at the start of a run then highly consistent bubble pressures could be achieved for several minutes. If the ends of the tubes were also chemically cleaned and degreased before insertion then reproducibility could be maintained for longer periods of up to 20 minutes. Inconsistency inevitably arose, however, after this period, which was not sufficiently long for a complete determination to be performed. Reproducible bubble pressures could be re-attained for short intervals by 'wiping' the end of the bubble tube 'in situ' with a remote-controlled graphite cleaning device.

(e) Highly accurate and reproducible maximum bubble pressures were obtained using mercury as the test liquid. A consistency of $\pm$ 0.01% was achievable in bubble pressure using the apparatus shown in fig. 8.5 with a hydrogen atmosphere in the furnace. This demonstrated that there was nothing intrinsically wrong with the apparatus, which was found to be quite adequate in monitoring such

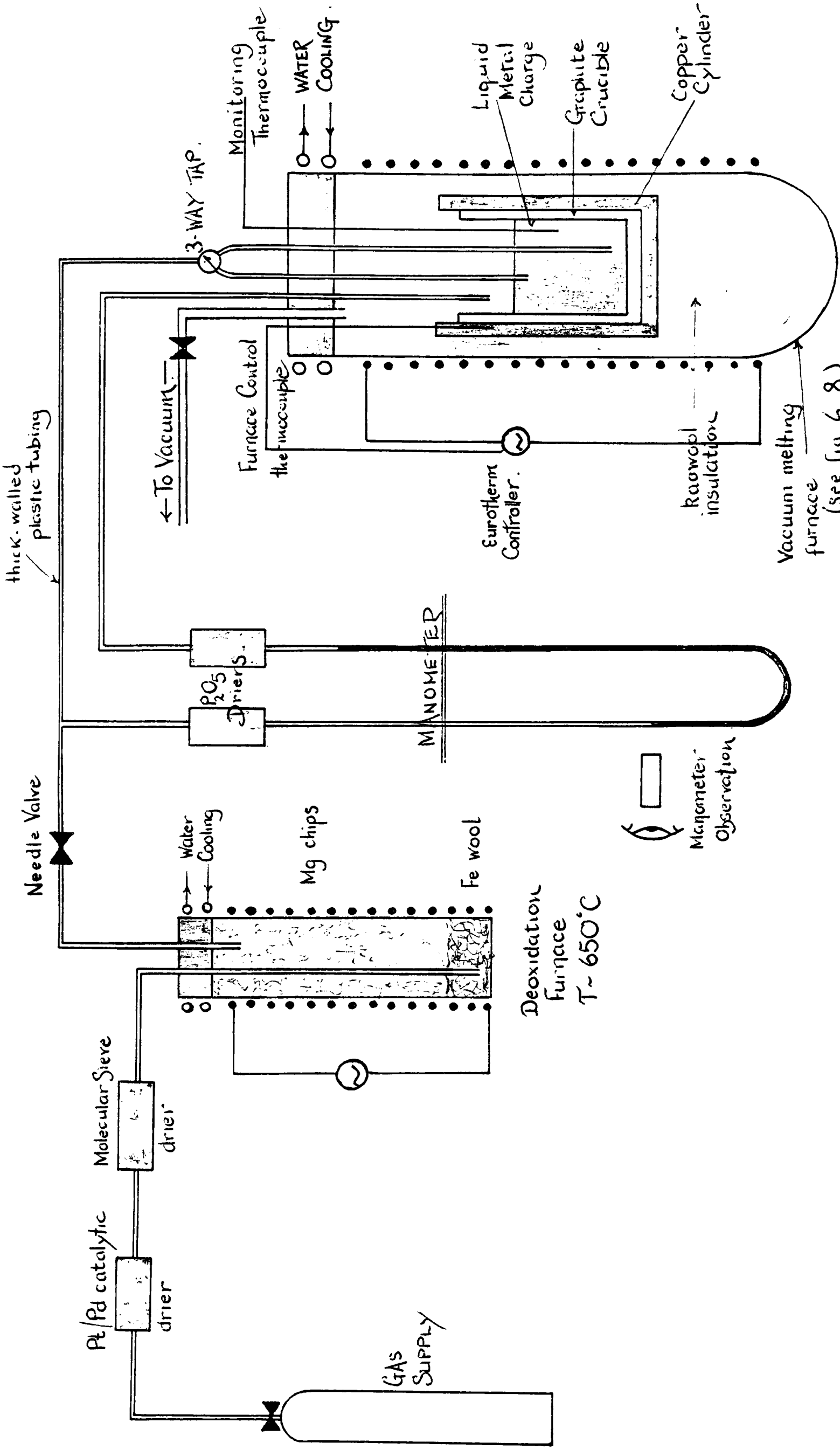


Fig 8.5. Schematic illustration of the second experimental arrangement for maximum bubble pressure measurements.

accuracies. The fact that successful determinations could be made on mercury and not on molten tin and lead was assumed to be because mercury has a lower oxidation potential.

The influence of oxide formation at the end of the bubble tube on maximum bubble pressure would have arisen from the 2S/R term in equation (8-13). Oxide adherence to the bubble tubes would have caused progressive changes both in surface tension forces and in bubble contact geometry.

Many experimental parameters were varied in order to improve bubble pressure consistency - usually without success. Silica, stainless steel, and alumina bubble tubes were used with a variety of internal and external diameters. Tube-end morphology was changed from the usual flat cut-off (perpendicular to the tube axis) to ones such as bevelled, or knife-edged, or with a 45^{o} profile, in an attempt to provide preferential, reproducible paths for bubble release. Tube ends were also ground and polished to various degrees. A number of gases were used for the bubble supply, these being argon, argon plus 10% hydrogen, and hydrogen. These gases were also used as protective furnace atmospheres. A platinum/palladium catalytic converter was inserted into the gas line in series with a magnesium de-oxidising unit in an attempt to eliminate oxygen in the gas supply. Water vapour from the manometer was isolated from the gas lines by drying tubes packed with phosphorous pentoxide. A variety of bubble rates from 1 per minute to 10 per minute was tried, and the rubber connecting tubing on both sets of apparatus was replaced with thick-walled plastic tubing.

The high accuracy mercury work was performed with 99.99% hydrogen as bubble gas and furnace atmosphere, bubbling at a rate of 2 per minute through alumina tubes with O.D. = 1.5 mm and I.D. = 1.0 mm, and end surfaces polished to 3μ diamond paste.

The final decision to abandon the technique came as a result of discussions with workers at Fulmer Research Institue[171]. They had carried out work on the bubble pressure technique in an attempt to establish standard values for liquid metal densities, and had achieved a similar lack of success. They, too, had concluded that the problems lay in incomplete removal of traces

of oxygen from the supply gas.

The only further steps which might have reasonably been taken to improve the technique were : (a) heating the incoming supply gas to prevent localised liquid metal cooling at the bubble tube-end; and (b) replacing the plastic connecting tubing on the apparatus with copper tubing which could be initially outgassed by heating. These modifications were not attempted due to lack of time and the expected low probability of success.

8.5 The Pycnometer technique

8.5.1 General Outline and Review

A pycnometer is essentially just a high temeperature version of the density bottle. The pycnometer technique for determining liquid metal densities therefore simply involves the measurement of the mass M_T of liquid metal required to fill the pre-calibrated volume of the pycnometer V_T at temperature T. The density is then given simply by:-

$$D_T = M_T/V_T \qquad (8.14)$$

The technique is therefore capable of providing an absolute determination of density by measurement of only two variables, mass and volume. Furthermore both of these variables, particularly mass, can be measured to a high degree of accuracy.

The mass of liquid metal, M_T, in the pycnometer is measured directly after the metal has been allowed to solidify. The volume of the pycnometer at the test temperature, V_T, is usually determined by measuring the volume at room temperature and then by calculating the expansion of this volume to the elevated temperature using the linear expansion coefficients of the pycnometer material. The room temperature volume may be established either directly using precision measuring techniques, or indirectly by calibration with mercury of accurately-known density.

The technique has been used only to a moderate extent by previous workers in determining liquid metal density. Urbain[154] in his review of liquid

metal density work stated that 'the pycnometer technique has been used to provide density data quickly and easily, but usually far from precisely.' However, this statement referred mainly to early work,[164,165] and Urbain noted that recent experiments, particularly those of Stott,[166] had improved accuracy by taking suitable precautions. Stott et al[166] employed alumina pycnometers to investigate the densities of commercial grades of liquid iron, using the mercury calibration technique for determination of initial pycnometer volumes. They quoted their results to an accuracy of $\pm$0.15%. Their precautions were mainly related to obtaining accurate values for the volumes of the pycnometers employed.

In another review of previous liquid metal density work Veazey and Roe[153] pointed out that the pycnometer method was particularly suited to measuring density variations at a particular temperature, since errors in the absolute value of V_T may then be neglected. In referring to the accuracy of the technique they pointed out that the present standard value for the density of pure mercury at 20°C was obtained by a pycnometer method to a reported accuracy of $\pm$ 0.8 x 10^{-6}%. This work was performed by Cook[167] using a large, cubical, fused silica box as a pycnometer, the internal dimensions of the box being determined by accurate interferometry.

Of particular relevance to the present experiment is the work of Crawley and co-workers.[151,168,169] They used the pycnometer technique to determine the liquid metal densities of a large number of low melting-point metal and alloy systems. An accuracy of $\pm$ 0.05% in absolute density values was claimed, which would be more than adequate for the purposes of the present experiment. Graphite pycnometers were employed for their work, these being precision machined to give an accurate room temperature volume. The metal, or alloy, to be studied was charged into the pycnometer as a solid ingot, melting being performed in a vacuum furnace equipped with an observation window which enabled them to visually inspect the pycnometer orifice when wiping away excess metal.

8.5.2 Apparatus

The design and construction of the pycnometer used for the present work is shown in figs. 8.6 and 8.7. All pieces were machined from a single length of austenitic (18:8 type) stainless steel bar. Stainless steel was used so that the time-consuming calibration of pycnometer volume need be performed only once at the start of the work. It was felt that the volume of a stainless steel pycnometer would not alter with successive density determinations because (a) it could be made to be robust; (b) the stable oxide layer on the stainless steel would prevent further oxidation (and hence volume change) at the elevated test temperatures, and (c) stainless steel was inert to the molten metals to be used in the experiment (Sn, Zn, Pb) and so would not be dissolved away.

The top and bottom end-plates of the pycnometer were each secured to the central cylinder by six stainless steel screws. The mating surfaces of the end-plates and central cylinder were finely ground and polished in order to ensure a leak-tight fit when assembled. A 1 mm. diameter hole was drilled through the top end-plate, in a position corresponding to the circumference of the internal pycnometer volume, to act as an exit hole for expanding liquid metal. By wiping the excess liquid away from this hole at the test temperature an accurately reproducible volume could be readily obtained. The device used to perform this operation is shown in figs. 8.6(a) and 8.7(b) and was a simple steel collar. In its rest position this fitted around the exit hole and so constituted a container for any excess liquid. It could however be pivoted so that it easily removed this liquid away from the hole.

Two 1.5 mm. diameter holes were also drilled in the top end-plate to take the monitoring and furnace control thermocouples, as shown in fig. 8.6. Both thermocouples were Pt/Pt13%Rh type. The bead of the thermocouple used for monitoring the liquid metal temperature lay within 1mm. of the ground surface of the top end-plate for maximum sensitivity.

The volume of the pycnometer cavity was machined to be approximately

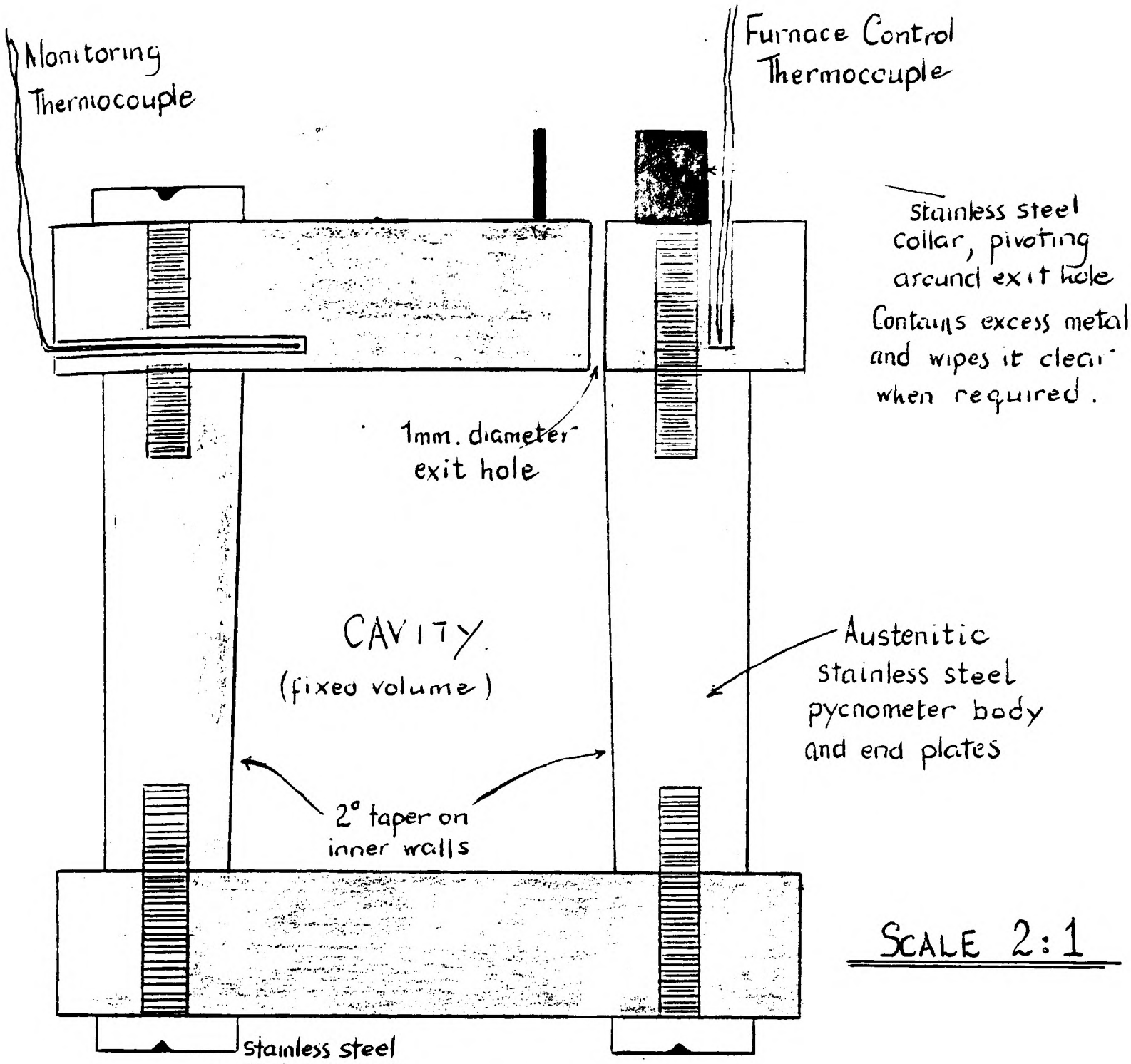


Fig.8.6(a) Schematic illustration of stainless steel pycnometer.

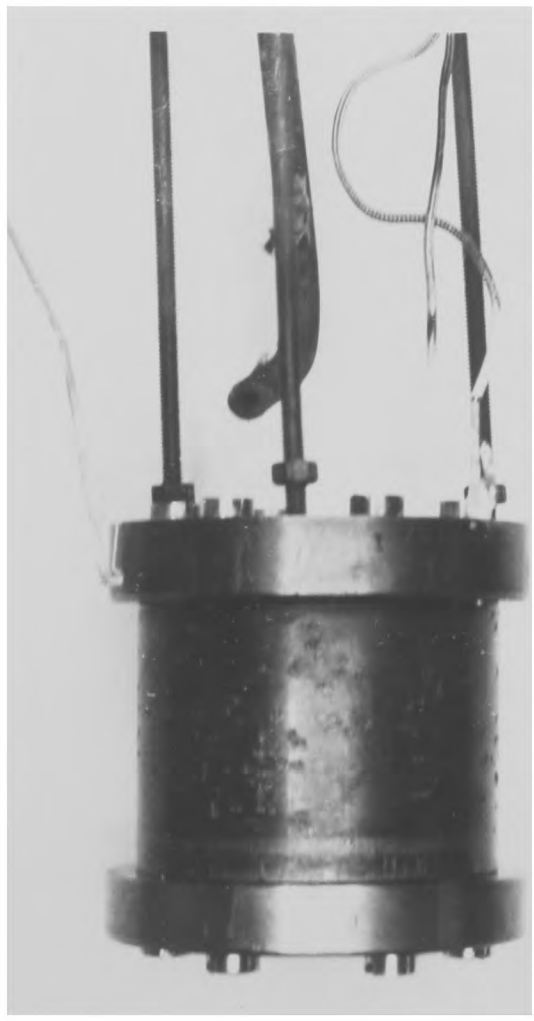


Fig 8.6(b). Photograph of the assembled pycnometer. Note the three rods screwed into the top plate which supported the pycnometer in the furnace cavity.

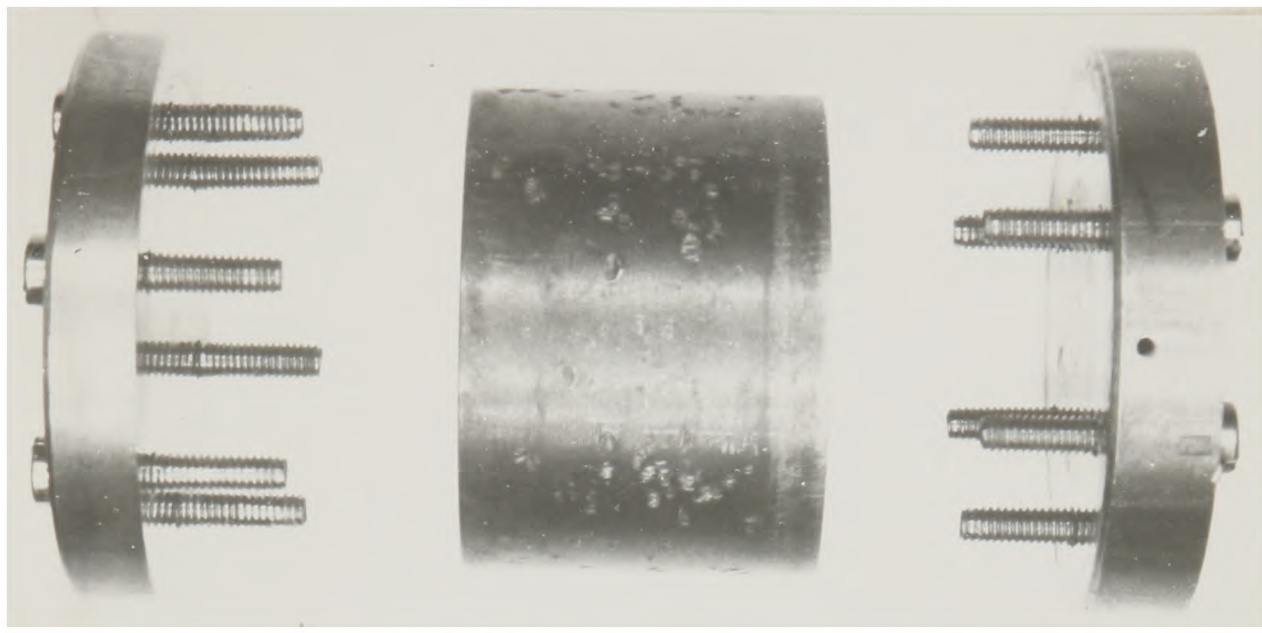


Fig 8.7(a). Exploded view of pycnometer assembly.

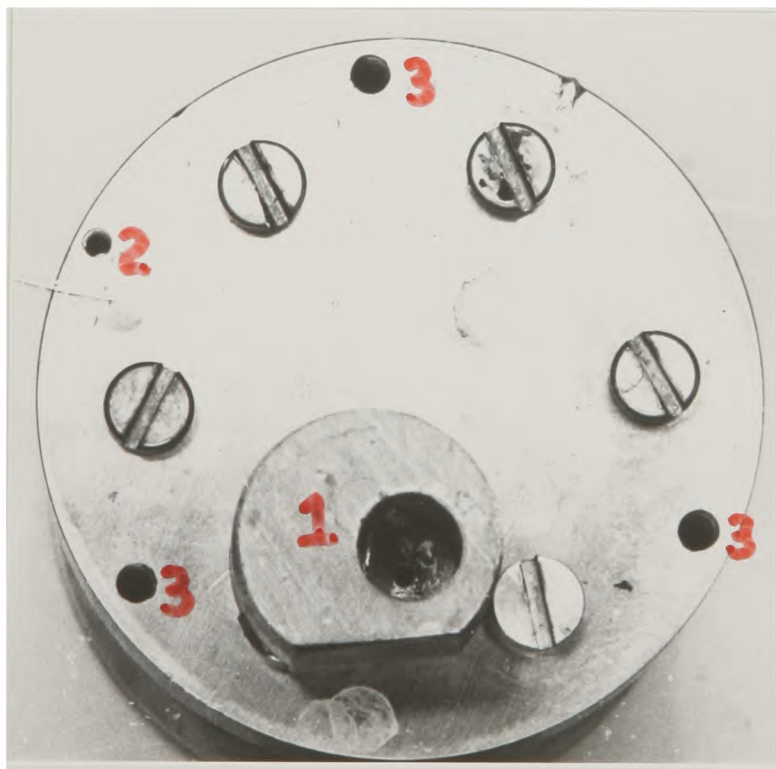


Fig 8.7(b). Plan view of top plate of pycnometer, showing :-

1. Stainless steel collar around exit hole
2. Hole for furnace control thermocouple
3. Holes for steel support rods.

20 ccs. This volume was a compromise between the higher accuracies obtainable at higher volumes and the weighing capacity of 200 gms. on the only accurate balance available. Since the stainless steel pycnometer itself weighed much more than 200 gms. it was necessary to remove the solidified specimen ingot from the pycnometer in order to weigh it accurately. The internal wall of the central cylinder of the pycnometer was therefore given a 2^{o} taper and was well polished in order to facilitate ingot removal.

The exact volume of the pycnometer was determined at room temperature using mercury of accurately known density. It was felt that this mercury calibration technique would give a more accurate value for the volume than an absolute measurement using machined dimensions, particularly in view of the inner wall taper. The volume of the pycnometer cavity at elevated temperatures was then calculated from this room temperature volume using quoted linear expansion coefficients for 18:8 stainless steel.

In view of the construction of the pycnometer it was felt that filling with liquid metal at elevated temperatures would be too difficult. It was therefore necessary to charge a solid ingot specimen into the pycnometer of sufficient size that the consequent volume of liquid at the test temperature would be just greater than that of the pycnometer. Initial solid ingot specimens of the required shape and size were produced using a casting technique, the pycnometer body itself being used as the mould. This casting arrangement is shown in fig. 8.8(a), the top plate of the pycnometer being replaced by an open-ended stainless steel collar which could be securely screwed to the top of the central cylinder. Each ingot was encouraged to solidify vertically upwards so that the majority of the shrinkage porosity would be confined to its top portion (in the region of the steel collar extension). This portion could then subsequently be machined away to give a sound ingot of the required height for the actual pycnometer cavity.

Melting of the solid specimen ingots in the pycnometer was performed in a resistance-heated, 500mm long vertical tube furnace which could be evacuated when required. The pycnometer was suspended in the furnace by three



Fig 8.8 (a) Exploded view of pycnometer assembly when set up for casting an ingot charge.

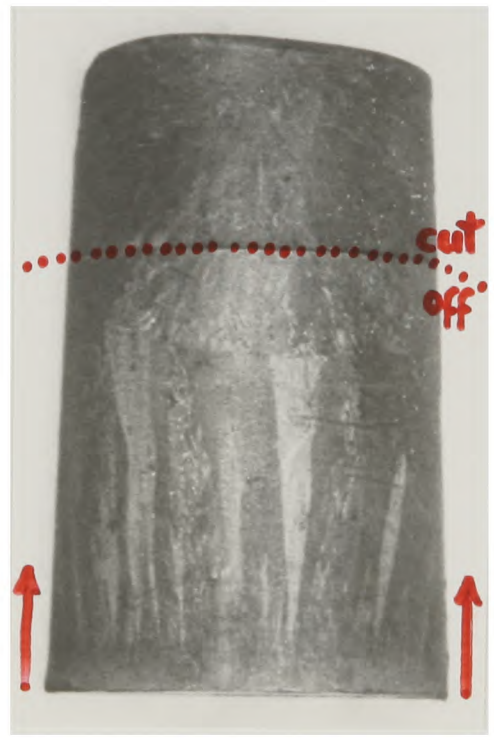


Fig 8.8 (b). Macro-etched ingot ; as cast. Showing columnar structure grown vertically upwards.

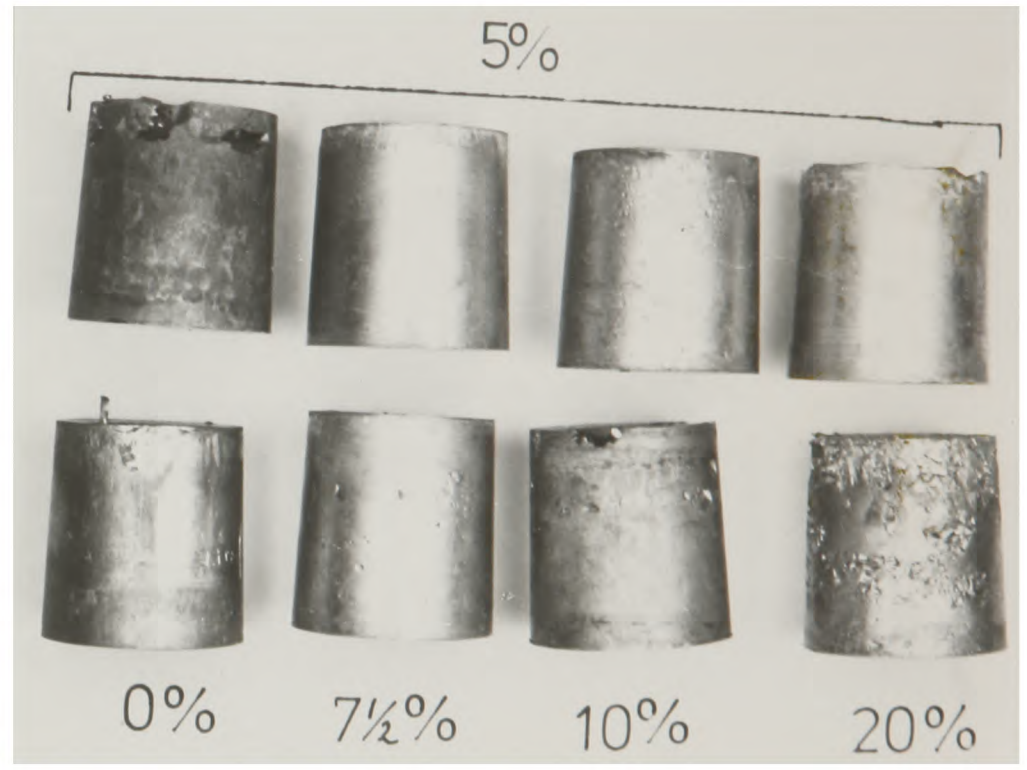


Fig 8.8 (c). Typical appearance of Sn-Zn alloy ingots after a density determination had been performed Alloy composition given in wt%Zn.

steel support rods (fig. 8.6). These were fastened into the water-cooled brass top plate of the furnace and were also screwed into three matching holes in the top end-plate of the pycnometer. The furnace windings were connected to a Eurotherm temperature controller capable of maintaining a very stable temperature. The control thermocouple for the Eurotherm was placed in the top end-plate of the pycnometer itself, as previously mentioned.

8.5.3 Experimental Procedure

The pycnometer volume was first calibrated at room temperature using high purity (triple distilled) mercury. All parts of the pycnometer were separated and thoroughly cleaned and degreased. The bottom end-plate was then tightly re-fastened onto the pycnometer body and pure dry mercury was poured in until the cavity was almost filled. This mercury was cooled to around $0^{o}C$ in an ice bath prior to pouring, so that on warming to room temperature it would expand and completely fill the pycnometer cavity. After pouring the mercury the top end-plate of the pycnometer was screwed tightly down into position. Great care was taken to ensure that the pool of mercury was not displaced during this operation in case any of it should find its way into the tapped holes on top of the pycnometer body. Once the pycnometer had been assembled,it,and the mercury charge,were allowed several hours to attain the ambient temperature of the laboratory. The excess mercury which had expanded through the 1mm. exit hole in the top plate of the pycnometer was contained by the steel collar which was fixed around the hole. When equilibrium had been attained this collar was scraped across the hole by manually pivoting it about its fixed point thereby removing the excess mercury. The pycnometer was then carefully inverted over a clean dry glass beaker, and the mercury was allowed to run into the beaker through the exit hole by slackening the base plate screws. After this the pycnometer was carefully dismantled and all traces of mercury remaining in it were transferred to the beaker. The mercury was then divided into two roughly equal portions each of which was weighed on an accurate balance. This division had to be performed because the total weight

of the mercury was greater than the capacity of the balance. The volume of mercury, and hence that of the pycnometer cavity, could then be calculated from the measured weight and the tabulated density of mercury. A mercury-in-glass thermometer was used to monitor laboratory temperature throughout the calibration procedure.

The first part of a liquid alloy density determination involved the manufacture of a solid alloy ingot which could be charged into the pycnometer. Suitable quantities of oxide-free, 99.99% purity elements were first melted up together under a protective argon atmosphere in an alumina crucible. The vertical tube resistance furnace was used for this purpose, the control temperature being set at around 300°C which ensured a superheat of at least 70°C for all of the alloys studied in these experiments. Once all the components had melted the liquid was thoroughly stirred to ensure complete alloy homogeneity. The modified pycnometer assembly, shown in fig. 8.8(a), was then set up with the stainless steel extension collar replacing the conventional top end-plate. This assembly was placed on a sheet of metal gauze on a tripod and was gently pre-heated using a bunsen burner. The superheated molten alloy, from which any small traces of oxide scum had previously been removed, was then poured from the crucible into the modified pycnometer until this was completely filled. A fast jet of compressed air was then played onto the base plate of the pycnometer assembly to try and encourage upward directional solidification of the alloy. When solidification was complete the assembly was allowed to cool in still air to room temperature, at which point the alloy ingot was removed from the mould by taking off the bottom end-plate. The top portion of this ingot was then machined away until the residual portion just fitted into the true pycnometer cavity. All surfaces of the residual ingot were then ground over with fine grade SiC paper to remove any traces of oxide, and finally the ingot was degreased and dried before being sealed into the pycnometer ready for a density determination.

High temperature density work was performed by suspending the pycnometer and its ingot charge in the vertical tube furnace described in the previous

section. The hot zone of the furnace was first measured and the length of the pycnometer support rods adjusted so that the pycnometer lay in the centre of the zone. Loose kaowool insulation fibre was packed around the pycnometer in the furnace tube in order to minimise any temperature fluctuations caused by convection currents in the furnace atmosphere. Once the pycnometer had been inserted into the furnace tube the vacuum pump was turned on and the tube was evacuated down to 1mm Hg pressure. The Eurotherm controller was then set to give the desired test temperature and the furnace was allowed to heat up.

The temperature of the alloy charge in the pycnometer was monitored from the thermocouple positioned at the centre of the top end-plate. The signal from this thermocouple was connected via a cold junction to an accurate potentiometer and thence to a chart recorder readout. The potentiometer allowed the signal voltage to be accurately backed-off so that the temperature could easily be read to better than $0.1^{o}C$ on the chart recorder scale. When the temperature readout indicated that the pycnometer was above the melting point of the alloy charge the vacuum in the furnace tube was released and replaced by an argon atmosphere. This was done in order to minimise errors caused by entrapment of gas bubbles within the pycnometer volume (see next section). After introduction of the argon,which tended to chill the pycnometer slightly,the system was allowed to continue towards the attainment of the set point temperature.

Providing the Eurotherm controller had been properly adjusted the warm-up overshoot of the set temperature was at most only $2^{o}C$. The collar fixed around the exit hole of the pycnometer was designed to contain all the liquid exuded during heating. This meant that the excess liquid exuded during overshoot of the set temperature could be easily sucked back down into the pycnometer from the pool of liquid above the exit hole. Temperature overshoot did not therefore cause any major errors in density determinations.

When the temperature of the pycnometer had remained stable within $\pm\frac{1}{4}^{o}C$ of the required temperature for at least 15 minutes the whole assembly was quickly and carefully removed from the furnace by manually raising the furnace

top plate. The steel collar was then quickly wiped across the exit hole on the top plate of the pycnometer to remove the excess liquid metal and prevent it from being sucked back into the pycnometer cavity during cooling. The entire operation was completed in less than 4 seconds and no significant fall in temperature was detected on the monitoring thermocouple trace in this time period (response time of chart recorder 0.1 secs.). The procedure had the advantage of allowing the removal of excess metal from the exit hole to be visually observed, thereby eliminating any errors caused by possible incomplete removal. Remote manipulation of the steel collar with the pycnometer still in the furnace had originally been attempted but was found to be unacceptable in this respect.

When the pycnometer had cooled to room temperature the bottom end-plate was unscrewed and the solidified alloy ingot was extracted from the tapered cylinder for weighing. Great care was taken to ensure complete removal of all traces of alloy from the inner surfaces of the pycnometer and from the exit hole. The typical appearance of alloy ingots after removal from the pycnometer is shown in fig. 8.8(c).

Finally it should be noted that all liquidus temperature determinations were performed on the original alloy charge prior to casting it into the modified pycnometer. The same technique was used as described in Chapter 6 of this thesis.

8.5.4 Experimental Difficulties and Precautions taken to minimise errors

The major problem encountered during the course of the experiments was associated with the way in which the solid alloy charge in the pycnometer expanded during melting. It was observed that in many of the solidified ingots removed from the pycnometer cavity after a density determination there was a small flash of metal around the base. This must have been formed by liquid metal being forced between the mating steel flats of the pycnometer body and the bottom end-plate. Additional evidence for some form of pressure being present at the base of the pycnometer was that the stainless steel screws used

to fasten the bottom end-plate onto the pycnometer body were susceptible to shearing failure on tightening after they had been used for several runs. It was concluded that the solid ingots charged into the pycnometer were melting from the base upwards, causing a high pressure to build up in the confined space at the bottom of the pycnometer due to the volume expansion on melting. This pressure was presumably capable of elastically deforming the bottom end-plate, producing slight concavity in it, and thereby allowing liquid metal seepage across the steel flats. The pressure must also have plastically deformed the stainless steel fixing screws, presumably because the initial screw tightening would probably have been close to the elastic limit. The taper on the internal surface of the pycnometer body would have amplified the melting pressure on the bottom end-plate while preventing it from being fully transmitted to the top end-plate. In order to overcome the problem the solid charge ingot was encouraged to melt from the top downwards by heavily insulating the base of the pycnometer with ceramic fibre blanket. The pycnometer support rods were also lengthened to bring the pycnometer nearer to the bottom of the furnace hot zone. Finally the bottom plate retaining screws were all replaced, and the bottom mating surfaces at the bottom of the pycnometer assembly were resurfaced and reground in order to remove any damage which might have been caused by the metal flash. These measures were successful in eliminating the flashing problems but the remachining did necessitate a recalibration of the pycnometer volume.

Two major areas of potential error were identified in the pycnometer technique used for these experiments, these being incomplete filling of the pycnometer volume and macrosegregation in the alloy charge. Gas entrapment was the major potential source of incomplete filling error and this was minimised by employing a vacuum melting technique. In addition, the vacuum was released to an argon atmosphere after melting in order to contract the volume of any gas bubbles present in the melt or pycnometer cavity. In releasing a vacuum of 1 mm Hg pressure to atmospheric pressure the volume of any gas bubble is reduced by a factor of almost 10^3, which reduces the error in volume caused by the

bubble by the same amount.

Macrosegregation in the alloy charge would clearly have caused major errors in density determinations. Potential sources for macrosegregation problems in this experiment were (a) in the melting of the pure elements to form the initial alloy; (b) in the casting and solidification of the alloy in the modified pycnometer mould; (c) during the remelting of the alloy in the pycnometer; and (d) during the holding period when the molten alloy was sitting in the furnace. Source (a) was eliminated by thoroughly stirring the initial melt to ensure complete homogeneity. Source (b) was a major problem particularly since some of the ingot was subsequently machined away. Care was therefore taken to ensure that solidification conditions were such that macrosegregation would be minimised in these ingots. Directional solidification was encouraged to prevent equi-axed mechanisms from operating, and the total solidification time was kept below 5 minutes so that the gravity flow mechanism would not have sufficient time to produce appreciable segregation (see Chapter 4). A certain amount of inverse segregation was considered to be inevitable but this was hopefully reduced to negligible proportions by pre-heating the mould prior to casting. Source (c) was also potentially a major problem particularly for those samples where density determinations were carried out just above the alloy liquidus temperature. Strangman et al[111] and Streat[96] have both demonstrated that dendritic fragments of low solute content may exist for long periods of time at a temperature which is above the liquidus temperature of the nominal solute concentration of the alloy. Any possibility of such retained dendrites occurring in these experiments was eliminated by superheating all alloys to 240°C (above the melting point of pure tin) before reversion to test temperature. The excess metal exuded from the pycnometer volume during this superheat period was easily contained by the steel collar around the exit hole and could therefore freely return to the pycnometer cavity during cooling. This superheat period should also have ensured complete homogeneity in the liquid through convection cycles. Finally, source (d) might have caused problems if, for example, one of the elements of the alloy was preferentially

oxidised during holding. This source of macrosegregation was therefore eliminated by holding the molten alloy either in a vacuum or under an argon atmosphere.

8.5.5 Density Results and Calculations

The results given in this section are presented in the order that they were obtained during the course of the various pycnometer experiments. The experiments followed the sequence:-

(a) determination of room temperature pycnometer volume by mercury calibration.

(b) Calculation of pycnometer volumes at elevated temperatures using standard linear expansion coefficients.

(c) Assessment of accuracy and consistency of technique by repeated measurement of pure liquid tin density at several elevated temperatures.

(d) Determination of $(dD/dT)_c$ for pure liquid tin.

(e) Determination of $(dD/dT)_c$ for Sn-8.73 at. %Zn, and comparison of this with the value for pure tin in order to assess the composition dependence of the term.

(f) Determination of $(dD/dc_{Zn})_T$ for binary Sn-Zn alloys at two temperatures, 240°C and 293°C. Assessment of temperature dependence of the term.

(g) Calculation of $(dD/dT)_c$ and $(dD/dc_{Pb})_T$ for binary Sn-Pb alloys from the data obtained by Thresh et al.[151] Assessment of composition and temperature dependence, respectively, of the terms.

(h) Calculation of ternary alloy composition for zero density change down the liquidus, using eqn. 8-12 with the values of the coefficients determined in (e) to (g) above .

(i) Determination of densities of ternary alloys of various R values down the liquidus slope. Experimental corroboration of zero density change at calculated value of R.

These various steps in the overall experiment are described and discussed

individually below.

(a) Pycnometer Volume - Room Temperature

Table 8.3 below lists the mercury masses measured in a total of twenty volume calibrations performed on the pycnometer throughout the course of the experiments. Ten of these relate to the original pycnometer and ten to the remachined pycnometer.

Table 8.3

Pycnometer	Original		Re-machined	
measured mass of mercury M gms.	277.062	277.023	276.774	276.910
	277.109	277.056	276.755	276.750
	277.072	277.043	276.730	276.781
	277.144	277.084	276.813	276.750
	277.013	277.122	276.824	276.730
$\bar{M}$ gms. (discarding highest and lowest)	277.071 $\pm$ 0.051		276.776 $\pm$ 0.048	

All of these measurements were made at a temperature of 21 $\pm$ 0.5°C. Several spurious values were obtained for M along with the figures listed above, and these have been ignored in the calculation of $\bar{M}$. They were presumably caused by random faults in the experimental procedure such as air entrapment beneath the pycnometer top plate or mercury droplet trapping in the threaded holes of the pycnometer cylinder.

The accepted value for the density of pure mercury at 21°C is

D_{Hg21} = 13.5434 g./cc. ($\pm$ 0.0012 g./cc. for temp. uncertainty of $\pm \frac{1}{2}$°C)

The volume of the pycnometer cavity is given by:-

$$V_{21} = \bar{M}/D_{Hg21} \qquad (8.15)$$

and so

$$V_{21} = 20.458 \text{ cm.}^3 \pm 0.005 \text{ cm.}^3$$

and

$$V^*_{21} = 20.436 \text{ cm.}^3 \pm 0.005 \text{ cm.}^3$$

where the starred value represents the re-machined pycnometer valume.

The errors in these volume figures are approximately $\pm$ 0.026% which represents a remarkable degree of consistency in the mercury calibration.

(b) Pycnometer Volume - Elevated Temperature

The linear expansion coefficient, L, quoted for the type of stainless steel used in making the pycnometer is

$$L = 17.7 \pm 0.7 \times 10^{-6}\ {}^{o}C^{-1}$$

The volume of the pycnometer V_T at any temperature T is given by the expression

$$V_T = V_{21}\ (1 + 3L\ (T-21)) \qquad (8.16)$$

for isotropic expansion, where L is small. Using the given value for L the pycnometer volume at 240°C was therefore:-

$$V_{240} = 20.458\ (1 + 53.1 \times 10^{-6} \times 219)\ cm^3$$

$$V_{240} = 20.696\ cm^3 \pm 0.01\ cm^3$$

and $$V^*_{240} = 20.674\ cm^3 \pm 0.01\ cm^3$$

which represents an accuracy of $\pm$ 0.048% in this high temperature volume figure.

(c) Assessment of technique accuracy for liquid metal densities

Pure tin was used for this work. Three density determinations were performed on pure tin at each of two temperatures 240°C and 293°C in order to examine the consistency of the technique. The measured values of M_T for these determinations are given in Table 8.4, below, together with the values of V_T and D_T calculated from eqns. (8.15) and (8.16)

Table 8.4

Pycnometer	T°C	M_T gms	V_T cm^3	D_T g./cc.	$\bar{D}_T$ g./cc.
Original	293	143.945	20.753	6.936	6.935 $\pm$ 0.004
	293	143.840	20.753	6.931	
	293	143.963	20.753	6.937	
Re-machined	241	144.315	20.675	6.980	6.974 $\pm$ 0.006
	240	144.100	20.674	6.970	
	240	144.148	20.674	6.972	

The average values of liquid tin density from these determinations indicated that the pycnometer technique was capable of accuracies of $\pm$ 0.072% of the density figures. This was within the required accuracy of the experiment (see section 8.3) and so the technique was used with confidence for the assessment of liquid metal density variations.

(d) Determination of $(dD/dT)_c$ for pure tin

Further determinations of liquid tin density were made in addition to those listed in Table 8.4. at temperatures greater than 293°C. It was felt that a more accurate value for (dD/dT) would be obtained if the temperature range of the determinations was increased. The data from the additional determinations is given in Table 8.5 below:-

Table 8.5

Pycnometer	$T^{\circ}C$	M_T gms	V_T cm^3	D_T g./cc.
Original	320	143.721	20.783	6.915
Re-machined	331	143.454	20.772	6.906
Original	440	142.918	20.913	6.834

The values of D_T listed in Tables 8.4 and 8.5 are plotted against T in fig. 8.9. The straight line of best fit drawn through the points had a slope of :-

$$(dD/dT)_{Sn} = -6.90 \times 10^{-4} \text{ g/cc./°C}$$

In order to assess the error in this value of (dD/dT) the following calculation was performed:-

$$M_T = V_T D_T$$

$$\therefore (dM/dT) = (dV/dT)_D D_T + (dD/dT)_V V_T \qquad (8.17)$$

$$\text{and } V_T = V_x + 3LV_x (T-T_x) \qquad (8.18)$$

$$\text{and } D_T = D_x + (dD/dT)_c (T-T_x) \qquad (8.19)$$

where V_x and D_x are the volume and density, respectively, of liquid at

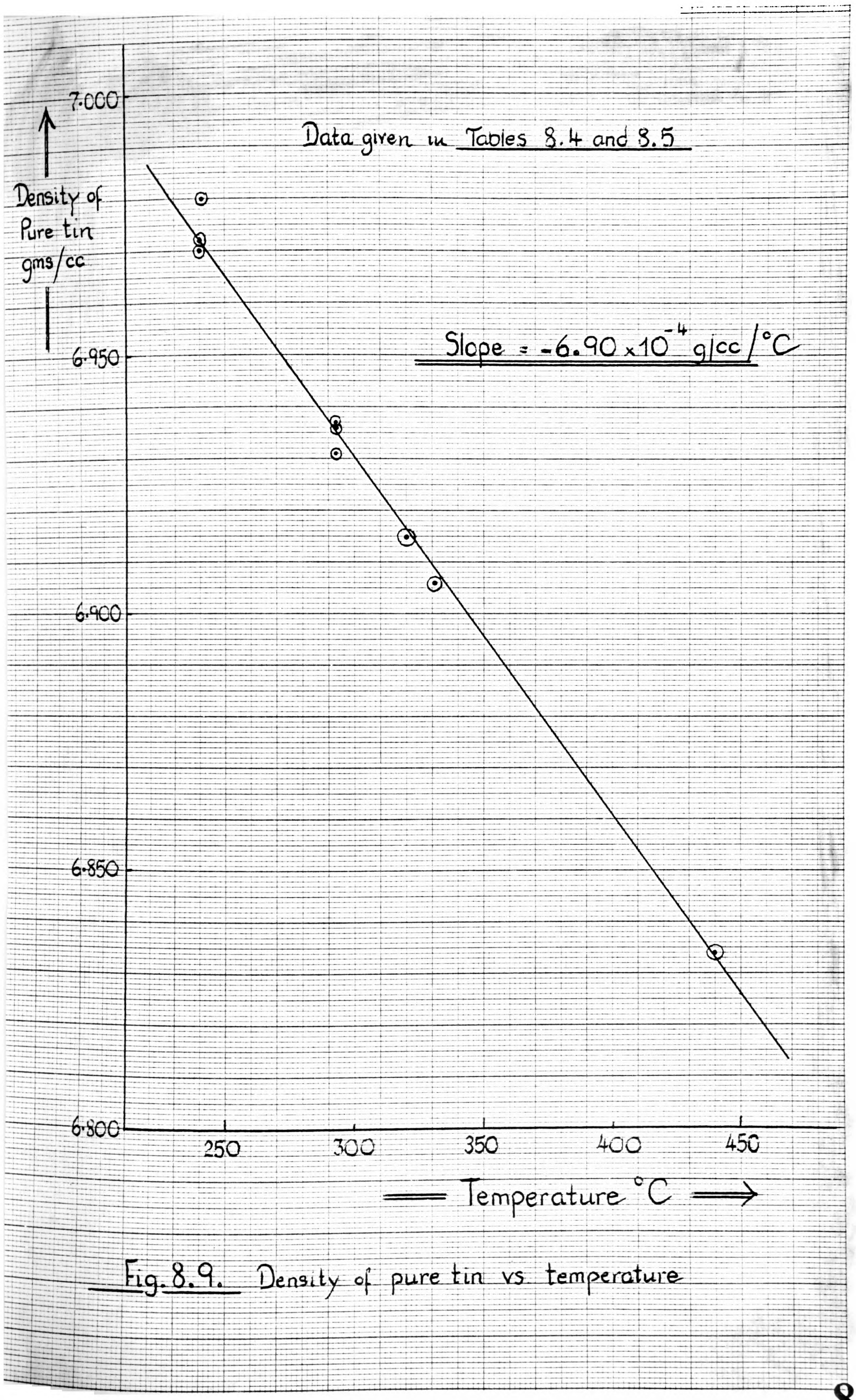


Fig. 8.9. Density of pure tin vs temperature

temperature T_x.

Differentiating eqns. (8.18) and (8.19) w.r.t. T gives

$$(dV/dT) = 3L\,Vx \qquad (8.20)$$

$$\text{and } (dD/dT) = (dD/dT)_c \qquad (8.21)$$

Substituting eqns. (8.18) to (8.21) into eqn. (8.17) gives

$$(dM/dT) = 3LV_x\left[D_x+(dD/dT)_c\,(T-T_x)\right] + (dD/dT)\left[V_x+3LV_x(T-T_x)\right] \qquad (8.22)$$

assuming that the product

$$L\,(dD/dT)_c = 0$$

then eqn. (8.22) reduces to:-

$$(dM/dT) = 3LV_x\,D_x + (dD/dT)_c V_x$$

which re-arranged gives:-

$$\left(\frac{dD}{dT}\right)_c = \frac{(dM/dT) - 3LV_xD_x}{V_x} \qquad (8.23)$$

taking $T_x = 293^{\circ}C$, then $V_{293} = 20.753 \pm 0.01$ ccs. from eqn. (8.16)

$\therefore\ V_{293}D_{293} = M_{293} = 143.916 \pm 0.076$ gms. from Table 8.4.

$$3L = 53.1 \pm 2.1 \times 10^{-6}\ {}^{\circ}C^{-1}$$

and from fig. 8.10 which plots the measured masses of liquid tin in the pycnometer against temperature $(dM/dT) = -7.02 \pm 0.60 \times 10^{-3}$ gms./°C.

Substituting these values into eqn. (8.23) gives

$$(dD/dT)_{Sn} = -7.06 \pm 0.44 \times 10^{-4}\ \text{g/cc/}^{\circ}C$$

which represents an error range of 6.2% in the coefficient. Published values of the thermal expansion coefficient of liquid tin in the literature range from -6.127×10^{-4} (ref.149) to -7.4×10^{-4} g/cc/°C (ref. 170).

(e) Determination of $(dD/dT)_c$ for a Sn-Zn alloy

A single alloy charge was used for these determinations. The composition of the charge was made up to be Sn-5.00 wt%Zn, which is equivalent to 8.73 at.% Zn. The results of the density determinations on this alloy over

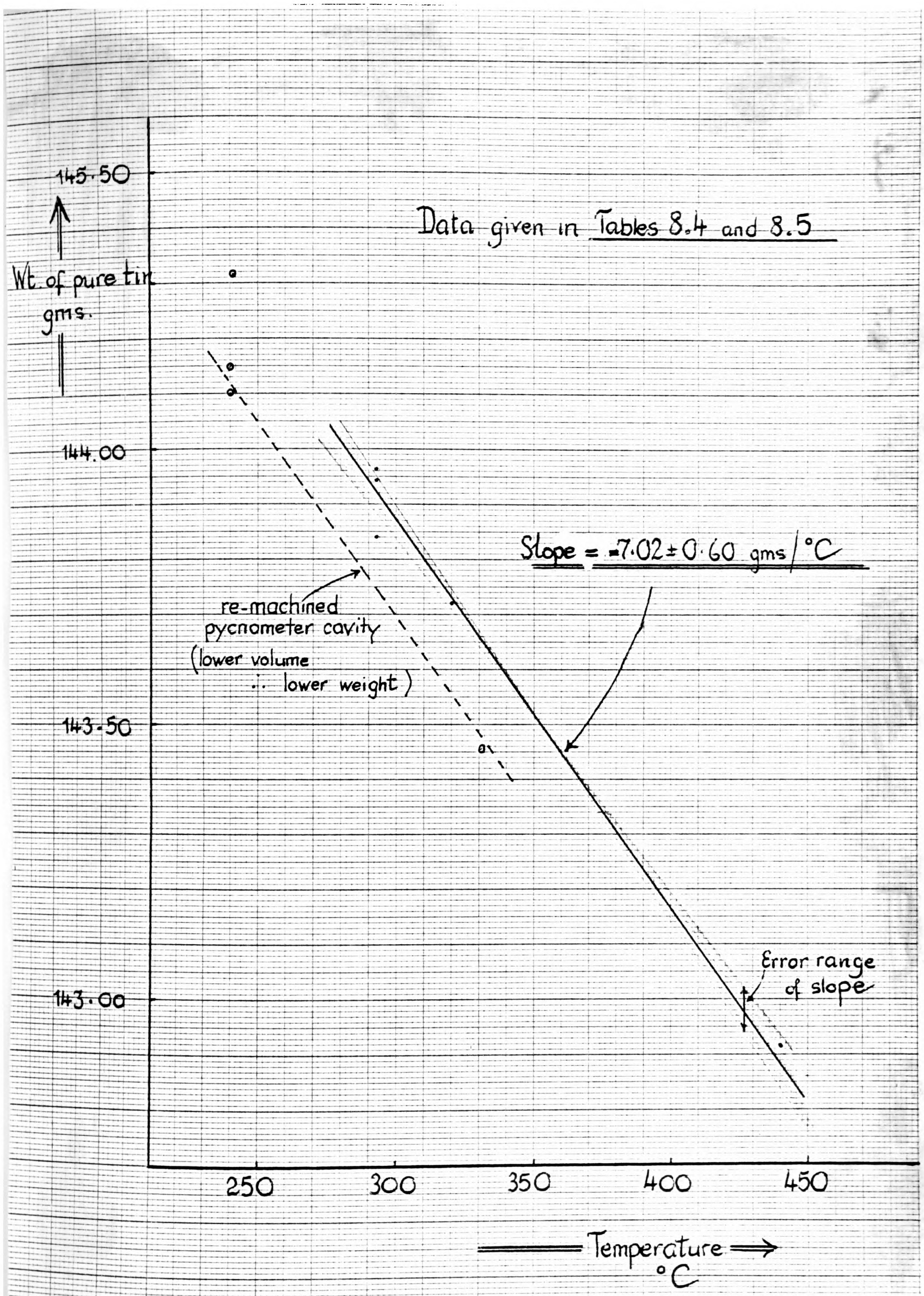


Fig. 8.10 Measured weight of pure tin metal required to fill the pycnometer cavity at various temperatures.

a wide range of temperatures are given in Table 8.6, below:-

Table 8.6

Pycnometer	$T^{o}C$	M_T gms
Original	240	143.705
"	220	143.935
"	231	143.880
"	233	143.880
"	252	143.547
"	260	143.503
"	322	143.021
Original	402	142.422

Alloy composition remained essentially constant throughout the sequence of determinations. Spectrophotometer analyses gave values of 4.98wt %Zn and 5.02wt %Zn for the composition at the start and finish of the sequence respectively. The difference between these values was within the error range of the determination, namely $\pm$ 0.10 wt %Zn.

Fig. 8.11. shows a plot of M_T vs T for the Sn-Zn alloy. The slope of the line of best fit through the points is

$$(dM/dT)_{8.73Zn} = -8.57 \pm 0.40 \times 10^{-3} \text{ gms}/^{o}C$$

Using eqn. (8.23) with $T_x = 240^{o}C$, and so $V_x = 20.696 \pm 0.01$ cm^3 and $M_x = 143.705$ ($\pm$ 0.1 gms. typically) then

$$(dD/dT)_{8.73Zn} = -7.83 \pm 0.35 \times 10^{-4} \text{ g/cc}/^{o}C$$

This value is appreciably different to that obtained for pure tin. Using the two experimental results this rate of change of $(dD/dT)_{Zn}$ with composition is

$$d/dc_{Zn}(dD/dT)_{Sn-Zn} = -8.82 \times 10^{-6} \text{ g/cc}/^{o}C/\text{at\%Zn}$$

(f) Determination of $(dD/dc)_T$ for Sn-Zn alloys

The coefficient $(dD/dc)_T$ was determined at two temperatures

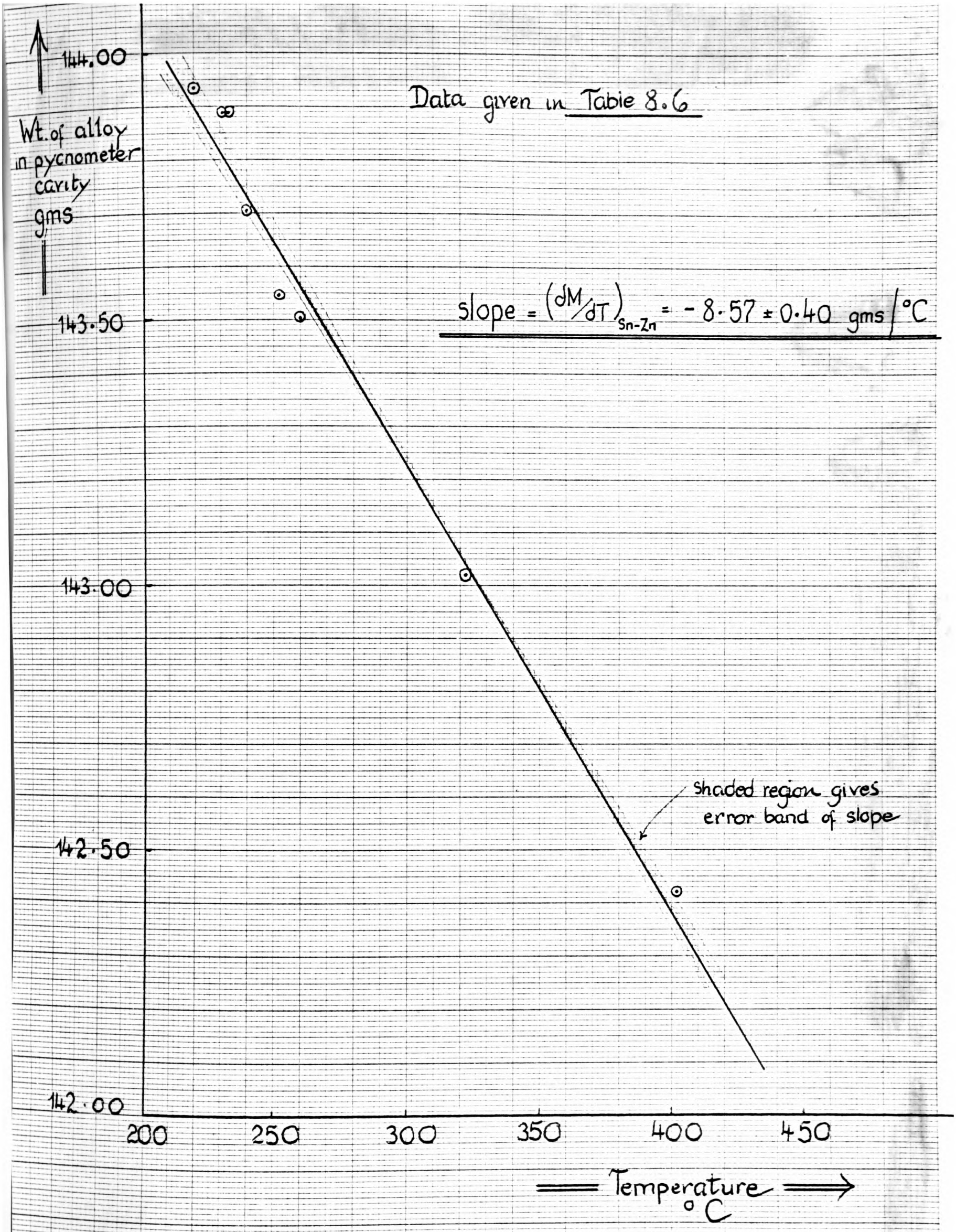


Fig. 8.11. Plot of the mass of a Sn-8·73 at.% Zn alloy required to fill the pycnometer cavity at various temperatures.

240°C and 293°C in order to investigate any dependence it might have had on the test temperature. The measurements performed at the higher temperature permitted a greater composition range to be used, which should have increased the accuracy of the determination. The results of the experiments at the two temperatures are given in Table 8.7., below:-

Table 8.7

Pycnometer	Alloy Compn. At.%Zn.	Temp. °C	M_T gms	V_T cm^3	D_T glcc.
Re-machined	0	240	144.124	20.674	6.971
Re-machined	8.73	240	143.519	20.674	6.942
Original	8.73	240	143.705	20.696	6.944
Re-machined	12.83	240	143.103	20.674	6.922
Original	16.79	240	142.981	20.696	6.909
Original	0	293	143.916	20.753	6.935
Original *1	8.73	293	143.295	20.753	6.905
Original	16.50	293	142.824	20.753	6.882
Original *2	24.15	293	141.973	20.753	6.841
Re-machined *2	31.30	293	141.380	20.731	6.813

*1 estimated from fig. 8.11.

*2 actual determination performed at 295°C. Mass values corrected to 293°C using $dM/dT = -8.57 \times 10^{-3}$ g/°C.

These values of density are plotted against composition for the two temperatures in fig. 8.12. The gradient of the line of best fit for each set of data was:-

$$(dD/dc_{Zn})_{240} = -38.1 \pm 5.1 \times 10^{-4} \text{ g/cc/at.\%Zn}$$

$$(dD/dc_{Zn})_{293} = -36.7 \pm 3.25 \times 10^{-4} \text{ g/cc/at.\%Zn}$$

The difference between the values for the coefficient is clearly smaller than

Data given in Table 8.7.

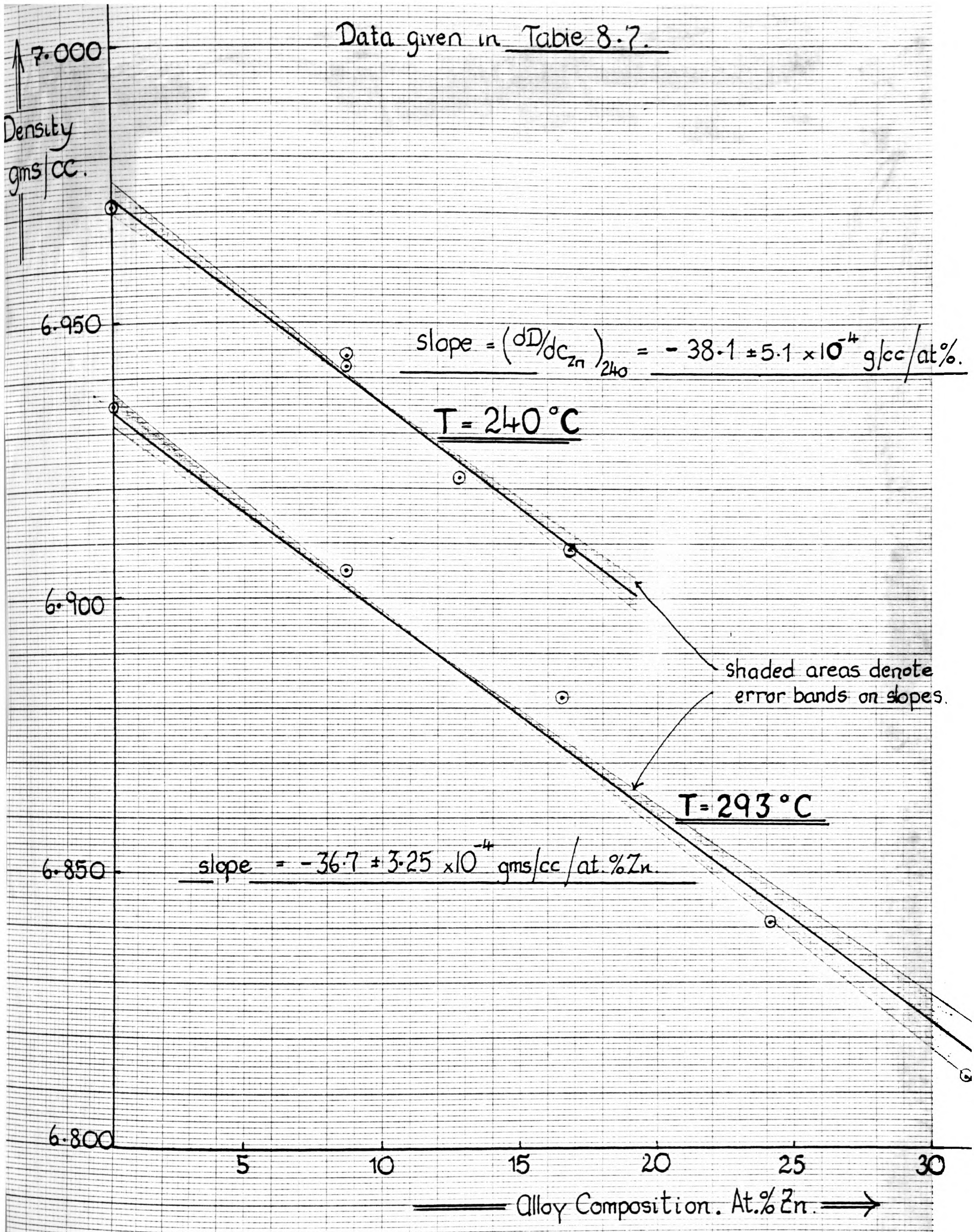


Fig. 8.12 Density of Sn-Zn binary alloys as a function of composition at two temperatures.

the error range on either of them. Assuming that the difference is a real one then

$$\underline{d/dT\ (dD/dc_{Zn}) = -2.64 \times 10^{-6}\ g/cc/at\ \%Zn/\ ^{o}C}$$

(g) Calculations of $(dD/dc)_T$ and $(dD/dT)_c$ for the Sn-Pb binary system

The data used to calculate values for those coefficients was obtained from the work of Thresh et al.[151] They found that the density D_T of liquid Sn-Pb alloys at temperature T could be represented by the formula

$$D_T = a + bT$$

the values of a and b being constant for any given alloy composition. Clearly from this formula $b = (dD/dT)_c$, and $(dD/dc)_T$ could easily be calculated by substituting the relevant values of a and b into the formula for a number of alloy compositions at one temperature. The relevant data used for determining the two coefficients is reproduced in Table 8.8., below:-

Table 8.8

Alloy Compn. At %Pb	a g/cc.	$b=(dD/dT)_c$ g/cc/°C	D_{240} g/cc	D_{400} g/cc
0	7.139	-7.125×10^{-4}	6.968	6.854
9.18	7.543	-7.775×10^{-4}	7.347	7.232
10.50	7.603	-7.760×10^{-4}	7.417	7.293
19.71	7.995	-8.443×10^{-4}	7.792	7.657
25.58	8.229	-8.652×10^{-4}	8.021	7.883
			± 0.004	± 0.004

In fig. 8.13 is plotted the values of D_{240} and D_{400} listed in the above Table against alloy composition. The lines of best fit of the two sets of data have slopes of

$$\underline{(dD/dc)_{240} = 4.116 \times 10^{-2}\ g/cc/\ at\%Pb}$$

$$\underline{(dD/dc)_{400} = 4.020 \times 10^{-2}\ g/cc/\ at\%Pb}$$

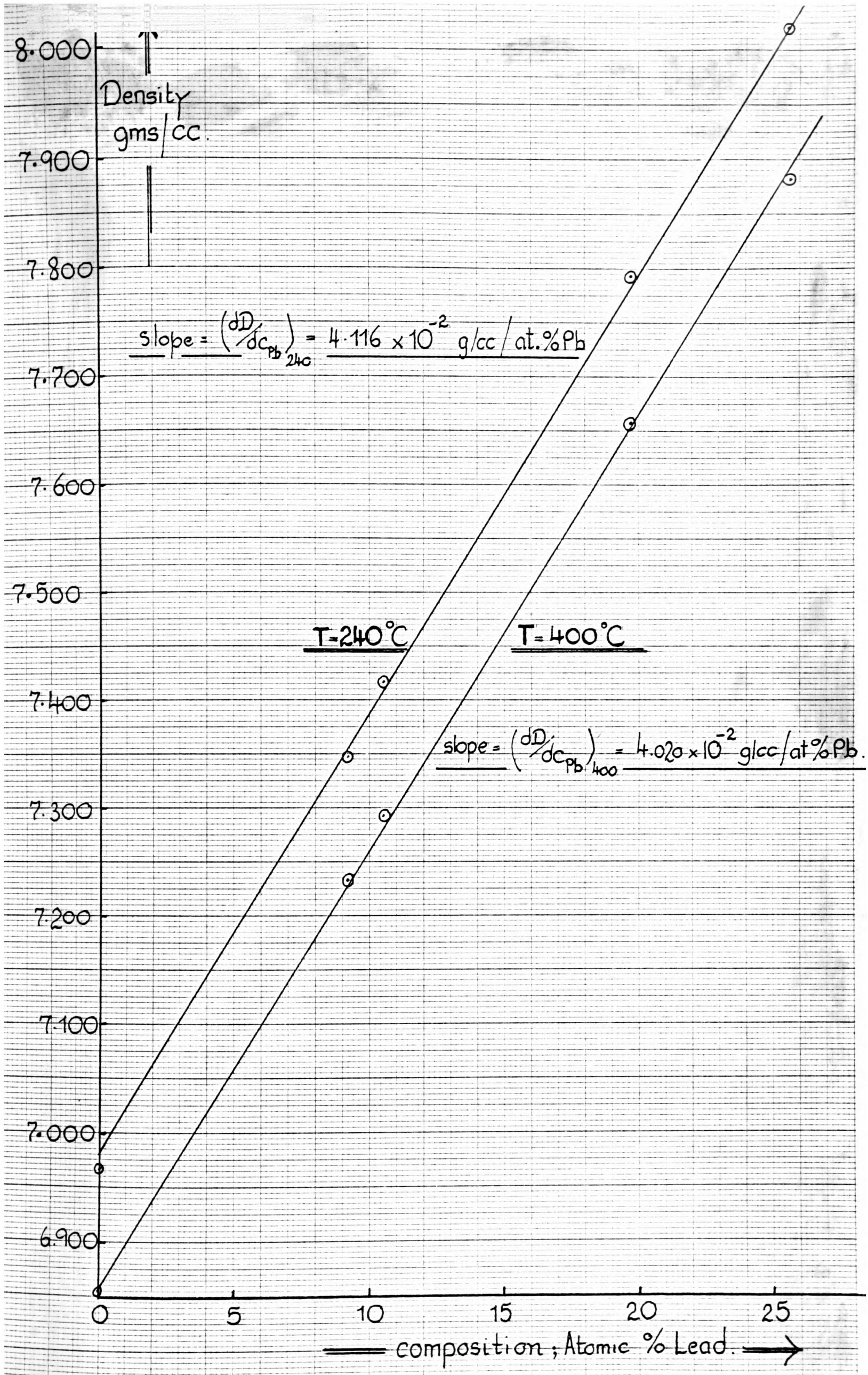


Fig 8.13. Plots of density of Sn-Pb binary alloys as a function of composition, at two temperatures. From work of Thresh et al.[151]

The variation of the coefficient with temperature is therefore fairly limited and is given by:-

$$d/dT\ (dD/dc_{Pb}) = -6.0 \times 10^{-6}\ g/cc/at\%Pb/^{o}C$$

The value of $(dD/dT)_c$ varies quite appreciably with alloy composition. Thresh et al quote:-

$$(dD/dT)_{Sn} = -7.125 \times 10^{-4}\ g/cc/^{o}C$$

and the variation of the coefficient with lead concentration may be estimated from their data as :-

$$d/dc_{Pb}\ (dD/dT)_{Sn-Pb} = -5.1 \times 10^{-6}\ g/cc/^{o}C/at\%Pb$$

It should be noted that the value of $(dD/dT)_{Sn}$ quoted by Thresh et al is very close to that determined for pure tin in the present work.

(h) Calculation of ternary alloy composition for zero density change

The values of the various coefficients used to calculate R in eqn. 8-12 were as follows:-

$(dD/dT)_{Sn-Zn} = -7.73 \pm 0.67 \times 10^{-4}\ g/cc/^{o}C$ This value should be that of a Sn-7.61 at%Zn alloy, as calculated by applying the d/dc (dD/dT) correction factor to the experimentally determined value of the Sn-8.73 at%Zn alloy. The Sn-7.61 Zn composition lies in the middle of the composition range of Sn-rich, Sn-Zn alloys (0→15.22 at%Zn). The error range quoted on the above figure covers the apparent variation of the coefficient within the composition range.

$(dD/dc_{Zn})_T = -38.8 \pm 3.25 \times 10^{-4}\ g/cc/at\%Zn$ This value was calculated to be that at T = 215°C, using the experimentally determined value at 240°C and the $d/dT\ (dD/dc_{Zn})$ correction factor. The temperature of 215°C should be midway in the freezing range of Sn-rich, Sn-Zn alloys. The error range on the figure was

taken from the error on the experimentally determined coefficient at 293°C; this error being greater than the variation of (dD/dc_{Zn}) in the alloy temperature range.

$(dD/dT)_{Sn-Pb} = -7.176 \times 10^{-4}$ g/cc/°C This value being calculated from Thresh's data assuming an average lead content in the alloy of approximately 1 at %Pb.

$(dD/dc_{Pb})_T = 4.131 \times 10^{-2}$ g/cc/at%Pb As calculated from the data of Thresh et al assuming an average temperature in the alloy freezing of 215°C .

m = -2.23 °C/at%solute This is calculated assuming a straight line liquidus slope on the Sn-Zn binary diagram. It was expected that small additions of lead would not alter the liquidus slope appreciably . This value of the liquidus slope was roughly confirmed by thermal analysis tests performed on the Sn-Zn binary alloys studied in section (f).

Substituting the above values into eqn. 8-12 gives:-

$$R = c_{Zn}/c_{Pb} = 19.90 \pm 3.60$$

(i) Determination of density variations in ternary Sn-Zn-Pb alloys

Five ternary Sn-Zn-Pb alloys were made up with the compositions shown in Table 8.9., overleaf. Alloys designated A and B were made up with a Zn:Pb ratio of around 20.0, which was approximately that predicted in the previous section to give zero density change down the liquidus. The approximate liquidus temperatures of the alloys, together with that of a sample of pure tin, were determined by thermal analysis. The values obtained are given in Table 8.9. The density of the alloy samples and that of pure tin were then determined using the pycnometer at a temperature approximately 8°C above their apparent liquidus temperature, in order to assess whether there was any significant density difference between them.

The alloys designated C and D in Table 8.9, below, were both made up with a Zn:Pb ratio of approximately 17.7:1, because calculations performed by Johnson[163] had originally indicated this to be the correct ratio. These two alloys, together with alloy E which had a Zn:Pb ratio of 37.75:1, were used to assess how critical the value of R was in terms of density variation down the liquidus.

Table 8.9 $T = (T_L + 8)\ ^{o}C$

Designation	Composition At %	R	T_L ^{o}C	M_T gms	V_T ccs	D_T gms/cc
Pure Sn	-	-	230	144.138*	20.673	6.972
A	14.37Zn-0.720 Pb	19.96	196	143.889	20.634	6.973
B	7.80Zn-0.389 Pb	20.05	210	143.903	20.650	6.969
C	12.08Zn-0.682 Pb	17.71	200	144.062	20.639	6.980
D	14.84Zn-0.836 Pb	17.75	195½	143.996	20.633	6.979
E	13.06Zn-0.346 Pb	37.75	199	143.604	20.638	6.958

*estimated from fig. 8.9. ±0.005 typically

The density values of these alloys are plotted against total alloy solute content in fig. 8.14. Also plotted on this figure are the calculated values for $(dD/dc)_{liquidus}$ for the Sn-Zn and Sn-Pb binary systems.obtained using the data in the previous section. It can be seen from fig. 8.14 and Table 8.9 that the density of the ternary alloys with R = 20.0 remained essentially constant with alloy solute content, certainly to within the error range on the individual density values. The alloys with R = 17.7 showed a slight increase in density with increasing composition down the liquidus line, although the errors bars on the density values did overlap. The alloy with R = 37.75 showed a definite decrease in density with increasing solute content down the liquidus line, which is consistent with the higher zinc content of the alloy. The values of $(dD/dc)_{liquidus}$ obtained from the density data for the various values of R are shown on fig. 8.14.

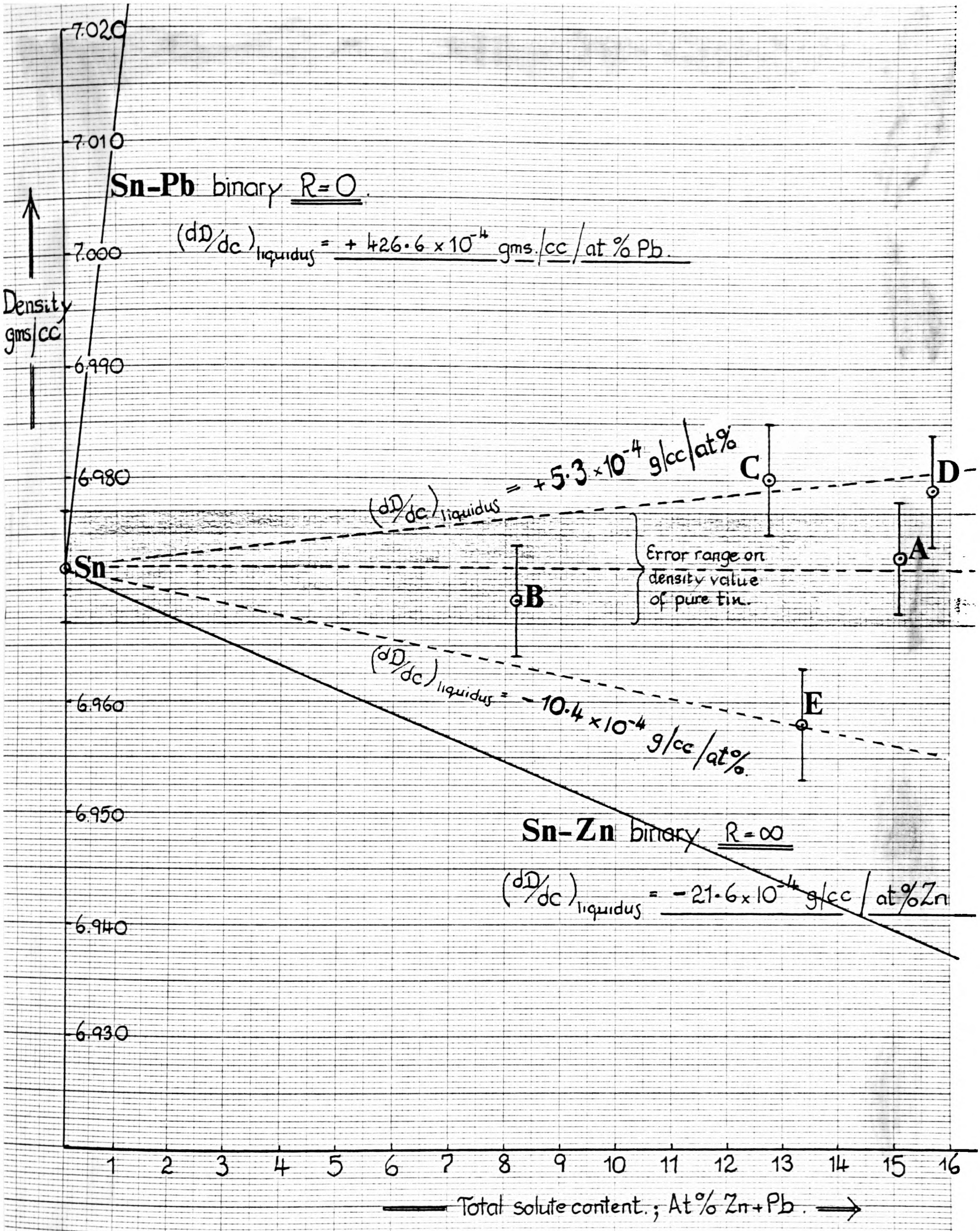


Fig. 8.14. Density values of ternary Sn-Zn-Pb alloys plotted against total alloy solute content. Alloy compositions are given in Table 8.9. Densities were measured at a temperature 8°C above the respective alloy liquidus temperature.

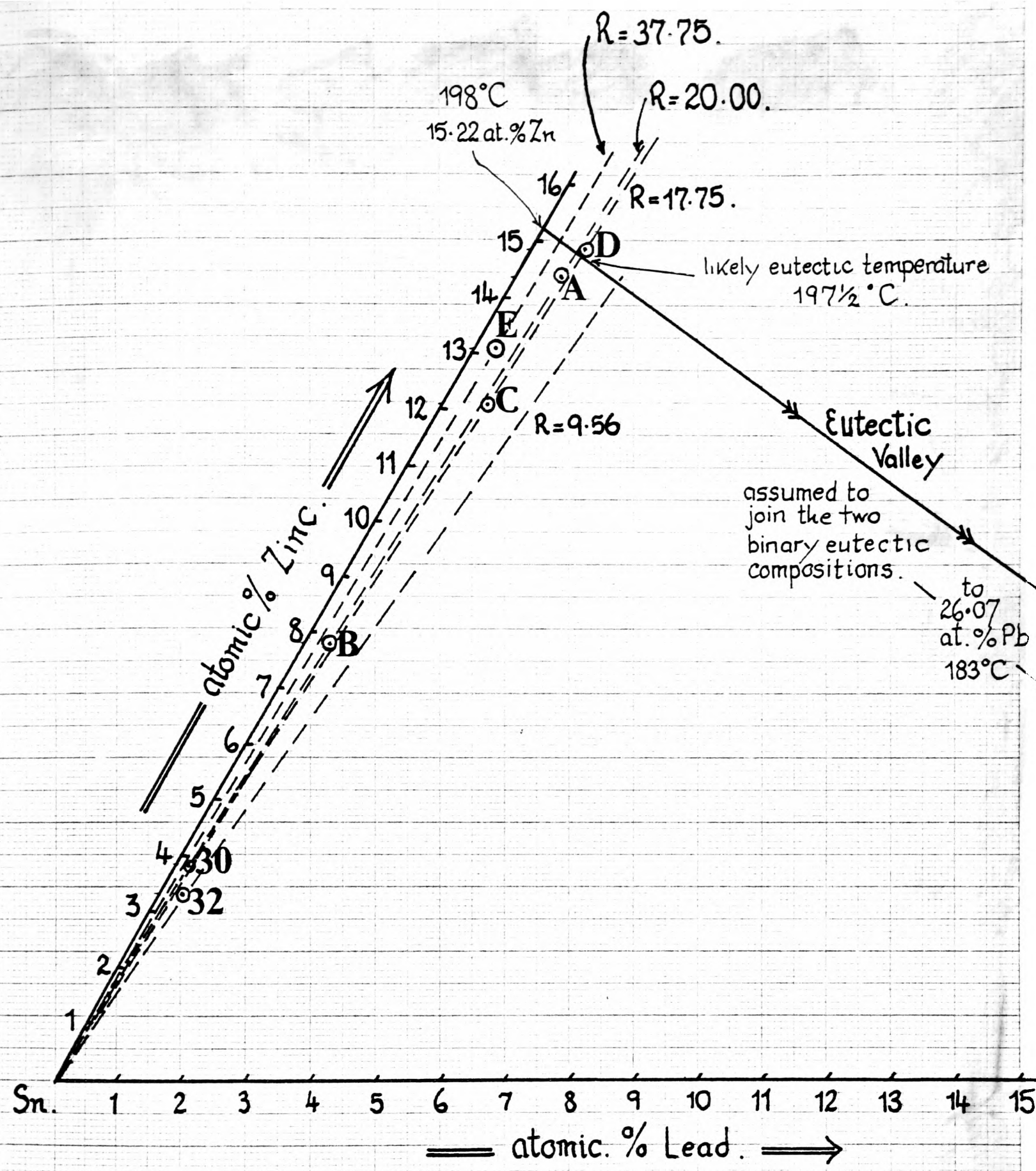


Fig 8.15. Sn-rich corner of the ternary Sn-Pb-Zn alloy liquidus surface. Dashed lines give paths down the liquidus surface assuming that the ratio C_{Zn}/C_{Pb} of the liquid remains constant until the ternary eutectic valley is reached.

Exact alloy compositions employed are given in Table 8.9 and Table 8.10.

The positions of these ternary alloy compositions on the ternary phase diagram are shown in fig. 8.15., together with the two ternary compositions studied in the slice casting apparatus as described in the next section. It can be seen from this figure that the density variation was studied down the whole length of the liquidus surface from pure tin down to the ternary eutectic valley. The fact that no significant density variation was observed between pure Sn and alloy compositions A and B therefore indicates that ternary Sn-Zn-Pb alloys with Zn:Pb ratio of 20:1 (in atomic %) should exhibit no gravitational flow effects during solidification.

8.6 Slice Cast Experiments

8.6.1 General Outline

It was mentioned in section 8.3 that Hebditch observed the effects of gravitational fluid flow in Sn-Zn binary alloys even though the density variations within this system were small. The apparatus which Hebditch used for his work was a fore-runner to the slice casting apparatus described in chapter 6 of this thesis. This suggested that the slice casting apparatus could be used to provide a sensitive indication of the extent of interdendritic gravity flow occurring in any alloy sample. A Sn-Zn-Pb alloy casting with a Zn:Pb ratio of 19.97 was therefore grown in the apparatus in order to corroborate, or otherwise, the density measurement findings of the previous section.

The same apparatus and experimental procedures were used as described in detail in chapter 6. The alloy charge was made up by carefully weighing out the relevant quantities of oxide-free, 99.99% purity elements. Melting was performed under an argon atmosphere and the charge was thoroughly stirred to ensure homogeneity. Thermal analysis was then carried out on the alloy charge in order to determine its approximate liquidus temperature. Once this had been done the charge was reheated to give a superheat of approximately 70^{o}C, re-stirred, and then poured into the pre-heated slice mould. The whole assembly was then allowed to attain thermal equilibrium at a temperature just above the

liquidus temperature of the alloy. At the start of cooling the charge was nucleated with a cold tin wire. Growth was allowed to continue until the interface had advanced approximately half-way along the length of the mould (as determined by the sample thermocouples) at which point the casting was quenched into cold water.

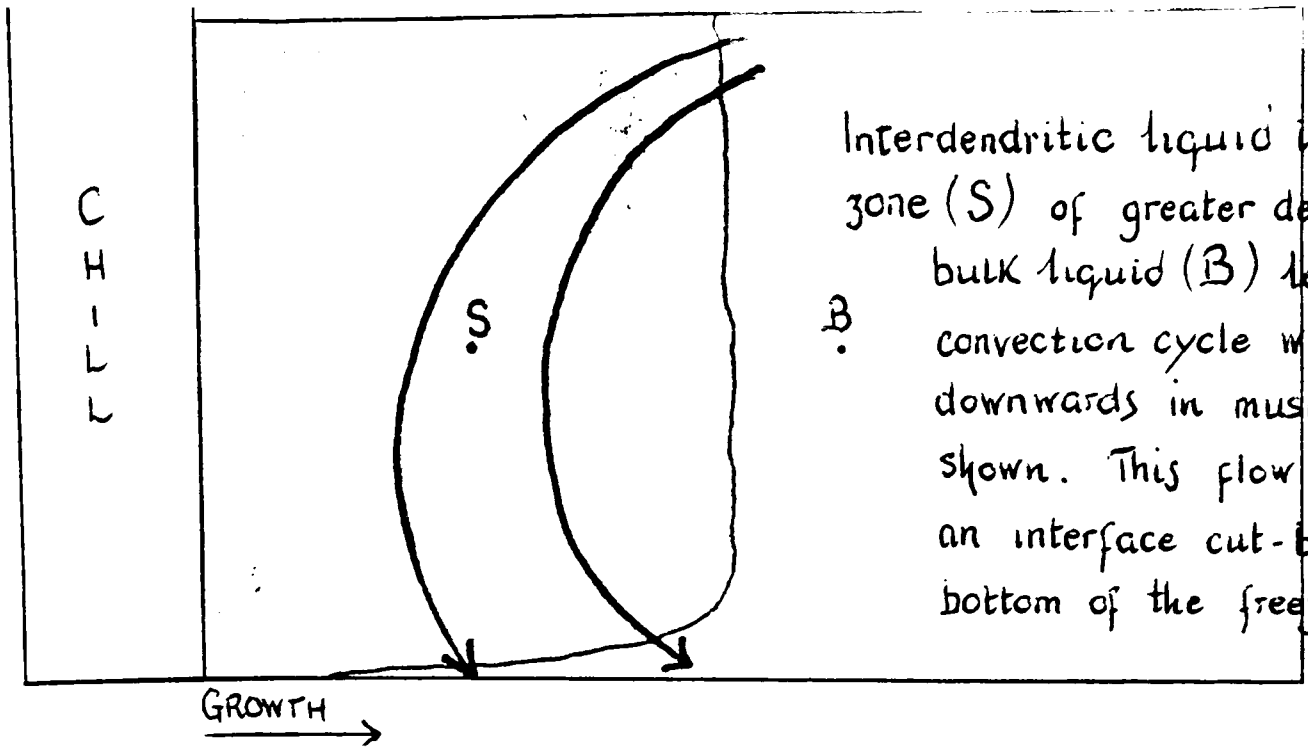
The quenched, macroscopic, dendrite tip interface shape was used to infer the presence, or absence, of interdendritic gravitational fluid flow. As explained in section 6.5.2.2, if the solute enrichment in the interdendritic liquid causes it to become denser than the bulk liquid then gravitational fluid flow occurs in a downwards direction in the semi-solid region. Solute-enriched liquid therefore moves out of the semi-solid zone towards the bottom of the casting and causes a cut-back in the dendrite tip interface in this region. Conversely if solute enrichment makes the interdendritic liquid lighter than the bulk then flow occurs in an upwards direction in the semi-solid, resulting in an interface cut-back at the top of the casting. For an alloy where solute-enrichment causes no change in interdendritic liquid density then no gravity flow of liquid should occur and the dendrite tip interface should remain vertical with no cut-back at either top or bottom. These three cases are illustrated in fig. 8.16.

8.6.2 Results and Discussion

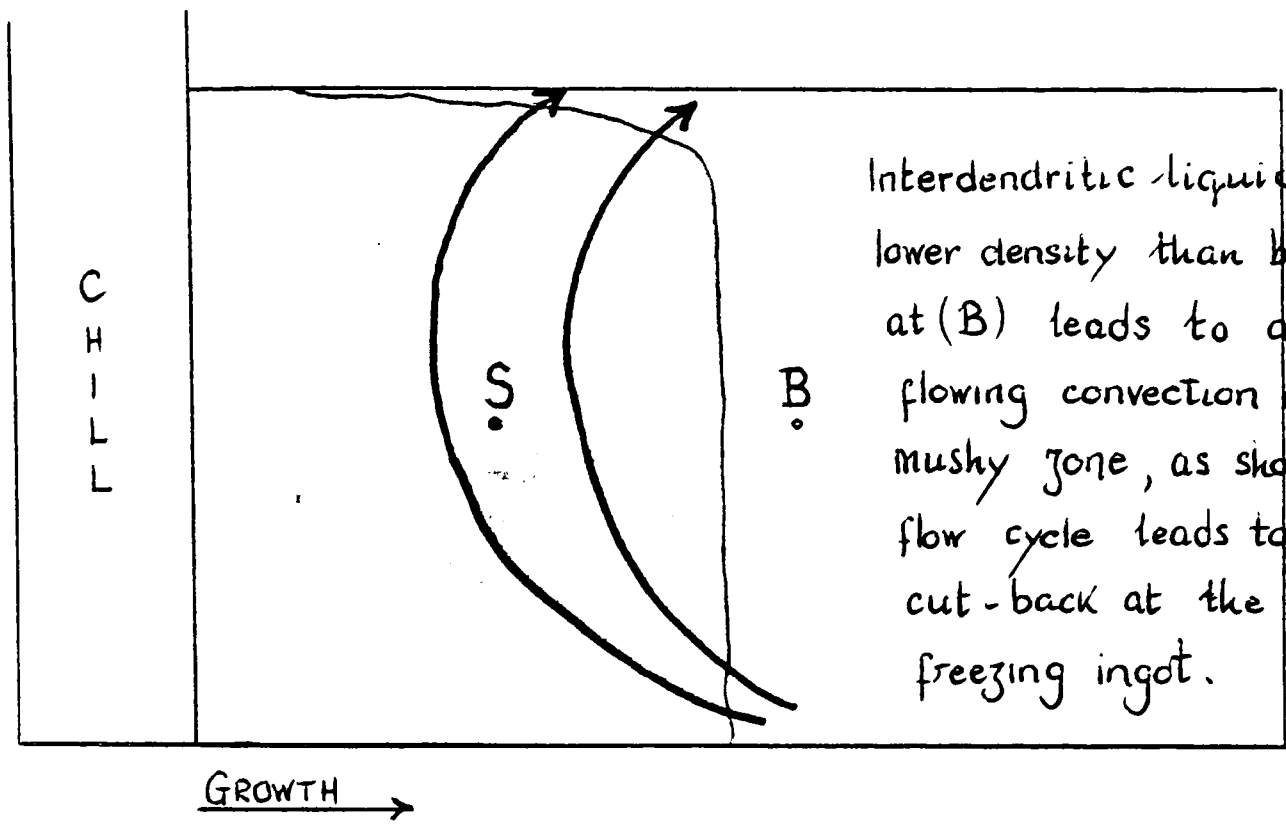
Four castings were grown for this experiment, having the compositions shown in Table 8.10., below:-

Table 8.10

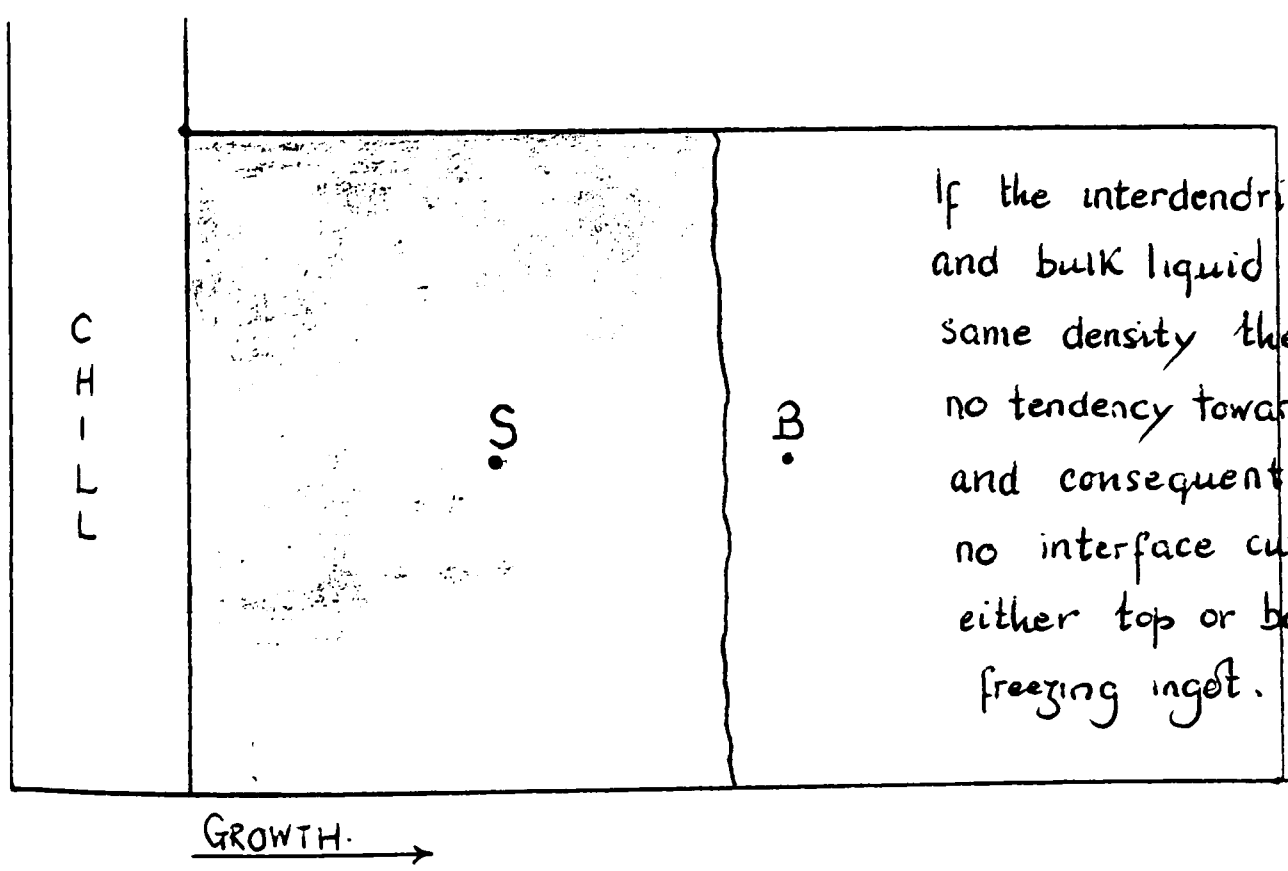
Run Number	Alloy Composition		R
	Wt.%	At.%	
30	Sn-2.158Zn-0.342Pb	Sn-3.855Zn-0.193Pb	19.97
31	Sn-2.5Zn	Sn-4.448Zn	∞
32	Sn-1.878Zn-0.622Pb	Sn-3.366Zn-0.352Pb	9.56
33	Sn-1.5Zn	Sn-2.690Zn	∞



Interdendritic liquid in semi-solid zone (S) of greater density than bulk liquid (B) leads to a convection cycle which flows downwards in mushy zone, as shown. This flow cycle causes an interface cut-back at the bottom of the freezing ingot.



Interdendritic liquid at (S) of lower density than bulk liquid at (B) leads to an upward flowing convection cycle in the mushy zone, as shown. This flow cycle leads to an interface cut-back at the top of the freezing ingot.



If the interdendritic liquid and bulk liquid are of the same density then there is no tendency towards convection and consequently there is no interface cut-back at either top or bottom of the freezing ingot.

The alloys used for runs number 30 to 32 all had a total solute content of $2\frac{1}{2}$ wt % . Of these three alloys the one used for run number 30 was a ternary Sn-Zn-Pb alloy having a Zn:Pb ratio equal to that which was found by the density technique to have zero density change down the liquidus. The alloy used for run 31 was a simple Sn-Zn binary, with $(dD/dc)_{liquidus}$ therefore being negative. That used for run 32 was a Sn-Zn-Pb ternary alloy which had a greater proportion of lead than that required for zero density change and so had a positive value of $(dD/dc)_{liquidus}$.

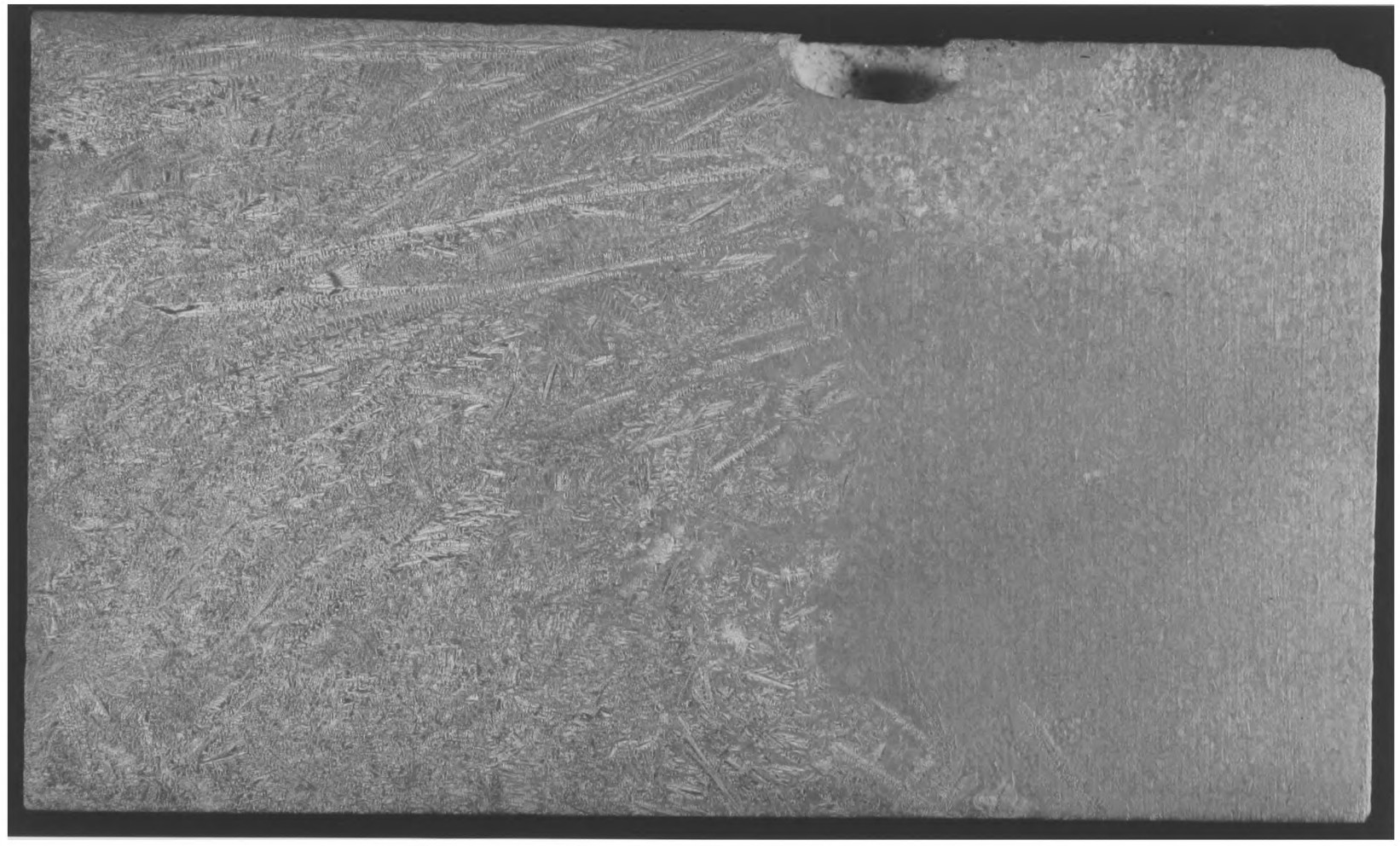
The casting data for the four runs is listed in Table 8.11., overleaf. The data follow the same general form as that obtained from the nucleated Sn-5 wt%Pb castings examined in chapter 6. Nucleation time was again observed to be dependent on initial melt superheat. Growth was essentially reproducible in castings 30, 31, and 32 which is not surprising in view of the similarity in solute content of these three castings. Growth velocity was initially around 7.2×10^{-3} cm/sec. which is the same as that measured in the Sn-5 wt%Pb castings, but the interface did appear to accelerate with time. The overall growth rate measured from quenched interface positions was around 8.15×10^{-3} cm/sec..

The quenched macrostructures of the four castings are shown in figs. 8.17 to 8.19. It can be seen from fig. 8.17 that the macroscopic dendrite tip interface of casting 30 lies roughly parallel with the chill face of the casting and has no cut-back at either top or bottom. This indicates the absence of gravitational interdendritic fluid flow in the casting, which therefore implies that the alloy composition used for casting 30 does indeed exhibit zero density change as it falls down the liquidus surface. This is further corroborated by the macrostructures of castings 31 to 33 in which gravitational fluid flow has clearly been operating. In castings 31 and 33, where the alloys were binary Sn-Zn, there is a cut-back at the top of the dendrite tip interface indicating an upward flow of interdendritic liquid during solidification (fig. 8.18). The magnitude of the cut-back in these castings is quite pronounced and yet, as mentioned previously, the driving force for flow in Sn-Zn alloys is very small

Table 8.11

Data concerning the slice casting runs performed to check the density variation of the interdendritic liquid of several alloys

Run N°	33	30	31	32
Approx. alloy composition Wt %	Sn - 1½ Zn	Sn - 2·16 Zn - 0·34 Pb	Sn - 2½ Zn	Sn - 1·83 Zn - 0·62 Pb
Inget Wt gms	628	630	629	630
Air flow rate (true) through chill l/min.	10	10	10	10
ΔT_s Holding Superheat °C	2¼	3½	3½	3°
Av. interface temperature T_p °C	223	219	218½	220
Nucleation time t_N	1m 00s	1m 40s	1m 40s	1m 20s
Time taken for the dendrite tip front to pass the various thermocouple positions t_A	2m 00s	2m 26s	2m 36s	2m 08s
t_B	7m 26s	7m 32s	7m 53s	7m 35s
t_C	10m 17s	10m 38s	10m 50s	10m 23s
t_D	12m 59s	13m 14s	13m 26s	12m 56s
Quench time t_Q	14m 25s	14m 46s	14m 56s	14m 46s
$t_A - t_N$	1m 00s	0m 46s	0m 56s	0m 48s
$t_B - t_N$	6m 26s	5m 52s	6m 13s	6m 15s
$t_C - t_N$	9m 17s	8m 58s	9m 10s	9m 03s
$t_D - t_N$	11m 59s	11m 34s	11m 46s	11m 36s
Total Growth time $t_Q - t_N$	13m 25s	13m 06s	13m 16s	13m 26s
cm/sec $\bar{V}_{A\to B}$	7.01×10^{-3}	7.47×10^{-3}	7.21×10^{-3}	6.99×10^{-3}
cm/sec $\bar{V}_{A\to C}$	7.30×10^{-3}	7.38×10^{-3}	7.35×10^{-3}	7.33×10^{-3}
cm/sec $\bar{V}_{A\to D}$	7.60×10^{-3}	7.73×10^{-3}	7.73×10^{-3}	7.73×10^{-3}
Distance of quenched interface from chill D	62·4 mm	63·6 mm	64·6 mm	65·0 mm.
Average grow velocity $D/t_Q - t_N$	7.75×10^{-3} cm/sec	8.09×10^{-3} cm/sec	8.12×10^{-3} cm/sec	8.06×10^{-3} cm/sec



Macro-etched for approx 15 minutes in hot, dilute nitric acid. A gelatinous precipitate produced on the ingot surface had first to be removed before the structure shown was revealed.

Fig. 8.17. Macrostructure of ingot 30. Alloy comp^{n} Sn - 3·855 at % Zn - 0·193 at % Pb. Zn : Pb ratio of 19·97 : 1 . No cut-back in interface shape at either top or bottom indicates that interdendritic gravitational fluid flow has not occurred. Alloy therefore has insignificant density change down its liquidus.

MAG^{n} x 1·5

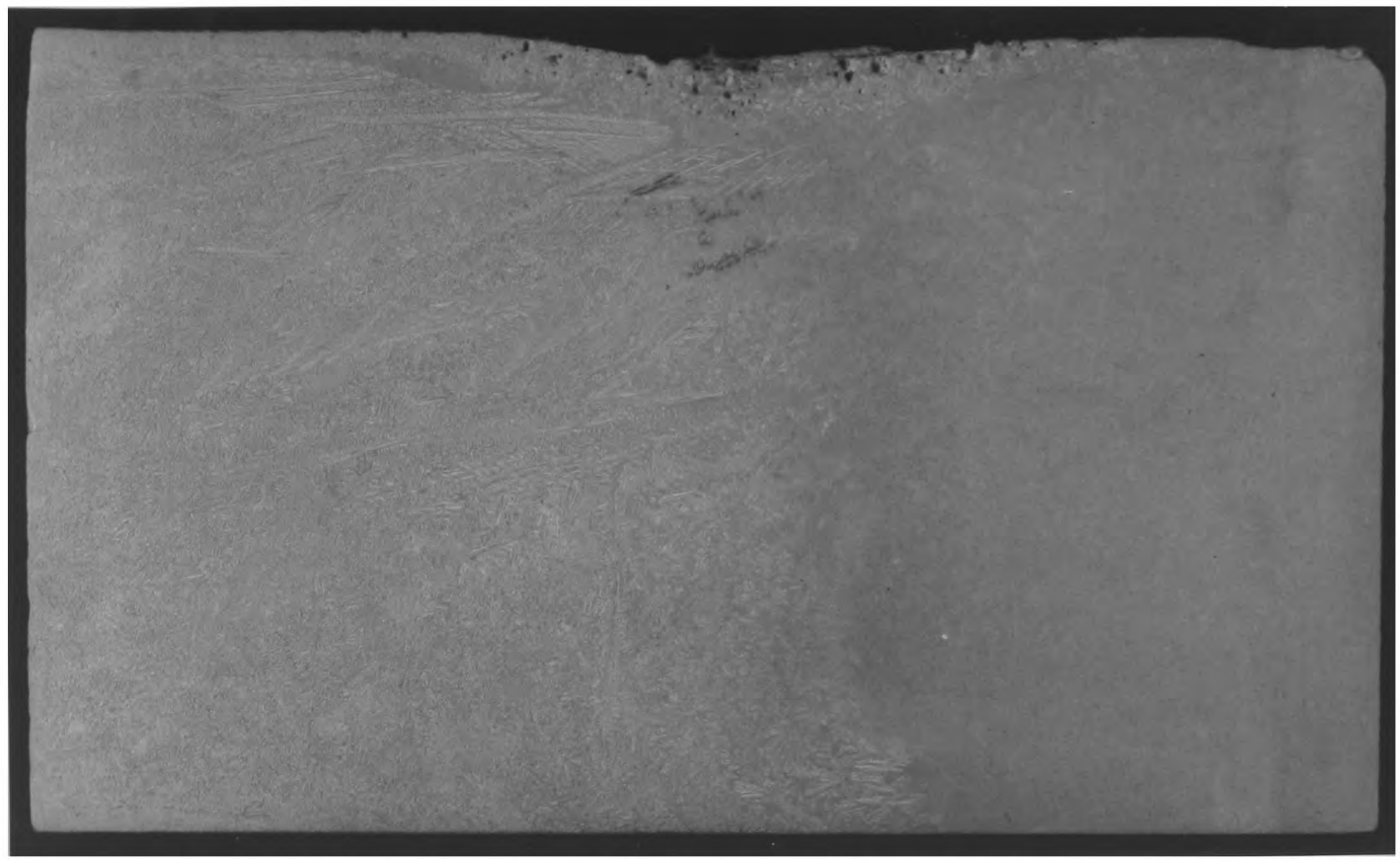


Fig 8.18 (a). Etched macrostructure of ingot 31; Sn-2½ wt% Zn.
Dendrite tip interface is cut-back at top of ingot, indicating upward gravity flow of liquid in the mushy zone.
Macro. etched as for ingot 30, fig. 8.17. MAG^N x 1.25



Fig 8.18 (b) Etched macrostructure of ingot 33; Sn-1½ wt% Zn.
Dendrite tip interface is also cut-back at the top of this ingot.
MAG^N x 1.25

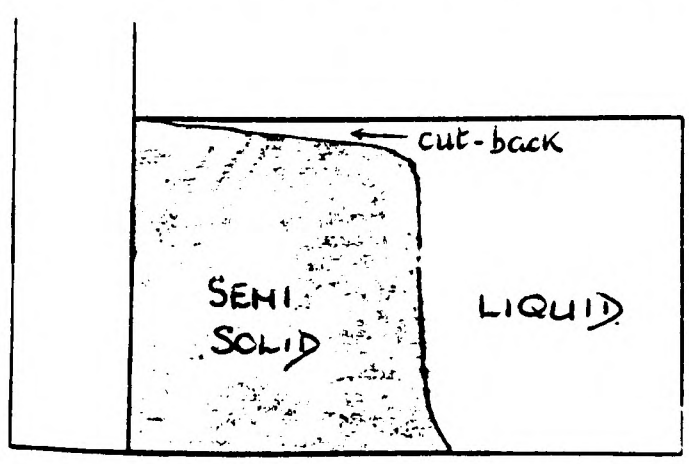
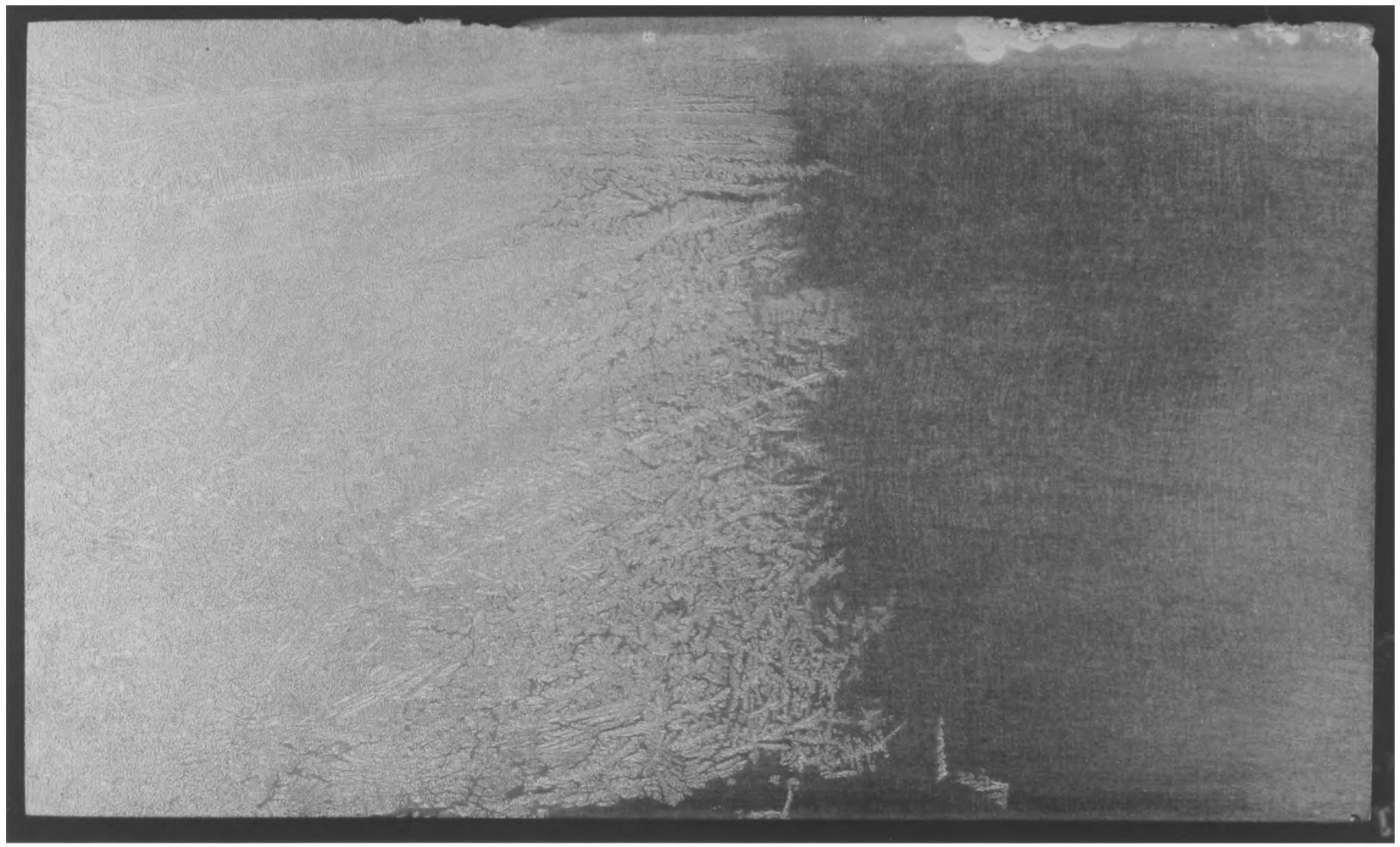


Fig. 8.18 (c). True extent of interface cut-back in ingots 31 and 33, deleting the confusing 'quench porosity structure' at the top surface of the ingots.



MAG^{N} x 1·5

Macro-etched for approx 15 minutes in a mixture of 1 pt. conc. HNO_3, 3 pts conc. HCl, 2 pts H_2O.

Fig. 8.19. Macrostructure of ingot 32 ; Sn - 3·366 at % Zn - 0·352 at. % Pb.

The higher Pb content of this alloy over that of ingot 30 has caused the interdendritic liquid to become denser than the bulk liquid. Gravity flow of solute-enriched liquid out of the mushy zone at the bottom of the ingot has therefore caused the dendrite tip interface to become cut back in this region.

(0.002 g/cc density change for 1 at.% Zn down the liquidus line). The absence of such a cut-back in casting 30 is therefore strong evidence that ternary alloys with Zn:Pb of 19.97:1 have zero liquid density change down their liquidus line. In casting 32 where the Pb content of the ternary is too high there is a clear cut-back in the dendrite tip interface at the bottom of the casting, fig. 8.19. This indicates that the interdendritic liquid was denser than the bulk liquid and flowed downwards through the semi-solid during solidification.

There are two further points worthy of mention in the quenched macrostructures of figs. 8.17 to 8.19. First the extent of the cut-back at the top of the dendrite tip front in castings 31 and 33 was masked to a certain extent, as shown in fig. 8.18. It was in order to verify that this feature was a 'real' effect that the Sn-Zn binary alloy run was repeated in casting 33. Microscopic examination of samples taken from the top region of both castings showed that the feature was an accumulation of porosity presumably brought about by inadequate feeding when the castings were quenched. The true extent of the interface cut-back prior to quenching was therefore as shown diagramatically in fig. 8.18(c). No primary dendritic material was observed in the micro-sections from the cut-back region. The second point worthy of note was the protrusion at the bottom of the dendrite tip interface which was present to a certain extent in all of the castings. This was probably caused by a combination of two factors. Firstly the equi-axed crystals which form just after nucleation tend to fall down the chill and subsequently lie on the bottom of the mould. Secondly there must be a certain amount of localised heat extraction from the melt by conduction among the relatively thick bottom stainless steel plate. Such a 'foot' was not noticed in the Sn-5 wt%Pb castings of chapter 6 because the heavily Pb enriched liquid which accumulated at the bottom of the castings re-dissolved the initial equi-axed dendrites and retarded growth in this region by depressing the liquidus temperature.

8.7 Summary and Conclusions

An alloy has been developed in which there is zero density change in the interdendritic liquid throughout the majority of the semi-solid region. This alloy lies in the Sn-rich corner of the ternary Sn-Zn-Pb system, and has a Zn:Pb ratio of 19.97:1 (concentration in atomic %) where the total solute content (Zn + Pb) is less than 15.2 at. %.

Gravity flow macrosegregation was found to be completely absent in a casting of such an alloy grown under conditions which normally favour the mechanism. The exact alloy composition used for this slice casting was Sn-3.855 at %Zn - 0.193 at.% Pb, the freezing range of the alloy being approximately 23°C. The alloy could therefore be usefully employed in the study and measuremen of dendrite spacings, as well as in the study of macrosegregation mechanisms other than gravity flow.

The alloy was developed using a combination of a theoretical treatment and a precision density measurement technique. The theoretical treatment involved the derivation of an expression for the density variation of an alloy down its liquidus line. The coefficient relating the density change in this expression to changes in temperature and alloy composition were then experimentally determined using the precision density measurement technique. These values for the coefficients were then substituted in the expression, and an alloy system and composition where liquid density did not change down the liquidus was predicted. The density measurement technique was then used again to verify that no density change did, in fact, occur in such an alloy.

Two precision density measurement techniques were employed during the cours of the experiment, these being maximum bubble pressure and pycnometer. The bubble pressure technique was found to be entirely unsuitable for the low melting-point metals employed in this study, contrary to the information available on the technique in the literature. In spite of increasing apparatus complexity no meaningful results could be obtained using the method. It was felt that the major problem lay in oxide contamination of the melt, and that no further refinement

beyond those already made could reasonably be attempted. The method was therefor reluctantly abandoned. The pycnometer technique, which had originally appeared less elegant and less suited to the experiment, was found to be very accurate, reproducible, and efficient in yielding data on low melting-point alloy densities It was this technique which was used in the successful prediction of the correct alloy system and composition for zero density change.

CHAPTER 9

CHEMICAL ANALYSIS. ATOMIC ABSORPTION SPECTROPHOTOMETRY

9.1 Introduction

Chemical analysis is clearly an important part of any quantitative work on macrosegregation. Careful consideration was therefore given to choosing the analytical technique best suited to the various experiments described in this thesis from the many different techniques available. At the start of the work it was envisaged that the chosen technique would need to fulfil the following requirements:-

(a) be capable of routine accuracies of < $2\frac{1}{2}\%$, and optimum accuracies of around 1%.

(b) be specific to known given volumes within a casting: these volumes being from as much as 30cm. apart to as little as 1mm. apart.

(c) be reliable and cheap (in terms of both capital and operating costs).

(d) be quick and easy to perform, in view of the large number of analyses required.

It was eventually decided that atomic absorption spectrophotometry was the technique which came closest to fulfilling all of these requirements, and so this technique was chosen for the work.

9.2 Outline of Analysis technique

Atomic absorption analysis is based on the ability of atoms of any given element to absorb electromagnetic radiation at characteristic wavelengths. Several types of absorption analysis exist, differing only in the way in which the free atoms are produced. In the most common technique, the one employed in this work, a population of free atoms is produced from a given sample using a high temperature flame. The sample is first dissolved into solution in order transform the elements into their ionic form. A small amount of this solution is then passed into the flame where a certain proportion of each of the ionic

species gets converted into free atoms. A light source, emitting the characteristic line spectrum of the element to be determined, is shone through the flame onto a detection device. If any atoms of that element are present in the flame then some of the light energy is absorbed and this is registered on the detector.

In flame absorption spectrometry the amount of radiation energy absorbed is proportional to the number of atoms of the element in the flame. Furthermore there is a fixed ratio between the number of atoms and the number of ions of a given element in the flame.

$$X^{n+} + ne^- \rightleftharpoons X$$

Consequently the concentration of the element in the sample solution may be worked out by comparing the amount of absorption with that given when standard solutions containing known concentrations of the element are introduced into the flame.

9.3 The Instrument

The spectrophotometer used in this work was a Pye Unicam SP90A Series 2. A schematic diagram showing the general layout of the machine is given in fig. 9.1(a).

Hollow cathode lamps provide the source of radiation in the instrument, a different lamp being used for each element analysed. The cathode of the lamps is made from the element which is to be determined and emits a characteristic line spectrum in which the resonance line is prominent. After the beam of radiation has passed through the flame this line is selected using a monochromator, and its intensity is monitored on a chart recorder readout via a photomultiplier and amplifier.

The SP90 sampling system is of the nebulizer-spray chamber-burner type shown in fig.9.1(b). The sample solution is sucked up into the nebulizer through a capillary tube by the action of the oxidant gas supply over the end of the capillary (see fig.9.1(c)). The solution emerges as a spray of droplets of various sizes, the droplets being further fragmented by collision with an impact

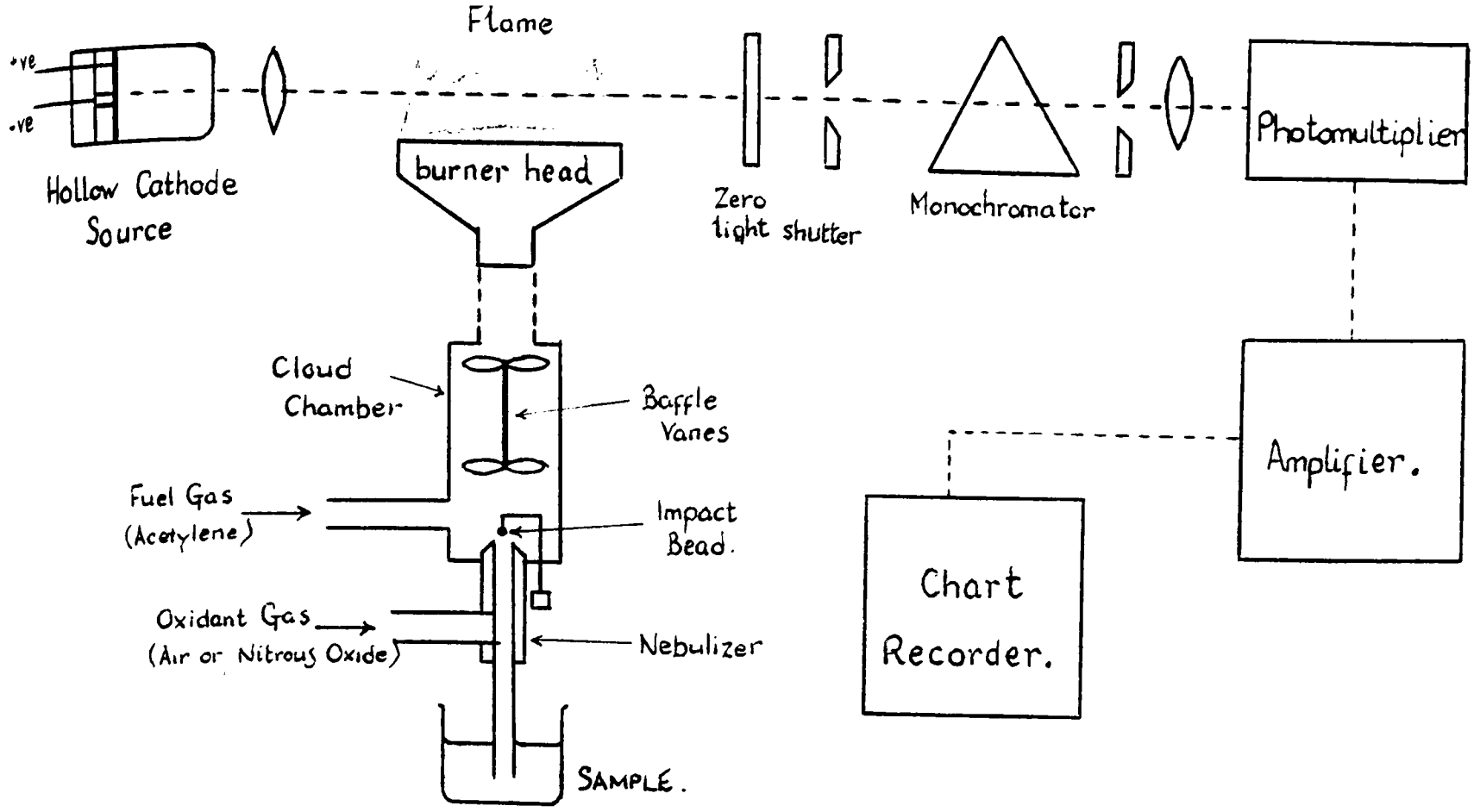


Fig. 9.1(a). General layout of the spectrophotometer analysis system.

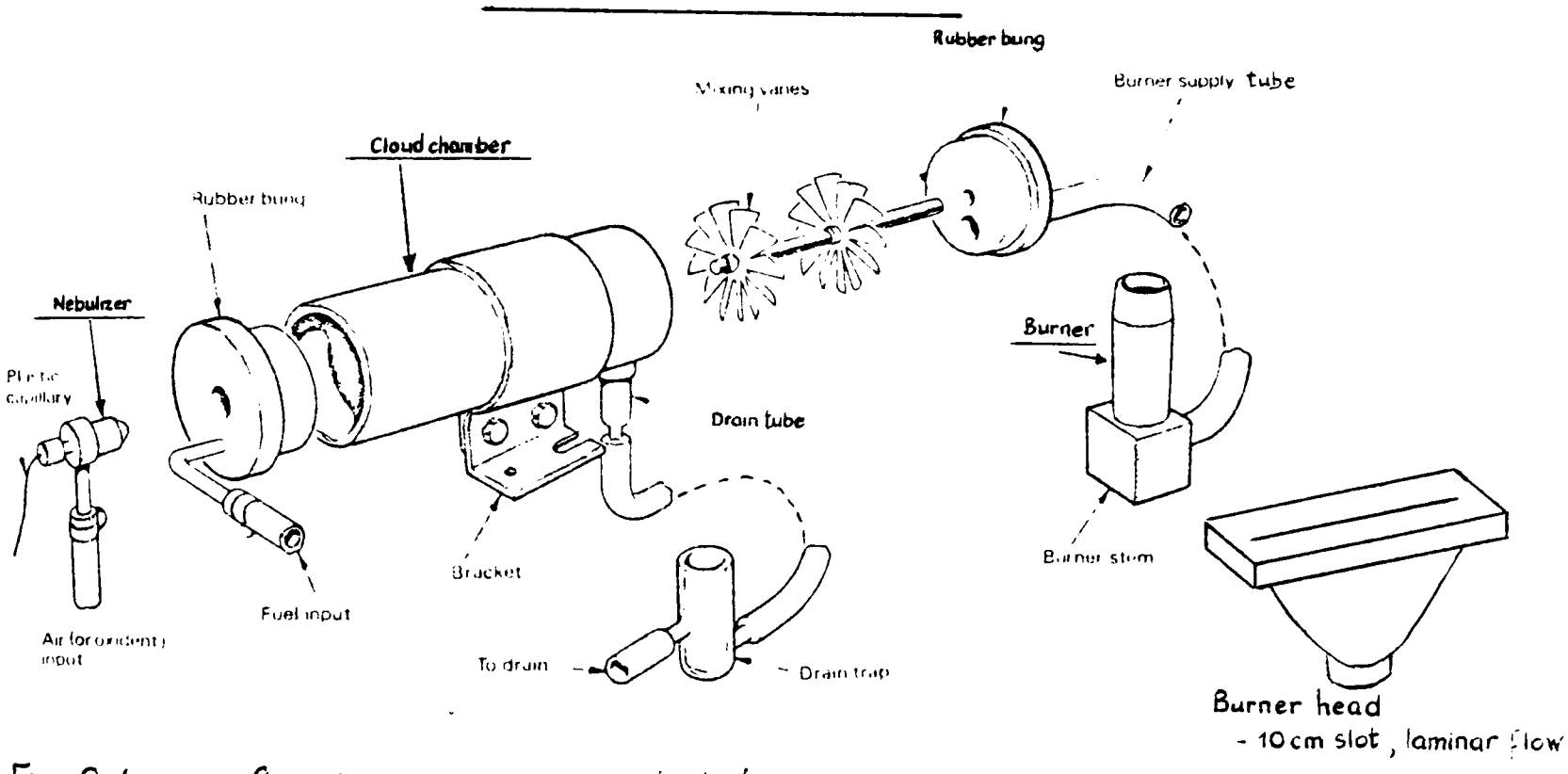


Fig. 9.1(b). Sampling system - exploded view.

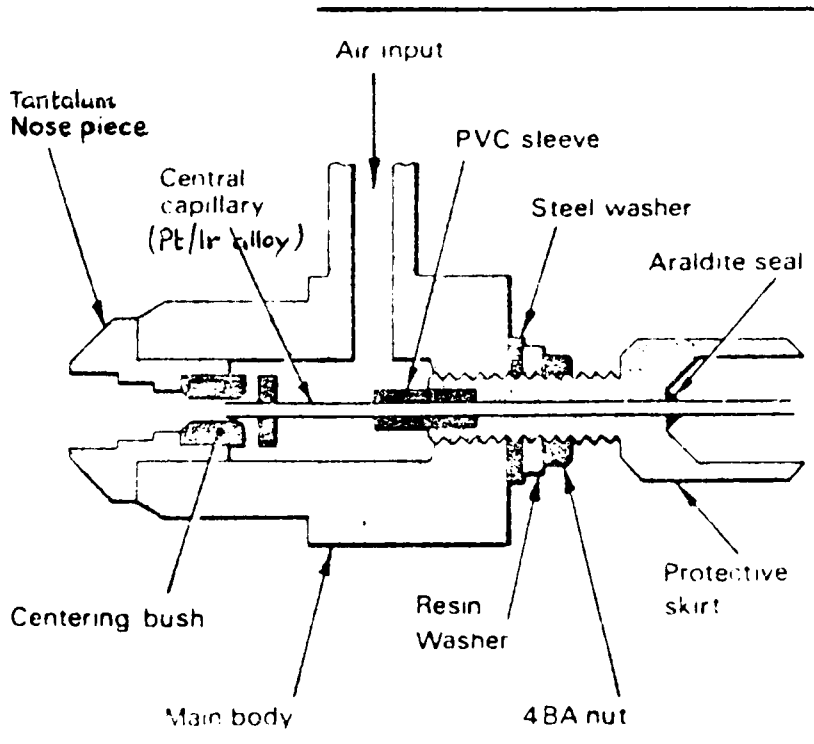
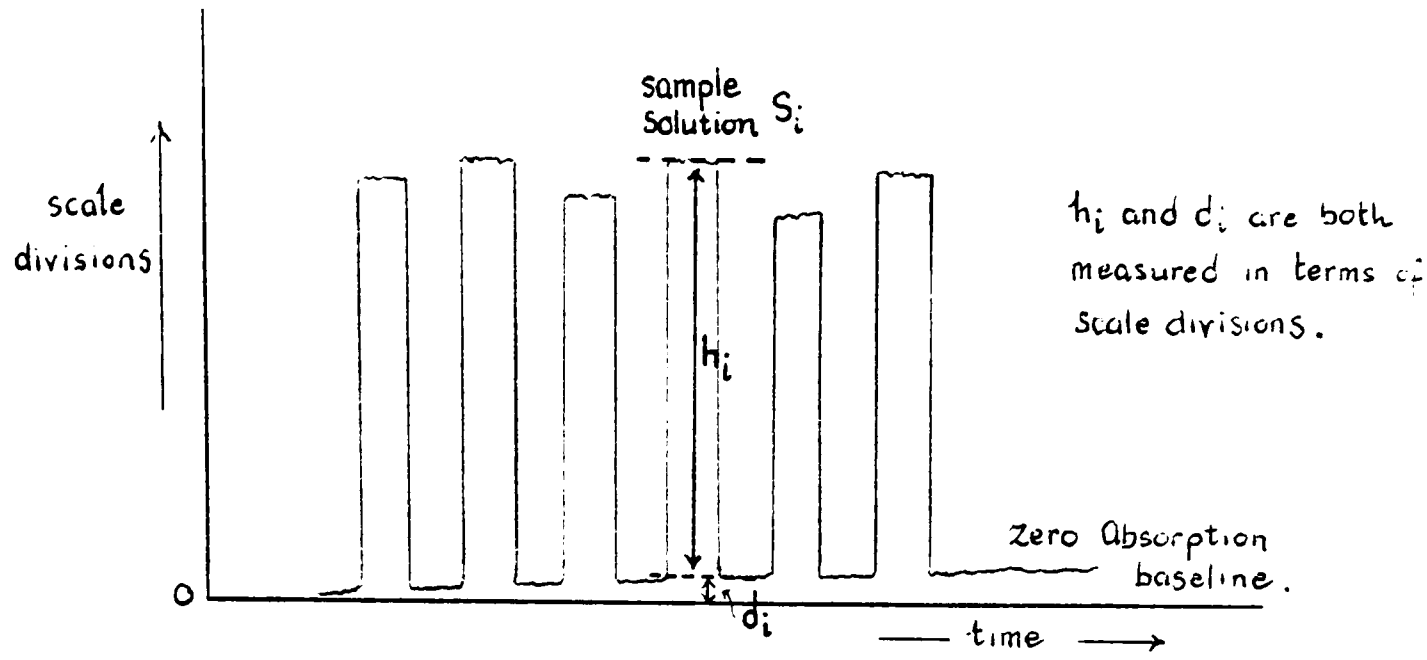


Fig. 9.1(c). Nebuliser Unit. - Inert type.



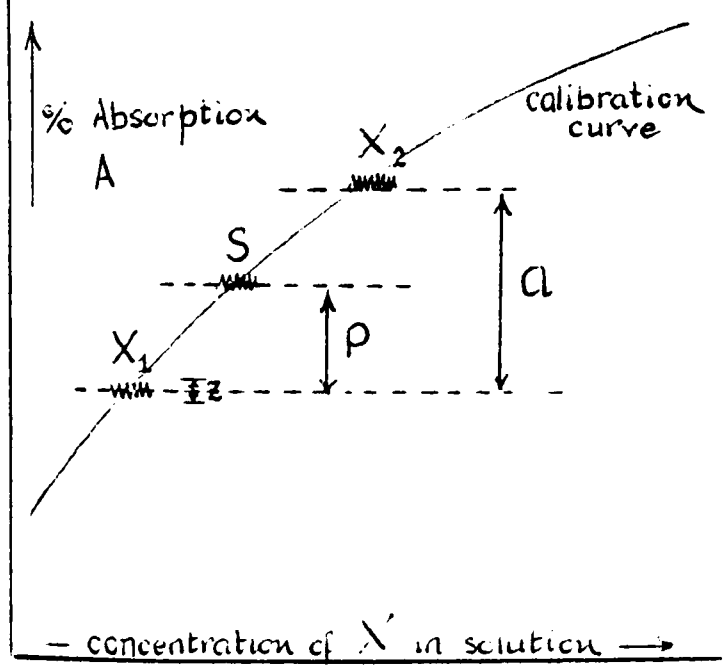
For ×1 scale expansion, because of baseline drift then at the ith solution, S_i, 0→100% absorption corresponds to $(100 - d_i)$ scale divisions.

. True % absorption of soln. $S_i = A_i = h_i \times \frac{100}{100 - d_i}$ — 9.1. (a).

For ×2 scale expansion, 0→100% absorption corresponds to $(200 - d_i)$ divisions

. True % absorption of soln. $S_i = A_i = h_i/2 \times \frac{200}{200 - d_i}$ — 9.1. (b).

Fig. 9.2(a). Correction applied to signal height to allow for the effects of baseline drift during a determination



The concentration of element X in the sample solution S lies somewhere between the two standard solutions X_1 and X_2, as shown. Assuming that the % abs. vs concn. X curve is linear between X_1 and X_2 (i.e. the two standard solutions are sufficiently close in compn. to allow a linear approximation) then :-

Av. concn. sample soln = $S = X_1 + \frac{p}{a}(X_2 - X_1)$

Now if each signal has an uncertainty of ± Z % absorption due to noise and standard deviation, then :-

$$S = X_1 + \frac{p \pm 2Z}{a}(X_2 - X_1)$$

∴ % error in calculating the concn = $E = \frac{\pm \frac{2Z}{a}(X_2 - X_1)}{\left(\frac{X_1 + X_2}{2}\right)} \times 100$ %

i.e. $E = \pm \frac{200ZY}{Wa}$ % — 9.2.

where $Y = X_2 - X_1$ = diff in concn between standard solns

and $W = \frac{1}{2}(X_1 + X_2)$ = av. value of concn of 2 standards

Fig. 9.2(b). Technique employed to determine the optimum range of sample concentration for minimisation of error.

bead assembly positioned just in front of the nebulizer orifice. The spray and oxidant gas are then directed into the cloud chamber where they are intimately mixed with the fuel gas and where the larger droplets are precipitated. Sets of baffles are placed within the chamber to help in both processes. The gases and spray then pass from the cloud chamber up to the burner head where combustion takes place.

Two types of burner head were used in this work one of which burnt an air/acetylene mixture and the other a nitrous oxide/acetylene mixture. Both were of the narrow slot type shown in fig. 9.1(b), with slot lengths of 10 cm. and 5 cm. respectively. The air/acetylene flame produces a temperature of around 2300 °C while the nitrous oxide/acetylene flame is hotter at around 2950 °C.[141] The higher temperature flame was required for the determination of silicon in order to dissociate stable compounds and so provide atoms for absorption. The air/acetylene flame was adequate for the rest of the elements studied.

9.4 Experimental Procedure

The procedure adopted for determining the macrosegregation present in any given ingot or casting was as follows:-

(a) The nominal composition of the alloy was examined and one of the solute elements, X, say, was chosen for analysis.

(b) The spectrophotometer was then calibrated for X using standard solutions containing known concentrations of the element. A calibration plot of % absorption versus concentration of X was made. This plot was then studied and the range of concentrations of X which gave the optimum analytical accuracy was determined.

(c) Samples were then taken from given positions in the casting, weighed, dissolved into solution, and diluted to a given volume. The sample weight and diluted volume were chosen, knowing the nominal alloy composition, to bring the concentration of X in the sample solution into the optimum concentration range of the instrument.

(d) Possible interference phenomena were then studied. The sample solutions contained many ions other than those of X and so it was necessary to see if any of them interfered with the absorption response of X in the flame. If any ionic species was found to cause interference then an appropriate addition of this species was made to all standard solutions. Interference then occurred equally in both sample and standard solutions, thereby eliminating any errors.

(e) The concentration of X in the sample solutions was determined by direct comparison with standard solutions. Two stages were used. A rough determination was made initially, and then each sample solution was closely bracketed by the two standards nearest to it in concentration.

(f) The composition of X in the original alloy sample could finally be easily calculated knowing the sample weight, the final diluted volume of the solution, and the concentration of X in the solution.

Steps (b) to (e) in the procedure are described in more detail in the following sections.

9.4.1 Spectrophotometer Calibration

A detailed account of the setting-up and operation of the instrument can be found in the instruction manual and so only a brief description will be attempted here.

When a new element, X, was to be examined the instrument had first to be calibrated for X, and the optimum concentration range for X determined. Calibration was performed using standard solutions containing known concentration of the element. These standards were made up volumetrically from a single concentrated stock solution of X. Table 9.1, overleaf, lists the ways in which the stock solutions were prepared for each of the elements studied in this work. The Table also gives the concentrations of the stock solutions employed, together with the various precautions which were taken during their preparation and storage.

The calibration run proceded as follows. The appropriate hollow cathode

TABLE 9.1. Preparation of stock solutions used in this work.

Element	Dissolution Procedure.	Dilution	Stock Soln Concn
Al	10.00 g metal dissolved in 250 mls conc. HCl + 10 mls conc. HNO_3	1 litre	10,000 p.p.m
Co	0.500 g metal dissolved in 20 mls 5N HNO_3	2 litres	250 p.p.m.
Cr	0.500 g. " " " 20 mls conc. HCl	2 litres	250 p.p m
Cu	0.500 g. " " " 40 mls 5N HNO_3	2 litres	250 p.p.m
Mg	0.500 g " " " 50 mls 5N HCl	5 litres	100 p.p.m.
Ni	0.500 g. " " " 20 mls 5N HNO_3	1 litre	500 p.p.m.
Pb	1.000 g " " " 40 mls 5N HNO_3	1 litre	1,000 p.p.m.
Si	7.552 gms. $Na_2SiO_3 . 5H_2O$ dissolved in H_2O	1 litre	1,000 p.p.m.
Sn	10.00 g. metal dissolved in 100 mls conc. HCl + 10 mls conc HNO_3	1 litre	10,000 p.p.m
Zn	0.500 g " " " 50 mls 5N HCl	10 litres.	50 p.p.m

Precautions Taken.

a. All metals were 99.99% purity minimum. All chemical reagents were AnalaR[144] grade.
b. All surface oxide was scraped from the metal pieces prior to dissolution.
c. Solutions were stored in polythene containers to avoid possible leaching from glassware.
d. Maximum storage time for stock solns was 3 months ; for standard solns. 1 week.

TABLE 9.2. Optimum concentration range and corresponding machine parameters.

Element.	Si	Cu	Pb	Zn	Cr	Co	Mg
Optimum Concn. Range p.p.m.	120→200	5 → 9	20→35	0.7→1.3	8 → 24	17 → 31	0.4→1.3
Scale Expansion	x 2	x 1	x 2	x 2	x 1	x 2	x 1
Oxidant Gas Flow Rate	N_2O 5 l/min.	Air 5 l/min	Air 5 l/min.	Air 5 l/min.	Air 5 l/min.	Air 5 l/min.	Air 5 l/min.
Fuel Gas Flow Rate	C_2H_2 4.8 l/min	C_2H_2 1 l/min.	C_2H_2 1·2 l/min	C_2H_2 1·5 l/min	C_2H_2 1·5 l/min	C_2H_2 1 l/min	C_2H_2 1·5 l/min
Monochromator Wavelength $\times 10^{-6}$ m.	251·6	324·8	283·3	213·9	357·9	240·7	285·2
Monochromator Slit Width mm.	0.10	0 C3	0.10	0.40	0.C3	C.10	0.C8
Burner Height (below radiation beam) mm.	10	8	8	10	10	10	10
Standard deviation of signals in optimum concn. range.	± ¾	± ¼	± ¼	± ½	± ½	± ¼	± ¼
Maximum uncertainty in sample concentration values %	±3.0	±1·5	±0·8	±2·0	±1·6	±0.9	±1·3
LAMP CURRENT mA.	12	4	4	6	8	5	3
Interference encountered.	Al	None	Sn	None	None	Ni	Al

lamp was first taken, plugged into the machine, and allowed to warm up for at least thirty minutes. The wavelength control of the monochromator was then adjusted to correspond to the resonance line wavelength of the element. After this the flame was ignited, and the chart recorder trace was calibrated so that the two extremes of the scale corresponded to 0% and 100% absorption. This condition was known as x1 scale expansion. Total absorption was achieved by placing a metal shutter between the lamp and the monochromator. Zero absorption was set by altering the gain control while distilled water was being sprayed into the flame. One of the most concentrated of the standard solutions was then sprayed into the flame and the operating controls of the instrument were adjusted until the % absorption signal of the standard was maximised. Further fine adjustments were then made to the controls to minimise any noise on the signal while keeping the absorption signal as high as possible. Those operating parameters which required adjustment are listed in Table 9.2. Of particular importance in minimising noise were the slit width setting, the fuel flow rate, and the burner height setting. The noise to signal ratio was also critically dependent on the performance of the nebulizer unit. Careful attention was paid to the relative positioning of the end of the capillary and the nose piece (see fig.9.1(c)), and attempts were made to try and prevent the capillary from becoming blocked during a run.

Once the instrument parameters had been optimised each of the standard solutions was sprayed in turn into the flame. The time allowed for spraying was around 30 seconds per solution, with distilled water being sprayed between each solution to flush out the instrument and establish a reference baseline for 0% absorption. All solutions were sprayed several times during any one run so that the standard deviations of the signal heights could be established. Fig. 9.8 shows a typical chart recorder trace taken from part of an actual sample determination run. A simplified, schematic version of this is shown in fig.9.2(a). It can be seen from these figures that there was a general drift in the baseline signal with time. This was caused mainly by a fall off in lamp intensity. It had the effect of compressing the scale so that 0 to 100%

absorption no longer corresponded to 100 scale divisions (x 1 scale expansion). A correction therefore had to be made to the signal heights h_i, fig. 9.2(a), in order to convert them into % absorption values for the relevant solutions. This correction is given by equation 9.1 below fig. 9.2(a). Once the correction had been applied to each signal an average value was calculated for the % absorption of each standard solution from the several readings taken throughout the run. A calibration curve of % absorption versus the concentration of X in the solutions was then drawn up. Typical curves are shown for the determination of copper, zinc, and chromium in figs. 9.3, and 9.4(b) and (a), respectively.

Each point on a calibration curve had an uncertainty of z_i % absorption in the overall average absorption figure of a_i %. In practice it was found that the standard deviation for the % absorption value of any particular solution throughout a determination run was only slightly greater than the average noise present on an individual signal peak and baseline. Furthermore, it was also generally observed that the level of noise (and hence the uncertainty z_i) was the same for all solution concentrations no matter what the magnitude of the % absorption value. It was therefore possible to use a single value of z in conjunction with the shape of the calibration curve to determine the concentration range of the curve where the error in concentration was at a minimum. The calculation employed is shown beneath fig. 9.2(b). The formula given in equation 9.2 was applied to each pair of adjacent standard solutions on the curve to give the error in the concentration (S ppm) of a sample solution lying in the concentration range between each pair of standards. The error given by equation 9.2 always exhibited a minimum at some part of the calibration curve because as W increased so A decreased (for constant Z and Y).

Owing to the finite thickness of the line scribed by the recorder pen on the chart trace it was not possible to obtain signal heights to an accuracy of better than $\pm\frac{1}{4}$ scale divisions ($\pm$1/8 division uncertainty on signal peak and baseline). This corresponded to an uncertainty of $\pm\frac{1}{4}$% absorption for x1 scale expansion. In cases where this was found to be the limiting factor to the

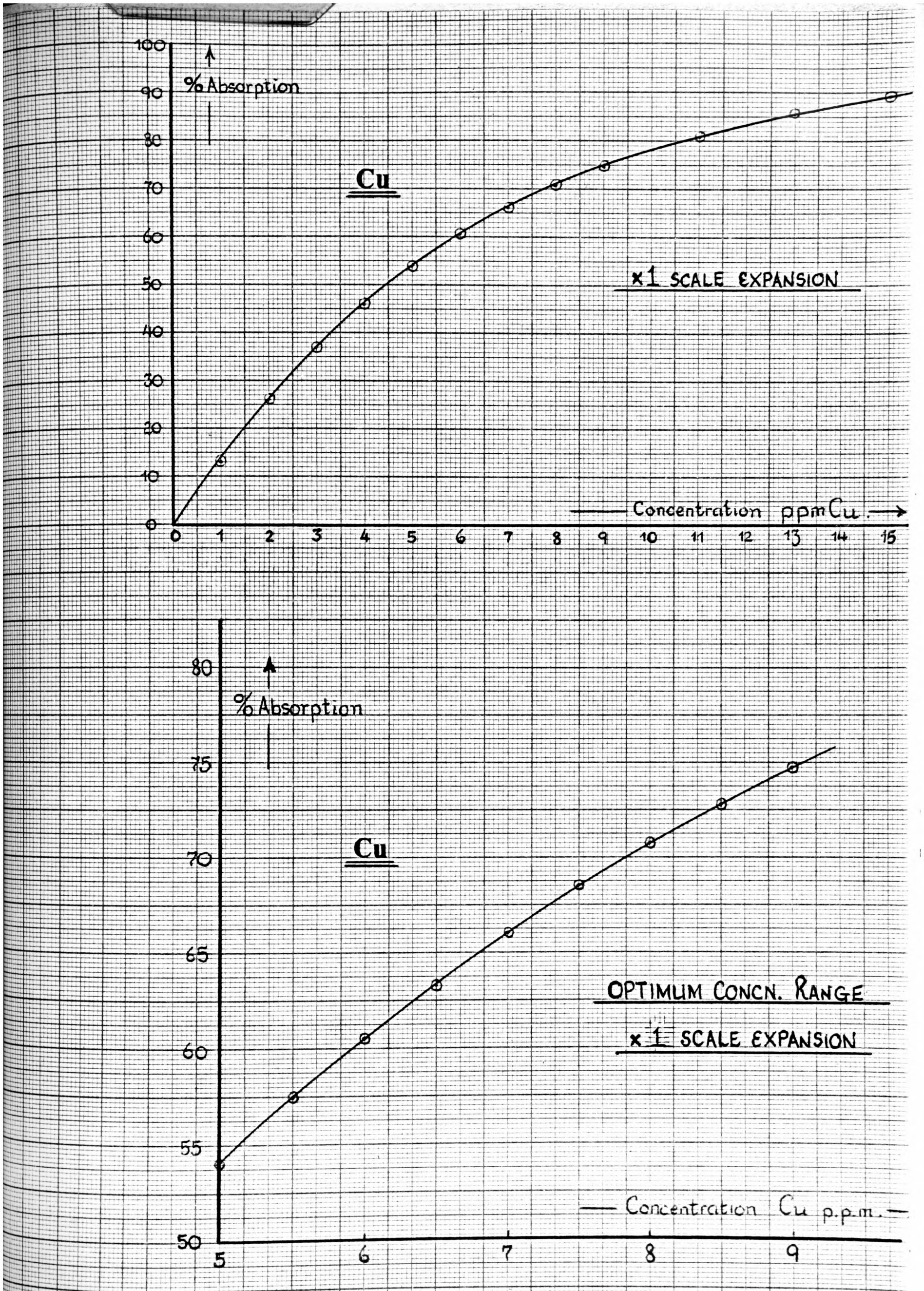


Fig. 9.3. Calibration curve for Copper standard solutions.

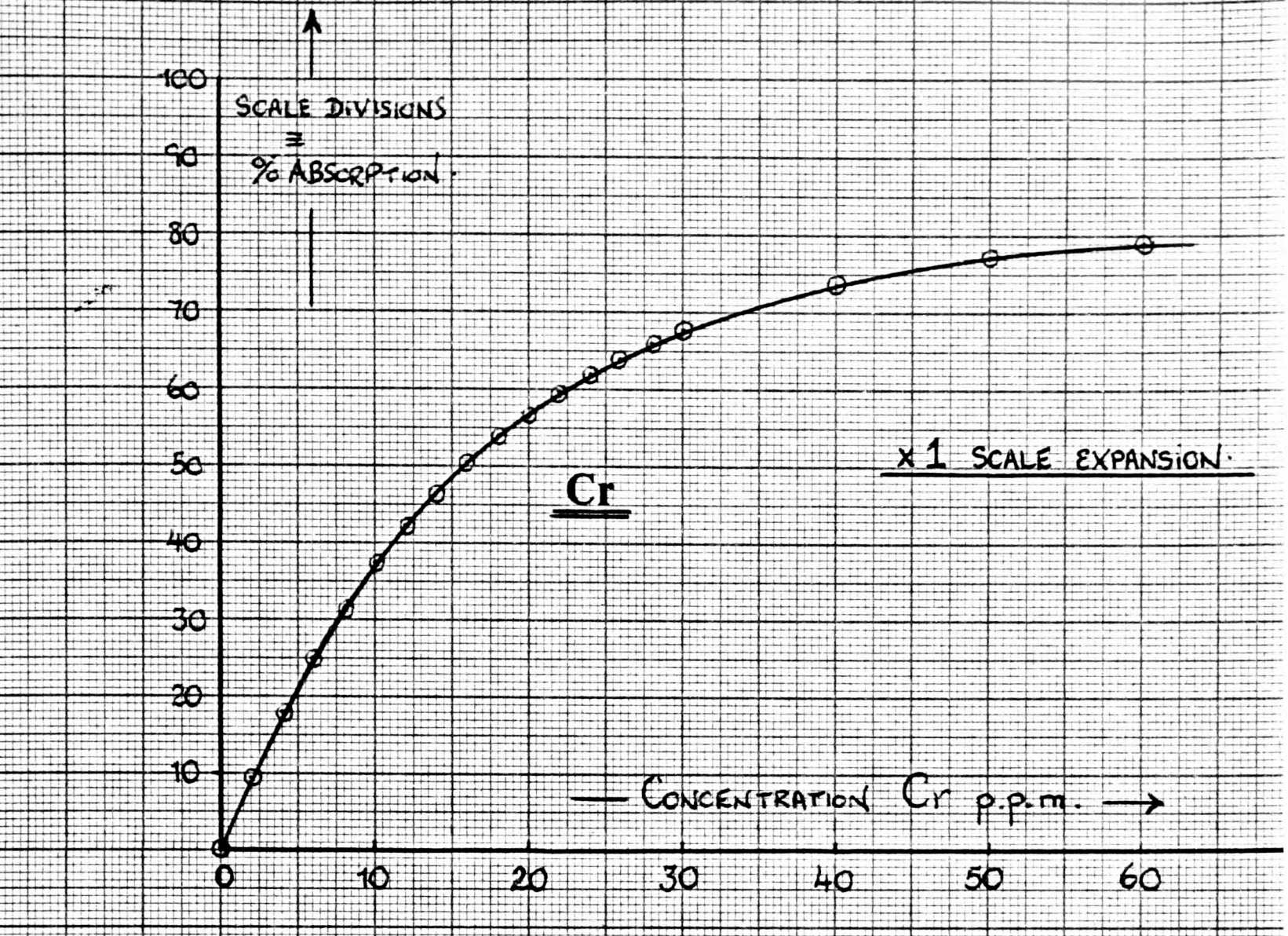


Fig 9.4(a) Calibration curve for CHROMIUM standard solutions

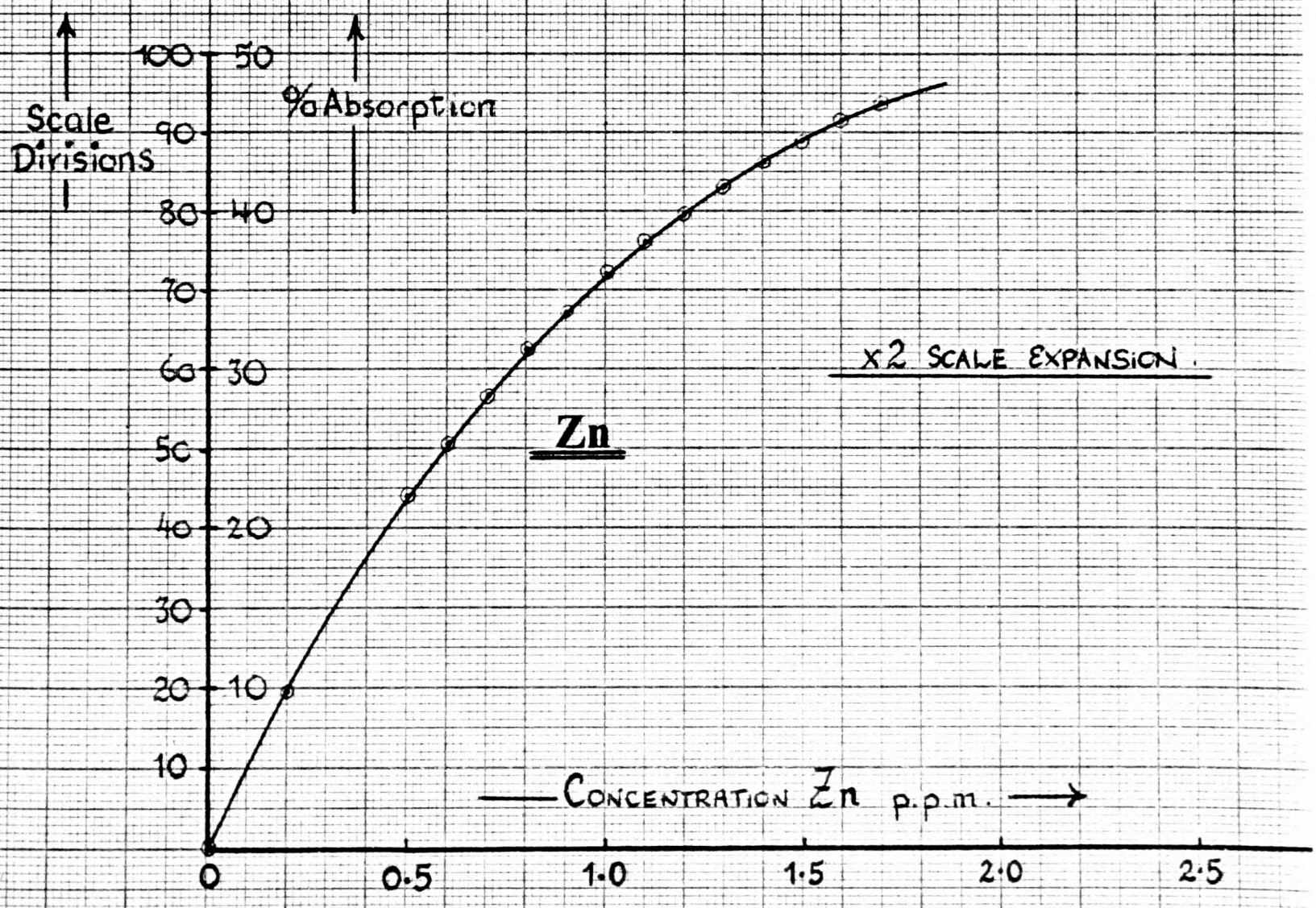


Fig. 9.4(b) Calibration curve for ZINC standard solutions.

accuracy of the determination (i.e. noise on signal height $< \pm\frac{1}{4}$ division) it was often possible to improve the accuracy by adjusting the spectrophotometer controls to give 2-fold scale expansion. In this arrangement the chart recorder scale was calibrated to read from 0% to 50% absorption, and the uncertainty of $\pm\frac{1}{4}$ scale divisions due to the pen width corresponded to only $\pm 1/8$ % absorption. Consequently, from equation 9.2, E is decreased by a factor of 2 by this reduction in z since W, Y, and A all effectively remain constant. Naturally, increasing the scale expansion in this way caused the noise on the signal to be magnified from its x1 expansion level but providing this did not cause an uncertainty in the signal height of greater than $\pm\frac{1}{2}$ division the accuracy was still improved. Increasing the scale expansion to x3 was never found to give any improvement in accuracy because of this corresponding magnification of signal noise.

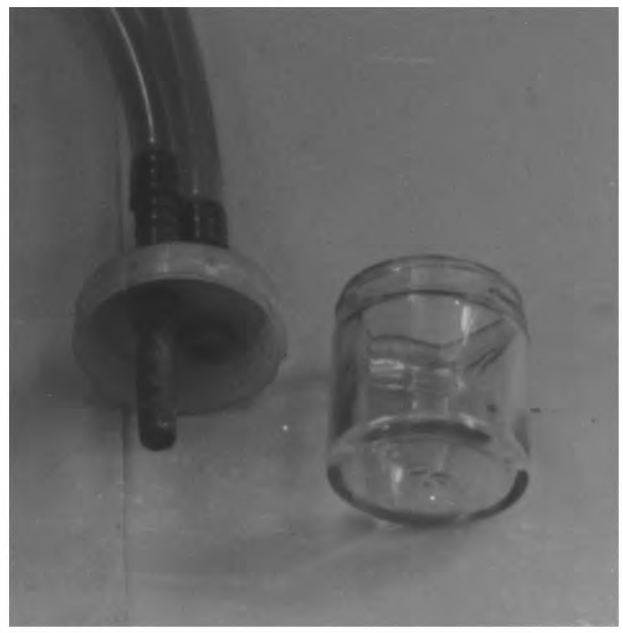
The application of equation 9.2 to the whole of the %absorption versus concentration of X calibration curve as described in the previous two paragraphs was considered to be a major breakthrough in achieving the optimum accuracy of the analysis technique. Previous workers in the Department had tended to use the steepest linear part of the calibration curve as their analysis range.[86,103,142,143] In this region A is at a maximum but W is at a minimum and so E is not necessarily minimised (see equation 9.2). In this work it was realised that the non-linear parts of the calibration curve at higher W could be used to reduce E, providing that the standard solution concentrations were sufficiently close to allow a linear approximation of % absorption versus concentration to be used between them.

The optimum concentration range determined for the analysis of each of the elements examined in this work is given in Table 9.2. Also listed in this Table are the values of the machine operating parameters used in each determination, the scale expansion employed, a typical value for the standard deviation of signal heights using these conditions, and an estimate of the error involved in sample solution concentration from spectrophotometer sources.

9.4.2 Sampling Procedure

The sampling technique involved four stages: machining the specimen from the casting, weighing the specimen, dissolving it completely into solution, and diluting the resultant solution to a known volume. The specimen weight and the final diluted volume of the solution were chosen so as to bring the concentration of the appropriate element into its optimum concentration range for the spectrophotometer given the nominal composition of the alloy.

Machining of specimens from castings was done either with a drill or with an end miller on a milling machine. In many ways this was the most important part of the whole analytical process. Not only was the actual sampling position important for the resultant 'picture' of macrosegregation in the casting, but it was also vital to ensure that the sample was truly representative of that position and did not become contaminated during machining. Any faults in the technique at this stage would have introduced errors into the composition of the specimen which would have stayed with it throughout the analysis and been almost impossible to detect. Contamination of the specimens was prevented by keeping the machines scrupulously clean; by removing all traces of dirt, grease, and loose material from the casting surface prior to machining; by using hardened tool steel drills and cutters; and by machining without lubricants. Furthermore, in order to obtain a truly representative sample from any position it was essential to collect every fragment of swarf machined from that position. Cardboard guards and trays were accordingly placed around the sampling position in order to contain all the swarf during machining, and the slowest machining speed consistent with adequate cutting was employed. A suction device was then used to ensure the complete transfer of the swarf into a sample jar. This device is shown in fig. 9.5. It was designed so that a glass sample jar could be used as the trap in the suction line, this being removable so that a different jar could be used for each sample. A fine mesh gauze was wrapped around and brazed to the exit tube of the trap to prevent the finer swarf particles from being sucked out. The plastic inlet line and the trap lid were inspected for any





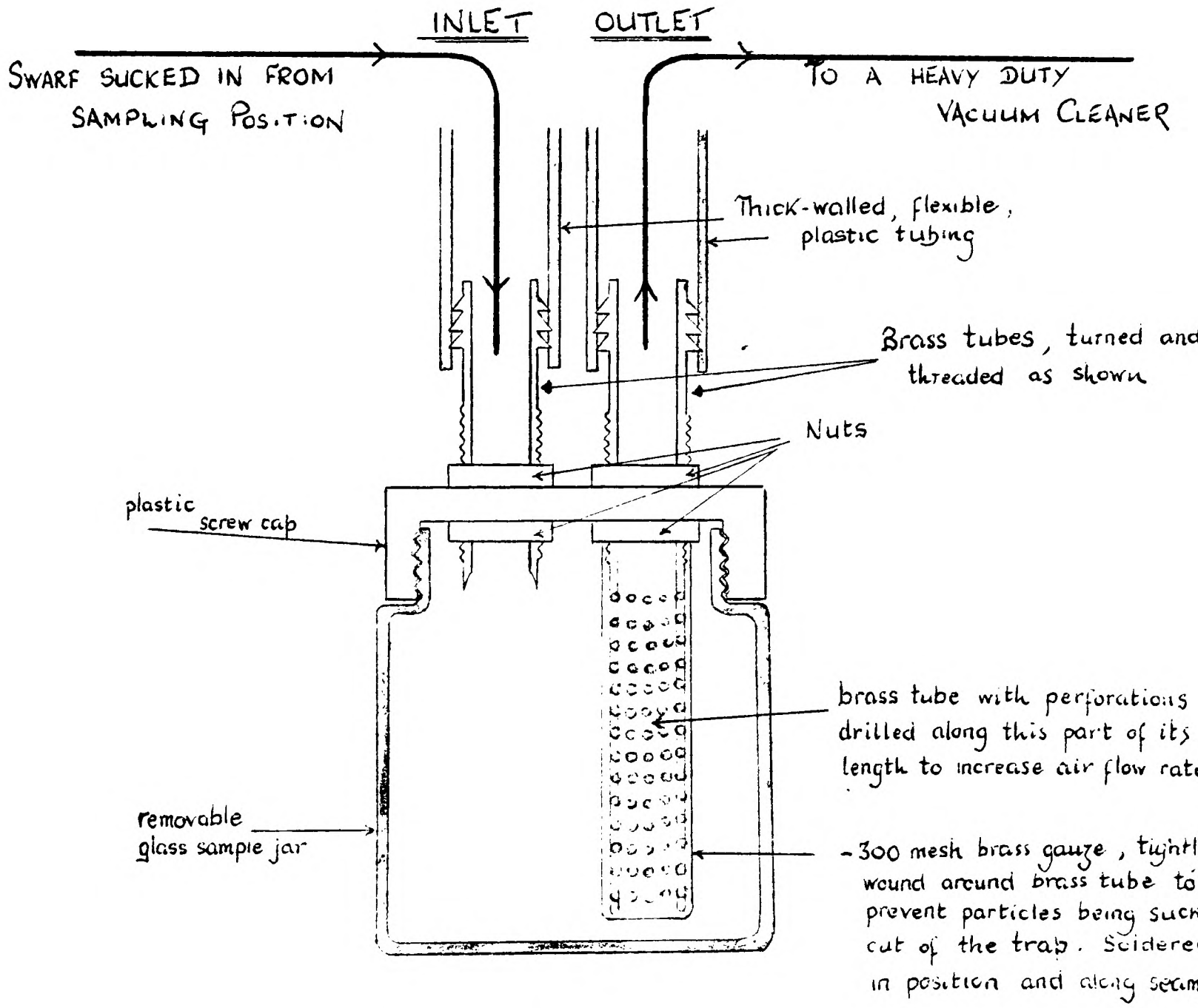


Fig 9.5. Suction device used to collect swarf from sampling position for subsequent dissolution and analysis.

contamination after each sample had been collected, and the sample jars were thoroughly cleaned and degreased before being connected up to the trap.

When a given batch of specimens had been collected each one was weighed. Weighing was carried out on an Oertling balance capable of measuring to 0.0001 gms.. After weighing each specimen was transferred to a clean, dry, 250 ml. conical flask and was dissolved in the relevant, Analar purity, reagents. A clean watch glass cover was placed over the top of each flask during dissolution to ensure that none of the specimen or solution would be lost. The individual dissolution techniques used for the various alloys encountered in this work are given in Table 9.3 overleaf.

Once the specimens had completely dissolved the solutions were diluted to a known volume with distilled water in 'grade A' volumetric glassware. Care was always taken to ensure complete transfer of each solution from its conical flask into the volumetric flask. The final diluted solutions were stored in plastic bottles to await analysis in the spectrophotometer. The storage time was never allowed to exceed two weeks in case the solutions began to deteriorate.

Finally, it should be noted that all pieces of glassware used in this work (sample jars, conical flasks, volumetric flasks, pipettes, and burettes) were regularly cleaned and degreased with a strong solution of sulphurchromic acid to ensure optimum accuracy and guard against contamination.

9.4.3 Investigation of possible interference phenomena

Flame absorption analysis is generally recognised to be free from spectral interference but chemical interference can often be a problem. The equilibria which exist between compounds, ions, and atoms can often be affected by other cations and anions in the solution. In this work the sample solutions always contained several species of ion. The standard solutions employed to determine the optimum concentration range on the other hand, usually only contained a single cation and anion. Consequently it was necessary to investigate possible interferences before proceding with the analysis.

Once the sample solutions had been prepared a note was made of the

TABLE 9.3. Individual dissolution techniques used on the alloys encountered in this work.

Alloy.	Thesis Chapter.	Alloy Comp^{n}%.	Av. Sample Weight. gms.	Dissolution Technique.	Diluted Volume. litres.	Comments.
Sn–Pb.	6	Pure binary Sn - 5 wt% Pb	0.6000	(a). Cover sample with approximately 3 mls distilled water (b). Add in portions 15 mls acid mixture (6 pts conc HCl : 1 pt. conc HNO_3)	1.	Dissolution relatively quick and easy - Water added to dampen initial reaction.
Al–Cu.	3	Various Al - 4Cu to Al - 10Cu	0.5000	(a). Cover sample with 3 mls. distilled H_2O. (b). Add 30 mls 1:1 conc HCl : H_2O in small portions. Soln colourless with filmy black pptate. (c). Add 5mls 20 vol H_2O_2 freshly prepared. Soln. turns green & some of black pptate dissolves. (d). Evaporate to a volume of ~ 15 mls (e). Add 10 mls hot $HClO_4$ (72% w/v). Soln. still green - black pptate slowly dissolves. (f). Continue to evaporate on hotplate for several hours. (g). Add 25 mls. cold H_2O. May still be some evidence of black pptate (h) Filter, and discard residue.	4 → 10	In the pure binary Al-Cu alloy, employed in Chapter 4, the black precipitate which appeared at step(b) was completely redissolved by step(c). Steps (d) to(h) were therefore unnecessary.
	4	Pure binary Al - 5.6 wt% Cu	0.2000		2.	
Al–Zn.	3	Al - 4 Zn.	0.5000	As for Al-Cu alloys above. Steps (a) to (c) only.	20.	No problem with black precipitate re-dissolving.
Al–Mg.	3	LM10 Al - 10Mg	0.5000	As for Al-Cu alloys above. Steps (a) to (c) only.	50.	No problem with black precipitate re-dissolving.
Al–Si.	3	Various Al - 6½ Si to Al - 10½ Si	0.5000	(a) Cover sample with 3 mls. distilled H_2O (b) Add 10 mls. warm 20% NaOH solution. (c) Add 3 mls 20 vol. H_2O_2 solution, freshly prepared. (d) Add 10 mls conc HNO_3 solution. (e) Add 20 mls dilute HCl solution.	0.250	The acid-base dissolution technique employed for Al-Cu, Al-Mg, and Al-Zn alloys did not work on Al-Si alloys.
Ni Superalloy	3	Complex.	0.3000	(a) Cover sample with 30 mls. aqua regia. (3 pts HCl : 1 pt HNO_3) (b) Warm occasionally and leave overnight. Produces dark green solution.	2	Dissolution is very slow.

types of ion present in the solutions, and their various concentrations were estimated. A given standard solution concentration was then chosen and a number of such solutions were made up, each one containing one of the other ionic species found in the sample solution at the same concentration level as in the sample solution. These modified standard solutions were then sprayed into the flame and any variation in the % absorption value from that of the original standard containing no additions was taken as evidence of interference by that particular ion. If an ion was found to interfere then it was added to all the standard solutions at a single concentration level which was similar to its level in the sample solutions. This was done during the stage when the various volumes of stock solution of X were being diluted to give the desired standard concentrations. A given volume of a solution containing the interfering ion was added to the volumes of stock solution before they were diluted.

Several examples of interference were encountered in this work. In the determination of lead, silicon, and cobalt,the matrix element in the alloy (tin, aluminium, and nickel, respectively) was found to give interference. This took the form of an increase in the % absorption value when the matrix ion was present in the solution. In fact in all three cases a solution which contained none of the solute ion (Pb, Si, or Co) but a large amount of the matrix ion still gave a finite absorption signal at the resonance wavelength of the solute atom. This type of interference is known as scatter interference and its causes are not well understood.[141] It is believed to arise, at least in part, from the scattering of radiation by solid particles in the flame. It is most commonly observed in the determination of elements whose resonance wavelengths are less than 300 nm. This was the case for lead, silicon and cobalt, although magnesium and zinc, which both have resonance wavelengths of less than 300 nm, were not found to be affected by scatter interference from the aluminium matrix in the alloys studied.

A different type of interference was found in the determination of magnesium from an Al-Mg alloy. The magnesium absorption signal was severely depressed when aluminium was present in the solution. This is an example of

anionic interference. The magnesium ions formed a stable compound with the aluminate anions in the solution. The compound could not be completely dissociated in the air/acetylene flame, thereby decreasing the number of atoms of magnesium in the flame and hence lowering the absorption signal. The interference was overcome by first adding aluminium ions to the magnesium standard solutions and then by adding the same concentration of strontium ions to all sample and standard solutions. The strontium ions have the effect of displacing the magnesium ions from the aluminate compound.

The calibration curves of % absorption versus concentration of X determined in this work for lead, silicon, magnesium, and cobalt are shown in figs. 9.6 and 9.7(a), (b), and (c), respectively. These curves have all been corrected to allow for the effect of the interfering ion.

9.4.4 Sample Determination Procedure

Once the optimum concentration range for a given element, X, had been determined a series of standard solutions were made up within this range together with the appropriate matrix, and other, additions. The gap between adjacent standard solution concentrations was chosen so that there was negligible error in assuming that the % absorption value varied linearly with the concentration of X between the two standards.

A rough determination of sample solution concentrations was initially carried out. The series of standard solutions was first sprayed into the flame in order to establish an approximate % absorption versus concentration of X curve and to ensure that the machine was operating at or near its optimum performance. The sample solutions were then sprayed in sets of five with a fixed standard solution being sprayed between each set. Finally the series of standards was re-sprayed. The time allowed for spraying each solution was approximately thirty seconds and distilled water was sprayed between each one. This rough determination allowed the concentration of each sample solution to be defined within the range of concentrations between two adjacent standards. Repeating the determination of a fixed standard solution throughout the run

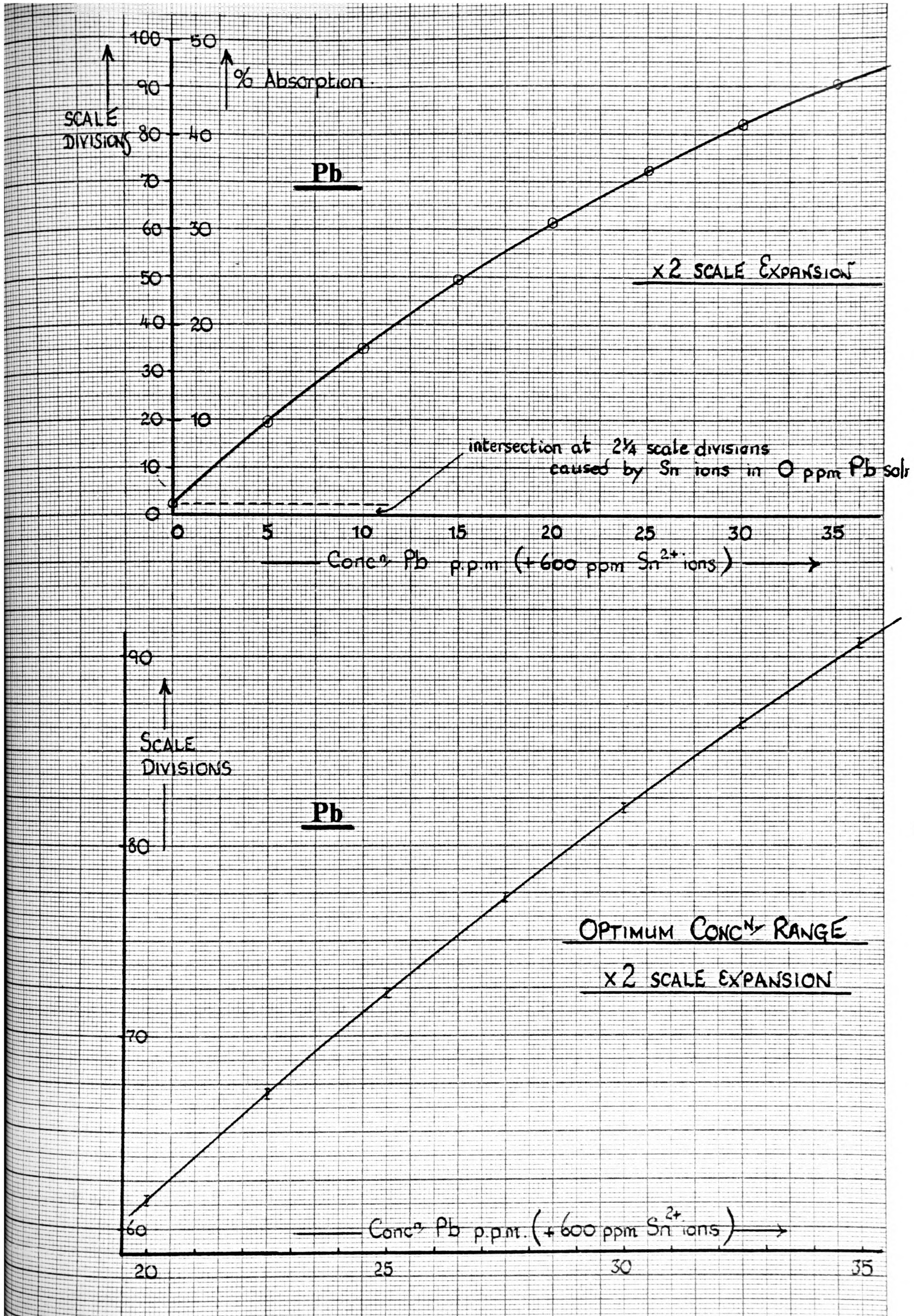


Fig. 9.6. Calibration curve for Lead standard solutions.

Fig. 9.7(a) - Calibration curve for SILICON standard solutions

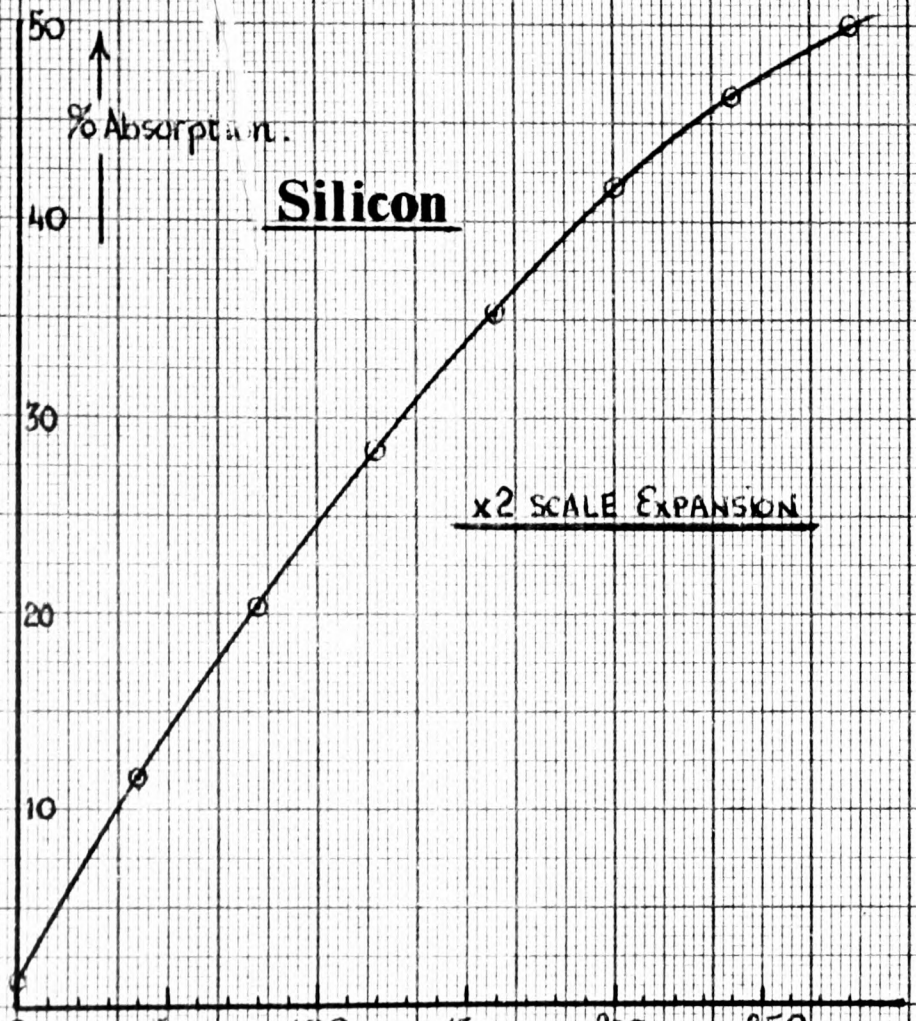


Fig. 9.7(b) Calibration curve for MAGNESIUM standard solutions.

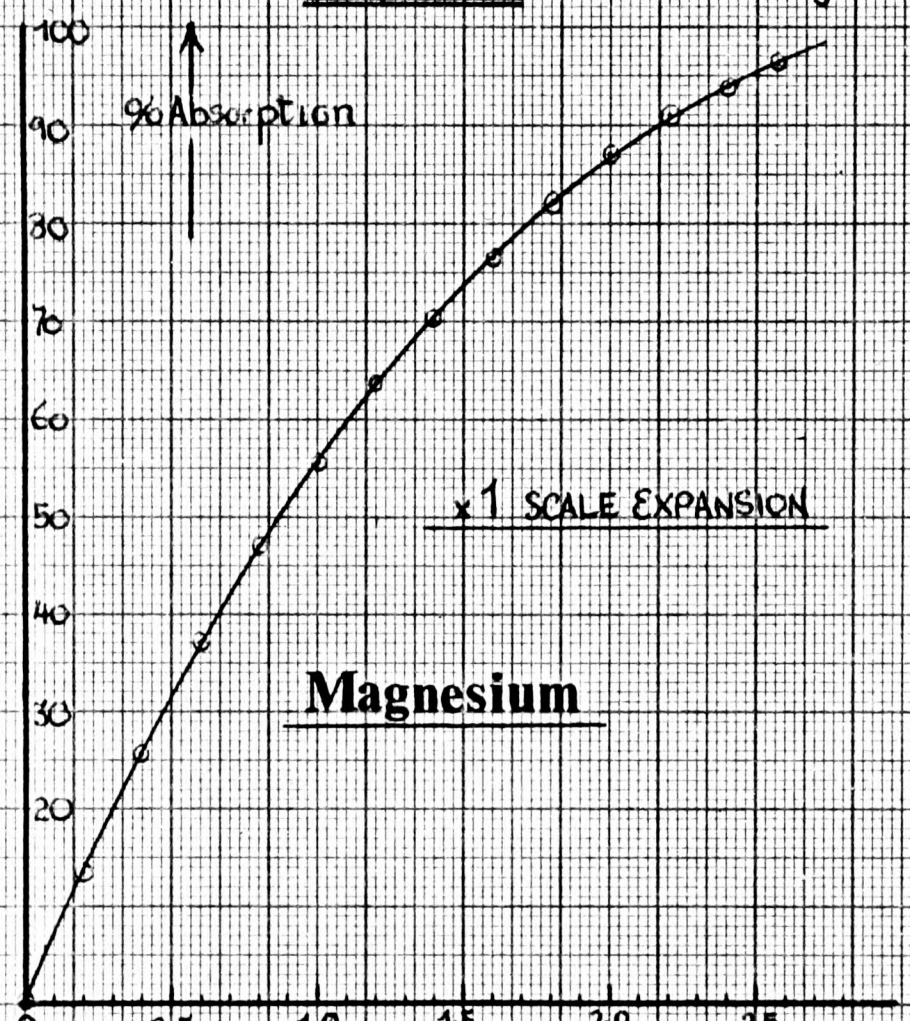
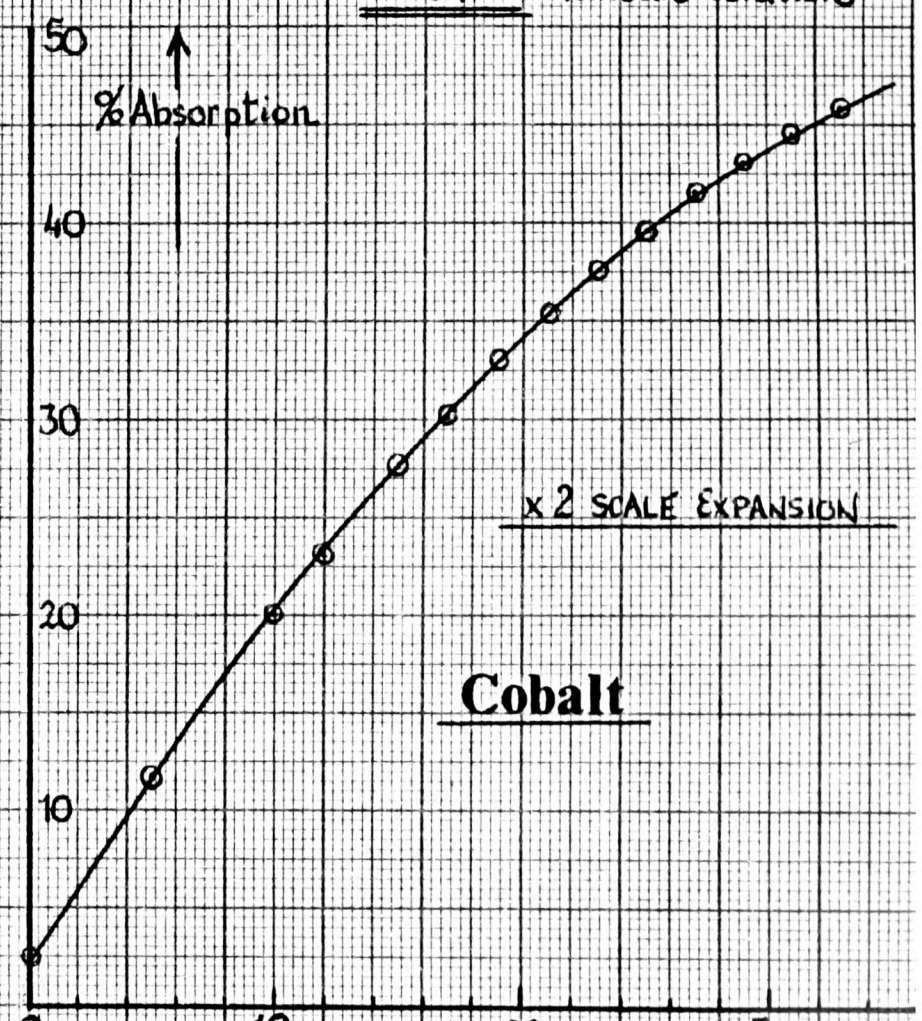


Fig. 9.7(c). Calibration curve for COBALT standard solutions



enabled any change in the sensitivity of the machine to be easily detected and corrected.

The second procedure, employed after the initial determination had been made, was developed to give optimum accuracy in the concentration measurements. The technique involved bracketing each sample solution by the two standard solutions nearest to it in concentration. Also during any given run a fixed standard solution was sprayed as every fifth reading. A typical chart trace obtained using the procedure is shown in figure 9.8. When the run was completed the baseline drift correction was applied to the signal heights. The corrected readings from the fixed standard solution sprayed throughout the run were then compared and the standard deviation of the signal was calculated. If this deviation was considered unacceptable then the set of results was scrapped and the run was repeated. In addition to this precaution against errors every sample solution concentration was determined using this technique at least twice. The concentration of the sample solution was calculated assuming a linear variation of % absorption with concentration between the two bracketing standards. The calculation is illustrated in fig.9.8. Once the concentration of element X in the sample solution had been determined then the composition of X in the orginal solid alloy sample could be calculated knowing the sample weight and the dilution of the solution.

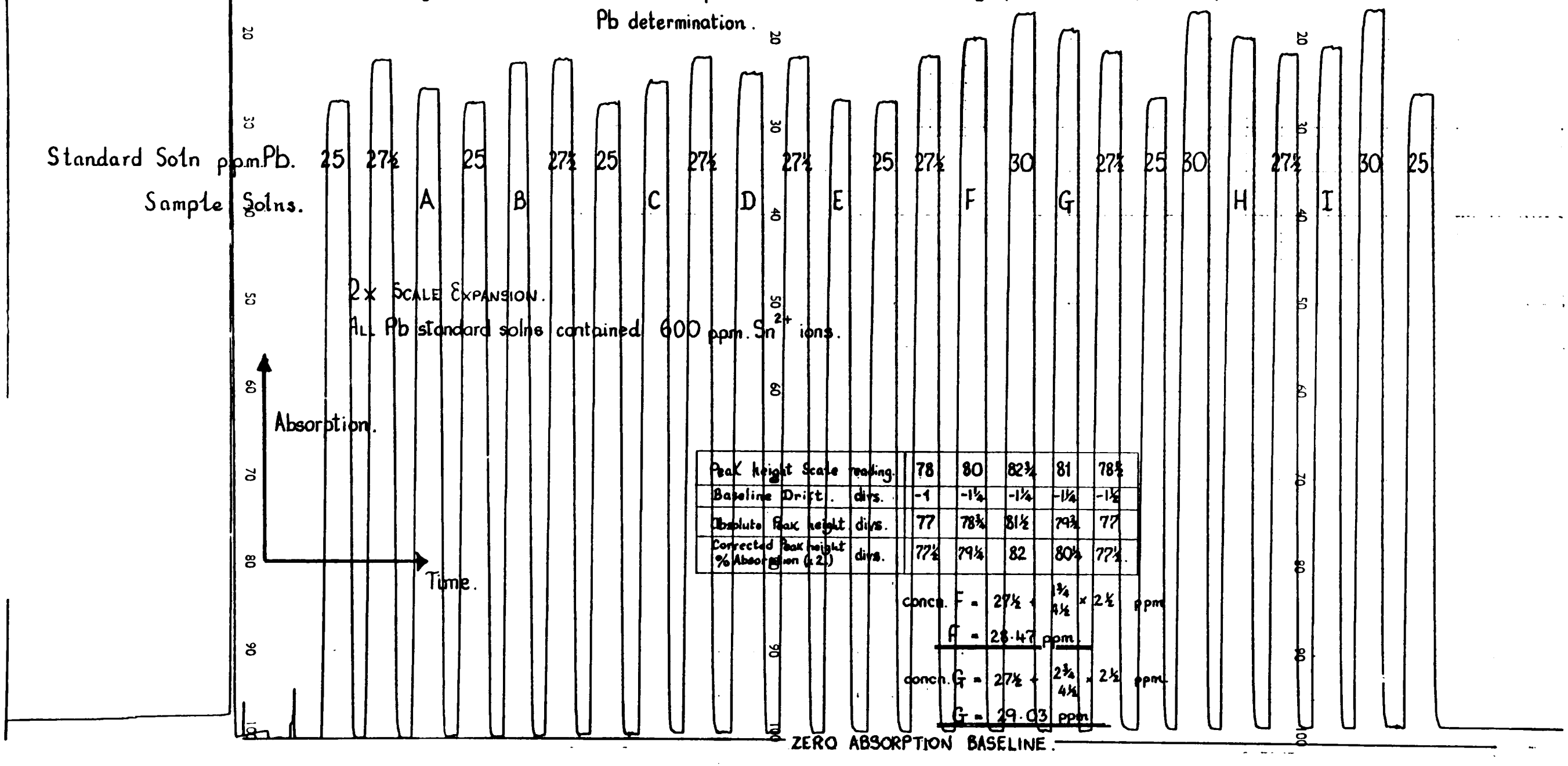
9.4.5 Practical Aspects of Spectrophotometer operation

In order for the machine to be able to perform at its optimum it was necessary to maintain it in a state of utmost cleanliness. Care was taken to cover the machine when not in use so as to prevent dust from entering the optical and electronic sections. All parts of the instrument which came into contact with the solutions were throughly washed out and dried at the end of each days work. The burners were also regularly dismantled and any deposit was cleaned from the edges of the slot using emery paper and soapy water.

Three major problems were encountered in machine operation during the course of the work. These were excessive baseline drift, burner tube blockage,

No. 990912

Fig. 9.8. Actual chart trace from spectrophotometer, using optimum accuracy technique Pb determination.



and nebulizer blockage.

Excessive baseline drift was encountered at the start of the work whenever the flame was turned on. A drift of only 4% absorption per hour before switching on the flame would increase to as much as 10 to 15% absorption per hour when the flame was on. The problem was inadvertently cured when the fume extraction hood was fitted over the chimney of the instrument for the nitrous oxide flame. Drifts in zero baseline level then remained at acceptable levels ($< 5\%$ abs. per hour) even when the flame was on. The reason for the excessive drift was therefore presumably a temperature rise within the instrument when the flame was being used,and this was prevented by the extractor fan.

The second major problem involved blockage of the plastic supply tube leading from the back of the cloud chamber to the burner stem (see fig.9.1(b)). The exit position of the tube from the chamber was only slightly below the level of the burner stem, and so it was extremely difficult to ensure that the tube sloped upwards continually along its length. If it did not slope continually upwards then any liquid droplets condensing in the tube could not drain back to the cloud chamber as required. Instead,a pool of liquid was gradually built up at the lowest point in the tube causing the absorption signal to be depressed and eventually extinguishing the flame. Since the problem lay essentially in poor instrument design the only solution was to ensure that the tube was carefully and correctly positioned for each run.

The third problem, that of nebulizer blockage, was probably the most important. Unfortunately it also proved to be the most difficult to eliminate. Nebulisation noise undoubtably constituted the major source of error in the determination of compositions by this technique, and a large part of this noise came from intermittent partial blockage of the nebulizer. Furthermore the nebulizer could become permanently blocked thereby leading to a sharp decrease in sample solution take-up rate and a corresponding depression of the absorption signal. The blockage was caused by solid particles suspended in the solutions and occurred in the central capillary. The problem could not be eliminated by

filtration since fibres from the filter paper proved to be just as effective in blocking the capillary. It was therefore necessary to ensure that there was as little solid material in the solutions as possible. Dissolution techniques were developed in an attempt to obtain total dissolution and when filtration was necessary only 'hard' grade filter papers were used. Glassware and polythene storage bottles were kept clean and were regularly rinsed out to prevent dust pick-up. The still used in distilling the water was also kept as clean and scale-free as possible. The problem of nebulizer blockage was never completely eliminated, however, and it was often necessary to stop the machine in order to clean out the capillary.

9.5 Error Calculations

In this analysis technique the composition of an alloy sample was calculated from the following data:-

sample weight=W mg.; final diluted volume of sample solution=V mls.; concentration of ions of element X in sample solution=P p.p.m. (mg/ml), by comparison with standard solutions. The calculation was as follows:-

Total weight of element X in whole of diluted solution=PV mg and this is equivalent to the weight of X in the original alloy sample

Therefore composition of X in alloy sample $=\frac{PV}{W} \times 100$ wt% X

The total error of the determination involves the sum of the errors in P, V, and W.

The possible factors which could have contributed to an error in W were:-

(a) incomplete collection of sample swarf from machined position, associated with segregation within swarf.

(b) weighing error.

(c) loss of sample after weighing and prior to dissolution.

(d) incomplete dissolution and

(e) contamination of sample solution with X after dissolution.

Factors (a), (c), (d), and (e) cannot be quantified but should have been

eliminated by the precautions which were taken. For factor (b) the balance employed was capable of measuring to 0.1 mg.. Furthermore, over a series of weighing operations on the same sample the reproducibility was found to be better than $\pm$0.5 mg.. This represents an error of $\pm$50/W% where W is the sample weight in mg.. In this work the sample weight was usually around 500 mg. and so the sample weighing operation typically introduced an error of $\pm$0.1%.

The factors which could have contributed to an error in V were:-

(f) incomplete transfer of solution during dilution operation;

(g) error in the graduation mark on the volumetric flask;

(h) error in making the solution up to the mark;

(i) error in using water at temperature other than 20°C;

(j) errors in subsequent dilutions involving pipettes.

Precautions were taken to ensure that factor (f) did not contribute to the error of the determination. For factors (g) and (j) grade A volumetric glassware was used throughout the work. The accuracy of the graduations on such glassware is closely defined by British Standards for each size of flask or pipette. The smallest size of volumetric flask employed was 100 ml. which had an allowed error in the graduation of $\pm$ 0.08%. The smallest size of pipette employed was 25 ml. which had a maximum error of $\pm$ 0.12% in the graduated volume. The errors decreased in the larger size vessels employed. With regard to factor (h) weighing tests were carried out to establish the error involved in making the meniscus of the solutions coincide with the graduation on the flask or pipette. It was estimated that for a 100 ml flask this error was $\pm$0.05%, while for a 25 ml. pipette it was $\pm$0.025%. Finally it was calculated that the error involved in not having the solution at 20°C during dilution was negligible providing the temperature was kept within $\pm$ 2°C of 20°C.

The factors causing an error in the value of P were:-

(k) uncertainty in the % absorption value for a given solution due to noise on the signal and systematic variations of the signal height with time;

(l) error in the absolute concentration values of the standard solutions; and

(m) error in assuming a linear variation in % absorption against concentration of X between adjacent standard solution concentrations.

The errors caused by factor (k) were minimised by suitable adjustment of the machine parameters, and by diluting the sample solutions so that their concentrations lay in the optimum range. Errors from this factor were estimated using equation 9.2 for each of the elements determined, and are listed in Table 9.2. They range from 0.8% to 3.0%. The errors in factor (l) arose from the preparation procedures of stock and standard solutions. The procedure for stock solutions involved a weighing operation followed by a dilution in a volumetric flask, while that for standard solutions involved a volume measurement using a pipette or burette followed by a further dilution in a volumetric flask. The typical magnitudes of the errors involved in such operations has been discussed for W and V previously, and usually totalled approximately 0.5%. Finally, factor (m) was made negligible by making up the standard solutions sufficiently close together in concentration to be able to effectively eliminate curvature.

Table 9.4, overleaf lists the total errors estimated to be involved in the composition determinations of the various elements studied in this work. The Table also lists the various contributions which individual parts of the procedur have made to the total error (i.e. factors (a) to (m) above). It can be seen fro the Table that the major causes of error were factors (k) and (l) in the determination of P, namely spectrophotometer error and error in the standard solution concentrations. The most accurate of the determinations was that for lead in the tin-lead alloy samples of Chapter 6, the error involved being only 1.30% of the composition figure.

Element	Errors ± %			
	Sample solution sources factors (b),(g),(h),(j)	Standard solution sources factors (b),(g),(h),(j)	Spectrophotometer sources factor (K)	Total Error.
Pb	± 0·13 %	± 0·35%	± 0·8 %	± 1·3%
Cu	± 0·30%	± 0·68%	± 1·5 %	± 2·5%
Si	± 0·15%	± 0·45%	± 3·0 %	± 3·6%
Zn	± 0·30%	± 0·50%	± 2·0%	± 2·8%
Mg	± 0·30%	± 0·50%	± 1·3 %	± 2·1%
Co	± 0·18 %	± 0·35%	± 0·9%	± 1·4%
Cr	± 0·18%	± 0·35%	± 1·6%	± 2·1%

9.6 Conclusions

A great deal of care, time, effort and attention was put into the sampling and analysis techniques used in this work since it was recognised that the success of the majority of the experiments was dependent upon them. The analysis was performed by atomic absorption flame spectrophotometry because this method best suited the particular requirements of the various experiments. The machine employed for the analysis was reliable but prone to certain inherent problems. The majority of these problems were eventually overcome and accuracies of up to $\pm$ 1¼% were achieved by suitable optimisation of machine parameters and by working within specific concentration ranges for each of the elements determined.

REFERENCES

1. V. Biringuccio — 'De la Pirotechnia' (1540) (transl. by C.S. Smith & M.T. Gnudi, AIME, New York (1942) p.259)
2. '1st. Report on the Heterogeneity of Steel Ingots' — J.I.S.I. 113 (1926) p.39
3. J. H. Dickenson — J.I.S.I. 113 (1926) p.177
4. I. G. Davies, M. Randle, & R. Widdowson — Metals Technology (1974) p.241
5. A. F. Giamei & B. H. Kear — Met. Trans. 1 (1970) p.2185
6. G. C. Gould — TMS-AIME 233 (1965) p.1345
7. M. C. Flemings & G. E. Nereo — TMS-AIME 242 (1968) p.50
8. 'Atlas of Defects in Castings' — Inst. of Brit. Fndrymen, (1961), London
9. W. Youdelis — I.S.I. publcn. 110, (1968), p.112
10. A. Goss, K. Benson, W. Pfann — Acta. Met. 4 (1956) p.332
11. J. Garland & G. Davies — Metal Constr. & Brit. Welding J. 2 (1970 p. 171
12. C. Jepson GKN Group Technological Centre — Private Communication
13. Metals Handbook, Vol.8, 8th.Edition, (1973), ASM Ohio.
14. K. M. Fisher — Unpublished research
15. N. Streat — Ph. D. Thesis (1973) Univ. of Brit. Columbia
16. J. W. Gibbs — Trans.Connecticut Acad. 3 (1876) p108
17. M. Hansen Constitution of Binary Alloys, 1st.suppt.,(1965),McGraw.
18. E. Scheuer — 2. Metallkunde 23 (1931) p.237
19. W. Tiller, K. Jackson, J. Rutter, & B. Chalmers — Acta. Met. 1 (1953) p.428
20. J. Burton, R. Prim, & W. Slichter — J. Chem. Phys. 21 (1953) p.1987
21. K. A. Jackson — Can. J. Phys. 36 (1958) p.683
22. E. Marburg — J. Metals 5 (1953) p.157
23. '7th. Report on the Heterogeneity of Steel Ingots' — I.S.I. Report No. 16 (1937) p.12
24. W. A. Tiller — J.I.S.I. 192 (1959) p.338
25. H. O. Howson — I.S.I. Publcn.110 (1968) p334
26. A. W. Brearley & H. Brearley — Ingots & Ingot Moulds. London. (1918)
27. N. Standish — Met. Trans. 1 (1970) p.2026
28. J. Blank & W. Johnson — Steel Times No. 5062 (1965) p.110
29. J. Blank & F. Pickering — I.S.I. Publcn. 110 (1968) p.370
30. K. Andrews & C. Gomer — I.S.I. Publcn. 110 (1968) p.363
31. W. Winegard — Inst. of Metals Monograph 29 (1964) p.55
32. B. Chalmers — 'Principles of Solidification' John Wiley & Sons, New York (1964)
33. J. W. Rutter & B. Chalmers — Can. J. Phys. 31 (1953) p.15
34. W. W. Mullins & R. F. Sekerka — J. Appl. Phys. 35 (1964) p.444
35. F. Weinberg — TMS-AIME 221 (1961) p.844
36. G. F. Bolling & W. A. Tiller — J. Appl. Phys. 32 (1961) p.2587
37. J. J. Kramer, G. F. Bolling, & W. A. Tiller — TMS-AIME 227 (1963) p.374
38. H. D. Brody & M. C. Flemings — TMS-AIME 236 (1966) p.615
39. T. F. Bower, H. D. Brody & M. C. Flemings — TMS-AIME 236 (1966) p.624
40. M. H. Burden & J. D. Hunt — J. Cryst. Growth 22 (1974) p.99

41. R. W. Ruddle 'The Solidification of Castings' — Inst. of Metals (1957)
42. T. F. Bower & M. C. Flemings — TMS-AIME 239 (1967) p.216
43. D. Walton & B. Chalmers — TMS-AIME 215 (1959) p.447
44. R. Doherty & D. Melford — J.I.S.I. 204 (1966) p.1131
45. J. Meier & A. Couture — Trans A.F.S. 68 (1960) p.636
46. G. S. Cole & G. F. Bolling — TMS-AIME 242 (1968) p.153
47. R. Morando, H. Biloni, G. S. Cole, & G. F. Bolling — Met. Trans. 1 (1970) p.1407
48. W. C. Winegard & B. Chalmers — Trans. A.S.M. 46 (1954) p.1214
49. B. Chalmers — J. Aust. Inst. Metals 8 (1963) p.255
50. K. Jackson, J. D. Hunt, D. R. Uhlmann, & T. P. Seward III — TMS-AIME 236 (1966) p.149
51. R. T. Southin — TMS-AIME 239 (1967) p.220
52. M. H. Burden & J. D. Hunt — Met. Trans. 6A (1975) p.240
53. G. S. Cole — Met. Trans 2 (1971) p.357
54. W. Bishop, H. F. Brandt, & W. Pellini — Trans A.F.S. 59 (1951) p.435
55. L. Backerud & B. Chalmers — TMS-AIME 245 (1969) p.309
56. M. H. Burden — D. Phil. Thesis (1974) Oxford University
57. G. S. Cole & G. F. Bolling — TMS-AIME 233 (1965) p.1568
58. M. J. Stewart & F. Weinberg — J. Cryst. Growth 12 (1971) p.228
59. ibid — TMS-AIME 245 (1969) p.2108
60. L. C. McAuley & F. Weinberg — Met. Trans. 4 (1973) p.2097
61. M. J. Stewart & F. Weinberg — Met. Trans. 3 (1972) p.333
62. J. Verhoeven — Met. Trans. 2 (1971) p.2673
63. N. B. Vaughan — J. Inst. Metals 61 (1937) p.35
64. O. Bauer & H. Arndt — Z. Metallkunde 13 (1921) p.497
65. G. Masing & C. Haase — Z. Metallkunde 17 (1925) p.251
66. E. Scheil — Metallforschung 2 (1947) p.69
67. D. E. Adams — J. Inst. Metals 75 (1948) p.809
68. J. S. Kirkaldy & W. V. Youdelis — TMS-AIME 212 (1958) p.833
69. M. C. Flemings & G. E. Nereo — TMS-AIME 239 (1967) p.1449
70. ibid — TMS-AIME 242 (1968) p.50
71. M. C. Flemings, R. Mehrabian, & G. E. Nereo — TMS-AIME 242 (1968) p.41
72. K. M. Fisher & J. D. Hunt 'Solidifcn.&Casting of Metals'Book192,Met.Soc.p.32
73. A.S.M. Handbook Vol. 8 (8th Edition) p.166 A.S.M., Ohio (1973)
74. A. Ohno — Iron & Steel Inst. Publcn. 110 (1968)p34
75. F. Badenheuer — Stahl u Eisen 54 (1934) p.1073
76. A. Hultgren — Scand. J. Metallurgy 2 (1973) p.217
77. B. M. Larsen — Trans. Met. Soc. AIME 162 (1945) p.414
78. R. Mehrabian, M. Keane, & M. C. Flemings — Met. Trans. 1 (1970) p.1209
79. P. R. Beeley — 'Solidification & Casting of Metals' Book 192, Metals Soc. (1979) p.319
80. I. Hagiwara & T. Takahashi — Tetsu-to-Hagane 53 (1967) p.27
81. R. J. McDonald & J. D. Hunt — Trans. Met. Soc. AIME 245 (1969) p.1993
82. ibid — Met. Trans. 1 (1970) p.1787
83. R. Mehrabian, M. Keane, & M. C. Flemings — Met. Trans. 1 (1970) p.3238
84. D. J. Hebditch & J. D. Hunt — Met. Trans. 4 (1973) p.2008
85. ibid — Met. Trans. 5 (1974) p.1557
86. K. M. Fisher — Part II Thesis, Oxford University, 1974
87. H. Fredriksson & S. O. Nilsson — Met. Trans. 9B (1978) p.111

88. F. Weinberg, J. Lait & R. Pugh — 'Solidification & Casting of Metals', Book 192, Metals Soc. (1979) p.334
89. J. Beech, Sheffield University — Private communication
90. G. S. Cole & G. F. Bolling — Trans. Met. Soc. AIME 239 (1967) p.1860
91. W. Salter & P. Waudby — Iron & Steel Inst. Publcn. 110 (1968) p. 412
92. K. M. Fisher — Unpublished research.
93. R. J. McDonald & J. D. Hunt — Met. Trans. 1 (1970) p.2027
94. S. Copley, A. Giamei, S. Johnson, & F. Hornbecker — Met. Trans. 1 (1970) p.2193
95. N. Streat & F. Weinberg — Met. Trans. 5 (1974) p.2539
96. N. Streat — D. Phil. Thesis, Univ. of Brit. Columbia, 1973
97. C. E. Smeltzer — Iron Age 184 (1959) p.188
98. R. P. DeVries & G. P. Mumau — J. Metals 20 (1968) p.33
99. M. H. Burden & J. D. Hunt — Metal Science (1976) p.156
100. P. R. Beeley — 'Foundry Technology' (1972) London, Butterworths
101. M. C. Flemings — 'Solidification Processing' (1974), McGraw-Hill
102. G. J. Davies — 'Solidification & Casting' (1973) Applied Science Publishers
103. D. J. Hebditch — D. Phil. Thesis, Oxford University, 1974
104. I. C. H. Hughes — Private Communication B.C.I.R.A.
105. D. A. Hudson — J. Inst. Metals 92 (1963-64) p.280
106. E. Kisakurek — Istanbul University. Private communication.
107. E. C. Ellwood — 'Tin and its alloys', (1960) p.248 London. Arnold.
108. J. V. Harding & W. T. Pell-Wallpole — J. Inst. Metals 75 (1948-49) p.115
109. G. J. Davies — J. Inst. Metals 93 (1964-65) p.197
110. T. Kawai & A. Keller — Phil. Mag. 8 (1936) p.1973
111. T. E. Strangman & T. Z. Kattamis — Met. Trans. 4 (1973) p.2219
112. R. Brett, B. K. L. Alloys Ltd., Telford, U.K. — Private communication
113. N. Streat & F. Weinberg — Met. Trans. 7B (1976) p.417
114. B. C. Allen & T. Isserow — Acta. Met. 5 (1957) p.465
115. J.V. McAllen — J. Aust. Inst. Metals 14 (1969) p.163
116. E. Kisakurek — Private Communication — Istanbul University
117. N. Standish — Iron & Steel (1969) p.354
118. J. E. Stead — Proc. Cleveland Instn. Engineers (1905-6) p.163
119. C. Benedicks — J.I.S.I. 117 (1928) p.557
120. P. H. Salmon-Cox & J. A. Charles — J.I.S.I. 201 (1963) p.863
121. M. H. Burden, D. J. Hebditch, & J. D. Hunt — Met. Trans. 6A (1975) p.230
122. Heterogeneity of Steel Ingots-Summary of Work — I.S.I. Report 29 (1943)
123. L. F. Mondolfo — 'Aluminium Alloys', (1976), Butterworths
124. G. McArtney — Private Communication — Oxford University.
125. K. Latimer — Private Communication — Alcan Laboratories, Banbury
126. I. G. Davies — Private Communication — Swinden Laboratories, B.S.C.
127. M. H. Burden — Private Communication — Tube Investments, Hinxton Hall.
128. A. Beardsley — Private Communication — Stanton & Staveley, B.S.C.
129. L. Northcott & V.Dicken — J. Inst. Metals 70 (1944) p.301
130. C. F. Walton — Grey Iron News (1962) p.4
131. M. G. Day — Private Communication — Newcastle Polytechnic.

132. N. Chvorinov — Giesserei 27 (1940) p.177
133. K. M. Fisher — Unpublished research
134. Code of Practice for the Protection of Persons exposed to Ionising Radiations in Research and Teaching. London HMSO (1968)
135. University of Oxford Local Regulations concerning work with Radioactive Materials in University Laboratories. Radiation Protection Committee (1975
136. C . R. C. Handbook of Chemistry & Physics — 53rd. Ed. (1972-73) Chemical Rubber Co., Ohio.
137. Dangerous Properties of Industrial Materials — N. Irving Sax 4th Ed. (1975) Van Nostrand.
138. W. Eastwood et alia — 'Radioactive tracers in Metallurgical Research', A.E.R.E., HMSO (1950)
139. R. Hultgren et alia — 'Selected Values of Thermod.Props. of Metals & alloys', (1963) Wiley, London
140. International Commission on Radiological Protection — (1966) Pergammon Press
141. P. Cooke — 'Atomic Absorption Spectrophotometry' 2nd. Ed. (1969) Pye Unicam Ltd.Cambridge
142. D. Bartholomew — D. Phil. Thesis, Oxford University (1971
143. M. Tassa — Private communication
144. Analar standards for laboratory chemicals — Analar Standards Ltd.
145. J. D. Hunt — Private communication
146. M. H. Burden — Private communication
147. M. H. Burden, D. J. Hebditch, & J. D. Hunt — J. Cryst. Growth 20 (1973) p.121
148. T. F. Bower, H. D. Brody, & M. C. Flemings — Trans. Met. Soc. AIME 236 (1966) p.624
149. C. J. Smithells — Metals Reference Handbook 2 4th Ed., Butterworths
150. D. J. Hebditch & J. D. Hunt — Met. Trans. 4 (1973) p.2474
151. H. R. Thresh, A. Crawley, & D. White — Trans. Met. Soc. AIME 242 (1968) p.819
152. H. J. Fisher & A. Phillips — Trans. Met. Soc. AIME 200 (1954) p.1060
153. S. D. Veazey & W. C. Roe — J. Mat. Science 7 (1972) p.445
154. G. Urbain — National Physical Laboratory Symposium No. 9 (1959) Vol. 1.
155. S. Glasstone — 'Textbook of Physics & Chemistry' p.448 Van Nostrand.
156. G. Lang — J. Inst. Metals 101 (1973) p.300
157. G. Taylor — J. Inst. Metals 83 (1954) p. 143
158. L. D. Lucas& G. Urbain — National Physical Laboratory Symposium No. 9 (1959) Vol. 2.
159. G. Uberlacker & L. D. Lucas — Compte Rendue 254 (1962) p.1622
160. W. J. Coy & R. S. Mateer — A.S.M. (1965) p.99
161. H. T. Greenaway — J. Inst. Metals 74 (1948) p.133
162. A. Kirschenbaum & J. Cahill — A.S.M. (1962) p.849
163. N. R. Johnson — Pt. II Thesis (1977) Oxford University
164. J. D. Edwards et alia — Chem. Met. Eng. 24 (1921) p.61,217,338
165. O. Smalley — Inst. Brit. Foundrymen 16 (1922) p.406
166. V. H. Stott & J. H. Rendall — J.I.S.I. 175 (1953) p.374
167. A. H. Cook — Phil. Trans. Roy. Soc. 254 (1961) p.125
168. A. Crawley — Trans. Met. Soc. AIME 242 (1968)p.859, 1483, 2237, 2309
169. A. Crawley & D. R. Kiff — Met. Trans. 2 (1971) p.609
170. T. R. Hogness — J. Am. Chem. Soc. 43 (1921) p.1621
171. J. Campbell, Fulmer Research Inst. — Private communication
172. A. W. Porter — Phil. Mag. 2 (1926) p.341
173. M. H. Burden & J. D. Hunt — J. Cryst. Growth 22 (1974) p328.
174 Saxonia Electrical Wire Co Ltd — Standard Thermocouple tables

APPENDIX 2 A

Production of macrosegregation by interdendritic fluid flow

Consider the simplified schematic model of a semi-solid zone advancing under steady-state growth conditions shown in fig.a, below, and in particular the volume element outlined. A moving co-ordinate system is used. Assume that the volume fractions of solid and liquid within the element, g_{sx} and g_{lx} respectively, are representative of the whole of the semi-solid region at the temperature T_x. Assume also that the compositions of the solid and liquid immediately in contact across the interface are given by the equilibrium phase diagram at each temperatur and furthermore that the liquid phase is fully mixed by diffusion at each position in the semi-solid zone. Using the equilibrium phase diagram shown in fig.b, the volume element appears as shown in fig.c. The composition of the liquid phase in

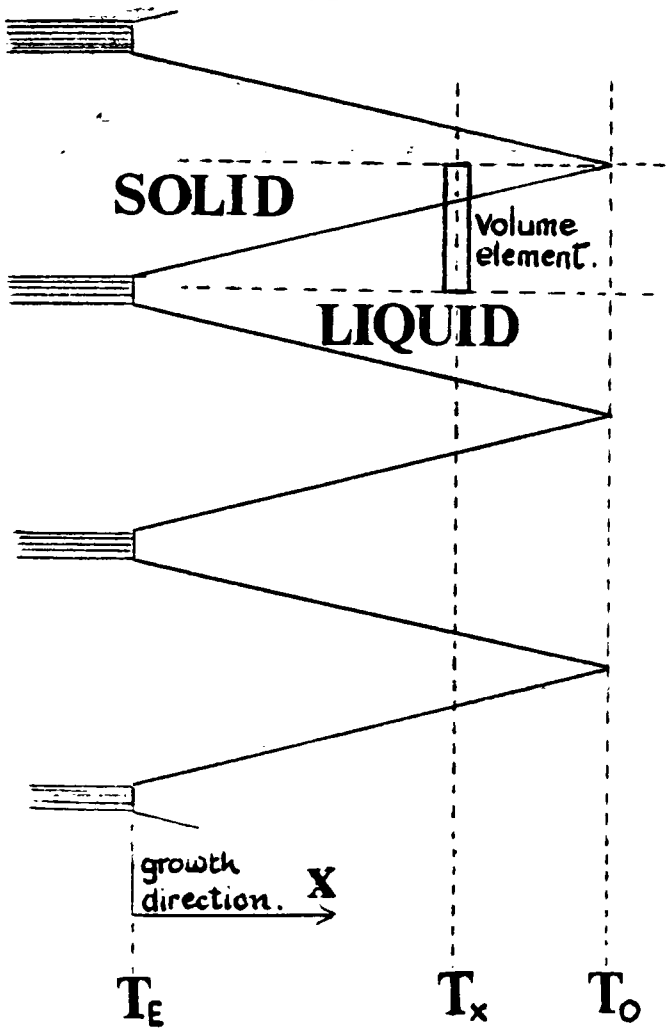


fig. a.

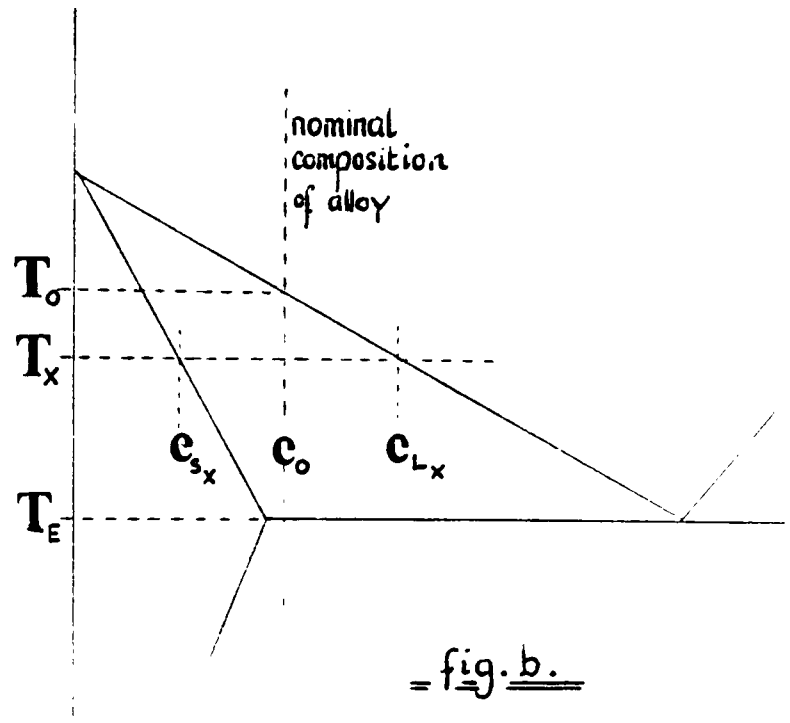


fig. b.

$$T_{x-1} < T_x < T_{x+1}$$

$$\therefore \quad C_{L_{x-1}} > C_{L_x} > C_{L_{x+1}}$$

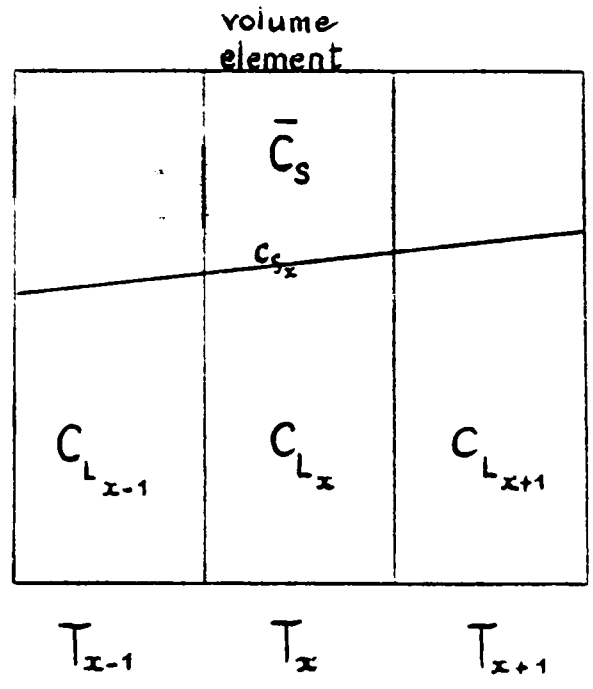


fig. c.

the volume element is uniform and is C_{lx} while the solid is non-uniform and has an average composition of $\bar{c}_s$ which is somewhat below C_{sx}. The average composition of the volume element at Tx is therefore given by the expression:-

$$\bar{C}x = \bar{C}_{Sx}g_{Sx} + C_{Lx}g_{Lx} \qquad - \quad 1$$

Consider now how flow of liquid through the element may affect this average composition. If flow occurs down the temperature gradient into the semi-solid zone then liquid of composition C_{Lx} leaves the volume element to the left and is replaced by liquid of composition $C_{I(x+1)}$ from the right. Now according to the phase diagram $C_{I(x+1)} < C_{Lx}$ and so the average liquid composition in the element is lowered. In order to maintain the equilibrium composition of liquid at T_x, as required by our second assumption, it is therefore necessary for more solid of composition C_{Sx} to be deposited. The new average composition of the element is therefore given by:-

$$\bar{C}'_x = \bar{C}'_{Sx}\, g'_{Sx} + C_{Lx}g'_{Lx} \qquad - \quad 2$$

and this is lower than the original composition of the volume element since there is now a greater volume fraction of the lower composition solid phase. Fluid flow down the temperature gradient therefore causes negative segregation (solute depletion) due to an increase in the amount of solid deposited.

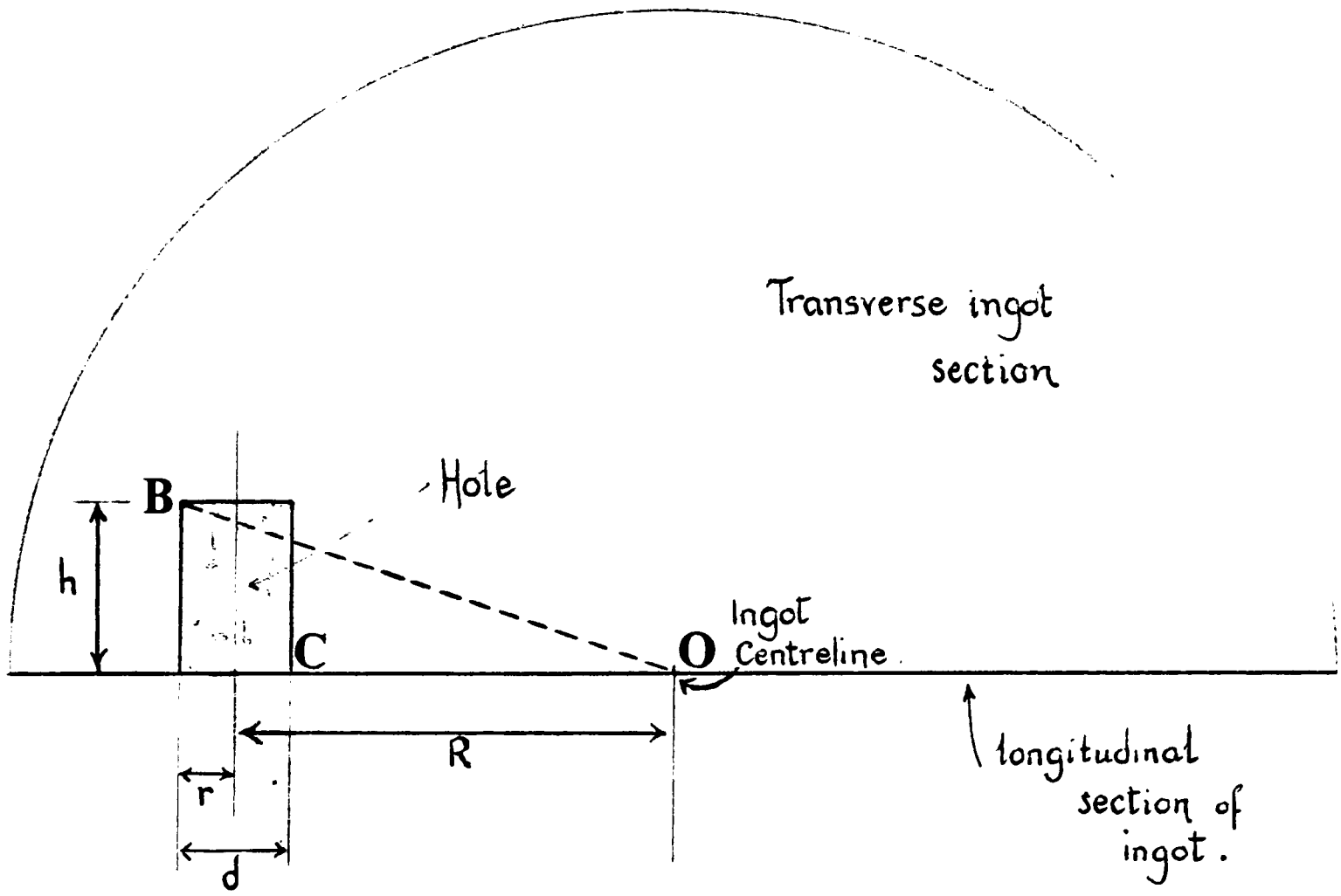
If flow occurs up the temperature gradient, out of the semi-solid region, then the reverse of the above argument occurs. Liquid of composition C_{Lx} leaves the volume element to the right and is replaced by liquid of a higher solute content $C_{I(x-1)}$ from the left. This therefore raises the average solute content of the liquid in the element, and the equilibrium composition can only be re-attained by dissolution of some of the solid phase. The average composition of the volume element is raised because the volume fraction of solid phase is reduced. Fluid flow up the temperature gradient therefore leads to positive segregation (solute enrichment) due to a dissolution of the solid phase. Furthermore such flow is unstable because the faster the rate of flow then the more solid has to be re-dissolved to maintain equilibrium. Small localised increases in flow rate therefore cause the flow resistance of the corresponding region of the semi-solid to decrease (because more solid has been dissolved) which

causes a further increase in flow rate, and so on. Flow up the temperature gradient out of the semi-solid therefore occurs in a small number of large channels.

It should be noted that interdendritic fluid flow occuring down the temperature gradient does not always produce negative segregation as suggested by the above treatment. For example, under conditions of steady-state growth no overall macrosegregation occurs and yet some inflow of liquid into the semi-solid region is required to fill solidification contraction. It is any excess inflow caused by gravitational forces which is responsible for the negative segregations under these growth conditions. When growth is not at steady-state and conditions are changing rapidly then inflow of liquid down the temperature gradient to feed contraction may cause positive segregation, as in inverse segregation. Unfortunately a simple model cannot be used to represent rapidly changing growth conditions and so this type of segregation is rather more difficult to understand.

APPENDIX 4.A

CALCULATIION OF OPTIMUM SAMPLE HOLE SIZE VS. POSITION



Now $OB = (h^2 + (R+r)^2)^{\frac{1}{2}}$ ①

$OC = R-r$ ②

Therefore $OB-OC = (h^2 + (R+r)^2)^{\frac{1}{2}} - (R-r)$ ③

And for subsequent analysis it is necessary for the sample to be of a fixed volume V, where:-

$V = \pi r^2 h$ ④, assuming a flat-bottomed cylindrical hole

Now if $r = zh$ ⑤, where z is a variable then

$V = \pi r^3 / z$ ⑥

Therefore $r^3 = Vz/\pi$ ⑦

i.e. $r = Kz^{\frac{1}{3}}$ ⑧ where $K = (V/\pi)^{\frac{1}{3}}$

Substituting equations (5) and (8) into (3) gives:-

$$OB - OC = (R^2 + 2RKz^{\frac{1}{3}} + K^2 z^{-4/3}(1 + z^2))^{\frac{1}{2}} - (R - Kz^{\frac{1}{3}}) \qquad (9)$$

when $R > r$

In this equation K is a constant. Therefore if R is specified then various values of z can be substituted into the equation to give values for OB -OC. This operation was performed numerically on a programmable calculator, and curves relating (OB -OC) to z were drawn for particular values of R. Some of these are shown in figure 4.A.1. Each curve has a definite minimum in OB -OC. The value of z corresponding to this minimum can be substituted into equations (8) and (5) to give to optimum values of hole depth and diameter at that particular radius from the ingot centreline. Some typical values are given in the table on figure 4.A.1.

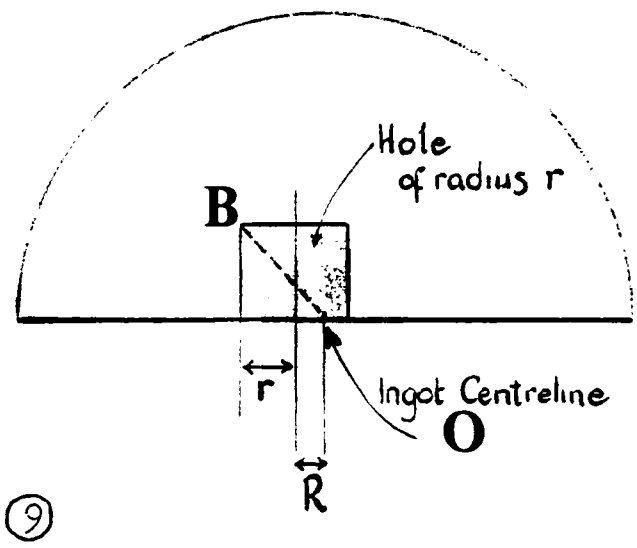
For analysis a sample of 0.200 gms. was required. The density of this Al-Cu alloy is approximately 2.98 gms/cc., therefore

$$V = {}^{0.200}/_{2.98} = 0.0672 \text{ ccs.}$$

Therefore $K = ({}^{V}/_{\pi})^{\frac{1}{3}} = 0.278$ cm.

The above calculation is not valid for $R < r$. In this situation we have material being sampled to a maximum radius of OB, as shown on the right:-

$$OB = (h^2 + (R+r)^2)^{\frac{1}{2}} \qquad (10)$$



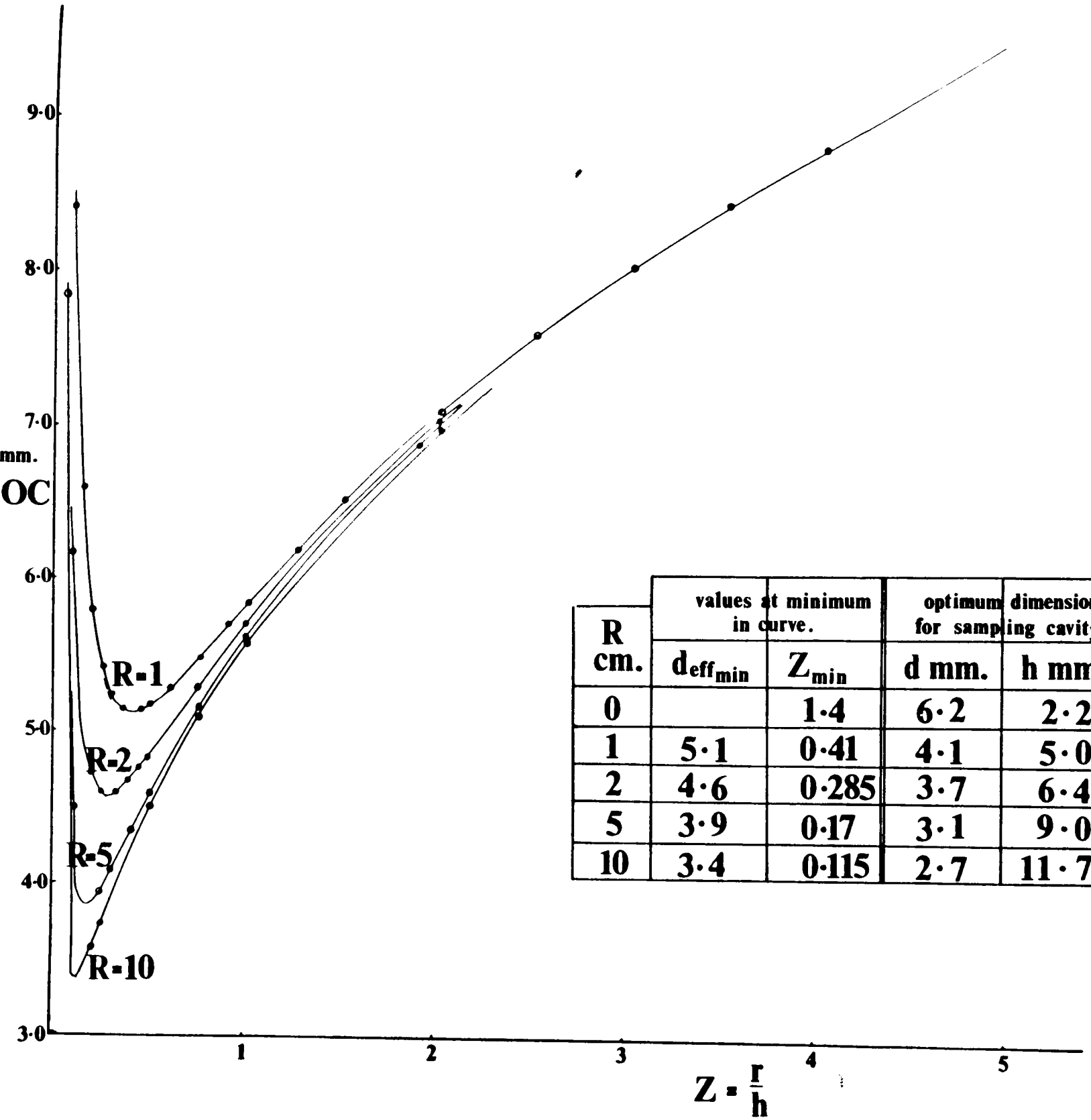
Substituting equations (5) and (8) into (10) gives:-

$$OB = (K^2 z^{-4/3}(1+z^2) + R^2 + 2RKz^{\frac{1}{3}})^{\frac{1}{2}} \qquad (11) \quad \text{for } R < r$$

which can be solved numerically as for equation (9)

The cross-over point for the two equations comes when R=r, which is found to be when R=0.25 cm..

Curves of OB vs z for R=0 and R=0.2 are given in figure 4.A.2.



R cm.	values at minimum in curve.		optimum dimensions for sampling cavity.	
	$d_{eff_{min}}$	Z_{min}	d mm.	h mm.
0		1·4	6·2	2·2
1	5·1	0·41	4·1	5·0
2	4·6	0·285	3·7	6·4
5	3·9	0·17	3·1	9·0
10	3·4	0·115	2·7	11·7

Fig. 4.A.1. Curves of 'effective sampling diameter' against hole aspect ratio at various distances from the ingot centreline

R cm	Values at min. in curves.		Dimensions of optimum sampling cavity.	
	$r_{eff\ min.}$ mm	Z	d mm	h mm
0	3·81	1·40	6·20	2·20
0·2	5·52	1·08	5·70	2·65

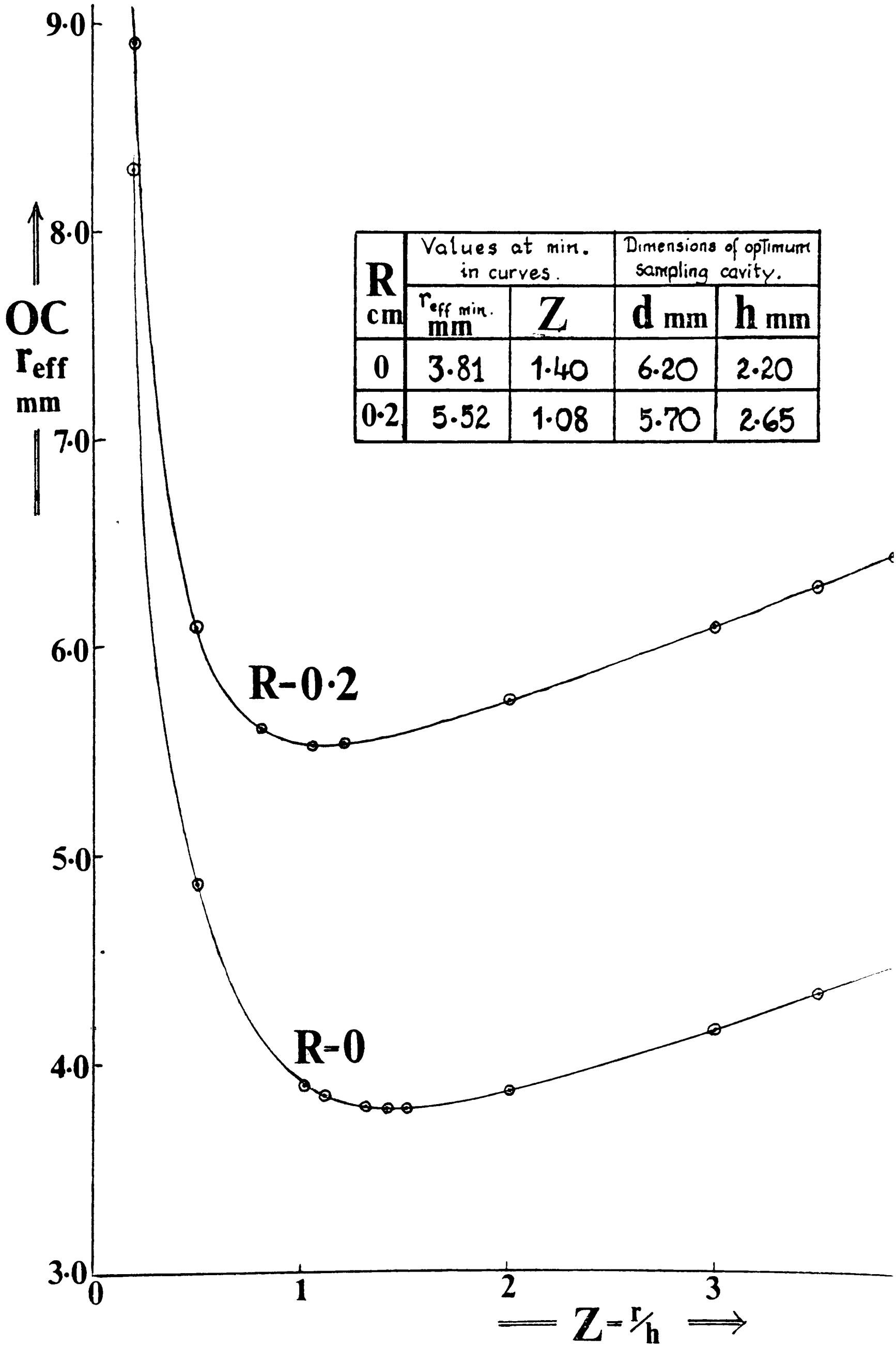


Fig.4.A.2. Curves of effective sampling radius versus aspect ratio of drill hole at various distances from the ingot centreline.

4A.2

APPENDIX 7.A.

CALCULATION OF THE AMOUNT OF Tl 204 REQUIRED IN THE EXPERIMENT

The number of β^- particles required to produce an acceptable autoradiograph is 10^8 β^-/cm^2 of film.[138] If 1 day is taken as a reasonable exposure time then the activity required for a good radiograph is approximately 10^3 $\beta^-/cm^2/sec$.

Now 1 mci = 3.7×10^7 disintegrations/sec

Activity required for radiograph = $a = 3 \times 10^{-5}$ mci/cm^2 1

The penetration depth of β^- particles in a medium of density ρ gm/cm^3 is given by:-[138]

$$t_M = {}^1/\rho\ (0.54E_M - 0.15)\text{cm}$$

where E_M is the maximum energy of the β^- particles in MeV. For tin with ρ = 7 gm/cm^3, and Tl 204 with E_M = 0.8 MeV then

$$t_M = 0.04 \text{ cm} \qquad 2$$

and the average penetration is approximately $\frac{1}{3}$rd of this, i.e.

$$tav = 0.013 \text{ cm} \qquad 3$$

From 1 and 3 the concentration of activity required in the ingot to give an adequate radiograph in 1 day is

$$a/t_{av} = 2.25 \times 10^{-3} \text{ mci/cm}^3$$

The total volume of one of the ingots was approximately 91 cm^3. Assuming that the radioisotope was inserted into the bulk liquid pool of the ingot at approximately $\frac{1}{2}$ growth then

$$\text{total activity required} = 2.25 \times 45.5 \times 10^{-3} \text{ mci}$$
$$= 10^{-1} \text{ mci}$$

In order not to disturb the growth process in the ingots it was felt that the maximum amount of radioactive alloy which could be inserted was 1 cm^3 (i.e. approximately 2% of the bulk liquid volume if inserted at half growth). This volume represents a weight of around 7 gms. of alloy, which corresponds to a weight of 7 mg. of thallium in an alloy of composition Sn-5wt% Pb-0.1wt% Tl. For such an alloy the required activity of the thallium source would have

had to be

$$0.1/0.007 = 15 \text{ mci/gm. of thallium}$$

which is far in excess of the maximum permitted source activity of 1 mci/gm. of thallium.

In order to satisfy all three constraints (i.e. total inserted activity 10^{-1} mci, maximum radioactive alloy insertion 7 gms., and maximum activity of thallium 1 mci/gm.) then the radioactive material inserted into the slice casting must contain at least 1.5wt% Tl.

APPENDIX 7.B.

CALCULATION OF THE IRRADIATION TIME NEEDED TO PRODUCE THE REQUIRED ACTIVITY OF Tl 204

$$\text{No. of atoms of element, E, in 1 gm.} = \frac{\text{Avogadros No.}}{\text{Atomic Weight}} = \frac{A}{W}$$

If the natural abundance of a particular stable isotope is a % then:-

$$\text{No. of atoms of isotope } E^{*} \text{ in 1 gm.} = \frac{Aa}{100W}$$

In the reactor the fraction of E^{*} atoms converted to E^{*+1} atoms is given by:-

$$\text{Fracn. converted} = Ft\,X$$

where F = neutron flux; t = time the sample was in the reactor;

X = thermal neutron capture cross section of E^{*} atoms.

$$\text{No. of atoms of } E^{*+1} \text{ produced} = \frac{Aa}{100\,W} \quad Ft\,X \quad gm^{-1}$$

Now if the decay half-life period of the E^{*+1} isotope is λ, then in this time half of the E^{*+1} atoms will have decayed.

$$\text{Activity} = \text{no. of disintegrations/second} = \frac{Aa\,FtX}{200\,W} \cdot \frac{1}{\lambda}$$

and 3.7×10^{7} disint./sec. = 1 mCi

$$\text{Activity} = \frac{Aa\,FtX}{W\lambda} \cdot \frac{1}{(7.4 \times 10^{9})} \quad \text{mCi/gm E}$$

Now $A = 6 \times 10^{23}$

and in this experiment:-

$$F = 7 \times 10^{12} \text{ n/cm}^2\text{/sec}$$

$$W = 204.37 \text{ for Thallium}$$

$$\text{Activity} = \frac{a\,X}{\lambda} \cdot t. \frac{(4.2 \times 10^{36})}{(1.51 \times 10^{12})} \quad \text{mCi/gm Thallium}$$

Now we require an activity of 1 mCi of Tl^{204} per gram of Thallium

$$t = \frac{\lambda}{a\,X} \cdot \frac{1.51}{4.2 \times 10^{24}} \text{ secs}$$

and for Tl^{203}

$X = 10 \text{ barns} = 10^{-23} \text{ cm}^2$

$a = 29.5\%$

for Tl^{204}

$\lambda = 3.8 \text{ yrs}$

$= 1.198 \times 10^{8} \text{ secs}$

$$\text{Irradiation time reqd. } t = \frac{1.198 \times 1.51}{2.95 \times 4.2} \times 10^6 \text{ secs.}$$

$$= 1.46 \times 10^5 \text{ secs}$$

$$= 40.5 \text{ hours}$$

For the other stable isotope Tl^{205} using the values of a, X, and $\lambda(Tl^{206})$ given in figure 7.2 then:-

$$\text{Activity} = \frac{(6\times10^{23})\times 70.5 \times(7\times10^{12})\times(1.46\times10^{5})\times(5\times10^{-25})}{204.37\times(4.3\times60)\times(7.4\times10^{9})} \text{ mCi/gm Thallium}$$

$$= 8.7 \times 10^4 \text{ mCi/gm Thallium}$$

$$= \underline{87 \text{ Ci/gm Thallium}}$$

which is clearly enormous, but luckily it decays away very quickly.

APPENDIX 7.C.

DEFINITIONS

Curie. (c.) Is a measure of the quantity of radioisotope present. It is 'that amount of radioactive substance in which the number of disintegrations per second is 3.7×10^{10}.'

mc. = millicurie = 3.7×10^{7} disintegrations/sec.

c. = microcurie = 3.7×10^{4} disintegrations/sec.

Rad. Is a measure of the absorbed dose from a radioisotope. It is 'The amount of energy imparted to matter by ionising particles per unit mass of irradiated material.'

1 rad = 100 ergs/gm..

Rem. Is a measure of the protection dose. It takes into account the different ionising powers of each type of radiation.

1 rem = 1 rad x Quality Factor

Quality Factor = 10 for α ; 1 for β^- and γ

Maximum Permissible doses

The values given below are taken from the International Commission on Radiological Protection,[140] and were adopted in 1965:-

Whole body. Gonads and red bone marrow	5 rems/yr.
	3 rems/calendar quarter.
Hands, forearms, feet, ankles	75 rems/yr.
	40 rems/calendar quarter.
Skin and bone	30 rems/yr.
	15 rems/calendar quarter.

The background radiation received by the general public from cosmic rays etc. is approximately 0.15 rads/yr..

APPENDIX 7.D.

CALCULATION OF SAFE OPERATING TEMPERATURES FOR MOLTEN THALLIUM AND ITS ALLOYS

Considering thallium vapour to be an ideal monatomic gas the ideal gas law can be used to find the no. of moles of thallium vapour per unit volume in equilibrium with liquid thallium at any temperature (T) and pressure (P).

$$PV = nRT$$

$$n/V = P/RT \quad \text{gm. mole/cc.}$$

Now if P is in mm. Hg., T in ^{o}K, and V in ccs, then the Gas Constant R is given by

$$R = 62{,}400 \quad \text{mm Hg cc/gm mole } ^{o}K$$

$$n/V = 1.603 \times 10^{-5}\ P/T \quad \text{gm mole/cc}$$

And molecular wt. of thallium is 204.37

$$n/V = 3.276 \times 10^{-3}\ P/T \quad \text{gms/cc}$$

$$= 3.276 \times 10^{6}\ P/T \quad \text{mg./m}^3$$

The safety limit for thallium vapour is 0.1 mg/m^3

Therefore for safety

$$P/T < 3.052 \times 10^{-8} \quad \text{mm Hg}/^{o}K$$

$$< 4.02 \times 10^{-11} \quad \text{atm}/^{o}K$$

Values of saturated vapour pressure for thallium are given below at different temps (see ref. 139).

T ^{o}K	P atm	P/T atm/^{o}K
577 (l)	3.43×10^{-11}	
600	1.38×10^{-10}	2.30×10^{-13}
700	2.07×10^{-8}	2.96×10^{-11}
800	8.72×10^{-7}	1.09×10^{-9}
900	1.57×10^{-5}	1.74×10^{-8}

The safety limit is therefore exceeded just above 700^{o}K for thallium vapour above molten thallium.

SUGGESTIONS FOR FUTURE WORK

The work on commercial castings and ingots described in chapter 3 should be extended to include castings of larger size and hence longer freezing times. This would permit the conclusions of the Al-Cu work on the critical freezing time for gravitational inter-dendritic fluid flow macrosegregation (Chapter 4) to be examined with relation to commercial solidification.

A theoretical quantitative model to describe macrosegregation produced by gravitational interdendritic fluid flow needs to be developed, possibly along the same lines as the model of Flemings et al.(69)for contraction fluid flow. The work described in Chapter 6 would provide quantitative data to insert into such a model.

The slice casting apparatus described in Chapter 6 could be used for accurate measurement of dendrite tip growth temperatures and dendrite spacings under horizontal growth conditions. Sufficient reproducibility in growth conditions was achieved for such experiments to be undertaken without large modifications being required on the apparatus.

The alloy developed for zero density change down its liquidus would be particularly suitable for dendrite spacing measurement experiments. It could also be used in future studies of macrosegregatio mechanisms such as contraction fluid flow and equi-axed sink/float, without the complicating effects of gravitational interdendritic fluid flow.

Further modifications could be made to the maximum bubble pressure apparatus as suggested in section 8.4.2., in an attempt to get it to produce results to the sort of accuracies quoted by previous workers.